VOLUME 19 NUMBER 1 2026 ISSN 2218-7979
eISSN 2409-370X

International Journal of Biology and Chemistry

Al-Farabi Kazakh National University

International Journal of Biology and Chemistry is published twice a year by
Al-Farabi Kazakh National University, al-Farabi ave., 71, 050040, Almaty, Kazakhstan
website: http://ijbch.kaznu.kz/

Any inquiry for subscriptions should be sent to:
Prof. Mukhambetkali Burkitbayev, Al-Farabi Kazakh National University
al-Farabi ave., 71, 050040, Almaty, Kazakhstan
e-mail: Mukhambetkali.Burkitbayev@kaznu.edu.kz

EDITORIAL

The most significant achievements in the field of natural sciences are reached in joint collaboration, where important roles are taken by biology and chemistry. Therefore publication of a Journal, displaying results of current studies in the field of biology and chemistry, facilitates highlighting theoretical and practical issues and distribution of scientific discoveries.

One of the basic goals of the Journal is to promote the extensive exchange of information between the scientists from all over the world. We welcome publishing original papers and materials of biological and chemical conferences, held in different countries (by prior agreement, after the process of their subsequent selection).

Creation of International Journal of Biology and Chemistry is of great importance, since scientists worldwide, including other continents, might publish their articles, which will help to widen the geography of future collaboration.

The Journal aims to publish the results of the experimental and theoretical studies in the field of biology, biotechnology, chemistry and chemical technology. Among the emphasized subjects are: modern issues of technologies for organic synthesis; scientific basis of the production of biologically active preparations; modern issues of technologies for processing of raw materials; production of new materials and technologies; study on chemical and physical properties and structure of oil and coal; theoretical and practical issues in processing of hydrocarbons; modern achievements in the field of nanotechnology; results of studies in various branches of biology, chemistry and related technologies.

We hope to receive papers from the leading scientific centers, which are involved in the application of the scientific principles of biological and chemical sciences on practice and fundamental research, related to production of new materials, technologies well ecological issues.

IRSTI 31.23.17:61.45.36 https://doi.org/10.26577/IJBCh20261911

S.M. Adekenov[1*], D.L. Savchenko[1], A. Syzdykova[1], A. Amanzhan[1], A.N. Kuprijanov[2]

[1]Research and Production Center "Phytochemistry", Karaganda, Kazakhstan
[2]Kuzbass Botanical Garden Russian Federal State Research Center of Coal and Coal Chemistry, Siberian Branch of the Russian Academy of Sciences, Kemerovo, Russia
*e-mail: arglabin@phyto.kz

SESQUITERPENE LACTONES OF PLANTS OF THE GENUS ACHILLEA L.

Abstract: Plants of the genus *Achillea* L. are considered promising sources of medicinal substances based on essential oils, sesquiterpene lactones, and flavonoids. In the present work, the results of a search for sesquiterpene γ-lactones in 13 Achillea species growing in Kazakhstan are summarized for the first time. The distribution of sesquiterpene lactones among the sections of the genus *Achillea* L. and their classification according to structural types are discussed. Based on chemical and biological screening, the presence of sesquiterpene γ-lactones was established in nine *Achillea* species. Three species –*Achillea inundata* Kondr., *Achillea salicifolia* Besser, and *Achillea tianschanica* Kupr. & Kulemin – were identified as promising sources for the isolation and identification of sesquiterpene lactones. From *Achillea nobilis* L. and *Achillea micrantha* Willd. 11 sesquiterpene lactones have been isolated, including 3 new compounds. The physicochemical characteristics of the isolated sesquiterpene lactones were determined, and their structures were elucidated using IR, UV, ^{1}H NMR, and ^{13}C NMR spectroscopy. An analysis was carried out on the influence of extraction methods, fractionation of crude plant extracts, and purification procedures on the yield of sesquiterpene lactones from *Achillea* species. Data on the biological activities of the isolated sesquiterpene lactones were compiled and summarized, including antitumor, antitrypanosomal, antileishmanial, anthelmintic activities, and cytotoxicity. The biosynthetic pathways of sesquiterpene lactones in *Achillea* species are discussed, along with the dynamics of their localization in different plant organs during various stages of vegetation. It was established that sesquiterpene lactones from *Achillea* species may serve as renewable starting materials for chemical modification and the synthesis of new compounds, representing potential sources of novel antitumor and antiparasitic agents.

Keywords: *Achillea* L., sesquiterpene lactones, qualitative reaction, molecular structure, infrared spectroscopy, nuclear magnetic resonance, X-ray crystallographic analysis, biological activity.

Introduction

Plants, as renewable biological resources, represent a potential source of new natural compounds with a wide range of pharmacological activities. The genus *Achillea* L. comprises approximately 150 species distributed throughout the countries of the Northern Hemisphere, with the greatest diversity occurring in Europe, Central Asia, and North America (Anderberg et al., 2007; Ehrendorfer et al., 2005). On the territory of Kazakhstan, 19 species of the genus *Achillea* L. occur: Sect. Filipendulinae (DC.) Afan.: *A. filipendulina* Lam.; Sect. Micranthae Klok. & Krytzka: *A. micrantha* Willd., *A. arabica* Kotschy; Sect. Nobilia Klok. & Krytzka: *A. nobilis* L.; Sect. Millefolium (Mill.) Koch: *A. asiatica* Serg., *A. kuprijanovii* Stepanov, *A. sergievskiana* Schaulo & Shmakov, *A. inundata* Kondr., *A. kamelinii* Kupr., *A. millefolium* L., *A. schmakovii* Kupr., *A. setacea* Waldst. & Kit., *A. tianschanica* Kupr. & Kulemin, *A. karatavica* Kamelin, *A. stepposa* Klokov & Krytzka, *A.* × *kasakhstanica* Kupr. & Alibekov; Sect. Ptarmica (Mill.) Koch: *A. impatiens* L., *A. ledebourii* Heimerl, *A. salicifolia* Besser.

The results of chemical investigations indicate that the aerial parts of *Achillea* L. species are a rich source of sesquiterpene γ-lactones. According to published data, a total of 103 sesquiterpene lactones have been identified in 27 species of this genus, including 79 guaianolides, 20 germacranolides, and 4 eudesmane-type lactones (Agatha et al., 2024; Alves et al., 2018; Frey et al., 2024). These compounds exhibit a broad range of biological activities, including antiparasitic (Sülsen & Martino, 2018), antiviral (Amen et al., 2025), antimicrobial (Ivanescu et al.,

2015), anti-inflammatory (Ivanescu et al., 2015), and antitumor effects (Laurella et al., 2022).

It is noteworthy that the overwhelming majority of sesquiterpene lactones from *Achillea* L. species are non-linear lactones. Their structures usually contain epoxy-, keto-, acetoxy-, and hydroxyl groups. Ten guaianolides bear a chlorine atom in their structure (Fraga, 2013). 23 of these compounds possess an exocyclic methylene group conjugated with the carbonyl group of the γ-lactone moiety, indicating the potential of searching for new sesquiterpene γ-lactones as promising pharmacologically active agents (Fraga, 2013).

Plants of section Millefolium (Mill.) Koch are widely distributed on the territory of Kazakhstan (Kupriyanov & Kulemin, 2023). The species of section Millefolium (Mill.) Koch are the most chemically studied with respect to the content of sesquiterpene lactones. Thus, from *Achillea millefolium* L., series Millefoliatae (DC.) Klok. & Krytzka, new sesquiterpene lactones with unusual structures have been isolated and described – 5 sesquiterpene dilactones and 12 guaianolides, including 9 halogen-containing guaianolides exhibiting comparatively high anti-inflammatory activity (Li et al., 2021; Li et al., 2023a; Li et al., 2023b; Li et al., 2023c). From *Achillea millefolium* L., a guaianolide with a peroxide bridge, α-peroxyachifolide, has been isolated, which is a skin sensitizer (Strzępek-Gomółka et al., 2021). By methanol extraction of the aerial part of *Achillea millefolium* L., three sesquiterpene lactones of the psilostachyin type, containing, in addition to the γ-lactone ring, a δ-lactone fragment, as well as a guaianolide and a germacranolide, have been isolated for the first time. Two guaianolides containing both γ- and δ-lactone rings exhibited antiproliferative activity towards HeLa, MCF-7, and A-431 cells, while the guaianolide achillinin A was active against the A549, RERF-LC-kj, and QG-90 cell lines (Csupor-Löffler et al., 2009; Yong et al., 2011). On the basis of terpenoids of the essential oil of *Achillea millefolium* L., a wound-healing and anti-inflammatory preparation, Akhizan, has been developed (Kalinkina et al., 1993). Australian researchers, by extraction with dichloromethane of the aerial part of *Achillea aspleniifolia* Vent., series Asplenifoliae Klok. & Krytzka, isolated a new pseudoguaianolide (Kasner et al., 1990). By HPLC analysis of an ultrasound-assisted dichloromethane extract of *Achillea collina* (Wirtg.) Becker ex Heimerl, the presence of five known guaianolides was determined (Rothwangl-Wiltschnigg et al., 2004). From *Achillea asiatica* Serg., three previously undescribed guaianolides were isolated (Glasl et al., 2001). In *Achillea setacea* Waldst. & Kit., 20 sesquiterpene γ-lactones have been detected, including an unusual guaianolide with a peroxide bridge (Todorova et al., 2000; Xue et al., 2025; Zitterl-Eglseer et al., 1991).

Another currently investigated plant of this genus is *Achillea alpina* L. of section Ptarmica (Mill.) Koch, series Lingulatae Botsch., from which 13 new sesquiterpene lactones have been isolated – 5 germacranolides, 6 guaianolides, and 2 dimeric guaianolides (Xue et al., 2022; Xue et al., 2023). Among them, a germacranolide and a guaianolide exhibit antidiabetic activity, while a 1,10-seco-guaianolide and a dimeric 1,10-seco-guaianolide show comparatively high hypoglycemic activity (Xue et al., 2022; Xue et al., 2023). From *Achillea arabica* Kotschy of section Filipendulinae (DC.) Afan., a new guaianolide, edremitin, has been isolated (Hanalp et al., 2022). From *Achillea ligustica* All. of section Achillea a new guaianolide, 3α-chloro-4β,10β-dihydroxy1β,2β-epoxy-5α,7αH-guai-11(13)-en-12,6α-olide, has been isolated (Mahmoud et al., 2012). By methanol extraction of the aerial part of *Achillea falcata* L. of section Babounya (DC.) Boiss., three known guaianolides have been isolated, exhibiting comparatively high cytotoxicity towards CT-116 colorectal cancer cells (Tohme et al., 2013).

The analysis of the literature and patent material for 2015–2025 on biologically active sesquiterpene lactones of plants of the genus *Achillea* L. testifies to the high potential of the above-mentioned taxon for the development of new antitumor and antiparasitic preparations.

The aim of this study was to search for potential sources of original medicinal agents based on biologically active sesquiterpene lactones from plants of the genus *Achillea* L.

Materials and methods

Plant material samples of *Achillea* L. species for chemical study were collected during the budding and flowering stages in different floristic regions of Kazakhstan, including Almaty, East Kazakhstan, Zhambyl, Ulytau, Karaganda, Turkistan, and Pavlodar regions. The collected herbarium specimens were identified and deposited in the herbarium of the Botanical Garden of the Research and Production Center "Phytochemistry" (Karaganda, Kazakhstan) (Table 1).

Table 1

Sites of raw material collection of the genus Achillea L. on the

Kazakhstan territory

№	Plant species	Collection site
	Section Filipendulinae (DC.) Afan.,	
1	*Achillea filipendulina* Lam.	Zhambyl region
	Section Micranthae Klok. & Krytzka	
2	*Achillea arabica* Kotschy	Turkistan region
3	*Achillea micrantha* Willd.	Ulytau region, Sarysu river valley
	Section Nobilia Klok. & Krytzka	
4	*Achillea nobilis* L.	Karaganda region, vicinity of Egindybulak village
	Section Millefolium (Mill.) Koch	
5	*Achillea asiatica* Serg.	Botanical Garden collection of JSC "RPC "Phytochemistry"
6	*Achillea inundata* Kondr.	Botanical Garden collection of JSC "RPC "Phytochemistry"
7	*Achillea karatavica* Kamelin	Almaty region
8	*Achillea millefolium* L.	Karaganda region, Karkaraly mountains
9	*Achillea setacea* Waldst. & Kit.	Pavlodar region, Bayanaul mountains
10	*Achillea tianschanica* Kupr. & Kulemin	Turkistan region, Sairam-Ugam National Park, slope and floodplain of the Sairamsu river
	Section Ptarmica (Mill.) Koch	
11	*Achillea impatiens* L.	Karaganda region, Kyzylarai mountains
12	*Achillea ledebourii* Heimerl	East Kazakhstan region, vicinity of Ridder town
13	*Achillea salicifolia* Bess.	Karaganda region, Abay district

Introduction and cultivation studies of *Achillea asiatica* Serg. and *Achillea inundata* Kondr. were carried out at the introduction plot of the Botanical Garden of JSC "Research and Production Center Phytochemistry" (Karaganda, Republic of Kazakhstan). Herbarium collections from this plot are deposited in the Herbarium Fund of JSC "Research and Production Center Phytochemistry".

To screen plants for the presence of sesquiterpene lactones, total extractive substances were isolated from the plant material. The obtained extracts were analyzed by a qualitative terpenoid assay, infrared (IR) spectroscopy of the crude extract, and chromatographic techniques, including thin-layer chromatography (TLC) and high-performance liquid chromatography (HPLC).

Total extractive substances were isolated from plant materials by carbon dioxide extraction (CO_2 extraction) using a USFE-5/2 supercritical fluid extraction system (manufactured by LLC "Goro-Engineering", Russia, under license from the Austrian company "Natex", Ternitz, Austria) at the following conditions (applied to all plant samples): pressure 160 bar, temperature 60°C, and extraction time 240 min. The resulting extracts were subsequently subjected to qualitative tests for terpenoids. Upon addition of a vanillin solution in sulfuric acid to the powdered extractive fraction, the mixture developed a red-violet coloration, indicating the presence of terpenoid compounds (Harborne, 1998). In samples of extracts that gave a positive reaction for terpenoids, the presence of sesquiterpene lactones was confirmed by IR spectroscopy through the absorption band characteristic of the γ-lactone carbonyl in the 1740–1800 cm^{-1} region. The IR spectrum was recorded on an Avatar 360 ESP spectrometer (Thermo Nicolet, USA) in KBr pellets. The extracts were analyzed by HPLC on a Hewlett Packard Agilent 1100 Series liquid chromatograph (USA) under isocratic conditions using a mobile phase of acetonitrile–acetic acid (50:50, v/v) at a flow rate of 0.5 $mL \cdot min^{-1}$. A stainless steel column (150 mm × 4.6 mm) packed with Zorbax SB-C18 sorbent (5 μm particle size) was used at a column temperature of 20°C. The injection volume was 20 μL. Detection was performed with a UV detector at wavelengths of 254 and 289 nm. The components were identified by comparison of their retention times with reference samples of sesquiterpenoids, the corresponding information on their content was obtained. Individual sesquiterpene lactones were isolated from the total extractive substances by liquid column chromatography on silica gel KSKG (macroporous coarse-grained granular silica gel) (Qingdao Shuoyuan Silica Gel Technology Co., Ltd.,

China) at a sample-to-sorbent ratio of 1:20. The column was eluted with benzene, benzene–diethyl ether mixtures (4:1, 1:1), diethyl ether, diethyl ether–ethyl acetate mixtures (4:1, 1:1), ethyl acetate, or petroleum ether–ethyl acetate mixtures with increasing content of the latter. The purity of the isolated compounds was monitored by thin-layer chromatography (TLC) and HPLC data.

For TLC, Silufol TLCP-AI A-UF plates manufactured by Imid (Krasnodar, Russia) were used with a benzene–ethanol (9:1) solvent system. The substances were visualized by spraying the plates with a 1% solution of vanillin in H_2SO_4 and a saturated solution of $KMnO_4$. Reference standards of the compounds were obtained from the Republican Bank of Biologically Active Compounds (Karaganda, Republic of Kazakhstan) (State Pharmacopoeia of the Republic of Kazakhstan, 2014).

HPLC was performed on an Agilent 1100 Series liquid chromatograph (USA) equipped with a Quat-Pump G1311A pump, a Rheodyne injection valve with a 20 μL loop, a G1322A column holder, and a G1314A ultraviolet (UV) detector. All analyses used a Zorbax SB-C18 column (15 cm × 0.46 cm, 5 μm particles; Agilent, Santa Clara, CA, USA) and the following solvents: methanol, acetonitrile, and water (analytical-grade reagents of purity ≥ 99.9%, supplied by Sigma-Aldrich (Merck-Millipore, USA). The maximum UV absorption at 205 nm was processed by ChemStation software (Agilent Technologies, USA).

Antiparasitic activity against extracellular forms was assessed using a standardized microplate assay. Parasite suspensions were adjusted to the appropriate density and distributed into 96-well plates. *Leishmania amazonensis* promastigotes in the stationary phase were diluted to 5×10^5 cells/well in phenol red-free RPMI medium. *Trypanosoma brucei brucei* bloodstream forms were diluted to 3.5×10^4 parasites/mL, and 200 μL aliquots were added per well. Test compounds were dissolved in dimethyl sulfoxide (DMSO) and further diluted in the corresponding culture medium to obtain final concentrations of 1, 10, and 50 μg/mL for *Leishmania amazonensis*, and 0.1, 1, and 10 μg/mL for *Trypanosoma brucei brucei*, in duplicate wells. The final DMSO concentration did not affect parasite viability and was used as a negative control. Following incubation (48 h at 24°C for *Leishmania amazonensis*; 72 h at 37 °C, 5% CO_2 for *Trypanosoma brucei brucei*), parasite viability was quantified: for promastigotes, 50 μL of XTT was added and incubated for 4 h at 24 °C, with absorbance measured at 450 nm using a microplate reader (Tecan); for bloodstream forms, parasites were counted directly using a Beckman Z2 Coulter counter. The percentage of inhibition was calculated for each compound at each concentration (Laurella et al., 2023).

Trypanocidal activity against intracellular forms of *Trypanosoma cruzi* was evaluated using a cell-based infection assay. Vero cells (5×10^3 per well) were infected with tissue culture-derived trypomastigotes of the *Trypanosoma cruzi* Tulahuen strain expressing β-galactosidase (MOI: 10). Following overnight incubation at 37°C, 5% CO_2, non-internalized parasites were removed by washing, and infected cells were incubated with test compounds at 10 μg/mL. After 5 days, cells were lysed with 1% Nonidet P-40, and chlorophenol red-β-D-galactopyranoside (CPRG) (100 μM) was added as a β-galactosidase substrate. The plates were incubated for 4 h at 37°C, and β-galactosidase activity was determined by measuring absorbance at 570 nm. The percentage of inhibition was calculated according to the following formula: 100 − {[(absorbance of treated infected cells) / (absorbance of untreated infected cells)] × 100} (Laurella et al., 2023).

Cytotoxicity was determined by the MTT method. Vero cells were seeded in flat-bottom 96-well plates and cultivated at 37°C in an atmosphere of 5% CO_2 in the presence of the sesquiterpene lactones of plants of the genus *Achillea* L. at a concentration of 10 μg/mL or DMSO as a viability control for 48 h. MTT was then added at a final concentration of 0.6 μg/mL, and after 2 h of incubation at 37°C, the formazan crystals were dissolved in 100 μL of isopropanol. Absorbance was measured at 595 nm in a microplate reader (Rayto RT-6000). Results were expressed as the percentage of cell viability: {(absorbance in the presence of compound) / (absorbance in the absence of compound)} × 100 (Borgo et al., 2023).

The *in vivo* anthelmintic activity of leucomisin (18) was evaluated at the Kazakh Scientific Research Veterinary Institute (Almaty, Kazakhstan) in accordance with methodological guidelines for determining the antiparasitic effects of pharmacological substances (Adekenov, 2023; Guidelines for the Experimental (Preclinical) Investigation of New Pharmacological Substances, 2000). Coproovoscopy of the collected feces was carried out by the Darling method using a digital microscope (Levenhuk D50 LNG, Levenhuk, Inc., USA/China). In accordance with the study protocol, fecal samples were taken from 20 sheepdogs to determine their initial helminth infestation. As a result of the coprological examination, 10 of the 20 dogs (50%) proved to be infested with various helminth species, with infestation inten-

sity (hereinafter – II) ranging from 1 to 15 eggs. Of the 10 infested dogs, eggs of *Trichuris vulpis* with II 1–15 were detected in 8 dogs (80%), and eggs of *Dipylidium caninum* in 2 dogs (20%). No other helminth species were detected in the feces of the sheepdogs by coproovoscopy. Based on the coproovoscopy results, the helminth-infested dogs (10 dogs) were divided into two experimental groups, 5 animals each. Dogs of the first group (5 animals) were administered capsules with leucomisin (18) at a dose of 150 mg (3 capsules) per 20–25 kg of body weight. In the comparison group, dogs received the preparation "CesTremForte" (LLP "Kazakh Scientific Research Veterinary Institute", Kazakhstan) at a dose of 150 mg (2 tablets) per 20–25 kg of body weight. The capsules with leucomisin (18) were administered as a single dose. Coproovoscopy of each fecal sample before and after deworming of the dogs was carried out twice. Four days after administration of the capsules with leucomisin (18), coproovoscopy of the dogs' feces was performed to determine the extens- and intens-efficacy of the test sample (18).

Statistical analysis of the results was performed using Statistica 8.0 software. The obtained data are expressed as mean ± standard error of the mean.

Ethical considerations

The study was conducted in accordance with the decree of the Minister of Health of the Republic of Kazakhstan No. KR DSM-181/2020 (November 4, 2020) and approved by the Local Bioethics Commission of the NJSC "Karaganda Medical University" (Protocol No. 18, October 21, 2025) (Order of the Minister of Healthcare of the Republic of Kazakhstan, 2020).

Results and discussion

The primary chemical screening of *Achillea* L. plant species for sesquiterpene lactones comprises qualitative reaction of total extractives for terpenoids, infrared spectroscopy and screening for biological activity. The results of the chemical evaluation and the bioscreening of the total extractive substances from *Achillea* L. species are presented in Table 2.

Table 2

Results of chemical and biological screening of plants of the genus Achillea L. for the content of sesquiterpene lactones

№	Plant species	Qualitative reaction for terpenoids	IR spectrum data of total extractive substances, cm^{-1}	Biological activity of total extractive substances
	Section Filipendulinae (DC.) Afan.			
1	*Achillea filipendulina* Lam.	-	1713	-
	Section Micranthae Klok. & Krytzka			
2	*Achillea arabica* Kotschy	+	1767, 1759, 1731	-
3	*Achillea micrantha* Willd.	+	1780, 1730, 1680, 1630	Antitumor, insecticidal, antifeedant
	Section Nobilia Klok. & Krytzka			
4	*Achillea nobilis* L.	+	1770, 1720,1650	Growth-regulating, antitumor, insecticidal
	Section Millefolium (Mill.) Koch			
5	*Achillea asiatica* Serg.	+	1775, 1715, 1650	Growth-regulating
6	*Achillea inundata* Kondr.	+	1745	-
7	*Achillea karatavica* Kamelin	-	1739, 1712	-
8	*Achillea millefolium* L.	+	1760, 1720, 1650	Fungicidal, insecticidal, antitumor, antibacterial
9	*Achillea setacea* Waldst. & Kit.	+	1770	Growth-regulating, antitumor
10	*Achillea tianschanica* Kupr. & Kulemin	+	1750, 1640,1620	-
	Section Ptarmica (Mill.) Koch			
11	*Achillea impatiens* L.	-	1722	Antitumor
12	*Achillea ledebourii* Heimerl	-	1710	Growth-regulating
13	*Achillea salicifolia* Bess.	+	1755, 1740, 1620	Antitumor

Based on the results of chemical screening, the absorption bands in the IR spectra of the total extractive substances from yarrow species in the 1740–1800 cm^{-1} region indicate the presence of sesquiterpene γ-lactones

in 9 species (69.23%) of the plants studied, which is confirmed by the qualitative reaction for terpenoids (Table 2). In addition, the total extractive substances from *Achillea millefolium* L., *Achillea micrantha* Willd., and *Achillea nobilis* L. exhibited growth-regulating, insecticidal, and antitumor activities.

According to the data of Table 2, among the thirteen plant species of the genus *Achillea* L. collected on the territory of Kazakhstan for chemical investigation, the presence of sesquiterpene lactones was established in 5 species (83.3%) of section Millefolium (Mill.) Koch, in 2 species (100%) of section Micranthae Klok. & Krytzka, and in 1 species (33.3%) of section Ptarmica (Mill.) Koch. Three species of the genus *Achillea* L. – *Achillea inundata* Kondr., *Achillea salicifolia* Besser, and *Achillea tianschanica* Kupr. & Kulemin – are promising, previously uninvestigated objects for the isolation and identification of sesquiterpene lactones.

Sesquiterpene Lactones of *Achillea* L. of the Flora of Kazakhstan

Achillea micrantha Willd. (small-flowered yarrow) is a plant widely distributed in the territory of Kazakhstan; it occurs on sands and sandy soils, more rarely in steppe, pasture, and solonetzic meadows from the forest-steppe to the desert zone (Flora of Kazakhstan, 1966).

We have previously established that the aerial parts of *Achillea micrantha* Willd. contain the guaianolides achillin (1), artilesin (2), and grossmisin (3), as well as the germacranolides micranthin (4) and achimicrin (5) (Barda et al., 2021).

Figure 1

The structure of Achillea micrantha Willd sesquiterpene lactones (guaianolides achillin (1), artilesin (2), grossmisin (3), germacranolides micranthin (4), achimicrin (5) and sintenin (6)

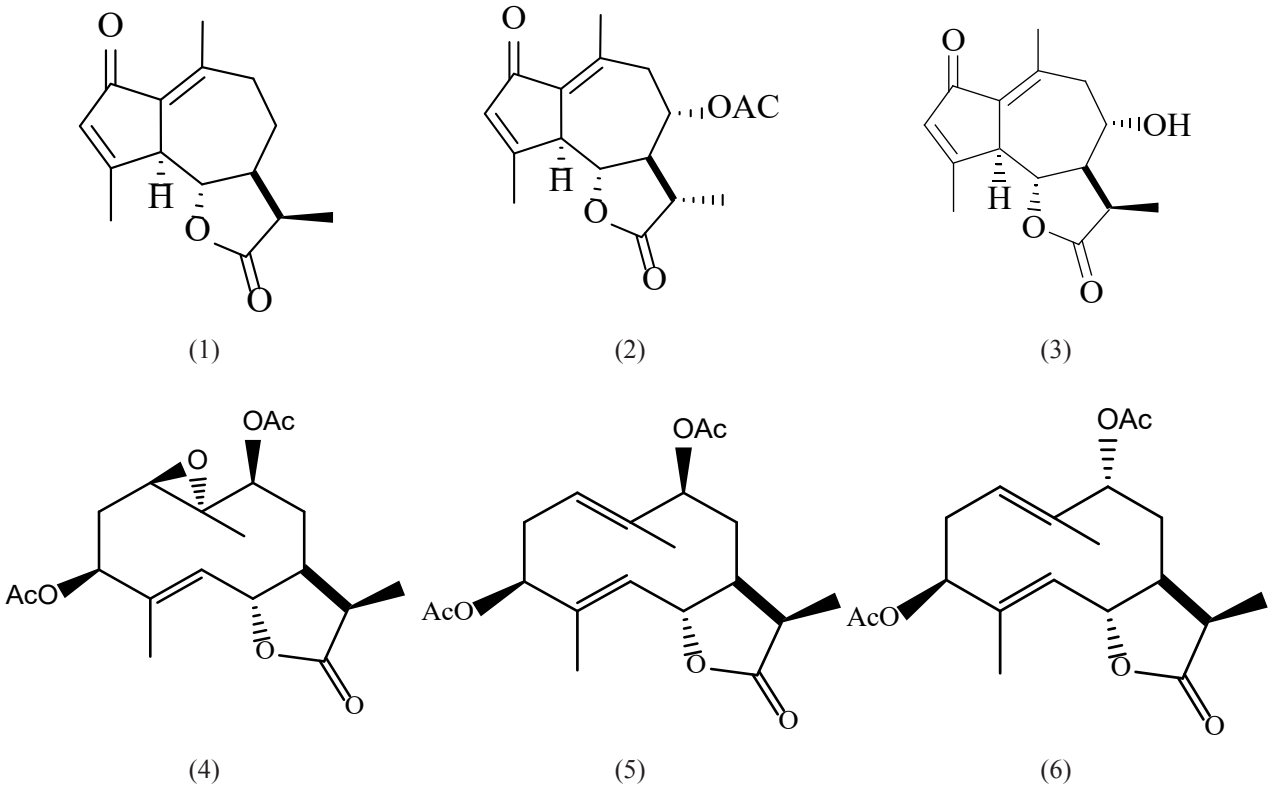

The quantitative yield of sesquiterpene lactones is provided by the method of extraction of the raw material with hot water followed by recovery of the total substances from the aqueous extract with chloroform and chromatographic separation of the total extractive substances on a silica gel column, which gives the yield (per air-dry raw material weight) of achillin (1) – 0.05%, artilesin (2) – 0.003%, grossmisin (3) – 0.005%, micranthin (4) – 0.003%, and achimicrin (5) – 0.003% (Barda et al., 2021).

A colorless crystalline substance of composition $C_{19}H_{26}O_6$, m.p. 220–222 °C (from a diethyl ether–chloroform mixture), $[\alpha]_D^{22}$ +15.5° (c 0.42; chloroform), M^+ 350, proved to be a new sesquiterpene lactone and was named achimicrin (5).

The IR spectrum of (4) shows absorption bands

characteristic of the γ-lactone carbonyl (1770 cm^{-1}), an ester group (1725, 1250 cm^{-1}), and a double bond (1660 cm^{-1}). The ^{1}H NMR and ^{13}C NMR data and their correlation with the literature (Natiq et al., 1992) allowed the structure of a *trans,trans*-germacradienolide of the 11,13-dihydrocostunolide series to be proposed for molecule (4). Signal assignments were made on the basis of comparative analysis of two-dimensional ^{1}H–^{1}H and ^{13}C–^{1}H NMR spectra.

In the ^{1}H NMR spectrum (recorded in $CDCl_3$), a doublet at 1.24 ppm (3H, J = 7.7 Hz) reflects the presence of a secondary methyl group in molecule (4); broad singlets at 1.50 and 1.72 ppm (3H each) correspond to two methyls at double bonds; and singlets at 2.03 and 2.10 ppm (3H each) correspond to two acetoxy groups. In the ^{13}C NMR spectrum, 5 quartets, 2 triplets, 7 doublets, and 5 singlets are observed, indicating that molecule (4) contains five methyl groups, two olefinic double bonds, and three carbonyl groups.

The presence of double bonds in the carbocycle is also confirmed by the signals of olefinic protons in the ^{1}H NMR spectrum (recorded in C_5D_5N): a broad doublet at 4.06 ppm (1H, J = 9.5 Hz) and a doublet of doublets of quartets at 5.24 ppm (1H, J = 12, 4.7, and 1 Hz). The triplet at 5.05 ppm (1H, J = 9.5 Hz) was assigned to the lactone proton, while the doublets of doublets at 5.18 ppm (1H, J = 10.5 and 5.6 Hz) and at 5.12 ppm (1H, J = 10.5 and 2.7 Hz) were assigned to gem-acyl protons. Upon decoupling of the Me-10 signal, the H-1 signal – a doublet of doublets of quartets at 5.24 ppm – simplifies to a doublet of doublets, while the H-2a signal – a broad doublet of doublets of doublets at 2.56 ppm – simplifies to a doublet of doublets of doublets. Moreover, H-2a is positioned such that the C–H-2a bond is almost perpendicular to the plane of the double bond, i.e. this proton is pseudo-equatorial and has the α-configuration.

One of the acetyl groups in the achimicrin (5) molecule is located at C-3, since the doublet of doublets at 5.18 ppm assigned to H-3 has J = 10.5 and 5.6 Hz, characteristic of the H-3/H-2a and H-3/H-2b couplings, respectively. The other acetoxy group is located at C-9, as follows from the correlation of the H-9 chemical shift in achimicrin (5) with that in sintenin (6).

The signal of the gem-acyl proton H-9 – a doublet of doublets at 5.12 ppm (J = 10.5 and 2.7 Hz) – simplifies, upon irradiation of H-8, to a doublet with J = 4 Hz, which is fully consistent with the presence of an axial H-9 proton whose signal is split through coupling with axial and equatorial vicinal H-8 protons. From Dreiding models it can be seen that, in the 1,5-*trans,trans*-germacradienolide conformation of the carbocycle, i.e. when both methyl groups have a syn-orientation and point upward, the data obtained correlate with 3β- and 9β-positions of the acetoxy function. According to the studies of Randall et al., C-11 in the γ-lactone ring has the α-configuration if the C-13 chemical shift in the ^{13}C NMR spectrum is observed in the 9.5–10 ppm range (Pregosin et al., 1972). Consequently, the methyl group at C-11 in achimicrin (5) is β-oriented, since the C-13 chemical shift is a quartet at 10.80 ppm.

The proposed configuration of Me-11 is also confirmed by the H-11/H-7 coupling (J = 7.7 Hz), indicating a pseudo-equatorial position of the proton at C-11. Thus, on the basis of the data obtained, it can be concluded that achimicrin (5) is an isomer of sintenin (6) at C9-OAc and has the structure of 11*R*-3-β,9β-diacetoxy-1,5-*trans,trans*-6β,7α(H)-germacra-1(10),4(5)-dien-6,12-olide.

It has been determined that aqueous and ethanolic extracts of *Achillea micrantha* Willd. exhibit antimicrobial activity against *Escherichia coli*, *Staphylococcus aureus*, and *Pseudomonas aeruginosa* (Astafyeva et al., 2018).

Achillea nobilis L. (noble yarrow) is a perennial plant whose range covers the steppe zone from the Western Mediterranean to Western Siberia. In the steppe part of Central Kazakhstan, it occurs on the slopes of granite hills. In certain districts of Central Kazakhstan, the exploitable reserve of noble yarrow on an area of 3916 hectares amounts to 136.6 tons (Flora of Kazakhstan, 1966).

From the aerial part of this plant, the flavonoids cosmosiin, cynaroside, and apigenin-7-glucuronide have been isolated and identified (Shevchenko et al., 2025).

From the raw material of *Achillea nobilis* L., the guaianolides anobin (7), chrysartemin A (8), canin (9), estafiatin (10), and anolide (11), as well as the germacranolide hanphyllin (12), have been isolated (Adekenov et al., 1984; Kishkentayeva et al., 2020; Turdybekov et al., 1994; Turmukhambetov et al., 1999).

Figure 2

The structure of Achillea nobilis L. sesquiterpene lactones (guaianolides anobin (7), chrysartemin A (8), canin (9), estafiatin (10), and anolide (11), germacranolide hanphyllin (12)

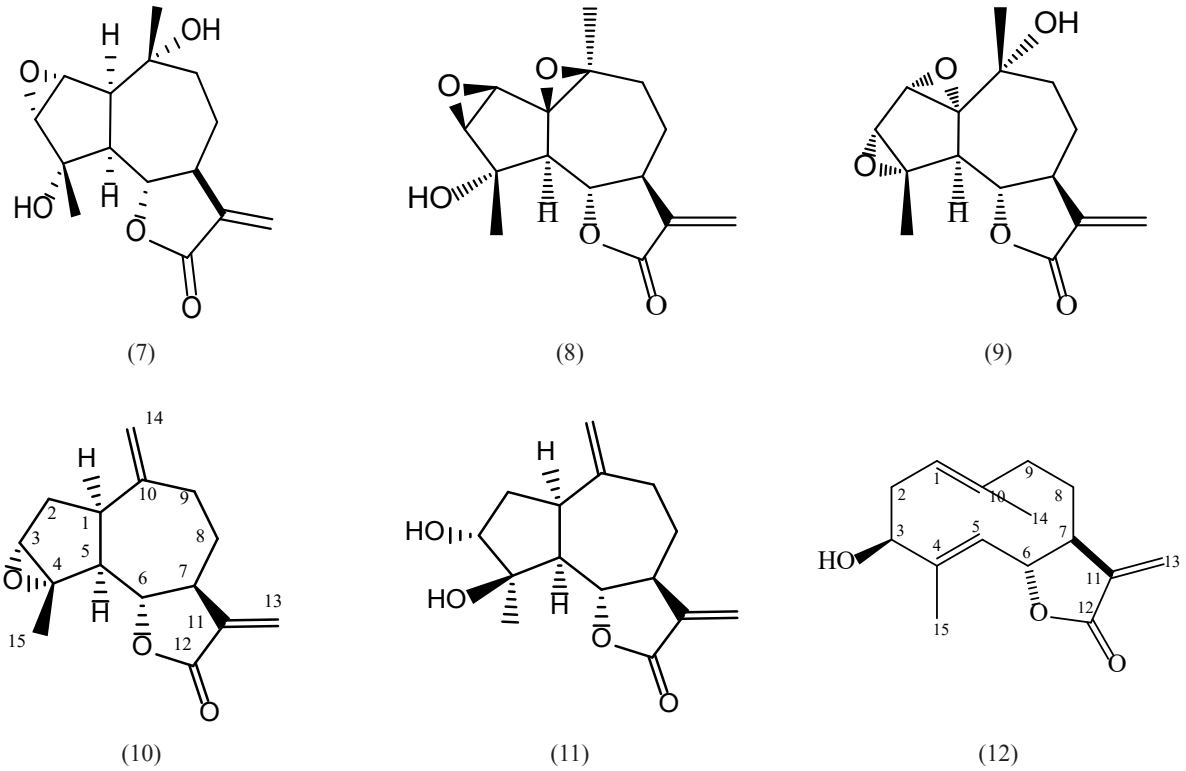

(7) (8) (9)

(10) (11) (12)

From the aerial part of *Achillea nobilis* L. collected at the flowering phase, by aqueous extraction followed by chromatographic separation of the isolated total extractive compounds on a silica gel column, a colorless crystalline substance of composition $C_{15}H_{20}O_5$, m.p. 175.5–177.5°C (from ethanol), M^+ 280 (mass spectrometry), was isolated. On the basis of the investigation of the physicochemical properties of the isolated substance and the comparison of the obtained constants and spectral data with the literature (Shevchenko et al., 2025), it was concluded that this compound differs from sesquiterpene lactones previously isolated from the genus *Achillea*. It proved to be a new sesquiterpene lactone and was named anobin (7).

Anobin (7) is soluble in alkalis on heating, and on acidification of the alkaline solution it precipitates out. The IR spectrum shows absorption bands characteristic of a hydroxyl group (3500 cm^{-1}), the γ-lactone carbonyl (1700 cm^{-1}), and a double bond (1660 cm^{-1}). The hydroxyl groups of anobin (7) are not acetylated by acetic anhydride in pyridine and are not oxidized by chromic anhydride, i.e. they are tertiary. In the ^{1}H NMR spectrum of anobin (7), the following signals are observed: singlets at 1.16 and 1.56 ppm (3H each) for tertiary methyls; weakly split doublets at 3.23 and 3.44 ppm (1H each, J = 2 Hz) for protons of the epoxy group; a multiplet at 3.93 ppm (1H) for H-7; a doublet of doublets at 4.38 ppm (1H, J = 12.4 and 9.5 Hz) for the lactone proton; a singlet at 4.93 ppm (2H) for the protons of the hydroxyl groups; and doublets at 5.28 and 6.10 ppm (1H each, J = 2.4 Hz) for the protons of the exomethylene group conjugated with the carbonyl. The doublet at 2.73 ppm (1H, J = 12.4 Hz) was assigned to H-5.

The fact that on dehydrogenation of anobin (7) chamazulene is formed, together with the spin–spin coupling constant of the protons of the exomethylene group of the lactone ring in the ^{1}H NMR spectrum, leads to the conclusion that anobin (7) has either a guaiane or a germacrane skeleton. Integration of the signals of the ^{1}H NMR spectrum reveals 20 hydrogen atoms. With this number of protons and the presence of an epoxide ring and two tertiary hydroxyl groups, a monocyclic (germacrane) structure is excluded for the compound under study. It can therefore be unambiguously stated that anobin (7) has a guaiane carbon skeleton.

The splitting pattern of the lactone proton signal in the ^{1}H NMR spectrum indicates that the lactone ring is fused at C6–C7, while the large coupling constant of the H-6 and H-5 protons (J = 12.4 Hz) indicates their mutual *trans*-disposition. Comparison with the ^{1}H NMR spectrum of the structurally related guaianolide canin (9) allows an α-orientation, rela-

tive to the main carbon skeleton, to be proposed for the epoxide ring and the hydroxyl groups of anobin (7).

The intensity of the molecular ion peak of anobin (7) at *m/z* 280 is low compared with the principal peaks in the mass spectrum, which is evidently due to the relative instability of the guaiane skeleton, enhanced by the presence of epoxy and hydroxyl groups. The fragments at *m/z* 216, 246, 250, and 262 reflect the initial fragmentation of the molecular ion through sequential elimination of methyls and hydroxyls. Loss of the neutral fragment CH_3OH gives the ion at *m/z* 216 and is followed by cleavage of rings A and B, which is supported by the ion at *m/z* 123. An alternative pathway leading to the ion at *m/z* 123 is the elimination from M^+ of an H_2O molecule with participation of the hydroxyl at C-4 and localization of the charge on the oxygen of the 2,3-epoxy group, which initiates cleavage of rings B and C. This process is enhanced by the presence of the OH group at C-10. The peak at *m/z* 250 can be explained because of simultaneous loss of methyls geminal to the hydroxyl groups, leading further to the ion at *m/z* 97. Simultaneous loss of OH groups from M^+ gives rise to the fragment at *m/z* 95.

Thus, on the basis of physicochemical constants, spectral data (IR, ^{1}H NMR, MS), and chemical transformations, it was concluded that anobin (7) has the structure and configuration of 2α,3α-epoxy-4α,10α-dihydroxy-5,7α(H),8β(H)-guai-11(13)-en-6,12-olide.

On further elution of the column, after the isolation of anobin (7), with benzene, with benzene–diethyl ether mixtures (4:1, 1:1), and with diethyl ether, four crystalline substances were obtained, three of which were identified as anobin (7), the guaiane-type sesquiterpene lactone estafiatin (10), and the germacranolide hanphyllin (12). Estafiatin (10) and hanphyllin (12) were isolated from noble yarrow for the first time.

A colorless crystalline substance of composition $C_{15}H_{20}O_4$, m.p. 167–169°C (from ethanol), $[\alpha]_D^{20}$ +52.9° (c 0.017; ethanol), proved to be a new sesqui-terpene lactone and was named anolide (11).

The IR spectrum of (11) shows absorption bands at 3550 (OH group), 1740 (γ-lactone carbonyl conjugated with an exomethylene group), 1670, and 1640 cm^{-1} (C=C). The UV spectrum displays a maximum at 204 nm (ε 18 521), characteristic of an exocyclic methylene in conjugation with the carbonyl of a γ-lactone ring.

The ^{13}C NMR spectra of (11) recorded under fully and partially decoupled ("off-resonance") conditions show signals of 5 sp^2-hybridized and 10 sp^3-hybridized carbon atoms, which is consistent with a guaiane carbon skeleton for anolide (11).

The ^{1}H NMR spectrum of (11) shows the following proton signals: a methyl group geminal to the hydroxyl group – singlet at 1.49 ppm (3H); hydroxyl protons – singlet at 2.08 ppm (2H); a gem-hydroxyl proton – doublet at 3.92 ppm (1H, J = 3.5 Hz); the lactone proton – doublet of doublets at 4.23 ppm (1H, J = 11.5 and 9.5 Hz); methylene protons – doublet at 4.92 ppm (2H, J = 3.5 Hz); and protons of the exocyclic methylene group conjugated with the γ-lactone carbonyl – doublets at 5.47 and 6.17 ppm (1H each, J = 3.5 Hz).

The multiplicity of the lactone proton signal indicates that the lactone ring is fused at the C6–C7 position, while the magnitude of J indicates its *trans*-junction relative to the main carbon skeleton.

Acetylation of the substance afforded a monoacetate of composition $C_{17}H_{22}O_5$, m.p. 182–185°C. The IR spectrum shows absorption bands at 3460 (OH group), 1740 (CO of γ-lactone), 1250 (ester group), 1665, and 1640 cm^{-1} (C=C). The ^{1}H NMR spectrum of the acetyl derivative of anolide shows signals of: a methyl group geminal to the hydroxyl group – singlet at 1.40 ppm (3H); a methyl group of the acetyl moiety – singlet at 2.02 ppm (3H); the lactone proton – triplet at 4.24 ppm (1H, J = 10 Hz); a gem-acyl proton – a signal centered at 4.95 ppm; and protons of the exocyclic methylene group conjugated with the lactone carbonyl – doublets at 5.46 and 6.17 ppm (1H each, J = 3.5 Hz). The acetylation results show that the structure of anolide (11) contains two hydroxyl groups: one secondary and the other tertiary, the latter being geminal to one of the methyl groups.

To establish the positions of the hydroxyl groups in the structure of anolide (11), as well as the relative configuration, an X-ray diffraction study of its molecule was carried out (Figure 3). It was established that ring A adopts an envelope conformation (see Figure 3). Atoms C-1, C-2, C-4, and C-5 are coplanar within 0.01 Å (torsion angle C-4, C-5, C-1, C-2 = 1.98°). Atom C-3 lies 0.09 Å below this plane. Ring B has a chair conformation. Atoms C-6, C-7, C-9, and C-10 are coplanar within 0.007 Å. Atoms C-1, C-5, and C-8 are displaced from the plane by 1.11–1.18 and 0.68 Å, respectively. The lactone ring is in an envelope conformation. Atoms C-6, C-11, and C-12 are coplanar within 0.03 Å. Atom C-7 is located 0.48 Å below the plane, while atoms C-13 and C-2 are 0.37 and 0.11 Å above it, respectively. Rings A and B are *cis*-fused, and rings B and C are *trans*-fused.

Figure 3
The structure of anolide (11) molecule

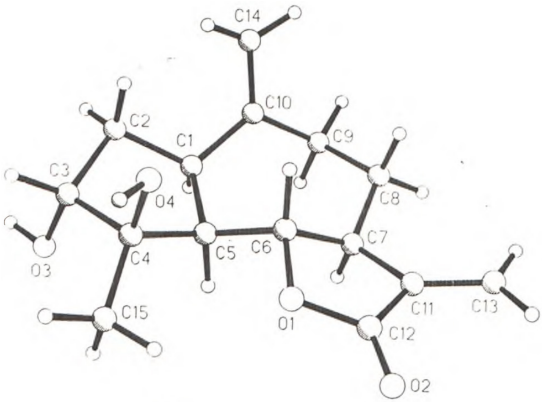

Thus, on the basis of the studies performed, it has been proved that anolide (11) has the structure and relative configuration of 3α,4β-dihydroxy-1,5,7α(H),6β(H)-guai-10(14),11(13)-dien-6,12-olide.

It was established that the quantitative yield of sesquiterpene lactones from the aerial part of *Achillea nobilis* L. is provided by aqueous extraction of the raw material: the yield of anobin (7) is 0.008% based on air-dry raw material, of estafiatin (10) – 0.01%, of hanphyllin (12) – 0.007%, and of anolide (11) – 0.01%. Whereas anobin (7) is isolated from the raw material of *Achillea nobilis* L. by both aqueous and chloroform extraction, anolide (11) is recovered only by aqueous extraction followed by chromatographic separation of the total substances on a silica gel column (Astafyeva et al., 2018).

In studying the dynamics of localization of sesquiterpene lactones in individual organs of *Achillea nobilis* L., it was established that estafiatin (10) and hanphyllin (12) are invariable components in all organs (Table 3).

Table 3
Content of sesquiterpene lactones in organs of Achillea nobilis L.

Vegetation phase	Plant organ	Raw material, g	Total extractive substances, g	Sesquiterpene lactones	Content, g	Content, % of air-dried raw material
Rosette	Leaves	2100	107.0	Estafiatin (10)	2.21	0.11
				Hanphyllin (12)	0.89	0.04
Budding	Leaves	1500	85.0	Estafiatin (10)	3.61	0.24
				Hanphyllin (12)	0.22	0.01
				Anobin (7)	0.16	0.01
	Buds	2000	81.3	Estafiatin (10)	1.76	0.09
				Hanphyllin (12)	0.08	0.01
				Anolide (11)	0.23	0.01
				Anobin (7)	0.18	0.01
Flowering	Leaves	500	42.0	Estafiatin (10)	0.72	0.14
				Anobin (7)	0.04	0.01
	Flower heads	2000	47.0	Anolide (11)	0.52	0.03

On chromatographic separation of the total substances from plants harvested in the juvenile state, on elution of the column with a benzene–diethyl ether mixture (9:1), were isolated colorless needle-like crystals of composition $C_{15}H_{18}O_3$, m.p. 102–104°C (from diethyl ether), identified as estafiatin (10). Its yield was 0.11% of the air-dry raw material weight (see Table 3). On elution of the column with a benzene – diethyl ether mixture (1:1), colorless plate-like crystals were obtained with R_f 0.76 (diethyl ether). After recrystallization from ethanol was obtained a crystalline substance of composition $C_{15}H_{20}O_3$, m.p. 190 °C (decomposition), identified as hanphyllin (12). Its yield was 0.04% of the air-dry raw material weight (see Table 3).

On chromatographic separation of the total extractive substances from leaves at the budding phase, from the fraction obtained on elution of the column

with a hexane–benzene mixture (1:1), estafiatin (10) was isolated in a yield of 0.24%. On elution of the column with benzene, hanphyllin (12) was isolated in a yield of 0.01%, and on further elution with a benzene–diethyl ether mixture (9:1), the new sesquiterpene lactone anobin (7) was obtained. Its yield was 0.011% of the air-dry raw material weight (see Table 3).

In the buds, the content of estafiatin (10) was 0.09%, of hanphyllin (12) – 0.004%, and of anobin (7) – 0.009%. On elution of the column with a benzene–diethyl ether mixture (1:1), plate-like crystals with R_f 0.53 precipitated. After recrystallization from ethanol, a colorless crystalline substance of composition $C_{15}H_{20}O_4$, m.p. 167–169 °C, was obtained, which was identified as the new sesquiterpene lactone anolide (11). The yield of anolide (11) was 0.01% based on air-dry raw material (see Table 3).

From the leaf extract at the flowering phase, on elution of the column with a benzene–diethyl ether mixture (9:1), estafiatin (10) (0.14%) was isolated, and on further elution of the column with a benzene–diethyl ether mixture (1:1), anobin (7) was isolated in a yield of 0.008% (see Table 3).

On chromatographic separation of the total extractive substances from the flower heads, crystals of anolide (11) were isolated in a yield of 0.03% (see Table 3).

The biosynthesis of the new sesquiterpene lactones anobin (7) and anolide (11) takes place at the budding and flowering phases of the plant. The data obtained on the localization of sesquiterpene lactones in noble yarrow, together with their correlation with literature data (Álvarez-Calero et al., 2021), allows a possible pathway to be proposed for the formation of the guaianolides estafiatin (10) and anolide (11) through epoxidation and successive cyclization of the germacranolide hanphyllin (12).

Since the hanphyllin (12) molecule belongs structurally to the *trans,trans*-germacradienolides, its epoxidation gives the 1β,10α-epoxy derivative; subsequent opening of the oxirane ring in this structure leads to ridentin (13). Nucleophilic attack of the 4,5-double bond at C-1 in molecule (13) brings about a 1,5-cyclization and gives rise to cation (A); hydroxylation at C-4 yields the 3β,4α-dihydroxyguaianolide (14), the subsequent dehydration of which, with elimination of C3–OH, gives the estafiatin (10) molecule. Opening of the α-epoxide ring in this molecule produces cation (B), and hydroxylation of the C-4 cationic center leads to the formation of anolide (11).

Figure 4
Proposed biosynthetic pathway of sesquiterpene lactones of Achillea nobilis L.

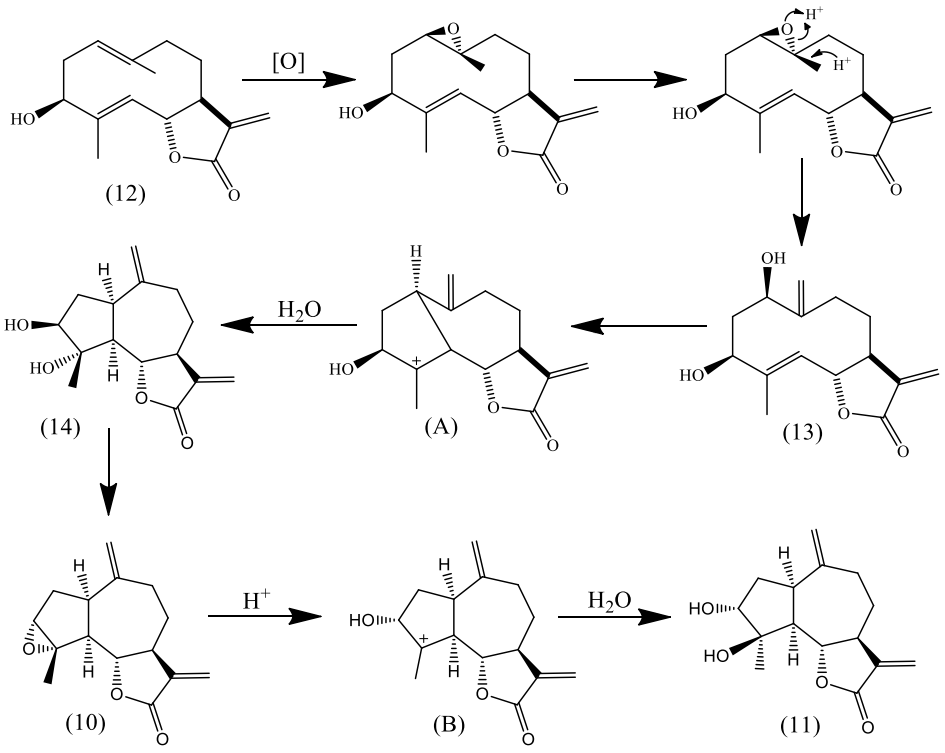

It is known that the biosynthesis of terpenoids proceeds via two different routes: the plastid non-mevalonate pathway, also called the methylerythritol-4-phosphate (MEP) pathway, which is responsible for the formation of monoterpenes, diterpenes, and tetraterpenes, and the cytosolic mevalonate (MVA) pathway, which mainly drives the biosynthesis of sesquiterpenes, triterpenes, and polyprenols. In both pathways, isopentenyl pyrophosphate (IPP) and dimethylallyl pyrophosphate (DMAPP) are synthesized; these are considered universal precursors in the biosynthesis of all terpenoids. Expression analysis of the genes involved in terpenoid biosynthesis in *Achillea millefolium* L. has shown that the DXR, LIS, PAL, and CHS genes are highly expressed specifically in glandular trichomes, whereas the expression of GPPS is ubiquitous (Fathi et al., 2019).

In plants, sesquiterpenes are formed with the participation of sesquiterpene synthases and perform a variety of ecological functions in higher plants, being localized in flowers, leaves, rhizomes, and roots. In a number of species of the family Asteraceae, germacrenes play an important role in the biosynthesis of various sesquiterpene derivatives, particularly sesquiterpene lactones. The key cytosolic enzyme in the biosynthesis of sesquiterpene lactones in *Achillea millefolium* L. is germacrene-A synthase (GAS) (Pazouki et al., 2015).

Analysis of the available literature data (Kupriyanov et al., 2023; Li et al., 2023c; Strzępek-Gomółka et al., 2021) indicates that *Achillea millefolium* L. contains sesquiterpene lactones with unusual structures, namely 5 dilactones – millefolactones A–E; 3 sesquiterpene lactones of the psilostachyin type bearing, in addition to the γ-lactone ring, a δ-lactone fragment – paulitin, isopaulitin, and psilostachyin C; 9 halogen-containing guaianolides – millefolactones B_1–B_9; and a guaianolide with a peroxide bridge – α-peroxyachifolide – which is connected with the specific features of sesquiterpenoid biosynthesis in this species.

Thus, as a result of the chemical study of 13 species of *Achillea* L. growing on the territory of Kazakhstan have been isolated 11 sesquiterpene lactones belonging to the guaianolides and germacranolides (Adekenov et al., 1984; Barda et al., 2021; Dracinsky et al., 2012). New sesquiterpene lactones – achimicrin (5), anobin (7), and anolide (11) – have been isolated and studied. The following compounds have been identified for the first time: from *A. millefolium* L. – 8-hydroxyachillin (grossmisin) (3); from *A. micrantha* Willd. – achillin (1), artilesin (2), and grossmisin (3); from *A. nobilis* L. – estafiatin (10) and hanphyllin (12).

Biological activity of sesquiterpene lactones isolated from *Achillea* L. plants

Sesquiterpene lactones from plants of the genus *Achillea* L. exhibit a wide spectrum of biological activity (Nemeth & Bernath, 2008).

Among the derivatives of estafiatin (10) isolated from *Achillea nobilis* L., comparatively high antitumor activity is exhibited by 3-keto-4-methylene-estafiatin (15), 3-keto-10(14)-epoxy-estafiatin (16), and 3-aceto-4-methylene-estafiatin (17), which inhibit the growth of Pliss lymphosarcoma, Walker carcinosarcoma, sarcoma 45, alveolar liver cancer PC-1, and sarcoma 180 by 68–90%, and of P-388 lymphocytic leukemia and lymphoid leukemia (ILS by 62–104%) (Adekenov, 2022).

Figure 5
The derivatives of estafiatin (10) isolated from Achillea nobilis L. (3-keto-4-methylene-estafiatin (15), 3-keto-10(14)-epoxy-estafiatin (16), and 3-aceto-4-methylene-estafiatin (17)

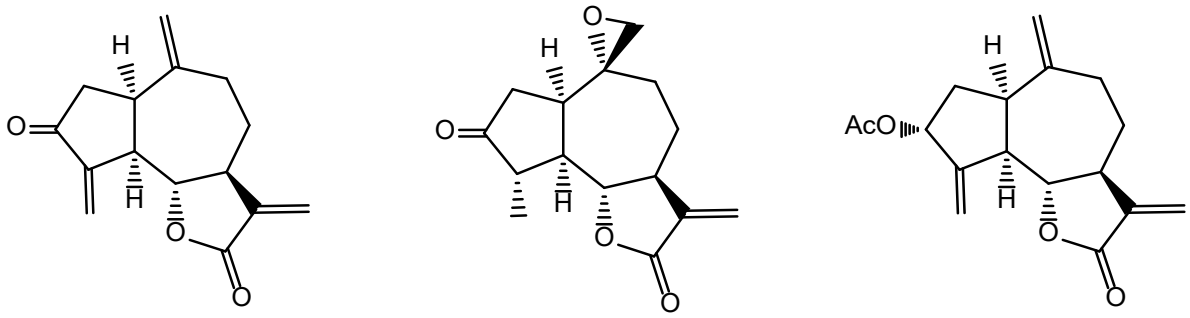

(15) (16) (17)

Among the germacranolides studied for antitumor activity, comparatively high activity is exhibited by hanphyllin (12) isolated from *Achillea nobilis* L. This germacranolide inhibits the growth of transplantable tumor strains – Guerin carcinoma, Pliss lymphosarcoma, alveolar liver cancer, and Pliss lymphosarcoma resistant to rubomycin (70–89% inhibition). In comparison with the analogue with the same indication – colchamine, a preparation of plant origin – the substances under study proved to be of low toxicity: the maximum tolerated dose (MTD) in chronic experiments is 20–70 mg/kg versus 1.0 mg/kg for colchamine (Sülsen & Martino, 2018). In-depth study of the antitumor activity of 3-keto-4-methylene-estafiatin (15) and 3-keto-10(14)-epoxy-estafiatin (16) is recommended. From *Achillea nobilis* L., the guaianolides anobin (7), exhibiting antitumor activity, and anolide (11), exhibiting acaricidal and insecticidal action, have also been isolated (Adekenov et al., 1984).

In the investigation of the antiparasitic activity of sesquiterpene lactones of plants of the genus *Achillea* L. against bloodstream trypomastigotes of *Trypanosoma brucei brucei*, amastigotes of *Trypanosoma cruzi*, and promastigotes of *Leishmania amazonensis*, a comparatively high antiparasitic activity has been established for estafiatin (10) and anabasinyl-estafiatin (20).

Table 4
Activity of Achillea L. sesquiterpene lactones against Trypanosoma brucei brucei bloodstream trypomastigotes

Compound	Inhibition, % ± SD		
	10 μg/mL	1 μg/mL	0.1 μg/mL
Achillin (1)	27.45 ± 11.02	1.47 ± 0.01	NI
Grossmisin (3)	1.47 ± 0.55	NI	NI
Estafiatin (10)	99.24 ± 0.18	72.91 ± 1.83	44.33 ± 1.83
Leucomisin (18)	4.71 ± 6.20	2.77 ± 1.83	2.77 ± 0.02
Cytisinyl-estafiatin (19)	4.77 ± 3.67	NI	NI
Anabasinyl-estafiatin (20)	99.31 ± 0.52	5.36 ± 1.83	NI
Suramin	99.74 ± 0.19	99.2 ± 0.31	29.4 ± 1.83
Note: NI – No Inhibition			

Figure 6
The derivatives of estafiatin (10) isolated from Achillea L. (leucomisin (18), cytisinyl-estafiatin (19), anabasinyl-estafiatin (20)

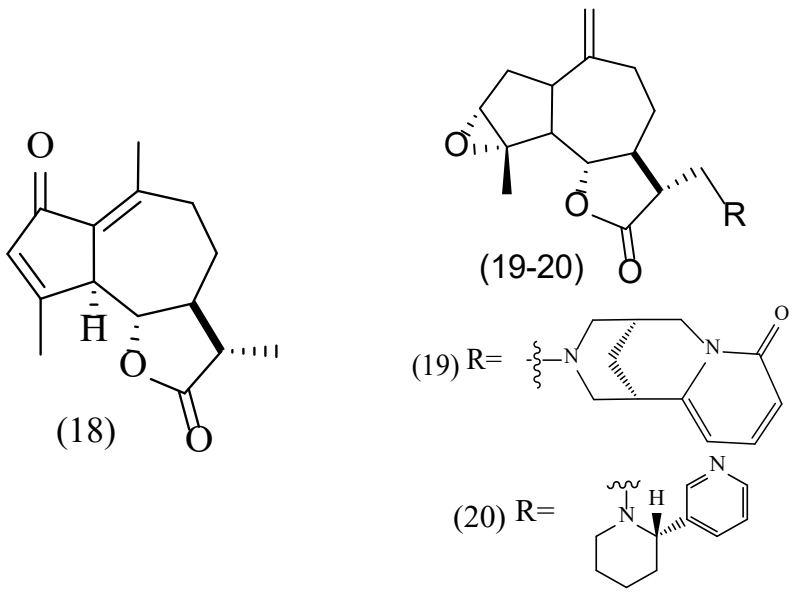

Table 5
Antiamastigote activity of Achillea L. sesquiterpene lactones against Trypanosoma cruzi at 10 μg/mL

Compound	Inhibition, %
Achillin (1)	13.63 ± 0.21
Grossmisin (3)	5.22 ± 5.35
Estafiatin (10)	97.24 ± 0.21
Leucomisin (18)	15.37 ± 3.18
Cytisinyl-estafiatin (19)	26.83 ± 0.17
Anabasinyl-estafiatin (20)	99.06 ± 0.31
Suramin	99.76 ± 0.18

Considering the comparatively high activity of *Achillea* L. sesquiterpene lactones at 10 μg/mL against *Trypanosoma cruzi* and *Trypanosoma brucei brucei*, we determined their cytotoxicity at the same concentration (Table 6).

It is important to note the comparatively high percentage of viable cells observed for the anabasinyl derivative of estafiatin (20), in comparison with the parent estafiatin (10), which indicates a decrease in the cytotoxicity of the sesquiterpene lactones as a result of Michael-type amination at position C-13.

Table 6
Cytotoxicity of Achillea L. sesquiterpene lactones against Vero cells at 10 μg/mL

Compound	Cell viability, %
Estafiatin (10)	3.15 ± 5.46
Anabasinyl-estafiatin (20)	25.72 ± 0.13
Suramin	99.2 ± 0.55

Table 7
Activity of Achillea L. sesquiterpene lactones against Leishmania amazonensis promastigotes

Compound	Inhibition, % ± SD		
	50 μg/mL	10 μg/mL	1 μg/mL
Achillin (1)	35.14 ± 7.90	30.51 ± 14.10	25.95 ± 4.76
Grossmisin (3)	40.49 ± 8.33	34.92 ± 0.03	31.84 ± 0.14
Estafiatin (10)	98.68 ± 0.28	100 ± 0.05	100 ± 0.91
Leucomisin (18)	17.87 ± 4.54	11.80 ± 4.28	8.09 ± 7.13
Cytisinyl-estafiatin (19)	22.80 ± 9.07	13.31 ± 0.01	13.52 ± 4.45
Anabasinyl-estafiatin (20)	100 ± 0.63	100 ± 1.20	17.39 ± 7.34
Amphotericin B	100.0± 0.03	100.0± 0.012	98.1± 0.53

Based on the experimental data presented above, it has been determined that Michael-type amination of estafiatin (10) at the C11=C13 exomethylene group leads to a decrease in the antiparasitic activity of its derivatives cytisinyl-estafiatin (19) and anabasinyl-estafiatin (20) against *Trypanosoma brucei brucei* and promastigotes of *Leishmania amazonensis*, as well as to a reduction in their cytotoxicity.

The guaianolide leucomisin (18) was isolated from the aerial part of *Achillea collina* Becker, *Achillea filipendulina* Lam., *Achillea millefolium* L., *Achillea santolina* L., and *Achillea sibirica* Ledeb. (Abdel-Baki et al., 2025; Glasl et al., 2002; Kaneko et al., 1971; Trendafilova et al., 2006) and determined on dogs infested with the helminths *Trichuris vulpis* and *Dipylidium caninum*. Based on the coproovoscopy results, the helminth-infested dogs (10 dogs) were divided into two experimental groups, 5 animals each. Dogs of the first group (5 animals) were administered capsules with leucomisin (18) at a dose of 150 mg (3 capsules) per 20–25 kg of body weight. In the comparison group, dogs received the preparation "CesTremForte" at a dose of 150 mg (2 tablets) per 20–25 kg of body weight. The capsules with leucomisin (18) were administered as a single dose. Coproovoscopy of each fecal sample before and after deworming of the dogs was carried out twice. Four days after administration of the capsules with leucomisin (18), coproovoscopy of the dogs' feces was performed to determine the extens- and intens-efficacy of the test sample (18). In all groups of animals, no side effects from the application of the test sample (18) were observed. As a result of the trials, no helminth eggs were detected in the dogs dewormed with capsules of leucomisin (18). Thus, the extens- and intens-efficacy of the capsules with leucomisin (18) is 100%

against the helminths *Trichuris vulpis* and *Dipylidium caninum*. The extens-efficacy and intens-efficacy of the comparison preparation "CesTremForte" are 80% and 83.33%, respectively. According to the results of the experiments, it was established that the extens-efficacy and intens-efficacy of capsules with leucomisin (18) are higher than those of the comparison preparation "CesTremForte" by 20% and 16.6%, respectively.

With a view to enhancing the water solubility of leucomisin (18) and, accordingly, the bioavailability of the pharmacologically active molecule in the body, a solid-phase synthesis was carried out on the basis of leucomisin (18) with disodium glycyrrhizinate (Adekenov et al., 2026).

Conclusion

Plants of the genus *Achillea* L. can be regarded as one of the promising taxa of the family Asteraceae as a renewable source of sesquiterpene lactones exhibiting antiparasitic and antitumor activity.

Based on the results of chemical screening of 13 species of plants of *Achillea* L. collected on the territory of Kazakhstan, the content of sesquiterpene lactones was confirmed in 9 (69.23%) of them. In the plants of section Millefolium (Mill.) Koch, the content of sesquiterpene lactones was determined in 5 species (83.3%); in plants of section Micranthae Klok. & Krytzka, in 2 species (100%); and in plants of section Ptarmica (Mill.) Koch, in 1 species (33.3%). Three species of the genus *Achillea* L. – *Achillea inundata* Kondr., *Achillea salicifolia* Besser, and *Achillea tianschanica* Kupr. & Kulemin – have been identified as promising, previously uninvestigated objects for the isolation and identification of sesquiterpene lactones.

The presence in *Achillea millefolium* L. of sesquiterpene lactones with unusual structures, namely 5 dilactones – millefolactones A–E; 3 sesquiterpene lactones of the psilostachyin type bearing, in addition to the γ-lactone ring, a δ-lactone fragment – paulitin, isopaulitin, and psilostachyin C; 9 halogen-containing guaianolides – millefolactones B_1–B_9; and a guaianolide with a peroxide bridge – α-peroxyachifolide – is connected with the specific features of the biosynthetic pathway in this species, the key cytosolic enzyme of which is germacrene-A synthase (GAS).

In Kazakhstan, the industrial reserves of the raw material of *Achillea nobilis* L., a source of the pharmacologically active estafiatin and hanphyllin, have been determined.

From *Achillea nobilis* L. and *Achillea micrantha* Willd. we have isolated 11 sesquiterpene lactones, including 3 new compounds. We have determined the physicochemical characteristics of the isolated sesquiterpene lactones and established their structures by IR, UV, ^{1}H NMR, and ^{13}C NMR spectroscopy.

The biosynthesis of sesquiterpene γ-lactones in *Achillea nobilis* L. is observed in flower heads, buds, and leaves. Their biosynthesis is carried out by specialized chloroplasts in the bracts of the buds and flower heads of the plant.

In the study of the dynamics of localization of sesquiterpene lactones in the leaves, buds, and flower heads of *Achillea nobilis* L., it has been established that estafiatin can be regarded as the main marker component for this species, since it is biosynthesized throughout almost the entire vegetation cycle, and quantitatively its content based on air-dry raw material was determined in the leaves of *Achillea nobilis* L. collected at the budding phase as 0.24%. The biosynthesis of anobin and anolide is closely linked to the development of the reproductive organs (buds and flower heads) of *Achillea nobilis* L., whereas hanphyllin is characteristic of the early developmental stages of the plant (rosette).

The quantitative yield of sesquiterpene lactones from the raw material of *Achillea micrantha* Willd. and *Achillea nobilis* L. is achieved by the methods of aqueous and supercritical fluid carbon dioxide extraction. By contrast, on chloroform extraction from the aerial part of *Achillea nobilis* L., the guaianolide anolide is not isolated, while estafiatin and hanphyllin have practically low yields and anobin is detected only in trace amounts, which indicates the comparatively low efficiency of this isolation method.

Based on the results of an *in vitro* study of sesquiterpene lactones of plants of the genus *Achillea* L., comparatively high antiparasitic activity has been determined for estafiatin and anabasinyl-estafiatin against bloodstream trypomastigotes of *Trypanosoma brucei brucei*, amastigotes of *Trypanosoma cruzi*, and promastigotes of *Leishmania amazonensis*. It has been established that Michael-type amination of estafiatin at the C11=C13 exomethylene group leads to a reduction of the antiparasitic activity of anabasinyl-estafiatin by approximately 6–13 times, and also reduces its cytotoxicity towards Vero cells by approximately 8 times.

Leucomisin, detected in 5 species of *Achillea* L., exhibits 100% extens- and intens-efficacy against the helminths *Trichuris vulpis* and *Dipylidium caninum*.

Based on leucomisin and disodium glycyrrhizinate, a solid dispersion has been synthesized whose water solubility is increased 18-fold, with a corresponding increase in the bioavailability of the pharmacologically active substance.

Estafiatin from *Achillea nobilis* L. is a renewable starting material for the synthesis of new biologically active compounds, including the compounds 3-keto-4-methylene-estafiatin and 3-keto-10(14)-epoxy-estafiatin, which possess potential antitumor activity.

Acknowledgments

This research was funded by the Science Committee of the Ministry of Science and Higher Education of the Republic of Kazakhstan under the Fundamental Research Program BR31714779 "Search for new plant metabolites and synthesis of biologically active compounds based on them".

Conflict of interest

All authors are aware of the article's content and declare no conflict of interest.

Appendix A. Supplementary data

Detailed data on the extraction of raw materials and the isolation of individual compounds are provided in the Supplementary material.

Author contributions

Sergazy M. Adekenov: Conceptualization, Methodology, Project Administration, Writing – Review & Editing

Dmitriy L. Savchenko: Writing – Original Draft, Writing – Review & Editing

Aylina B. Syzdykova: Investigation, Writing – Original Draft, Formal Analysis

Asel Amanzhan: Investigation, Methodology, Writing – Original Draft

Andrey N. Kuprijanov: Methodology, Supervision, Data Curation, Writing – Review & Editing

References

1. Abdel-Baki, P. M., Mahdy, N. E., Ibrahim, R. M., El Badawy, S. A., Ali, S. E., Ibrahim, M. A., et al. (2025). Phytochemical analysis and neuroprotective potential of Achillea santolina L. fractions. *Scientific Reports, 15*(1), 16070. https://doi.org/10.1038/s41598-025-98887-z

2. Adekenov, S. (2022). Syntheses based on 3,4α-epoxy-1,5,7α,6β(H)-guai-10(14),11(13)-dien-6,12-olide. *Molecules, 27*(6), 1862. https://doi.org/10.3390/molecules27061862

3. Adekenov, S. M. (2023). 2-oxo-5α,7α,6β,11β(H)-guai-1(10),3(4)-dien-6,12-olide possessing anthelmintic activity. Patent of the Republic of Kazakhstan, No. 2023/0509.1.

4. Adekenov, S. M., Amanzhan, A., Savchenko, D. L., Krasnyuk, I. I., Solovieva, N. L., & Krasnyuk, I. I. (Sr.). (2026). Solid-State Synthesis Based on Natural Leucomisine. *Molecules*, *31*(8), 1307-1332. https://doi.org/10.3390/molecules31081307

5. Adekenov, S. M., Mukhametzhanov, M. N., Kagarlitskii, A. D., & Turmukhambetov, A. Zh. (1984). A chemical investigation of Achillea nobilis. *Chem. Nat. Compd*., *20*(5), 568–571. https://doi.org/10.1007/BF00580067

6. Agatha, O., Mutwil-Anderwald, D., Tan, J. Y., & Mutwil, M. (2024). Plant sesquiterpene lactones. *Philos. Trans. R. Soc. Lond. B Biol. Sci., 379*(1914), 20230350. https://doi.org/10.1098/rstb.2023.0350

7. Alves, M. F., Scotti, L., Da Costa, F. B., & Scotti, M. T. (2018). *Chemotaxonomic Study of Sesquiterpene Lactones of Asteraceae: Classical and Modern Methods.* Springer International Publishing, 31-45. https://doi.org/10.1007/978-3-319-78274-4_3

8. Álvarez-Calero, J. M., Ruiz, E., López-Pérez, J. L., Jaraiz, M., Rubio, J. E., Jorge, Z. D., & Massanet, G. M. (2021). 15-Hydroxygermacranolides as Sources of Structural Diversity: Synthesis of Sesquiterpene Lactones by Cyclization and Rearrangement Reactions. *J. Org. Chem., 83*(10), 1-12. https://doi.org/10.1021/acs.joc.8b00407

9. Amen, Y., Abdelwahab, G., Heraiz, A., Sallam, M., & Othman, A. (2025). Exploring sesquiterpene lactones: structural diversity and antiviral therapeutic insights. *RSC Advances, 15*, 1970-1988. https://doi.org/10.1039/D4RA08125K

10. Anderberg, A. A., Baldwin, B. G., & Bayer, R. G., et al. (2007). *Compositae. The Families and Genera of Vascular Plants.* (Vol.VIII. Flowering Plants. Eudicots). Asterales. Springer.

11. Astafyeva, O., Sukhenko, L. T., Kurashov, E., Krylova, J., Egorov, M. A., Bataeva, Y., & Baimukhambetova, A. (2018). Chemical composition and antibacterial properties of Achillea micrantha. *Indian J. Pharm. Sci., 80,* 1-10. https://doi.org/10.4172/pharmaceutical-sciences.1000376

12. Barda, C., Grafakou, M. E., Tomou, E. M., & Skaltsa, H. (2021). Phytochemistry and evidence-based traditional uses of the genus Achillea L.: an update (2011–2021). *Scientia Pharmaceutica, 89*(4), 1-50. https://doi.org/10.3390/scipharm89040050

13. Borgo J, Elso OG, Gomez J, Coll M, Catalán CAN, Mucci J, Alvarez G, Randall LM, Barrera P, Malchiodi EL, et al. (2023). Anti-Trypanosoma cruzi Properties of Sesquiterpene Lactones Isolated from Stevia spp.: In Vitro and In Silico Studies. Pharmaceutics.; 15(2):647. https://doi.org/10.3390/pharmaceutics15020647

14. Csupor-Löffler, B., Hajdú, Z., Zupkó, I., Réthy, B., Falkay, G., Forgo, P., & Hohmann, J. (2009). Antiproliferative effect of flavonoids and sesquiterpenoids from Achillea millefolium s.l. on cultured human tumour cell lines. *Phytother. Res., 23*(5), 672-676. https://doi.org/10.1002/ptr.2697

15. Dracinsky, M., Budesinsky, M., Warzajtis, B., & Rychlewska, U. (2012). Solution and solid-state effects on NMR chemical shifts in sesquiterpene lactones: NMR, X-ray, and theoretical methods. *The Journal of Physical Chemistry, 116*(1), 680-688. https://doi.org/10.1021/jp209408b

16. Ehrendorfer, F., & Guo, Y. P. (2005). Changes in the circumscription of the genus Achillea (Compositae-Anthemideae) and its subdivision. *Willdenowia, 35*(1), 49-54. https://doi.org/10.3372/wi.35.35102

17. Fathi, E., Majdi, M., Dastan, D., & Maroufi, A. (2019). The spatio-temporal expression of some genes involved in the biosynthetic pathways of terpenes/phenylpropanoids in yarrow (Achillea millefolium). *Plant Physiol. Biochem., 142*, 43-52. https://doi.org/10.1016/j.plaphy.2019.06.036

18. Fraga, B. M. (2013). Natural sesquiterpenoids. *Nat. Prod. Rep., 30*, 1226-1264. https://doi.org/10.1039/c3np70047j

19. Frey, M., Vahabi, K., & Cankar, K., et al. (2024). Sesquiterpene Lactones – Insights into Biosynthesis, Regulation and Signalling Roles. *Critical Reviews in Plant Sciences, 43*(3), 131-157. https://doi.org/10.1080/07352689.2024.2307240

20. Glasl, S., Mucaji, P., Werner, I., & Presser, A. (2002). Sesquiterpenes and flavonoid aglycones from a Hungarian taxon of the Achillea millefolium group. *Zeitschrift fur Naturforschung. C, Journal of biosciences*, *57*(11-12), 976–982. https://doi.org/10.1515/znc-2002-11-1203

21. Glasl, S., Presser, A., Gunbilig, D., Werner, I., Narantuya, S., Haslinger, E., Jurenitsch, J., & Kubelka, W. (2001). Highly hydroxylated guaianolides of Achillea asiatica and Middle European Achillea species. *Phytochemistry, 58*(8), 1189-1194. https://doi.org/10.1016/s0031-9422(01)00281-3

22. Hanalp, H. C., Dogan, A., Saygi, T. K., Donmez, F., & Battal, A. (2022). Exploring phytochemical constituents of Achillea arabica Kotschy (ethanolic extract). *Research Square, 78*(5-6), 189-199. https://doi.org/10.21203/rs.3.rs-1207243/v2

23. Harborne, J. B. (1998). *Phytochemical Methods: A Guide to Modern Techniques of Plant Analysis* (3rd edition) Chapman and Hall.

24. Ivanescu, B., Miron, A., & Corciova, A. (2015). Sesquiterpene lactones from Artemisia genus: biological activities and methods of analysis. *J. Anal. Methods Chem., 247685*, 1-21. https://doi.org/10.1155/2015/247685

25. Kalinkina, G. I., Berezovskaya, T. P., Taran, D. D., Prishchep, T. P., Saratikov, A. S., & Vengerovskii, A. I. (1993). *Method for obtaining an essential oil exhibiting wound-healing and anti-inflammatory activity*. Russian Federation Patent, No. 1297279.

26. Kaneko, H., Naruto, S., & Takahashi, S. (1971). Sesquiterpenes of Achillea sibirica. *Phytochemistry, 10*(12), 3305-3306. https://doi.org/10.1016/S0031-9422(00)97402-8

27. Kasner, U., Reznicek, G., Jurenitsch, J., Kubelka, W., Baumann, A., Robien, W., Sosa, S., & Loggia, R. D. (1990). A new proazulene from Achillea aspleniifolia. *Biology and Chemistry of Active Natural Substances, 56*(6), 531. https://doi.org/10.1055/s-2006-961092

28. Khabriev, R. U. (Ed.). (2000). *Guidelines for the Experimental (Preclinical) Investigation of New Pharmacological Substances*. Remedium, 309-311.

29. Kishkentayeva, A. S., Mantler, S. N., Zhakanov, M. M., & Adekenov, S. M. (2020). Biologically active substances from Achillea nobilis L. Bulletin of Karaganda University. *Chemistry Series, 4*, 52-59. https://doi.org/10.31489/2020Ch4/52-59

30. Kupriyanov, A. N., & Kulemin, Y. E. (2023). Synopsis of the genus Achillea L. (Asteraceae) in Kazakhstan. *Turczaninowia, 26*(2), 190-201. https://doi.org/10.14258/turczaninowia.26.2.15

31. Laurella, L. C., Elso, O. G., Rodriguez, R. N., Viecenz, J. M., Alonso, M. R., Bontempi, E. J., et al. (2023). Antiprotozoal compounds from Mikania periplocifolia (Asteraceae). Fitoterapia, 167, 105499. https://doi.org/10.1016/j.fitote.2023.105499

32. Laurella, L. C., Mirakian, N. T., Garcia, M. N., Grasso, D. H., Sülsen, V. P., & Papademetrio, D. L. (2022). Sesquiterpene lactones as promising candidates for cancer therapy: focus on pancreatic cancer. *Molecules, 27*(11), 1-25. https://doi.org/10.3390/molecules27113492

33. Li, H., Li, J., Liu, M., Xie, R., Zang, Y., Li, J., & Aisa, H. A. (2021). Guaianolide sesquiterpene lactones from Achillea millefolium L. *Phytochemistry, 186*, 1-9. https://doi.org/10.1016/j.phytochem.2021.112733

34. Li, H., Liu, L., Gou, G., Xin, X., Li, J., & Aisa, H. A. (2023a). Guaianolides from Achillea millefolium L. and their anti-inflammatory activity. *Phytochemistry, 210*, 113647. https://doi.org/10.1016/j.phytochem.2023.113647

35. Li, H., Liu, L., Liu, G., Li, J., & Aisa, H. A. (2023b). Chlorine-containing guaianolide sesquiterpenoids from Achillea millefolium L. with inhibitory effects against LPS-induced NO release in BV-2 microglial cells. *Phytochemistry, 207*, 113567. https://doi.org/10.1016/j.phytochem.2022.113567

36. Li, H., Xu, N., Li, J., & Aisa, H. A. (2023c). Guaianolide-type sesquiterpene lactones from Achillea millefolium L. and their anti-inflammatory activity. *Phytochemistry, 216*, 113894. https://doi.org/10.1016/j.phytochem.2023.113894

37. Li, Y., Zhang, M. L., & Cong, B., et al. (2011). Achillinin A, a cytotoxic guaianolide from the flower of yarrow, Achillea millefolium. *Biosci. Biotechnol. Biochem., 75*(8), 1554-1556. https://doi.org/10.1271/bbb.110234

38. Mahmoud, A. A., Al-Shihry, S. S., & Hegazy, M. E. F. (2012). A new epimeric sesquiterpene lactone from Achillea ligustica. *Rec. Nat. Prod., 6*(1), 21-27.

39. Ministry of Healthcare of the Republic of Kazakhstan. (2020). Order of the Minister of Healthcare of the Republic of Kazakhstan No. KR DSM-181/2020 of November 4, 2020. *On approval of the rules for the assessment of materials and compliance of preclinical (non-clinical) studies with Good Laboratory Practice (GLP) requirements of the Republic of Kazakhstan and/or the Eurasian Economic Union within the framework of pharmaceutical inspection*. (Registered under No. 21596). https://adilet.zan.kz/eng/docs/V2000021596

40. Natiq, A. R. H., Nahia, J. Y., Andrea, P., & Karlheinz, S. (1992). Sesquiterpene lactones from Achillea micrantha. *Phytochemistry, 31*(6), 2160-2162. https://doi.org/10.1016/0031-9422(92)80389-v

41. Nemeth, E., & Bernath, J. (2008). Biological activities of yarrow species (Achillea spp.). *Curr. Pharm. Des., 14*(29), 3151-3167. https://doi.org/10.2174/138161208786404281

42. Pavlov, N. V. (Ed.). (1966). *Flora of Kazakhstan* (Vol. IX). Publishing House of the Academy of Sciences of the Kazakh SSR.

43. Pazouki, L., Memari, H. R., Kännaste, A., Bichele, R., & Niinemets, Ü. (2015). Germacrene A synthase in yarrow (Achillea millefolium) is an enzyme with mixed substrate specificity: gene cloning, functional characterization and expression analysis. *Front. Plant Sci., 6*, 111. https://doi.org/10.3389/fpls.2015.00111

44. Pregosin, P. S., Randall, E. W., & McMurry, T. B. H. (1972). 13C fourier studies. The configurational dependence of the carbon-13 chemical shifts in santonin derivatives. *J. Chem. Soc. Perkin Trans., 3*, 299-301. https://doi.org/10.1039/P19720000299

45. Rothwangl-Wiltschnigg, K., Glasl, S., Werner, I., & Reznicek, G. (2004). Analysis of the sesquiterpenes in Achillea species using liquid chromatography–mass spectrometry with positive ion atmospheric pressure chemical ionization. *Sci. Pharm., 72*(3), 249-258. https://doi.org/10.3797/scipharm.aut-04-21

46. Shevchenko, A., & Akhelova, A., et al. (2025). Phytochemistry, Pharmacological Potential, and Ethnomedicinal Relevance of Achillea nobilis and Its Subspecies: A Comprehensive Review. *Molecules, 30*(11), 2460. https://doi.org/10.3390/molecules30112460

47. State Pharmacopoeia of the Republic of Kazakhstan (Volume 3). (2014). Zhibek Zholy Publishing House, 122.

48. Strzępek-Gomółka, M., Gaweł-Bęben, K., & Kukula-Koch, W. (2021). Achillea species as sources of active phytochemicals for dermatological cosmetic applications. *Oxid. Med. Cell. Longev., 2021*(1), 1-14. https://doi.org/10.1155/2021/6643827

49. Sülsen, V., & Martino, V. (2018). *Sesquiterpene Lactones: Advances in Their Chemistry and Biological Aspects*. Springer International Publishing, 1-391. https://doi.org/10.1007/978-3-319-78274-4

50. Todorova, M., Vogler, B., & Tsankova, E. (2000). Terpenoids from Achillea setacea. Z. Naturforsch. *C J. Biosci., 55*(9-10), 840-842. https://doi.org/10.1515/znc-2000-9-1028

51. Tohme, R., Al Aaraj, L., & Ghaddar, T., et al. (2013). Differential growth inhibitory effects of highly oxygenated guaianolides isolated from the Middle Eastern indigenous plant Achillea falcata in HCT-116 colorectal cancer cells. *Molecules, 18*(7), 8275-8288. https://doi.org/10.3390/molecules18078275

52. Trendafilova, A., Todorova, M., Mikhova, B., Vitkova, A., & Duddeck, H. (2006). Sesquiterpene lactones from Achillea collina J. Becker ex Reichenb. *Phytochemistry, 67*(8), 764-770. https://doi.org/10.1016/j.phytochem.2006.01.033

53. Turdybekov, K. M., Turmukhambetov, A. Zh., Adekenov, S. M., & Struchkov, Y. T. (1994). Anolide – a new guaianolide from Achillea nobilis. *Chem. Nat. Compd., 30*(4), 460-463. https://doi.org/10.1007/BF00630399

54. Turmukhambetov, A. Zh., Buketova, G. K., Gafurov, N. M., & Adekenov, S. M. (1999). Chrysartemin A and canin from Achillea nobilis. *Chem. Nat. Compd., 35*(1), 102. https://doi.org/10.1007/BF02238225

55. Xue, G. M., Xue, J. F., Duan, J. J., Yang, H. Y., Sun, Y. J., Chen, H., Zhi, Y. L., Zhang, Z. Q., Li, R., Zhu, D. R., & Li, G. S. (2025). Sesquiterpenoids from Achillea setacea Waldst. & Kit. with anti-inflammatory activity by inhibiting the glycolytic pathway. *Phytochemistry, 239*, 114608. https://doi.org/10.1016/j.phytochem.2025.114608

56. Xue, G. M., Zhao, C. G., Xue, J. F., Duan, J. J., Pan, H., Jia, Y., Du, K., Zhi, Y. L., & Feng, W. S. (2023). Monomeric and dimeric guaianolide sesquiterpenoids with hypoglycemic activity from Achillea alpina. *Fitoterapia, 166*, 1-19. https://doi.org/10.1016/j.fitote.2023.105472

57. Xue, G. M., Zhao, C. G., Xue, J. F., Duan, J. J., Pan, H., Li, M., Chen, H., Sun, Y. J., Feng, W. S., Ma, T., & Zhang, W. D. (2022). Germacranolide- and guaianolide-type sesquiterpenoids from Achillea alpina L. reduce insulin resistance in palmitic acid-treated HepG2 cells via inhibition of the NLRP3 inflammasome pathway. *Phytochemistry, 202*, 113297. https://doi.org/10.1016/j.phytochem.2022.113297

58. Zitterl-Eglseer, K., Jurenitsch, J., Korhammer, S., Haslinger, E., Sosa, S., Della Loggia, R., Kubelka, W., & Franz, C. (1991). Sesquiterpene lactones of Achillea setacea with antiphlogistic activity. *Planta Med., 57*(5), 444-446. https://doi.org/10.1055/s-2006-960146

Information about the authors:

Sergazy M. Adekenov – Doctor of Chemical Sciences, Professor, Chairman of the Board, JSC "Research and Production Center "Phytochemistry" (Karaganda, Kazakhstan, e-mail: arglabin@phyto.kz).

Dmitriy L. Savchenko – Researcher, Laboratory of Terpenoids Chemistry, JSC "Research and Production Center "Phytochemistry" (Karaganda, Kazakhstan, e-mail: SavchenkoD_pharmatech@mail.ru).

Aylina B. Syzdykova – Researcher, Laboratory of Terpenoids Chemistry, JSC "Research and Production Center "Phytochemistry" (Karaganda, Kazakhstan, e-mail: syzdykova.aylina@gmail.com).

Asel Amanzhan – PhD, Head of the Laboratory of Alkaloids Chemistry, JSC "Research and Production Center "Phytochemistry" (Karaganda, Kazakhstan, e-mail: asel.amanzhan@bk.ru).

Andrey N. Kuprijanov – Doctor of Biological Sciences, Professor, Chief Researcher, Kuzbass Botanical Garden Russian Federal State Research Center of Coal and Coal Chemistry (Kemerovo, Russia, e-mail: kupr-42@yandex.ru)

Received 25 March 2026;
received in revised form 23 June 2026;
accepted 26 June 2026

IRSTI 34.17.35 https://doi.org/10.26577/IJBCh20261912

A. Baikatov[1,2*], D. Zhumakhanov[1,2]

[1]Al-Farabi Kazakh National University, Almaty, Kazakhstan
[2]Neurolab Neurorehabilitation Center, Almaty, Kazakhstan
*e-mail: amir.sapar@zoho.com

LOW-FREQUENCY TRANSCRANIAL MAGNETIC STIMULATION FOR ENHANCING COMMUNICATION IN CHILDREN WITH AUTISM AND SPECIFIC LANGUAGE IMPAIRMENT

Abstract: To evaluate whether low-frequency transcranial magnetic stimulation (TMS) is associated with improvement in speech-language function in children with autism spectrum disorder (ASD) and Specific Language Impairment (SLI), a treatment response difference by stimulation frequency and cortical target was assessed**.** This retrospective observational study analyzed clinical data from 131 children treated at Neurolab Neurorehabilitation Center (Almaty, Kazakhstan), between April 3, 2023, and July 30, 2024. The cohort included 58 children with ASD and 73 children with SLI. Speech-language function was rated before and after treatment using a structured 10-point clinical scale. TMS was delivered to the bilateral dorsolateral prefrontal cortex (DLPFC), with additional stimulation of Broca's and/or Wernicke's areas in selected participants. Frequencies of 0.3 Hz, 0.5 Hz, and 1.0 Hz were analyzed. Each course consisted of 10 daily sessions. Across the total cohort, mean speech-language rating improved from 3.46 to 3.96 points, with a mean improvement of 0.50 points. Improvement was greater in children with ASD than in children with SLI (0.83 vs. 0.25 points). The strongest response was observed in the ASD subgroup treated at 1.0 Hz, where mean improvement reached 2.13 points. In an adjusted linear regression model, the ASD x 1.0 Hz interaction remained significant (coefficient=1.55, p=0.004), while number of treatment courses was positively associated with improvement and motor delays were negatively associated with improvement. Low-frequency TMS was associated with improvement in clinician-rated speech-language function, but the effect was not uniform across stimulation protocols. The findings support the potential of TMS as a protocol-sensitive neuromodulation approach and indicate the need for prospective studies comparing stimulation parameters directly.

Keywords: transcranial magnetic stimulation, autism spectrum disorder, specific language impairment, low-frequency stimulation, speech development, neuromodulation.

Introduction

Human communication and socialization fundamentally rely on speech and language, which are guided by complex neural mechanisms regulated by functional networks in the central nervous system. Excitability and plasticity of cortical regions within these networks are considered to play a critical role in fostering the development of effective communication skills (Nasios et al., 2019). In cases of delayed speech development, such as in individuals with autism spectrum disorder (ASD) or Specific Language Impairment (SLI), they are disrupted, resulting in adverse effects on socialization, cognitive development, and quality of life. ASD is characterized by impairments in social interaction and communication, and by restricted or repetitive interests and behaviors. A major challenge for children with ASD is speech and language development delays, which can be displayed as delays in acquiring language skills or even a complete absence of speech (Mottron & Bzdok, 2020). In contrast, SLI is an isolated speech impairment with preserved cognitive and sensory functions.

Both conditions are the subjects of active research aimed at understanding their neurophysiological bases, developing effective support, and identifying potential treatments. Studies have reported altered brain oscillations, particularly in low-frequency and gamma ranges, in individuals with both ASD and SLI. These disruptions along with the atypical excitation/inhibition signaling and connectivity are theorized to impact the functional activity of cortical networks, reducing the efficiency of language processing (Arutiunian et al., 2024; Bruining et al., 2020; Kessler et

al., 2016; Larson et al., 2023). In SLI and developmental language disorder, current models emphasize procedural and sequence learning, auditory discrimination, and broader functional network differences (Doucet et al., 2025; Hsu & Bishop, 2014; Kujala & Leminen, 2017; Ullman et al., 2020). Considering the association of these disorders with altered cortical excitability and impaired neuroplasticity, neuromodulation methods such as transcranial magnetic stimulation (TMS), which aim to stabilize excitability and promote neuroplasticity, hold promise for improving communication-related symptoms in these patients.

TMS is a non-invasive brain stimulation technique that uses magnetic fields to modulate neural network activity. Repeated low-frequency application of magnetic impulses (LF-TMS; <1 Hz pulses) has been shown to suppress neuronal activity, reduce hyperconnectivity in specific cortical regions, and normalize brain signaling rhythms (Casanova et al., 2020; Gao et al., 2022). In adult patients with post-stroke aphasia, LF-TMS protocols have been shown to promote speech fluency, comprehension, and writing skills (Yao et al., 2020). Its application in pediatric populations opens new avenues for addressing speech and language impairments, considering the high plasticity of the developing brain (Bethlehem et al., 2022). The recent migration of the technique from academic to clinical practice has yielded abundant data useful for establishing specific stimulation protocols across various conditions (Scheper et al., 2022). Of particular interest is low-frequency TMS targeting the dorsolateral prefrontal cortex (DLPFC), involved in cognitive and executive functions related to language processes. LF-TMS reduces hyperactivity in gamma oscillations of children with ASD, improves cognitive performance, and decreases stereotypical behaviors (Casanova et al., 2020; Casanova et al., 2021). Improvements in nonverbal communication and language skills were also reported following LF-TMS to the prefrontal cortex in children with ASD (Tarhan et al., 2023). Several EEG markers of cognitive control in underage participants with ASD were normalized after six to twelve 1 Hz stimulation sessions, along with the improvements in oddball test performance (Sokhadze et al., 2018). One of the challenges in making inferences with this protocol is the wide array of conditions with described results, including improvements in healthy participants' performances in language tasks (Noda, 2021; Quet al., 2022).

Despite growing evidence for the application of TMS in neurological and neurodevelopmental conditions, its impact on speech development in ASD and SLI remains underexplored. Modeling neural circuits in children, whose brains exhibit heightened plasticity, offers unique opportunities to address speech impairments. However, precise parameters for optimizing therapeutic outcomes have yet to be determined. Given the complex relationship between cortical excitability and speech development, we hypothesize that LF-TMS (≤1 Hz) will significantly improve speech development in children with ASD compared to other neurodevelopmental disorders. This hypothesis is based on the unique neural characteristics of ASD, such as increased cortical excitability and altered neuroplasticity, which may facilitate a stronger response to neuromodulation interventions. Previous studies have shown that LF-TMS at 1 Hz targeting the DLPFC can normalize cortical excitability and reduce hyperconnectivity in prefrontal regions, improving cognitive and behavioral outcomes (Hamilton, 2026). Stimulation of the inferior frontal gyrus (IFG), commonly referred to as Broca's area, improved general accuracy in semantic and phonological, but not syntactic tasks or reaction times (Berent et al., 2015). In cases of SLI, additional stimulation of these areas may aid language acquisition. Studies on aphasia recovery suggest that targeting speech-related areas can improve language-related performance, which may be effective for children with speech disorders (Caulfield & Brown, 2022; Noda, 2021).

The primary objective of this study is to explore the therapeutic potential of LF-TMS in children with speech impairments, particularly those diagnosed with ASD and SLI. We aim to assess whether LF-TMS at 1 Hz yields greater improvements compared to other stimulation frequencies and to determine whether additional stimulation of speech-related areas (Broca's and Wernicke's regions) enhances communication. Additionally, the study investigates variables such as delays in gross motor skills development and the number of TMS sessions, which may significantly influence therapeutic outcomes. Preliminary data suggest that patients with ASD may benefit most from 1 Hz stimulation, and factors such as session frequency and motor delays are critical to speech and language development.

Materials and methods

Data was collected from children who underwent LF-TMS between April 3, 2023, and July 30, 2024. The analyzed cohort included 131 children with available pre- and post-treatment speech-language assessments, including 58 children with ASD and 73 children with SLI. A total of 131 children aged 3 to

12 years participated in the study, with a mean age of 7.2 years (SD = 2.3). Participants were required to have completed at least two courses of TMS therapy, and all underwent comprehensive pre- and post-treatment assessments of speech and language abilities. Children with significant neurological comorbidities unrelated to speech and language impairments were excluded, while motor delays, when present, were recorded for subgroup analysis. Baseline speech-language impairment differed between diagnostic groups. Children with ASD had lower baseline scores than children with SLI (mean 2.57 vs. 4.16), indicating greater initial severity in the ASD subgroup. Sex-based subgroup analysis was not performed because sex/gender was not included as a structured variable in the analysis dataset.

Magnetic pulses were delivered using the Neuro-MS/D transcranial magnetic stimulator manufactured by Neurosoft (Ivanovo, Russia). The equipment included a figure-of-eight coil for precise targeting of specific brain regions, including the dorsolateral prefrontal cortex (DLPFC), Broca's area, and Wernicke's area. Stimulation frequencies of 0.3 Hz, 0.5 Hz, and 1 Hz were utilized, with stimulation intensity calibrated individually at 80% of each participant's resting motor threshold (RMT). All 131 participants received DLPFC stimulation. In the structured dataset, 92 participants received additional Broca's area stimulation, 33 received Wernicke's area stimulation, and 19 received combined Broca's and Wernicke's area stimulation. Target combinations were distributed as follows: DLPFC only, n=25; DLPFC + Broca, n=73; DLPFC + Wernicke, n=14; DLPFC + Broca + Wernicke, n=19 Each treatment course consisted of 10 daily sessions. In the analyzed cohort, the number of completed courses ranged from 2 to 8.

To quantify severity and treatment progress, a structured impairment scale was adapted from validated models, mapping clinician-reported observations to a numerical scale ranging from 1 (severe impairment) to 10 (normal development). The scale mapped clinician-reported observations, such as response to name, use of simple words, and functional communication, onto predefined score ranges. This approach was used to standardize retrospective clinical descriptions into an analyzable ordinal outcome, consistent with previous work showing that clinician-rated global scales can be useful for tracking social-communication change in minimally verbal children with ASD (Toolan et al., 2021). Collected data was processed and analyzed using Pandas, Numpy, and Statsmodels Python libraries in the Google Colab environment. Linear regression models were applied to investigate relationships between TMS parameters and speech and language outcomes. Interaction effects were evaluated using linear regression models with interaction termsresults were visualized using Matplotlib and Seaborn libraries.

Ethical Considerations

All procedures were approved by the Local Ethical Committee of Al-Farabi Kazakh National University (Protocol No. IRB-A843, IRB00010790, approval date: 23.02.2023), with written informed consent obtained from caregivers before enrollment.

Results and discussion

The final analysis included 131 children, the ASD subgroup included 58 participants and the SLI subgroup included 73 participants (Table 1) Across the total cohort, mean speech-language rating improved from 3.46 before treatment to 3.96 after treatment, corresponding to a mean improvement of 0.50 points. The paired pre/post comparison showed a statistically significant overall improvement in speech-language rating (paired t-test, t=-3.82, p=0.00021). Children with ASD showed a larger mean improvement than children with SLI (0.83 vs. 0.25 points), although baseline severity also differed between groups. The ASD subgroup had lower baseline speech-language scores, suggesting greater initial impairment and a larger potential range for observable improvement. Among stimulation parameters, 1.0 Hz stimulation was associated with the largest speech-language improvement in children with ASD. In the adjusted linear regression model, the ASD x 1.0 Hz interaction remained significant (coefficient=1.55, p=0.004). Assessments of children with ASD were higher in vocabulary comprehension, speech fluency, and sentence construction after a 1 Hz stimulation course, regardless of additional stimulation sites. This aligns with prior literature suggesting that 1 Hz Repetitive Transcranial Magnetic Stimulation (rTMS) of DLPFC can normalize hyperactive cortical oscillations and improve neuroplasticity in individuals with ASD (Casanova et al., 2020; Casanova et al., 2021; Kessler et al., 2016; Sokhadze et al., 2018; Tarhan et al., 2023). Stimulation at lower impulse frequencies did not show comparable effects in this dataset. This may be explained by subgroup size and clinical heterogeneity, but it may also reflect the broader theoretical problem of rTMS parameter selection. Recent reviews emphasize that rTMS outcomes are shaped not only by frequency, but by a wider parameter space including intensity, pulse number, intersession inter-

val, target engagement, and endogenous brain activity (Caulfield & Brown, 2022). Therefore, the present results should not be read as proof that 1.0 Hz is universally optimal, but rather as evidence that the ASD subgroup in this sample was more responsive to this protocol (Figure 1).

Figure 1
Speech-language improvement by stimulation frequency in patients with SLI and ASD. Bars show mean change in the structured speech-language rating from first to last visit; error bars show standard error (SE). Sample sizes are shown on the figure. The largest mean improvement was observed in children with ASD treated at 1.0 Hz

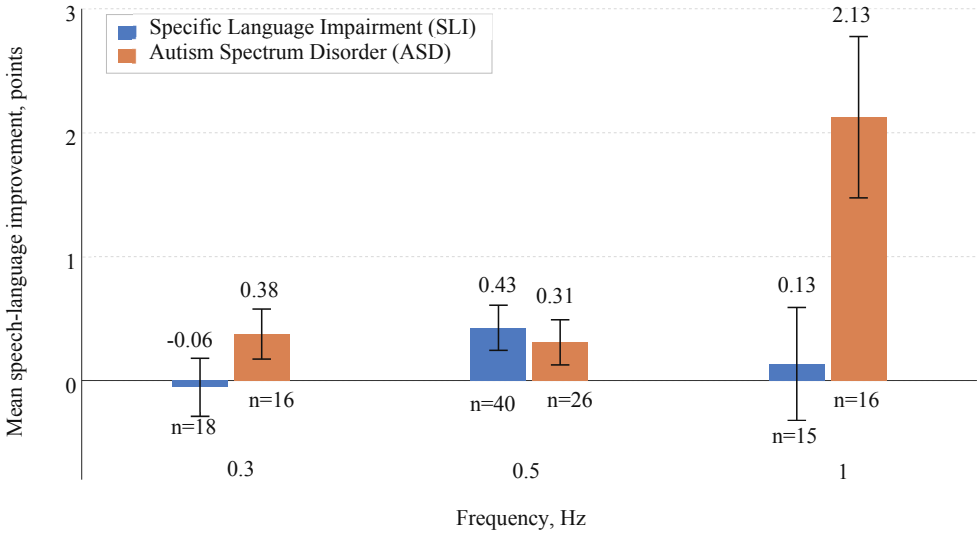

This interpretation is also consistent with network-level models of rTMS. Stimulation of DLPFC may influence not only local cortical excitability, but also distributed networks connected with executive, salience, language, and sensorimotor functions. Systematic review evidence indicates that rTMS can alter resting-state connectivity beyond the stimulated node, and that the classical low-frequency/high-frequency excitability heuristic does not fully explain distal network effects (Beynel et al., 2020). In this context, the interaction between ASD diagnosis and 1.0 Hz stimulation may reflect a better fit between the protocol and the functional network state of this subgroup, rather than a simple frequency effect.

Table 1
Cohort characteristics and speech-language severity by diagnosis

Diagnosis	N	Age, mean	Age, SD	Baseline score, mean	Final score, mean	Improvement, mean	Improvement, SD
ASD	58	5.14	1.89	2.57	3.4	0.83	1.73
SLI	73	4.66	1.80	4.16	4.41	0.25	1.27

In the ASD subgroup, mean improvement was 0.38 points at 0.3 Hz, 0.31 points at 0.5 Hz, and 2.13 points at 1.0 Hz. In the SLI subgroup, mean improvement was -0.06 points at 0.3 Hz, 0.43 points at 0.5 Hz, and 0.13 points at 1.0 Hz (Table 2). Thus, 1.0 Hz appeared to be the most effective frequency for children with ASD in this sample, whereas the frequency-related pattern was less clear in SLI. The small negative mean at 0.3 Hz in the SLI subgroup should not be interpreted as proof of harm, but it is consistent with the broader observation that poorly matched or weakly justified stimulation parameters may produce little benefit and, in individual cases, even minor setbacks.

Table 2
Speech-language improvement by frequency and diagnosis

Frequency, Hz	Diagnosis	N	Mean	SD	SE
0.3	ASD	16	0.375	0.806	0.202
0.3	SLI	18	-0.056	0.998	0.235
0.5	ASD	26	0.308	0.928	0.182
0.5	SLI	40	0.425	1.152	0.182
1	ASD	16	2.125	2.604	0.651
1	SLI	15	0.133	1.767	0.456

Preexisting delays in motor abilities were associated with slower speech-language development (β = -1.2028, p = 0.014), consistent with the interconnected nature of motor and language development (Hamilton, 2026). Integrating motor rehabilitation alongside TMS may enhance outcomes for this subgroup. Additionally, the number of TMS sessions was positively correlated with improvements in speech and language abilities scores (β = 0.4748, p < 0.001), which may support the theoretical cumulative effect of intervention, or benefit from sustained rhythmicity of the TMS course (Bethlehem et al., 2022). The model accounted for the time passed between sessions and measures.

Subset of patients with SLI that received LF-TMS on Broca and Wernicke areas expressed better language comprehension and production, with the in-group effects (β = 1.5176, p = 0.004 and β = 1.1497, p = 0.019), respectively. In the overall cohort, the largest mean improvement was observed in children who received DLPFC + Broca + Wernicke stimulation (0.84 points), followed by DLPFC + Broca stimulation (0.59 points), DLPFC-only stimulation (0.24 points), and DLPFC + Wernicke stimulation (0.07 points). These results are consistent with findings in aphasia patients, in whom stimulation of these regions facilitated recovery in language processing (Hamilton, 2026; Nasios et al., 2019; Yao et al., 2020). However, this difference has not shown to be statistically significant in between-group analysis, as well as in the results of participants from the ASD group (Figure 2).

Figure 2
Speech-language improvement by TMS stimulation target in SLI and ASD patients.
Bars show mean change in the structured speech-language rating from first to last visit; error bars show standard error (SE). Sample sizes (n) are shown on the figure. Target-specific findings should be interpreted cautiously because several subgroups were small.

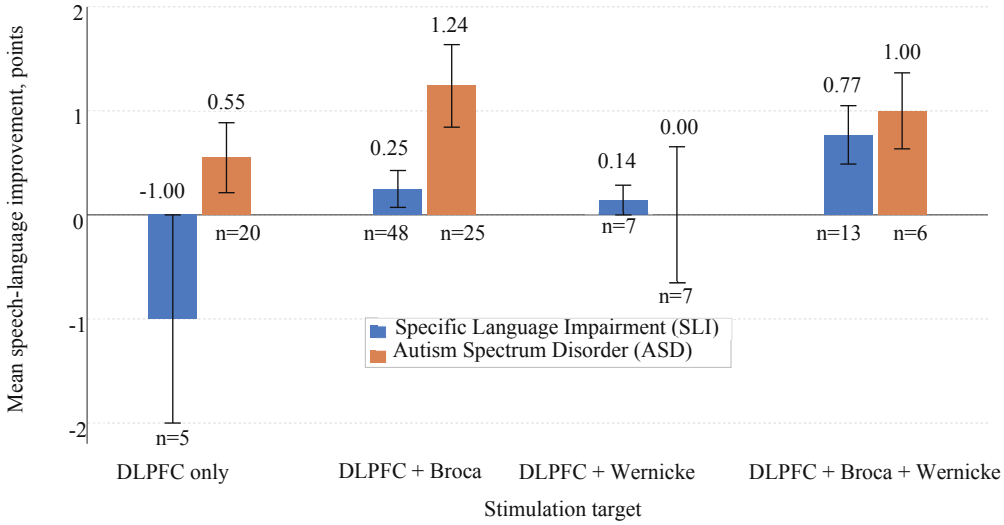

Patterns differed by diagnosis. In children with ASD, DLPFC + Broca stimulation was associated with the largest mean improvement (1.24 points), followed by DLPFC + Broca + Wernicke stimulation (1.00 point), DLPFC-only stimulation (0.55 points), and DLPFC + Wernicke stimulation (0.00 points). In children with SLI, the largest mean improvement was observed in the DLPFC + Broca + Wernicke group (0.77 points), followed by DLPFC + Broca (0.25 points), DLPFC + Wernicke (0.14 points), and DLPFC-only stimulation (-1.00 point) (Table 3). Due to the inequal distribution throughout target-by-diagnosis subgroups, these target-specific results should be interpreted cautiously.

Table 3
Speech-language improvement by stimulation target and diagnosis

Stimulation target	Diagnosis	N	Mean	SD	SE
DLPFC + Broca	ASD	25	1.24	1.99	0.40
DLPFC + Broca	SLI	48	0.25	1.23	0.18
DLPFC + Broca + Wernicke	ASD	6	1.00	0.89	0.37
DLPFC + Broca + Wernicke	SLI	13	0.77	1.01	0.28
DLPFC + Wernicke	ASD	7	0.00	1.72	0.66
DLPFC + Wernicke	SLI	7	0.14	0.38	0.14
DLPFC only	ASD	20	0.55	1.50	0.34
DLPFC only	SLI	5	-1.00	2.24	1.00

The overall pre/post change was statistically significant, but the magnitude and direction of improvements varied across diagnostic, frequency, and target subgroups. The adjusted linear model is summarized visually in Figure 3. The strongest positive association was observed for the ASD x 1.0 Hz interaction, while motor delays were associated with lower improvement. The relatively large variability observed in several subgroups should therefore be considered part of the result rather than only a statistical limitation. Brain stimulation effects are increasingly understood as state-dependent: the same external stimulation can have different consequences depending on ongoing oscillatory activity, connectivity, prior neural activity, and individual neurodevelopmental profile (Bergmann, 2018; Jannati et al., 2022). This framework is compatible with our observation that diagnosis, stimulation frequency, number of courses, and motor delays jointly influenced speech-language change.

Figure 3
Adjusted linear regression model of speech-language improvement.
Markers show regression coefficients in structured speech-language rating-score units, and horizontal bars show 95% confidence intervals. Positive coefficients indicate greater improvement in the structured speech-language rating. The model included diagnosis, stimulation frequency, ASD x 1.0 Hz interaction, number of completed courses, and motor delays

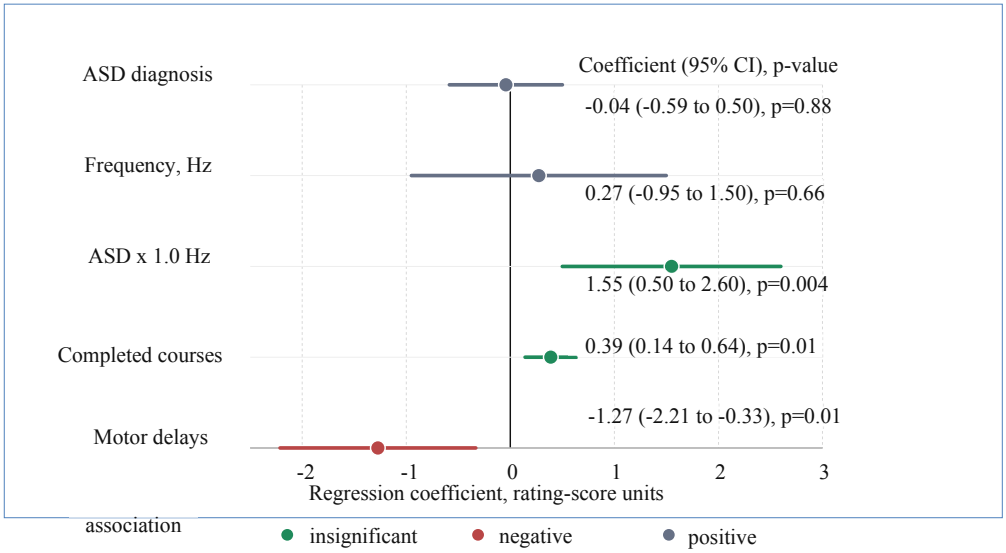

Conclusion

This study provides another argument for the therapeutic potential of LF-TMS for improving speech and language abilities in children with developmental delays. The analysis of the clinical data demonstrates that children with both ASD and SLI diagnoses may benefit from LF-TMS, but the outcomes varied significantly between the two populations. Practitioners are encouraged to rely on diagnostic and neurophysiological profiles of their patients to imply optimal individualized approaches to support and treatment.

A significant improvement in speech and language acquisition was observed in the ASD subset of our sample after 1 Hz TMS on bilateral DLPFC. This observation is consistent with both the literature and clinical practice, as 1 Hz is the most common lf-TMS frequency, as well as the one yielding results more consistently than sub-1 Hz protocols (Casanova et al., 2020; Casanova et al., 2021; Qu et al., 2022). Although the theoretical mechanism is hypothesised to be the same across lf-TMS protocols, our results suggest that a more intrinsic difference may take place instead of a capability to deliver more impulses. On the other hand, improvements in various measures, including speech and language metrics across different disorders and in healthy subjects, may be due to a mechanism non-specific to the condition (Kessler et al., 2016; Qu et al., 2022). More research involving the registry of occilatory and cortical connectivity biomarkers across various stimulation paradigms is highly encouraged. The additional stimulation of the language network nodes yielded conservative, yet noticeable enhancements of the treatment, especially within the subset of patients with SLI. In contrast, lf-TMS, which focused only on the DLPFC, has shown no observable effect in this subset of patients, underscoring the importance of considering the disorder's pathophysiology in the choice of protocol. Despite minimal improvements, the differences in observations across TMS parameters may deem implementation of the method to support the treatment of isolated language impairments a promising direction for future research (Hamilton, 2016).

Network-level models of rTMS suggest that stimulation effects may spread across connected regions and interact with distributed language, executive, and sensorimotor systems (Beynel et al., 2020). This framework may explain why a protocol that is useful in one diagnostic subgroup can be weak or unstable in another. Delays in motor development, on the other hand, were identified as a limiting factor influencing observed improvements in both groups. This finding is consistent with developmental and network-based accounts of language acquisition, in which motor development contributes to communicative experience, gesture, interaction with objects and people, and later speech-language development (Iverson, 2010; Leonard & Hill, 2014; Skipper et al., 2017). It is also consistent with evidence that speech perception and language functions recruit distributed motor-language networks rather than isolated classical language areas (Berent et al., 2015). From this perspective, motor delay may reduce the readiness of the broader motor-language system to benefit from stimulation, and integrating motor rehabilitation strategies with TMS may enhance therapeutic outcomes.

This study takes advantage of the increased use of TMS in clinical settings to explore possible improvements in current practices by analyzing existing data. Apart from the confirmation of the establishing protocol for support in ASD efficacy, the analysis revealed apparent under-performance of the sub-1 Hz protocols as well as added to the scarce data on application of TMS in SLI. We encourage clinical practitioners to consider recent studies and diagnostic profiles of patients in choice of the treatment and stimulation parameters. Measuring and collecting data would also be beneficial to establish standardized supporting approaches to various conditions. More controlled studies are needed to refine protocols and establish magnetic stimulation as an efficient tool for neurorehabilitation.

Acknowledgments

This research was funded by the Science Committee of the Ministry of Science and Higher Education of the Republic of Kazakhstan, grant number BR27198099.

Conflict of interest

The authors declare that they have no conflicts of interest.

Author contributions

Amir Baikatov: Conceptualization, Methodology, Formal Analysis, Visualization, Writing – Original draft, Writing – Review and Editing.

Dauren Zhumakhanov: Investigation, Data Curation, Resources, Project Administration, Writing – Review and Editing.

References

1. Arutiunian, V., Santhosh, M., Neuhaus, E., Borland, H., Tompkins, C., Bernier, R. A., et al. (2024). The relationship between gamma-band neural oscillations and language skills in youth with Autism Spectrum Disorder and their first-degree relatives. *Mol Autism, 15*(1), 21. https://doi.org/10.1186/s13229-024-00598-1
2. Bergmann, T. O. (2018). Brain State-Dependent Brain Stimulation. *Front Psychol, 9*, 2108. https://doi.org/10.3389/fpsyg.2018.02108
3. Berent, I., Brem, A., Zhao, X., Seligson, E., Pan, H., Epstein, J., et al. (2015). Role of the motor system in language knowledge. *Proc Natl Acad Sci U S A, 112*(7), 1983-1988. https://doi.org/10.1073/pnas.1416851112
4. Bethlehem, R. A. I., Seidlitz, J., White, S. R., Vogel, J. W., Anderson, K. M., Adamson, C., et al. (2022). Brain charts for the human lifespan. *Nature, 604*(7906), 525-533. https://doi.org/10.1038/s41586-022-04554-y
5. Beynel, L., Powers, J. P., & Appelbaum, L. G. (2020). Effects of repetitive transcranial magnetic stimulation on resting-state connectivity: A systematic review. *NeuroImage, 211*, 116596. https://doi.org/10.1016/j.neuroimage.2020.116596
6. Bruining, H., Hardstone, R., Juarez-Martinez, E., Sprengers, J., Avramiea, E. A., Simpraga, S., et al. (2020). Measurement of excitation-inhibition ratio in autism spectrum disorder using critical brain dynamics. *Sci Rep, 10*(1), 9195. https://doi.org/10.1038/s41598-020-65500-4
7. Casanova, M., Shaban, M., Ghazal, M., El-Baz, A., Casanova, E., & Sokhadze, E. (2021). Ringing Decay of Gamma Oscillations and Transcranial Magnetic Stimulation Therapy in Autism Spectrum Disorder. *Appl Psychophysiol Biofeedback, 46*, 161-173. https://doi.org/10.1007/s10484-021-09509-z
8. Casanova, M., Sokhadze, E., Casanova, E., & Li, X. (2020). Transcranial Magnetic Stimulation in Autism Spectrum Disorders: Neuropathological Underpinnings and Clinical Correlations. *Semin Pediatr Neurol, 35*, 100832. https://doi.org/10.1016/j.spen.2020.100832
9. Caulfield, K., & Brown, JC. (2022). The Problem and Potential of TMS' Infinite Parameter Space: A Targeted Review and Road Map Forward. *Front Psychiatry, 13*, 867091. https://doi.org/10.3389/fpsyt.2022.867091
10. Doucet, G. E., Kruse, J. A., Eden, N., Goffman, L., & McGregor, K. K. (2025). Initial evidence of altered functional network connectivity in children with developmental language disorder. *Brain Lang, 270*, 105637. https://doi.org/10.1016/j.bandl.2025.105637
11. Gao, L., Wang, C., Song, X., Tian, L., Qu, Z., Han, Y., et al. (2022). The Sensory Abnormality Mediated Partially the Efficacy of Repetitive Transcranial Magnetic Stimulation on Treating Comorbid Sleep Disorder in Autism Spectrum Disorder Children. *Front Psychiatry, 12*, 820598. https://doi.org/10.3389/fpsyt.2021.820598
12. Hamilton, RH. (2026). Noninvasive Brain Stimulation in Translational Cognitive Neuroscience: Applications in Aphasia and Beyond. *Neurology, 106*(5), e214611. https://doi.org/10.1212/WNL.0000000000214611
13. Hartwigsen, G., & Volz, L. J. (2021). Probing rapid network reorganization of motor and language functions via neuromodulation and neuroimaging. *NeuroImage, 224*, 117449. https://doi.org/10.1016/j.neuroimage.2020.117449
14. Hsu, H. J., & Bishop, D. V. M. (2014). Sequence-specific procedural learning deficits in children with specific language impairment. *Dev Sci, 17*(3), 352-365. https://doi.org/10.1111/desc.12125
15. Iverson, J. M. (2010). Developing language in a developing body: the relationship between motor development and language development. *J Child Lang, 37*(2), 229-261. https://doi.org/10.1017/S0305000909990432
16. Jannati, A., Oberman, L. M., Rotenberg, A., & Pascual-Leone, A. (2022). Assessing the mechanisms of brain plasticity by transcranial magnetic stimulation. *Neuropsychopharmacology, 48*(1), 191-208. https://doi.org/10.1038/s41386-022-01453-8
17. Kessler, K., Seymour, R. A., & Rippon, G. (2016). Brain oscillations and connectivity in autism spectrum disorders (ASD): new approaches to methodology, measurement and modelling. *Neurosci Biobehav Rev, 71*, 601-620. https://doi.org/10.1016/j.neubiorev.2016.10.002
18. Kujala, T., & Leminen, M. (2017). Low-level neural auditory discrimination dysfunctions in specific language impairment: A review on mismatch negativity findings. *Dev Cogn Neurosci, 28*, 65-75. https://doi.org/10.1016/j.dcn.2017.10.005
19. Larson, C., Thomas, H. R., Crutcher, J., Stevens, M. C., & Eigsti, I. M. (2023). Language Networks in Autism Spectrum Disorder: A systematic review of connectivity-based fMRI studies. *Rev J Autism Dev Disord, 12*(1), 110-137. https://doi.org/10.1007/s40489-023-00382-6
20. Leonard, H. C., & Hill, E. L. (2014). Review: The impact of motor development on typical and atypical social cognition and language: a systematic review. *Child Adolesc Ment Health, 19*(3), 163-170. https://doi.org/10.1111/camh.12055
21. Mottron, L., & Bzdok, D. (2020). Autism spectrum heterogeneity: fact or artifact? *Mol Psychiatry, 25*(12), 3178-3185. https://doi.org/10.1038/s41380-020-0748-y
22. Nasios, G., Dardiotis, E., & Messinis, L. (2019). From Broca and Wernicke to the Neuromodulation Era: Insights of Brain Language Networks for Neurorehabilitation. *Behav Neurol, 2019*, 9894571. https://doi.org/10.1155/2019/9894571
23. Noda, Y. (2021). Potential Neurophysiological Mechanisms of 1Hz-TMS to the Right Prefrontal Cortex for Depression: An Exploratory TMS-EEG Study in Healthy Participants. *J Pers Med, 11*(2), 68. https://doi.org/10.3390/jpm11020068
24. Qu, X., Wang, Z., Cheng, Y., Xue, Q., Li, Z., Li, L., et al. (2022). Neuromodulatory effects of transcranial magnetic stimulation on language performance in healthy participants: Systematic review and meta-analysis. *Front Hum Neurosci, 16*, 1027446. https://doi.org/10.3389/fnhum.2022.1027446
25. Scheper, A., Rosenfeld, C., & Dubljevic, V. (2022). The public impact of academic and print media portrayals of TMS: shining a spotlight on discrepancies in the literature. *BMC Med Ethics, 23*(1), 25. https://doi.org/10.1186/s12910-022-00760-5
26. Skipper, J. I., Devlin, J. T., & Lametti, D. R. (2017). The hearing ear is always found close to the speaking tongue: Review of the role of the motor system in speech perception. *Brain Lang, 164*, 77-105. https://doi.org/10.1016/j.bandl.2016.10.004

27. Sokhadze, E. M., Casanova, E. L., Li, X., Coben, R., Wang, Y., Li, L., et al. (2018). Exploratory Study of rTMS Neuromodulation Effects on Electrocortical Functional Measures of Performance in an Oddball Test and Behavioral Symptoms in Autism. *Front Syst Neurosci, 12*, 20. https://doi.org/10.3389/fnsys.2018.00020

28. Tarhan, N., Aydogdu, M., Ibadi, Y., Gokten, E., & Metin, B. (2023). Low-frequency prefrontal cortex magnetic stimulation improves autism spectrum disorder symptoms: A pilot study. *J Neurobehav Sci, 10*, 3-7. https://doi.org/10.4103/jnbs.jnbs_24_22

29. Toolan, C., Holbrook, A., Schlink, A., Shire, S. Y., Brady, N., & Kasari, C. (2021). Using the Clinical Global Impression Scale to Assess Social Communication Change in Minimally Verbal Children with Autism Spectrum Disorder. *Autism Res, 15*, 284-295. https://doi.org/10.1002/aur.2638

30. Ullman, M. T., Earle, F. S., Walenski, M., & Janacsek, K. (2020). The Neurocognition of Developmental Disorders of Language. *Annu Rev Psychol, 71*(1), 389-417. https://doi.org/10.1146/annurev-psych-122216-011555

31. Yao, L., Zhao, H., Shen, C., Liu, F., Qiu, L., & Fu, L. (2020). Low-Frequency Repetitive Transcranial Magnetic Stimulation in Patients With Poststroke Aphasia: Systematic Review and Meta-Analysis of Its Effect Upon Communication. *J Speech Lang Hear Res, 63*(11), 3801-3815. https://doi.org/10.1044/2020_JSLHR-19-00077

Information about the authors:

Amir Baikatov – M.Sc., Researcher, Brain Institute, Al-Farabi Kazakh National University (Almaty, Kazakhstan, e-mail: amir.sapar@zoho.com).

Dauren Zhumakhanov – M.Sc., Chief Physician, Neurolab Neurorehabilitation Center (Almaty, Kazakhstan, e-mail: daurjuma@gmail.com).

Received 14 January 2026;
received in revised form 21 June 2026;
accepted 26 June 2026

IRSTI 34.31.15; 34.31.37 https://doi.org/10.26577/IJBCh20261913

G. Doktyrbay[1*], S.S. Kenzhebayeva[1], S.D. Atabayeva[1], S.A. Shoinbekova[1], S.Sh. Asrandina[1], M.A. Abdulzhanova[1], A. Rsatayeva[1], A. Distelfeld[2]

[1]Al-Farabi Kazakh National University, Almaty, Kazakhstan
[2]Institute of Evolution, University of Haifa, Haifa, Israel
*e-mail:gulina.kaznu@gmail.com

GAMMA IRRADIATION–INDUCED VARIATION IN GRAIN PROTEIN CONTENT AND DAYS FROM SOWING TO HEADING IN M_5 MUTANT LINES OF SPRING WHEAT (CV. ERITROSPERMUM-35)

Abstract: Bread wheat (*Triticum aestivum* L.) is a major staple crop providing essential calories for human diets. However, intensive breeding for yield has reduced genetic diversity for quality traits, including grain protein content (GPC). Induced mutagenesis offers an effective strategy to broaden the genetic base and generate novel alleles affecting agronomic traits. In this study, M_5 mutant lines of the spring wheat cultivar Eritrospermum-35 were developed through gamma irradiation at 100 Gy and 200 Gy. Lines were evaluated for variation in GPC and days from sowing to heading under controlled greenhouse conditions. GPC was measured using near-infrared reflectance spectroscopy (NIR), and allelic variation at the candidate gene Eps-Am1 was analyzed using PCR-based markers. Substantial variation in GPC was observed. The 100 Gy lines showed GPC values ranging from 12.60% to 14.43% (mean 13.56 ± 0.57%), whereas the 200 Gy lines had a mean GPC of 13.76 ± 0.63%. Eleven mutant lines (37%) exhibited significantly higher GPC (5.7–11.0%) than the parent. Importantly, the increase in GPC was not associated with a reduction in thousand kernel weight; TKW values were higher in irradiated lines compared with the parent. Days to heading differed between treatments: 100 Gy lines headed earlier, while 200 Gy lines showed delayed heading. Molecular screening identified new alleles of *Eps-A^m1*, with allele carriers generally exhibiting earlier heading. Overall, gamma irradiation generated valuable genetic variation for improving grain protein content and adaptive traits in spring wheat.

Keywords: gamma irradiation, grain protein content, days to heading, thousand kernel weight, spring wheat, *Eps-A^m1*, mutation breeding.

Introduction

Bread wheat (*Triticum aestivum* L.) is a major cereal crop of global importance and plays a central role in food and nutrition security (Shewry & Hey, 2015). In many developing countries, wheat-based foods dominate the diet, providing a substantial portion of daily caloric intake as well as essential plant proteins and micronutrients (Guzmán et al., 2019). However, wheat-based diets often lack sufficient protein quality and micronutrients, leading to “hidden hunger” and contributing to malnutrition-related diseases and impaired development (Bouis & Saltzman, 2016).

Grain protein content (GPC) represents a key determinant of wheat grain quality, as it influences both nutritional characteristics and processing performance, particularly baking properties (Sun et al., 2025). However, efforts to enhance GPC through conventional breeding remain constrained by substantial environmental effects (Rybicki et al., 2016), the well-documented inverse relationship between protein concentration and grain yield, limited genetic diversity in modern germplasm (Simmonds, 1995), and the complex polygenic nature of this trait. Together, these factors complicate the development of high-protein wheat cultivars (Welch & Graham, 2004), and complex polygenic inheritance involving genotype-by-environment interactions (Marcotuli et al., 2025). These factors make selection for enhanced grain protein particularly challenging (Shewry, 2009).

In addition to protein concentration, thousand kernel weight (TKW) represents a key yield-related trait reflecting grain size and overall productivity in wheat. Improvement of grain protein content is frequently associated with a potential trade-off with

kernel weight and yield components. Therefore, simultaneous evaluation of GPC and TKW is essential to determine whether enhanced protein levels are accompanied by unintended reductions in grain weight.

Adaptation to diverse or changing environments requires flexible control of developmental traits such as heading time (Kamran et al., 2014). In wheat, heading time is primarily regulated by three genetic systems: vernalization response mediated by VRN genes (Allard et al., 2012), photoperiod sensitivity controlled by PPD genes (Kitagawa et al., 2012), and earliness per se (*Eps*) genes that fine-tune heading independently of vernalization and photoperiod (Ochagavía et al., 2019). *Eps* genes allow wheat to synchronize reproductive development with favorable environmental windows, supporting yield stability (Alvarez et al., 2016). Among these, the *Eps-Am1* locus has been identified as an important determinant of heading time, spike development, and yield components (Appendino & Slafer, 2003). In the present study, *Eps-Am1* was selected as a candidate gene because it represents a well-characterized intrinsic earliness locus regulating heading time independently of vernalization and photoperiod pathways. Since the experiments were conducted under controlled greenhouse conditions minimizing environmental variation, differences in heading time were expected to reflect underlying genetic factors. Targeting *Eps-Am1* allowed us to examine whether gamma irradiation induced allelic variation at a major developmental regulator associated with intrinsic earliness. Additional studies have shown that *Eps* genes contribute significantly to local ecological adaptation (Horváth et al., 2023; Zhang et al., 2022).

Induced mutagenesis is a powerful approach for expanding genetic diversity by creating novel alleles not available in natural germplasm (Shu et al., 2012). Both physical and chemical mutagens are widely used to generate beneficial mutants for crop improvement (Chaudhary et al., 2019). Gamma irradiation, especially using a 60 Co source, is one of the most effective and widely applied physical mutagens in plant breeding (Spencer-Lopes et al., 2018). It has been responsible for developing numerous improved crop varieties across the world, including cereals (Ahloowalia et al., 2004). In wheat, gamma irradiation has successfully increased variability in agronomic traits (Kenzhebayeva et al., 2017), yield components (Maree et al., 2025), grain micronutrient content (Kenzhebayeva et al., 2018b), and grain quality traits (Kenzhebayeva et al., 2013). The biological effects of gamma rays, including increased mutation frequency and altered gene expression, have been well documented (Zulfiqar et al., 2021). Gamma-induced mutants are often screened in early generations, and promising genotypes are advanced for further evaluation (Tahir et al., 2023).

Several studies have also demonstrated increases in protein content, gluten strength, and other quality parameters in wheat mutants developed using gamma irradiation (Köksel et al., 1998; von Well et al., 2023). Mutation breeding continues to play an important role in wheat research, especially for traits with limited natural variation (Holme et al., 2019). Evaluation of mutant lines under diverse environments provides opportunities to identify novel alleles affecting grain quality and developmental traits (Oury et al., 2006).

The local spring wheat cultivar Eritrospermum-35 is an important variety in Kazakhstan, but like many modern cultivars, it has limited genetic variability for some agronomic and quality traits. Previous research in Kazakhstan has emphasized the need to expand genetic diversity through modern breeding and mutagenesis approaches (Kenzhebayeva et al., 2018a). Studies on wheat adaptation in Central Asia further highlight the importance of improving both nutritional quality and resilience traits. Kazakhstan wheat breeding programs continue to explore new genetic sources for improving grain quality, stress tolerance, and yield potential (Kenzhebayeva et al., 2022; Kenzhebayeva et al., 2015).

Recent advances in wheat genomics have provided new tools for understanding complex traits such as protein content and flowering time (Song et al., 2023). The use of molecular markers accelerates the identification of key alleles and supports marker-assisted selection in breeding programs (Appels et al., 2018). Wheat genome research has shed light on the structure and evolution of polyploid wheat, improving the efficiency of genetic analysis (Uauy et al., 2006). Regulatory genes, including transcription factors influencing grain protein content, have also been identified (Velu et al., 2018). Improving wheat nutritional quality remains a global objective, particularly in the context of food security challenges (Gupta et al., 2020).

Biofortification through genetic and breeding approaches is recognized as a promising strategy to address micronutrient deficiencies worldwide (Velu et al., 2011). Wheat is a primary target for biofortification due to its central role in human diets (Velu et al., 2014). Enhancing grain zinc and iron concentrations, along with improving protein quality, is essential for combating hidden hunger. Wheat adaptation studies in Kazakhstan further support the need for breeding

nutritionally enhanced cultivars suited to local condition. Consequently, enhancing grain nutritional traits continues to be a central objective of both international and regional wheat improvement programs (Wan Teng et al., 2022).

Therefore, the objective of this study was to evaluate gamma irradiation–induced variation in grain protein content and heading time in M_5 mutant lines of spring wheat (cv. Eritrospermum-35), and to assess allelic variation in the candidate gene *Eps-A^{m}1* associated with heading traits.

Materials and methods

Development of M_5 mutant lines through gamma irradiation. The experimental material included M_5 mutant lines obtained from the local spring bread wheat cultivar *Eritrospermum-35* (*Triticum aestivum* L.). Dry seeds were exposed to gamma radiation at doses of 100 and 200 Gy using a ^60Co source at the Kazakh Nuclear Centre in accordance with established protocols for mutation induction in cereal crops (Ahloowalia et al., 2004; Zhang et al., 2022). The irradiated seeds were then sown to produce the M_2 generation.

Subsequent generations (M_2–M_4) were cultivated under field conditions at the Kazakh Research Institute of Agriculture and Plant Growing (Almaty, Kazakhstan). Selection of superior plants was performed mainly based on yield-related parameters, including grain weight per plant (GWP) and grain weight per main spike (GWS), in comparison with the non-irradiated parental cultivar grown under identical conditions. Following harvest of the M_5 generation, fifteen lines from each radiation treatment (100 and 200 Gy) were selected for further evaluation of grain protein content, Thousand kernel weight and flowering time. These mutant lines, together with the parental cultivar Eritrospermum-35, were used for subsequent analyses

Field and greenhouse experiments. To evaluate yield performance and grain quality traits, the M_5 mutant lines together with the parental cultivar Eritrospermum-35 were cultivated in replicated field trials. The experiment was conducted at the Institute for Cereal Crops Improvement, Department of Molecular Biology and Ecology of Plants, Tel Aviv University. A randomized design with three replications was applied. Each experimental unit consisted of three rows (2 m in length and 1.2 m in width) with 20 cm spacing between rows and a planting density of 30 seeds per row. Standard agronomic management practices, including fertilization, weed control and plant protection, were applied according to local recommendations. Flowering time assessment was performed under controlled greenhouse conditions to reduce environmental variation. Seeds were initially germinated on moist filter paper, and four-day-old seedlings were transferred to plastic pots (16 cm upper diameter, 12 cm lower diameter, 18 cm height) containing 2 kg of soil substrate.

Plants were maintained at 23°C under a 16 h photoperiod in a naturally illuminated greenhouse. Soil moisture was maintained at approximately 70% of field capacity. Thirty plants were grown per pot, and each genotype was represented by three independent biological replicates.

Grain protein content determination. The GPC was measured on whole grains using near-infrared reflectance (NIR) spectroscopy. For each M_5 line and the Eritrospermum-35 parent, three subsamples were analyzed using a ZX50 Portable Grain Analyzer (Zeltex, Hagerstown, MD, USA) with proprietary calibration software. Each subsample consisted of 25 grains per line. Results are expressed as percentage of protein in the grain on a mass basis. For the Eritrospermum-35 mutant population, summary statistics (minimum, maximum, mean and standard deviation) of GPC were calculated separately for the 100 Gy and 200 Gy treatments. Superior high-protein lines were identified using analysis of variance (ANOVA) followed by pairwise comparisons.

Thousand kernel weight determination. Thousand kernel weight (TKW) was determined according to standard grain analysis procedures. For each genotype, mature and healthy grains were randomly selected after harvest, and measurements were performed in three biological replicates. TKW values were expressed in grams as mean ± standard deviation (SD). All genotypes were grown under field conditions during the same growing season and harvested at physiological maturity to ensure reliable comparison of TKW values.

Molecular analysis of Eps-A^{m}1. To investigate the genetic basis of flowering time and the earliness per se candidate gene *Eps-A^{m}1* was analyzed by PCR. Total genomic DNA was extracted from young leaf tissue of 10-day-old seedlings using a modified CTAB method adapted from previously published protocols and optimized according to Kenzhebayeva et al. (2016). DNA pellets were dried and resuspended in TE buffer, and DNA concentration was determined using a Bio Photometer (Eppendorf AG, Hamburg, Germany). For *Eps-A^{m}1*, candidate gene-specific primers *Eps-A^{m}1* -F (5'-CACATATCTGGCACCCACA-3') and *Eps-A^{m}1* -R (3'-TGCTCAT-

GAGTTTTCC-TCTGAA-5') (Eurofins Genomics, Germany) were used to amplify a fragment of around 780 bp associated with the presence of the *Eps-A^{m}1* allele (Kenzhebayeva et al., 2016). PCR amplification was performed under the following conditions: initial denaturation at 95°C for 5 min; followed by 37 cycles of denaturation at 94°C for 30 s, annealing at 57°C for 30 s, and extension at 72°C for 30 s; with a final extension at 72°C for 5 min. PCR products were separated on 1% agarose gels and visualized under UV light using a Gel Documentation System (the ENDURO™ GDS, Labnet International, Inc). The presence or absence of the diagnostic bands for *Eps-A^{m}1* was recorded for each Eritrospermum-35 M_5 mutant line and the parent, and the frequency of alleles in the mutant populations was compared between the 100 Gy and 200 Gy treatments.

Recording of heading time. Heading time was recorded in the greenhouse experiment as the number of days from sowing to spike emergence (heading). Pots were inspected every two days, and heading date was defined as the day when spikes first emerged from the flag leaf sheath. For each genotype, the mean heading time (days from sowing) was calculated based on three replicated pots. In addition, the number of main spikes per pot at heading was recorded as an indicator of tillering and reproductive development. For Eritrospermum-35, summary statistics of heading time (mean ± standard deviation) were calculated for the parent, the 100 Gy mutant lines, and the 200 Gy mutant lines.

Statistical analysis. All data were analyzed using standard statistical procedures. The GPC data were evaluated by one-way analysis of variance (ANOVA) to test the effect of irradiation dose (parent vs 100 Gy vs 200 Gy) within the Eritrospermum-35 background. Coefficients of variation (CV, %) were calculated to assess the relative variability of GPC in each group of lines. Multiple comparisons of mutant lines with the parent were performed using appropriate post hoc tests (e.g. Dunnett's test), and a significance level of $p \leq 0.05$ was considered statistically significant. For flowering time, mean values and standard deviations were calculated for the parent and the 100 Gy and 200 Gy mutant populations. Differences between means were interpreted considering the presence or absence of *Eps-A^{m}1* alleles. Frequency distributions and boxplots of GPC and flowering time are presented to visualize the response of the parent and mutant populations and to facilitate interpretation of irradiation effects on the studied traits.

Results and discussion

Gamma-Induced Variation in Grain Protein Content of Eritospermum-35 M_5 Mutant Line. The population derived from the 100 Gy treatment displayed protein values between 5.60% and 14.43%, with a mean of 13.56 ± 0.57% (n = 45). Lines exposed to 200 Gy showed a marginally higher average GPC (13.76 ± 0.63%). Compared with the parental cultivar (13.27 ± 0.31%), eleven mutant genotypes (37%) demonstrated an increase in protein concentration ranging from 5.7% to 11.0%.

Among the most promising high-protein genotypes were lines 108(1), 118(3), 135(1), 156(1), 140(2), 149(2), 150(7), 152(5), 153(6), 153(7) and 153(8). The coefficient of variation for GPC in Eritrospermum-35 mutant lines was 4.2% for the 100 Gy population and 4.58% for the 200 Gy population, indicating a moderate level of variability in GPC within each Gy group. The boxplots (Figure 1. a, b) clearly illustrate that both irradiation doses increased the spread of GPC values relative to the parent, with several outlier lines exceeding the parental mean by more than one standard deviation.

Statistical evaluation using one-way ANOVA demonstrated that irradiation dose significantly influenced GPC levels ($p \leq 0.05$). Pairwise comparisons indicated that both irradiated populations differed from parental control, and irradiation explained a considerable proportion of total phenotypic variation in protein content (Figure 1).

Gamma irradiation induced substantial variation in grain protein content (GPC) among M5 lines, consistent with earlier findings that mutagenesis generates novel alleles affecting grain quality. Both 100 Gy and 200 Gy groups showed increased mean GPC relative to the parent (Table 1). In addition to protein content, thousand kernel weight (TKW) was evaluated to assess the potential impact of irradiation on grain size and yield-related traits. The mutant populations exhibited higher mean TKW values (47.19 ± 8.54 g for 100 Gy and 48.68 ± 5.95 g for 200 Gy) compared with the parent cultivar (34.19 ± 0.32 g). Importantly, the increase in GPC was not accompanied by a reduction in kernel weight, suggesting that protein enhancement did not result in an evident yield penalty. Analysis of variance indicated a significant effect of irradiation dose on TKW ($p \leq 0.05$). These results indicate that gamma irradiation generated favorable combinations of quality and agronomic traits in the Eritrospermum-35 mutant lines.

Figure 1
Grain protein content (GPC) distribution in the parental cultivar Eritrospermum-35 and in M_5 mutant lines generated after exposure to 100 Gy and 200 Gy gamma irradiation (b) shows box-and-whisker plots representing median values, interquartile ranges and extreme data points for each treatment group

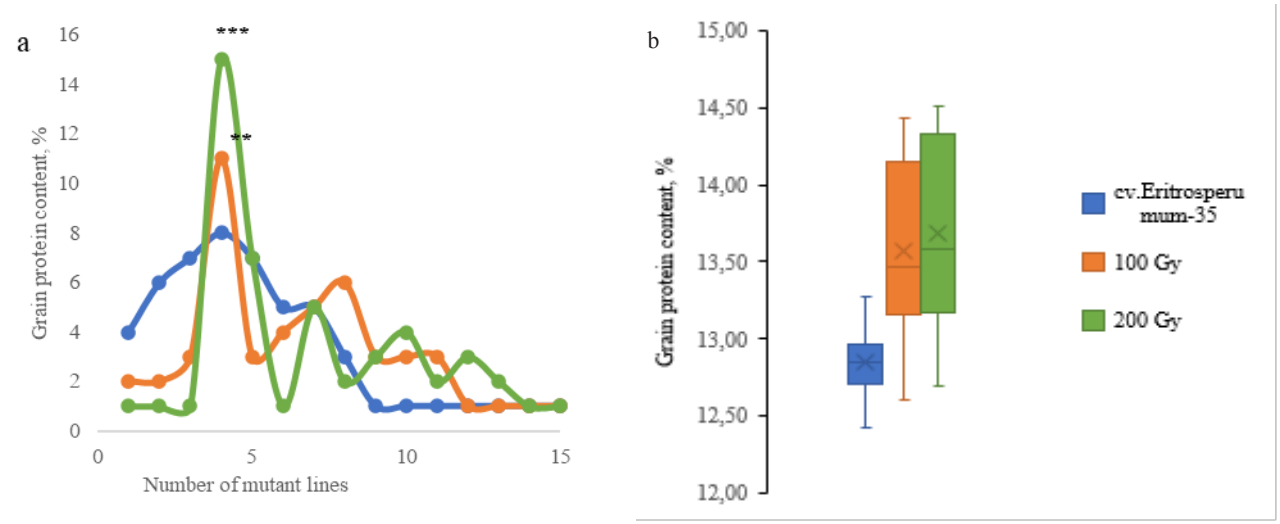

Table 1
Mean values (± SD) of grain protein content (GPC) and thousand kernel weight (TKW) in parental cultivar and M_5 mutant lines of Eritrospermum-35 developed under different gamma irradiation doses

Genotype	Grain protein content, % on db	TKW, g
Eritrospermum-35 (parent)	13.27 ± 0.31	34.19 ±0.32
Eritrospermum-35 M_5 mutant lines (100 Gy)	13.56 ± 0.57	47.19 ±8.54
Eritrospermum-35 M_5 mutant lines (200 Gy)	13.76 ± 0.63	48.68 ±5.95

Gamma irradiation induced substantial variation in GPC among M_5 lines, consistent with earlier findings that mutagenesis generates novel alleles affecting grain quality. Both 100 Gy and 200 Gy groups showed increased mean GPC relative to the parent (Table 1).

Variation in days to heading in Eritrospermum-35 mutant lines. Days to heading showed clear differences between the parental cultivar and the Eritrospermum-35 mutant populations (Table 2). The parent exhibited a mean heading time of 106 ± 8.13 days from sowing to spike emergence under greenhouse conditions. The 100 Gy-treated M_5 lines headed substantially earlier, with a mean of 88 ± 10.41 days, corresponding to an advance of approximately 18 days relative to the parent. In contrast, the 200 Gy-treated lines headed later, with a mean of 114 ± 5.45 days, about 8 days later than the parent.

Table 2
Days to heading (mean ± SD) in the parental cultivar and M_5 mutant lines of Eritrospermum-35 developed under different gamma irradiation doses

Genotype	Number of lines	Days to heading (mean ± SD)
Eritrospermum-35 (parent)	1	106 ± 8.13
Eritrospermum-35 M_5 mutant lines (100 Gy)	15	88 ± 10,41
Eritrospermum-35 M_5 mutant lines (200 Gy)	15	114 ± 5.45

Eritrospermum-35 mutants showed strong shifts in days to heading. Early heading at 100 Gy aligns with observations that moderate irradiation doses often generate beneficial developmental mutations (Chaudhary, 2019; von Well et al., 2023). In contrast, delayed heading at 200 Gy corresponds to findings that higher irradiation doses cause broader genomic perturbations.

Molecular characterization of Eps-A^m1 alleles. Molecular analysis revealed differences in allelic

composition at the *Eps-A^{m}1* locus between the parent cultivar Eritrospermum-35 and its M_5 mutant lines. For the *Eps-A^{m}1* candidate gene, a relatively high frequency of the diagnostic PCR fragment was found in the Eritrospermum-*35* 100 Gy-dose mutant lines. Sex out of fifteen 100 Gy lines (66.7%) carried the *Eps-A^{m}1* allele, including lines 105(1); 118(1); 118(2); 136(1); 140(3) and 232(1). In the 200 Gy mutant lines, the *Eps-A^{m}1* allele was not present. These results indicate that 100 Gy dose was more efficient than the 200 Gy dose in generating allelic variation at *Eps-A^{m}1* in Eritrospermum-*35* mutant populations.

Figure 2
Agarose gel electrophoresis of PCR amplification products of the Eps-Am1 gene.
M – 100 bp DNA ladder; lane 1 – Eritospermum-35 (parent); lanes 2-16 – M_5 mutant lines (200 Gy) [105(1), 108(1), 113(1), 113(5), 118(1), 118(2), 118(3), 135(1), 136(1), 138(6), 140(2), 140(3), 140(4), 232(1) and 242(2)]

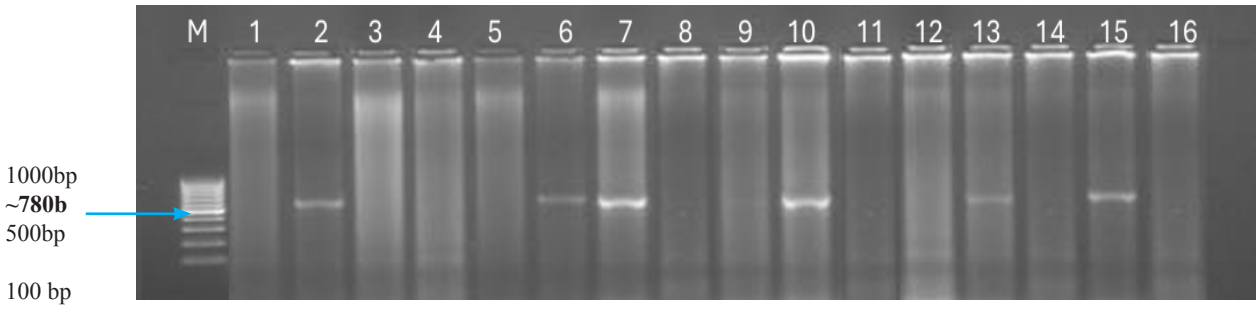

The frequency distribution of days to heading (not shown) demonstrated a clear shift toward earlier heading in the 100 Gy population and toward delayed heading in the 200 Gy population. Lines carrying the Eps-Am1 allele tended to head 12–28 days earlier than the parent, depending on genotype and irradiation dose, confirming the contribution of this locus to intrinsic earliness. The presence of early-heading *Eps-A^{m}1* alleles, combined with enhanced GPC, supports their potential breeding value, especially in environments prone to heat and drought stress (Appendino & Slafer, 2003).

Treatment of Eritrospermum-35 seeds with gamma radiation at 100 and 200 Gy led to the formation of M_5-derived mutants characterized by substantial variation in both grain protein content and heading time. These findings confirm that induced mutagenesis is an effective strate Gy to broaden genetic variability for important agronomic and quality traits in locally adapted wheat varieties (Chaudhary et al., 2019).

An increased grain protein content was detected in a considerable number of M_5 mutant lines, particularly within the 100 Gy and 200 Gy treatments, compared with the parental cultivar. The occurrence of these high-protein genotypes indicates that gamma irradiation may have induced genetic alterations influencing nitrogen assimilation, remobilization efficiency, or protein accumulation in the grain (Maree et al., 2025). Although breeding for high GPC is often hampered by its negative correlation with yield, the mutant lines in this study were selected from earlier generations based on yield components, indicating that at least some of the high-protein lines may maintain acceptable productivity.

The observed variation in days to heading among Eritrospermum-35 mutant lines has important implications for adaptation and yield stability. Earlier heading can help wheat escape terminal heat and drought stress in continental climates, whereas slightly later heading may be advantageous in cooler or more humid regions (Alvarez et al., 2016; Ochagavía et al., 2019). The 100 Gy mutant population showed generally earlier heading than the parent, whereas the 200 Gy lines tended to head later, suggesting that different sets of mutations affecting developmental regulators were recovered in the two irradiated populations. The molecular data suggest that allelic variation at *Eps-A^{m}1* contributed to these differences. In particular, the higher frequency of the *Eps-A^{m}1* allele in the 100 Gy population is consistent with the reduced days to heading in these lines.

The *Eps* genes are believed to control intrinsic earliness by affecting developmental rates after vernalization and photoperiod requirements are satisfied (Appendino & Slafer, 2003). Thus, the appearance of novel *Eps-A^{m}1* alleles in the Eritrospermum-35 mutant lines likely enabled fine-tuning of heading time independently of external cues. The PCR products observed in Figure 2 confirm that irradiation generated additional allelic variants at this locus.

From a breeding perspective, the combination of enhanced GPC, favorable heading time and novel alleles at *Eps-Am1* makes the Eritrospermum-35 M_5 mutant lines valuable genetic resources. High-protein, early-heading lines are particularly attractive for regions where short growing seasons and climatic stresses limit wheat productivity and quality. Such lines could be used directly as mutant varieties after agronomic evaluation or as donors in crossing programs to transfer desirable alleles into elite breeding lines (von Well et al., 2023).

Overall, the study highlights the potential of gamma irradiation and mutation breeding for improving both grain quality and adaptation traits in spring wheat. Further work should focus on (i) detailed phenotypic characterization of the most promising mutant lines in multi-environment field trials, (ii) fine mapping of the novel *Eps-A^m1* alleles and (iii) integration of mutation-derived alleles into marker-assisted selection schemes for spring wheat improvement.

Conclusions

Gamma irradiation of Eritrospermum-35 seeds at 100 Gy and 200 Gy generated M_5 mutant lines exhibiting significant variation in grain protein content (GPC), thousand kernel weight (TKW), and flowering time. A considerable proportion of mutant lines showed GPC values 5.7–11.0% higher than the parental cultivar, demonstrating the effectiveness of induced mutagenesis for improving wheat grain nutritional quality.

Importantly, the increase in GPC was not accompanied by a reduction in grain weight. Both irradiation treatments resulted in significantly higher mean TKW compared with the parent (34.19 ± 0.32 g), reaching 47.19 ± 8.54 g at 100 Gy and 48.08 ± 5.95 g at 200 Gy. Analysis of variance confirmed a significant effect of irradiation dose on TKW, indicating favorable combinations of quality and yield-related traits. The 100 Gy population headed earlier (88 ± 10.41 days) than the parent (106 ± 8.13 days), whereas the 200 Gy population headed later (114 ± 5.45 days), suggesting dose-dependent shifts in developmental timing. Molecular analysis revealed novel allelic variation at the *Eps-A^m1* locus, with the 100 Gy treatment showing greater allelic diversity. Lines carrying the *Eps-A^m1* allele tended to head 12–28 days earlier than the parental genotype.

Overall, M_5 mutant lines combining enhanced GPC, increased TKW, modified days to heading, and favorable allelic variation represent promising material for breeding high-quality and well-adapted spring wheat cultivars for Kazakhstan and similar environments.

Acknowledgments

The authors sincerely thank Prof. Assaf Distelfeld and his research team at the Institute for Cereal Crops Improvement, Tel Aviv University, for providing greenhouse facilities and technical support during the experimental work.

Conflict of interest

The authors declare that they have no conflicts of interest.

Author contributions

Gulina Doktyrbay: Conceptualization, Investigation, Visualization, Writing – Original Draft.

Saule S. Kenzhebayeva: Investigation, Writing – Review & Editing.

Saule D. Atabayeva: Methodology, Formal Analysis

Sabina A. Shoinbekova: Data Curation, Formal Analysis

Saltanat Sh. Asrandina: Data Curation, Methodology

Malika A. Abdulzhanova: Visualization, Formal Analysis

Adel Rsatayeva: Data Curation, Methodology

Assaf Distelfeld: Writing – Resources, Analysis, Methodology

References

1. Ahloowalia, B. S., Maluszynski, M., & Nichterlein, K. (2004). Global impact of mutation-derived varieties. *Euphytica, 135*(2), 187–204. https://doi.org/10.1023/B:EUPH.0000014914.85465.4f

2. Allard, V., Veisz, O., Köszegi, B., Rousset, M., Le Gouis, J., & Martre, P. (2012). The quantitative response of wheat vernalization to environmental variables indicates that vernalization is not a response to cold temperature. *Journal of Experimental Botany, 63*(2), 847–857. https://doi.org/10.1093/jxb/err316

3. Alvarez, M. A., Tranquilli, G., Lewis, S., Kippes, N., & Dubcovsky, J. (2016). Genetic and physical mapping of the earliness per se locus Eps-Am1 in Triticum monococcum identifies EARLY FLOWERING 3 (ELF3) as a candidate gene. *Functional & Integrative Genomics, 16*(4), 365–382. https://doi.org/10.1007/s10142-016-0490-3

4. Appendino, M. L., & Slafer, G. A. (2003). Earliness per se and its dependence upon temperature in diploid wheat lines differing in the major gene Eps-Am1 alleles. *Journal of Agricultural Science, 141*(2), 149–154. https://doi.org/10.1017/S0021859603003472

5. Appels, R., Eversole, K., Feuillet, C., Keller, B., Rogers, J., Stein, N., Pozniak, C. J., Choulet, F., Distelfeld, A., Poland, J., et al. (2018). Shifting the limits in wheat research and breeding using a fully annotated reference genome. *Science, 361*(6403), eaar7191. https://doi.org/10.1126/science.aar7191

6. Bouis, H. E., & Saltzman, A. (2017). Improving nutrition through biofortification: A review of evidence from HarvestPlus, 2003 through 2016. *Global Food Security, 12*, 49–58. https://doi.org/10.1016/j.gfs.2017.01.009

7. Chaudhary, J., Deshmukh, R., & Sonah, H. (2019). Mutagenesis Approaches and Their Role in Crop Improvement. *Plants, 8*(11), 467. https://doi.org/10.3390/plants8110467

8. Gupta, P. K., Balyan, H. S., Sharma, S., & Kumar, R. (2020). Improving Wheat Nutritional Quality through Biofortification. *IntechOpen Chapters, Springer*, 135–154. https://doi.org/10.1007/978-3-030-34163-3_9

9. Guzmán, C., Ammar, K., Govindan, V., & Singh, R. (2019). Genetic improvement of wheat grain quality at CIMMYT. *Frontiers of Agricultural Science and Engineering, 6*(3), 265–272. https://doi.org/10.15302/J-FASE-2019260

10. Holme, I. B., Gregersen, P. L., & Brinch-Pedersen, H. (2019). Induced Genetic Variation in Crop Plants by Random or Targeted Mutagenesis: Convergence and Differences. *Frontiers in Plant Science, 10*, 1468. https://doi.org/10.3389/fpls.2019.01468

11. Horváth, Á., Kiss, T., Berki, Z., Horváth, Á. D., Balla, K., Cseh, A., Veisz, O., & Karsai, I. (2023). Effects of genetic components of plant development on yield-related traits in wheat (Triticum aestivum L.) under stress-free conditions. *Frontiers in Plant Science, 13*, 1070410. https://doi.org/10.3389/fpls.2022.1070410

12. Kamran, A., Iqbal, M., & Spaner, D. (2014). Flowering time in wheat (Triticum aestivum L.): A key factor for global adaptability. *Euphytica, 197*(1), 1–26. https://doi.org/10.1007/s10681-014-1075-7

13. Kenzhebayeva, S., Abekova, A., Zhan, G., Zharassova, D., Dai, F., Doktyrbay, G., & Tashenev, D. (2018a). Improved iron and zinc bioavailability in spring wheat mutant lines. *Journal of Biotechnology, 280*(Suppl.), S53. https://doi.org/10.1016/j.jbiotec.2018.06.170

14. Kenzhebayeva, S., Alybayeva, R., Atabayeva, S., Doktyrbay, G., Kaldybekkyzy, G., Asrandina, S., & Kaukaeva, G. (2013). Improvement of spring wheat protein quality and quantity by mutation breeding. *Current Opinion in Biotechnology, 24*(Suppl. 1), S85. https://doi.org/10.1016/j.copbio.2013.05.247

15. Kenzhebayeva, S., Atabayeva, S., Sarsu, F., Abekova, A., Shoinbekova, S., Omirbekova, N., Doktyrbay, G., Beisenova, A., & Shavrukov, Y. (2022). Organ-specific expression of genes involved in iron homeostasis in wheat mutant lines with increased grain iron and zinc content. *PeerJ, 10*, e13515. https://doi.org/10.7717/peerj.13515

16. Kenzhebayeva, S., Capstaff, N. M., Doktyrbay, G., Sarsu, F., Omirbekova, N. Zh., Eilam, T., Tashenev, D. K., & Miller, A. J. (2017). Searching a spring wheat mutation resource for correlations between yield, grain size, and quality parameters. *Journal of Crop Improvement, 31*(2), 209–228. https://doi.org/10.1080/15427528.2016.1276990

17. Kenzhebayeva, S., Doktyrbay, G., Alybayeva, R., Atabayeva, S. D., Zharasova, D., & Asrandina, S. Sh. (2015). Genetic variability on grain zinc concentrations of advanced mutant lines of spring wheat obtained through gamma irradiation and their evaluation for yield associated trait. *The 3rd Conference of Cereal Biotechnology and Breeding, Book of Abstracts*, 39.

18. Kenzhebayeva, S., Doktyrbay, G., Omirbekova, N., Sarsu, F., Tashenev, D., & Aibekova, A. (2016). Frequency of vernalization requirement associated dominant VRN-A1 gene and earliness related Eps-A1 candidate genes in advanced wheat mutant lines and effect of allele on flowering time. *International Journal of Biology and Chemistry, 9*(1), 24–30. https://doi.org/10.26577/2218-7979-2016-9-1-24-30

19. Kenzhebayeva, S., Doktyrbay, G., Sarsu, F., Omirbekova, N., Abekova, A., & Tashenev, D. (2018b). Improvement of spring wheat grain micronutrients concentrations through mutation breeding. *FAO/IAEA International Symposium on Plant Mutation Breeding and Biotechnology, Book of Abstracts*, 141. https://conferences.iaea.org/event/145/contributions/5094/contribution.pdf

20. Kitagawa, S., Shimada, S., & Murai, K. (2012). Effect of Ppd-1 on the expression of flowering-time genes in vegetative and reproductive growth stages of wheat. *Genes & Genetic Systems, 87*(3), 161–168. https://doi.org/10.1266/ggs.87.161

21. Köksel, H., Sapirstein, H. D., Çelik, S., & Bushuk, W. (1998). Effects of gamma-irradiation of wheat on gluten proteins. *Journal of Cereal Science, 28*(3), 243–250. https://doi.org/10.1016/S0733-5210(98)90004-2

22. Marcotuli, I., Cabas-Lühmann, P., Carafa, D., Mores, A., Giove, S. L., Colasuonno, P., Muciaccia, S., Simone, M., Schwember, A. R., & Gadaleta, A. (2025). Genome-Wide Association Study for Protein and Color Content in a Tetraploid Wheat Collection. *Current Plant Biology, 42*, 100483. https://doi.org/10.1016/j.cpb.2025.100483

23. Maree, A., Baloch, M., Mari, S. N., Sial, M. A., Laghari, K. A., Sootaher, J. K., Jamshaid, M., Attaullah, & Muneer, S. (2025). Gamma radiation-induced variation in wheat (Triticum aestivum L.) mutants for yield and agronomic traits. *International Journal of Agronomy and Agricultural Research, 27*(5), 23–36. https://doi.org/10.12692/ijaar/27.5.23-36

24. Morgounov, A., Gómez-Becerra, H. F., Abugalieva, A., Dzhunusova, M., Yessimbekova, M., Muminjanov, H., Zelenskiy, Y., Ozturk, L., & Cakmak, I. (2007). Iron and zinc grain density in common wheat grown in Central Asia. *Euphytica, 155*(1-2), 193–203. https://doi.org/10.1007/s10681-006-9321-2

25. Ochagavía, H., Prieto, P., Zikhali, M., Griffiths, S., & Slafer, G. A. (2019). Earliness Per Se by Temperature Interaction on Wheat Development. *Scientific Reports, 9*, 2584. https://doi.org/10.1038/s41598-019-39201-6

26. Oury, F. X., Leenhardt, F., Rémésy, C., Chanliaud, E., Duperrier, B., Balfourier, F., & Charmet, G. (2006). Genetic variability and stability of grain magnesium, zinc and iron concentrations in bread wheat. *European Journal of Agronomy, 25*(2), 177–185. https://doi.org/10.1016/j.eja.2006.04.011

27. Rybicki, M., Voss-Fels, K. P., Snowdon, R. J., & Wittkop, B. (2016). Genotype × environment interaction effects on grain quality in wheat. *Journal of Agricultural Science, 154*(7), 1218–1230. https://doi.org/10.1017/S0021859615001097

28. Shewry, P. R. (2009). Wheat. *Journal of Experimental Botany, 60*(6), 1537–1553. https://doi.org/10.1093/jxb/erp058

29. Shewry, P. R., & Hey, S. J. (2015). The contribution of wheat to human diet and health. *Food and Energy Security, 4*(3), 178–202. https://doi.org/10.1002/fes3.64

30. Shu, Q. Y., Forster, B. P., & Nakagawa, H. (2012). *Plant Mutation Breeding and Biotechnology*. CABI Publishing, Wallingford. https://www.cabidigitallibrary.org/doi/book/10.1079/9781780640853.0000

31. Simmonds, N. W. (1995). The relation between yield and protein in cereal grain. *Journal of the Science of Food and Agriculture, 67*(3), 309–315. https://doi.org/10.1002/jsfa.2740670306

32. Song, L., Wang, R., Yang, X., Zhang, A., & Liu, D. (2023). Molecular Markers and Their Applications in Marker-Assisted Selection (MAS) in Bread Wheat (Triticum aestivum L.). *Agriculture, 13*(3), 642. https://doi.org/10.3390/agriculture13030642

33. Spencer-Lopes, M. M., Forster, B. P., & Jankuloski, L. (Eds.). (2018). *Manual on Mutation Breeding* (3rd ed.). FAO/IAEA, Vienna, Austria, pp. 1–319. https://openknowledge.fao.org/handle/20.500.14283/i9285en

34. Sun, X., Hu, B., Li, W. X., & Ning, H. L. (2025). Genetic basis and simulated breeding strategies for enhancing soybean seed protein content across multiple environments. *Plants, 14*(14), 2117. https://doi.org/10.3390/plants14142117

35. Tahir, O., Bangash, S. A. K., Ibrahim, M., Shahab, S., Khattak, S. H., Din, I. U., Khan, M. N., Hafeez, A., Wahab, S., Ali, B., Makki, R. M., & Harakeh, S. (2023). Evaluation of Agronomic Performance and Genetic Diversity Analysis Using Simple Sequence Repeats Markers in Selected Wheat Lines. *Sustainability, 15*(1), 293. https://doi.org/10.3390/su15010293

36. Uauy, C., Distelfeld, A., Fahima, T., Blechl, A., & Dubcovsky, J. (2006). A NAC gene regulating senescence improves grain protein, zinc, and iron content in wheat. *Science, 314*(5803), 1298–1301. https://doi.org/10.1126/science.1133649

37. Velu, G., Ortiz-Monasterio, I., Cakmak, I., Hao, Y., & Singh, R. P. (2014). Biofortification strategies to increase grain zinc and iron concentrations in wheat. *Journal of Cereal Science, 59*(3), 365–372. https://doi.org/10.1016/j.jcs.2013.09.001

38. Velu, G., Singh, R. P., Crespo-Herrera, L., et al. (2018). Genetic dissection of grain zinc concentration in spring wheat for mainstreaming biofortification in CIMMYT wheat breeding. *Scientific Reports, 8*, 13526. https://doi.org/10.1038/s41598-018-31951-z

39. Velu, G., Singh, R., Huerta-Espino, J., Peña, J., & Ortiz-Monasterio, I. (2011). Breeding for enhanced zinc and iron concentration in CIMMYT spring wheat germplasm. *Czech Journal of Genetics and Plant Breeding, 47*(Special Issue), S174–S177. https://doi.org/10.17221/3275-CJGPB

40. von Well, E., Booyse, M., & Fossey, A. (2023). Gamma Irradiation as Tool for Mutation Breeding in Wheat. *Wheat Research and Utilization, IntechOpen*. https://doi.org/10.5772/intechopen.111713

41. Wan, T., Xue, H., & Tong, Y. (2022). Genetic Control of Efficient Nitrogen Use for High Yield and Grain Protein Concentration in Wheat: A Review. *Plants, 11*(4), 492. https://doi.org/10.3390/plants11040492

42. Welch, R. M., & Graham, R. D. (2004). Breeding for micronutrients in staple food crops from a human nutrition perspective. *Journal of Experimental Botany, 55*(396), 353–364. https://doi.org/10.1093/jxb/erh064

43. Zhang, T., He, Y., DePauw, R., Jin, Z., Garvin, D., Yue, X., Anderson, W., Li, T., Dong, X., Zhang, T., & Yang, X. (2022). Climate change may outpace current wheat breeding yield improvements in North America. *Nature Communications, 13*(1), 5591. https://doi.org/10.1038/s41467-022-33265-1

44. Zulfiqar, S., Ishfaq, S., Ikram, M., Nawaz, M. A., & Rahman, M. U. (2021). Characterization of Gamma-Rays-Induced Spring Wheat Mutants for Morphological and Quality Traits through Multivariate and GT Bi-Plot Analysis. *Agronomy, 11*(11), 2288. https://doi.org/10.3390/agronomy11112288

Information about the authors:

Gulina Doktyrbay – PhD, Acting Associate Professor, Department of Biotechnology, Al-Farabi Kazakh National University (Almaty, Kazakhstan, e-mail: gulina.kaznu@gmail.com).

Saule Kenzhebayeva – Doctor of Biological Sciences, Professor, Department of Biotechnology, Al-Farabi Kazakh National University (Almaty, Kazakhstan, e-mail: saule.kenzhebayeva@kaznu.kz).

Saule Atabayeva – Doctor of Biological Sciences, Professor, Department of Biotechnology, Faculty of Biology and Biotechnology, Al-Farabi Kazakh National University (Almaty, Kazakhstan, e-mail: Saule.Atabayeva@kaznu.edu.kz).

Sabina Shoinbekova – Doctor of Chemical Science, Professor, Department of Biotechnology, Al-Farabi Kazakh National University (Almaty, Kazakhstan, e-mail: Sabina.Shoinbekova@kaznu.edu.kz).

Saltanat Asrandina – Candidate of Biological Sciences, Professor, Department of Biotechnology, Al-Farabi Kazakh National University (Almaty, Kazakhstan. e-mail: Saltanat.Asrandina@kaznu.edu.kz).

Malika Abdulzhanova – PhD, Senior Lecturer, Department of Biotechnology, Al-Farabi Kazakh National University (Almaty, Kazakhstan, e-mail: Malika.Abdulzhanova@kaznu.edu.kz).

Rsatayeva Adel – Master Student, Department of Biotechnology, Al-Farabi Kazakh National University (Almaty, Kazakhstan. e-mail: adelrsatayeva@gmail.com).

Assaf Distelfeld – PhD, Professor, Department of Evolutionary and Environmental Biology, Institute of Evolution, University of Haifa, (Haifa, Israel, e-mail: adistelfeld@evo.haifa.ac.il).

Received 25 November 2025;
received in revised form 24 June 2026;
accepted 26 June 2026

IRSTI 34.35.15 https://doi.org/10.26577/IJBCh20261914

N.M. Joldasbayeva[1,2], Z.B. Tungushbaeva[1,2], M.B. Zhaksybaev[1]*, N.N. Pravin[2]*

[1]Abai Kazakh National Pedagogical University, Almaty, Kazakhstan
[2]Aliyev Kazakh-Russian Medical University, Almaty, Kazakhstan
*e-mail: zh.murat_1966@mail.ru(M.B.Zh.), n.pravin@medkrmu.kz (N.N.P.)

EFFECT OF CADMIUM CHLORIDE ON THE CARDIAC MUSCLE ULTRASTRUCTURE OF RATS

Abstract: Cadmium is a heavy metal and environmental pollutant that plays a significant role in the development of cardiovascular diseases. Chronic exposure to low concentrations of cadmium in experimental animals leads to various biochemical and pathophysiological changes, such as increased blood pressure, accelerated formation of cholesterol plaques in arterial walls, conduction disturbances in the heart, and reduced contractile function of the myocardium. This study aimed to evaluate ultrastructural changes in the heart muscle of rats poisoned with cadmium chloride, as well as to determine the extent of recovery of these changes after cadmium exposure was discontinued. Wistar rats weighing 180 – 200 grams were administered cadmium chloride orally at a dose of 1.5 mg/kg daily. The poisoning lasted for 10 weeks. After the cadmium administration was stopped, heart tissue samples were collected on the first day, one week, and two weeks later for analysis. Following cadmium administration, ultrastructural examination of the cardiac muscle fibers revealed an increased number of mitochondria with significant cristae damage. The number of myofibrils and myofilaments was reduced. Z-discs were partially displaced, and A and I bands were poorly distinguishable. Intercalated discs were irregularly positioned, and the sarcolemma was damaged. Two weeks after cadmium withdrawal, these structural changes were partially reduced. Thus, exposure to cadmium chloride is associated with ultrastructural alterations in the heart that may underline physiological dysfunctions, and it is suggested that these changes are partially reversible after the cessation of cadmium exposure.

Keywords: cadmium chloride, cardiac muscle, ultrastructure, myofibrils, myofilaments, rat.

Introduction

Cadmium (Cd) – is a ubiquitous, non-essential, toxic metal that has harmful effects on the environment and human health upon exposure. These effects have been the focus of research for several decades. Cd occurs naturally in ore form. Its release into the environment from natural or anthropogenic sources can lead to contamination of soil and food products. Although acute Cd intoxication is now rare due to international regulations, people are continuously exposed to low levels of Cd, primarily through food and water consumption, cigarette smoke, polluted air, and occupational contact (Järup & Hazards, 2003). Once absorbed, Cd is not effectively eliminated and thus accumulates in the human body over a lifetime, with a long biological half-life of 15–30 years (Thevenod & Lee, 2013). Cd mainly accumulates in the kidneys, liver, and lungs. However, with chronic exposure, Cd can also accumulate in other parts of the body, including the heart, aorta, bones and intestines (Tai, et al., 2022b), leading to various diseases. Cadmium toxicity causes kidney problems (tubular and glomerular damage), osteomalacia, osteoporosis, testicular dysfunction, and cancer (Honda et al., 2003).

Furthermore, epidemiological studies have demonstrated a link between Cd exposure and the risk of cardiovascular diseases, such as heart failure, stroke, myocardial infarction, and diseases of the coronary and peripheral arteries (Barregard et al., 2016; Deering et al., 2018; Everett & Frithsen, 2008; Peters et al., 2010; Satarug et al., 2010; Tellez-Plaza et al., 2013; Tinkov et al., 2018). For example, Tellez-Plaza et al. (2013), reported an increased risk of ischemic heart disease (hazard ratio [HR]: 1.22; 95% confidence interval [CI]: 1.08–1.38), stroke (HR: 1.75; 95% CI: 1.17–2.59), and heart failure (HR: 1.39; 95% CI: 1.01–1.94) in individuals exposed to high Cd levels (80th vs. 20th percentile of urinary Cd concentration) (Tellez-Plaza et al., 2013). Additionally, Barregard et al. (2016) compared individuals with the highest and lowest quartiles of blood Cd levels and found that

those in the highest quartile had an increased risk of acute coronary events (HR: 1.8; 95% CI: 1.2–2.7) and stroke (HR: 1.9; 95% CI: 1.3–2.9) (Barregard et al., 2016). In the aforementioned studies, the association between Cd exposure and cardiovascular risk was consistent among never-smokers; therefore, this link cannot be entirely attributed to the confounding effects of smoking. As a major toxin in cigarettes, Cd may partially mediate the pro-atherosclerotic effects of smoking. Mediation analysis showed that Cd contributed to approximately 50% of the total increase in cardiovascular risk among current smokers (Andersson et al., 2018; Li et al., 2019).

Despite epidemiological data linking Cd exposure to cardiovascular risk, the underlying mechanisms remain unclear. Cd induces cell apoptosis and tissue damage by causing DNA damage, oxidative stress, mitochondrial injury, and endoplasmic reticulum stress (Genchi et al., 2020). The toxic effects of Cd on cardiomyocytes, vascular endothelial cells, and smooth muscle cells have been described both *in vivo* (animal studies) and in vitro (Ghosh & Indra, 2018; Messner et al., 2016; Shen et al., 2018; Washington et al., 2006). In the present study, we investigated the toxicity of Cd in the cardiovascular system of mice, evaluating its impact on baseline hemodynamics, cardiac function, and histology and ultrastructure of cardiac and arterial tissues. Matrix metalloproteinases (MMPs) influence heart failure and atherosclerosis by regulating extracellular matrix (ECM) turnover (Johnson, 2017; Olejarz et al., 2020; Spinale et al., 2013). Therefore, we further examined the effect of cadmium on the expression of cardiac and arterial MMPs, particularly MMP-2, MMP-9, and MMP-14, and their significance in cardiovascular diseases.

Ozturk et al. (2009) in his research, the systemic hemodynamics induced by acute and chronic cadmium (Cd^{2+}) intoxication in the cardiovascular system of rats using thoracic electrical bioimpedance were examined and the acute and chronic effects of Cd^{2+} intoxication on the activities of antioxidant enzymes and malondialdehyde (MDA) were compared. Also, in this study, ultrastructural changes in the heart and aorta of rats were evaluated. Thirty-eight male Wistar albino rats were randomly divided into control, acute, and chronic groups. Chronic group was administered by oral gavage an aqueous solution of $CdCl_2$ for 60 days, at dose of 15 mg Cd^{2+}/kg/day. Acute group was administered by oral gavage an aqueous solution of $CdCl_2$ with a single dose of 15mg Cd^{2+}/kg. Cadmium increased the stroke volume and cardiac output of rats in the chronic group but did not change the heart rate significantly. Antioxidant enzymes activities and MDA level significantly increased in the chronic group. In ultrastructural examination, there were widespread degenerative changes in heart muscle cells of the chronic group but endothelial cells and smooth muscle cells in the aorta tissue samples had normal morphological features in all groups. All of the findings indicate that Cd^{2+} toxication can cause deformation in heart muscle cells due to an increase in free radicals and lipid peroxidation. Also, this study has confirmed that a long-term-Cd^{2+} exposure increased stroke volume (SV) and cardiac output (CO) but did not change the heart rate (HR).

The novelty of the study lies in demonstrating that subchronic cadmium exposure induces a mitochondria-driven structural destabilization of cardiomyocytes, resulting in sarcomeric disorganization secondary to impaired bioenergetic support. The observed mitochondrial – sarcomeric dissociation represents a morphological substrate of toxic cardiomyopathy, highlighting disruption of the energetic – mechanical continuum in myocardial tissue. By incorporating post – exposure recovery intervals, the study further establishes that toxic myocardial injury is a dynamic and partially reversible process, redefining cadmium cardiotoxicity as a structurally phased pathology rather than a static degenerative condition.

This study aimed to evaluate the effects of subchronic cadmium chloride exposure on the ultrastructure of the rat myocardium and to determine whether these alterations are reversible during a post-exposure recovery period.

Materials and methods

The experimental animals were Wistar white rats that had been bred for several generations in the university laboratory to ensure genetic homogeneity. Healthy male rats weighing 180–200 grams were used in the study. The animals were divided into two groups: a control group (6 rats) and an experimental group, subdivided into three time points with 6 rats each. Rats in the experimental group were administered cadmium chloride orally at a dose of 1.5 mg/kg of body weight, dissolved in 0.2 ml 0.9% physiological saline, daily for 10 weeks. The control group received 0.2 ml of 0.9% NaCl solution orally on the same schedule. After completing cadmium administration, rats from the experimental group were euthanized at three time points: on the first day, 1 week, and 2 weeks after cessation of cadmium exposure (6 animals per time point). The left ventricular myocardium was collected from all animals for analysis (Table 1).

The experimental animals were male Wistar albino rats obtained from the animal vivarium at the B. Atchabarov Institute of Fundamental and Applied Medicine (Almaty, Kazakhstan). Healthy rats aged 3-4 months, weighing 180–200 g, were used in the study. The animals were bred under controlled conditions over several generations to ensure genetic homogeneity and the reproducibility of experimental results.

Animals were maintained under standard vivarium conditions: ambient temperature 22 ± 2°C, relative humidity 50–60%, and a 12 h light/12 h dark cycle. Ventilation was provided by a supply and exhaust system with controlled air quality. The animals were housed under barrier system conditions ("clean/dirty zones"). Rats were kept in polycarbonate cages (approximately 40 × 25 × 20 cm), with no more than 6 animals per cage. Animals were fed a standard pelleted diet, with free access to water (ad libitum). The animals were divided into two groups: a control group (6 rats) and an experimental group, subdivided into three time points with 6 rats each. Rats in the experimental group were administered cadmium chloride ($CdCl_2$) orally at a dose of 1.5 mg/kg body weight, dissolved in 0.2 mL of 0.9% physiological saline, once daily for 10 weeks. Animals in the control group received 0.2 mL of 0.9% NaCl solution orally according to the same schedule. After completion of cadmium administration, animals from the experimental group were euthanized at three time points: on day 1, 1 week, and 2 weeks after cessation of cadmium exposure (n = 6 per time point). The left ventricular myocardium was collected from all animals for subsequent analysis. The selected dose of cadmium chloride (1.5 mg/kg body weight) corresponds to a subchronic exposure level commonly used in recent experimental studies to induce organ-specific toxicity without excessive mortality. Subchronic cadmium exposure has been shown to cause cardiotoxic effects, including impaired myocardial contractility and altered hemodynamic parameters associated with oxidative stress and molecular damage (Protsenko et al., 2020).

Experimental data indicate that doses in the range of approximately 1–2 mg/kg/day produce consistent morphological and functional alterations in tissues while maintaining animal viability, which is essential for studying both injury progression and recovery. Similar dosing regimens (e.g., ~2 mg/kg $CdCl_2$) have been successfully used in recent studies to induce oxidative stress and structural tissue damage under subchronic conditions (Hu et al., 2024).

Higher doses (≥5 mg/kg) are associated with severe toxicity and pronounced tissue damage, limiting their suitability for long-term experimental models (Razooqi et al., 2924).

Therefore, the selected dose of 1.5 mg/kg represents a biologically relevant and methodologically justified model of chronic cadmium intoxication.

The duration of cadmium administration (10 weeks) was selected to induce stable chronic intoxication and ensure sufficient accumulation of the toxicant in tissues. Cadmium is characterized by cumulative properties and a long biological half-life; therefore, prolonged exposure is required to produce consistent morphological and ultrastructural alterations.

Post-exposure time points (day 1, 1 week, and 2 weeks after cessation) were included to evaluate the dynamics of tissue injury and recovery following withdrawal of the toxic agent. This design allows assessment of both the persistence and potential reversibility of cadmium-induced myocardial damage.

Euthanasia was performed under deep general anesthesia using Ketamine (80–100 mg/kg) and Xylazine (10 mg/kg), administered intraperitoneally. Adequate depth of anesthesia was confirmed by the absence of pain reflex and corneal reflex. Following induction of surgical anesthesia, euthanasia was completed by decapitation.

All procedures were carried out in accordance with international guidelines for the care and use of laboratory animals and were approved by the local ethics committee (Table 1).

Table 1
Experimental animal group

Group	Condition	Number of animals	Cadmium dose, mg/kg
control	no treatment	6	–
experiment	1st day post-cadmium	6	1.5
	1 week post-cadmium	6	1.5
	2 weeks post-cadmium	6	1.5

Immediately after excision, myocardial tissue samples (~1 mm³) were fixed at 4°C in 0.1 M Millonig's phosphate buffer (pH 7.2) containing 2% glutaraldehyde and 2.5% paraformaldehyde (Sigma-Aldrich, USA). Post-fixation was performed in 1% osmium tetroxide at 4 °C for 2 hours (Electron Microscopy Sciences, USA). The specimens were dehydrated in graded ethanol and acetone (Merck, Germany) and embedded in Epon-812 resin. Ultrathin sections (70–80 nm) were prepared using an AK-VIII ultramicrotome, positioned on copper grids, and stained with 2% uranyl acetate and lead citrate (0.04 M). The samples were processed at the Atchabarov Research Institute of Fundamental and Applied Medicine (Almaty, Kazakhstan).

Ultrastructural analysis was performed using a Hitachi H-600 transmission electron microscope (Japan) at 80 kV at the Kazakh Research Institute of Oncology and Radiology (Almaty, Kazakhstan).

Cadmium chloride ($CdCl_2$, ≥99% purity, analytical grade) was obtained from a certified supplier of chemical reagents in the Republic of Kazakhstan, Lab Time (product code 79037, CAS No. 10108-64-2). A sterile 0.9% sodium chloride solution (physiological saline, pharmaceutical grade) was purchased from a licensed pharmaceutical manufacturer by Kelun-Kazpharm, Kazakhstan. All reagents used in the study were of analytical or pharmaceutical grade and complied with relevant quality standards. Solutions were prepared under standard laboratory conditions in accordance with established protocols.

Ethical considerations

All experimental procedures involving animals were approved by the Local Ethics Committee of Asfendiyarov Kazakh National Medical University (Protocol No. 38 dated 28.01.2026) and were conducted in accordance with international guidelines for the care and use of laboratory animals.

All procedures were carried out in accordance with the Order of the Ministry of Health of the Republic of Kazakhstan dated December 11, 2020, №. Ministry of Health of the Republic of Kazakhstan-248/2020. The movement of personnel and materials was ensured through sanitary airlocks with the mandatory use of personal protective equipment. To prevent bacterial contamination, cleaning procedures, feeding, and animal care were performed strictly in accordance with the established regulations.

Housing and care of laboratory animals were organized according to barrier system principles, with strict separation of "clean" and "dirty" flows. The maintenance, care, and use of laboratory animals were conducted based on the following regulatory documents: the sanitary rules approved by the Order of the Ministry of Health of the Republic of Kazakhstan dated December 25, 2020, №. Ministry of Health of the Republic of Kazakhstan-331/2020; generally accepted international guidelines for working with laboratory animals (GLP, *Guide for the Care and Use of Laboratory Animals*); and the internal standard operating procedures (SOPs) of the vivarium.

Results and discussion

Electron microscope findings of the control white mouse myocardial cells. The nucleus and nucleus of the spindle type are clearly observed and the nuclear membrane of the double membrane was easily observed. Myofibril was distributed in large numbers and between the myofibril, the circumferential privates were distributed bearing the privates (Figure 1a). Myofibrils were clearly separated by sarcomere due to the limit of the Z-line and I band (1), A band and H band were observed. Some T tubules were also observed. M lines were observed in the center of eradication. myofilaments were arranged regularly at regular intervals and sharpened at each root (Figure 1b).

Electron microscopic findings of white rat cardiomyocytes in the experimental group in the myocardium of white rats sacrificed on the first day after daily administration of cadmium for 10 weeks, most of the myofibrils were shrunk or reduced, and the sarcoplasmic reticulum was proliferated between the myofibrils, but some of the sarcoplasmic reticulum was damaged or reduced (Figure 2a). The Z lines of the root fibers show an irregular arrangement and the myofibrils are reduced or damaged. Distinctions between bands and bands were rarely observed. The structure of the sarcoplasmic reticulum (interdisc) was observed to be irregular and the fascicle (in the sarcolemma) was observed to have disconnected phases (Figure 2b).

Figure 1
Electron micrographs of cardiac muscle fibers in control rat (a) X 8000 and (b) X 20000)
Round oval nucleus (N) of a cardiac cell is clearly seen. Numerous myofibrils (m) and myofilaments are clearly arranged. A few mitochondria (M) are located at interfibrillar region and adjacent nucleus. In myofibril, Z-line, A-band, I-band and H-line showed their fine structures.
Mitochondria contains numerous cristae.

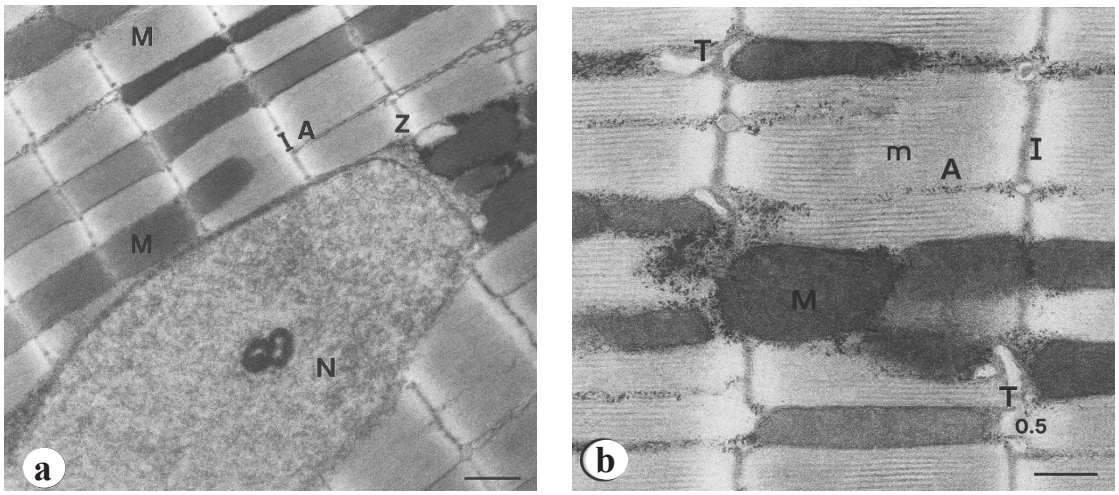

Figure 2
Electron micrographs of rat cardiac muscle fibers at 1st day after cadmium chloride administration of 10 weeks (a) X 8000 and (b) X 20000)
The number of mitochondria (M) is increased, and their cristae are severely damaged. Consequently, cardiac myofibrils (My) are decreased, and few myofilaments (mf) are observed. The Z-discs show irregular structures and are partially dislocated. Additionally, irregularly arranged intercalated discs (Ic) and a disrupted sarcolemma are visible.

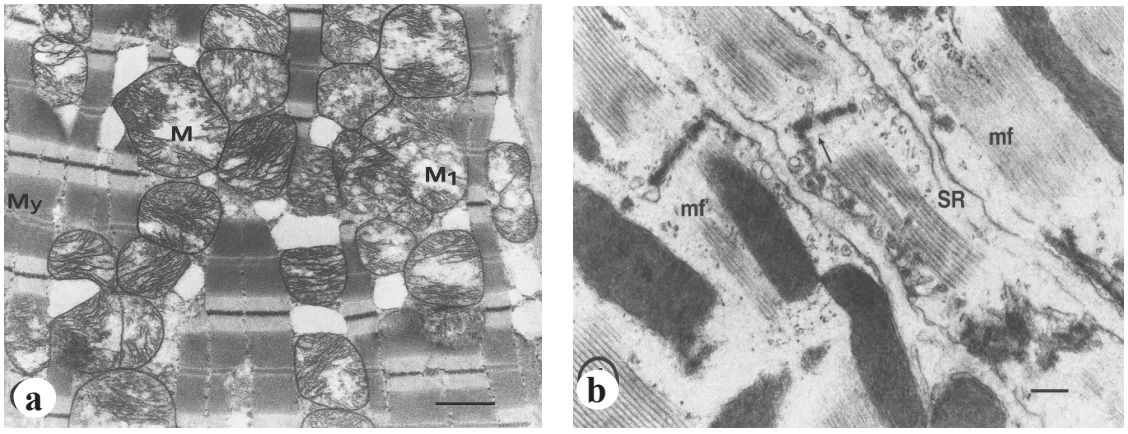

In the cardiomyocytes of white rats treated with cadmium 10 for a week and recovered after 1 week, the number of myofibrils is significantly reduced, numerous private bodies are observed, the connection of sarcolemmal plates is disrupted, and some of the myofilaments are lost, and the loss of private bodies and the loss of A and h bands are also observed (Figure 3a, 3b).

Figure 3
Electron micrographs of rat cardiac muscle fibers at l week after cadmium chloride administration of 10 weeks (a) X 8000 and (b) X 20000)
Few myofibrils (My) are seen, and mitochondria (M) are increased in numbers. Mitochondria lost a lot of cristae. Myofilaments (mf) are reduced and A-bands and I-bands are not clearly defined. Z-disc are partly observed. Sarcolemma (Sl) are segregated from myofibrils (Mf).

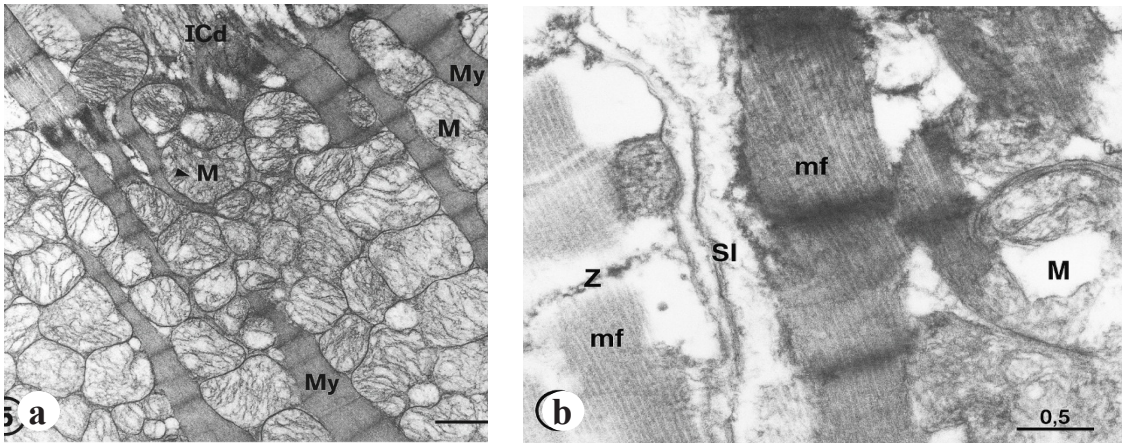

In the cardiomyocytes of white rats treated with cadmium 10 for a week and recovered after 2 weeks, the number of myofibrils is similar to that of the control group, but the number of private bodies is slightly increased, and the myofilaments are also recovered.

Figure 4
Electron micrographs of rat cardiac muscle fibers at 2 weeks after cadmium chloride administration of 10 weeks (a) X 8000 and (b) X 20000)
The myofibrils(mf) of cardiac muscle fibers were increased in numbers. Mitochondria (M) are reduced in number similar to control rat mitochondria. Z-disc, I-band and A-band are seen.

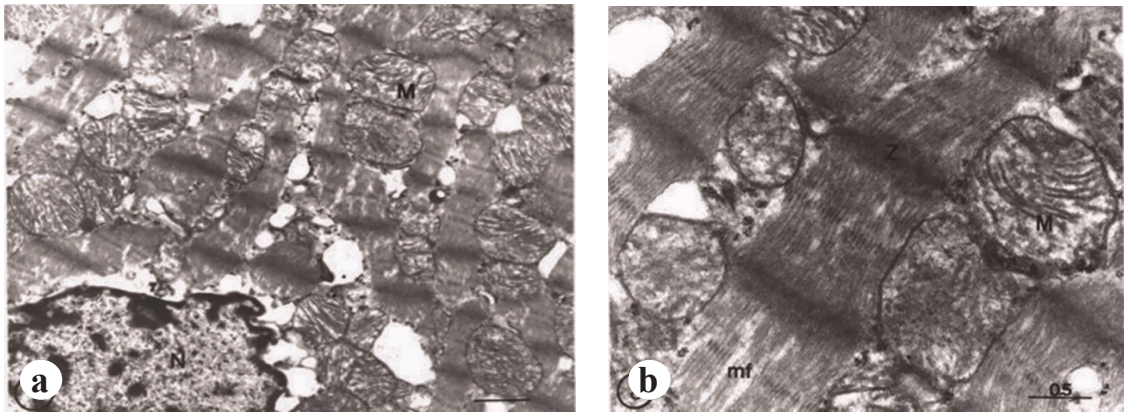

Cadmium is a heavy metal widely used for industrial purposes, and in recent years, due to the development of industry in the world, an increase in intake through air pollution, smoking, drinking water and food has been reported.

The results of a study by Reda A. Ali et al. (2024), showed that exposure to various low doses of Cd in chick embryos affects key stages of myocardial development, which may predispose offspring to cardiovascular disease in the future. This study showed that exposure to Cd caused inflammation of embryonic cardiomyocytes, thickening and hyperplasia of the heart muscle. In addition, Cd causes underdevelopment of the heart, as well as microstructural and histopathological damage, which is reflected in a decrease in the efficiency of the heart. The cardio-

toxic effects of Cd on the structure and function of the heart depend on the dose (Reda et al., 2024).

Yu-Ting Tai et al. (2022a) demonstrated the successful establishment of a mouse model of chronic cadmium (Cd) accumulation. Cadmium deposition was detected in multiple tissues, including the spine, femur, aorta, heart, kidneys, lungs, liver, intestines, serum, and urine, confirming systemic distribution following prolonged exposure. The authors reported that Cd accumulation in the kidneys and aorta reached near-saturation levels in the higher-dose group. In addition, calcium concentrations in bone and kidney tissues decreased with increasing Cd exposure, indicating direct toxic effects on mineralized tissues. Although no significant changes in body weight, blood pressure, or heart rate were observed, histological examination revealed pronounced structural alterations in cardiac tissue. These findings suggest that Cd accumulation plays an important role in mediating pathophysiological changes, particularly in the heart and skeletal system (Tai et al., 2022a).

Shing-Hsien Chou et al. (2023) showed epidemiological studies have reported an association between chronic cadmium (Cd) exposure and increased cardiovascular risk; however, their causal relationship remains unclear. The aim of this study is to explore the effects of Cd exposure on the cardiac and arterial systems in mice. According to the concentration of cadmium chloride in drinking water, male mice were randomly divided into control and low-dose and high-dose Cd exposure groups. The intervention duration was 12 weeks. In cardiac tissues, Cd exposure led to focal necrosis, myofibril disarray, perivascular and interstitial fibrosis, and disorganized sarcomere structures. Cd also induced the apoptosis of cardiomyocytes and increased the expression levels of matrix metalloproteinase (MMP)-2 and MMP-14 in cardiac tissues. In the arterial tissues, Cd exposure damaged the intimal and medial layers of the aorta. Cd further reduced the viability of aortic smooth muscle cells in vitro. This study provides evidence for the Cd-induced damage of the cardiovascular system, which may contribute to various cardiovascular diseases (Chou et al., 2023).

Sepulchro Mulher et al. (2024) demonstrated that cadmium, a widespread environmental heavy metal, acts not only as a cardiovascular risk factor but also as a potential metalloestrogen capable of inducing sex-dependent vascular effects. Using isolated aortic preparations from female Wistar rats, the authors investigated the in vitro effects of cadmium chloride ($CdCl_2$, 5 μM) on vascular reactivity. Exposure to $CdCl_2$ resulted in structural damage to the vascular endothelium, increased production and release of reactive oxygen species (O_2), reduced the involvement of potassium (K^+) channels, and enhanced activation of the angiotensin II pathway in response to phenylephrine. In addition, estrogen receptor alpha (ERα) was found to modulate vascular reactivity in the presence of cadmium, supporting the hypothesis that cadmium may function as a metalloestrogen. The study concluded that cadmium exposure promotes endothelial injury and oxidative stress in the isolated aorta of female rats, potentially contributing to the development of vasculopathies (Sepulchro Mulher et al., 2024).

Rossi et al. (2024) reported that chronic cadmium exposure is associated with vascular alterations and increased arterial pressure; however, the short-term cardiovascular effects remain insufficiently characterized. In their experimental study, Wistar rats were exposed to cadmium chloride ($CdCl_2$) at a concentration of 100 mg/L in drinking water for 7 days, which corresponds to an approximate daily intake of ~10–15 mg/kg body weight, depending on fluid consumption. The authors demonstrated that, despite relatively low plasma cadmium levels, the exposed animals exhibited elevated systolic blood pressure and enhanced vascular contractility in response to phenylephrine. Endothelium removal and nitric oxide synthase (NOS) inhibition increased contractile responses in both control and cadmium-treated groups. In the aorta of cadmium-exposed rats, increased phosphorylation of endothelial nitric oxide synthase (eNOS, Ser1177) and elevated basal nitric oxide production were observed. Furthermore, cadmium exposure was associated with decreased catalase expression and increased basal hydrogen peroxide (H_2O_2) release. Catalase incubation attenuated the enhanced contractile response. In vessels pre-contracted with phenylephrine, cadmium-treated rats showed impaired endothelium-dependent (acetylcholine-induced) and endothelium-independent (sodium nitroprusside-induced) relaxation. However, responses to sodium nitroprusside were comparable between groups when pre-contraction was induced by KCl. These findings indicate that even short-term cadmium exposure can induce early alterations in vascular function and blood pressure regulation, potentially mediated by impaired antioxidant defense and increased H_2O_2 bioavailability.

El Bakary et al. (2025) reported that exposure to cadmium (Cd) induces pronounced cardiotoxic effects, primarily mediated by oxidative stress and inflammatory responses. In their experimental study, male albino rats were divided into five groups (con-

trol, Cd, Cd+R, Cd+RES, and Cd+RES+R). Cadmium chloride was administered intraperitoneally at a dose of 2 mg/kg body weight, five times per week for six consecutive weeks. Resveratrol (50 mg/kg/day) was administered for 35 days, starting from the second week of cadmium exposure, and low-dose gamma radiation (0.75 Gy) was applied at the end of the experimental period. The authors demonstrated that cadmium exposure significantly increased serum levels of cardiac injury markers, including creatine kinase-MB (CK-MB), troponin I, and lactate dehydrogenase (LDH), along with alterations in lipid profile parameters. Moreover, a marked downregulation of key metabolic and antioxidant regulators was observed in cardiac tissue, including AMP-activated protein kinase (AMPK), Sirtuin 1 (SIRT1), nuclear factor erythroid 2-related factor 2 (NRF2), and suppressor of cytokine signaling 3 (SOCS3). Notably, resveratrol exerted a protective effect by modulating AMPK-mediated signaling pathways and attenuating oxidative stress and inflammatory responses in cadmium-treated animals.

Raktim et al. (2026) reported that cadmium induces cardiotoxicity even at low doses through endocrine disruption and oxidative stress. This investigation assessed age-related susceptibility in female albino rats by comparing pre-pubertal (30-day-old) and post-pubertal (60-day-old) animals that were administered $CdCl_2$ at a dosage of 5.12 mg/kg body weight per day via oral gavage for 15 days. Despite greater Cd accumulation in pre-pubertal rats, post-pubertal animals exhibited heightened cardiac injury. This paradox correlated with impaired induction of metallothionein (MT), enhanced glutathione and vitamin C depletion, and reduced enzymic antioxidants (SOD, CAT, GPx). Concomitantly, altered adrenal function with increased corticosterone (CORT) and reduced estradiol (E2) reflected differential hypothalamic–pituitary–adrenal (HPA) axis responsiveness, further compromising antioxidant defenses. Biomarkers of cardiac function confirmed this vulnerability: increased serum CK-MB and troponin I, electrocardiographic (ECG) abnormalities (ST elevation, QT prolongation, tachycardia), and larger infarct volume. Collectively, these findings demonstrate that post-pubertal susceptibility is driven by reduced MT inducibility and HPA axis–mediated endocrine dysregulation, which amplify oxidative injury and structural remodeling of ventricular myocardium. From a translational standpoint, our findings identify adolescence and early adulthood as critical windows during which females exhibit heightened vulnerability to environmental $CdCl_2$ exposure. Variations in metallothionein (MT) expression capacity and estradiol levels may serve as informative biomarkers for predicting individual susceptibility. These results also suggest the potential value of targeted interventions such as MT induction, antioxidant therapy, or modulation of hormonal pathways, that merit further investigation. Collectively, the study emphasizes the urgent need for stricter regulation of cadmium exposure, particularly among peripubertal populations, to reduce lifelong cardiovascular risk.

Xiao et al. (2026) demonstrated that cadmium (Cd^{2+}) exposure exacerbates atherosclerotic lesions through endothelial dysfunction. In their study, a positive correlation was observed between cadmium levels and atherosclerotic plaque burden in human vascular samples. In vivo experiments using apolipoprotein E-deficient ($ApoE^{-/-}$) mice fed a high-fat diet showed that cadmium chloride ($CdCl_2$) exposure led to a dose-dependent increase in atherosclerotic plaque formation. Histological analysis revealed enhanced lipid deposition within the vascular wall, as confirmed by Oil Red O staining, along with increased signs of vascular inflammation. Similarly, in zebrafish models, cadmium exposure intensified high-fat diet–induced vascular lipid accumulation and inflammatory changes. These findings indicate that cadmium contributes to the progression of atherosclerosis by promoting structural and histopathological alterations in the vascular wall.

During the experimental period, no mortality was observed in either the control or cadmium-treated groups. All animals completed the study according to the experimental protocol; therefore, the final sample size remained unchanged (control: n = 6; cadmium-treated: n = 18, with n = 6 per time point). Histological examination revealed no significant differences in the morphology of small arteries, capillaries, or cardiomyocytes between the cadmium-treated and control groups. However, pronounced ultrastructural alterations were observed in the sarcoplasmic reticulum (SR) of papillary muscle cardiomyocytes in the cadmium-treated animals. These changes were characterized by dilatation of the SR cisternae, reflected by an increased intermembrane distance, as well as disruption of junctional complexes. Such structural damage to the SR may impair intracellular calcium handling and, consequently, affect myocardial electrical conductivity and contractile function. In addition, an increase in electron density of the SR in the interventricular septum was observed, suggesting alterations in ionic homeostasis and intercellular signaling. These findings support the hypothesis that cadmium exposure may interfere with cell-to-cell

electrical coupling in myocardial tissue. Minor differences in the degree of SR electron density reported across studies are unlikely to be solely attributable to variations in cadmium dose or duration of exposure.

Subchronic exposure to cadmium for 10 weeks induced degenerative alterations in myocardial myofibrils and myofilaments, suggesting that sarcoplasmic reticulum dysfunction may impair cardiac contractility and electrical conduction. Notably, partial attenuation of these ultrastructural changes was observed after cessation of cadmium administration (1 day, 1 and 2 weeks), indicating a degree of reversibility. However, these findings should be interpreted with caution, as the extent of structural recovery requires further confirmation by quantitative morphometric analysis and additional ultrastructural evidence. These results highlight the need for further studies aimed at elucidating the mechanisms of cadmium-induced myocardial injury and potential strategies for its prevention.

Conclusion

The present study confirms that long-term oral administration of cadmium chloride at a dose of 1.5 mg/kg causes notable degenerative changes in the ultrastructure of myocardial tissue in Wistar albino rats. Morphological alterations were evident as early as one day after the exposure period ended. These included shrinkage and partial loss of myofibrils, disorganization of Z-lines, disappearance of A and I bands, disconnection of the sarcoplasmic reticulum, and proliferation of electron-dense (private) bodies between the myofibrils. Such damage indicates impaired structural integrity and potential compromise of cardiac function.

Interestingly, one week after cadmium withdrawal, the myocardial structure remained abnormal, although some signs of improvement were noted. However, two weeks post-exposure, most of the structural features of the myocardium were restored to a state resembling normal tissue, suggesting that the cadmium-induced damage is, to a significant extent, reversible if exposure is discontinued in time.

These findings suggest that cadmium has a direct toxic effect on myocardial ultrastructure, but the myocardium also possesses a certain regenerative capacity. This highlights the importance of early detection and removal of cadmium exposure to prevent long-term or irreversible cardiac damage. Further studies are recommended to explore the molecular mechanisms of this recovery and its impact on heart function.

Funding

This research received no external funding.

Acknowledgments

The authors express their gratitude to the Vivarium of the B. Atchabarov Research Institute of Fundamental and Applied Medicine (Almaty, Kazakhstan), the M.A. Aitkhozhin Institute of Molecular Biology and Biochemistry (Almaty, Kazakhstan), and the Kazakh Research Institute of Oncology and Radiology (Almaty, Kazakhstan) for their assistance in conducting experimental studies and electron microscopy analysis.

Conflicts of Interest

The authors declare that they have no conflicts of interest.

Author contributions

Nurzhamal M. Joldasbayeva: Conceptualization, Investigation, Methodology, Writing – Original Draft & Review & Editing.

Zina B. Tungushbaeva: Conceptualization, Supervision, Data Curation, Formal Analysis, Visualization.

Murat B. Zhaksybaev: Conceptualization, Discussion of the research results.

Nariman N. Pravin: Conceptualization, Discussion of the research results.

All authors have read and approved the final version of the manuscript.

References

1. Andersson, E. M., Fagerberg, B., Sallsten, G., et al. (2018). Cadmium and carotid plaques. *Am J Epidemiol, 187*(4), 806–816. https://doi.org/10.1093/aje/kwx306

2. Barregard, L., Sallsten, G., Fagerberg, B., et al. (2016). Blood cadmium and cardiovascular events. *Environ Health Perspect, 124*(5), 594–600. https://doi.org/10.1289/ehp.1509735

3. Chou, S. H., Lin, H. C., Chen, S. W., et al. (2023). Cadmium-induced cardiovascular damage. *Food Chem Toxicol, 175*, 113740. https://doi.org/10.1016/j.fct.2023.113740

4. Deering, K. E., Callan, A. C., Prince, R. L., et al. (2018). Cadmium exposure and cardiovascular outcomes. *Int J Hyg Environ Health, 221*(2), 347–354. https://doi.org/10.1016/j.ijheh.2017.12.007

5. El Bakary, N. M., Abdelhamid, G. R., Anees, L. M., & Rihan, S. (2025). Resveratrol mitigates cadmium cardiotoxicity. *Ecotoxicol Environ Saf, 302*, 118749. https://doi.org/10.1016/j.ecoenv.2025.118749

6. Everett, C. J., & Frithsen, I. L. (2008). Urinary cadmium and myocardial infarction. *Environ Res, 106*(2), 284–286. https://doi.org/10.1016/j.envres.2007.10.009

7. Genchi, G., Sinicropi, M. S., Lauria, G., Carocci, A., & Catalano, A. (2020). The effects of cadmium toxicity. *Int J Environ Res Public Health, 17*(11), 3782. https://doi.org/10.3390/ijerph17113782

8. Ghosh, K., & Indra, N. (2018). Cadmium-induced cardiac damage in rats. *Environ Toxicol Pharmacol, 59*, 43–52. https://doi.org/10.1016/j.etap.2018.02.009

9. Hartwigsen, G., & Volz, L. J. (2021). Probing rapid network reorganization of motor and language functions via neuromodulation and neuroimaging. *NeuroImage, 224*, 117449. https://doi.org/10.1016/j.neuroimage.2020.117449

10. Honda, R., Tsuritani, I., Noborisaka, Y., Suzuki, H., Ishizaki, M., & Yamada, Y. (2003). Urinary cadmium excretion is correlated with calcaneal bone mass in Japanese women. *Environ Res, 91*(2), 63–70. https://doi.org/10.1016/S0013-9351(02)00035-X

11. Hu, Y., Zhang, L., & Chen, X. (2024). Subchronic cadmium exposure induces oxidative stress and structural tissue damage in experimental rats. *Toxicol Rep, 11*, 245–256. https://doi.org/10.1016/j.toxrep.2024.01.015

12. Järup, L. (2003). Hazards of heavy metal contamination. *Br Med Bull, 68*(1), 167–182. https://doi.org/10.1093/bmb/ldg032

13. Johnson, J. L. (2017). Metalloproteinases in atherosclerosis. *Eur J Pharmacol, 816*, 93–106. https://doi.org/10.1016/j.ejphar.2017.09.007

14. Li, H., Fagerberg, B., Sallsten, G., et al. (2019). Smoking-related cadmium and cardiovascular risk. *Environ Health, 18*(1), 56. https://doi.org/10.1186/s12940-019-0495-1

15. Messner, B., Turkcan, A., Ploner, C., Laufer, G., & Bernhard, D. (2016). Cadmium-induced endothelial damage. *Cell Mol Life Sci, 73*(8), 1699–1713. https://doi.org/10.1007/s00018-015-2094-9

16. Olejarz, W., Lacheta, D., & Kubiak-Tomaszewska, G. (2020). MMPs as biomarkers of plaque instability. *Int J Mol Sci, 21*(11), 3946. https://doi.org/10.3390/ijms21113946

17. Ozturk, I. M., Buyukakilli, B., Balli, E., Cimen, B., & Gunes, S. (2009). Effects of cadmium on the cardiovascular system. *Toxicol Mech Methods, 19*(4), 308–317. https://doi.org/10.1080/15376510802662751

18. Peters, J. L., Perlstein, T. S., Perry, M. J., McNeely, E., & Weuve, J. (2010). Cadmium exposure and cardiovascular disease. *Environ Res, 110*(2), 199–206. https://doi.org/10.1016/j.envres.2009.12.004

19. Protsenko, Y. L., Klinova, S. V., Gerzen, O. P., & Katsnelson, B. A. (2020). Changes in rat myocardium contractility under subchronic intoxication with lead and cadmium salts administered alone or in combination. *Toxicol Rep, 7*, 433–442. https://doi.org/10.1016/j.toxrep.2020.03.001

20. Raktim, M., Megha, D., Selvaraj, J., et al. (2026). Cadmium-induced cardiac injury. *Cardiovasc Toxicol, 26*(6). https://doi.org/10.1007/s12012-025-10082-8

21. Razooqi, A., Hassan, M., & Al-Shaeli, S. (2024). Dose-dependent toxic effects of cadmium chloride on organ morphology and oxidative balance in rats. *Environ Sci Pollut Res, 31*(18), 27411–27423. https://doi.org/10.1007/s11356-024-32841-7

22. Reda, A. A., Eatemad, A. A., Amal, S. H., & Dalia, E. F. M. (2024). Cadmium cardiotoxicity in embryogenesis. *Cardiovasc Toxicol, 24*, 982–1003. https://doi.org/10.1007/s12012-024-09894-x

23. Rossi, K. A., Almenara, C. C. P., Simoes, R. P., et al. (2024). Cadmium effects on blood pressure. *Biol Trace Elem Res, 202*, 2645–2656. https://doi.org/10.1007/s12011-023-03851-5

24. Satarug, S., Garrett, S. H., Sens, M. A., & Sens, D. A. (2010). Cadmium, environmental exposure, and health outcomes. *Environ Health Perspect, 118*(2), 182–190. https://doi.org/10.1289/ehp.0901234

25. Sepulchro Mulher, D., de Oliveira, B. F., de Souza, L. L., et al. (2024). Cadmium exposure impairs vascular reactivity and endothelial integrity in isolated aortas of female Wistar rats. *Environ Toxicol Pharmacol, 107*, 104438. https://doi.org/10.1016/j.etap.2024.104438

26. Shen, J., Wang, X., Zhou, D., et al. (2018). Cadmium-induced cardiotoxicity in stem cell-derived cardiomyocytes. *J Cell Mol Med, 22*(9), 4221–4235. https://doi.org/10.1111/jcmm.13702

27. Spinale, F. G., Janicki, J. S., & Zile, M. R. (2013). Matrix proteolysis and heart failure. *Circ Res, 112*(1), 195–208. https://doi.org/10.1161/CIRCRESAHA.112.266882

28. Tai, Y. T., Chen, K. C., Hsu, Y. C., et al. (2022a). Chronic cadmium exposure induces tissue accumulation and histopathological alterations in mice. *J Appl Toxicol, 42*(9), 1458–1472. https://doi.org/10.1002/jat.4305

29. Tai, Y. T., Chou, S. H., Cheng, C. Y., Ho, C. T., & Lin, H. C. (2022b). The preferential accumulation of cadmium ions among various tissues in mice. *Toxicol Rep, 9*, 111–119. https://doi.org/10.1016/j.toxrep.2022.01.002

30. Tellez-Plaza, M., Guallar, E., Howard, B. V., et al. (2013). Cadmium exposure and incident cardiovascular disease. *Epidemiology, 24*(3), 421–429. https://doi.org/10.1097/EDE.0b013e31828b0631

31. Tellez-Plaza, M., Jones, M. R., Dominguez-Lucas, A., Guallar, E., & Navas-Acien, A. (2013). Cadmium exposure and clinical cardiovascular disease. *Curr Atheroscler Rep, 15*(10), 356. https://doi.org/10.1007/s11883-013-0356-2

32. Thevenod, F., & Lee, W. K. (2013). Toxicology of cadmium and its damage to mammalian organs. *Met Ions Life Sci, 11*, 415–490. https://doi.org/10.1007/978-94-007-5179-8_14

33. Tinkov, A. A., Filippini, T., Ajsuvakova, O. P., et al. (2018). Cadmium and atherosclerosis. *Environ Res, 162*, 240–260. https://doi.org/10.1016/j.envres.2018.01.008

34. Washington, B., Williams, S., Armstrong, P., et al. (2006). Cadmium toxicity in vascular smooth muscle. *Int J Environ Res Public Health, 3*(4), 323–328. https://doi.org/10.3390/ijerph2006030040

35. Xiao, J., Xie, Y., Zhang, L., Ye, R., & Zeng, X. (2026). GADD45G and cadmium-induced endothelial dysfunction. *Biochem Mol Toxicol, 40*(1). https://doi.org/10.1002/jbt.70672

Information about the authors:

Nurzhamal M. Joldasbayeva – PhD Student (3rd year), Abai Kazakh National Pedagogical University (Almaty, Kazakhstan; e-mail: nurimazhitovna@mail.ru).

Zina B. Tungushbaeva – Doctor of Biological Sciences, Professor, Abai Kazakh National Pedagogical University (Almaty, Kazakhstan; e-mail: alua2002@yandex.kz).

Murat B. Zhaksybaev – Candidate of Biological Sciences, Associate Professor, Abai Kazakh National Pedagogical University (Almaty, Kazakhstan; e-mail: zh.murat_1966@mail.ru).

Nariman N. Pravin – Master of Science, Senior Lecturer, Kazakhstan–Russia Medical University named after M. Aliyev (Almaty, Kazakhstan; e-mail: n.pravin@medkrmu.kz).

Received 26 March 2026;
received in revised form 20 June 2026;
accepted 26 June 2026

IRSTI 34.23.41; 34.15.23; 34.47.51 https://doi.org/10.26577/IJBCh20261915

N. Kabysheva[1], O. Khamdiyeva[1], L. Tenelbayeva[1,2], G. Koishekenova[1], N. Altynova[1], L. Djansugurova[1], E. Djangalina[1], C. Cakir-Kiefer[3], G. Baratzhanova[1*]

[1]Institute of Genetics and Physiology, Almaty, Kazakhstan
[2]Al-Farabi Kazakh National University, Almaty, Kazakhstan
[3] Université de Lorraine, Nancy, France
* e-mail: baratzhanova.gulminyam@gmail.com

THE ADVANTAGES AND LIMITATIONS OF HUMAN LIVER MODELS IN *IN VITRO* TOXICOLOGY STUDY

Abstract: This review collects and analyses information about modern liver models used in toxicological studies from 2015 to January 2026. Currently, human liver models are increasingly being improved and various approaches being explored, including the selection of different cell types and advanced cultivation methods, to more accurately simulate the *in vivo* liver environment to replace animal models. These new methods are increasing the complexity of *in vitro* systems. However, the complex liver models currently available are not yet a complete replacement for animal models and does not have all the characteristics of the liver. Since many models undergo phenotypic changes during prolonged cultivation, this limits their suitability for long-term studies of repeated administration toxicity. Moreover, they have limited suitability, lack of vascularization, labour demanding and expensive. However, compared to early 2D hepatocyte cultures, these modern systems demonstrate significantly improved prediction accuracy and physiological relevance. With continued development, it may be possible to create models capable of tracking the occurrence, progression, and potential reversibility of liver drug toxicity.
Keywords: liver cells, HepG2, HepaRG, 2D culture, 3D culture, toxicology.

Introduction

The liver is the central organ for the metabolism and transformation of xenobiotics and is therefore a major focus of toxicological research. The toxicological effect of drugs is one of the main reasons for drug elimination during development (Guengerich, 2011). Moreover, proper liver models are also used to study mechanism of action of different environmental pollutions (Baratzhanova et al., 2025). This highlights the need for reliable preclinical models capable of predicting hepatotoxicity. Although animal models have traditionally been used to assess safety, interspecies differences and ethical considerations have stimulated the development of human-relevant *in vitro* systems (Poh & Stanslas, 2024).

The use of human cell culture systems makes it possible to study human metabolism and physiology, which are difficult to accurately reproduce in *in vivo* studies (Philippeos et al., 2012). Cell culture mimics the reaction of target tissue cells in the human body in response to chemicals. However, there are important differences between systems of whole organisms and isolated cellular systems regarding the types and complexity of toxic effects that can be measured. In animal studies, toxicity assessment often focuses on one or two critical endpoints that appear first when the dose of a xenobiotic is increased. Although such models provide valuable systemic information, they may not reflect the full range of biological reactions occurring in the body, and some effects may go unnoticed during experimental observation. In contrast, cell culture models allow the assessment of specific cellular and molecular mechanisms of toxicity. Nevertheless, the results obtained *in vitro* require careful verification of compliance with the *in vivo* data obtained in humans to confirm their physiological significance.

In vitro systems are particularly advantageous for screening purposes because localized toxicity can be assessed more quickly under controlled exposure conditions. In addition, cellular toxicity data can be

compared with calculated *in vivo* exposure levels to improve risk assessment. The other advantage of cell culture models is the relative homogeneity of the cell population, which reduces variability resulting from genetic and environmental factors. This makes possible to manipulate genes and molecular pathways. It allows generation of data with high reproducibility and consistency, which cannot be guaranteed when studying entire organ systems (Segeritz & Vallier, 2017).

Nowadays, significant progress has been made in the development and application of cellular systems, which has led to the stability and functionality of liver models. An important and main criteria for evaluating liver models in fundamental or pharmacological studies is their ability to perform basic liver functions and maintain appropriate metabolic pathways. As mentioned above, liver plays a central role in the metabolism of endogenous substrates and exogenous compounds, the regulation of homeostasis of amino acids, carbohydrates and lipids, the synthesis of plasma proteins such as albumin and transferrin, as well as in the activation of inflammatory and immune responses after damage caused by diseases, drugs or toxic effects (Zeilinger et al., 2016).

Hepatocytes are generally considered to be metabolically adequate models for *in vitro* assessment of hepatotoxicity. They are increasingly being used in studies on xenobiotic toxicity, including genotoxic effects (Guo et al., 2020). Over the past decades, liver modelling has progressed from traditional two-dimensional (2D) hepatocyte cultures to more advanced three-dimensional (3D) systems, including spheroids, organoids, extracellular matrix 3D models, and organs on a chip. These models aim to more accurately reproduce the structural and functional complexity of the human liver. However, increasing the complexity of the model does not always lead to improved predictive characteristics, and cultivation conditions, endpoints, and applications vary significantly (Fukunaga & Takebe, 2025).

Given this rapid development of liver modelling technologies and their growing role in toxicological assessment, it is necessary to conduct a comprehensive analysis of the available models and their applications. The purpose of this review study is to systematically examine existing *in vitro* human liver models used in toxicology, summarize their advantages and limitations, and identify gaps that need to be addressed to increase their predictive value regarding the toxicity of xenobiotics to the liver.

Data collection method

This scoping review was conducted to map existing and new literature on hepatocyte models which can be used in toxicology studies. A comprehensive literature search was conducted through online library sources in PubMed, Science Direct, Web of Science from 2015 to January 2026. The specific search criteria for Science Direct and Web of Science was (“2D liver cells” OR “3D liver cells” OR “liver cell” OR “HepG2” OR “HepaRG” OR “PHH liver cell” OR “HuH-7 “) AND (“toxicology research” OR “ drug discovery”). For PubMed search criteria was (“Primary human hepatocytes” OR “HepG2” OR “HepaRG” OR “HuH-7” OR “Fa2N-4”) AND (toxicolog* OR toxico* OR “toxicity” OR “toxic effects” OR “toxic response”). Key words such as “2D hepatocyte models”, “3D hepatocyte models”, “toxicology research on liver cells”, etc. were used.

Reference list of included studies was manually screened to identify other relevant articles. Included articles were describing or evaluating hepatocyte-based models used in toxicology studies. Only studies published in English were included. The results were summarized in a descriptive form. Hepatocyte models were classified according to their structural complexity (2D, 3D, organoids, etc). Research trends, advantages, limitations, and gaps in the literature were summarized in Tables and Figures.

Results

The database search yielded 518 articles in Web of Science and 4761 articles for Science Direct, and 1424 for PubMed. Search depending on liver cell types was also performed and showed that among three databases article concerning usage of HepG2 in toxicological studies was predominant (Fig.1). After removing duplicate, articles were screened by title and abstract.

Figure 1
Literature search results for human liver cell publications across three databases (from January 2015 to January 2026)

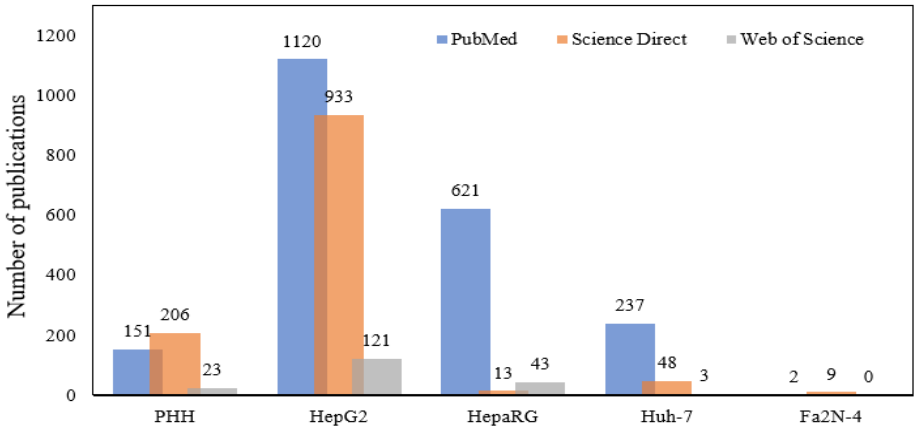

2D cultures

Primary human hepatocytes (PHH) isolated from the liver have morphological and biochemical characteristics that are most similar to the original tissue (Segeritz & Vallier, 2017). Such cells are considered the gold standard for the creation of human-appropriate models for the cultivation of liver cells *in vitro*. They recreate the functionality of the liver as *in vivo*, and provide fairly accurate results in pharmacological and toxicological studies *in vitro*. Also, these cells allow analysing a wide range of genetic polymorphisms, since they are derived from an individual donor. However, this fact also complicates model standardization due to interindividual variability and alterations induced during isolation procedure. In addition, the limited availability and complex logistical requirements associated with PHH cells prevent their large-scale application (Shulman & Nahmias, 2013; Zeilinger et al., 2016). The characteristics of the donor, including age, liver fat content and pre-existing liver damage, as well as procedural factors such as tissue conditions and transportation time, significantly affect cell viability (Richert et al., 2004). Immediately after tissue extraction, hepatocytes become very sensitive to ischemic damage and quickly lose their viability. Regardless of preservation method there is usually a significant decrease in the activity of enzymes that metabolize phase I and phase II drugs (Godoy et al., 2013; Kammerer & Küpper, 2018). These disadvantages makes them also expensive to use (Van den Hof et al., 2014).

Several approaches have been proposed to overcome the limited cell viability of PHH (Castell et al., 2006). One such strategy involves cellular immortalisation. Immortalized cell lines are characterized by their ability to proliferate indefinitely *in vitro*, overcoming normal replicative senescence. This state is usually achieved through genetic modifications such as ectopic expression of telomerase reverse transcriptase (hTERT) or introduction of viral oncogenes that suppress key cell cycle regulators (e.g., p53 and Rb), or by culturing tissues derived from tumours.

Viral oncogene introduction. Transformed Human Liver Epithelial-2 cells (THLE-2), derived from healthy human liver, were immortalized by the introduction of the simian virus 40 large T antigen (SV40) (Pfeifer et al., 1993). Yalda Soltanpour *et al.* in their study analysed the expression of 96 representative genes involved in drug absorption, distribution, metabolism, and excretion of drugs (ADME) in THLE-2 cells. These genes encode various transporters, phase I and II drug-metabolizing enzymes, and nuclear hormone receptors (Table 1). During their study, it was shown that the expression of most genes was absent or at a low level, with the exception of some cytochrome P450 (CYP) genes, CYP2C9 and CYP3A4 (Soltanpour et al., 2012).

Other human hepatocytes immortalised by transfection with SV40 are Fa2N-4 cells. They were derived from a 12-year-old female donor. These cells show ability to induce *CYP3A4, CYP2C9, CYP1A2, UGT1A,* and MDR1 mRNA in response to known in-

ducers similar to PHH. Moreover, this induction also can be noticed at the enzyme activity level (Mills et al., 2004). Youdim *et al.* confirmed that Fa2N-4 cells are suitable model for evaluation of P450 induction using cocktail approach (Youdim et al., 2007). Moreover, they are easily available and can be grown in culture as needed for experimental use, unlike freshly isolated human hepatocytes, whose availability depends on access to suitable donor liver tissue (Mills et al., 2004). Hariparsad *et al.* showed that the expression of PXR and AhR is similar between Fa2N-4 cells and human hepatocytes, but CAR and some hepatic uptake transporters, the organic anion-transporting polypeptides, were significantly reduced in this cell line compared to primary cells (Hariparsad et al., 2008).

Hepatocarcenoma cell lines. Considerable efforts were made to develop reliable cell models of human liver cells that would show a fairly accurate prediction of results after exposure to genotoxic chemicals for effective screening. As a result, several models of human hepatocarcinoma cell cultures were created, which are used in toxicological studies, like HepG2 (Knasmüller et al., 2004), HepaRG (Mandon et al., 2019), HuH-7 (Nakabayashi et al., 1982), etc (Table 1). Cells obtained from liver tumour tissue have been widely used as models for toxicological studies *in vitro*. These cell lines have good availability, high ability to proliferate and stable metabolism. However, the high potential for proliferation of these cells usually leads to the loss of differentiated functions. Because of this, for toxicological studies, it is necessary to take into account the specific functional characteristics of the cell lines (Zeilinger et al., 2016).

HepG2 cell line, derived from hepatocellular carcinoma, was obtained from a 15-year-old Caucasian male diagnosed with hepatoblastoma. This cell line has been extensively characterised and retains a number of functional properties of normal hepatocytes (Roe et al., 1993). HepG2 cells are cheap and easy to cultivate, and over the years, a significant amount of experimental data has been accumulated, allowing for the creation of an extensive reference database (Figure 1) (Mišík et al., 2019). Moreover, HepG2 cells are less technically demanding than PHH and demonstrate superior experimental reproducibility (Ramirez et al., 2018). However, there have been still some reports of showing interlaboratory variability, as well as inconsistency in the reproducibility of experiments with individual compounds (Waldherr et al., 2018).

These cells express a wide range of CYP enzymes; However, both mRNA and protein levels are generally lower than those observed in normal hepatocytes. In addition, they are also capable of performing second-phase metabolic reactions, including glutathione conjugation as well as glucuronidation and sulfation reactions (Donato et al., 2008). Notably, HepG2 cells exhibit relatively high levels of antioxidant enzymes and intracellular glutathione compared to many other human cell lines. Similar metabolic responses to dioxin and dibenzofurans have been reported in HepG2 and PHH (Dehn et al., 2005). In addition, transcriptomic analysis showed that HepG2 cells exhibit increased expression of genes involved in DNA, RNA, and protein metabolism, as well as cell cycle-related processes compared to HepaRG and PHH cells (Jennen et al., 2010).

HepG2 cells have been shown to be suitable for cytotoxicity screening by assessing reactive oxygen species (ROS) formation, glutathione depletion, and loss of membrane integrity (Schoonen et al., 2005). In addition, comparable modulation of gene expression profiles was observed in both PHH and HepG2 cells after exposure to the hepatotoxic compound trovafloxacin (Liguori et al., 2008). Magkoufopoulou *et al.* further showed that the integration of transcriptome analysis with the Ames test improves the prediction of genotoxic potential *in vitro* (Magkoufopoulou et al., 2012). Moreover, transcriptomic profiling of HepG2 cells exposed to toxic substances allowed the development of an *in vitro* screening test for phospholipidosis (Sawada et al., 2005). Van den Hof *et al.* applied gene expression analysis in HepG2 cells to classify chemical compounds according to their hepatotoxic properties (Van den Hof et al., 2014).

HepG2 often used as well to study human Apolipoprotein-B100 metabolism because they secretes predominately higher density Apolipoprotein-B100 -containing particles and low density lipoproteins, unlike normal human liver, which secretes Apolipoprotein-B100 mainly associated with VLDL particles (Meex et al., 2011). In the study of Meex *et al.*, they showed that HepG2 cells are more efficient in lipidation of apoB100 than Huh-7 cells. Compared to PHH, HepG2 cells has defect in assembly of hepatic VLDL. Tsai *et al.* showed that through inhibition of the overactive ras-MEK-ERK pathway this defect can be corrected (Tsai et al., 2007).

HepG2 cells also wildly used model to predict mitochondrial dysfunction and hepatotoxicity (Berger et al., 2016; Kamalian et al., 2015; Ramirez et al., 2018; Stanley & Wolf, 2022). Unlike many mammalian cells, HepG2 cells exhibit metabolic flexibility, allowing them to switch between glycolysis and oxidative phosphorylation to sustain proliferation, even

under low-oxygen conditions. This capacity to rely on glycolysis can render them less sensitive to mitochondrial toxicants (Marroquin et al., 2007). However, Kamalian *et al.* demonstrated that HepG2 cells subjected to acute glucose deprivation become more dependent on mitochondrial respiration and therefore represent a suitable model for detecting mitochondrial toxicity. The combined assessment of ATP levels and cytotoxicity in both metabolic states provides a more comprehensive evaluation of the underlying mechanisms of toxicity (Kamalian et al., 2015).

Huh-7 cells is a well-differentiated and characterized *in vitro* model of hepatocellular carcinoma (HCC) that is widely used in metabolic research. The cell line was isolated in 1982 from 57-year-old man with highly differentiated HCC and was proposed as an alternative to PHH and HepG2 cells (Nakabayashi et al., 1982). Huh-7 cells are often used to evaluate the efficacy and metabolism of anticancer drugs that affect the liver. For example, Huh-7 cells have proven valuable for studying drug distribution in the liver mediated by transporter proteins and for studying interactions with proteins associated with multidrug resistance (Jouan et al., 2016; Malinen et al., 2019). In addition, Huh-7 cells have also been effectively used in toxicity studies and are capable of bioactivating certain compounds, including acetaminophen, which leads to the formation of the hepatotoxic metabolite *N*-acetyl-*p*-benzoquinone imine (Nelson et al., 2015). Jouan *et al.* showed that Huh-7 cells exhibit significant activity of the multidrug-resistant protein (MRP), which probably reflects the expression of several liver MRPs, including MRP2. However, these cells lack the functional activity of key uptake transporters such as organic anion-transporting polypeptides, sodium-taurocholate co-transporting polypeptide, and organic cation transporter 1, as well as tubular transporters including P-glycoprotein and breast cancer resistance protein (Jouan et al., 2016).

Huh-7 cells have several distinctive features. In particular, they are homozygous for the null CYP3A5*3 null allele, indicating that the metabolism of CYP3 substrates is mediated exclusively by CYP3A4 (Dorr et al., 2017). Another characteristic is that Huh-7 cells secreted more Apolipoprotein-B100 than HepG2 cells did, according to the mass data (normalized to cell protein) (Meex et al., 2011). HuH-7 cells are also highly susceptible to the hepatitis C virus (HCV) which make them perfect model to study HCV (Lohmann et al., 1999). However, genomic analyses revealed significant chromosomal abnormalities in Huh-7 cells, including changes affecting all chromosomes and extensive loss of heterozygosity covering approximately 55.3% of the genome, consistent with the presence of numerous homozygous variants identified by sequencing (Kasai et al., 2018).

HepaRG cell line was derived from the liver tumour of a patient with chronic hepatitis C and macronodular cirrhosis (Marion et al., 2010). In culture, HepaRG cells typically differentiate into a mixed population of hepatocyte-like cells and cholangiocyte-like cells (Aninat et al., 2006). These cells retain the ability to express a wide range of liver-specific genes involved in carbohydrate, bile acid, and lipid metabolism, as well as in xenobiotic detoxification processes (Guo et al., 2020). HepaRG cells express key drug transporters such as ATP-binding cassettes (ABCs), nuclear receptors (e.g., CAR and PXR), CYP enzymes, phase II conjugating enzymes, and functional proteins such as albumin, transferrin, aldolase B, as well as various apical and tubular proteins (Zheng et al., 2021). It is important to note that differentiated HepaRG cells are considered one of the most comparable *in vitro* liver models to PHH (Cerec et al., 2007).

It was shown that genes located in 7th chromosome are highly expressed in HepaRG cells in comparison to PHH due to extra copy of this chromosome (Hart et al., 2010). Complex proteomic and secretomic analyses have shown that HepaRG cells have functional mitochondria and retain the ability to secrete hepatokines (Tascher et al., 2019). Compared to HepG2 cells, HepaRG cells exhibit higher activity of CYP enzymes and phase II conjugation enzymes. The differences in expression levels in the major drug-response gene families, such as CYPs, ALDHs, ADHs, NATs, FMOs, GSTs, UGTs, SULTs, ABCBs, ABCCs, ABCGs, and SLCOs showed that HepG2 and PHH were have much larger differences than the differences between HepaRG and PHH for most genes (Hart et al., 2010). In addition, HepaRG cells have been shown to be more sensitive to detecting DNA damage caused by xenobiotics, which confirms their suitability for genotoxicity assessment (Guo et al., 2020; Seo et al., 2019, 2020).

However, HepaRG cells less sensitive in detecting some direct- and indirect acting genotoxic carcinogens, such as cadmium chloride, etoposide, 2-amino-3-methylimidazo, and 2,4-diaminotoluene (Mandon et al., 2019; Mišík et al., 2019). Another limitation of this cells are their expansivity, scarce, and recurrence in higher levels of maintenance (Donato et al., 2013).

HepaRG cells are highly proliferative, they can differentiate toward hepatocytic and biliary lineage and into functional hepatocytes *in vivo*. Moreover,

probably due to their tumour origin, HepaRG cells have the potential to transdifferentiate through a hepatic bipotent progenitor (Cerec et al., 2007). It was also shown that HepaRG cells have higher galactose/sorbitol elimination rates and albumin production in comparison to PHH, however urea production was not observed. As well CYP expression was found to be more stable over cultivation in HepaRG cells (Lübberstedt et al., 2011).

Human Induced pluripotent stem cells (iPSCs). Recently human iPSCs became popular a renewable starting material for generating primary cell types, as they enable the recapitulation of human tissue from a sustainable source (Gracey & Lampe, 2025). In liver research, most teams focus on differentiating iPSCs into hepatocyte-like cells (HLC) that will replicate the metabolic activity of PHH. Multiple studies have demonstrated the applicability of HLC in drug metabolism studies, toxicity screening and modelling of specific liver diseases (Dao Thi et al., 2020; Donowitz et al., 2020; Gómez-Lechón & Tolosa, 2016; Mann, 2015; Matsui et al., 2020). Nevertheless, full maturation and restoration of HLC metabolic activity to adult levels remains a challenge, and none of the existing protocols for differentiating iPSCs into HLCs can produce cells that fully replicate the phenotype of adult human liver (Graffmann et al., 2022).

Table 1
Overview of 2D liver cells used in toxicology studies

Models	Advantages	Disadvantages	Application	References
PHH	+ Functionality of the liver as *in vivo* + Diversity in genetic polymorphisms	– Limited availability – Instability of the phenotype – Short time cultivation – Higher Cost	• Hepatotoxicity • DILI prediction • Inter-individual variability test	(Parmentier et al., 2018; Segeritz & Vallier, 2017; Shulman & Nahmias, 2013; Zeilinger et al., 2016)
THLE-2	+ Non-tumorigenic + Expression of CYP2C9 and CYP3A4 genes + Stable cell culture	– Expression of ADME genes is absent or in low level – Low receptor abundance	• Oxidative stress • inflammatory responses • Cytotoxic assays	(Sefried et al., 2018; Shah et al., 2014; Soltanpour et al., 2012; Şahin et al., 2024)
Fa2N-4	+ Consistent and reproducible + Express ADME genes like PHH + Higher mRNA level of MDR1	– Low basal level of CAR nuclear receptor and some enzymes such as CYP1A2, CYP1A1, CYP2D6, CYP2E1, UGT1A1, UGT1A6 etc – Incapable of metabolizing compounds	• Cocktail approach • Pathway-Specific Toxicological Studies	(Mills et al., 2004; Ramboer et al., 2015; Youdim et al., 2007)
HepG2	+ Easy handling and low cost + Stable growth + Active phase II metabolism enzymes + High antioxidant capacity + Metabolic specificity	– Low CYPs expression compared to PHH – Tumour-Derived Phenotype – Altered lipid metabolism – Interlaboratory variability	• Cytotoxic assays • Pathway-Specific Toxicological Studies • ROS formation assays • Transcriptomic profiling • Mitochondrial toxicity screening • Genotoxicity prediction (combined with Ames's test) • Phospholipidosis screening	(Donato et al., 2008; Jennen et al., 2010; Kamalian et al., 2015; Magkoufopoulou et al., 2012; Meex et al., 2011; Mišík et al., 2019; Ramirez et al., 2018; Sawada et al., 2005; Schoonen et al., 2005; Stanley & Wolf, 2022; Waldherr et al., 2018)
HuH-7	+ High susceptibility to hepatitis C virus + Higher ability to secrete lipoproteins + Capable of bioactivating acetaminophen + Significant activity of the multidrug-resistant protein	– Tumor-Derived Phenotype – Genomic Instability – Altered CYPs expression compared to PHH	• Drug Transport and Multidrug Resistance Studies • studying HCV biology	(Jouan et al., 2016; Lohmann et al., 1999; Malinen et al., 2019; Marroquin et al. 2007; Nelson et al., 2015; Sawada et al., 2005)

Continuation of the table

Models	Advantages	Disadvantages	Application	References
HepaRG	+ High similarity to PHH + High expression and inducibility of CYPs + Functional Phase II Enzymes and Transporters + Mixed population of hepatocytes and cholangiocytes	– Complex and time-consuming differentiation – Higher Cost in comparison to HepG2 – Less sensitive in detecting some direct- and indirect genotoxic carcinogens	• Hepatotoxicity • DILI prediction • Metabolism and biotransformation of xenobiotics • Genotoxicity prediction • Oxidative stress assays • Detection of drug-induced mitochondrial toxicity	(Aninat et al., 2006; Cerec et al., 2007; Guo et al., 2020; Hart et al., 2010; Mandon et al., 2019; Mišík et al., 2019; Seo et al., 2019, 2020; Tascher et al., 2019; Zheng et al., 2021)

3D cultures

The 3D cellular model combines the advantages of conventional 2D cultivation models, such as lower labour intensity, fever ethically debates compared to live animal models, which makes 3D culture more powerful and widely used *in vitro* model. Currently, 3D models are widely used in fields such as biology, medicine, and pharmacy (Brancato et al., 2020). In addition, 3D culture can also provide a good cellular microenvironment that resembles the real internal conditions of the human body (Fig.2), and thus respond more realistically to environmental pollution (S. Yang et al., 2021; H. Wang et al., 2023).

Spherical hepatic culture. As mentioned before, PHH in 2D monolayer culture rapidly de-differentiate and lose hepatocyte-specific functions. To overcome this issue PHH can be cultured as 3D spheroids. It was shown that this 3D culture can be maintained for longer time in comparison to 2D PHH and produce albumin and urea. It was found that in comparison to 2D PHH the level of expression of proteins involving in drug ADME and catalytic activities of CYPs enzymes, were significantly higher in 3D spheroid cultures (Bell et al., 2018). Moreover, they can form a functional network of bile channels extending from the surface to the inside of the spheroids after 3-4 weeks of cultivation (Tostões et al., 2012). PHH spheroids can also be obtained using bioreactors (Mueller et al., 2011). However, there are some limitations connected to 3D PHH spheroids such as inability to control spheroids` size, difficulty in suspension of them in medium and its replacement.

Except PHH spheroids nowadays several 3D HepaRG models were obtained, which can mimic *in vivo* like microenvironments. In comparison to 2D HepaRG they show improved differentiation, functionality and longevity (Darnell et al., 2012; Gunness et al., 2013; Leite et al., 2012). There are as well HepG2 spheroids that actively used as biosensor-like cell based system to evaluate genotoxicity (Štampar et al., 2022). Compared to 2D HepG2 cells, 3D HepG2 spheroids showed time-dependent decrease in cell proliferation, increased liver function specificity and demonstrated strong physiological relevance in terms of the expression of liver marker genes and metabolic enzymes (Štampar et al., 2020).

3D hepatic organoids. Organoids are 3D self-organised cells derived mostly from stem cells that mimic tissues and organs by recreating their basic functions on a small scale through cell-cell and cell-matrix interaction (Lancaster & Knoblich, 2014). They allow modelling human diseases to evaluate therapeutic strategies. For instance, Ramli *et al.* developed liver organoid with gene expression signature of nonalcoholic steatohepatitis, destruction of the bile duct network and ductal reactions (Ramli et al., 2020). Another model is CFTR-mutant cholangiocyte organoids, which were used to study the patient-specific response to CFTR modulators in patients with cystic fibrosis (Sampaziotis et al., 2021). De Crignis *et al.* generated transgenic organoids to model hepatitis B and C virus infections, which can enables drug screening and identification of cancer-related gene signatures in hepatitis B-infected tissues obtained from patients (De Crignis et al., 2021).

Organoids are also widely used in the assessment of drug toxicity, drug development, and pharmacological research. For example, Bronsard *et al.* obtained 3D multi-cell-type liver organoids using different cell cultures such as primary human macrophages, HepaRG, and hepatic-stellate-cell-derived LX-2 cells to model drug-induced liver injury (Bronsard et al., 2024). Another example is the human liver organoid model developed by Wu *et al.* which has successfully model liver fibrogenesis after stimulation of TGF-β or LPS and has demonstrated application in screening of antifibrotic drugs and drug safety testing (Wu et al., 2023).

Extracellular matrix 3D models. The understanding that the interaction of cells with the extracellular matrix (ECM) affects the morphology, function of cells, as well as their therapeutic response has influenced the development of other types of 3D models that are embedded in the matrix. For example, researchers from Italy have presented a hybrid alginate and ECM hydrogel for creating 3D *in vitro* models of the liver called Hep3Gel to reproduce the chemical and mechanical behaviour of the liver with the possibility of adapting its shape to various production technologies. The viscoelastic properties of Hep3Gel were adjusted considering the available knowledge about liver biomechanics, which made it possible to reproduce the properties of a physiological organ. In addition, this model can be used as a bioink for 3D printing (Guagliano et al., 2023).

Another example of ECM use a method that makes it possible to isolate and further use the main types of human liver cells from cryopreserved material which was developed by Belgium team (Alevra Sarika et al., 2020). Calitz *et al.* showed that composition of ECM can influence on HCC behaviour and increase liver stiffness (Calitz et al., 2023). There are some studies which applied hepatic spheroids of PHH or HepaRG cells into collogen I ECM (Rose et al., 2021, 2022). Liao et al. showed that HepaRG spheroids embedded with collagen accelerate differentiation of cells compared to spheroids grown in suspension (Liao et al., 2022). However, most of the ECM are made from animal origin hydrogels which can create ethical issues and limit its use in human toxicity testing. Another option is synthetic hydrogels, which have reproducible quality, lower immunogenicity, greater mechanical strength, and are easily modifiable. However, they are less biologically active and lack viscoelasticity (Ye et al., 2019). One of the examples of synthetic hydrogen is HepMat gel developed by Kumar *et al.* a fully defined polyethylene glycol-based synthetic hydrogel functionalized to support co-culture of pluripotent stem cell derived hepatocyte- and non-parenchymal cellular -like cells. This system can model the key molecular and functional features of fatty acid-induced inflammation, TGFβ-induced liver fibrosis better than monocultures (Kumar et al., 2021).

The other method that can be related to ECM is collagen-based sandwich culture, where PHH cultured between two layers of collogen gel. Sandwich culture is better replicates the *in vivo* liver microenvironment and preserves key liver functions, including albumin and urea secretion, CYP activity, liver polarity, and bile duct formation in comparison to 2D cells (Dunn et al., 1989; Keemink et al., 2015). Consequently, this system is widely used for studies of drug clearance and polarity-dependent processes such as endocytosis (Treijtel et al., 2004; Zeigerer et al., 2017). Despite these advantages, sandwich cultures prone to cholestasis due to changes in bile metabolism, which limits their long-term preservation (Swift et al., 2010).

3D bioprinting. Currently, 3D printing is a widely popular field and has expanded its applications in regenerative medicine, tissue engineering, and drug screening. This technology allows to construct complex 3D structures which contains multiple cell types and biomaterials. Using this technology researcher can control of the mechanical and biological characteristics of 3D structures with high resolution along three dimensions. Using special bio-inks, it is possible to precisely tune the response or activity of cells to mimic the *in vitro* environment (Ma et al., 2018). There are various methods for 3D bioprinting such as extrusion-based bioprinting, inkjet-based bioprinting, acoustic bioprinting, laser-based bioprinting, at photopolymerization bioprinting (VPB) and magnetic bioprinting (Matai et al., 2020; Shukla et al., 2022)

Extrusion-based bioprinting allows the printing of the main components of liver units, while requiring only a simple and easily installed experimental setup. For applications involving microvessels, high-resolution DLP technology can be used to produce more complex matrices with excellent resolution. For 3D liver bioprinting bioinks contains hydrogels and different cells such as hepatic parenchymal cells (hepatocytes) and liver nonparenchymal cells (hepatic stellate cells, hepatic sinusoidal endothelial cells, and Kupffer cells) (W. Li et al., 2023). This technology was already used to mimic different diseases such as hepatocellular carcinoma (Xie et al., 2021) and fibrosis (van Grunsven, 2017). 3D bioprinter liver also can be applied in organ regeneration (Y. Yang et al., 2023) and drug screening (J.-Z. Wang et al., 2018). One of the latest bioprinted liver tissue on the basis of functional hepatocyte organoids derived from human chemically induced pluripotent stem cells was constructed by Li *et al.*, 2025. They showed that this model significantly reduced liver damage, inflammation, and fibrosis, while promoting liver regeneration and expression of biological functions in mice with acute chronic liver failure caused by CCl_4, as well as *Fah* -/- mice (G. Li et al., 2025). Another recently developed method is a 3D model of the human liver made of a disc-shaped structure from a mixture of PHH cells and collagen-1 placed in a highly permeable support medium made of polyethylene glycol

(PEG) microgels. This method has proven to be accurate, precise, and scalable. One hundred tissues can be produced per hour with a variability and error in diameter of about 4%. Histological and immunohistochemical evaluation showed self-organisation, cell cohesion, and expression of key markers in the liver (Subramaniam et al., 2025). Bioprinting represents a promising approach for use in liver toxicity testing, drug development, and organ regeneration. However, a number of challenges remain, including the manufacture of perfused vascular networks that play an important role in liver function, the accurate reproduction of the complex liver microenvironment, and the limited effectiveness of currently available bioinks (W. Li et al., 2023).

Organ-on-chip. The liver on a chip recreates the real conditions of liver functioning in an *in vitro* environment, such as a constant flow of blood and bile. With the help of this technology, a continuous flow of nutrient medium passes through microchannels, which delivers nutrients, oxygen and removes metabolic products (Ehrlich et al., 2019). Thanks to this flow, the liver cells on the chip retain their specialization better, metabolize drugs more actively, synthesize albumin and urea, and react correctly to toxic substances.

Liver in chip mostly used in disease modelling. For example, Gori *et al.* presented liver-on-chip *in vitro* models of human Non-alcoholic fatty liver disease, which enables higher hepatic cell viability, minimal oxidative stress and gradual and lower intracellular lipid accumulation (Gori et al., 2016). Hou *et al.* developed integrated Biomimetic Array Chip which is co-culture model that simultaneously evaluates anti-cancer efficacy and liver toxicity by integrating 3D models of liver and tumour tissues, which improves the accuracy of drug screening at early stages (Hou et al., 2020). Another study tested if liver-in-chip reliably detects toxicity of known hepatotoxin Diglycolic acid. They showed that this method allows reliable detect the hepatotoxicity with high sensitivity, low variability and improved physiological significance compared to traditional PHH multiwell plate format, which confirms its potential use in the regulatory assessment of drug safety (Eckstrum et al., 2020). Recent study also demonstrated the use of liver-on-chip for liver metabolism study and for genotoxicity assay to detect both direct and metabolically activated DNA damage, providing a promising, animal-free tool for early drug safety testing (Kopp et al., 2024). It was even shown that liver on-chip can model in some extend gut-liver interaction. This study demonstrated a multiorgan-on-a-chip platform that combines the human microbial-crosstalk gut-on-chip and the Dynamic42 liver-on-chip platform. This platform captures the influence of gut microbes on human drug metabolism, exemplified by E. coli converting irinotecan metabolites back into toxic forms. This is offering a human-relevant tool for studying microbiome-drug interactions and improving drug safety prediction (Lucchetti et al., 2024). Despite their advantages, liver-on-a-chip models still face several limitations. Their manufacture is a time-consuming and expensive process, and the accuracy and reproducibility of chips largely depend on the choice of materials and methods used in their creation (Liu et al., 2024).

Figure 2
3D culture methods and their disadvantages (ECM – extracellular matrix)

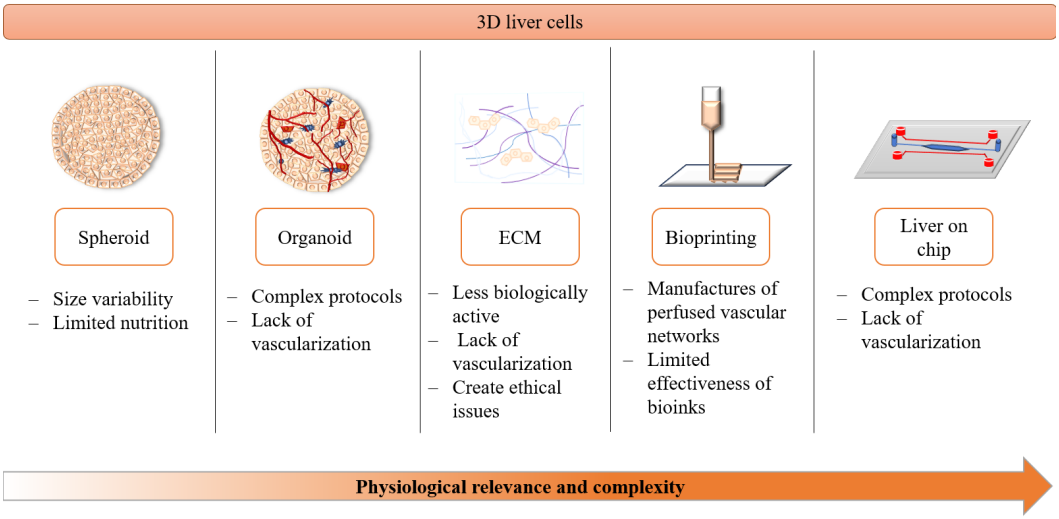

Conclusion

This review compiles and analyses information on modern liver models used in toxicological research. Currently, human liver models are being increasingly refined and various approaches are being explored, including the selection of different cell types and advanced culture techniques, with the aim of more accurately modelling the conditions of liver function *in vivo* to replace animal liver models.

Both 2D and 3D liver models play critical role in toxicology studies. Traditional 2D cultures remain widely used due to their simplicity, cost-effectiveness, reproducibility. They provide valuable insights into basic cellular mechanisms, toxicity testing and early stage of drug development. However, their inability to accurately reproduce the complex processes of native liver tissues limit their physiological relevance.

In contrast, modern *in vitro* liver models have significantly advanced toxicological studies by providing more physiologically relevant systems than early 2D hepatocyte cultures. The 3D cell models combine the advantages of conventional 2D cultivation models, such as lower labour intensity and the absence of ethical issues compared to live animal models, which makes the 3D culture a more powerful and widely used *in vitro* model. The use of various cell types and sophisticated cultivation methods has improved the prediction of the compounds' effects on the liver. However, problems such as phenotypic drift during long-term cultivation, limited suitability, lack of vascularization, etc., still limit their full-fledged use as an alternative to animal models. Despite these limitations, the continuous improvement of these models promises to provide more accurate tools for studying the occurrence, progression, and potential reversibility of hepatotoxicity. This will contribute to a safer and more effective assessment of chemicals and drugs in preclinical toxicology.

Acknowledgements

This research was funded by the Science Committee of the Ministry of Science and Higher Education of the Republic of Kazakhstan, grant number AP26199563 "Study the mechanisms of toxicity of various classes of organochlorine pesticides".

Conflict of interest

All authors are aware of the article's content and declare no conflict of interest.

Author contributions

Nailya P. Kabysheva: Conceptualization, Investigation, Writing – Original Draft

Ozada Khamdiyeva: Writing – Review & Editing

Lyazzat Tenelbayeva: Formal Analysis, Visualization

Gulshat Koishekenova: Writing – Review & Editing

Nazym K. Altynova: Writing – Review & Editing

Leyla B. Djansugurova: Conceptualization, Writing – Review & Editing

Erika D. Djangalina: Project Administration, Funding Acquisition, Writing – Review & Editing

Céline Cakir-Kiefer: Conceptualization, Methodology, Investigation, Writing – Review & Editing

Gulminyam S. Baratzhanova: Supervision, Conceptualization, Methodology, Investigation, Visualization, Writing – Review & Editing

References

1. Alevra Sarika, N., Payen, V. L., Fléron, M., Ravau, J., Brusa, D., Najimi, M., De Pauw, E., Eppe, G., Mazzucchelli, G., Sokal, E. M., des Rieux, A., & El Taghdouini, A. (2020). Human Liver-Derived Extracellular Matrix for the Culture of Distinct Human Primary Liver Cells. *Cells, 9*(6), 1357. https://doi.org/10.3390/cells9061357

2. Aninat, C., Piton, A., Glaise, D., Le Charpentier, T., Langouët, S., Morel, F., Guguen-Guillouzo, C., & Guillouzo, A. (2006). Expression of cytochromes P450, conjugating enzymes and nuclear receptors in human hepatoma HepaRG cells. *Drug Metabolism and Disposition, 34*(1), 75–83. https://doi.org/10.1124/dmd.105.006759

3. Baratzhanova, G., El Sheikh Saad, H., Fournier, A., Huguet, M., Joubert, O., Paul, A., Djansugurova, L., & Cakir-Kiefer, C. (2025). Comparison of the impact of chlordecone and its metabolite chlordecol on genes involved in pesticide metabolism in HepG2 cell line. *Environmental Toxicology and Pharmacology, 116,* 104701. https://doi.org/10.1016/j.etap.2025.104701

4. Bell, C. C., Dankers, A. C. A., Lauschke, V. M., Sison-Young, R., Jenkins, R., Rowe, C., Goldring, C. E., Park, K., Regan, S. L., Walker, T., Schofield, C., Baze, A., Foster, A. J., Williams, D. P., van de Ven, A. W. M., Jacobs, F., van Houdt, J., Lähteenmäki, T., Snoeys, J., … Ingelman-Sundberg, M. (2018). Comparison of Hepatic 2D Sandwich Cultures and 3D Spheroids for Long-term Toxicity Applications: A Multicenter Study. *Toxicological Sciences, 162*(2), 655–666. https://doi.org/10.1093/toxsci/kfx289

5. Berger, B., Donzelli, M., Maseneni, S., Boess, F., Roth, A., Krähenbühl, S., & Haschke, M. (2016). Comparison of Liver Cell Models Using the Basel Phenotyping Cocktail. *Frontiers in Pharmacology, 7*. https://doi.org/10.3389/fphar.2016.00443

6. Brancato, V., Oliveira, J. M., Correlo, V. M., Reis, R. L., & Kundu, S. C. (2020). Could 3D models of cancer enhance drug screening? *Biomaterials, 232*, 119744. https://doi.org/10.1016/j.biomaterials.2019.119744

7. Bronsard, J., Savary, C., Massart, J., Viel, R., Moutaux, L., Catheline, D., Rioux, V., Clement, B., Corlu, A., Fromenty, B., & Ferron, P. J. (2024). 3D multi-cell-type liver organoids: A new model of non-alcoholic fatty liver disease for drug safety assessments. *Toxicology in Vitro: An International Journal Published in Association with BIBRA, 94*, 105728. https://doi.org/10.1016/j.tiv.2023.105728

8. Calitz, C., Rosenquist, J., Degerstedt, O., Khaled, J., Kopsida, M., Fryknäs, M., Lennernäs, H., Samanta, A., & Heindryckx, F. (2023). Influence of extracellular matrix composition on tumour cell behaviour in a biomimetic in vitro model for hepatocellular carcinoma. *Scientific Reports, 13*(1), 748. https://doi.org/10.1038/s41598-023-27997-3

9. Castell, J. V., Jover, R., Martnez-Jimnez, C. P., & Gmez-Lechn, M. J. (2006). Hepatocyte cell lines: Their use, scope and limitations in drug metabolism studies. *Expert Opinion on Drug Metabolism & Toxicology, 2*(2), 183–212. https://doi.org/10.1517/17425255.2.2.183

10. Cerec, V., Glaise, D., Garnier, D., Morosan, S., Turlin, B., Drenou, B., Gripon, P., Kremsdorf, D., Guguen-Guillouzo, C., & Corlu, A. (2007). Transdifferentiation of hepatocyte-like cells from the human hepatoma HepaRG cell line through bipotent progenitor. *Hepatology, 45*(4), 957–967. https://doi.org/10.1002/hep.21536

11. Dao Thi, V. L., Wu, X., Belote, R. L., Andreo, U., Takacs, C. N., Fernandez, J. P., Vale-Silva, L. A., Prallet, S., Decker, C. C., Fu, R. M., Qu, B., Uryu, K., Molina, H., Saeed, M., Steinmann, E., Urban, S., Singaraja, R. R., Schneider, W. M., Simon, S. M., & Rice, C. M. (2020). Stem cell-derived polarized hepatocytes. N*ature Communications, 11*(1), 1677. https://doi.org/10.1038/s41467-020-15337-2

12. Darnell, M., Ulvestad, M., Ellis, E., Weidolf, L., & Andersson, T. B. (2012). In vitro evaluation of major in vivo drug metabolic pathways using primary human hepatocytes and HepaRG cells in suspension and a dynamic three-dimensional bioreactor system. *The Journal of Pharmacology and Experimental Therapeutics, 343*(1), 134–144. https://doi.org/10.1124/jpet.112.195834

13. De Crignis, E., Hossain, T., Romal, S., Carofiglio, F., Moulos, P., Khalid, M. M., Rao, S., Bazrafshan, A., Verstegen, M. M., Pourfarzad, F., Koutsothanassis, C., Gehart, H., Kan, T. W., Palstra, R.-J., Boucher, C., IJzermans, J. N., Huch, M., Boj, S. F., Vries, R., … Mahmoudi, T. (2021). Application of human liver organoids as a patient-derived primary model for HBV infection and related hepatocellular carcinoma. *eLife, 10*, e60747. https://doi.org/10.7554/eLife.60747

14. Dehn, P. F., Allen-Mocherie, S., Karek, J., & Thenappan, A. (2005). Organochlorine insecticides: Impacts on human HepG2 cytochrome P4501A, 2B activities and glutathione levels. *Toxicology in Vitro, 19*(2), 261–273. https://doi.org/10.1016/j.tiv.2004.10.002

15. Donato, M. T., Jover, R., & Gómez-Lechón, M. J. (2013). Hepatic cell lines for drug hepatotoxicity testing: Limitations and strategies to upgrade their metabolic competence by gene engineering. *Current Drug Metabolism, 14*(9), 946–968. https://doi.org/10.2174/1389200211314090002

16. Donato, M. T., Lahoz, A., Castell, J. V., & Gómez-Lechón, M. J. (2008). Cell lines: A tool for in vitro drug metabolism studies. *Current Drug Metabolism, 9*(1), 1–11. https://doi.org/10.2174/138920008783331086

17. Donowitz, M., Turner, J. R., Verkman, A. S., & Zachos, N. C. (2020). Current and potential future applications of human stem cell models in drug development. *The Journal of Clinical Investigation, 130*(7), 3342–3344. https://doi.org/10.1172/JCI138645

18. Dorr, C. R., Remmel, R. P., Muthusamy, A., Fisher, J., Moriarity, B. S., Yasuda, K., Wu, B., Guan, W., Schuetz, E. G., Oetting, W. S., Jacobson, P. A., & Israni, A. K. (2017). CRISPR/Cas9 Genetic Modification of CYP3A5 *3 in HuH-7 Human Hepatocyte Cell Line Leads to Cell Lines with Increased Midazolam and Tacrolimus Metabolism. *Drug Metabolism and Disposition, 45*(8), 957–965. https://doi.org/10.1124/dmd.117.076307

19. Dunn, J. C., Yarmush, M. L., Koebe, H. G., & Tompkins, R. G. (1989). Hepatocyte function and extracellular matrix geometry: Long-term culture in a sandwich configuration. *FASEB Journal: Official Publication of the Federation of American Societies for Experimental Biology, 3*(2), 174–177. https://doi.org/10.1096/fasebj.3.2.2914628

20. Eckstrum, K., Striz, A., Ferguson, M., Zhao, Y., Welch, B., Solomotis, N., Olejnik, N., & Sprando, R. (2020). Utilization of a model hepatotoxic compound, diglycolic acid, to evaluate liver Organ-Chip performance and in vitro to in vivo concordance. *Food and Chemical Toxicology: An International Journal Published for the British Industrial Biological Research Association, 146*, 111850. https://doi.org/10.1016/j.fct.2020.111850

21. Ehrlich, A., Duche, D., Ouedraogo, G., & Nahmias, Y. (2019). Challenges and Opportunities in the Design of Liver-on-Chip Microdevices. *An. Rev. of Biomed. Engineering, 21*, 219–239. https://doi.org/10.1146/annurev-bioeng-060418-052305

22. Fukunaga, I., & Takebe, T. (2025). In vitro liver models for toxicological research. Drug Metabolism and *Pharmacokinetics, 62*, 101478. https://doi.org/10.1016/j.dmpk.2025.101478

23. Godoy, P., Hewitt, N. J., Albrecht, U., Andersen, M. E., Ansari, N., Bhattacharya, S., Bode, J. G., Bolleyn, J., Borner, C., Böttger, J., Braeuning, A., Budinsky, R. A., Burkhardt, B., Cameron, N. R., Camussi, G., Cho, C.-S., Choi, Y.-J., Craig Rowlands, J., Dahmen, U., … Hengstler, J. G. (2013). Recent advances in 2D and 3D in vitro systems using primary hepatocytes, alternative hepatocyte sources and non-parenchymal liver cells and their use in investigating mechanisms of hepatotoxicity, cell signaling and ADME. *Archives of Toxicology, 87*(8), 1315–1530. https://doi.org/10.1007/s00204-013-1078-5

24. Gómez-Lechón, M. J., & Tolosa, L. (2016). Human hepatocytes derived from pluripotent stem cells: A promising cell model for drug hepatotoxicity screening. *Archives of Toxicology, 90*(9), 2049–2061. https://doi.org/10.1007/s00204-016-1756-1

25. Gori, M., Simonelli, M. C., Giannitelli, S. M., Businaro, L., Trombetta, M., & Rainer, A. (2016). Investigating Nonalcoholic Fatty Liver Disease in a Liver-on-a-Chip Microfluidic Device. *PloS One, 11*(7), e0159729. https://doi.org/10.1371/journal.pone.0159729

26. Gracey, E. G., & Lampe, J. N. (2025). Novel emerging cell and organoid systems for the study of drug metabolism and toxicity in humans. *Drug Metabolism and Disposition, 53*(12), 100188. https://doi.org/10.1016/j.dmd.2025.100188

27. Graffmann, N., Scherer, B., & Adjaye, J. (2022). In vitro differentiation of pluripotent stem cells into hepatocyte like cells – Basic principles and current progress. *Stem Cell Research, 61*, 102763. https://doi.org/10.1016/j.scr.2022.102763

28. Guagliano, G., Volpini, C., Sardelli, L., Bloise, N., Briatico-Vangosa, F., Cornaglia, A. I., Dotti, S., Villa, R., Visai, L., & Petrini, P. (2023). Hep3Gel: A Shape-Shifting Extracellular Matrix-Based, Three-Dimensional Liver Model Adaptable to Different Culture Systems. *ACS Biomaterials Science & Engineering, 9*(1), 211–229. https://doi.org/10.1021/acsbiomaterials.2c01226

29. Guengerich, F. P. (2011). Mechanisms of Drug Toxicity and Relevance to Pharmaceutical Development. *Drug Metabolism and Pharmacokinetics, 26*(1), 3–14. https://doi.org/10.2133/dmpk.dmpk-10-rv-062

30. Gunness, P., Mueller, D., Shevchenko, V., Heinzle, E., Ingelman-Sundberg, M., & Noor, F. (2013). 3D organotypic cultures of human HepaRG cells: A tool for in vitro toxicity studies. *Toxicological Sciences: An Official Journal of the Society of Toxicology, 133*(1), 67–78. https://doi.org/10.1093/toxsci/kft021

31. Guo, X., Seo, J.-E., Petibone, D., Tryndyak, V., Lee, U. J., Zhou, T., Robison, T. W., & Mei, N. (2020). Performance of HepaRG and HepG2 cells in the high-throughput micronucleus assay for in vitro genotoxicity assessment. *Journal of Toxicology and Environmental Health, Part A, 83*(21–22), 702–717. https://doi.org/10.1080/15287394.2020.1822972

32. Hariparsad, N., Carr, B. A., Evers, R., & Chu, X. (2008). Comparison of immortalized Fa2N-4 cells and human hepatocytes as in vitro models for cytochrome P450 induction. *Drug Metabolism and Disposition: The Biological Fate of Chemicals, 36*(6), 1046–1055. https://doi.org/10.1124/dmd.108.020677

33. Hart, S. N., Li, Y., Nakamoto, K., Subileau, E., Steen, D., & Zhong, X. (2010). A Comparison of Whole Genome Gene Expression Profiles of HepaRG Cells and HepG2 Cells to Primary Human Hepatocytes and Human Liver Tissues. *Drug Metabolism and Disposition, 38*(6), 988–994. https://doi.org/10.1124/dmd.109.031831

34. Hou, Y., Ai, X., Zhao, L., Gao, Z., Wang, Y., Lu, Y., Tu, P., & Jiang, Y. (2020). An integrated biomimetic array chip for high-throughput co-culture of liver and tumor microtissues for advanced anticancer bioactivity screening. *Lab on a Chip, 20*(14), 2482–2494. https://doi.org/10.1039/d0lc00288g

35. Jennen, D. G. J., Magkoufopoulou, C., Ketelslegers, H. B., van Herwijnen, M. H. M., Kleinjans, J. C. S., & van Delft, J. H. M. (2010). Comparison of HepG2 and HepaRG by whole-genome gene expression analysis for the purpose of chemical hazard identification. *Toxicological Sciences: An Official Journal of the Society of Toxicology*, 115(1), 66–79. https://doi.org/10.1093/toxsci/kfq026

36. Jouan, E., Vée, M. L., Denizot, C., Parmentier, Y., & Fardel, O. (2016). Drug Transporter Expression and Activity in Human Hepatoma HuH-7 Cells. *Pharmaceutics, 9*(1). https://doi.org/10.3390/pharmaceutics9010003

37. Kamalian, L., Chadwick, A. E., Bayliss, M., French, N. S., Monshouwer, M., Snoeys, J., & Park, B. K. (2015). The utility of HepG2 cells to identify direct mitochondrial dysfunction in the absence of cell death. *Toxicology in Vitro, 29*(4), 732–740. https://doi.org/10.1016/j.tiv.2015.02.011

38. Kammerer, S., & Küpper, J.-H. (2018). Human hepatocyte systems for in vitro toxicology analysis. *Journal of Cellular Biotechnology, 3*(2), 85–93. https://doi.org/10.3233/JCB-179012

39. Kasai, F., Hirayama, N., Ozawa, M., Satoh, M., & Kohara, A. (2018). HuH-7 reference genome profile: Complex karyotype composed of massive loss of heterozygosity. *Human Cell, 31*(3), 261–267. https://doi.org/10.1007/s13577-018-0212-3

40. Keemink, J., Oorts, M., & Annaert, P. (2015). Primary Hepatocytes in Sandwich Culture. Methods in *Molecular Biology, 1250*, 175–188. https://doi.org/10.1007/978-1-4939-2074-7_12

41. Knasmüller, S., Mersch-Sundermann, V., Kevekordes, S., Darroudi, F., Huber, W. W., Hoelzl, C., Bichler, J., & Majer, B. J. (2004). Use of human-derived liver cell lines for the detection of environmental and dietary genotoxicants; current state of knowledge. *Toxicology, 198*(1–3), 315–328. https://doi.org/10.1016/j.tox.2004.02.008

42. Kopp, B., Khawam, A., Di Perna, K., Lenart, D., Vinette, M., Silva, R., Zanoni, T. B., Rore, C., Guenigault, G., Richardson, E., Kostrzewski, T., Boswell, A., Van, P., Valentine Iii, C., Salk, J., & Hamel, A. (2024). Liver-on-chip model and application in predictive genotoxicity and mutagenicity of drugs. Mutation Research. *Genetic Toxicology and Environmental Mutagenesis, 896*, 503762. https://doi.org/10.1016/j.mrgentox.2024.503762

43. Kumar, M., Toprakhisar, B., Van Haele, M., Antoranz, A., Boon, R., Chesnais, F., De Smedt, J., Tricot, T., Idoype, T. I., Canella, M., Tilliole, P., De Boeck, J., Bajaj, M., Ranga, A., Bosisio, F. M., Roskams, T., van Grunsven, L. A., & Verfaillie, C. M. (2021). A fully defined matrix to support a pluripotent stem cell derived multi-cell-liver steatohepatitis and fibrosis model. *Biomaterials, 276*, 121006. https://doi.org/10.1016/j.biomaterials.2021.121006

44. Lancaster, M. A., & Knoblich, J. A. (2014). Organogenesis in a dish: Modeling development and disease using organoid technologies. *Science, 345*(6194), 1247125. https://doi.org/10.1126/science.1247125

45. Leite, S. B., Wilk-Zasadna, I., Zaldivar, J. M., Airola, E., Reis-Fernandes, M. A., Mennecozzi, M., Guguen-Guillouzo, C., Chesne, C., Guillou, C., Alves, P. M., & Coecke, S. (2012). Three-dimensional HepaRG model as an attractive tool for toxicity testing. T*oxicological Sciences: An Official Journal of the Society of Toxicology, 130*(1), 106–116. https://doi.org/10.1093/toxsci/kfs232

46. Li, G., He, J., Shi, J., Li, X., Liu, L., Ge, X., Chen, W., Jia, J., Wang, J., Yin, M., Sakai, Y., Sun, W., Deng, H., & Pang, Y. (2025). Bioprinting functional hepatocyte organoids derived from human chemically induced pluripotent stem cells to treat liver failure. *Gut, 74*(7), 1150–1164. https://doi.org/10.1136/gutjnl-2024-333885

47. Li, W., Liu, Z., Tang, F., Jiang, H., Zhou, Z., Hao, X., & Zhang, J. M. (2023). Application of 3D Bioprinting in Liver Diseases. *Micromachines, 14*(8), 1648. https://doi.org/10.3390/mi14081648

48. Liao, F.-C., Wang, Y.-K., Cheng, M.-Y., & Tu, T.-Y. (2022). A Preliminary Investigation of Embedding In Vitro HepaRG Spheroids into Recombinant Human Collagen Type I for the Promotion of Liver Differentiation. *Polymers, 14*(9). https://doi.org/10.3390/polym14091923

49. Liguori, M. J., Blomme, E. A. G., & Waring, J. F. (2008). Trovafloxacin-induced gene expression changes in liver-derived in vitro systems: Comparison of primary human hepatocytes to HepG2 cells. *Drug Metabolism and Disposition: The Biological Fate of Chemicals, 36*(2), 223–233. https://doi.org/10.1124/dmd.107.017608

50. Liu, J., Du, Y., Xiao, X., Tan, D., He, Y., & Qin, L. (2024). Construction of in vitro liver-on-a-chip models and application progress. *BioMedical Engineering OnLine, 23*(1), 33. https://doi.org/10.1186/s12938-024-01226-y

51. Lohmann, V., Körner, F., Koch, J., Herian, U., Theilmann, L., & Bartenschlager, R. (1999). Replication of subgenomic hepatitis C virus RNAs in a hepatoma cell line. *Science (New York, N.Y.), 285*(5424), 110–113. https://doi.org/10.1126/science.285.5424.110

52. Lübberstedt, M., Müller-Vieira, U., Mayer, M., Biemel, K. M., Knöspel, F., Knobeloch, D., Nüssler, A. K., Gerlach, J. C., & Zeilinger, K. (2011). HepaRG human hepatic cell line utility as a surrogate for primary human hepatocytes in drug metabolism assessment in vitro. *Journal of Pharmacological and Toxicological Methods, 63*(1), 59–68. https://doi.org/10.1016/j.vascn.2010.04.013

53. Lucchetti, M., Aina, K. O., Grandmougin, L., Jäger, C., Pérez Escriva, P., Letellier, E., Mosig, A. S., & Wilmes, P. (2024). An Organ-on-Chip Platform for Simulating Drug Metabolism Along the Gut-Liver Axis. *Advanced Healthcare Materials, 13*(20), e2303943. https://doi.org/10.1002/adhm.202303943

54. Ma, X., Liu, J., Zhu, W., Tang, M., Lawrence, N., Yu, C., Gou, M., & Chen, S. (2018). 3D bioprinting of functional tissue models for personalized drug screening and in vitro disease modeling. *Advanced Drug Delivery Reviews, 132*, 235–251. https://doi.org/10.1016/j.addr.2018.06.011

55. Magkoufopoulou, C., Claessen, S. M. H., Tsamou, M., Jennen, D. G. J., Kleinjans, J. C. S., & van Delft, J. H. M. (2012). A transcriptomics-based in vitro assay for predicting chemical genotoxicity in vivo. *Carcinogenesis, 33*(7), 1421–1429. https://doi.org/10.1093/carcin/bgs182

56. Malinen, M. M., Ito, K., Kang, H. E., Honkakoski, P., & Brouwer, K. L. R. (2019). Protein expression and function of organic anion transporters in short-term and long-term cultures of Huh7 human hepatoma cells. *European Journal of Pharmaceutical Sciences, 130*, 186–195. https://doi.org/10.1016/j.ejps.2019.01.022

57. Mandon, M., Huet, S., Dubreil, E., Fessard, V., & Le Hégarat, L. (2019). Three-dimensional HepaRG spheroids as a liver model to study human genotoxicity in vitro with the single cell gel electrophoresis assay. *Scientific Reports, 9*(1), Article 1. https://doi.org/10.1038/s41598-019-47114-7

58. Mann, D. A. (2015). Human induced pluripotent stem cell-derived hepatocytes for toxicology testing. *Expert Opinion on Drug Metabolism & Toxicology, 11*(1), 1–5. https://doi.org/10.1517/17425255.2015.981523

59. Marion, M.-J., Hantz, O., & Durantel, D. (2010). The HepaRG Cell Line: Biological Properties and Relevance as a Tool for Cell Biology, Drug Metabolism, and Virology Studies. In P. Maurel (Ed.), Hepatocytes (Vol. 640, pp. 261–272). Humana Press. https://doi.org/10.1007/978-1-60761-688-7_13

60. Marroquin, L. D., Hynes, J., Dykens, J. A., Jamieson, J. D., & Will, Y. (2007). Circumventing the Crabtree Effect: Replacing Media Glucose with Galactose Increases Susceptibility of HepG2 Cells to Mitochondrial Toxicants. *Toxicological Sciences, 97*(2), 539–547. https://doi.org/10.1093/toxsci/kfm052

61. Matai, I., Kaur, G., Seyedsalehi, A., McClinton, A., & Laurencin, C. T. (2020). Progress in 3D bioprinting technology for tissue/organ regenerative engineering. *Biomaterials, 226*, 119536. https://doi.org/10.1016/j.biomaterials.2019.119536

62. Matsui, T., Miyamoto, N., Saito, F., & Shinozawa, T. (2020). Molecular Profiling of Human Induced Pluripotent Stem Cell-Derived Cells and their Application for Drug Safety Study. *Current Pharmaceutical Biotechnology, 21*(9), 807–828. https://doi.org/10.2174/1389201021666200422090952

63. Meex, S. J. R., Andreo, U., Sparks, J. D., & Fisher, E. A. (2011). Huh-7 or HepG2 cells: Which is the better model for studying human apolipoprotein-B100 assembly and secretion?. *Journal of Lipid Research, 52*(1), 152–158. https://doi.org/10.1194/jlr.D008888

64. Mills, J. B., Rose, K. A., Sadagopan, N., Sahi, J., & de Morais, S. M. F. (2004). Induction of Drug Metabolism Enzymes and MDR1 Using a Novel Human Hepatocyte Cell Line. T*he Journal of Pharmacology and Experimental Therapeutics, 309*(1), 303–309. https://doi.org/10.1124/jpet.103.061713

65. Mišík, M., Nersesyan, A., Ropek, N., Huber, W. W., Haslinger, E., & Knasmueller, S. (2019). Use of human derived liver cells for the detection of genotoxins in comet assays. Mutation Research. *Genetic Toxicology and Environmental Mutagenesis, 845*, 402995. https://doi.org/10.1016/j.mrgentox.2018.12.003

66. Mueller, D., Tascher, G., Müller-Vieira, U., Knobeloch, D., Nuessler, A. K., Zeilinger, K., Heinzle, E., & Noor, F. (2011). In-depth physiological characterization of primary human hepatocytes in a 3D hollow-fiber bioreactor. *Journal of Tissue Engineering and Regenerative Medicine, 5*(8), e207–e218. https://doi.org/10.1002/term.418

67. Nakabayashi, H., Taketa, K., Miyano, K., Yamane, T., & Sato, J. (1982). Growth of human hepatoma cells lines with differentiated functions in chemically defined medium. *Cancer Research, 42*(9), 3858–3863.

68. Nelson, L. J., Navarro, M., Treskes, P., Samuel, K., Tura-Ceide, O., Morley, S. D., Hayes, P. C., & Plevris, J. N. (2015). Acetaminophen cytotoxicity is ameliorated in a human liver organotypic co-culture model. *Scientific Reports, 5*(1), 17455. https://doi.org/10.1038/srep17455

69. Parmentier, C., Hendriks, D. F. G., Heyd, B., Bachellier, P., Ingelman-Sundberg, M., & Richert, L. (2018). Inter-individual differences in the susceptibility of primary human hepatocytes towards drug-induced cholestasis are compound and time dependent. *Toxicology Letters, 295*, 187–194. https://doi.org/10.1016/j.toxlet.2018.06.1069

70. Pfeifer, A. M., Cole, K. E., Smoot, D. T., Weston, A., Groopman, J. D., Shields, P. G., Vignaud, J. M., Juillerat, M., Lipsky, M. M., & Trump, B. F. (1993). Simian virus 40 large tumor antigen-immortalized normal human liver epithelial cells express hepatocyte characteristics and metabolize chemical carcinogens. *Proceedings of the National Academy of Sciences, 90*(11), 5123–5127. https://doi.org/10.1073/pnas.90.11.5123

71. Philippeos, C., Hughes, R. D., Dhawan, A., & Mitry, R. R. (2012). Introduction to Cell Culture. In R. R. Mitry & R. D. Hughes (Eds), Human Cell Culture Protocols (Vol. 806, pp. 1–13). Humana Press. https://doi.org/10.1007/978-1-61779-367-7_1

72. Poh, W. T., & Stanslas, J. (2024). The new paradigm in animal testing – "3Rs alternatives". Regulatory *Toxicology and Pharmacology, 153*, 105705. https://doi.org/10.1016/j.yrtph.2024.105705

73. Ramboer, E., Vanhaecke, T., Rogiers, V., & Vinken, M. (2015). Immortalized human hepatic cell lines for in vitro testing and research purposes. Methods in Molecular Biology (Clifton, N.J.), 1250, 53–76. https://doi.org/10.1007/978-1-4939-2074-7_4

74. Ramirez, T., Strigun, A., Verlohner, A., Huener, H.-A., Peter, E., Herold, M., Bordag, N., Mellert, W., Walk, T., Spitzer, M., Jiang, X., Sperber, S., Hofmann, T., Hartung, T., Kamp, H., & van Ravenzwaay, B. (2018). Prediction of liver toxicity and mode of action using metabolomics in vitro in HepG2 cells. *Archives of Toxicology, 92*(2), 893–906. https://doi.org/10.1007/s00204-017-2079-6

75. Ramli, M. N. B., Lim, Y. S., Koe, C. T., Demircioglu, D., Tng, W., Gonzales, K. A. U., Tan, C. P., Szczerbinska, I., Liang, H., Soe, E. L., Lu, Z., Ariyachet, C., Yu, K. M., Koh, S. H., Yaw, L. P., Jumat, N. H. B., Lim, J. S. Y., Wright, G., Shabbir, A., … Chan, Y.-S. (2020). Human Pluripotent Stem Cell-Derived Organoids as Models of Liver Disease. *Gastroenterology, 159*(4), 1471-1486.e12. https://doi.org/10.1053/j.gastro.2020.06.010

76. Richert, L., Alexandre, E., Lloyd, T., Orr, S., Viollon-Abadie, C., Patel, R., Kingston, S., Berry, D., Dennison, A., Heyd, B., Mantion, G., & Jaeck, D. (2004). Tissue collection, transport and isolation procedures required to optimize human hepatocyte isolation from waste liver surgical resections. A multilaboratory study. *Liver International, 24*(4), 371–378. https://doi.org/10.1111/j.1478-3231.2004.0930.x

77. Roe, A. L., Snawder, J. E., Benson, R. W., Roberts, D. W., & Casciano, D. A. (1993). HepG2 cells: An in vitro model for P450-dependent metabolism of acetaminophen. *Biochemical and Biophysical Research Communications, 190*(1), 15–19. https://doi.org/10.1006/bbrc.1993.1003

78. Rose, S., Cuvellier, M., Ezan, F., Carteret, J., Bruyère, A., Legagneux, V., Nesslany, F., Baffet, G., & Langouët, S. (2022). DMSO-free highly differentiated HepaRG spheroids for chronic toxicity, liver functions and genotoxicity studies. *Archives of Toxicology, 96*(1), 243–258. https://doi.org/10.1007/s00204-021-03178-x

79. Rose, S., Ezan, F., Cuvellier, M., Bruyère, A., Legagneux, V., Langouët, S., & Baffet, G. (2021). Generation of proliferating human adult hepatocytes using optimized 3D culture conditions. *Scientific Reports, 11*(1), 515. https://doi.org/10.1038/s41598-020-80019-4

80. Şahin, S., Azarkan, S. Y., & Türksoy, V. A. (2024). Evaluation of the effect of cannabidiol on the THLE-2 liver cell line exposed to lead. *The Science of the Total Environment, 923*, 170901. https://doi.org/10.1016/j.scitotenv.2024.170901

81. Sampaziotis, F., Muraro, D., Tysoe, O. C., Sawiak, S., Beach, T. E., Godfrey, E. M., Upponi, S. S., Brevini, T., Wesley, B. T., Garcia-Bernardo, J., Mahbubani, K., Canu, G., Gieseck, R., Berntsen, N. L., Mulcahy, V. L., Crick, K., Fear, C., Robinson, S., Swift, L., … Vallier, L. (2021). Cholangiocyte organoids can repair bile ducts after transplantation in the human liver. *Science, 371*(6531), 839–846. https://doi.org/10.1126/science.aaz6964

82. Sawada, H., Takami, K., & Asahi, S. (2005). A toxicogenomic approach to drug-induced phospholipidosis: Analysis of its induction mechanism and establishment of a novel in vitro screening system. Toxicological Sciences: An *Official Journal of the Society of Toxicology, 83*(2), 282–292. https://doi.org/10.1093/toxsci/kfh264

83. Schoonen, W. G. E. J., Westerink, W. M. A., de Roos, J. A. D. M., & Débiton, E. (2005). Cytotoxic effects of 100 reference compounds on Hep G2 and HeLa cells and of 60 compounds on ECC-1 and CHO cells. I mechanistic assays on ROS, glutathione depletion and calcein uptake. *Toxicology in Vitro, 19*(4), 505–516. https://doi.org/10.1016/j.tiv.2005.01.003

84. Sefried, S., Häring, H.-U., Weigert, C., & Eckstein, S. S. (2018). Suitability of hepatocyte cell lines HepG2, AML12 and THLE-2 for investigation of insulin signalling and hepatokine gene expression. *Open Biology, 8*(10), 180147. https://doi.org/10.1098/rsob.180147

85. Segeritz, C.-P., & Vallier, L. (2017). Cell Culture. In Basic Science Methods for Clinical Researchers (pp. 151–172). https://doi.org/10.1016/B978-0-12-803077-6.00009-6

86. Seo, J.-E., Tryndyak, V., Wu, Q., Dreval, K., Pogribny, I., Bryant, M., Zhou, T., Robison, T. W., Mei, N., & Guo, X. (2019). Quantitative comparison of in vitro genotoxicity between metabolically competent HepaRG cells and HepG2 cells using the high-throughput high-content CometChip assay. *Archives of Toxicology, 93*(5), 1433–1448. https://doi.org/10.1007/s00204-019-02406-9

87. Seo, J.-E., Wu, Q., Bryant, M., Ren, L., Shi, Q., Robison, T. W., Mei, N., Manjanatha, M. G., & Guo, X. (2020). Performance of high-throughput CometChip assay using primary human hepatocytes: A comparison of DNA damage responses with in vitro human hepatoma cell lines. *Archives of Toxicology, 94*(6), 2207–2224. https://doi.org/10.1007/s00204-020-02736-z

88. Shah, F., Louise-May, S., & Greene, N. (2014). Chemotypes sensitivity and predictivity of in vivo outcomes for cytotoxic assays in THLE and HepG2 cell lines. *Bioorganic & Medicinal Chemistry Letters, 24*(12), 2753–2757. https://doi.org/10.1016/j.bmcl.2014.04.039

89. Shukla, P., Yeleswarapu, S., Heinrich, M. A., Prakash, J., & Pati, F. (2022). Mimicking tumor microenvironment by 3D bioprinting: 3D cancer modeling. *Biofabrication, 14*(3). https://doi.org/10.1088/1758-5090/ac6d11

90. Shulman, M., & Nahmias, Y. (2013). Long-term culture and coculture of primary rat and human hepatocytes. Methods in Molecular Biology (Clifton, N.J.), 945, 287–302. https://doi.org/10.1007/978-1-62703-125-7_17

91. Soltanpour, Y., Hilgendorf, C., Ahlström, M. M., Foster, A. J., Kenna, J. G., Petersen, A., & Ungell, A.-L. (2012). Characterization of THLE-cytochrome P450 (P450) cell lines: Gene expression background and relationship to P450-enzyme activity. *Drug Metabolism and Disposition: The Biological Fate of Chemicals, 40*(11), 2054–2058. https://doi.org/10.1124/dmd.112.045815

92. Štampar, M., Breznik, B., Filipič, M., & Žegura, B. (2020). Characterization of In Vitro 3D Cell Model Developed from Human Hepatocellular Carcinoma (HepG2) Cell Line. *Cells, 9*(12), 2557. https://doi.org/10.3390/cells9122557

93. Štampar, M., Žabkar, S., Filipič, M., & Žegura, B. (2022). HepG2 spheroids as a biosensor-like cell-based system for (geno) toxicity assessment. *Chemosphere, 291*, 132805. https://doi.org/10.1016/j.chemosphere.2021.132805

94. Stanley, L. A., & Wolf, C. R. (2022). Through a glass, darkly? HepaRG and HepG2 cells as models of human phase I drug metabolism. *Drug Metabolism Reviews, 54*(1), 46–62. https://doi.org/10.1080/03602532.2022.2039688

95. Subramaniam, V., Abrahan, C., Higgins, B. R., Chisolm, S. J., Sweeney, B., Duraivel, S., Balzano-Nogueira, L., Monjure, T., Wang, C.-Y., Palmer, G. D., & Angelini, T. E. (2025). A functional human liver tissue model: 3D bioprinted co-culture discoids. *Biomaterials Advances, 173,* 214288. https://doi.org/10.1016/j.bioadv.2025.214288

96. Swift, B., Pfeifer, N. D., & Brouwer, K. L. R. (2010). Sandwich-cultured hepatocytes: An in vitro model to evaluate hepatobiliary transporter-based drug interactions and hepatotoxicity. *Drug Metabolism Reviews, 42*(3), 446–471. https://doi.org/10.3109/03602530903491881

97. Tascher, G., Burban, A., Camus, S., Plumel, M., Chanon, S., Le Guevel, R., Shevchenko, V., Van Dorsselaer, A., Lefai, E., Guguen-Guillouzo, C., & Bertile, F. (2019). In-Depth Proteome Analysis Highlights HepaRG Cells as a Versatile Cell System Surrogate for Primary Human Hepatocytes. *Cells, 8*(2), 192. https://doi.org/10.3390/cells8020192

98. Tostões, R. M., Leite, S. B., Serra, M., Jensen, J., Björquist, P., Carrondo, M. J. T., Brito, C., & Alves, P. M. (2012). Human liver cell spheroids in extended perfusion bioreactor culture for repeated-dose drug testing. *Hepatology (Baltimore, Md.), 55*(4), 1227–1236. https://doi.org/10.1002/hep.24760

99. Treijtel, N., Barendregt, A., Freidig, A. P., Blaauboer, B. J., & van Eijkeren, J. C. H. (2004). Modeling the in vitro intrinsic clearance of the slowly metabolized compound tolbutamide determined in sandwich-cultured rat hepatocytes. *Drug Metabolism and Disposition: The Biological Fate of Chemicals, 32*(8), 884–891. https://doi.org/10.1124/dmd.32.8.884

100. Tsai, J., Qiu, W., Kohen-Avramoglu, R., & Adeli, K. (2007). MEK-ERK inhibition corrects the defect in VLDL assembly in HepG2 cells: Potential role of ERK in VLDL-ApoB100 particle assembly. *Arteriosclerosis, Thrombosis, and Vascular Biology, 27*(1), 211–218. https://doi.org/10.1161/01.ATV.0000249861.80471.96

101. Van den Hof, W. F. P. M., Coonen, M. L. J., van Herwijnen, M., Brauers, K., Wodzig, W. K. W. H., van Delft, J. H. M., & Kleinjans, J. C. S. (2014). Classification of Hepatotoxicants Using HepG2 Cells: A Proof of Principle Study. *Chemical Research in Toxicology, 27*(3), 433–442. https://doi.org/10.1021/tx4004165

102. van Grunsven, L. A. (2017). 3D in vitro models of liver fibrosis. *Advanced Drug Delivery Reviews, 121*, 133–146. https://doi.org/10.1016/j.addr.2017.07.004

103. Waldherr, M., Mišík, M., Ferk, F., Tomc, J., Žegura, B., Filipič, M., Mikulits, W., Mai, S., Haas, O., Huber, W. W., Haslinger, E., & Knasmüller, S. (2018). Use of HuH6 and other human-derived hepatoma lines for the detection of genotoxins: A new hope for laboratory animals? *Archives of Toxicology, 92*(2), 921–934. https://doi.org/10.1007/s00204-017-2109-4

104. Wang, H., Xu, T., & Yin, D. (2023). Emerging trends in the methodology of environmental toxicology: 3D cell culture and its applications. *Science of The Total Environment, 857*, 159501. https://doi.org/10.1016/j.scitotenv.2022.159501

105. Wang, J.-Z., Xiong, N.-Y., Zhao, L.-Z., Hu, J.-T., Kong, D.-C., & Yuan, J.-Y. (2018). Review fantastic medical implications of 3D-printing in liver surgeries, liver regeneration, liver transplantation and drug hepatotoxicity testing: A review. *International Journal of Surgery, 56*, 1–6. https://doi.org/10.1016/j.ijsu.2018.06.004

106. Wu, X., Jiang, D., Yang, Y., Li, S., & Ding, Q. (2023). Modeling drug-induced liver injury and screening for anti-hepatofibrotic compounds using human PSC-derived organoids. *Cell Regeneration, 12*(1), 6. https://doi.org/10.1186/s13619-022-00148-1

107. Xie, F., Sun, L., Pang, Y., Xu, G., Jin, B., Xu, H., Lu, X., Xu, Y., Du, S., Wang, Y., Feng, S., Sang, X., Zhong, S., Wang, X., Sun, W., Zhao, H., Zhang, H., Yang, H., Huang, P., & Mao, Y. (2021). Three-dimensional bio-printing of primary human hepatocellular carcinoma for personalized medicine. *Biomaterials, 265*, 120416. https://doi.org/10.1016/j.biomaterials.2020.120416

108. Yang, S., Chen, Z., Cheng, Y., Liu, T., Lihong Yin, Pu, Y., & Liang, G. (2021). Environmental toxicology wars: Organ-on-a-chip for assessing the toxicity of environmental pollutants. *Environmental Pollution, 268*, 115861. https://doi.org/10.1016/j.envpol.2020.115861

109. Yang, Y., Yu, Z., Lu, X., Dai, J., Zhou, C., Yan, J., Wang, L., Wang, Z., & Zang, J. (2023). Minimally invasive bioprinting for in situ liver regeneration. *Bioactive Materials, 26*, 465–477. https://doi.org/10.1016/j.bioactmat.2023.03.011

110. Ye, S., Boeter, J. W. B., Penning, L. C., Spee, B., & Schneeberger, K. (2019). Hydrogels for Liver Tissue Engineering. *Bioengineering, 6*(3), 59. https://doi.org/10.3390/bioengineering6030059

111. Youdim, K. A., Tyman, C. A., Jones, B. C., & Hyland, R. (2007). Induction of Cytochrome P450: Assessment in an Immortalized Human Hepatocyte Cell Line (Fa2N4) Using a Novel Higher Throughput Cocktail Assay. *Drug Metabolism and Disposition, 35*(2), 275–282. https://doi.org/10.1124/dmd.106.012864

112. Zeigerer, A., Wuttke, A., Marsico, G., Seifert, S., Kalaidzidis, Y., & Zerial, M. (2017). Functional properties of hepatocytes in vitro are correlated with cell polarity maintenance. *Experimental Cell Research, 350*(1), 242–252. https://doi.org/10.1016/j.yexcr.2016.11.027

113. Zeilinger, K., Freyer, N., Damm, G., Seehofer, D., & Knöspel, F. (2016). Cell sources for in vitro human liver cell culture models. *Experimental Biology and Medicine, 241*(15), 1684–1698. https://doi.org/10.1177/1535370216657448

114. Zheng, P., Xu, Y., Ren, Z., Wang, Z., Wang, S., Xiong, J., Zhang, H., & Jiang, H. (2021). Toxic Prediction of Pyrrolizidine Alkaloids and Structure-Dependent Induction of Apoptosis in HepaRG Cells. *Oxidative Medicine and Cellular Longevity, 2021*, 1–12. https://doi.org/10.1155/2021/8822304

Information about the authors:

Nailya Kabysheva – Candidate of Biological Sciences, Head of the Laboratory of Experimental Mutagenesis, Institute of Genetics and Physiology (Almaty, Kazakhstan, e-mail: nailya.kabysheva@gmail.com).

Ozada Khamdiyeva – Senior Researcher, Laboratory of Experimental Mutagenesis, Institute of Genetics and Physiology (Almaty, Kazakhstan, e-mail: azadahamdieva@gmail.com).

Lyazzat Tenelbayeva – Junior Researcher, Laboratory of Experimental Mutagenesis, Institute of Genetics and Physiology (Almaty, Kazakhstan, e-mail: tenelbayevalyazzat@gmail.com).

Gulshat Koishekenova – Researcher, Laboratory of Experimental Mutagenesis, Institute of Genetics and Physiology (Almaty, Kazakhstan, e-mail: ms.gulshat7@mail.ru).

Nazym Altynova – PhD, Head of the Laboratory of Population Genetics, Institute of Genetics and Physiology (Almaty, Kazakhstan, e-mail: naz10.79@mail.ru).

Leyla Djansugurova – Candidate of Biological Sciences, Head of the Center for Paleogenetics and Ethnogenomics, Professor, Academician of MAIN, Institute of Genetics and Physiology, Al-Farabi Kazakh National University (Almaty, Kazakhstan, e-mail: leylad@mail.ru).

Erika Djangalina – Candidate of Biological Sciences, Assistant Professor, Leading researcher, Institute of Genetics and Physiology (Almaty, Kazakhstan, e-mail: djangalina@rambler.ru).

Céline Cakir-Kiefer – Professor, Head of the Master's Programme in Nutrition and Food Science, University of Lorraine, Faculty of Science and Technology, Animal and Agroecosystems Laboratory (L2A) (UR 200515254N, ex-URAFPA), École Nationale Supérieure d'Agronomie et des Industries Alimentaires (Vandœuvre-lès-Nancy Cedex, France, e-mail: celine.cakir@univ-lorraine.fr).

Gulminyam Baratzhanova – PhD, Senior Researcher, Laboratory of Experimental Mutagenesis, Institute of Genetics and Physiology (Almaty, Kazakhstan, e-mail: baratzhanova.gulminyam@gmail.com).

Received 02 March 2026;
received in revised form 24 June 2026;
accepted 26 June 2026

IRSTI 34.27.51; 34.31.15 https://doi.org/10.26577/IJBCh20261916

H. Khosravi[1*], A. Otadi[1], H. Etesami[2], H. Alikhani[2]

[1]Soil and Water Research Institute, Agricultural Research, Education and Extension Organization, Karaj, Iran
[2]University of Tehran, Karaj, Iran
*e-mail: hkhosravi@areeo.ac.ir

PLANT GROWTH-PROMOTING RHIZOBACTERIA INOCULATION MITIGATES DROUGHT STRESS AND ENHANCES GROWTH AND NUTRIENT UPTAKE IN WHEAT

Abstract: Drought is one of the most critical environmental constraints limiting wheat productivity worldwide, especially under organic and low-input agricultural systems where synthetic fertilizers are restricted. Microbial inoculants, particularly plant growth-promoting rhizobacteria (PGPR), offer a sustainable strategy for enhancing plant tolerance to water deficit by improving physiological performance and nutrient acquisition. In this study, germinated seeds of the wheat cultivar 'Rakhshan' were inoculated with eight PGPR strains – *Azotobacter chroococcum* (Azto478), *A. salinestris* (Azto474), *Azospirillum lipoferum* (A443), *Pseudomonas* sp. (P196 and P241), *Pseudomonas fluorescens* (P187), *Pseudomonas putida* (P186), and *Bacillus subtilis* (B271). The experiment was conducted under greenhouse conditions using a completely randomized factorial design. Drought stress was applied at three moisture levels corresponding to 100%, 60%, and 40% of field capacity (FC), and soil moisture was maintained throughout the 100-day growth period. Measured traits included grain, shoot, and root dry weights; plant height; spike length; grain nitrogen, phosphorus, and potassium concentrations. As expected, increasing drought severity markedly reduced all growth and nutrient parameters. However, PGPR inoculation substantially mitigated these declines, demonstrating the capacity of specific bacterial strains to counteract drought-induced physiological limitations. Among the tested inoculants, *Pseudomonas fluorescens* P187 consistently exhibited the strongest positive effects. Under moderate drought, P187 increased grain dry weight by approximately 95%, and under severe drought it enhanced shoot and root dry weights by approximately 75% compared with the uninoculated control. P187 also improved macronutrient accumulation, outperforming all other strains across nitrogen, phosphorus, and potassium contents. *Pseudomonas* sp. P196 ranked second, showing notable but comparatively lower improvements. Overall, the findings identify P187 and to a lesser extent P196 as highly promising PGPR candidates for developing microbial biofertilizers aimed at enhancing drought resilience and nutrient use efficiency in wheat. These strains warrant further evaluation under field conditions and in multi-strain or consortium-based formulations to maximize their agronomic potential.
Keywords: biofertilizers, drought, inoculation, stress mitigation, water deficit, wheat.

Introduction

Drought stress is one of the most critical limiting factors affecting plant growth and crop productivity worldwide (Kuwayama et al., 2019). Iran, located between latitudes 25° and 38°N, lies within arid and semi-arid climatic zones and has recently experienced a significant decline in precipitation along with an increased frequency of drought events. As a substantial portion of the country's water resources is allocated to agriculture, this sector is the most severely impacted by drought (Yazdandoost, 2016; Yousefi et al., 2024).

A promising and environmentally sustainable strategy for mitigating drought stress in agriculture is the application of microbial inoculants containing plant growth-promoting rhizobacteria (PGPR) (Ali & Glick, 2025). Representative genera of PGPR include *Azotobacter*, *Pseudomonas*, *Bacillus*, and *Azospirillum* (Shah et al., 2021). These bacteria enhance plant drought tolerance primarily by promoting root development through phytohormone production, facilitating biological nitrogen (N_2) fixation, mediating iron uptake via siderophores, and solubilizing insoluble phosphate compounds in the soil. Additional mechanisms include the production of exopolysaccharides (EPS) and the enzyme ACC deaminase, both of which contribute to drought stress alleviation (Ali & Glick, 2025; Khosravi, 2019; Khosravi & Mahmoudi, 2013; Khosravi et al., 2024; Shirinbayan et al., 2019).

Wheat bread is a major source of caloric intake in Iranian households and plays a fundamental role in the national diet (Abdi et al., 2016). Currently, approximately 58% of Iran's cultivated land is dedicated to wheat production (Center for Statistics, Information Technology, and Communications, 2024). Given wheat's strategic importance, extensive cultivation area, and the increasing occurrence of drought and water scarcity, the adoption of biotechnology-based approaches such as microbial inoculants is essential for promoting sustainable agricultural development.

This study aimed to evaluate the effects of inoculating wheat with selected native PGPR strains under different soil moisture regimes and drought stress levels. The ultimate objective is to develop effective microbial formulations that enhance wheat resilience to drought stress and improve crop performance under water-limited conditions.

Material and methods

Bacterial selection and inoculum preparation

In this study, the bacterial strains *Azotobacter chroococcum* Azto478, *Azotobacter salinestris* Azto474, *Azospirillum lipoferum* A443, *Bacillus subtilis* B271, *Pseudomonas sp.* P241, *Pseudomonas sp*. P196, *Pseudomonas putida* P186, and *Pseudomonas fluorescens* P187 were used to prepare the inoculants for the greenhouse experiments. These strains were selected from a collection of 63 isolates maintained in the microbial collection of the Soil and Water Research Institute (SWRI) (https://gcm.wdcm.org/cc?wdcmnumber=891). They were originally isolated from cultivated soils across Iran and had previously been screened for plant growth-promoting traits. The plant growth-promoting characteristics of the selected bacterial strains used in this study are summarized in Table 1 (Khosravi et al., 2025).

Table 1

Characteristics of the selected plant growth-promoting bacteria (Khosravi et al., 2025)

Bacterial strain	Indole-3-acetic acid (IAA)	Inorganic phosphorus solubilization	Organic phosphorus solubilization	Potassium release from muscovite	Potassium release from biotite	Exopolysaccharide production	Insoluble iron compounds solubilization	Siderophore production
			$\mu g \cdot mL^{-1}$			$g \cdot L^{-1}$	halo/colony diameter ratio	
Azospirillum lipoferum A443	24.90	34.20	40.35	16.67	29.59	0.00	1.90	1.42
Azotobacter chroococcum Azto478	27.89	27.06	17.27	5.33	7.33	4.79	0.00	0.00
Azotobacter salinestris Azto474	40.67	11.16	17.35	5.37	5.92	0.70	0.00	0.00
Pseudomonas putida P186	8.00	274.18	46.51	22.33	15.86	5.21	3.55	2.33
Pseudomonas fluorescens P187	43.90	334.31	74.78	14.31	13.79	5.38	3.77	1.92
Pseudomonas sp. P241	44.93	214.15	48.55	14.38	16.45	5.92	3.88	1.66

To prepare the inoculate, a loopful of each purified single colony grown on agar plates was transferred into a 100 mL Erlenmeyer flask containing the appropriate selective medium. The flasks were incubated at 30°C for 72 hours on a Rotary Shaker Incubator (AG CH, Infors, Switzerland). The following media were used for bacterial cultivation: Winogradsky medium for *Azotobacter*, RC medium for *Azospirillum*, *Bacillus* agar medium for *Bacillus*, and King's B medium for *Pseudomonas* (Himedia, India).

Soil and water testing used for greenhouse cultivation

The soil samples used in this study were collected from the top 20 cm of a field at the Central Research Station of the SWRI (Karaj, Iran). Soil and water analyses were subsequently performed at the institute's Chemistry, Physics, and Fertilizer Technology Laboratory to determine the physicochemical properties of the samples. Total nitrogen (N) content was measured using the Kjeldahl method, available potassium (K) was extracted using 1N am-

monium acetate, and available phosphorus (P_2O_5) was determined using the Olsen method (Sparks et al., 2020). Micronutrients (Zn, Fe, Cu, and Mn) were extracted using the DTPA method and quantified by atomic absorption spectrophotometry (Novaspec II, Pharmacia, Sweden). Electrical conductivity (EC) was determined using a conductivity meter (4510, Jenway, UK), while pH was measured with a pH meter (691, Metrohm, Switzerland). Organic carbon content in the soil saturation extract was determined using the Walkley–Black method (Standard volumetric titration method) (Sparks et al., 2020). Soil calcium carbonate equivalent was determined using the Total Neutralizing Value (TNV) method based on acid neutralization, following standard soil chemical procedures (Sparks et al., 2020). Soil texture components – sand, silt, and clay – were determined using the Bouyoucos hydrometer method, and the soil texture class was identified using the soil texture triangle. Field capacity (FC) was measured using the pressure plate method at 0.3 bar, and the permanent wilting point (PWP) was determined at 15 bars using the same technique (Soil moisture Equipment Corp) (Dane & Topp, 2020).

Irrigation water samples were collected following standard hydrochemical sampling procedures in pre-cleaned, acid-washed polyethylene bottles to avoid contamination. Samples were immediately transported to the laboratory and stored at 4°C prior to analysis to preserve their chemical integrity.

Soluble cations (Na^+, Ca^{2+}, Mg^{2+}, and K^+) were determined after filtration of samples through 0.45 µm membrane filters. Sodium and potassium concentrations were measured using flame photometry (PFP7, Jenway, Germany), while calcium and magnesium were determined by atomic absorption spectrophotometry (Novaspec II, Pharmacia, Sweden), following standard methods used in soil and irrigation water studies (Sparks et al., 2020).

Soluble anions (Cl^-, SO_4^{2-}, and NO_3^-) were analyzed using standard colorimetric and titrimetric methods, in accordance with established soil science laboratory procedures (Sparks et al., 2020).

The sodium adsorption ratio (SAR) was calculated based on soluble cation concentrations expressed in meq L^{-1} using the following equation: $SAR = Na^+ / \sqrt{((Ca^{2+} + Mg^{2+}) / 2)}$ (Sparks et al., 2020).

Plastic pots measuring 23 cm in height and 29 cm in top diameter, each equipped with drainage holes, were used in the experiment. Each pot was filled with 10 kg of soil sieved through a 5 mm mesh. Based on the soil analysis results, nitrogen deficiency was corrected through split applications at three key growth stages: one week after planting, during stem elongation, and at heading.

Experimental design

The experiment was conducted in the greenhouse of the Central Research Station of the SWRI, Karaj, Iran, using a factorial arrangement based on a completely randomized design (CRD) with three replications. Treatments included two factors: drought stress and bacterial inoculation.

Drought stress was applied at three levels:

- D0 (non-stress): soil moisture maintained at 100–80% of field capacity (FC), corresponding to irrigation at 20% moisture depletion;
- D1 (moderate stress): soil moisture maintained at 60% of FC, corresponding to 40% depletion;
- D2 (severe stress): soil moisture maintained at 40% of FC, corresponding to 60% depletion.

The inoculation factor consisted of nine levels: a non-inoculated control (B0) and inoculation with the bacterial strains A443, B271, Azto474, Azto478, P186, P187, P196, and P241. Inoculation was performed at sowing by applying 1 mL of bacterial suspension to each seed, with a concentration of approximately 1.5×10^7 cells mL^{-1}.

Planting, growth conditions, and harvesting

Four pre-germinated seeds of the wheat cultivar ‘Rakhshan’, provided by the Seed and Plant Improvement Institute (Karaj, Iran) were sown in each pot. One week after sowing, seedlings were thinned to maintain two plants per pot. The greenhouse was kept under a 12-hour photo period, with temperatures ranging from 20 to 30°C, for 100 consecutive days.

At the end of the experiment, the plants were harvested, and the following traits were measured: grain dry weight, shoot dry weight, root dry weight, plant height, spike length, and the percentage concentrations of nitrogen (N), phosphorus (P), and potassium (K) in dry grains. To determine grain N, P, and K contents, oven-dried grain samples were ground and digested using an H_2SO_4–H_2O_2 acid mixture. Total nitrogen was quantified using the Kjeldahl method, phosphorus was measured colorimetrically with a spectrophotometer, and potassium was determined by flame photometry (Sparks et al., 2020). All nutrient concentrations were expressed as percentages (%).

Data was analyzed using DSAASTAT.XLS software (Version 2010.5.04). A one-way ANOVA was used to determine treatment effects, and mean comparisons were performed using the least significant difference (LSD) test at the 5% significance level.

Results and discussion

Soil and water test results. The physical and chemical properties of the soil used for greenhouse cultivation are presented in Table 2.

The characteristics of the irrigation water are shown in Table 3.

Effect of inoculation treatments and drought stress on growth plant indices. The results of the analysis of variance (ANOVA) for the effects of different treatments and drought stress on wheat growth indices are presented in Table 4.

Comparison of mean values showed that under non-stress conditions (D0), all bacterial treatments significantly increased grain dry weight compared to the uninoculated control (B0), with the highest value observed for inoculation with strain P187. Under moderate drought stress (D1), strain P187 again exhibited the highest grain dry weight, showing a 95% increase relative to the control. However, under severe drought stress (D2), inoculation did not result in a significant enhancement of grain dry weight compared to the control (Figure 1).

Table 2
Physical and chemical properties of the soil

Texture	Clay	Sand	Silt	Organic C (OC)	Total Neutralizing Value (T.N.V.)	FC	PWP	pH	EC	N	K	P_2O_5	Zn^{2+}	Cu^{2+}	Fe^{2+}	Mn^{2+}
	%								$dS \cdot m^{-1}$	%	mg·kg⁻¹					
Sandy Clay Loam	28	46	26	0.65	14.5	18.25	11.93	7.78	1.44	0.065	285	12.6	1.21	1.21	1.8	5.46

Table 3
Chemical properties of irrigation water

EC, $dS \cdot m^{-1}$	pH	SAR, $meq \cdot L^{-1}$	K^+, $mmol \cdot L^{-1}$	Na^+, $mmol \cdot L^{-1}$	Ca^{2+}, $mmol \cdot L^{-1}$	Mg^{2+}, $mmol \cdot L^{-1}$	Ca^{2+}/Mg^{2+}, $mmol \cdot L^{-1}$	Cl^-, $mmol \cdot L^{-1}$	SO_4^{2+}, $mmol \cdot L^{-1}$	NO_3^+, $mmol \cdot L^{-1}$
0.42	7.92	1.8	0.015	1.87	0.84	0.24	3.54	0.17	0.69	0.31

Table 4
Variance analysis of inoculation and drought stress on various growth indices (mean square)

S.O.V.	df	Grain dry weight, g/pot	Shoot dry weight, g/pot	Root dry weight, g/pot	Plant height, cm	Spike length, cm	Nitrogen content, %	Phosphorous content, %	Potassium content, %
Inoculation	8	45.25**	72.20**	10.70**	13.13**	10.43**	3.20**	0.0014**	0.07**
Drought stress	2	492.91**	1130.12**	32.11**	156.94**	37.28**	11.89**	0.0142**	0.09**
Inoculation * Drought stress	16	10.91**	14.27**	1.70**	2.43**	0.53**	0.33*	0.0006**	0.01**
Error	54	4.12	3.10	0.40	1.11	0.29	0.00019	0.00	0.001
CV, %		15.98	8.24	7.80	2.42	7.11	15.78	3.82	3.42

*Note: * significant at $p < 0.05$; ** significant at $p < 0.01$*

Figure 1
Effect of inoculation and drought stress on grain dry weight
(D0: no stress, D1: 60% of field capacity, D2: 40% of field capacity)

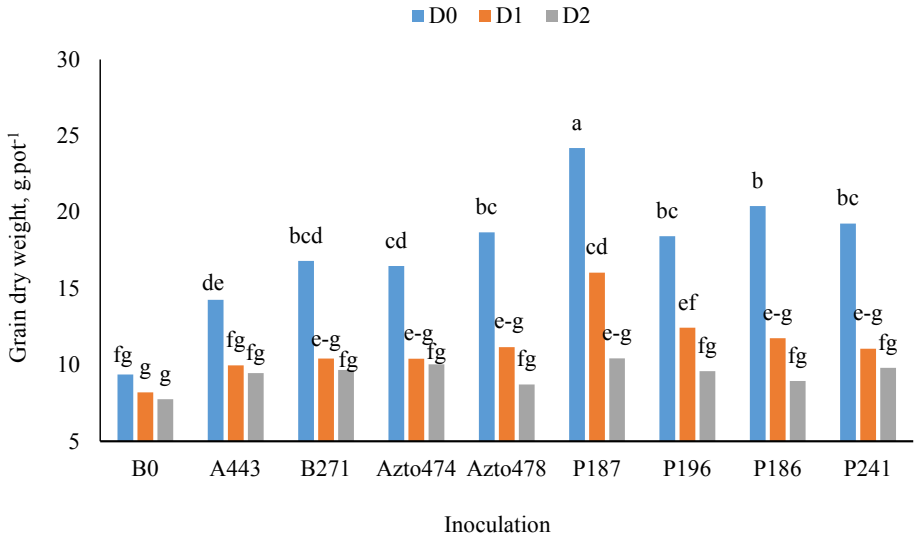

With increasing drought severity, shoot dry weight decreased significantly in most treatments. Under D2 conditions, shoot dry weight was reduced by 47% compared with D0. Inoculation with all bacterial strains under D0 and D1 significantly increased shoot dry weight relative to the uninoculated control (B0). Under D2 conditions, all strains except B271 enhanced shoot dry weight, with the highest value recorded for strain P187, which resulted in a 75% increase compared with the control (Figure 2).

Figure 2
Effect of inoculation and drought stress on shoot dry weight
(D0: no stress, D1: 60% of field capacity, D2: 40% of field capacity)

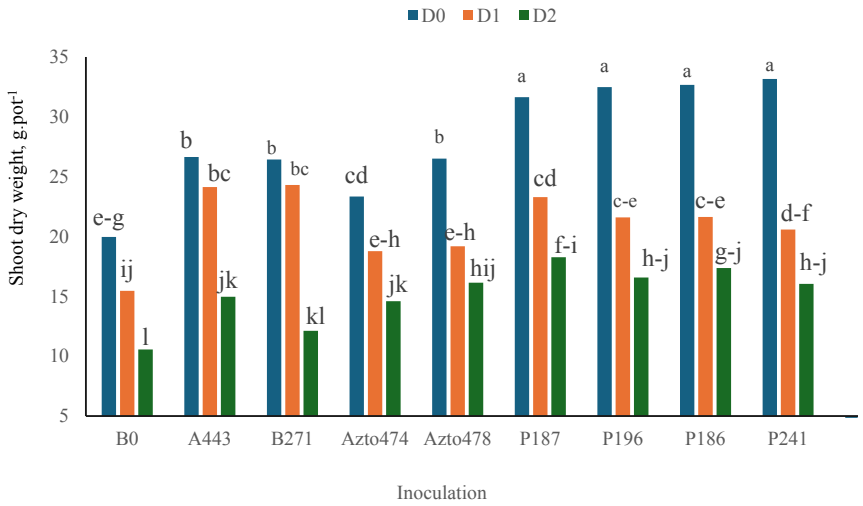

An increase in drought stress was associated with a reduction in root dry weight. Under severe stress (D2), the lowest root dry weight was observed in the B0 treatment. Under both D1 and D2 conditions, all inoculated treatments significantly increased root dry weight relative to the control

(B0), with strains P187 and P196 showing the most pronounced effects. Under D1, P187 increased root weight by approximately 75% compared to the control (Figure 3)

Plant height decreased across all treatments with increasing drought stress. In the uninoculated control (B0), plant height under D2 was reduced by 17% compared to D0. Inoculation under D2 had a significant effect, as all treated groups showed considerable increases in plant height relative to the control, with strains Azto474 and P187 producing the tallest plants (Figure 4).

Figure 3
Effect of inoculation and drought stress on root dry weight
(D0: no stress, D1: 60% of field capacity, D2: 40% of field capacity)

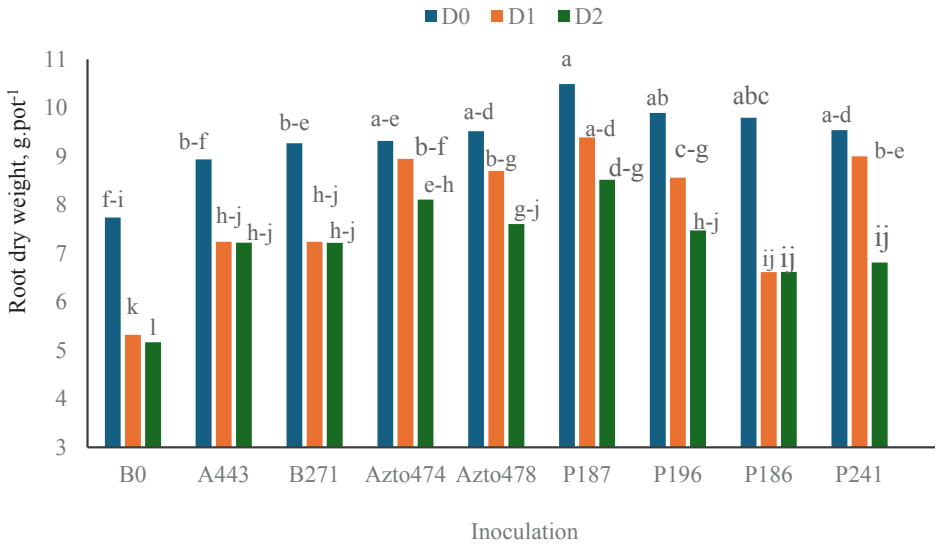

Figure 4
Effect of inoculation and drought stress on plant height
(D0: no stress, D1: 60% of field capacity, D2: 40% of field capacity)

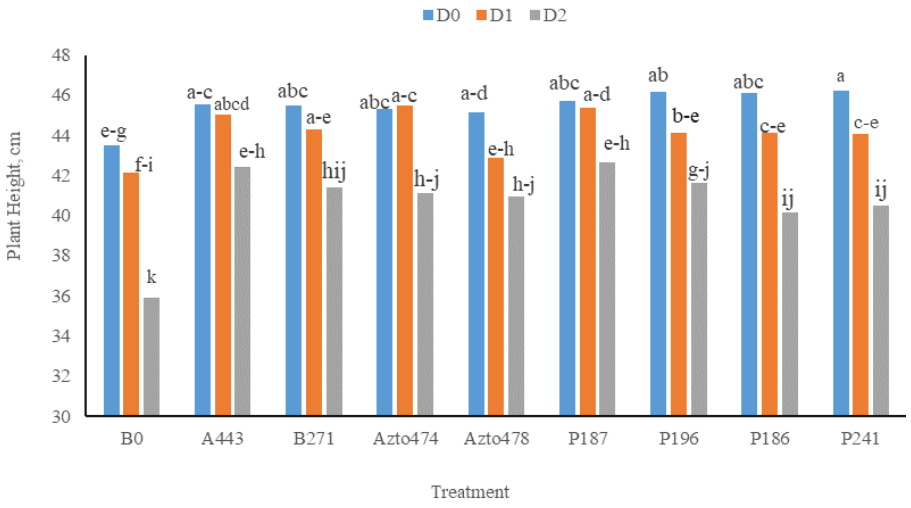

Under D1 conditions, the most significant increases in spike length were observed for strains P196 and P187. However, under D2, inoculation did not significantly affect spike length (Figure 5).

Mean comparisons revealed that drought stress led to a reduction in grain nitrogen content. Under moderate stress (D1), only inoculation with strain P187 resulted in a significant increase in nitrogen content compared to the control. Under severe stress (D2), strains P187, P196, and B271 significantly increased nitrogen content, with P187 showing the highest value (Figure 6).

Figure 5
Effect of inoculation and drought stress on spike length
(D0: no stress, D1: 60% of field capacity, D2: 40% of field capacity)

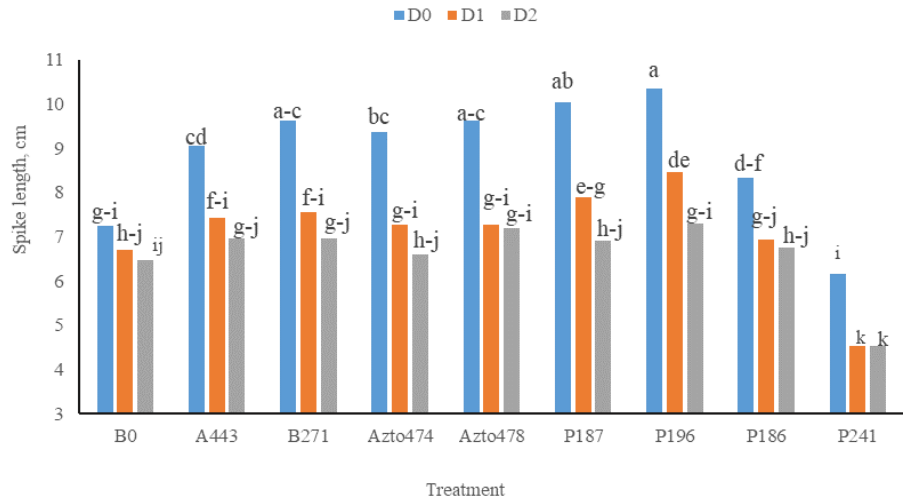

Figure 6
Effect of inoculation and drought stress on nitrogen content in plants
(D0: no stress, D1: 60% of field capacity, D2: 40% of field capacity)

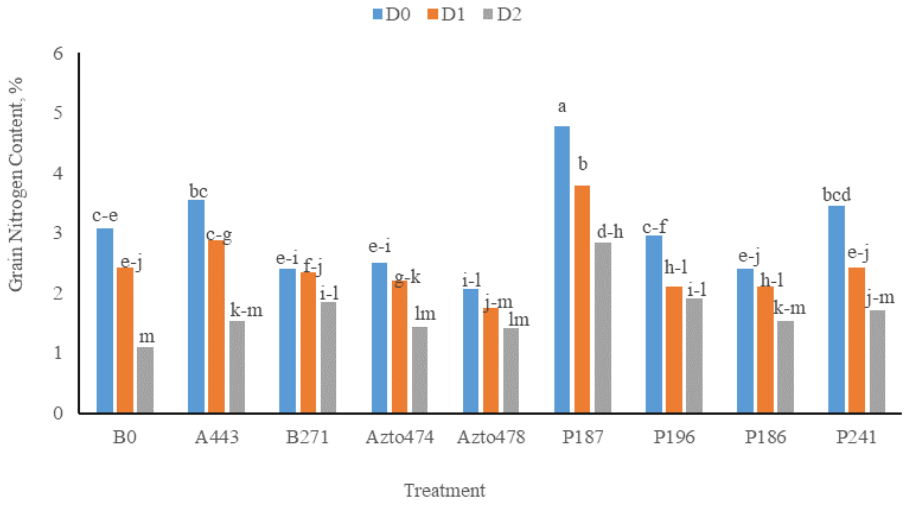

Analysis of mean values indicated that drought stress reduced grain phosphorus content. Under D1, only strain P187 caused a significant increase in phosphorus levels. Under D2, all treatments except P196 significantly increased phosphorus content compared to the control, with strain P187 showing the greatest enhancement (Figure 7).

Drought stress also led to a reduction in grain potassium content. Under D1, inoculation with strains P196, P187, and P186 significantly increased potassium levels compared to the control. Under D2, strains P196 and P187 significantly elevated potassium content relative to the control (Figure 8).

Figure 7
Effect of inoculation and drought stress on phosphorous content in plants (D0: no stress, D1: 60% of field capacity, D2: 40% of field capacity)

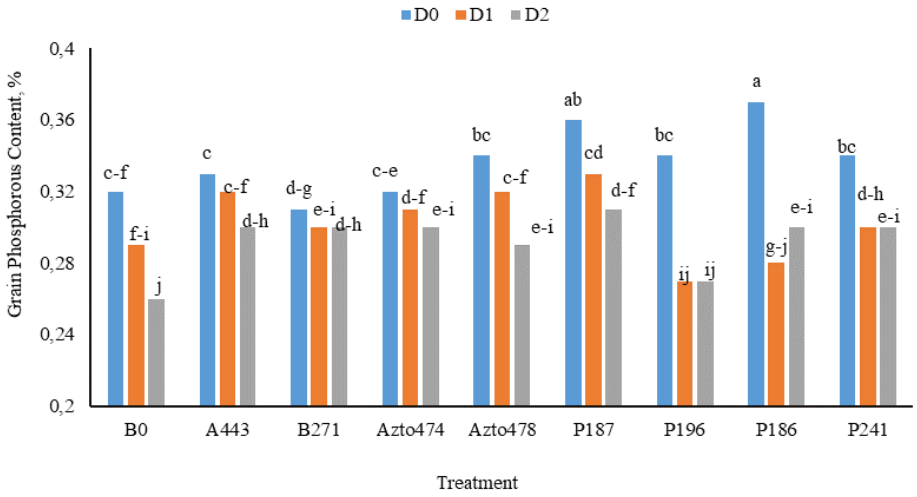

Figure 8
Effect of inoculation and drought stress on potassium content in plants (D0: no stress, D1: 60% of field capacity, D2: 40% of field capacity)

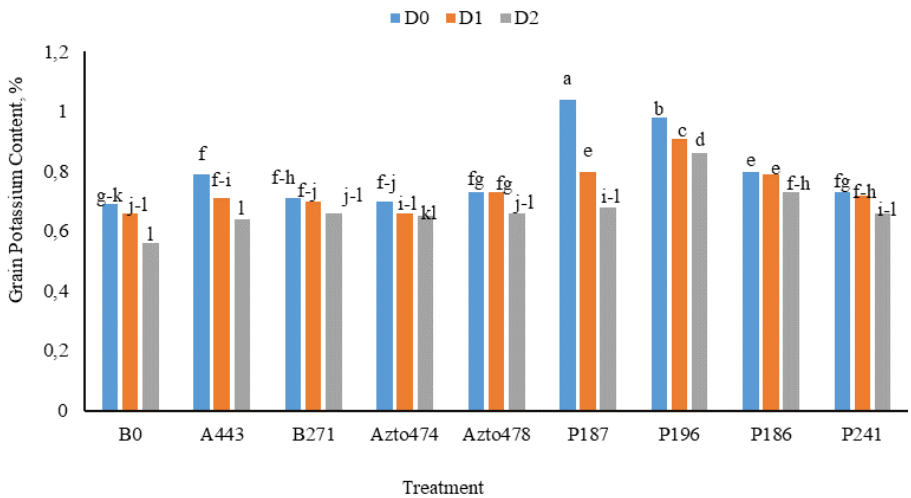

The results demonstrated that drought stress, at both moderate (D1) and severe (D2) levels, significantly reduced wheat growth indices and the concentrations of nitrogen (N), phosphorus (P), and potassium (K) in grains. However, inoculation with selected bacterial strains mitigated these adverse effects by enhancing several growth parameters and nutrient concentrations under drought conditions (Figures 1-8).

Among the tested strains, *Pseudomonas fluorescens* P187 led to a significant increase in grain dry weight under moderate drought stress (D1) compared to the uninoculated control (Figure 1). This finding is consistent with previous studies reporting that inoculation with plant growth-promoting rhizobacteria improves wheat yield under drought conditions (Creus et al., 2004). *Pseudomonas spp.* has been shown to enhance grain yield in both irrigated and water-limited environments (Chandra et al., 2019).

Shoot dry weight also increased significantly at both drought levels following inoculation with all strains, P187 showing the highest mean values (Figure 2). These observations align with earlier reports demonstrating the beneficial effects of *Pseudomonas* on straw biomass (Chandra et al., 2019) and of *Bacillus* and *Azospirillum* on shoot biomass under drought stress (Kasim et al., 2013).

Similarly, root dry weight was significantly improved under both D1 and D2 conditions across all treatments, P187 again producing the greatest increase (Figure 3). The role of *Azospirillum* in promoting root biomass under drought has been well-documented. Enhanced root development under stress is particularly important for improving water and nutrient uptake, thereby supporting overall plant growth (Agami et al., 2014).

Drought stress led to a reduction of plant height, but inoculation significantly mitigated this effect, especially under severe drought (D2) (Figure 4). This result is consistent with prior findings indicating that PGPR can enhance plant height under stress conditions (Kasim et al., 2013).

Although spike length declined with increasing drought severity, significant improvement due to inoculation was observed only under moderate stress (D1), with strains P187 and P196 producing the longest spikes (Figure 5). These findings agree with earlier studies showing that PGPR can enhance spike length under water-deficient conditions (Chandra et al., 2019). Additionally, *Azospirillum lipoferum* was previously reported to increase spike length under 60% evapotranspiration (ETc) relative to 100% ETc (Agami et al., 2014).

Drought stress also decreased grain macronutrient concentrations, but inoculation partially offset this reduction (Figures 6-8). Under moderate drought (D1), only strain P187 significantly improved nitrogen and phosphorus levels, and it showed the strongest effect under severe stress (D2) as well. A similar trend was noted for potassium content (Figure 8). These outcomes are supported by prior research indicating that PGPR can improve N, P, and K concentrations in grains under drought stress (Chandra et al., 2019). Likewise, inoculation with *Azotobacter* has been shown to enhance macronutrient uptake in maize grown under drought conditions in greenhouse trials (Shirinbayan et al., 2019).

PGPR enhance plant growth through several mechanisms, including the production of phytohormones (e.g., auxins), biological nitrogen fixation, solubilization of insoluble phosphates, siderophore release, silicate decomposition, and mobilization of essential nutrients such as potassium (Khosravi et al., 2024). The bacterial strains used in the present study were previously screened and characterized based on these functional traits (Khosravi et al., 2025).

Previous research has also demonstrated that bacterial inoculation can mitigate drought-induced damage and increase wheat stress tolerance via both direct mechanisms (e.g., hormone production) and indirect mechanisms (e.g., improved nutrient availability) (Kasim et al., 2013).

Interestingly, although *Azotobacter* strains (Azto478 and Azto474) and *Azospirillum* (A443) are known nitrogen (N_2) fixers, they did not significantly influence grain nitrogen content. In contrast, *Pseudomonas fluorescens* P187, which lacks nitrogen-fixing ability, significantly enhanced nitrogen content under all moisture conditions (D0, D1, and D2) compared to the control (Figure 6). This suggests that mechanisms other than nitrogen fixation – likely involving plant growth-promoting activities such as enhanced root development – are responsible for the observed improvements in nitrogen uptake. Laboratory analyses have confirmed that P187 exhibits superior traits, including indole-3-acetic acid (IAA) production, phosphate solubilization, and exopolysaccharide secretion (Khosravi et al., 2025). Similar enhancements were observed for phosphorus and potassium concentrations, further underscoring the effectiveness of this strain (Figures 7 and 8). These results are consistent with other reports highlighting the central role of microbial growth-promoting traits in improving root and shoot development and, subsequently, nutrient accumulation in plants (Ahmed & Hasnain, 2014; Alaskar & Al-Shwaiman, 2023; Çakmakçı et

al., 2020; Grover et al., 2021; Pantoja-Guerra et al., 2023).

Conclusion

This study provides clear evidence that inoculating wheat with selected PGPR strains, including *Azotobacter*, *Azospirillum*, *Bacillus*, and *Pseudomonas*, can significantly enhance plant performance under drought stress, both in terms of growth attributes and macronutrient acquisition. Among all evaluated strains, *Pseudomonas fluorescens* P187 consistently produced the strongest positive responses across multiple growth and nutrient parameters, indicating substantial drought-mitigating potential. The performance of *Pseudomonas sp.* P196, although slightly lower, further supports the superior adaptability and functional versatility of *Pseudomonas* species in water-limited environments. These results collectively highlight the value of exploring multi-strain or consortium-based inoculation strategies in future research, as such formulations may broaden the functional spectrum and yield more stable improvements under variable field conditions.

A particularly noteworthy finding is the marked increase in grain nitrogen content in plants inoculated with P187, despite the strain's lack of nitrogen-fixing ability. This suggests that indirect mechanisms such as stimulation of root system architecture, enhancement of rhizosphere nutrient mobilization, or modulation of hormone-mediated nutrient uptake pathways may play a central role in improving nitrogen assimilation under drought. In contrast, classical nitrogen-fixing PGPR such as *Azotobacter* and *Azospirillum* did not produce comparable effects, indicating that nitrogen fixation alone is insufficient to guarantee improved N accumulation when plants are exposed to moisture stress.

Overall, these observations emphasize the need to adopt a mechanism-oriented and trait-based perspective when selecting bacterial inoculants for wheat drought tolerance. Considering attributes such as phytohormone production, siderophore release, osmotic-adjustment facilitation, and nutrient-mobilization capacity will be essential for developing reliable PGPR-based bioformulations aimed at strengthening crop resilience and maintaining yield stability under increasingly frequent drought events.

Author contributions

Houshang Khosravi: Conceptualization, Investigation, Data Curation, Writing-Original Draft Preparation, Writing-Review and Editing, Visualization, Supervision, and Project Administration

Akram Otadi: Conceptualization, Investigation, Data Curation, and Writing-Original Draft Preparation

Hassan Etesami: Conceptualization, Visualization, and Supervision

Hosseinali Alikhani: Supervision and Visualization

Acknowledgments

This research was conducted as part of the project approved under project number "2-10-10-013-980061" by the Soil and Water Research Institute, and as part of A. Otadi's MSc thesis at the University of Tehran (Karaj, Iran). The authors would like to extend their sincere gratitude to the Soil and Water Research Institute (Karaj, Iran) for their valuable support. The authors also declare that no external funding or grants were received for this study.

Conflict of interest

The authors declare that they have no conflicts of interest.

References

1. Abdi, F., Atarodi, Z., Mirmiran, P., & Esteki, T. (2016). Review of nutritional status in Iranian population. *Focus on Sciences, 2*(3), 1–4. https://doi.org/10.20286/focsci-020332

2. Agami, R. A., Ghramh, H. A., & Hasheem, M. (2017). Seed inoculation with *Azospirillum lipoferum* alleviates the adverse effects of drought stress on wheat plants. *Journal of Applied Botany and Food Quality, 90*(1), 165–173.

3. Ahmed, A., & Hasnain, S. (2014). Auxins as one of the factors of plant growth improvement by plant growth promoting rhizobacteria. *Polish Journal of Microbiology, 63*(3), 261–266. https://doi.org/10.33073/pjm-2014-035

4. Alaskar, A. A., & Al-Shwaiman, H. A. (2023). The effect of plant growth-promoting rhizobacteria on soil properties and the physiological and anatomical characteristics of wheat under water-deficit stress conditions. *Agriculture, 13*(11), 2042. https://doi.org/10.3390/agriculture13112042

5. Ali, S., & Glick, B. (2025). Bacterial alleviation of drought stress in plants: recent advances and future challenges. In H. Etesami & Y. Chen (Eds.), *Sustainable Agriculture under Drought Stress* (pp. 367-383). Academic Press. https://doi.org/10.1016/B978-0-443-23956-4.00022-3

6. Çakmakçı, R., Mosber, G., Milton, A. H., Alatürk, F., & Ali, B. (2020). The effect of auxin and auxin-producing bacteria on the growth, essential oil yield, and composition in medicinal and aromatic plants. *Current Microbiology, 77*(4), 564–577. https://doi.org/10.1007/s00284-020-01917-4

7. Center for Statistics, Information Technology, and Communications. (2024). *Agricultural statistics* (Vol. 1). Ministry of Agricultural-Jahad. (In Persian)

8. Chandra, D., Srivastava, R., Gupta, V. V., Franco, C. M., Paasricha, N., Saifi, S. K., et al. (2019). Field performance of bacterial inoculants to alleviate water stress effects in wheat (*Triticum aestivum* L.). *Plant and Soil, 441*, 261–281. https://doi.org/10.1007/s11104-019-04115-9

9. Creus, C. M., Sueldo, R. J., & Barassi, C. A. (2004). Water relations and yield in *Azospirillum*-inoculated wheat exposed to drought in the field. *Canadian Journal of Botany, 82*(2), 273–281. https://doi.org/10.1139/b03-119

10. Dane, J. H., & Topp, C. G. (Eds.). (2020). *Methods of soil analysis: Part 4. Physical methods*. John Wiley & Sons.

11. Grover, M., Bodhankar, S., Sharma, A., Sharma, P., Singh, J., & Nain, L. (2021). PGPR mediated alterations in root traits: way toward sustainable crop production. *Frontiers in Sustainable Food Systems, 4*, 618230. https://doi.org/10.3389/fsufs.2020.618230

12. Kasim, W. A., Osman, M. E., Omar, M. N., Abd El-Daim, I. A., Bejai, S., & Meijer, J. (2013). Control of drought stress in wheat using plant-growth-promoting bacteria. *Journal of Plant Growth Regulation, 32*, 122–130. https://doi.org/10.1007/s00344-012-9283-7

13. Khosravi, H. (2019). Response of maize to inoculation with *Azotobacter* under drought stress conditions. *Journal of Water Research in Agriculture, 33*(1), 29–38. (In Persian) https://doi.org/10.22092/jwra.2019.119112

14. Khosravi, H., Khoshru, B., Nosratabad, A. F., & Mitra, D. (2024). Exploring the landscape of biofertilizers containing plant growth-promoting rhizobacteria in Iran: progress and research prospects. *Current Research in Microbial Sciences, 6*, 100268. https://doi.org/10.1016/j.crmicr.2024.100268

15. Khosravi, H., Mahmoudi, M. (2013). Evaluation of effects of *Azotobacter* inoculation and manure on growth of rainfed wheat. *Journal of Soil Management and Sustainable Production, 3*(2), 205–219. (In Persian).

16. Khosravi, H., Otadi, A., Alikhani, H., & Etesami, H. (2025). Evaluation and comparative analysis of plant growth-promoting traits in diverse groups of rhizosphere bacteria. *Journal of Soil Biology, 12*(2), 235–260. https://doi.org/10.22092/sbj.2025.367286.271

17. Kuwayama, Y., Thompson, A., Bernknopf, R., Zaitchik, B., & Vail, P. (2019). Estimating the impact of drought on agriculture using the US Drought Monitor. *American Journal of Agricultural Economics, 101*(1), 193–210. https://doi.org/10.1093/ajae/aay037

18. Pantoja-Guerra, M., Valero-Valero, N., & Ramírez, C. A. (2023). Total auxin level in the soil–plant system as a modulating factor for the effectiveness of PGPR inocula: a review. *Chemical and Biological Technologies in Agriculture, 10*(1), 6. https://doi.org/10.1186/s40538-022-00370-8

19. Shah, A., Nazari, M., Antar, M., Msimbira, L. A., Naamala, J., Lyu, D., & Smith, D. L. (2021). PGPR in agriculture: a sustainable approach to increasing climate change resilience. *Frontiers in Sustainable Food Systems, 5*, 667546. https://doi.org/10.3389/fsufs.2021.667546

20. Shirinbayan, S., Khosravi, H., & Malakouti, M. J. (2019). Alleviation of drought stress in maize (*Zea mays*) by inoculation with *Azotobacter* strains isolated from semi-arid regions. *Applied Soil Ecology, 133*, 138–145. https://doi.org/10.1016/j.apsoil.2018.09.015

21. Sparks, D. L., Page, A. L., Helmke, P. A., & Loeppert, R. H. (Eds.). (2020). *Methods of soil analysis: Part 3. Chemical methods*. John Wiley & Sons.

22. Yazdandoost, F. (2016). Dams, drought and water shortage in today's Iran. *Iranian Studies, 49*(6), 1017–1028. https://doi.org/10.1080/00210862.2016.1241626

23. Yousefi, H., Ahani, A., Moridi, A., & Razavi, S. (2024). The future of droughts in Iran according to CMIP6 projections. *Hydrological Sciences Journal, 69*(7), 951–970. https://doi.org/10.1080/02626667.2024.2348720

Information about the authors:

Houshang Khosravi – Associate Professor, Soil Biology Department, Soil and Water Research Institute (Karaj, Iran, e-mail: hkhosravi@areeo.ac.ir).

Akram Otadi – M.Sc., Laboratory Specialist, Soil and Water Research Institute (Karaj, Iran, e-mail: mahnaz.otadi@gmail.com).

Hassan Etesami – Associate Professor, Department of Soil Sciences, Faculty of Agriculture, University of Tehran (Karaj, Iran, e-mail: hassanetesami@ut.ac.ir).

Hosseinali Alikhani – Professor, Department of Soil Sciences, Faculty of Agriculture, University of Tehran (Karaj, Iran, e-mail: halikhan@ut.ac.ir).

Received 07 December 2026;
received in revised form 21 June 2026;
accepted 26 June 2026

IRSTI 34.29.35 https://doi.org/10.26577/IJBCh20261917

R.K. Anatoliy[1], M.S. Kurmanbayeva[1*], T.E. Darbayeva[2], A.B. Kusmangazinov[1], D.E. Karabalayeva[1], A.R. Aldibekova[1], G. Sramkó[3]

[1] Al-Farabi Kazakh National University, Almaty, Kazakhstan
[2] Makhambet Utemisov West Kazakhstan University, Uralsk, Kazakhstan
[3] University of Debrecen, Debrecen, Hungary
*e-mail: Meruyert.Kurmanbayeva@kaznu.edu.kz

THE RATIO OF BOREAL AND STEPPE FLORISTIC ELEMENTS IN PHYTOCOENOSES INVOLVING *POPULUS ALBA*, *P NIGRA*, *P. TREMULA* AND *P.* × *CANESCENS* IN THE ZHAIYK RIVER FLOODPLAIN

Abstract: The article presents the results of a comprehensive ecological, phytocoenotic, and floristic study of forest communities involving representatives of the genus Populus L. in the Ural River valley within Western Kazakhstan. The research was conducted in 2024-2026 across steppe, semi-desert, and desert zones. Based on 26 geobotanical releves, a syntaxonomic analysis of floodplain and ravine forests was carried out, encompassing various elements of floodplain relief and moisture gradients. Four populations of the genus Populus were identified and characterized, represented by the species *Populus alba* L., *Populus nigra* L., *Populus canescens* (Aiton) Sm., and *Populus tremula* L. The studied phytocoenoses are characterized by pronounced vertical stratification, high floristic diversity, and a mosaic vegetation structure determined by differences in soil and hydrological conditions. The total number of vascular plant species within the communities ranges from 16-55. Species of the family Salicaceae plays a leading role in forming the coenotic core, while the herb layer is mainly represented by members of Poaceae, Asteraceae, and Fabaceae. Chorological analysis revealed the predominance of boreal forest and Eurasian floristic elements, with a significant contribution of steppe and Pontic species, reflecting the ecotonal nature of the region's floodplain forests. An expansion of the ecological-coenotic amplitude of certain species was observed under changing hydrological conditions, particularly within the desert zone.The obtained data supplement existing knowledge on the structure, floristic composition, and geographical distribution of poplar forests in Western Kazakhstan and are important for the monitoring and conservation of floodplain ecosystems.
Keywords: Populus, floodplain forests, phytocoenoses, floristic structure, boreal and steppe elements, Zhaiyk river.

Introduction

The genus *Populus* L. comprises deciduous forest-forming tree species belonging to the family *Salicaceae* (Mirbel). and plays an important role in the formation of floodplain and riparian forest ecosystems. In Western Kazakhstan, representatives of the genus *Populus* L. are mainly confined to the valley of the region's principal hydrological feature: the Zhaiyk river and are distributed along both its right and left banks over a stretch of approximately 700 km (Chibilev et al., 2023).

Within the study area, plantations of the genus *Populus* L. are represented by species belonging to two sections. Section Leuce Duby includes white and aspen-like poplars and is subdivided into two subsections. Subsection Albidae Dode comprises *Populus alba* L., occupying an area of 10,334.2 ha, and *Populus canescens* (Aiton) Sm., distributed over 8 ha. Subsection Trepidae Dode is represented by *Populus tremula* L., whose plantations cover 1,334 ha (Anatoliy et al., 2025).

Section Aigeiros Lunell, which includes black poplar forms, is represented by *Populus nigra* L., whose plantations occupy 16,667.7 ha (Klimov & Proshkin, 2024). This species is one of the principal forest-forming components of the Zhaiyk River floodplain ecosystems and plays a significant role in bank stabilization, regulation of the hydrological regime, and maintenance of biodiversity.

Within the floodplain, the channel, near-channel, central, and terrace-adjacent zones are distinguished, differing in relief morphology, hydrological regime, and vegetation cover. The indigenous (upland) banks are mainly represented by zonal steppe communities formed by feather-grass and Artemisia lerchiana formations (Figure 1).

The river floodplain is characterized by the development of azonal vegetation complexes, including floodplain forests and meadow communities. In the northern part of the valley, the average width of the floodplain is 12–13 km, locally increasing to 16 – 18 km, whereas southward it gradually narrows to 3–5 km (Khlyustov et al., 2019).

Morphologically, the floodplain has a flat-ridged relief formed by alternating ridges, interridge depressions, low-lying depressions, lakes, and oxbow channels.

The near-channel part of the floodplain, 200 – 400 m wide, is characterized by the predominance of arboreal phytocoenoses represented by white willow *Salix alba* and black poplar communities.

The central floodplain occupies the largest area, features a weakly expressed ridged relief, and ranges in width from 4 to 12 km. The terrace-adjacent floodplain forms a strip 1–2 km wide, locally narrowing to 400 – 500 m, and is predominantly overgrown with shrub vegetation.

The Trans-Ural – Turgai (West Kazakhstan) subprovince has not always been regarded as an independent unit and, in some literature sources, was included either within the Volga–Ural and Mugodzhar-Turgai subprovinces or within the Trans-Volga–West Kazakhstan subprovince (Petrenko et al., 1998).

The western boundary of the subprovince runs along the marginal part of the Southern Urals and the Ural River valley, corresponding to the boundary of the moderately continental climate, and extends eastward to the Turgai Plateau.

Figure 1
Forest phytocoenoses of the Zhaiyk river valley, June, 2025

The relief of the Trans – Ural -Turgai Province is predominantly flat. In its southern part, the marginal areas of the Mugodzhar Hills are located, with a maximum elevation of 657 m above sea level. In the eastern part, north of the Zhaiyk River, plains composed of alluvial and deluvial deposits prevail, with absolute elevations ranging from 450 to 300 m, whereas in the southern part the Pre-Ural Plateau is distinguished, with elevations from 450 to 100 m (Viktorov, 1951). In recent years, within the field of botanical geography, during the study of arid and subarid territories of the Palearctic and the vegetation

cover of the Eurasian steppe zone, E.M. Lavrenko developed a botanical-geographical regionalization and established the latitudinal and longitudinal boundaries of steppe territories (Lavrenko, 1979).

The Pre-Ural Plateau is characterized by a diversity of parent materials: in addition to loamy deluvial deposits, chalk formations, Cretaceous sandy rocks, and saline clays are widespread. In combination with varied microrelief conditions, this determines the considerable diversity of vegetation cover.

I.N. Safronova subdivided the Pre-Ural Plateau into two subzonal types of dry sod-grass steppes formed on dark chestnut and chestnut soils (Safronova, 2002). The northern dry steppes on dark chestnut soils are characterized by the dominance of *Stipa lessingiana* and *Festuca valesiaca*, sometimes with a notable presence of *Stipa capillata*. The forb layer is mainly represented by xerophytic species such as *Tanacetum achilleifolium*, *Serratula dissecta*, and *Crinitaria tatarica* (Mirkin et al., 2015).

The aim of this article is to provide a detailed ecological-phytocoenotic and floristic characterization of the poplar forests of the Zhaiyk River, studied in its middle and lower reaches within the western region of Kazakhstan, as well as to identify their syntaxonomic diversity, structure, species composition, and geographical-ecological features under the conditions of steppe, semi-desert and desert natural zones.

Materials and methods

During the period from May 2024 to April 2026, a total of 26 geobotanical relevés were conducted in floodplain and ravine forests, and the resulting data were subsequently classified according to syntaxonomic principles. The size of the sampling plots was determined according to the homogeneity and structure of the community and measured 20 × 20 m. Species abundance was assessed using the Braun-Blanquet scale (Martynenko et al., 2008). In the synoptic table of syntaxa, species constancy is presented using an equal-interval scale with the following constancy classes: 1 – 1-20%; 2 – 21-40%; 3 – 41-60%; 4 – 61-80%; 5 – 81-100%. Species constancy within communities was evaluated using a five-point scale: I – 1-20%; II – 21-40%; III – 41-60%; IV – 61-80%; V – 81-100% (Ermakov & Martynenko, 2022).

The syntaxonomic analysis was performed in accordance with the generally accepted principles of ecological-floristic classification. The Latin names of plant species follow the checklist by M.M.Fartushinam (Chekalin & Fartushina, 2014) and were harmonized with the requirements of the International Code of Phytosociological Nomenclature (Theurillat et al., 2021).

Taxonomic identification of plants was carried out using fundamental floristic sources, including Flora of Kazakhstan (Pavlov, 1960), Key to Plants of Central Asia (Novikov, et al., 2018), as well as the generalizing works of V.V. Ivanov (Darbaeva et al., 2011). Species nomenclature is presented in accordance with current data from the international database Plants of the World Online (POWO) and the electronic resource Plantarium (http://www.ipni.org; https://powo.science.kew.org; https://www.plantarium.ru/).

In the geographical regionalization of the vegetation cover of the study area, the monograph by E.M. Lavrenko "Steppes of Eurasia" (Lavrenko, 1991) served as the theoretical basis. To analyze the steppe zones and classify the plant communities of Western Kazakhstan, we integrated data from I.N. Safronova article (2002) and were guided by the general provisions of R.V. Kamelin (2012). The geographical regionalization of floodplain forests in the desert and semi-desert zones was carried out using data from the monograph Akzhigitova et al. (2003).

Field research was conducted across the West Kazakhstan Region within various natural zones. In the Terekty District, on the lands of the Chagan Forestry (village of Kabyltobe), floodplain forest communities of the first population were studied: twelve geobotanical relevés were carried out across extensive plots during the period from late April to late May (51°15.711′ N, 51°54.173′ E) at an absolute elevation of 5 m above sea level. The second population comprises four geobotanical relevés of ravine forests, completed in early May and mid-July (51°21.238′ N, 51°56.512′ E) at an elevation of 41 m above sea level.

In the semi-desert zone of the region, within the Baiterek District (village of Bogatskoye), the third population was investigated: five geobotanical releves were established during early spring and early autumn at sites with coordinates 50°40′20″ N, 51°08′24″ E and 51°05′73″ N, 51°14′41″ E, at absolute elevations of 45-46 m above sea level.

In the southern part of the region, within the desert zone, fieldwork was conducted on the territory of the Taipak Forestry, where the fourth population was studied: five geobotanical releves were carried out during the summer period, following the recession of floodwaters, at coordinates 49°09′64″ N, 51°32′50″ E and 49°09′422″ N, 51°33′185″ E, absolute relief elevations in this area reach – 6 m above sea level (Figure 2).

Figure 2
Map of the sampling locations of the described plant communities

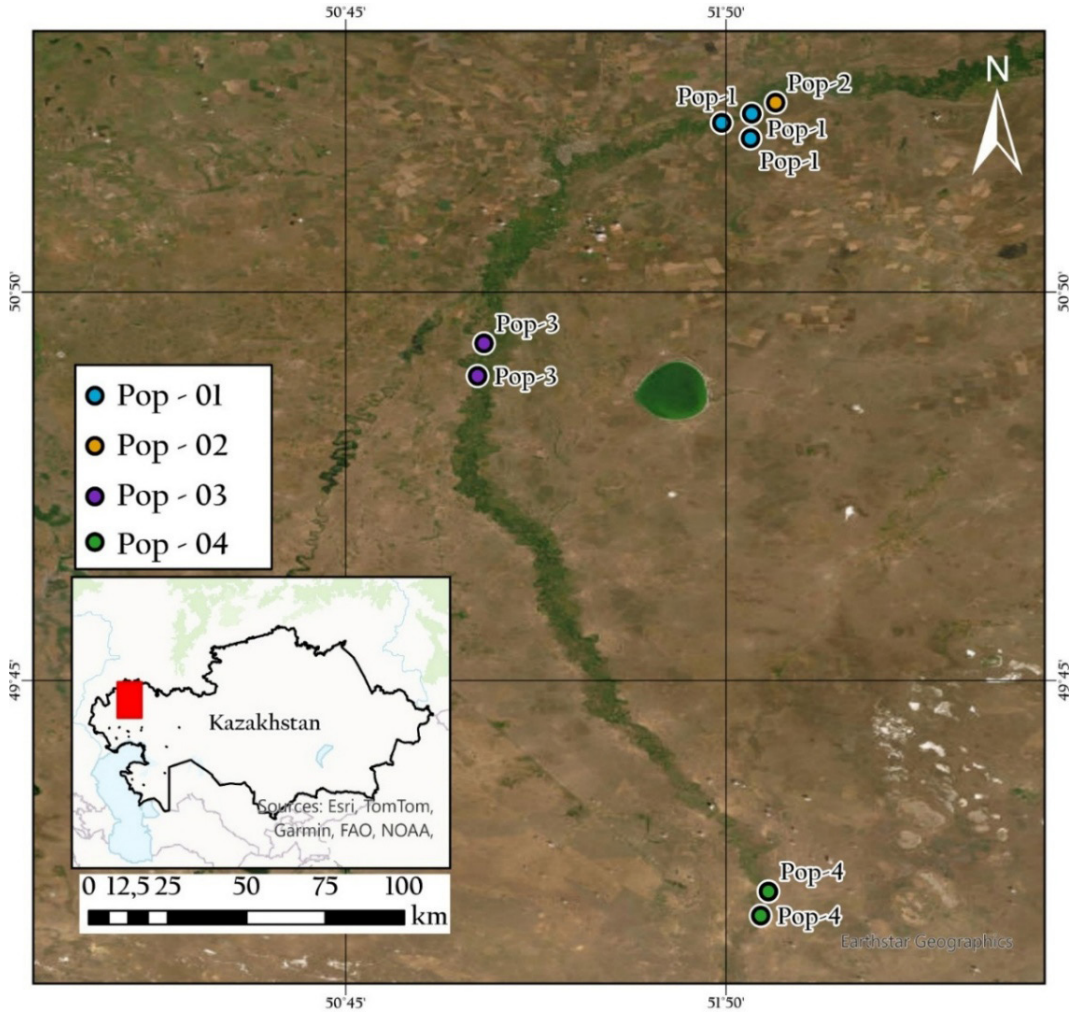

Results and discussion

In Western Kazakhstan, within the Zhaiyk River valley, four populations of the genus Populus were identified. An ecological and phytocoenotic survey of plant communities involving species of the genus *Populus* was conducted, which made it possible to characterize their environmental conditions and community structure (Table 1).

The studied phytocoenoses are confined to floodplain and above-floodplain sites located within the steppe, semi-desert, and desert zones. Geobotanical relevés were carried out on 20 m² sample plots, in accordance with standard requirements for the study of tree – shrub and herbaceous communities. Absolute elevations range from – 6 to 46 m, reflecting both floodplain depressions and elevated terraces.

The soil cover is represented mainly by forest-meadow alluvial soils, dark chestnut meadow soils, and sandy soils, which determine the high mosaic structure of the vegetation cover and the diversity of ecological plant groups.

In all described communities, a clearly expressed vertical structure is observed:

Table 1

Differentiating groups of species formed with the participation of the genus Populus L.

Association	*Populus* × *canescens – Convallaria majalis*		*Populus alba – Carex vulpine*		*Populus nigra – Rubus caesius*		*Populus tremula -Aegopodium podagraria*		*Populus alba – Glycyrrhiza glabra*		*Populus nigra -Bromopsis inermis*		*Populus nigra – Melilotus albus*		*Populus nigra – Pseudosophora alopecuroides*		Species constancy
Zone	Steppe								Semi-desert				Desert				
Plot area, m²	20		20		20		20		20		20		20		20		
Mean tree height, m	18		20		21		12,5		21		22		18		19		
Total vegetation cover, %	75		70		65		55		60		65		50		40		
Absolute elevation, m	21		16		18		41		46		45		-6		-6		
Soil	Forest-meadow alluvial soil								Dark chestnut meadow soil				Sandy soil				
Number of species	25		19		16		30		29		25		20		18		
GPS	N51°15.711′ E51°54.173′		N51°19.741′ E51°54.199′		N51°20.461′ E51°55.528′		N51°21.238′ E51°56.512′		N50°40′.20′′ E 51°8.24′′		N 51°5.73′ E 51°14.41′		N 49°9.64′ E52°32.50′		N 49°9.422′ E 52°33.185′		
Releve number / layer designation	1.1		1.2		1.3		2.1		3.1		3.2		4.1		4.2		
Salicaceae																	
Populus alba L.	t1	2	t1	3	t1	2	t1	r	t1	4	t1	2	t1	2	·	·	III
Populus nigra L.	·	·	t1	+	t1	2	·	·	t1	2	t1	3	t1	3	t1	3	III
Populus × *canescens* (Aiton) Sm.	t1	5	·	·	·	·	·	·	·	·	·	·	·	·	·	·	I
Populus tremula L.	·	·	·	·	·	·	t1	5	·	·	·	·	·	·	·	·	I
Salix alba L.	t1	2	t1	1	t1	1	·	·	t1	2	·	·	t1	1	t1	1	III
Salix caspica Pall.	·	·	·	·	·	·	·	·	·	·	·	·	s1	r	·	·	I
Poaceae																	
Bromopsis riparia (Rehmann) Holub	·	·	·	·	·	·	·	·	h1	1	·	·	·	·	·	·	I
Bromopsis inermis (Leyss.) Holub	·	·	·	·	·	·	h1	+	·	·	h1	2	·	·	·	·	I
Setaria glauca (Poir.) Roem. & Schult.	·	·	·	·	·	·	·	·	h1	1		.	·	·	·	·	I
Poa pratensis L.	h1	1	.	.	·	·	h1	1	·	·	·	.	·	·	·	·	I
Calamagrostis epigeios (L.) Roth	·	·	h1	1	·	·	·	·	·	·	·	.	·	·	·	·	I

Continuation of the table

Calamagrostis neglecta (Ehrh.) Gaerth., Mey. et Scherb.	h1	1																		I
Festuca valesiaca Gaudin					h1	1														I
Melica nutans L.	h1	1																		I
Eremopyrum orientale L. Jaub. & Spach															h1	1				I
Melica altissima L.							h1	1												I
Cyperaceae																				
Carex vulpine L.			h1	2																I
Carex acuta L.																	h1	1		I
Carex melanostachya M. Bieb. ex Willd.							h1	1							h1	1				I
Carex leporina L.							h1	1												I
Alliaceae																				
Allium lineare L.									h1	r					h1	r				II
Liliaceae																				
Fritillaria meleagris L.	h1	r																		I
Iridaceae																				
Iris pseudacorus L.			h1	1					h1	1										II
Juncaceae																				
Juncus compressus Jacq.									h1	1										I
Asparagaceae																				
Asparagus officinalis L.									h1	1										I
Amaranthaceae																				
Amaranthus albus L.									h1	+	h1	1								I
Convallariaceae																				
Convallaria majalis L.	h1	3					h1	+												I
Aceraceae																				
Acer negundo L.	t1	1	t1	1	t1	1	t1	+							t1	+				II
Fagaceae																				
Quercus robur L.	t1	r																		I

Continuation of the table

Oleaceae																	
Fraxinus americana L.							t1	r									I
Betulaceae																	
Betula pendula Roth							t1	r									I
Aristolochiaceae																	
Aristolochia clematitis L.	ss1	+			ss1	1											I
Rosacaeae																	
Prunus spinosa L.			s1	1					s1	1							II
Rubus caesius L.					ss1	2									ss1	2	II
Cerasus fruticosa Pall.							s1	r									I
Spiraea hypericifolia L.							s1	1									I
Amygdalus nana L.							s1	2									I
Rosa canina L.							s1	+									I
Crataegus ambigua C.A. Mey. ex A.K. Becker							s1	1									I
Celastraceae																	
Euonymus verrucosus Scop.	s1	+															I
Brassicaceae																	
Chorispora tenella (Pall.) DC.			h1	1	h1	1											I
Sisymbrium altissimum L.			h1	+													I
Ranunculaceae																	
Thalictrum flavum L.					h1	1											I
Thalictrum minus L.			h1	1													I
Lamiaceae																	
Phlomoides tuberosa (L.) Moench									h1	+							I
Mentha aquatica L.									h1	+							I
Salvia pratensis L.									h1	1							I
Glechoma hederacea L.									h1	+							I
Leonurus cardiaca L.							h1	r	.	.	h1	r	h1	1			II
Lycopus europaeus L.									.	.	h1	+					I
Stachys palustris L.	.	.											h1	1			I

Continuation of the table

Lamium amplexicaule L.	h1	+	·	·	·	·	·	·	·	·	·	·	·	·	·	·	·	I
Lythraceae																		
Lythrum salicaria L.	h1	2	·	·	·	·	·	·	·	·	·	·	·	·	·	·	·	I
Rubiaceae																		
Galium boreale L.	h1	2	·	·	·	·	h1	1	·	·	·	·	·	·	·	·	·	I
Fabaceae																		
Glycyrrhiza glabra L.	·	·	·	·	·	·	·	·	h1	3	.	.	h1	1	·	·	·	II
Glycyrrhiza aspera Pall.	·	·	·	·	·	·	·	·	·	·	·	·	h1	2	·	·	·	I
Lathyrus tuberosus L.	h1	1	·	·	·	·	·	·	h1	2	·	·	·	·	·	·	·	II
Medicago falcata L.	·	·	h1	2	·	·	·	·	·	·	·	·	·	·	h1	1	·	II
Melilotus albus Medik.	·	·	·	·	h1	2	·	·	·	·	·	·	h1	3	.	.	·	II
Trifolium arvense L.	h1	+	·	·	·	·	·	·	·	·	·	·	·	·	·	·	·	I
Trifolium repens L.	·	·	·	·	·	·	h1	+	·	·	·	·	·	·	·	·	·	I
Lotus corniculatus L.	·	·	·	·	·	·	·	·	·	·	·	·	h1	+	.	.	·	I
Alhagi pseudalhagi (M. Bieb.) Desv. ex Wangerin	·	·	·	·	·	·	·	·	·	·	·	·	·	·	h1	3	·	I
Pseudosophora alopecuroi-des (L.) Sweet	·	·	·	·	·	·	·	·	·	·	·	·	·	·	h1	2	·	I
Cytisus borysthenicus (Gruner) Klásk.	·	·	·	·	·	·	s1	+	·	·	·	·	·	·	·	·	·	I
Polygonaceae																		
Rumex confertus Willd.	·	·	·	·	·	·	·	·	h1	+	·	·	h1	1	·	·	·	II
Polygonum aviculare L.	·	·	·	·	·	·	·	·	h1	1	·	·	h1	1	·	·	·	II
Persicaria amphibia (L.) Delarbre	·	·	·	·	·	·	·	·	·	·	h1	+	·	·	·	·	·	I
Solanaceae																		
Solanum dulcamara L.	·	·	·	·	·	·	·	·	h1	r	·	·	h1	+	·	·	·	II
Tamaricaceae																		
Tamarix ramosissima Ledeb.	·	·	·	·	·	·	·	·	·	·	·	·	·	·	h1	2	·	I
Chenopodiaceae																		
Atriplex cana C.A. Mey.	·	·	·	·	·	·	·	·	ss1	1	·	·	ss1	1	·	·	·	I
Atriplex micrantha Ledeb.	·	·	·	·	·	·	·	·	·	·	h1	1	·	·	·	·	·	I
Bassia prostrata (L.) Beck	·	·	·	·	·	·	·	·	·	·	·	·	·	·	h1	+	·	I

Continuation of the table

Plantaginaceae																				
Plantago maxima Juss. ex Jacq.											h1	1								I
Plantago lanceolata L.													h1	+						I
Plantago major L.	h1	+																		I
Scrophulariaceae																				
Gratiola officinalis L.											h1	r								I
Veronica longifolia L.											h1	+								I
Linaria vulgaris Mill.															h1	1				I
Dodartia orientalis L.																	h1	1		I
Scrophularia nodosa L.	h1	r																		I
Plumbaginaceae																				
Limonium gmelinii (Willd.) Kuntze											h1	1								I
Euphorbiaceae																				
Euphorbia palustris L.											h1	1								I
Euphorbia seguieriana Neck.					h1	1														I
Butomaceae																				
Butomus umbellatus L.											h1	+								I
Ulmaceae																				
Ulmus laevis Pall.	t1	2	t1	1	t1	2					t1	+								II
Rhamnaceae																				
Rhamnus cathartica L.											s1	+								I
Frangula alnus Mill.	s1	r																		I
Caprifoliaceae																				
Lonicera tatarica L.							s1	1												I
Crassulaceae																				
Hylotelephium triphyllum (Haw.) Holub													h1	+						I
Apiaceae																				
Eryngium planum L.	h1	1																		I
Silaum silaus (L.) Schinz & Thell.													h1							I

Continuation of the table

Sium latifolium L.	.	.	.	.	.	.	h1	+	.	.	.	.	.	.	.	.	.	.	.	.	I
Aegopodium podagraria L.	.	.	.	.	.	.	h1	1	.	.	.	.	.	.	.	.	.	.	.	.	I
Malvaceae																					
Malva thuringiaca (L.) Vis.	.	.	.	.	.	.	.	.	.	.	h1	.	.	.	.	.	.	.	.	.	I
Cannabaceae																					
Cannabis sativa L.	.	.	.	.	.	.	.	.	.	.	.	.	.	.	.	.	h1	2	.	.	I
Urticaceae																					
Urtica dioica L.	.	.	.	.	.	.	h1	+	.	.	.	.	.	.	.	.	.	.	.	.	I
Elaeagnaceae																					
Elaeagnus commutata Bernh. ex Rydb.	.	.	.	.	.	.	.	.	.	.	.	.	.	.	s1	+	.	.	.	.	I
Oberna behen (L.) Ikonn.	h1	+	.	.	.	.	.	.	.	.	.	.	.	.	.	.	.	.	.	.	I
Silene nutans L.	.	.	h1	+	.	.	.	.	.	.	.	.	.	.	.	.	.	.	.	.	I
Herniaria glabra L.	.	.	.	.	.	.	.	.	.	.	.	.	.	.	.	.	h1	+	.	.	I
Convolvulaceae																					
Convolvulus arvensis L.	.	.	h1	+	.	.	.	.	.	.	h1	1	.	.	h1	1	.	.	.	.	III
Campanulaceae																					
Campanula sibirica L.	h1	+	.	.	.	.	.	.	.	.	.	.	.	.	.	.	.	.	.	.	I
Campanula ruthenica M. Bieb.	.	.	.	.	.	.	h1	+	.	.	.	.	.	.	.	.	.	.	.	.	I
Violaceae																					
Viola canina L.	.	.	h1	+	.	.	.	.	.	.	.	.	.	.	.	.	.	.	.	.	I
Viola elatior Fries.	.	.	.	.	h1	+	.	.	.	.	.	.	.	.	.	.	.	.	.	.	I
Asteraceae																					
Inula salicina L.	.	.	.	.	.	.	.	.	.	.	h1	1	.	.	h1	+	II				
Arctium lappa L.	.	.	.	.	.	.	h1	+	.	.	.	.	.	.	.	.	.	.	.	.	
Inula britannica L.	.	.	h1	1	.	.	.	.	.	.	h1	1	.	.	h1	1	II				
Inula germanica L.	.	.	.	.	h1	1	.	.	.	.	.	.	.	.	.	.	.	.	.	.	I
Inula helenium L.	.	.	.	.	.	.	h1	1	.	.	.	.	.	.	.	.	.	.	.	.	I
Xanthium spinosum L.	.	.	.	.	.	.	.	.	.	.	h1	1	h1	.	.	.	.	.	.	.	II
Senecio erucifolius L.	.	.	.	.	.	.	.	.	.	.	h1	1	.	.	.	.	.	.	.	.	I
Artemisia marschalliana Spreng.	.	.	.	.	.	.	.	.	ss1	1	.	.	.	.	.	.	.	.	.	.	I

Continuation of the table

Artemisia prasina Krasch. ex Poljak.	.	.	.	.	.	.	.	.	.	.	ss1	1	.	.	.	.	I
Artemisia absinthium L.	h1	+	.	.	.	.	.	.	.	.	.	.	.	.	.	.	I
Artemisia vulgaris L.	.	.	h1	+	.	.	.	.	.	.	.	.	.	.	.	.	I
Artemisia lercheana Weber ex Stechm.	.	.	.	.	.	.	.	.	.	.	.	.	.	.	h1	2	I
Sonchus arvensis L.	.	.	.	.	.	.	.	.	.	.	h1	1	.	.	.	.	I
Cichorium intybus C. Presl Arcang.	.	.	.	.	.	.	.	.	.	.	h1	1	.	.	h1	1	II
Lactuca tatarica (L.) C.A. Mey.	.	.	.	.	.	.	.	.	.	.	h1	+	.	.	.	.	I
Tripleurospermum inodorum (L.) Sch. Bip.	.	.	.	.	.	.	.	.	.	.	h1	2	.	.	h1	1	II
Arctium lappa L.	.	.	.	.	.	.	.	.	.	.	h1	1	.	.	.	.	I
Pulicaria vulgaris Gaertn.	.	.	.	.	.	.	.	.	.	.	h1	+	.	.	.	.	I
Taraxacum officinale F.H. Wigg.	.	.	.	.	.	.	.	.	.	.	h1	1	.	.	.	.	I
Achillea millefolium L.	.	.	h1	+	.	.	.	.	.	.	.	.	.	.	.	.	I
Conyza canadensis (L.) Cronquist	.	.	.	.	h1	1	.	.	.	.	.	.	.	.	.	.	I
Lactuca tatarica (L.) C.A. Mey.	.	.	.	.	h1	+	.	.	.	.	.	.	.	.	.	.	I
Lactuca serriola L.	.	.	.	.	.	.	h1	r	.	.	.	.	.	.	.	.	I
Centaurea scabiosa L.	.	.	.	.	.	.	.	.	.	.	.	.	.	.	h1	1	I
Hieracium echioides (Lumn.) F.W. Schultz & Sch. Bip.	.	.	.	.	.	.	h1	r	.	.	.	.	.	.	.	.	I

Note: t1 – first tree layer (upper tree canopy), s1 – shrub layer,ss1 – subshrub layer, h1 – herbaceous layer.Constancy classes (%):I – 1-20 %, II – 21-40 %, III – 41–60 %, IV – 61–80 %,V – 81–100 %. Species abundance according to the Braun-Blanquet scale: r – solitary individuals, negligible cover – few individuals, cover < 1 % 1 – numerous individuals, but cover 1–5 %, 2 – 6-25 % , 3 – 26–50 %, 4 – 51–75 %, 5 – 76–100 %

Tree layer (t1). Dominated by species of the family Salicaceae, primarily *Populus alba*, *Populus nigra*, and *Populus canescens*; less frequently *Populus tremula* and *Salix alba*. The average height of the tree stand ranges from 12.5 to 22 m, indicating mature and middle-aged plantations.

Shrub and subshrub layers (s1, ss1). Developed unevenly. The most common species include Rubus caesius, *Prunus spinosa*, *Euonymus verrucosus*, as well as halophytic and xerophytic subshrubs such as *Artemisia marschalliana* and *Atriplex cana*.

Herb layer (h1). Characterized by high floristic diversity and plays a key role in forming the total projective cover. Total projective cover varies from 40 to 75%, reflecting differences in community closure, moisture, and light conditions.

The number of species in the communities ranges from 16 to 30, which is typical for floodplain and transitional ecosystems. The highest species richness was recorded in communities involving *Populus tremula* and *Aegopodium podagraria*, where favorable mesophytic conditions are formed.

In the herb layer, representatives of the following families dominate: Poaceae: *Bromopsis inermis, Calamagrostis epigeios, Poa pratensis; Asteraceae: Inula britannica, Artemisia vulgaris, Achillea millefolium*; Fabaceae: *Glycyrrhiza glabra, Melilotus albus, Medicago falcata;* Cyperaceae*: Carex vulpina, Carex acuta.*

The presence of Fabaceae species indicates increased soil trophicity and their capacity for biological nitrogen fixation.

Ecological and phytocoenotic interpretation based on the constancy scale shows that most species belong to class I (1–33%), reflecting the high dynamism and mosaic structure of the vegetation cover (Golovanov et al., 2025). Species of constancy class III (*Populus alba*, *Populus nigra*, *Salix alba*) form the coenotic core of the communities and determine their physiognomic appearance.

The first population was identified in the Terekti District, within the Chagan Forestry, compartment №4 (GPS: N 51°19.758′, E 051°54.208′), at an elevation of 5 m above sea level. Geographically, this population is confined to a ravine-gully system originating from the Pre-Ural Plateau and transitioning into the central floodplain. The microclimatic conditions of forests with *Populus canescens* create favorable conditions for its growth on alluvial-meadow soils (GBIF Backbone Taxonomy, 2026).

The plant community of the first population is represented by a mixed tree – shrub – herb phytocoenosis. The most widespread formations are: *Populus canescens – Convallaria majalis*, *Populus alba – Carex vulpina*, *Populus nigra – Rubus caesius*.

The tree layer is formed by *Populus canescens, Populus tremula, Fraxinus Americana* and *Ulmus laevis.*

The understory (second layer) includes shrub species such as *Rhamnus cathartica*, *Rosa cinnamomea* and *Prunus spinosa*.

The third layer is formed by the subshrub *Rubus caesius*.

The herbaceous cover (fourth layer) is distinguished by high species diversity and includes *Festuca ovina, Lathyrus tuberosus, Convallaria majalis, Aristolochia clematitis, Carex vulpina, Artemisia vulgaris, Chelidonium majus, Veronica longifolia, Medicago falcata*, *Trifolium montanum, Cichorium intybus, Euphorbia seguieriana, Bromus inermis, Conyza canadensis, Elytrigia repens* and other species.

The phytocoenosis is characterized by pronounced vertical stratification and high heterogeneity of the herb layer, which is typical of floodplain forest ecosystems with well-developed microrelief and optimal moisture conditions.

The floristic composition of the herb layer shows considerable taxonomic diversity. The largest number of species belongs to the family Asteraceae – 8 species 14.5%. The second position in terms of species richness is occupied by Fabaceae – 5 species 11.9%. The third place belongs to Poaceae, represented by 4 species 7.2%.

Several families are represented by single species, including Aristolochiaceae, Cyperaceae, Papaveraceae, Convallariaceae, Euphorbiaceae, Polygonaceae, Ranunculaceae, and Scrophulariaceae.

Overall, within the central floodplain, the first population includes 55 species of vascular plants belonging to 20 families and 41 genera, indicating high floristic richness of the studied phytocoenosis.

In the flora of the investigated community, 11 geographical elements were identified (Table 2).

Figure 3
Association of the central floodplain
Populus × canescens – Convallaria majalis, April, 2025

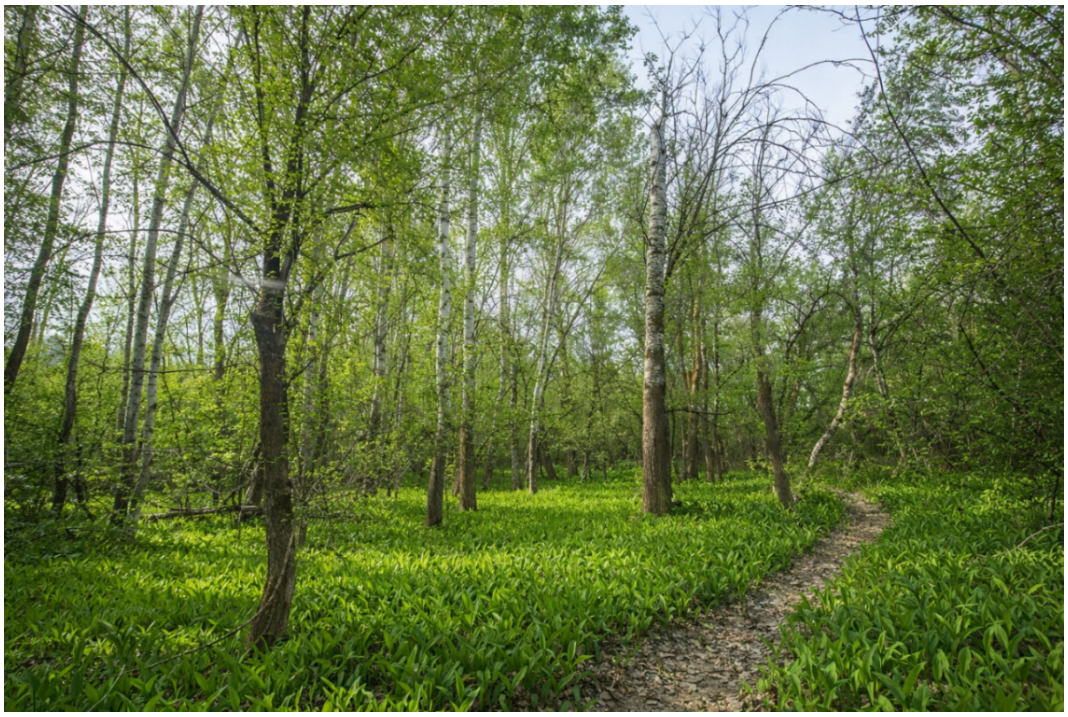

Table 2
Distribution of plant species by geographical ranges for the first population

Range group	Floral elements	Number of species	% of the total number
Boreal forest		40	72.7
	Eurasian	11	20.3
	Euro-Siberian	8	14.8
	European	9	16.6
	Holarctic	5	9
	East European	1	1.8
Steppe		11	20.3
	Pontic	3	5.5
	Ancient Mediterranean	3	5.5
	Mediterranean	4	7.2
	Pontic–Trans-Volga–Kazakhstan	1	1.8
Adventive ruderal (Pluriregional)		4	7.4
	North American	4	7.4
Total		**55**	**100**

Among the geographical elements of the first population, Eurasian species predominate (11 species; 20.3%), including *Prunus spinosa*, *Rhamnus cathartica*, *Rosa cinnamomea*, and *Bromopsis inermis*. The Euro-Siberian element comprises 8 species (14.8%); *Rubus caesius*, *Chelidonium majus*, *Festuca valesiaca*. The Holarctic element (5 species; 9%) includes *Bidens tripartita*, *Artemisia vulgaris*, and *Cichorium intybus*. These groups belong to the Boreal chorological group.

The Mediterranean element (4 species; 7.2%) includes *Populus alba* and *Convallaria majalis*, while the Ancient Mediterranean element (3 species; 5.5%) is represented by *Medicago falcata* and *Lactuca tatarica*. The Pontic element (3 species; 5.5%) includes *Euphorbia seguieriana* and *Polygonum aviculare*. Steppe species account for 11 species (20.3%) and are well developed along forest edges.

Weedy or adventive species are few (4 species; 7.4%), including *Fraxinus americana*, *Conyza canadensis*, and *Acer negundo*.

In the second population, the studied phytocoenosis is represented by a ravine deciduous forest of the forest-steppe zone, confined to the bottoms and slopes of gullies. The community develops under conditions of increased moisture and a moderated

microclimate typical of depressed relief forms. The vegetation cover belongs to the association *Populus tremula – Aegopodium podagraria* and is located at 51°21.238′ N, 51°56.512′ E, at an absolute elevation of 41 m above sea level.

Within this phytocoenosis, 30 species of vascular plants were recorded, belonging to the division *Magnoliophyta* (angiosperms), represented by two classes – *Magnoliopsida* (dicotyledons) and *Liliopsida* (monocotyledons). Dicotyledonous plants predominate, which is typical of ravine forest communities of the forest-steppe zone.

The flora of the phytocoenosis includes 14 families and 27 genera, indicating relatively high taxonomic diversity and stability of the vegetation cover under dissected relief and increased moisture conditions.

The most represented families are: Rosaceae – 6 species (20%): *Cerasus fruticosa*, *Spiraea hypericifolia*, *Amygdalus nana*, *Rosa canina*, *Crataegus ambigua*, *Fragaria vesca*, Asteraceae – 4 species (13.3%): *Inula helenium*, *Hieracium echioides*, *Lactuca serriola*, *Arctium lappa*, Poaceae – 3 species (10%): *Bromopsis inermis*, *Poa pratensis*, *Melica altissima*, Apiaceae – 2 species (6.6%): *Sium latifolium*, *Aegopodium podagraria*; Salicaceae – 2 species (6.6%): *Populus tremula*, *Populus alba*.

The tree layer is composed of deciduous species, with an average tree height of about 12,5 m. The dominant species is *Populus tremula*, forming the basis of the association. The layer also includes *Populus alba*, *Fraxinus americana*, *Acer negundo*, and *Betula pendula*. The canopy closure is moderate, allowing sufficient light penetration to the lower layers.

The shrub layer is well developed but heterogeneous. It is mainly represented by species of the family Rosaceae and steppe elements: *Cerasus fruticosa*, *Spiraea hypericifolia*, *Amygdalus nana*, *Rosa canina*, *Crataegus ambigua*, as well as *Lonicera tatarica*. Shrubs form a sparse understory, especially pronounced on gully slopes and forest edges.

The herbaceous layer is the richest in species composition and exhibits a mosaic structure. The dominant species is *Aegopodium podagraria*, forming a dense ground cover. Grasses and sedges (*Bromopsis inermis*, *Poa pratensis*, *Carex melanostachya*) are widely represented, along with forest, meadow and edge forbs (*Convallaria majalis*, *Galium boreale*, *Inula helenium*, *Fragaria vesca*). The presence of ruderal and adventive species indicates moderate anthropogenic impact.

A total of 30 species of vascular plants belonging to various floristic–geographical elements were identified within the phytocoenosis.

Analysis of the distribution of species by range groups makes it possible to assess the origin of the flora and the ecological specificity of the community (Table 3).

Figure 4
Ravine forest phytocoenoses of Populus tremula, June, 2025

Table 3
Distribution of plants by geographical ranges in the second population

Range group	Floral elements	Number of species	% of the total number
Boreal forest		20	66.6
	Eurasian	8	26.6
	Euro-Siberian	5	16.6
	European	2	6.6
	Holarctic	5	16.6
Steppe		8	26.6
	Pontic	5	16.6
	Mediterranean	2	6.6
	Lower Volga	1	3.3
Adventive ruderal (Pluriregional)		2	6.6
	North American	1	3.3
	Canada	1	3.3
Total		**30**	**100**

The boreal forest geo-element is the most widely represented, comprising 20 species (66.6% of the total flora). Within this group, the following are distinguished: Eurasian elements 8 species (26.6%): *Populus tremula*, *Bromopsis inermis*, *Carex melanostachya*, *Melica altissima*, *Rosa canina*, *Galium boreale*, Euro-Siberian elements 5 species (16.6%): *Sium latifolium*, *Inula helenium*, *Betula pendula*, *Aegopodium podagraria*, Holarctic elements 5 species (16.6%): *Poa pratensis*, *Arctium lappa*, *Fragaria vesca*, European elements 2 species (6.6%): *Convallaria majalis*, *Leonurus cardiaca*.

The high proportion of boreal species indicates the forest character of the phytocoenosis and its connection with moderately moist growing conditions typical of ravine forests.The steppe geo-element is represented by 8 species (26.6% of the flora), including:Pontic species 5 (16.6%): *Cerasus fruticosa*, *Spiraea hypericifolia*, *Amygdalus nana*, *Hieracium echioides*, *Cytisus borysthenicus*, Mediterranean species; 2 (6.6%): *Lactuca serriola*, *Populus alba*;Lower Volga element; 1 (3.3%): *Crataegus ambigua*.The significant share of steppe and Pontic species reflects the ecotonal character of ravine forests formed within the forest-steppe zone and influenced by adjacent steppe communities.The adventive (pluriregional) ruderal group includes 2 species (6.6%) North American element – *Acer negundo* (3.3%), Canadian element – *Fraxinus americana* (3.3%).

The presence of adventive species indicates anthropogenic influence and a certain degree of transformation of the natural vegetation cover.

Thus, the chorological analysis shows that the flora of the *Populus tremula – Aegopodium podagraria* phytocoenosis is characterized by dominance of boreal forest geo-elements significant participation of steppe and Pontic species, presence of adventive elements.

This confirms the forest-steppe, ecotonal nature of the ravine forest formed at the junction of forest and steppe floristic complexes, under moderate anthropogenic influence.

The first and second populations are confined to the North Caspian region, within the physical-geographical province of the Koshim-Zhaiyk steppe district of the Caspian – Turanian country. This territory covers the steppe zone of the upper course of the Zhaiyk River.

The boreal forest geo-element is the most widely represented and includes 20 species, accounting for 66.6% of the total number of species. Within this group the following elements predominate: Eurasian elements – 8 species (26.6%): *Populus tremula*, *Bromopsis inermis*, *Carex melanostachya*, *Melica altissima*, *Rosa canina*, *Galium boreale*. Euro-Siberian elements 5 species (16.6%) – *Sium latifolium*, *Inula helenium*, *Betula pendula*, *Aegopodium podagraria*, *Sium latifolium*. Holarctic elements 5 species (16.6%): *Poa pratensis*, *Arctium lappa*, *Fragaria vesca*. European elements 2 species (6.6%): *Convallaria majalis*, *Leonurus cardiaca*.

The high proportion of boreal species indicates the forest character of the phytocoenosis and its association with moderately humid growing conditions typical of ravine forests.

The steppe geo-element is represented by 8 species, which corresponds to 26.6% of the flora. The following elements are distinguished within it: Pontic species 5 (16.6%) – *Cerasus fruticosa*, *Spiraea hypericifolia*, *Amygdalus nana*, *Hieracium echioides*, *Cytisus borysthenicus*. Mediterranean species – 2 (6.6%): *Lactuca serriola*, *Populus alba*. Lower Volga element – 1 (3.3%): *Crataegus ambigua*.

The third population was identified at the boundary of the semi-desert zone, near the village of Bogatsk (GPS: N 50°39.282′, E 051°08.578′), in compartment No. 49 of the Ural Forestry. At an elevation of 46 m above sea level, forest formations involving *Populus alba* and *Populus nigra* were studied under conditions of the central floodplain.

The third population is located in the Zhayik River valley and belongs to the semi-desert arid

zone extending for approximately 200 km. Annual precipitation is relatively low (210 – 260 mm), with most of it falling during the warm season and largely evaporating. In winter, snow cover does not exceed 20 – 30 cm, strong winds redistribute snow, causing its accumulation in depressions. This results in insufficient spring soil moisture, leading to changes in vegetation cover.

Within the third population, the dominant community types are: *Populus alba – Aristolochia clematitis*, *Populus nigra – Glycyrrhiza glabra*.

The tree layer of the floodplain forest is formed by *Populus alba*, *Populus nigra*, *Salix alba*, *Acer negundo* and *Ulmus pumila*.

The shrub layer is represented by *Rhamnus cathartica*, *Elaeagnus commutata* and *Rosa cinnamomea*.

Over the past two years, spring flooding in the central floodplain lasting 45–50 days has promoted the active development of the herbaceous layer, which spreads intensively across the surface soil horizons. The most widespread species is *Glycyrrhiza glabra*, whose annual shoot length has doubled under these conditions.

Within the studied area of the central floodplain, the flora is represented by three range groups and comprises 10 geographical elements (Table 4).

Figure 5
Association of the semi-desert zone Populus alba – Glycyrrhiza glabra, June, 2025

Table 4
Distribution of plant species by geographical ranges for the third population

Range group	Floral elements	Number of species	% of the total number
Boreal forest		40	74
	Eurasian	14	25.9
	Euro-Siberian	5	9.2
	European	9	16.6
	Holarctic	12	22.2
	Boreal	1	1.8

Continuation of the table

Range group	Floral elements	Number of species	% of the total number
Steppe		11	21.8
	Pontic	4	7.4
	Ancient Mediterranean	5	9.2
	Mediterranean	2	3.6
Adventive ruderal (Pluriregional)		3	5.5
	American	1	1.8
	Pluriregional	2	3.6
Total		**54**	**100**

For the third population, the flora is distributed among the following geographical elements:

Boreal forest group Eurasian element (14 species; 25.9%): *Rhamnus cathartica*, *Inula salicina*, *Hylotelephium triphyllum*, *Thalictrum flavum*, *Bromopsis inermis*, *Eryngium planum*. Holarctic element (12 species; 22.2%): *Artemisia marschalliana*, *Artemisia prasina*, *Sonchus arvensis*, *Cichorium intybus*, *Polygonum aviculare*, *Persicaria amphibia*, *Silene vulgaris*. European element (9 species; 16.6%): *Ulmus laevis*, *Asparagus officinalis*, *Mentha aquatica*, *Tripleurospermum inodorum*, *Solanum dulcamara*, *Leonurus cardiaca*, *Salix alba*, *Iris pseudacorus*. Euro-Siberian element (5 species; 9.2%): *Gratiola officinalis*, *Euphorbia palustris*, *Senecio erucifolius*, *Rumex confertus*, *Veronica longifolia*.

Steppe group Ancient Mediterranean element (5 species; 9.2%): *Lactuca tatarica*, *Atriplex cana*, *Atriplex micrantha*, *Allium lineare*, *Glycyrrhiza glabra*.Pontic element (4 species; 7.4%): *Phlomoides tuberosa*, *Salvia pratensis*, *Limonium gmelinii*.Mediterranean element (2 species; 3.6%): *Plantago lanceolata*, *Populus alba*.

Adventive (ruderal) group Pluriregional elements: *Setaria glauca*, *Convolvulus arvensis*.American element (1 species; 1.8%): *Xanthium spinosum*.

The flora of the third population is diverse and includes 38 species belonging to 16 families and 25 genera. The dominant families are:Asteraceae – 13 species 26.5%; Fabaceae – 9 species 18.3%; Polygonaceae – 6 species 12.2%; Cyperaceae and Poaceae – 5 species each 10.2%; Salicaceae – 3 species 6.1%. Other families (*Scrophulariaceae*, *Lythraceae*, *Rhamnaceae*, *Elaeagnaceae*, *Solanaceae*) are represented by single species about 2% each.

The fourth population is located within a forest massif in the desert zone near the village of Taipak, at the extreme boundary of the middle course of the Ural River. The site is situated in compartment №10 (GPS: N 49°05.714′, E 051°56.493′), where *Populus nigra* and *Populus alba* occur. The absolute elevation of the territory is 6 m relative to sea level. Despite its proximity to the central floodplain, soils are predominantly clayey and loose sandy.

This population belongs to the desert zone. The main forest-forming phytocoenotic groups are represented by *Populus nigra – Melilotus albus* communities, and locally by small patches of *Populus alba – Rubus caesius*.

During the study, particular attention was drawn to the fact that following strong floods in recent years within the desert zone, in the central floodplain *Rubus caesius* began to grow together with representatives of the genus *Populus*. This indicates a noticeable expansion of the species' range and a possible shift in its ecological-coenotic preferences.

Such co-occurrence may also suggest restructuring of plant communities in floodplain areas of the desert zone, likely associated with changes in the hydrological regime and increased habitat moisture following flooding events.

The analysis of life forms revealed that perennial polycarpic plants predominate in the population – 34 species 89.4%. Perennial forest species are characterized by a long growing season and the ability to renew shoots annually.

Annual monocarpic plants account for 4 species 10.5% and include *Thlaspi arvense*, *Capsella bursa-pastoris, Silene dichotoma, Conyza canadensis,* and *Bidens tripartita* which grow in floodplain forests mainly during spring and summer.

In maintaining the stability of forest plant communities, the dominant role among herbaceous species is played by representatives of the following families: Poaceae – 4 species 10.2% – *Bromus inermis*, *Elytrigia repens*, *Festuca rubra*, *Calamagrostis epigeios*, Fabaceae – 4 species 10.2% – *Melilotus albus*, *Vicia cracca*, *Lathyrus pisiformis*, *Alhagi pseudalhagi*, Asteraceae – 8 species 20.5%: *Taraxacum officinale*, *Lactuca tatarica*, *Conyza canadensis*, *Bidens tripartita*, *Cichorium intybus*, *Artemisia vulgaris*, *Inula germanica*.

Representatives of Polygonaceae – 2 species 5.1% – *Rumex confertus*, *Polygonum aviculare* as well as single species from Scrophulariaceae – *Dodartia orientalis*, Cannabaceae – *Cannabis sativa*, Lamiaceae – *Marrubium vulgare* and Plantaginaceae – *Plantago media* were recorded, together accounting for approximately 2.5%.

In the shrub layer, unlike the first, second, and third populations, *Tamarix laxa* was recorded.

Within the desert zone, in comparison with the other studied populations, a dominance of steppe-type geographical ranges was established. As a result, 13 geographical elements characteristic of the region were identified within this territory (Table 5).

Figure 6
Community of the central floodplain in the desert zone Populus nigra – Melilotus albus, June, 2025

Table 5
Distribution of plant species by geographical ranges for the fourth population

Range group	Floral elements	Number of species	% of the total number
Boreal forest		21	55.2
	Eurasian	11	28.9
	Euro-Siberian	5	13.1
	European	3	7.8
	Holarctic	2	5.2
Steppe		13	34.2
	Pontic	1	2.6
	Ancient Mediterranean	8	21
	Mediterranean	1	2.6
	Asian	1	2.6
	Central Asian	1	2.6
	Caspian	1	2.6

Continuation of the table

Range group	Floral elements	Number of species	% of the total number
		4	10.5
Adventive ruderal (Pluriregional)	North American	2	5.2
	American	1	2.6
	Pluriregional	1	2.6
Total		**38**	**100**

Within the flora of the fourth population, the boreal forest group of ranges is dominated by Eurasian species – 11 species (28.9%), including *Populus nigra*, *Carex acuta*, *Carex melanostachya*, *Glycyrrhiza aspera* and *Melilotus albus*. The Euro-Siberian element comprises 5 species 13.1%, such as *Rubus caesius*, *Centaurea scabiosa*, *Linaria vulgaris* and *Rumex confertus*. European elements account for 3 species 7.8% – *Salix alba*, *Leonurus cardiaca*, *Stachys palustris*, *Lotus corniculatus*. The Holarctic element includes 2 species 5.2%: *Polygonum aviculare* and *Sonchus arvensis.*

In the steppe group of ranges, the most significant is the Ancient Mediterranean element, represented by 8 species 21%*: Eremopyrum orientale, Allium lineare, Glycyrrhiza glabra, Medicago falcata, Alhagi pseudalhagi, Atriplex cana, Bassia prostrata, Tamarix ramosissima.* Other range elements are represented by single species: Asian element – *Cannabis sativa* (1 species; 2.6%*);* Mediterranean element – *Populus alba* (1 species; 2.6%), Central Asian element – *Dodartia orientalis* (1 species; 2.6%), Caspian element – *Artemisia lercheana* (1 species; 2.6%).

The adventive ruderal group includes species of various origins: North American element – 2 species (5.2%): *Acer negundo*, *Elaeagnus commutata*;American element – *Xanthium spinosum* (1 species; 2.6%), Pluriregional element – *Convolvulus arvensis* (1 species; 2.6%). Overall, the territory where the fourth population is located belongs to the Saharo – Gobian floristic region, the Irano – Turanian subregion, the North Turanian province and the Caspian lowland subprovince. This is confirmed by the predominance of steppe and Ancient Mediterranean floristic elements within the flora.

According to Darbaeva & Chukalina (2011), communities dominated by *Populus nigra* and *Populus alba* prevailed in the floodplain poplar forests of the middle reaches of the Zhaiyk River; however, their floristic composition was presented in a generalized form, without differentiation by natural zone. The present study, based on 26 geobotanical relevés conducted along a gradient from steppe to desert, documents changes that have occurred in these communities: an expansion of the ecological – coenotic amplitude of several species – in particular, *Rubus caesius* and *Melilotus albus* – previoussly unrecorded in the desert zone, as well as intensified development of *Glycyrrhiza glabra* in the semi-desert zone under the influence of increased spring flood events in recent years. The obtained data thus reflect the dynamics of floristic composition against the backdrop of shifting hydrological conditions.

The influence of latitudinal zonation on the species composition of phytocoenoses is analyzed in detail in the chorological section of the present study. It was established that from north to south – from the steppe to the desert zone – the proportion of boreal-forest floristic elements consistently decreases: from 72.7% in the first population (steppe zone) to 55.2% in the fourth population (desert zone). Concurrently, the share of steppe and Ancient Mediterranean elements increases from 20.3% to 34.2%. Species absent from northern populations – including *Tamarix ramosissima*, *Bassia prostrata*, *Alhagi pseudalhagi*, *Dodartia orientalis* and *Artemisia lercheana* – were recorded exclusively in the desert zone. These findings confirm the ecotonal character of the region's floodplain forests, which develop at the interface of boreal and arid floristic complexes.

Comparison with Russian data was conducted with reference to studies carried out in adjacent territories. The closest floristic analogues are the floodplain poplar forests of the Ural River valley on the Russian side (Orenburg Region), described by Chibilev et al. (2023), as well as investigations of the chalk uplands of the Sub-Ural region Golovanov & Yamalov (2025). The chorological structure of the flora of the Zhaiyk floodplain communities is broadly consistent with data reported for the Russian sector of the basin, with Eurasian and Holarctic elements of the boreal group predominating and a substantial contribution of Pontic and Ancient Mediterranean species. At the same time, the Kazakhstani sector is distinguished by a markedly higher proportion of arid

floristic elements – Caspian, Central Asian, and Irano -Turanian – reflecting the more pronounced aridization of the climate in the southward direction and underscoring the significance of the studied communities as refugia of boreal flora within an arid landscape matrix.

Conclusion

As a result of the comprehensive ecological-phytocoenotic and floristic study of the floodplain and ravine forests of the Zhaiyk River within the western region Kazakhstan, four populations of the genus *Populus* L. were identified and characterized, represented by the species *Populus alba, Populus nigra, Populus tremula, and Populus canescens*. The studied populations are distributed along a latitudinal gradient of natural zones – from steppe to desert – which determines significant differences in their floristic composition, phytocoenotic structure, and ecological growing conditions.

Based on 26 geobotanical relevés, eight plant associations were distinguished: *Populus canescens – Convallaria majalis*, *Populus alba – Carex vulpina*, *Populus nigra – Rubus caesius*, *Populus tremula – Aegopodium podagraria*, *Populus alba – Glycyrrhiza glabra*, *Populus nigra – Bromopsis inermis*, *Populus nigra – Melilotus albus*, *Populus nigra – Pseudosophora alopecuroides*.

The phytocoenoses are characterized by pronounced vertical stratification, high floristic diversity, and a mosaic vegetation structure. The total number of vascular plant species in individual communities ranges from 16 to 55.

Chorological analysis showed that boreal forest floristic elements (Eurasian, Euro-Siberian, European, and Holarctic) dominate in all four populations. At the same time, a clear geographical pattern was revealed: from north to south – from the steppe to the desert zone – the proportion of boreal species consistently decreases (from 72.7% in the first population to 55.2% in the fourth), whereas the share of steppe and Ancient Mediterranean elements increases (from 20.3% to 34.2%). This confirms the ecotonal character of the region's floodplain forests, formed at the junction of boreal and arid floristic complexes.

In the desert zone, an expansion of the ecological–coenotic amplitude of several species was recorded under the influence of changes in the hydrological regime. In particular, following strong floods in recent years, *Rubus caesius* began to spread within the central floodplain together with representatives of the genus *Populus*, indicating restructuring of plant community structure. The significant development of *Glycyrrhiza glabra* in the semi-desert zone also points to increased spring moisture in floodplain habitats.

It should also be noted that *Melilotus albus* was newly recorded in the desert zone after the passage of floodwaters. This finding may indicate an expansion of the species' ecological amplitude and its capacity to colonize extreme environments.

The obtained data substantially supplement existing knowledge on the structure, floristic composition, and geographical distribution of poplar forests in Western Kazakhstan

Author contributions

Raiymbek K. Anatoliy – Conceptualization, Writing – Original Draft

Meruyert S. Kurmanbayeva – Supervision, Funding Acquisition.

Talshen E. Darbayeva – Writing – Review & Editing, Methodology

Adil B. Kusmangazinov – Data Curation, Investigation

Dina E. Karabalayeva – Writing – Original Draft, Formal Analysis

Almagul R. Aldibekova – Data Curation

Gábor Sramkó – Supervision, Methodology

Conflict of interest

All authors are aware of the article's content and declare no conflict of interest.

References

1. Anatoliy, R., Kurmanbaeva, M., & Karabalaeva, D. (2025). Evolutionary development of the genus *Populus* L. (Salicaceae Mirb.) in western Kazakhstan. *Experimental Biology, 104*(3), 44–58. (In Russian). https://doi.org/10.26577/bb202510434

2. Akzhigitova, N., Brekle, Z., Volkova, E., Winkler, G., Vukhrer, B., Ogar, Ya., & Kurochkina, L. (2003). *Botanical geography of Kazakhstan and Central Asia*. (In Russian).

3. Chekalin, S., & Fartushina, M. (2014). Soil fertility and the main ways of its regulation. *Bulletin of the Orenburg State Agrarian University, 3*(1), 14–17. (In Russian).

4. Chibilev, A., Ramazanov, S., Grudinin, D., & Padalko, Yu. (2023). On the conservation of natural heritage sites of the Burlin-Terekty left bank of the Ural River in the West Kazakhstan region. *Issues of Steppe Studies, 4*, 4–13. (In Russian). https://doi.org/10.24412/2712-8628-2023-4-4-13

5. Darbaeva, T., & Chukalina, O. (2011). Current state of poplar forests in the middle reaches of the Ural within the West Kazakhstan region. *Engineering Technologies and Systems, 4*, 128–133. (In Russian).

6. Ermakov, N., & Martynenko, V. (2022). Higher units of dark coniferous forests of the eastern part of Europe, the Southern Urals and Western Siberia in the Braun-Blanquet system. *Vegetation of Russia, 44*, 76–96. (In Russian). https://doi.org/10.31111/vegrus/2022.44.76

7. GBIF Backbone Taxonomy. (2026). *Global Biodiversity Information Facility dataset*. https://doi.org/10.15468/ab3s5x

8. Golovanov, Y., & Yamalov, S. (2025). Features of the flora of chalk uplands of the Sub-Ural and adjacent territories. *Arid Ecosystems, 15*(1), 58–68. (In Russian). https://doi.org/10.31111/vegrus/2025.51.3

9. Kamelin, R. (2012). Floristic zoning of land: new solutions to some problems. *Botanical Journal, 97*(12), 1481–1488. (In Russian).

10. Khlyustov, V., Elekesheva, M., Izteleu, T., Baysynova, A., & Nuradinova, N. (2019). Growth and productivity of forest elements in the basins of the Ural River. *Agrarian Scientific Journal, 1*, 32–38. (In Russian).

11. Klimov, A., & Proshkin, B. (2024). Origin and evolution of the genus *Populus* L. (family Salicaceae). *Social and Ecological Technologies, 14*(2), 205–238. (In Russian). https://doi.org/10.31862/2500-2961-2024-14-2-205-238

12. Lavrenko, E. (1970). Provincial division of the Black Sea-Kazakhstan subregion of the steppe region of Eurasia. *Botanical Journal, 55*(5), 609–625. (In Russian).

13. Lavrenko, E., Karamysheva, Z., & Nikulina, R. (1991). *Steppes of Eurasia*. (In Russian).

14. Martynenko, V., Shirokikh, P., Muldashev, A., & Solomeshch A. (2008). On the new association of steppe oak forests on the South Urals. *Vegetation of Russia, 2*(13), 49–60. (In Russian). https://doi.org/10.31111/vegrus/2008.13.49

15. Mirkin, B., Naumova, L., Martynenko, V., & Shirokih, P. (2015). Contribution of syntaxonomy based on the Braun-Blanquet approach to the study of plant community successions. *Ecology, 4*(4), 153–243. (In Russian). https://doi.org/10.7868/S0367059715040137

16. Novikov, V., Tikhomirov, V., Gubanov, I., & Kiseleva, K. (2018). *Illustrated key to plants of central Russia* (Vol. 3). (In Russian).

17. Pavlov, N. V. (Ed.). (1960). *Flora of Kazakhstan* (Vol. 3). Academy of Sciences of the KazSSR. (In Russian).

18. Petrenko, A., Dzhubanov, A., Fartushina, M., Irkalieva, M., Ramazanov, S., Sdykov, M., & Chernyshev, D. (1998). *Natural resource potential and planned objects of the protected area of the West Kazakhstan region*. ZKSU. (In Russian).

19. Plantarium. (2025). *Plants and lichens of Russia and neighboring countries: Open online galleries and key to species*. https://www.plantarium.ru/

20. Safronova, I. (2002). Phytoecological mapping of the Northern Caspian region. *Geobotanical Mapping, 44*, 44–65. (In Russian).

21. The International Plant Names Index and World Checklist of Vascular Plants. (2025). http://www.ipni.org and https://powo.science.kew.org/

22. Theurillat, J., Willner, W., Fernández-González, F., Bültmann, H., Čarni, A., Gigante, D., & Weber, H. (2021). International code of phytosociological nomenclature. *Applied Vegetation Science, 24*(1), 125–164. https://doi.org/10.1111/avsc.12491

23. Viktorov, S. (1951). Vegetation as an indicator of lithological conditions in the Northern Ustyurt and the West Kazakhstan steppes. *Bulletin of the Moscow Society of Naturalists, Biological Section, 1*(1), 81–85. (In Russian).

Information about the authors:

Raiymbek K. Anatoliy – Master of Pedagogical Sciences, PhD student, Al-Farabi Kazakh National University (Almaty, Kazakhstan, e-mail:anatoliy_raiymbek@live.kaznu.kz).

Meruyert S. Kurmanbayeva – Doctor of Biological Sciences, Professor, Al-Farabi Kazakh National University (Almaty, Kazakhstan, e-mail: Meruyert.Kurmanbayeva@kaznu.edu.kz).

Talshen E. Darbayeva – Doctor of Biological Sciences, Professor, Makhambet Utemisov West Kazakhstan University (Uralsk, Kazakhstan, email: dtalshen@mail.ru).

Adil B. Kusmangazinov – PhD, Al-Farabi Kazakh National University (Almaty, Kazakhstan, e-mail: adil_06.1996@mail.ru).

Dina E. Karabalayeva – Master of Engineering and Technology,Al-Farabi Kazakh National University (Almaty, Kazakhstan, e-mail: dina.20.1996@mail.ru).

Almagul R. Aldibekova – PhD, Al-Farabi Kazakh National University (Almaty, Kazakhstan, e-mail: alma_rakhat@mail.ru).

Gábor Sramkó – PhD, University of Debrecen MTA–ELTE–MTM Ecology Research Group (Budapest, Hungary, e-mail: sramko.gabor@science.unideb.hu).

Received 10 March 2026;
received in revised form 23 June 2026;
accepted 26 June 2026

IRSTI 34.45.21; 31.21.27 https://doi.org/10.26577/IJBCh20261918

A.S. Sokolenko[1,2], A.B. Kaldybayeva[2,3*], L.K. Baktybaeva[2], G. Deniz[4], V.K. Yu[3]

[1]Abai Kazakh National Pedagogical University, Almaty, Kazakhstan
[2]Al-Farabi Kazakh National University, Almaty, Kazakhstan
[3]A.B. Bekturov Institute of Chemical Sciences, Almaty, Kazakhstan
[4]Istanbul University, Istanbul, Turkey
[*]e-mail: altin_28.94@mail.ru

SYNTHESIS AND HEMATOPOIESIS-STIMULATING ACTIVITY OF NEW IMIDAZOLYL-CONTAINING PHOSPHONATE INCLUSION COMPLEXES

Abstract: A series of novel imidazole-containing α-aminophosponate derivatives were synthesized based on 1-(3-aminopropyl)imidazole using the absolute benzene under the one-pot, three-component Kabachnik–Fields reaction. The hematopoiesis-stimulating activity was evaluated for the compounds 7βCD-12βCD. The structure of the obtained compounds was confirmed using nuclear magnetic resonance (NMR) spectroscopy, infrared spectroscopy (IR), and elemental analysis. All tested compounds were β-cyclodextrin inclusion complexes of dialkyl(3-(1*H*-imidazol-1-yl)propylamino)(fluoro- and trifluoromethylphenyl) methyl)phosphonates to enhance aqueous solubility, improve bioavailability, and modulate the pharmacokinetic profile of the phosphonates. Among the tested derivatives, compounds 7βCD, 8βCD, 10βCD, and 11βCD exhibited low hematopoiesis-stimulating activity, whereas 9βCD and 12βCD demonstrated a moderate stimulatory effect on leukopoiesis. Biological evalution in a cyclophosphamide-induced pancytopenia model revealed that several complexes exhibit hematopoietic properties. Notably, 9βCD and 12βCD moderately stimulated leukopoiesis at a level comparable to methyluracil, significantly restoring the total leukocyte and lymphocyte counts and normalizing the Harkavy index. Despite their positive effects on leukopoiesis, compounds 9βCD and 12βCD showed limited influence on erythropoiesis and thrombopoiesis. In contrast, other derivatives (7βCD, 8βCD, 11βCD) did not exhibit stimulatory activity and, in some cases, even suppressed hematopoietic parameters. Taken together, these findings indicate that complexes of β-cyclodextrin with imidazole-containing α-aminophosphonates – particularly the complex of dimethyl(((3-(1*H*-imidazol-1-yl)propyl)amino)(4-fluorophenyl)methyl)phosphonate with β-cyclodextrin (9βCD) and complex of dimethyl ((3-(1*H*-imidazol-1-yl)propylamino)(4-(trifluoromethylphenyl)-methyl) phosphonate with β-cyclodextrin (12βCD) – represent promising scaffolds for the development of novel modulators of hematopoiesis. The observed biological activity may be associated with the presence of electron-withdrawing substituents (fluoro- and trifluoromethyl groups) and the imidazole fragment, which can contribute to intermolecular interactions with biological targets and participate in hydrogen bonding, facilitating binding to enzyme active sites, while the phosphonate moiety provides enhanced metabolic stability. Overall, these holdings suggest the potential of certain phosphonate derivatives, particularly 9βCD and 12βCD, as possible candidates for the further development of immunomodulating agents.

Keywords: hematopoiesis-stimulating activity; phosphonate derivatives; β-cyclodextrin inclusion complexes of dialkyl ((3-(1*H*-imidazol-1-yl)propylamino) (fluoro- and trifluoromethylphenyl)methyl)phosphonate.

Introduction

The need for effective and safe immunomodulatory and leukopoiesis-stimulating agents remains one of the pressing challenges in modern pharmaceutical science. Disorders of hematopoiesis – whether caused by autoimmune diseases, chemotherapy, infections, or toxic exposures – often require pharmacological correction (El-Badry et al., 2025; Gholami et al., 2023; Regina et al., 2025; Strzelec et al., 2023; Zhang et al., 2025). The most common conditions associated with the acquired form of leukopoiesis deficiency, requir-

ing mandatory treatment for systemic infections, include: sepsis, purulent meningitis, etc.; chronic bronchitis with frequent relapses, concomitant with ENT conditions (purulent sinusitis, otitis media, lymphadenitis) resistant to standard treatments and with a history of pneumonia; recurrent pneumonia and bronchopleuropneumonia; bronchiectasis; chronic bacterial infections of the skin and subcutaneous tissue (pyoderma, furunculosis, abscesses, phlegmon, septic granuloma, recurrent paraproctitis in adults); chronic mycoses of the skin and mucous membranes, candidiasis, parasitic infections; recurrent aphthous stomatitis, concomitant with an increased incidence of acute viral respiratory infections. Recurrent herpesvirus infections of various sites; gastrointestinal conditions with chronic diarrhea of unknown etiology, intestinal dysbiosis; lymphadenopathy, recurrent lymphadenitis. Persistent low-grade fever and fever of unclear origin. However, the therapeutic options currently available to clinicians are limited (Bahrami et al., 2020; Cabañero-Navalon et al., 2024; Gubernatorova et al., 2021; Zaman & Toth, 2013).

Existing leukocytosis-inducing drugs include small molecules such as levamisole and high-molecular immunomodulators such as polyoxidonium (Gago et al., 2025; Ikeda et al., 2025; Tavakol et al., 2022; Wang et al., 2014). Despite their established clinical use, these agents possess significant limitations: a narrow activity spectrum, variable efficacy, adverse side effects, and limited applicability in long-term therapy. Therefore, the search for new low-toxicity compounds capable of safely stimulating hematopoiesis remains highly relevant.

Phosphonate derivatives represent a promising class of small molecules with significant immunotropic potential. Their unique chemical structure ensures high metabolic stability, resistance to enzymatic degradation, and strong binding interactions (Groaz & De Jonghe, 2021; Krečmerová et al., 2022). These features allow phosphonates to exhibit a wide range of biological activities, including anti-inflammatory, antitumor, and immunomodulatory effects. Structural modification of the phosphonate scaffold provides opportunities for targeted regulation of immune responses and the design of compounds with improved pharmacological profiles.

In aim of the present study to synthesize the dialkyl ((3-(1*H*-imidazol-1-yl)propylamino)(fluoro- and trifluoromethylphenyl)methyl)phosphonates and their inclusion complexes with β-cyclodextrin and evaluate their potential as myelostimulators to activation of hematopoiesis.

Materials and methods

All used chemicals (analytical grade) were purchased from Sigma Chemical Co. (Sigma-Aldrich Chemie Gmbh, Steinheim, Germany) and were used without further purification. These chemicals are as follows: benzene (C_6H_6≥98%), 1-(3-aminopropyl)imidazole ($C_6H_{11}N_3$≥97%), 2-fluorobenzaldehyde (FC_6H_4CHO≥97%), 3-fluorobenzaldehyde (FC_6H_4CHO≥97%), 4-fluorobenzaldehyde (FC_6H_4CHO≥97%), 2-(trifluoromethyl)benzaldehyde ($CF_3C_6H_4CHO$≥98%), 3-(trifluoromethyl)benzaldehyde ($CF_3C_6H_4CHO$≥98%), 4-(trifluoromethyl)benzaldehyde ($CF_3C_6H_4CHO$≥98%).

The course of the reaction and the purity of the compounds was monitored using TLC (by Al_2O_3, II degrees). Infrared spectra were recorded using a Nicolet 5700 spectrometer (Thermo Fisher Scientific, USA) on tablets containing potassium bromide that were sealed between potassium bromide plates. ^1H and ^{13}C nuclear magnetic resonance (NMR) spectra of the chemicals under study, dissolved in deuterated chloroform or dimethyl sulfoxide, were recorded using a JEOL JNM-ECA400 NMR spectrometer (JEOL Ltd, Japan) operating at 400 megahertz (MHz) for hydrogen nuclei. Tetramethylsilane (TMS) was used as an internal standard.

*Synthesis dimethyl (((3-(1H-imidazol-1-yl)propyl)amino)(2-fluorophenyl)methyl)-phosphonate (**1**).* A three-neck conical flask with a flat bottom and equipped with a Dean-Stark trap and reflux condenser was filled with 2.1 mL (0.018 mol of 1-(3-aminopropyl)imidazole and 185 mL of absolute benzene. Then 1.9 mL (0.018 mol) of 2-fluorobenzaldehyde and 1.7 mL (0.018 mol) of dimethyl phosphite were added successively. The reaction mixture is boiled with constant stirring for 63 h. After the reaction had completed, the solvent was removed and the resulting oily liquid was washed several times with hot hexane. This process yielded 3.71 grams of the desired product, dimethyl (((3-(1*H*-imidazol-1-yl)propyl) amino)(2-fluorophenyl)methyl)phosphonate, in the form of colorless crystals. Yield 3.71 g (62 %), R_f = 0.14 (hexane:chloroform – 1:3), Tm = 83-86 ^{0}C. $C_{15}H_{21}FN_3O_3P$, calculated, %: C 52.78; H 6.20; F 5.57; N 12.31; O 14.06; P 9.07. $C_{15}H_{21}FN_3O_3P$, found, %: C 52.76; H 6.17; F 5.59; N 12.34; P 9.05. IR spectra, cm^{-1}: 1044 (C-N); 1211 (P=O); 1044 (C-F). ^1H NMR (400 MHz, DMSO-d_6), δ, ppm: 2.19 (2H, m, J = 2.67 Hz, $NCH_2CH_2CH_2N$), 3.08-3.10, 3.85 (4H, t, J = 2.67 Hz, $NCH_2CH_2CH_2N$), 3.63 (6H, s, $POCH_3$), 4.72 (s, 1H, CH), 6.92-7.45 (3H, m, J = 3.40, 1.86, 1.15 Hz,

CH_{im}), 7.12-7.63 (4H, d, J = 7.84, 7.41, 1.52 Hz, J = 8.35, 1.52, 0.55 Hz, CH_{benz}). ^{13}C NMR (100 MHz, DMSO-d_6), δ, ppm: 26.55 ($NCH_2CH_2CH_2N$), 47.22-47.37 ($NCH_2CH_2CH_2N$), 53.51 ($POCH_3$), 58.37 (CH), 116.11-162.13 (CH_{benz}), 120.45-136.33 (CH_{im}).

*Synthesis of diethyl (((3-(1H-imidazol-1-yl)propyl)amino)(3-fluorophenyl)methyl)-phosphonate (**2**)* is carried out in a similar way. Yield 3.85 g (58 %), R_f = 0.19 (hexane:chloroform – 1:3), Tm = 40-43 ^{0}C. $C_{17}H_{25}FN_3O_3P$, calculated, %: C 55.28; H 6.82; F 5.14; N 11.38; O 12.99; P 8.39. $C_{17}H_{25}FN_3O_3P$, found, %: C 55.26; H 6.80; F 5.11, N 11.36; P 8.42. IR spectra, cm^{-1}: 1039 (C-N); 1238 (P=O); 1039 (C-F). ^1H NMR (400 MHz, DMSO-d_6), δ, ppm: 1.15 (6H, t, J = 7.02, 7.00 Hz, $POCH_2CH_3$), 2.19 (2H, m, J = 2.67 Hz, $NCH_2CH_2CH_2N$), 3.08-3.10, 3.85 (4H, t, 2.67 Hz, $NCH_2CH_2CH_2N$), 3.90-3.97 (6H, q, J = 7.02 Hz, $POCH_2CH_3$), 4.46 (1H, s, CH), 6.92-7.45 (3H, m, J = 3.40, 1.87 Hz, J = 3.40, 1.87 Hz, CH_{im}), 6.72-7.31 (4H, s, J = 8.09, 1.57, 1.25 Hz, J = 8.03, 1.25, 1.22 Hz, CH_{benz}). ^{13}C NMR (100 MHz, DMSO-d_6), δ, ppm: 16.45 ($POCH_2CH_3$), 26.55 ($NCH_2CH_2CH_2N$), 47.22-47.37 ($NCH_2CH_2CH_2N$), 60.59 (CH), 63.10 ($POCH_2CH_3$), 115.32-163.99 (CH_{benz}), 120.45-136.33 (CH_{im}).

*Synthesis of dimethyl (((3-(1H-imidazol-1-yl) propyl)amino)(4-fluorophenyl)methyl)-phosphonate (**3**)* is carried out in a similar way. Yield 2.25 g (38 %), R_f = 0.27 (hexane:chloroform – 1:3), n_D^{20}=1,526. $C_{15}H_{21}FN_3O_3P$, calculated, %: C 52.78; H 6.20; F 5.57; N 12.31; O 14.06; P 9.07. $C_{15}H_{21}FN_3O_3P$, found, %: C 52.81; H 6.18; F 5.55; N 12.34; P 9.10. IR spectra, cm^{-1}: 1054 (C-N); 1220 (P=O); 1054 (C-F). ^1H NMR (400 MHz, DMSO-d_6), δ, ppm: 2.19 (2H, m, J = 2.67 Hz, $NCH_2CH_2CH_2N$), 3.08-3.10, 3.85 (4H, t, J = 2.67 Hz, $NCH_2CH_2CH_2N$), 3.63 (s, 6H, $POCH_3$), 4.47 (s, 1H, CH), 6.92-7.45 (3H, m, J = 3.40, 1.86 Hz, J = 3.40, 1.15 Hz, CH_{im}), 7.19-7.34 (4H, s, J = 8.40, 1.18, 0.55 Hz, J = 8.40, 1.18, 0.55 Hz, CH_{benz}). ^{13}C NMR (100 MHz, DMSO-d_6), δ, ppm: 26.55 ($NCH_2CH_2CH_2N$), 47.22-47.37 ($NCH_2CH_2CH_2N$), 53.51 ($POCH_3$), 60.70 (CH), 115.48-163.81 (CH_{benz}), 120.45-136.33 (CH_{im}).

*Synthesis of dimethyl (((3-(1H-imidazol-1-yl) propyl)amino)(2-(trifluoromethyl)phenyl)methyl) phosphonate (**4**)* is carried out in a similar way. Yield 4.93 g (79 %), R_f = 0.32 (hexane:chloroform – 1:3), n_D^{20}=1,520. $C_{16}H_{21}F_3N_3O_3P$, calculated, %: C 49.11; H 5.41; F 14.56; N 10.74; P 7.92. $C_{16}H_{21}F_3N_3O_3P$, found, %: C 49.12; H 5.39; F 14.54, N 10.72; P 7.89. IR spectra, cm^{-1}: 1035 (C-N); 1166 (P=O); 1314 (C-F). ^1H NMR (400 MHz, $CDCl_3$), δ, ppm: 2.19 (2H, m, J = 2.67 Hz, $NCH_2CH_2CH_2N$), 3.08-3.10, 3.85 (4H, t, J = 2.67 Hz, $NCH_2CH_2CH_2N$), 3.63 (6H, s, $POCH_3$), 4.13 (1H, s, CH), 6.92-7.45 (3H, m, J = 3.40, 1.87 Hz, J = 3.40, 1.15 Hz, CH_{im}), 7.47-7.93 (4H, s, J = 7.91, 7.39, 1.93 Hz, J = 7.59, 7.39, 1.60 Hz, CH_{benz}). ^{13}C NMR (100 MHz, $CDCl_3$), δ, ppm: 26.55 ($NCH_2CH_2CH_2N$), 47.22-47.37 ($NCH_2CH_2CH_2N$), 53.51 ($POCH_3$), 58.51 (CH), 125.98-132.77 (CH_{benz}), 120.45-136.33 (CH_{im}).

*Synthesis of dimethyl (((3-(1H-imidazol-1-yl) propyl)amino)(3-(trifluoromethyl)phenyl)methyl) phosphonate (**5**)* is carried out in a similar way. Yield 5.1 g (82%), R_f = 0.27 (hexane:chloroform – 1:3), n_D^{20}=1,517. $C_{16}H_{21}F_3N_3O_3P$, calculated, %: C 49.11; H 5.41; F 14.56; N 10.74; P 7.92. $C_{16}H_{21}F_3N_3O_3P$, found, %: C 49.07; H 5.43; F 14.58; N 10.77; P 7.95. IR spectra, cm^{-1}: 1030 (C-N); 1166 (P=O); 1329 (C-F). ^1H NMR (400 MHz, $CDCl_3$), δ, ppm: 2.19 (2H, m, J = 2.67 Hz, $NCH_2CH_2CH_2N$), 3.08-3.10, 3.85 (4H, t, J = 2.67 Hz, $NCH_2CH_2CH_2N$), 3.63 (6H, s, $POCH_3$), 4.40 (1H, s, CH), 6.92-7.45 (3H, m, J = 3.40, 1.87 Hz, J = 3.40, 1.15 Hz, CH_{im}), 7.05-8.05 (4H, s, J = 7.71, 7.56, 0.45 Hz, J = 7.56, 1.52, 1.23 Hz, CH_{benz}). ^{13}C NMR (100 MHz, $CDCl_3$), δ, ppm: 26.55 ($NCH_2CH_2CH_2N$), 47.22-47.37 ($NCH_2CH_2CH_2N$), 53.51 ($POCH_3$), 62.25 (CH), 126.04-131.62 (CH_{benz}), 120.45-136.33 (CH_{im}).

*Synthesis of dimethyl (((3-(1H-imidazol-1-yl) propyl)amino)(4-(trifluoromethyl)phenyl)methyl) phosphonate (**6**)* is carried out in a similar way. Yield 5.68 g (91 %), R_f = 0.30 (hexane:chloroform – 1:3), n_D^{20}=1,517. $C_{16}H_{21}F_3N_3O_3P$, calculated, %: C 49.11; H 5.41; F 14.56; N 10.74; P 7.92. $C_{16}H_{21}F_3N_3O_3P$, found, %: C 49.08; H 5.40; F 14.59; N 10.76; P 7.90. IR spectra, cm^{-1}: 1038 (C-N); 1161 (P=O); 1314 (C-F). ^1H NMR (400 MHz, $CDCl_3$), δ, ppm: 2.19 (2H, m, J = 2.67 Hz, $NCH_2CH_2CH_2N$), 3.08-3.10, 3.85 (4H, t, J = 2.67 Hz, $NCH_2CH_2CH_2N$), 3.63 (6H, s, $POCH_3$), 4.47 (1H, s, CH), 6.92-7.45 (3H, m, J = 3.40, 1.87 Hz, J = 3.40, 1.15 Hz, CH_{im}), 7.61-7.72 (4H, s, J = 8.49, 1.92, 0.48 Hz, CH_{benz}). ^{13}C NMR (100 MHz, $CDCl_3$), δ, ppm: 26.55 ($NCH_2CH_2CH_2N$), 47.22-47.37 ($NCH_2CH_2CH_2N$), 53.51 ($POCH_3$), 60.70 (CH), 126.75-140.49 (CH_{benz}), 120.45-136.33 (CH_{im}).

*The complex of dimethyl (((3-(1H-imidazol-1-yl) propyl)amino)(2-fluorophenyl)methyl)-phosphonate with β-cyclodextrin (**7βCD**)*. Hot solutions of 0.4 g (0.001 mol) of dimethyl (((3-(1*H*-imidazol-1-yl)propyl)amino) (2-fluorophenyl) methyl) phosphonate (1) were mixed in 25 mL of ethyl alcohol and 1.13 g (0.001 mol) of β-cyclodextrin in 40 mL of distilled water. The mixture was placed in a drying chamber, and ethanol and water were evaporated at a temperature of 50-55 ^{0}C. Dimethyl (((3-(1*H*-imidazol-1-yl) propyl)amino) (2-fluorophenyl) methyl)phosphonate and β-cyclodextrin inclusion complex were obtained as a white powder. Yield 2.23 g (91 %).

$C_{57}H_{91}FN_3O_{38}P$, calculated, %: C 46.36; H 6.17; F 1.29; N 2.85; P 2.09. $C_{57}H_{91}FN_3O_{38}P$, found, %: C 46.39; H 6.19; F 1.32; N 2.87; P 2.06.

*The complex of diethyl (((3-(1H-imidazol-1-yl) propyl)amino)(3-fluorophenyl)methyl)-phosphonate with β-cyclodextrin (***8βCD***)* is carried out in a similar way. Yield 1.74 g (86 %). $C_{59}H_{95}FN_3O_{38}P$, calculated, %: C 47.09; H 6.32; F 1.26; N 2.79; P 2.06. $C_{59}H_{95}FN_3O_{38}P$, found, %: C 47.12; H 6.27; F 1.29; N 2.77; P 2.09.

*The complex of dimethyl (((3-(1H-imidazol-1-yl) propyl)amino)(4-fluorophenyl)methyl)-phosphonate with β-cyclodextrin (***9βCD***)* is carried out in a similar way. Yield 4.32 g (98 %). $C_{57}H_{91}FN_3O_{38}P$, calculated, %: C 46.36; H 6.17; F 1.29; N 2.85; P 2.09. $C_{57}H_{91}FN_3O_{38}P$, found, %: C 46.33; H 6.21; F 1.31; N 2.84; P 2.07.

*The complex of dimethyl (((3-(1H-imidazol-1-yl)propyl)amino)(2-(trifluoromethyl)phenyl)) methyl)phosphonate with β-cyclodextrin (***10βCD***)* is carried out in a similar way. Yield 7.24 g (93 %). $C_{58}H_{91}F_3N_3O_{38}P$, calculated, %: C 45.63; H 5.97; F 3.74; N 2.75; P 2.03. $C_{58}H_{91}F_3N_3O_{38}P$, found, %: C 45.67; H 5.95; F 3.77; N 2.78; P 2.01.

*The complex of dimethyl (((3-(1H-imidazol-1-yl)propyl)amino)(3-(trifluoromethyl)phenyl)) methyl)phosphonate with β-cyclodextrin (***11βCD***)* is carried out in a similar way. Yield 7.2 g (92 %). $C_{58}H_{91}F_3N_3O_{38}P$, calculated, %: C 45.63; H 5.97; F 3.74; N 2.75; P 2.03. $C_{58}H_{91}F_3N_3O_{38}P$, found, %: C 45.66; H 5.99; F 3.76; N 2.72; P 2.06.

*The complex of dimethyl (((3-(1H-imidazol-1-yl)propyl)amino)(4-(trifluoromethyl)phenyl)) methyl)phosphonate with β-cyclodextrin (***12βCD***)* is carried out in a similar way. Yield 7.27 g (93 %). $C_{58}H_{91}F_3N_3O_{38}P$, calculated, %: C 45.63; H 5.97; F 3.74; N 2.75; P 2.03. $C_{58}H_{91}F_3N_3O_{38}P$, found, %: C 45.61; H 5.96; F 3.72; N 2.72; P 2.05.

Hematopoietic-stimulating activity. The experimental group included female white rats aged two and three months weighing 220-280 g, 24 individuals. The difference in groups compared to the initial body weight did not exceed 10%. The animals were obtained simultaneously from the same nursery, the biological clinic of the Faculty of biology and biotechnology of the Al–Farabi Kazakh National University. Before and during the experiment, control and experimental animals were kept under the same standard conditions, 6 individuals per cage. Animals were divided into the following groups: untreated (UT), placebo (PL), control (MU), experimental (6 groups). Eachgroup consisted of 6 rats. Hematopoiesis was inhibited by administration of the cytostatic cyclophosphamide (Baxter Oncology GmbH, Baxter Healthcare Corporation, Deerfield, IL 60015 USA, Made in Italy, Product of Germany). On days 1st, 3d and 5th of the experiment, animals in groups PL, MU and experimental groups received an intramuscular injection of 3% sodium cyclophosphamide solution at a dose of 30 mg/kg (solvent: isotonic sodium chloride solution). The average volume of the administered drug was 0.2-0.24 ml. Then, on the 6th, 7th and 8th days of the experiment, at 9:00 a.m., the newly synthesized compounds were injected into the animals of the experimental groups respectively (the compounds were dissolved in saline solution, administered intramuscularly at a dose of 10 mg/kg, in a volume of 0.2-0.25 ml (1% solution)), the control group (MU) animals were injected with 6-methyluracil (dissolved in saline solution, administered intramuscularly at a dose of 10 mg/kg, in a volume of 0.2-0.25 ml (1% solution)), animals of the placebo group (PL) were injected with a saline solution of 0.2-0.25 ml. Animals in the intact group did not receive any treatment.. In preclinical studies of newly synthesized compounds, an intermittent regimen of administration every other day is widely used, including a limited number of injections (for example, three doses), which reduces cumulative toxicity and provides a more accurate assessment of pharmacological activity in vivo (Liao et al., 2022).On the 15th day of the experiment (7 days after the last injection), at 9:00 AM animals were anesthetized under light anesthesia induced by intraperitoneal administration of ketamine/xylazine (91 mg/kg ketamine and 9.1 mg/kg xylazine), which corresponds to commonly used anesthetic regimens in rats (Wellington et al., 2013) blood was collected from the occipital sinuses of the rats into VF-052SDK hematology tubes (2 ml, Terumo Venosafe,Ukraine) containing 3.9 mg K2-EDTA The feed was removed from the feeders 12 hours before blood sampling. Blood analyses were performed using a MicroCC-20 Plus animal hematological analyzer (High Technology Inc, China). The device was configured to determine the following cell categories: WBC – total number of leukocytes ($\times 10^9$/L), LYM – absolute number of lymphocytes ($\times 10^9$/L); MON – absolute number of monocytes ($\times 10^9$/L); NEU – absolute number of neutrophils ($\times 10^9$/L); EO – absolute number of eosinophils ($\times 10^9$/L); BAS – absolute number of basophils ($\times 10^9$/L); LYM – comparative lymphocytic index (%); MON – comparative index of monocytes (%); NEU – comparative neutrophil index (%); EO – comparative index of eosinophils (%); BAS – comparative basophilic index (%), RBC – total value of erythrocytes (red blood cells) ($\times 10^{12}$/L); HGB – hemoglobin (g/L); HCT – hematocrit (%); MCV – average volume of erythrocytes

(fL); MCH – average hemoglobin content HGB/RBC (pg); MCHC – average concentration of hemoglobin in erythrocytes HGB/HCT (g/L); RDW-cv – relative width of red blood cell distribution by volume (coefficient of variation) (%); RDW-sd – relative width of red blood cell distribution by volume) (fL); PLT – total platelet volume ($\times 10^9$/L); PCT – thrombocrit volume (%); MPV – average platelet volume (fL). Blood smears were prepared for repeat cytological examination to determine the number of leukocytes. These smears were stained with Giemsa grade and counted under a Leica microscope (Wetzlar, Germany) (at 7x100 magnification), 100 cells were dipped into each sample. The relative number of each cell type was then converted to an absolute value.

Statistical data processing. The data obtained were processed by mathematical statistics methods using Microsoft Excel and the "Statistica 6.0" software. The data are presented as an average value (M) ± standard deviation (SD) (n=6 mice/group). We used one-way (single factor) ANOVA (analysis of variance) to determine a statistically significant difference, and the values were considered reliable at $p<0.05$ and $F>Fcrit$.

Ethical considerations

The study was conducted in accordance with the decree of the Minister of Health of the Republic of Kazakhstan No. KR DSM-181/2020 (November 04, 2020) and approved by the Local Ethics Commision of Asfendiyarov Kazakh National University (Protocol No.470, June 10, 2022) (Order of the Minister of Healthcare of the Republic of Kazakhstan, 2020).

Results and discussion

Synthesis of compounds. Based on initial research (Baktybayeva et al., 2026; Kaldybayeva et al., 2022), it has been demonstrated that the incorporation of an imidazole group into a system may provide beneficial biological effects. Additionally, ionic liquids containing an imidazole ring may have potential applications in the fields of agrochemistry and agriculture (Ten et al., 2020). The combination of two chemical compounds, phosphonates and imidazoles, has the potential to generate hybrid molecules that may exhibit positive effects. These effects include the promotion of the formation of new compounds with potential applications in the fields of medicine, agriculture, and corrosion inhibition (Kaldybayeva et al., 2020). The complexation of these compounds with medical polymers has been shown to increase their solubility (Seilkhanov et al., 2024). As a result, aminophosphonate derivatives have been developed based on 1-(3-aminopropyl) imidazole and novel complexes with β-cyclodextrin (βCD),

The reaction of 1-(3-aminopropyl)imidazole with *o-,m-,p*-fluorobenzaldehyde and *o-,m-,p*-(trifluoromethyl)benzaldehyde in the presence of dimethyl- and diethylphosphite under the conditions of the one-pot, three-component Kabachnik–Fields reaction in benzene at temperatures between 70 and 80°C, using a Dean–Stark trap for the removal of water from the reaction mixture by distillation of its azeotrope with benzene, resulted in the formation of α-aminophosphonate products with yields ranging from 58 to 91% (Figure 1, Table 1).

Figure 1
Synthesis of new systems with imidazole fragment

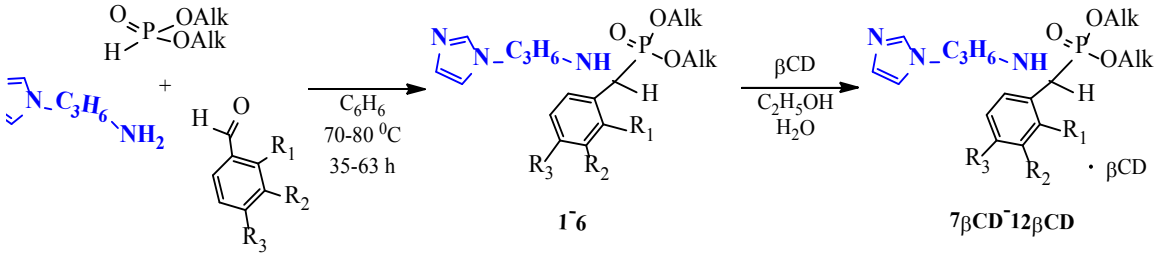

1, 7βCD Alk= CH_3; R_1=F, R_2 = R_3 = H
2, 8βCD Alk= C_2H_5; R_2=F, R_1 = R_3 = H
3, 9βCD Alk= CH_3; R_3=F, R_1 = R_2 = H
4, 10βCD Alk= CH_3; R_1=CF_3, R_2 = R_3 = H
5, 11βCD Alk= CH_3; R_2=CF_3, R_1= R_3= H
6, 12βCD Alk= CH_3; R_3=CF_3, R_1= R_2= H

Table 1
Physical and chemical characteristics of aminophosphonates 1-6

Compounds	Yield, %	R_f*	Calculated found, %		IR spectra, cm^{-1}					$t_{mel.}$ ^0C / n_D^{20} (liq.)*
			C	H	C=C	C-N	P=O	P-C	C-F	
1	62	0,14	52,78 52,76	6,20 6,17	1618	1044	1211	762	1044	83-86
2	58	0,19	55,28 55,26	6,82 6,80	1621	1039	1238	805	1039	40-43
3	38	0,27	52,78 52,81	6,20 6,18	1607	1054	1220	763	1054	1,526*
4	79	0,32	49,11 49,12	5,41 5,39	1578	1035	1166	770	1314	1,520*
5	82	0,27	49,11 49,07	5,41 5,43	1509	1030	1166	741	1329	1,517*
6	91	0,30	49,11 49,08	5,41 5,40	1558	1038	1161	773	1314	1,517*

The IR spectra of the α-aminophosphonate compounds **1-6** exhibit signals corresponding to the C-N bond at 1030–1054 cm^{-1}, the P=O bond at 1161–1238 cm^{-1} and the C-F bond at 1039–1054 and 1314–1329 cm^{-1} respectively. In the ^{13}C NMR spectrum, the carbon atoms of the propyl group (C-6–8) appear at 26.55 and 47.22–47.37 ppm. The carbon atoms belonging to the imidazole ring are resonated at 120.45–136.33 ppm, while the aromatic carbon atoms are observed at 115.32–163.99, and 125.98–140.49 ppm respectively. The tertiary carbon atom is located at 58.37–60.70 ppm, while the carbon atoms from the methoxy and ethoxy groups are recorded at 16.45 and 53.51–63.10 ppm respectively.

In the ^1H NMR spectra of compounds **1-6**, imidazole protons were observed as single-proton peaks at 6.92, 7.03, and 7.45 ppm. Aromatic protons from the phenyl ring were detected as single-proton doublets in a range between 6.72 and 8.05 ppm. Protons from the methylene group of the propyl group (H-6, H-7, and H-8) were observed as multiplets between 2.19 and 3.11 ppm. Proton H-10 appeared as a doublet between 4.13 and 4.72 ppm. Methoxy and ethoxy protons were detected at 1.15 ppm and 3.63 ppm, respectively.

The reaction products 1-6 were soluble only in organic solvents. Complexes 7βCD-12βCD with β-CD were obtained as solids and studied for myelostimulating activity, which includes stimulation of erythropoiesis, leukopoiesis and thrombocytopoiesis.

Hematopoietic-stimulating activity. The intact group of animals had leukocyte, platelet, and red blood cell counts within normal limits for obviously healthy animals. The total erythrocytes count was $(7.5 \pm 0.9) \cdot 10^{12}$ /L of blood, with a hemoglobin level (140.70 ± 8.90) g/L. The average amount of hemoglobin in red blood cells was (350.60 ± 14.28) g/L of blood. Hematocrit value and mean corpuscular volume were (21.21 ± 7.79)% and (82.6 ± 0.23) fl, respectively, within the normal range.

Platelet counts. The total platelet count, mean platelet volume, and platelet crit were (660.0±12.2) $\cdot 10^9$/L of blood, (7.90±0.10) fl, and (0.44±0.01)%, respectively, which were also within normal limits.

Leukocyte count. The total leukocyte count was $(12.10\pm0.80) \cdot 10^9$/L of blood which was within the normal range. In the leukogram, the relative lymphocyte count, relative granulocyte count, and relative monocyte count were (63.72±1.1) %, (30.0±0.8) %, and (6.28±0.1)%, respectively. The normal absolute values of lymphocytes, granulocytes and monocytes were $(7.71\pm0.10) \cdot 10^9$/l of blood, $(3.63\pm0.01) \cdot 10^9$/l of blood, $(0.76\pm0.01) \cdot 10^9$/l of blood, respectively.

The introduction of the cytostatic cyclophosphamide resulted in a 2.0-2.6-fold decrease in all peripheral blood parameters. The red blood cell count decreased 1.52-fold to $(4.67\pm0.1) \cdot 10^{12}$ /L of blood, with a 1.54-fold decrease in the hemoglobin level to (96.60±10.00) g/L of blood. The average hemoglobin concentration in the red blood cell mass decreased insignificantly to (342.50±6.50) g/L of blood, the hematocrit and the average corpuscular volume decreased to (28.1±0.47)% and (50.00±11.30) fl, respectively. It is the erythrocytes that primarily make up the volume of formed elements of the blood, and the decrease in the hematocrit reflected a decrease in the volume

of erythrocytes to the volume of blood plasma. The platelet mass showed a significant decrease in the platelet count by 6.34 times to (70.50±23.33) · 10^9/L of blood. The average platelet volume and platelet crit decreased by 1.34 and 1.6 times to (5.28±2.00) fl and (0.05±0.03)%, respectively.

Significant changes in absolute and relative leukocyte counts were observed in placebo group. The total leukocyte count decreased by 5.10 times to (3,83±0,73) · 10^9/L of blood. A leftward shift in the leukogram occurred, with a decrease in agranulocyte leukocytes, specifically lymphocytes, and an increase in the relative granulocyte count. Absolute counts decreased more significantly than relative counts. The absolute lymphocyte count decreased to (2.22±0.90) · 10^9/L of blood, a 6.88-fold decrease, while the absolute granulocyte count decreased to (1.44±0.13) · 10^9/L of blood, a 5.85-fold decrease.

Thus, we observed a decrease in the proliferative activity of erythropoiesis, thrombocytopoiesis, and leukopoiesis in experimental groups.

Reduction of erythrocytes, leukocytes and platelets with cyclophosphamide in an experiment with mice due to its pronounced anti-cytotoxic and marrow-suppressive effects. Cyclophosphamide is widely used in preclinical studies as a standard model of induced myelosuppression and immunodeficiency in experimental animals (Sharata et al., 2026). Cyclophosphamide is a prodrug that is activated in the liver and produces cytotoxic metabolites, including the phosphoramide mustard. These compounds stimulate DNA alkylation and form interlinked networks within and between cells, thereby disrupting transcription and copying, as well as inducing cell cycle arrest and controlled cell death. Experimental studies in mice have shown that cyclophosphamide mainly affects rapidly growing bone marrow cells, thereby inhibiting hematopoiesis and changing the bone marrow microenvironment (Sun et al., 2025). This is accompanied by a significant decrease in the number of cells in the blood and the development of hemocytopenia, including anemia, leukemia and thrombocytopenia. Therefore, the use of cyclophosphamide in experimental models allows replicating cytotoxic stimulation by inhibiting the proliferation of hematopoietic cells, which makes it a suitable tool for studying the processes of hemotoxic action and evaluating potential protective or therapeutic agents (Gao et al., 2025).

Furthermore, against the background of erythropoiesis, thrombocytopoiesis, and leukopenia, experimental newly synthesized compounds were administered intramuscularly to stimulate erythropoiesis, thrombopoiesis, and leukopoiesis.

Next, against a background of pancytopenia, the test compounds of the βCD-complexes series were administered: 7βCD-12βCD. Among the compounds studied, 7βCD, 8βCD, and 11βCD not only showed a hematopoietic-stimulating effect, but even inhibited the hematopoietic system, as blood counts in these experimental groups were lower than in the placebo group. Therefore, 9βCD, 10βCD, and 12βCD exhibit hematopoietic activity comparable to that of methyluracil as the parent drug. 9βCD and 12βCD exhibited similar hematopoietic activity. Both compounds exhibited moderate leukopoiesis-stimulating activity without affecting the Harkavi index. The total leukocyte count in the 9βCD and 12βCD injection groups was (7.09÷7.40) · 10^9/L blood, which was slightly higher than the MU blood group count (5.20±0.80) · 10^9/L blood, but significantly exceeded the PL group count by 3.22 times (3.84±0.93) · 10^9/L blood. The Harkavi index reflects the body's recovery process after stress. During the experiment, it demonstrated rapid hematopoiesis recovery without disrupting the lymphocyte-to-granulocyte ratio. In rats, the relative lymphocyte count prevails over the relative neutrophil count. It is due to this ratio that the adaptive immune system of rodents is more reactive than that of other animal species. The relative lymphocyte index of the blood in the group with compounds 9βCD and 12βCD was (91.16÷91.27)%, significantly exceeding the values of the intact group of animals (63.72±1.10)%, being at the upper limit of the norm, which indicated a significant increase in lymphocyte values. The absolute indices of peripheral blood lymphocytes in the group receiving compounds 9βCD and 12βCD were also high and amounted to (6,73± 2,27)·10^9/l of blood, which exceeded the indices of the MU group (3,32± 0,04)·109/l of blood by 2.88 times ($p \leq 0.01$), the indices of the PL group (2.22±0.90) · 10^9/l of blood by 4.17 times, and the UT group (7.71±0.10)·10^9/l of blood by 1.20 times.

Compound 9βCD did not exhibit erythropoiesis-stimulating activity. The total erythrocyte count was (4.61 ± 0.2) · 10^{12}/L of blood, lower than the UT group count (7.50 ± 0.9) · 10^{12}/L. Hemoglobin levels were also low (89.50 ± 4.2) g/L, close to placebo group and lower than those in the UT and MU groups. The mean hemoglobin concentration in erythrocyte mass, hematocrit, and mean corpuscular volume corresponded to those in the placebo group and were lower than those in the intact and control groups.

Table 2
Hemogram parameters of peripheral blood in experimental groups

	7βCD	8βCD	9βCD	10βCD	11βCD	12βCD	PL	MU	UT	P
	1	2	3	4	5	6	7	8	9	10
WBC, $\times 10^9$/L	2.43±0.1	3.29±0.1	7.40±1.2	5.33±0.91	2.66±0.18	7.09±3.06	3.83±0.73	5.20±0.80	12.10±0.80	P_{1-8}= 0.004 P_{1-9}= 0.01 P_{2-8}= 0.02 P_{2-9}= 0.03 P_{3-8}= 0.01 P_{3-9}= 0.01 P_{4-9}= 0.1 P_{5-8}= 0.003 P_{5-9}= 0.004
LYM, $\times 10^9$/L	1.88±1.0	3.16±0.5	6.78±0.9	3.47±0.38	1.67 ±0.08	6.73±2.27	2.22 ±0.90	3.32±0.04	7.71±0.10	P_{1-8}= 0.003 P_{1-9}= 0.02 P_{2-8}= 0.01 P_{2-9}= 0.02 P_{3-8}= 0.02 P_{3-9}= 0.03 P_{4-9}= 0.1 P_{5-8}= 0.002 P_{5-9}= 0.003
MON, $\times 10^9$/L	0.46±0.05	0.28±0.13	0.54±0.17	0.31±0.03	0.21± 0.01	0.19± 0.09	0.19 ±0.01	0.27± 0.00	0.76±0.01	P_{1-8}= 0.002 P_{1-9}= 0.02 P_{2-8}= 0.02 P_{2-9}= 0.03 P_{3-8}= 0.01 P_{3-9}= 0.02 P_{4-9}= 0.1 P_{5-8}= 0.003 P_{5-9}= 0.003
NEU, $\times 10^9$/L	0.09±0.01	0.11±0.01	0.09±0.02	1.54 ±0.00	0.76±0.01	0.15±0.01	1.44±0.13	1.70±0.04	3.63±0.01	P_{1-8}= 0.001 P_{1-9}= 0.01 P_{2-8}= 0.01 P_{2-9}= 0.03 P_{3-8}= 0.01 P_{3-9}= 0.02 P_{4-9}= 0.1 P_{5-8}= 0.001 P_{5-9}= 0.002

Continuation of the table

	7βCD	8βCD	9βCD	10βCD	11βCD	12βCD	PL	MU	UT	P
	1	2	3	4	5	6	7	8	9	10
LYM, %	72.05±4.2	88.16±4.5	91.27±9.9	65.67±1.18	63.07± 0.47	92.16± 2.07	57.60±1.65	62.04± 3.93	63.72±1.10	ND
MI, %	24.22±4.5	7.34±0.50	7.56±0.80	7.15± 2.43	7.84±1.12	2.40± 0.20	4.84± 5.30	5.28± 0.40	6.28 ±0.10	ND
NEU, %	3.78±0.50	4.67±0.30	1.33±0.01	26.73±3.83	29.10±0.65	4.99±2.05	37.56±9.30	32.68±1.60	30.00±0.80	P_{1-7}=0.04 P_{1-8}=0.02 P_{2-8}= 0.01 P_{2-9}= 0.02 P_{3-8}= 0.01 P_{3-9}= 0.02 P_{6-8}= 0.01 P_{6-9}= 0.03
RBC, × 10^{12}/L	1.81±0.10	2.88±0.10	4.61±0.20	6.29±0.42	5.29±0.43	5.14±0.01	4.67±0.10	5.69± 0.36	7.50±0.90	P_{1-8}= 0.003 P_{1-9}= 0.006 P_{2-8}= 0.01 P_{2-9}= 0.03
HGB, g/L	40.00±1.2	59.50±4.6	89.50±4.20	111.50± 4.33	94.00±10.67	89.00±2.67	96.60±10.00	106.0±12.20	140.70±8.90	P_{1-8}= 0.003 P_{1-9}= 0.005 P_{2-8}= 0.01 P_{2-9}= 0.002
MCHC, g/L	437.00±37.5	400.00±22.2	360.00±16.6	297.50±1.00	301.00±4.67	299.00±2.00	342.50±6.50	34.69±0.70	350.6±14.28	P_{1-7}=0.01 P_{3-8}= 0.01 P_{4-8}= 0.01 P_{4-9}= 0.01 P_{5-8}= 0.01 P_{5-9}= 0.01
MCH, pg	22.72±2.10	21.11±3.20	19.50±1.20	17.70± 0.50	17.70±0.53	17.30±0.47	17.00±0.30	52.50 ±1.50	27.30±5.27	P_{1-7}=0.03
MCV, fL	51.72±1.50	52.67±11.20	54.00±4.60	59.70 ±1.87	58.80± 0.87	57.95±1.17	50.00±11.30	18.45±0.55	82.60±0.23	P_{1-8}= 0.004 P_{2-8}= 0.02 P_{2-9}= 0.002 P_{3-8}= 0.01 P_{3-9}= 0.02 P_{4-8}= 0.005 P_{4-9}= 0.007 P_{5-8}= 0.001 P_{5-9}= 0.002 P_{6-8}= 0.002 P_{6-9}= 0.002

Continuation of the table

	7βCD	8βCD	9βCD	10βCD	11βCD	12βCD	PL	MU	UT	P
	1	2	3	4	5	6	7	8	9	10
RDW-CV, %	14.83±2.30	14.22±0.30	16.33±1.30	12.20±0.20	11.65±0.03	12.50± 0.80	12.25±0.30	17.2±0.20	12.40±0.17	$P_{1\text{-}9}$ = 0.01 $P_{2\text{-}9}$ = 0.002 $P_{3\text{-}9}$ = 0.02 $P_{4\text{-}8}$ =0.0001 $P_{4\text{-}9}$ = 0.008 $P_{5\text{-}8}$ = 0.001 $P_{5\text{-}9}$ = 0.003 $P_{6\text{-}8}$ = 0.004 $P_{6\text{-}9}$ = 0.002
RDW-SD, fL	27.83±7.50	28.28±6.20	29.11±2.10	25.20±0.60	23.45±0.43	24.50± 0.93	23.00±0.40	12.70±0.40	23.6±0.20	$P_{1\text{-}8}$ = 0.001 $P_{1\text{-}9}$ = 0.01 $P_{2\text{-}7}$ = 0.02 $P_{2\text{-}8}$ = 0.002 $P_{3\text{-}7}$ = 0.01 $P_{3\text{-}8}$ = 0.02 $P_{4\text{-}7}$ =0.0001 $P_{4\text{-}8}$ = 0.008 $P_{5\text{-}7}$ = 0.001 $P_{5\text{-}8}$ = 0.003 $P_{6\text{-}7}$ = 0.004 $P_{6\text{-}8}$ = 0.002
HCT, %	9.17±0.90	14.94±0.90	24.94±1.10	37.35±1.37	31.20±3.00	29.80± 0.60	28.10±0.84	28.10±0.47	21.21±2.79	$P_{1\text{-}8}$ = 0.01 $P_{1\text{-}9}$ = 0.02
PLT, × 10^9/L	174.50±5.50	189.1±13.20	397.0±18.90	503.0±50.00	362.0±62.00	309.5±21.33	70.50 ±7.33	518.25±19.9	670.0±14.20	ND
MPV, fL	6.44±0.50	7.72±0.80	7.72±0.10	6.10±0.40	5.70±0.01	6.20±0.20	5.28±2.00	6.63±0.30	7.90±0.10	ND
PDW, %	7.67±0.10	9.78±0.90	9.00±.0.01	14.40±2.47	10.90±0.07	11.40±0.20	7.10±0.00	12.25±0.57	11.40±0.43	ND
PCT, %	0.12±0.01	0.12±0.01	0.31±0.01	0.31± 0.05	0.21±0.04	0.19±0.04	0.05±0.04	0.31±0.25	0.44±0.01	ND
P-LCR, %	10.06±0.90	15.38±1.30	13.89±0.80	4.75±1.70	3.30±0.20	6.15±0.67	2.5±0.47	4.95± 0.46	2.1± 0.15	ND

Note: ND – not discussed (non-informative values)

The compound 9βCD showed moderate platelet-stimulating activity.The total trombocyte count was (397,0±18,9)·10^9/L of blood. This indicator was lower than the UT group (670,00 ±14,20)·10^9/L blood and the MU group (518.25 ± 19.90) ·10^9/L blood. The platelet crit, platelet distribution width, and mean platelet count in the blood were also low. Thus, compound 9βCD had low thrombopoiesis-stimulating activity.

Compound 12βCD slightly exceeded compound 9βCD in erythro- and thrombopoiesis-stimulating activity. The total erythrocyte count was (5.14 ± 0.01) · 10^{12}/L blood and was at the level of the MU group. The hemoglobin level was low (89.00 ± 2.67) g/L and was close to the blood values of animals of the PL group and inferior to the blood values of animals of the UT group and MU group. The values of the average concentration of hemoglobin in the erythrocyte mass, the hematocrit index, and the average volume of erythrocytes corresponded to the blood values of the animals in the PL group were lower than in the UT and MU groups. The level of platelet-stimulating activity of compound 12βCD was low. The total platelet index was (309.5 ± 48.33) ·10^9/l of blood. This indicator was lower than the value of the UT group (660.00 ± 12.20) ·10^9/l of blood and the MU group (518.25 ± 19.90) ·10^9/l of blood. The values of thrombocrit, platelet distribution width and average platelet index in the blood were also low. Thus, compound 12βCD had low thrombocytopoiesis-stimulating activity. The observed effects are likely due to the effects of the compound on redox homeostasis and cytokine-mediated signaling pathways that regulate hematopoietic cell proliferation and differentiation. In general, phosphonates are characterized by a range of biological activities, including antioxidant and immunomodulatory properties (Cui & Ju, 2025).

The obtained results indicate the presence of strong structural and functional dependence and confirm the possibility of directed synthesis of phosphate derivatives with selective influence on various foci of hematopoiesis (Krečmerová et al., 2022).

Conclusion

A series of α-aminophosphonate compounds were synthesized through a one-pot reaction involving 1-(3-aminopropyl)imidazole, fluoro- or trifluoromethyl-substituted benzaldehydes, and dialkyl phosphite under azeotropic drying conditions using benzene as the solvent. The target compounds were obtained with yields ranging from 58% to 91%. Spectroscopic analysis (IR, ^{1}H and ^{13}C NMR) confirmed the anticipated structures, revealing the presence of characteristic signals for C–N, P=O, and C–F groups, as well as for the imidazole, aromatic, alkoxy, and propyl moieties. The α-aminophosphonates were converted into β-cyclodextrin inclusion complexes (7βCD–12βCD) to improve solubility, enabling biological evaluation.

Biological testing demonstrated that several complexes exhibited hematopoiesis-stimulating properties in a cyclophosphamide-induced pancytopenia model. Among them, 9βCD and 12βCD showed the most promising activity, producing moderate stimulation of leukopoiesis comparable to methyluracil, with significant recovery of total leukocyte and lymphocyte counts and restoration of the Harkavi index. However, their effects on erythro- and thrombopoiesis were limited. Other derivatives (7βCD, 8βCD, 11βCD) did not exhibit stimulatory effects and further suppressed hematopoietic parameters.

Overall, the data indicate that β-cyclodextrin complexes of imidazole-containing α-amino phosphonates, particularly 9βCD and 12βCD, represent promising skeletons for the development of novel small-molecule hematopoietic system modulators.

Authors contributions

A.S. Sokolenko: Conceptualization, Methodology, Investigation, Writing – Original Draft;

A.B.Kaldybayeva: Data Curation, Formal Analysis, Visualization, Writing – Review & Editing;

L.B. Baktybayeva: Conceptualization, Methodology, Investigation, Writing – Original Draft;

G. Deniz: Supervision, Funding Acquisition, Project Administration, Writing – Review & Editing;

V.K. Yu: Supervision, Funding Acquisition, Project Administration, Writing – Review & Editing.

Acknowledgements

This research was funded by the Science Committee of the Ministry of Science and Higher Education of the Republic of Kazakhstan, grant number AP22688235, BR27101179.

Conflict of interest

The authors declare that they have no conflicts of interest.

References

1. Agami, R. A., Ghramh, H. A., & Hasheem, M. (2017). Seed inoculation with *Azospirillum lipoferum* alleviates the adverse effects of drought stress on wheat plants. *Journal of Applied Botany and Food Quality, 90*(1), 165–173.

2. Ahmed, A., & Hasnain, S. (2014). Auxins as one of the factors of plant growth improvement by plant growth promoting rhizobacteria. *Polish Journal of Microbiology, 63*(3), 261–266. https://doi.org/10.33073/pjm-2014-035

3. Alaskar, A. A., & Al-Shwaiman, H. A. (2023). The effect of plant growth-promoting rhizobacteria on soil properties and the physiological and anatomical characteristics of wheat under water-deficit stress conditions. *Agriculture, 13*(11), 2042. https://doi.org/10.3390/agriculture13112042

4. Bahrami, A., Sayyahfar, S., Soltani, Z., Khodadost, M., Moazzami, B., & Rezaei, N. (2020). Evaluation of the frequency and diagnostic delay of primary immunodeficiency disorders among suspected patients based on the 10 warning sign criteria: A cross-sectional study in Iran. *Allergologia et Immunopathologia, 48*, 711–719. https://doi.org/10.1016/j.aller.2020.03.005

5. Baktybayeva, L., Kaldybayeva, AB., Sokolenko, A., Tursynova, B., Ten, AY., Daulet, G., Svambayev, E., Thevis, M., Yu, VK., & Tassibekov, KS. (2026). Targeting leukopoiesis: Pharmacological and biotechnological strategies for the treatment of leukopenia. *Biomedicines, 14*(3), 624. https://doi.org/10.3390/biomedicines14030624

6. Cabañero-Navalon, MD., Garcia-Bustos, V., Balastegui-Martin, H., Bracke, C., Mateu, L., et al. (2024). The impact of immune dysregulation on the risk of malignancy in common variable immunodeficiency: Insights from a multicenter study. *Frontiers in Immunology, 15**, 1465159. https://doi.org/10.3389/fimmu.2024.1465159

7. Cui, J., & Ju, KS. (2025). Recent advances in natural and synthetic phosphonate therapeutics. *Current Opinion in Microbiology, 87**, 102630. https://doi.org/10.1016/j.mib.2025.102630

8. El-Badry, E., Chen, L., Ghneim, K., Li, Z., Brooks, K., Rhodes, J., Sekaly, R., Kilembe, W., Allen, S., Wu, H., & Hunter, E. (2025). Heightened expression of Type I interferon signaling genes in CD4+ T cells from acutely HIV-1-infected women is associated with lower viral loads. *Frontiers in Immunology, 15**, 1507530. https://doi.org/10.3389/fimmu.2024.1507530

9. Gago, C., Serralheiro, A., & Miguel, MG. (2025). Anti-inflammatory activity of thymol and thymol-rich essential oils: Mechanisms, applications, and recent findings. *Molecules, 30*(11), 2450. https://doi.org/10.3390/molecules30112450

10. Gao, F., Wang, Y., Liu, J., Xie, Y., Geng, Y., He, Z., Geng, J., Li, J., Chen, W., & Du, R. (2025). Protective effects of velvet antler polypeptides on cyclophosphamide-induced myelosuppression in mouse and bone marrow mesenchymal stem cells. *Nutrients, 17*(21), 3428. https://doi.org/10.3390/nu17213428

11. Gholami, MH., Rassouli, A., Mirzaei, S., & Hashemi, F. (2023). The potential immunomodulatory effect of levamisole in humans and farm animals. *Journal of Advanced Veterinary and Animal Research, 10*(4), 620–629. https://doi.org/10.5455/javar.2023.j717

12. Giemsa, G. (1904). Eine Vereinfachung und Vervollkommnung meiner Methylenazur-Methylenblau-Eosin-Färbemethode zur Erzielung der Romanowsky-Nochtschen Chromatinfärbung. *Centralblatt für Bakteriologie, 37**, 308–311.

13. Groaz, E., & De Jonghe, S. (2021). Overview of biologically active nucleoside phosphonates. *Frontiers in Chemistry, 8*, 616863. https://doi.org/10.3389/fchem.2020.616863

14. Gubernatorova, EO., Namakanova, OA., Gorshkova, EA., Medvedovskaya, AD., Nedospasov, SA., & Drutskaya, MS. (2021). Novel anti-cytokine strategies for prevention and treatment of respiratory allergic diseases. *Frontiers in Immunology, 12**, 601842. https://doi.org/10.3389/fimmu.2021.601842

15. Ikeda, M., Morizane, C., Ueno, M., Okusaka, T., Ishii, H., & Furuse, J. (2025). Systemic therapy for hepatocellular carcinoma, from the early to the advanced stage: A Japanese perspective. *Japanese Journal of Clinical Oncology, 55*(5), 465–476. https://doi.org/10.1093/jjco/hyaf017

16. Kaldybayeva, AB., Yu, VK., Malmakova, AE., Li, T., Ten, AY., Seilkhanov, TM., Praliyev, KD., & Berlin, KD. (2022). Novel complexes of 3-[3-(1H-imidazol-1-yl)propyl]-3,7-diaza-bispidines and β-cyclodextrin as coatings to protect and stimulate sprouting wheat seeds. *Molecules, 27*(21), 7406. https://doi.org/10.3390/molecules27217406

17. Kaldybayeva, AB., Malmakova, AE., Yu, VK., & Pyraliev, KZh. (2020). Synthesis and biological properties of some α-aminophosphonates. *Chemical Journal of Kazakhstan, 3**, 63–84. https://doi.org/10.22159/ijap.2021.v13s1.Y1013

18. Krečmerová, M., Majer, P., Rais, R., & Slusher, BS. (2022). Phosphonates and phosphonate prodrugs in medicinal chemistry: Past successes and prospects. *Frontiers in Chemistry, 10**, 889737. https://doi.org/10.3389/fchem.2022.889737

19. Liao, Y., Xiao, N., Wang, X., Dai, S., & Wang, G. (2022). Promoting effect of Tmsb4x on the differentiation of peripheral blood mononuclear cells to dendritic cells during septicemia. *International Immunopharmacology, 111**, 109002. https://doi.org/10.1016/j.intimp.2022.109002

20. Ministry of Health of the Republic of Kazakhstan. (2005). *Instructions for conducting preclinical trials and (or) studies of biologically active substances in the Republic of Kazakhstan* (Order No. 51).

21. Ministry of Healthcare of the Republic of Kazakhstan. (2020). *On approval of the rules for the assessment of materials and compliance of preclinical (non-clinical) studies with Good Laboratory Practice (GLP) requirements of the Republic of Kazakhstan and/or the Eurasian Economic Union within the framework of pharmaceutical inspection* (Order No. KR DSM-181/2020). https://adilet.zan.kz/eng/docs/V2000021596

22. Regina, J., Doms, J., Kampouri, E., et al. (2025). Immunodeficiencies in adults: Key considerations for diagnosis and management. *Clinical Reviews in Allergy & Immunology, 68**, 92. https://doi.org/10.1007/s12016-025-09103-9

23. Seilkhanov, T., Ten, A., Tassibekov, K., Seilkhanov, O., Zharkynbek, T., Tursynova, B., & Yu, V. (2024). Supramolecular cyclodextrin complexes of biologically active nitrogen heterocycles. *Chemical Bulletin of Kazakh National University, 112*(3), 22–33. https://doi.org/10.15328/cb1379

24. Sharata, EE., Bakry, T., Atta, HG., Mohammed, HA., Diab, NS., Atef, RA., Hosney, RS., Omar, MM., & Hemeida, RAM. (2026). Molecular mechanisms underlying cyclophosphamide-induced ovarian injury and protective strategies. *Naunyn-Schmiedeberg's Archives of Pharmacology, 399*(2), 1951–1985. https://doi.org/10.1007/s00210-025-04550-9

25. Strzelec, M., Detka, J., Mieszczak, P., Sobocińska, MK., & Majka, M. (2023). Immunomodulation-a general review of the current state-of-the-art and new therapeutic strategies for targeting the immune system. *Frontiers in Immunology, 14**, 1127704. https://doi.org/10.3389/fimmu.2023.1127704

26. Sun, M., Wu, S., Yi, G., & Yu, L. (2025). Protective effects of *Althaea officinalis* L. against cyclophosphamide-induced immunosuppression and bone marrow/spleen injuries in rats. *Pharmacognosy Magazine*. https://doi.org/10.1177/09731296251396325

27. Tavakol, M., Delavari, S., Salami, F., Ansari, S., Rasouli, SE., Chavoshzadeh, Z., et al. (2022). Diversity of malignancies in patients with different types of inborn errors of immunity. *Allergy, Asthma & Clinical Immunology, 18*(1), 106. https://doi.org/10.1186/s13223-022-00747-2

28. Ten, A., Zazybin, A., Zolotareva, D., Dauletbakov, A., Rafikova, K., Yu, V., & Giner, B. (2020). Ionic liquids in agrochemistry. *Current Organic Chemistry, 24*(11), 1181–1195. http://dx.doi.org/10.2174/1385272824999200608135522

29. Wang, Y., Cao, Y., Meng, Y., You, Z., Liu, X., & Liu, Z. (2014). The novel role of thymopentin in induction of maturation of bone marrow dendritic cells (BMDCs). *International Immunopharmacology, 21*(2), 481–487. https://doi.org/10.1016/j.intimp.2014.05.011

30. Wellington, D., Mikaelian, I., & Singer, L. (2013). Comparison of ketamine-xylazine and ketamine-dexmedetomidine anesthesia and intraperitoneal tolerance in rats. *Journal of the American Association for Laboratory Animal Science, 52*(4), 481–487.

31. Zhang, M., Liu, C., Tu, J., Tang, M., Ashrafizadeh, M., Nabavi, N., Sethi, G., Zhao, P., & Liu, S. (2025). Advances in cancer immunotherapy: Historical perspectives, current developments, and future directions. *Molecular Cancer, 24*(1), 136. https://doi.org/10.1186/s12943-025-02305-x

Information about the authors:

Anastassiya S. Sokolenko – M.Sc,Phd student, Department of Biology, Abai Kazakh National Pedagogical University, (Almaty, Kazakhstan, e-mail: sokolenko.anastassiya@gmail.com).

Altynai B.Kaldybayeva – PhD, Department of Chemistry and Technology of Organic Substances, Natural Compounds and Polymers, Al-Farabi Kazakh National University; Laboratory of Chemistry of Synthetic and Natural Medicinal Compounds, A.B. Bekturov Institute of Chemical Sciences (Almaty, Kazakhstan, e-mail: altin_28.94@mail.ru).

Layilya B. Baktybayeva – Associated Professor (biophysics and biomedicine), Al-Farabi Kazakh National University (Almaty, Kazakhstan, e-mail: lilaturap707@gmail.com).

Gunnur Deniz – Prof. Dr. Department of Immunology, Istanbul University,(Istanbul, Turkey, e-mail:gdeniz@istanbul.edu.tr).

Valentina K. Yu – Full Professor, Laboratory of Chemistry of Synthetic and Natural Medicinal Compounds, A.B. Bekturov Institute of Chemical Sciences (Almaty, Kazakhstan, e-mail: yuvkconst@gmail.com).

Received 09 December 2025;
received in revised form 22 June 2026;
accepted 26 June 2026

IRSTI 61.67.99 https://doi.org/10.26577/IJBCh20261919

A. El-Hashani[1], K.M. Elsherif[2*], G.F. Musbah[1], A. Imragaa[1], H.F. Emrayed[3]

[1]Department of Chemistry, Faculty of Science, University of Benghazi, Benghazi, Libya
[2]Department of Medical Laboratory Science, Faculty of Health Science, Misurata University, Misurata, Libya
[3]Department of Chemistry, Faculty of Science, Omar Al-Mukhtar University, Al-Bayda, Libya
*e-mail: elsherif27@yahoo.com

CHEMICAL FUNCTIONALIZATION OF PALM FIBERS FOR IMPROVED DYE ADSORPTION: SUSTAINABILITY AND EFFICIENCY

Abstract: The potential of chemically modified palm fibres (CMPF) as effective, economical, and eco-friendly sorbents for wastewater treatment – more specifically, for dye removal – is highlighted in this study. Two adsorbents were produced from palm fibres: acid-base treated palm fibres (A-BTPF), treated with H_2SO_4 and NaOH, and CMPF, treated with CS_2. The addition of xanthate and aldehyde functional groups to CMPF, which enhanced its adsorption ability, was validated by FT-IR analysis. Adsorption behavior was assessed for neutral red (NR) and methyl green (MG) dyes under varying pH, contact time, adsorbent dose, initial dye concentration, and temperature. Both adsorbents demonstrated significant removal efficiencies, with maximum adsorption of NR at pH 4 and MG at pH 10. The enhanced adsorption of MG at basic pH is consistent with the adsorbent's pH_{PZC} value of 9.0. Adsorption data were best described by the Langmuir isotherm model, with maximum adsorption capacities of 19.88 mg/g for NR and 7.45 mg/g for MG, and correlation values of 0.9935 and 0.9869, respectively. Kinetic investigations showed that adsorption followed a pseudo-second-order model ($R^2 = 0.9988$ for NR and 0.9989 for MG). Thermodynamic analysis confirmed that the process was spontaneous and endothermic (negative $\Delta G°$ and positive $\Delta H°$ values). CMPF exhibited superior adsorption efficiency and capacity compared to A-BTPF, demonstrating its suitability as a high-performance, sustainable biosorbent for wastewater treatment. Given its low cost, abundance, and enhanced adsorption performance, CMPF has strong potential for industrial-scale applications, particularly in textile, pharmaceutical, and dye-producing industries, offering a green alternative to conventional adsorbents in water purification.

Keywords: Biosorption, Xanthated palm fiber, Dye removal, Wastewater treatment, Adsorption isotherms, Adsorption kinetics.

Introduction

The textile, food, cosmetics, and paper industries release large amounts of dyes into the environment annually, which can prove harmful to ecosystems and human health. An estimated 10–15% of the more than 1,000 tonnes of commercially available colours used in the textile industry alone end up in wastewater systems, largely untreated (Al-Saeedi et al., 2023; Elsherif, Yaghi, 2017; Ibrahim et al., 2021). About 60–70% of the world's dye output, which surpasses 700,000 tonnes per year, is composed of azo dyes, which are highly preferred because of their ease of synthesis and stability (Djama et al., 2023; Pietrzyk et al., 2023). Synthetic dyes have complex, durable structures that resist biodegradation, persisting in aquatic environments. Their stability threatens ecosystems and human health by depleting oxygen, harming aquatic life, and causing mutagenic and carcinogenic effects (Alkherraz et al., 2023; Alshorifi et al., 2022; Elsherif et al., 2019). Commonly used dyes like Rhodamine B, methyl green, methylene blue (MB), neutral red, Congo red, and Reactive Black-5 can be anionic, neutral, or cationic (Alardhi et al., 2023; El-Shafie et al., 2023). Their persistent discharge – particularly from textile wastewater – threatens human health and the environment, challenging conventional water treatment methods (El-Hashani et al., 2018b). These toxic, non-biodegradable dyes disrupt microbial ecosystems and, with prolonged exposure, may cause cancer or skin irritation in humans (El-Hashani et al., 2018a; Fito et al., 2023).

The growing global emphasis on advanced wastewater treatment underscores the urgent need for effective industrial dye waste management (Hammad et al., 2024; Harouache et al., 2024; Tenev et al., 2023). Despite various existing methods – such as membrane separation (Elsherif et al., 2014a; Huang et al., 2024), adsorption (Alkherraz et al., 2020b; Islam et al., 2024; Matić et al., 2024; Olusegun et al., 2023), photocatalytic oxidation (Zhou et al., 2024), electrochemical techniques (Bibikov et al., 2024; Elsherif et al., 2014b), biopolymer sorption (Lakshmi et al., 2024), and biodegradation (Nasiri et al., 2023) – water pollution remains a critical environmental challenge (Rashid et al., 2021). Among these, adsorption stands out for its efficiency, cost-effectiveness, ease of implementation, and versatility in removing diverse pollutants (Alkherraz et al., 2020a).

Activated carbon is widely used for adsorption due to its high surface area and capacity, but its high cost limits large-scale applications (Devi et al., 2023; Sghiouri Idrissi et al., 2024). Researchers are exploring low-cost alternatives like biosorbents derived from natural materials, including coffee grounds, cellulose, and algae (Elsherif et al., 2022). Carbonized coffee grounds show promise for removing pollutants like bisphenol A due to their porous structure (Elsherif et al., 2018a; Memetova et al., 2023), while cellulose and algal biomass effectively adsorb heavy metals (e.g., Pb, Cd, Zn) (Li et al., 2021). Microalgae, with their large surface area, can capture diverse contaminants (Wang et al., 2021). Agricultural wastes (e.g., rice husks, sugarcane bagasse, pine leaves) achieve >90% removal efficiency for dyes (methylene blue, reactive orange, rhodamine B) at 5–300 mg/L concentrations, proving viable as activated carbon substitutes (Elsherif et al., 2018b; Gutiérrez et al., 2021; Hamedi et al., 2023; Sanou et al., 2024).

Researchers continue exploring sustainable, low-cost adsorbents with favorable surface properties and regeneration potential for large-scale water treatment. Palm trees, abundant in tropical regions like the Middle East, offer promising solutions. Libya alone hosts ~20 million palms across 23,000 hectares, yielding over 20 kg of dry residues per tree annually (Racchi & Camussi, 2018). Palm fiber's high functional group density (especially from southern Libya) enhances its adsorption capacity, making it an eco-friendly biosorbent (Geddeda & Abdassalam, 2010). Modified date palm residues have demonstrated effective removal of heavy metals and dyes (Din et al., 2024; Melliti et al., 2021; Rambabu et al., 2021), positioning them as sustainable alternatives for industrial wastewater treatment.

This study evaluates sustainable, bio-based sorbents from palm fibres for dye removal in water treatment. We compare the adsorption performance of Acid-Base Treated Palm Fibres (A-BTPF) and Chemically Modified Palm Fibres (CMPF), prepared via H_2SO_4/NaOH and CS_2 treatments respectively. FTIR confirmed C-S group formation in CMPF, enhancing adsorption capacity. Batch experiments analyzed removal efficiency under varying conditions (pH, temperature, dose, contact time, concentration). Adsorption mechanisms were characterized through kinetic, isotherm, and thermodynamic studies. Results demonstrate CMPF's superior performance as an eco-friendly alternative to conventional sorbents.

Materials and methods

Neutral Red (NR), Methyl Green (MG), sodium hydroxide, hydrochloric acid, sulphuric acid, and carbon disulphide were among the analytical-grade chemical reagents that were purchased from Merck Darmstadt, Germany. They were used without any additional purification. Figure 1 shows both the NR and MG dyes' chemical structures. Double-distilled water was utilized to prepare all solutions.

Figure 1
Structure of dyes: (a) methyl green (b) neutral red (Al-Saeedi et al., 2023; Ibrahim et al., 2021)

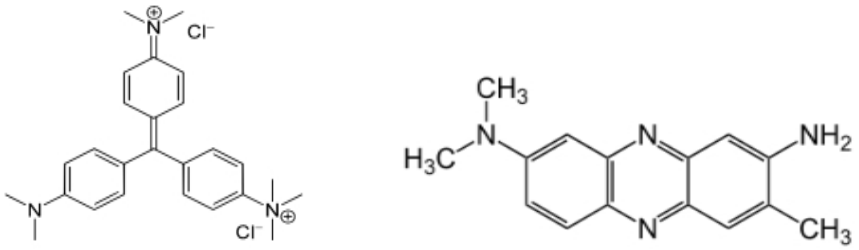

(a) (b)

Preparation of adsorbent materials: Palm fibers were sourced from Galu City, southern Libya. The fibers were initially cut into 1 cm segments, followed by thorough washing with double-distilled water (DDW) to eliminate impurities. Subsequent drying at 150 ± 2°C for 48 hours and cooling to room temperature were performed.

To prepare the first adsorbent material, the dried fibers were ground and sieved to obtain particles smaller than 75 μm and this material is designed as dry palm fiber powder (DPFP). A 50 g sample of this powder was subjected to acid treatment using 100 ml of 4 M H_2SO_4 for 60 minutes, followed by overnight incubation. This acid treatment facilitates ring-opening reactions, as reported by Homagai et al. (2010). After being acid-treated, the material was cleaned with DDW to remove any remaining excess acid, and then dried at 70 ± 2°C. Lastly, 200 ml of 4 M NaOH solution was added to 25 g of the acid-treated powder, agitated for 60 minutes, and then left overnight. The resulting product, labelled as Acid-Base Treated Palm Fibers (A-BTPF), was filtered, washed, and dried at 70 ± 2°C.

To prepare the second adsorbent material, the previously obtained A-BTPF was further treated with 25 ml of CS_2, stirred for 3 hours, and allowed to stand overnight. The resulting product was filtered, washed, and dried at 70 ± 2°C. This chemically modified material, labelled as Chemically Modified Palm Fibers (CMPF), was employed as an adsorbent. The synthetic procedure for CMPF was adapted from Pathania et al., 2017.

Characterization of adsorbent materials: FT-IR spectroscopy of the DPFP, A-BTPF, and CMPF adsorbents was carried out using an FT-IR Spectrometer fitted with a universal ATR sample attachment from PerkinElmer.

The Point of Zero Charge (pH_{PZC}) is the pH at which the net surface charge of the adsorbent becomes neutral, meaning the positive and negative surface charges are balanced. This property indicates the acidic or basic nature of the adsorbent surface. Below the pH_pzc, the surface carries a positive charge, while above it, the surface is negatively charged.

The Madadgar et al. (2023) method was used to determine the pH_{pzc}. In six Erlenmeyer flasks, 50 mL of a 0.01 M NaCl solution and 0.15 g of the biosorbent was mixed. The proper amounts of HCl or NaOH were added to each mixture to adjust its pH down to 2, 4, 6, 8, 10, and 12. Each mixture was shaken for 24 hours at room temperature before its final pH was determined. The pH_{pzc} was identified as the point of intersection of a plot that showed the change in final pH vs beginning pH.

Dyes adsorption efficiency and capacity: The adsorption behavior of methylene green and neutral red onto both A-BTPF and CMPF adsorbent materials was examined and assessed by determining the adsorption efficiency (%E) and adsorption capacity (Q_e) using the following equations (Elsherif et. al., 2017):

$$Q_e = \frac{(C_0 - C_e) * V}{M} \quad (1)$$

$$\%E = \frac{(C_0 - C_e)}{C_0} * 100 \quad (2)$$

where V is the solution's volume in L; M is the mass of the adsorbent material in g; Q_e is the amount of adsorbed dye in mg/g; C_o is the initial dye concentration in mg/L; and C_e is the equilibrium dye concentration in mg/L. UV-Vis spectrophotometry (Molecular Absorption Spectrophotometer 6305 from JENWAY) was used to measure the dyes concentrations both before and after adsorption. In an aqueous solution with defined initial and equilibrium concentrations, a decline in adsorption was observed at 540 nm for NR and at 640 nm for MG. A calibration curve was used to convert the adsorption to concentration.

Adsorption experiments: Batch adsorption studies evaluated NR and MG dye removal using A-BTPF and CMPF, examining key parameters (contact time, adsorbent dose, pH, initial concentration, temperature) as outlined in Table 1. Each trial combined a fixed adsorbent mass with 50 mL dye solution in 100 mL Erlenmeyer flasks, agitated at 150 rpm in a water bath shaker. pH adjustments used HCl/NaOH solutions. After reaching equilibrium, samples were filtered and analyzed via UV-Vis spectrophotometry at λ_{max} to determine residual dye concentrations, enabling calculation of removal efficiency and adsorption capacity.

Table 1
Operating Condition Variations for Adsorption Experiments

Investigated parameter	Variation range
Reaction time (min)	15 – 90
pH	2.0 – 7.0* 2.0 – 12.0**
Adsorbent mass (g)	0.02 – 0.14
Initial dye concentration (ppm)	9.0 – 18.0* 4.5 – 8.5**
Temperature (K)	298 – 318

**for NR dye, **for MG dye*

Equilibrium isotherms and kinetic investigations: The adsorption of NR and MG onto CMPF was analyzed using linear isotherm and kinetic models (Table 2) for initial concentrations (9-18 mg/L) and contact times (15-90 min). These models, with their equations and parameters, helped identify the adsorption mechanism and determine the best-fitting model for our system.

Table 2

Equations and Parameters of Isotherm and Kinetic Models (Alkherraz et al., 2023; Dural et al., 2011; Elsherif et al., 2019; Elsherif et al., 2020; Hammad et al., 2024)

Isotherms Models			
Model	Linear equation	No.	Parameters
Langmuir	$\frac{1}{Q_e} = \frac{1}{Q_m} + \frac{1}{bQ_mC_e}$	(3)	Q_e (mg/g): adsorption capacity C_e (mg/L): Equilibrium concentration b (L/mg): Langmuir constant Q_m (mg/g): Maximal adsorption capacity
Freundlich	$\log Q_e = \log K_F + \frac{1}{n}\log C_e$	(4)	K_F (mg/g (L/mg)1/n): Freundlich adsorption constants n: Empirical constant
Temkin	$Q_e = B_T \ln K_T + B_T \ln C_e$	(5)	B_T (J/mol): Temkin adsorption constant K_T (L/mg): Temkin isotherm constant
D-R	$\log Q_e = \log Q_m - \beta \varepsilon^2$ $\varepsilon = RT \log\left(1 + \frac{1}{C_e}\right)$	(6) (7)	B (mol²/J²): D-R constant ε (J/mol): Polanyi potential R (kJ/mol K): Gas constant T (K): absolute Temperature
Kinetic Models			
Model	Linear equation	No.	Parameters
Pseudo-first-order	$\ln(Q_e - Q_t) = \ln(Q_e) - \frac{k_1}{2.303} * t$	(8)	Q_t (mg/g): Capacity at t time k_1 (min^{-1}): Adsorption rate constant
Pseudo-second-order	$\frac{t}{Q_t} = \frac{1}{k_2 * Q_e^2} + \frac{1}{Q_e}$	(9)	k_2 (g/mg.min): Adsorption rate constant.
Intra-particle diffusion	$Q_t = k_d t^{1/2} + C$	(10)	k_d (mg/g $min^{1/2}$): Intraparticle diffusion rate constant
Elovich equation	$Q_t = \frac{1}{\beta}\ln(\alpha\beta) + \frac{1}{\beta}\ln t$	(11)	β (g/mg): Amount of surface covering and activation energy α (mg/g min): Initial sorption rate

Thermodynamic investigation: The analysis of thermodynamics is crucial to understanding adsorption processes because it provides significant insights into the spontaneity, sustainability, and nature of the adsorption interactions. Key thermodynamic parameters that impact the total energy dynamics that can be calculated to assess the favorability of the adsorption process include Gibbs free energy (ΔGº, kJ/mol), entropy change (ΔSº, J/mol.k), and enthalpy change (ΔHº, kJ/mol). These parameters can be determined via the following formulas (Alkherraz et al., 2023), which allow for a comprehensive evaluation of the process's thermal characteristics:

$$\Delta G = \Delta H - T\,\Delta S \quad (12)$$

$$\Delta G = -RT\,\mathrm{Ln}\,K_d \quad (13)$$

To accurately determine the apparent equilibrium constant of adsorption (K_d), it is essential to use the standard thermodynamic equilibrium constant calculated based on activity, rather than concentration, to reflect the true thermodynamic behavior of the system (Alkherraz et al., 2020b):

$$K_d = \frac{Q_e}{C_e} \quad (14)$$

The interrelationship between entropy, enthalpy, and the distribution coefficient (K_d) is presented by Van't Hoff equation (Alkherraz et al., 2020b), illustrating how these factors collectively contribute to the adsorption mechanism:

$$\ln K_d = \frac{\Delta S}{R} - \frac{\Delta H}{RT} \quad (15)$$

Results and discussion

Adsorbent characterization

FTIR spectra: FTIR spectroscopy was used for analysing chemically modified palm fibres (CMPF), acid-base treated palm fibres (A-BTPF), and dried palm fibre powder (DPFP). A prominent absorption band was seen in all samples (Figures 2a, 2b, and 2c) at about 1020 cm^{-1}. This band was likely caused by inorganic silicates found in the palm fibre samples and might be ascribed to either C–O stretching vibrations or Si–O vibrations. Furthermore, in each case, a broad peak at 3351 cm^{-1} that corresponded to O–H stretching vibrations was seen. The hydroxyl (OH) groups on the carbon surface and any remaining moisture may be partially responsible for this peak.

Figures 2a, 2b, and 2c show the FT-IR spectra of palm fibre adsorbents that were processed differently, such as DPFP, A-BTPF, and CMPF. The structural and chemical alterations brought about by the different treatments are highlighted in the analysis.

Figure 2
Characterization of different adsorbents by FTIR

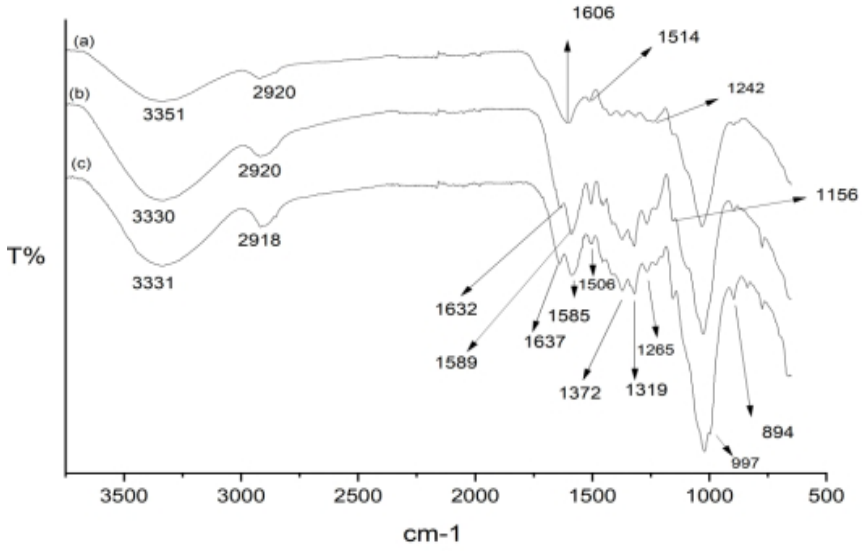

Aromatic, C–C, C–O, and C–O–C groups are present in the DPFP spectrum (Figure 2a), which is typical of characteristics derived from plants. The C–C stretching vibrations are represented by a band at 1606 cm^{-1}, the C–O stretching vibrations by a band at 1514 cm^{-1}, and the C–O–C and aromatic stretching vibrations by a band at 1242 cm^{-1}. These are significant absorption peaks. These peaks confirm the inherent structural properties of the untreated palm fibre.

The A-BTPF spectrum (Figure 2b) reveals significant structural modifications, with original DPFP peaks shifting to higher wavenumbers (1589, 1504, and 1265 cm^{-1}) and new aldehyde group vibrations appearing at 1632 (C=O), 1372, and 1319 cm^{-1} (C-O). These changes confirm the acid-base treatment successfully introduced new functional groups, altering the palm fiber's chemical properties.

The CMPF spectra (Figure 2c) reveal successful xanthation, evidenced by new C–S (997 cm^{-1}) and C=S (894 cm^{-1}) stretching vibrations. The C=S group further confirms xanthate incorporation through a broad absorption band (1632–1156 cm^{-1}), demonstrating effective chemical modification of the palm fiber.

pH at the point of zero charge: The pH_{PZC} (point of zero charge), where the adsorbent surface maintains charge neutrality, was ~9.0 for DPFP (Figure 3). Below this pH, the surface becomes positively charged; above it, negatively charged (Abate et al., 2023; Caldeira et al., 2018).

Figure 3
Point of zero charge (pH_{pzc}) for DPFP

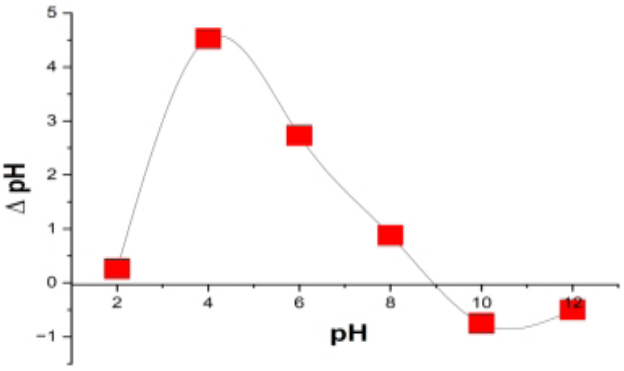

The pH_{PZC} critically influences adsorption behavior. Above pH 9.0, DPFP's negatively charged surface enhances cationic dye uptake. This explains methyl green's (MG) increased adsorption at higher pH, as its protonated amine groups (Figure 1) facilitate electrostatic attraction to the adsorbent surface.

On the other hand, the adsorption behaviour varies for neutral dyes like neutral red. Neutral red is protonated in acidic solutions, which causes the dye molecules and hydronium ions to compete for the adsorption sites on the adsorbent. The adsorption effectiveness may be decreased by this competition, emphasising the need of pH optimisation for various adsorbate types (Ben-Ali et al., 2017).

Effect of pH: Solution pH critically influences dye adsorption by modifying surface charges and adsorbent-dye interactions (Alver et al., 2020; Madadgar et al., 2023). For neutral red (NR), both removal efficiency (%R) and adsorption capacity (Q_e) increased with pH, peaking at pH 4. As shown in Figures 4A & 4B, CMPF achieved 72% removal while A-BTPF reached 61% at this optimal pH.

Removal efficiency and dye uptake declined as pH increased beyond 4 (Figure 4B), consistent with previous reports (Xu et al., 2006). At pH < 4, excessive surface protonation hindered dye ion access. CMPF capacity decreased from 10 to 7.8 mg/g (pH 3-7), while A-BTPF dropped from 7.7 to 6.6 mg/g. This reduction stems from deprotonation in alkaline conditions, creating electrostatic repulsion between dye molecules and the adsorbent surface (Ramesha, 2011). Additional adsorption mechanisms included hydrophobic interactions, van der Waals forces, and hydrogen bonding.

Figure 4 (C and D) illustrates how the methyl green (MG) dye's removal percentage (%R) and adsorption capacity (Q_e) increased with pH, peaking at pH 10 for both A-BTPF and CMPF. At this pH, CMPF and A-BTPF had the highest removal efficiencies of 68% and 61%, respectively, indicating that a basic medium is the best option for adsorption. Since there were no discernible variations in the biosorption capability above pH 10, further research was conducted at this pH.

The pH_{PZC} (9.0) governs MG dye adsorption by controlling surface charge. Below pH 9.0, protonation creates a positively charged surface that repels cationic MG, reducing uptake. Above pH 9.0, deprotonation generates negative surface charges that enhance electrostatic attraction to MG, significantly improving adsorption efficiency, as demonstrated by Belgacem et al. (2022).

Further evidence that CMPF continuously demonstrated greater removal efficiency and biosorption capacity than A-BTPF across all pH levels can be found in Figures 4A, 4B, 4C, and 4D. This demonstrates how the biosorption capabilities of palm fibre for neutral red dye were successfully improved by CS_2 treatment.

Effect of adsorbent dose: Adsorbent dosage significantly influences dye removal efficiency by determining available adsorption sites for a given dye concentration (Elsherif et al., 2024a). Figure 5 (A-D) demonstrates the relationship between biosorbent dose and dye uptake capacity.

The study revealed an inverse relationship between adsorbent dosage and removal efficiency. At the lowest tested dose (0.02 g), A-BTPF and CMPF achieved 70% and 81% NR removal, and 84% and 91% MG removal, respectively. This enhanced performance at lower doses (≤0.14 g) results from greater surface area availability and unoccupied active sites, consistent with Abuzerr et al. (2018).

Conversely, as the adsorbent dose increases, the adsorption capacity decreases. The decline is most likely due to particle aggregation, which reduces the surface area available for adsorption and reduces the efficacy of dye removal (Elsherif et al., 2024b).

Figure 4
Effect of pH on adsorption of NR (A & B) and MG (C & D) onto both A-BTPF and CMPF biosorbents

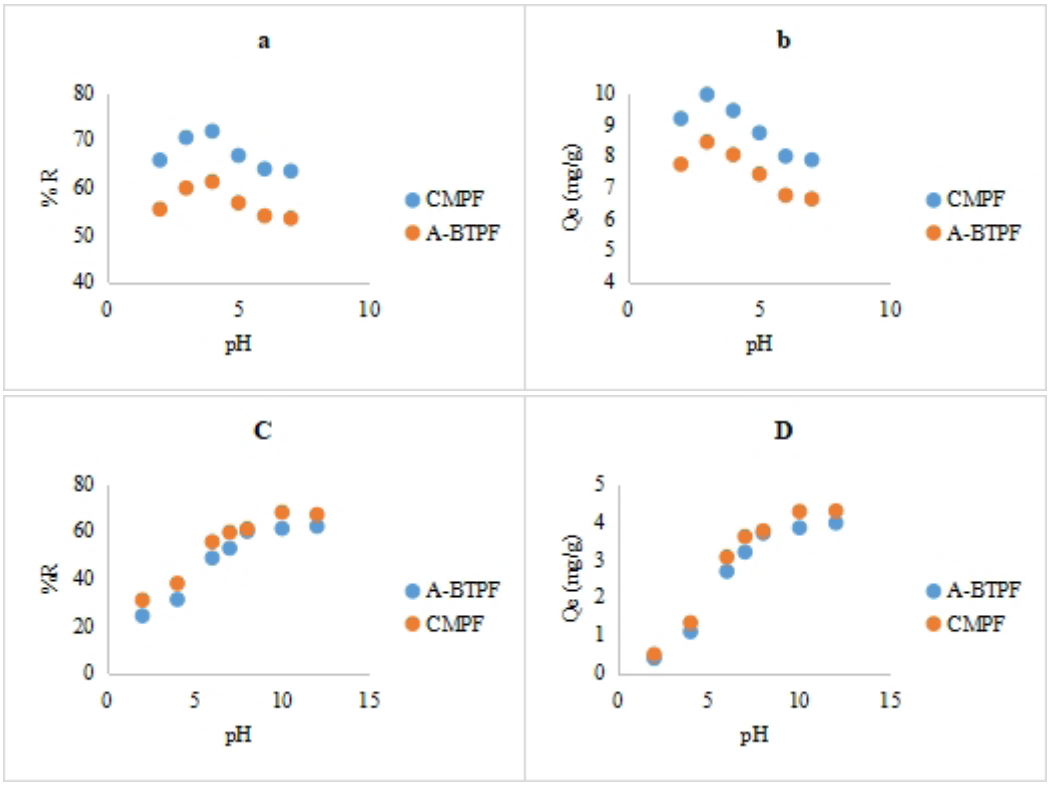

Effect of contact time: Contact time significantly affects adsorption equilibrium between dyes and biosorbents. Tests with A-BTPF and CMPF at 15–90-minute intervals (Figure 6A-B) revealed peak removal efficiencies at equilibrium: 75% (MG) and 65% (NR) for A-BTPF versus 83% and 76% for CMPF. Prolonged contact beyond this point marginally reduced removal rates, suggesting optimal adsorption times.

The results align with Ansari and Mosayebzadeh's findings (2010), demonstrating increasing dye removal with contact time until equilibrium, beyond which additional time yields diminishing returns. Adsorption occurs rapidly initially, then slows as active sites become occupied.

CMPF showed rapid adsorption within the first hour, followed by equilibrium plateauing as active sites became saturated (Alkherraz et al., 2022). Extended contact led to negligible additional uptake, suggesting potential desorption. Optimal contact times were established at 45 minutes for NR and 60 minutes for MG in subsequent tests.

Effect of initial concentration: Initial dye concentration significantly affects removal efficiency by influencing interactions with adsorbent active sites. Studies examined MG (4.5-8.5 ppm) and NR (9-18 ppm) adsorption on A-BTPF and CMPF, with results shown in Figures 7A-D.

Both removal efficiency (%R) and adsorption capacity (Q_e) of NR dye increased with concentration up to 13.5 ppm. For MG dye, CMPF achieved 75% removal (5.5 mg/g) versus A-BTPF's 65% (4 mg/g). These results agree with Alardhi et al. (2023), demonstrating enhanced adsorption at higher concentrations due to increased driving force. The enhanced adsorption at higher concentrations stems from stronger electrostatic dye-adsorbent interactions. However, MG adsorption plateaued above 6.5 ppm due to site saturation, consistent with Pietrzyk et al. (2023), who attributed superior low-concentration removal to higher site availability. Across all tests, CMPF outperformed A-BTPF in both removal efficiency and capacity, confirming its superior biosorbent performance for NR and MG dyes.

Figure 5
Effect of adsorbent dose on adsorption of NR (A & B) and MG (C & D) onto both A-BTPF and CMPF biosorbents

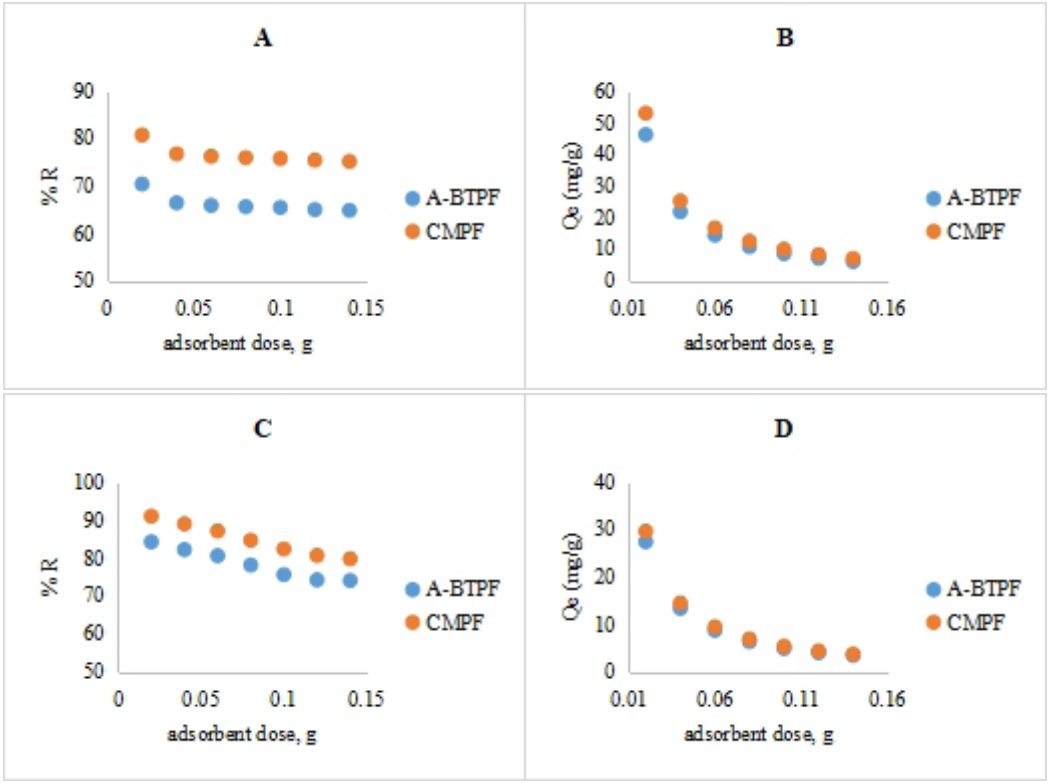

Figure 6
Effect of contact time on adsorption of NR (A) and MG (B) onto both A-BTPF and CMPF biosorbents

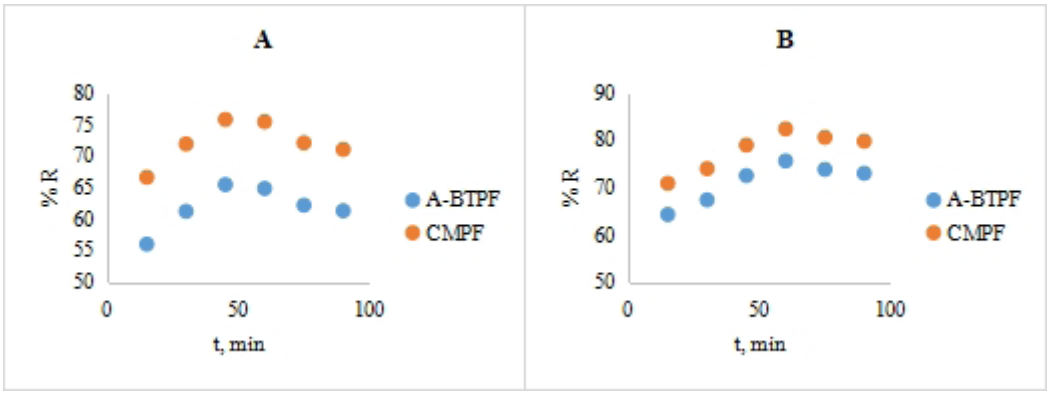

Figure 7
Effect of initial dye concentration on adsorption of NR (A & B) and MG (C & D) onto both A-BTPF and CMPF biosorbents

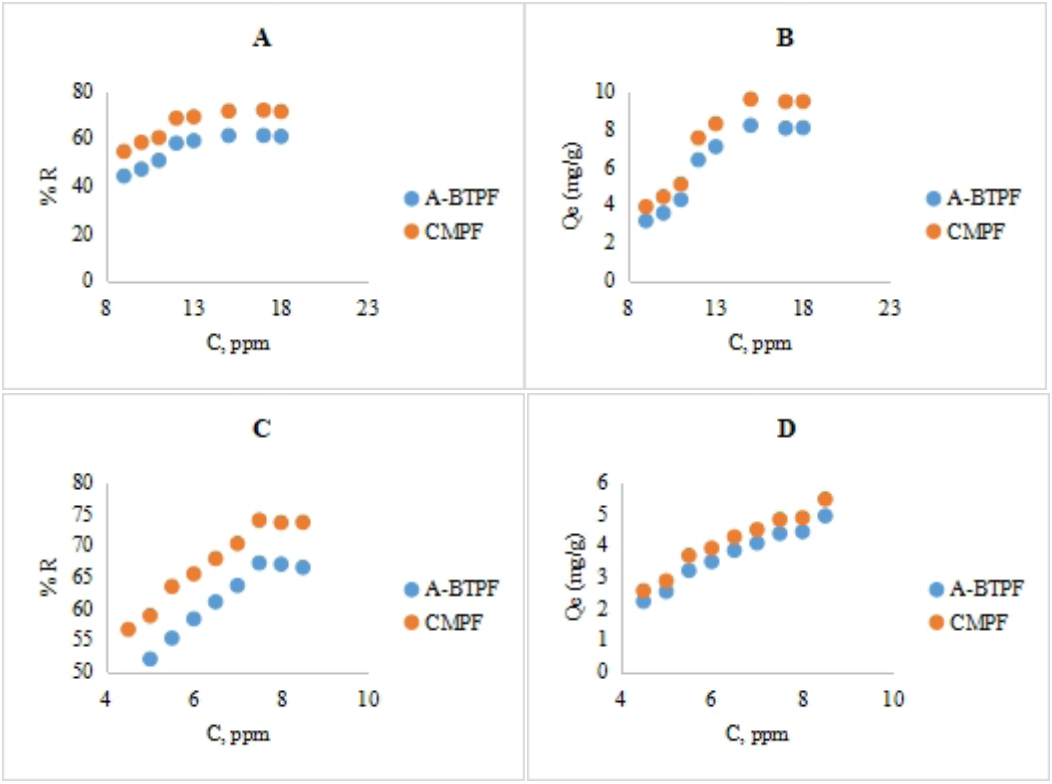

Effect of temperature: The influence of temperature on adsorption capacity is governed by both adsorbent characteristics and experimental conditions, reflecting either endothermic or exothermic behavior (Budi et al., 2018; Elsherif et al., 2024b). Our batch experiments (25-45°C) demonstrated a gradual improvement in removal efficiency with increasing temperature (Figures 8A-B). For neutral red (NR), A-BTPF showed an increase from 70% to 74% removal, while CMPF improved from 81% to 84%. Similarly, methyl green (MG) removal rose from 84% to 86% for A-BTPF and from 90% to 93% for CMPF over the same temperature range, confirming the endothermic nature of the process (Abate et al., 2023). This modest temperature dependence suggests physical adsorption dominates, where enhanced molecular mobility facilitates access to active sites. However, the relatively small effect indicates that other factors – particularly dye chemistry and adsorbent surface properties – play more significant roles in determining adsorption efficiency (Alkherraz et al., 2023; Hammad et al., 2024; Olusegun et al., 2023).

From the previous investigations, carbon disulphide (CS_2)-treated palm fibre showed a notable increase in adsorption capacity for Neutral Red dye following the optimisation process. CMPF's exceptional performance highlights its potential as a strong biosorbent. Accordingly, we will concentrate on examining equilibrium isotherms in order to better understand its adsorption behaviour. These are important indicators of the adsorbent's surface characteristics, adsorption capacity, and interaction mechanisms.

Figure 8
Effect of temperature on adsorption of NR (A) and MG (B) onto both A-BTPF and CMPF biosorbents

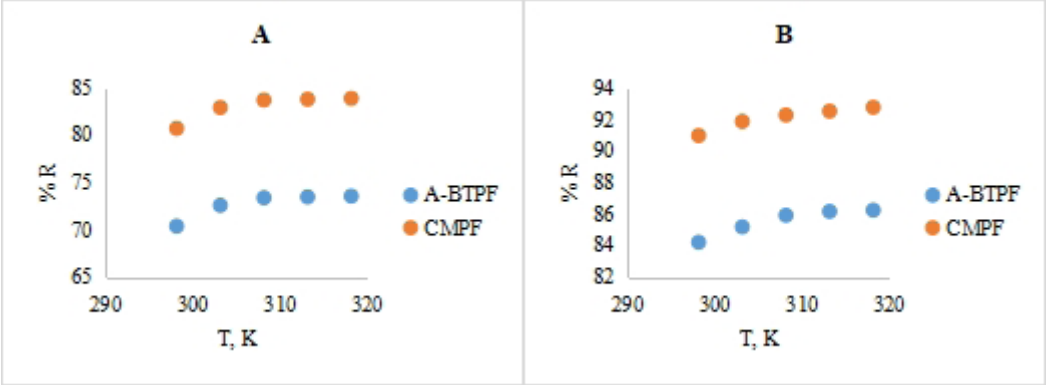

Equilibrium adsorption isotherms: Understanding the adsorption mechanism and designing and optimising adsorption systems depend heavily on equilibrium data, which are typically represented by adsorption isotherms. The most popular isotherm models were used in this investigation to assess the chemically treated palm fiber's (CMPF) adsorption capabilities. Among the models utilised are: The Freundlich isotherm, which provides information about the maximum adsorption capacity, the Langmuir isotherm, which assumes monolayer adsorption onto a surface with a finite number of identical sites; the Temkin isotherm, which describes adsorption on heterogeneous surfaces and indicates the adsorption intensity and capacity; the Dubinin-Radushkevich (D-R) isotherm, which takes into account the effects of indirect adsorbate-adsorbent interactions on adsorption and suggests a uniform distribution of binding energies; and the energy of adsorption (Alkherraz et al., 2023; Elsherif et al., 2022; Matić et al., 2024).

Langmuir isotherm model: The Langmuir adsorption isotherm model was used to evaluate the adsorption behaviour of Methyl Green (MG) and Neutral Red (NR) dyes onto CMPF. Using the linear version of the Langmuir equation (equation 3), the slope and intercept of the plot of $1/Q_e$ vs 1/Ce (Figures 9A and 9B) were used to calculate the parameters Q_m (maximum adsorption capacity) and b (Langmuir constant). The correlation coefficient R^2 and the values of Q_m and b are shown in Table 3.

As demonstrated by the high correlation coefficients (R^2) of 0.9935 for NR dye and 0.9869 for MG dye, which show a strong alignment with the experimental data, the Langmuir model successfully characterises the adsorption process for both dyes. Indicating a greater contact between NR dye and the adsorbent surface, the Langmuir constant b, which measures the affinity between the adsorbent and the adsorbate, was higher for NR dye (0.730 L/mg) than for MG dye (0.513 L/mg). Furthermore, the Langmuir isotherm yielded maximum adsorption capacities (Q_m) of 19.88 mg/g for NR dye and 7.45 mg/g for MG dye, which closely matched the values of 14.5 mg/g and 9.5 mg/g, respectively, that were found experimentally. These results show that the observed adsorption behaviour and model predictions are consistent.

The dimensionless separation factor R_L, which is defined by the equation (Harouache et al., 2024), can be used to assess the favourability of the adsorption process because the experimental results closely matched the linear form of the Langmuir model:

$$R_L = \frac{1}{1 + bC_0} \qquad (16)$$

The R_L values for both dyes ranged between 0 and 1, specifically from 0.07 to 0.13 for NR and from 0.21 to 0.33 for MG, indicating that the adsorption process was favorable under the studied experimental conditions.

Figure 9
Langmuir isotherm plot of NR (A) and MG (B) dyes onto CMPF

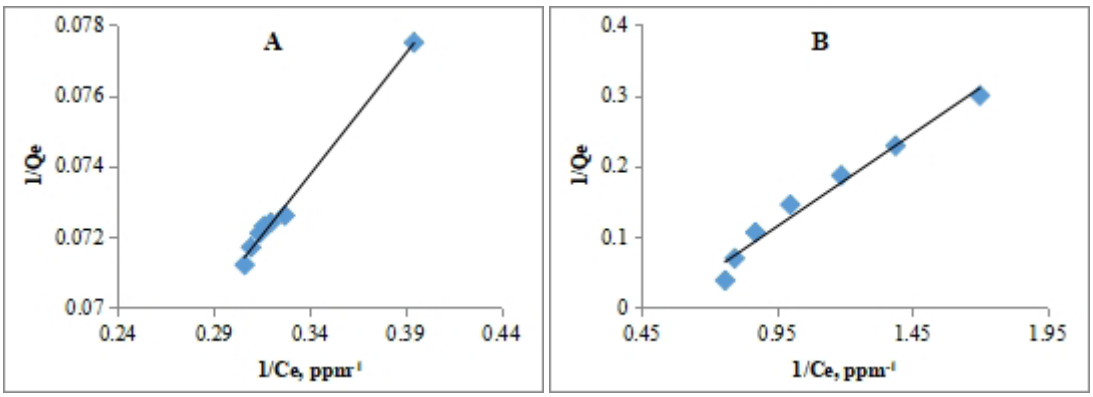

Freundlich isotherm model: The Freundlich isotherm characterises a physical adsorption process that occurs in several layers with comparatively weak connections, assuming heterogeneity of the adsorption sites (Matić et al., 2024). Equation 4 was used to get the Freundlich equilibrium constants from the linear plot of Log Q_e vs. Log C_e, which is displayed in Figure 10 (A & B). Even though it is empirical, the Freundlich isotherm provides valuable insights into the behaviour of adsorption, particularly in heterogeneous systems. The parameter n indicates the adsorption intensity; lower n values often suggest chemical adsorption rather than physical adsorption (Elsherif et al., 2024a). As shown in Table 3, the n values derived from the Freundlich equation were 3.995 for NR dye and 0.634 for MG dye. For NR dye adsorption, the n value of 3.995 indicates a mostly physical contact, but the n value of 0.634 for MG dye shows a potential chemical interaction. The high R^2 values show that the Freundlich model fits well the experimental data quite well (0.9965 for NR and 0.9698 for MG).

Figure 10
Freundlich isotherm plot of NR (A) and MG (B) dyes onto CMPF

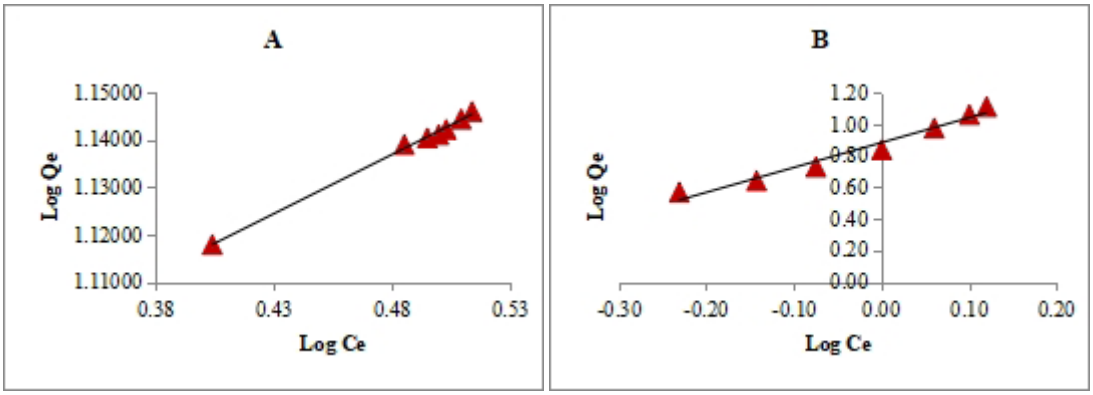

Temkin isotherm model: The Temkin isotherm states that the adsorption mechanism requires interactions between the adsorbent and adsorbate, the adsorption process assumes a uniform distribution of binding energy across the adsorbent surface, and the heat of adsorption decreases linearly as the adsorbent surface coverage increases (El-Shafie et al., 2023; Hammad et al., 2024). The isotherm constants (Figures 11A and 11B) obtained by plotting Q_e against Ln Ce are summarised as follows (Table 3): B_T = 2.127 and 17.14 J/mol (the heat of biosorption, which gives information on the energy changes during adsorption) and K_T = 215.8 and 1.804 L/mg (the equilibrium binding constant) for NR and MG dyes, respectively.

Stronger interactions between the adsorbent and adsorbate are indicated by a greater equilibrium

binding constant (K_T), which is linked to the maximal binding energy (Olusegun et al., 2023; Rashid et al., 2021). Additionally, the Temkin isotherm model and the experimental results show a good agreement, as indicated by the correlation coefficients (R^2) of 0.7381 for MG and 0.9234 for NR.

Figure 11
Temkin isotherm plot of NR (A) and MG (B) dyes onto CMPF

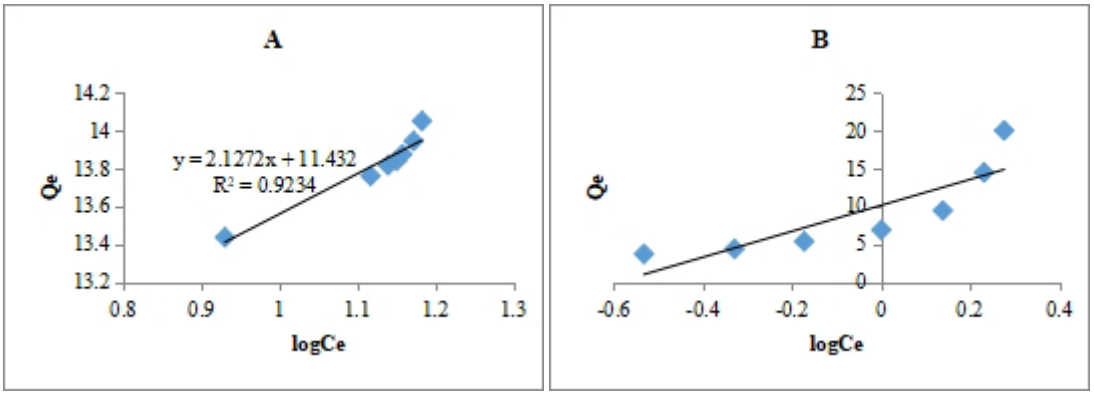

Dubinin-Radushkevich isotherm model: The Dubinin-Radushkevich (D-R) isotherm describes adsorption processes on adsorbents with heterogeneous surfaces or pore architectures and provides information on the free energy of adsorption. This theory states that micropore volume filling causes adsorption to occur (Elsherif et al., 2022; Memetova et al., 2023). Using the slope and intercept of the linear plots (Figures 12A and 12B), equations 6 and 7 were utilised to determine the D-R isotherm parameters, β and Q_m. An overview of the calculated values is given in Table 3. The experimental data and the D-R model showed a reasonable connection, with R^2 values of 0.9874 for NR dye and 0.8363 for MG dye.

Using Equation 17, the free energy of adsorption (E) per adsorbate molecule was calculated (Alkherraz et al., 2023):

$$E = \frac{1}{\sqrt{2k}} \qquad (17)$$

The energy required to extract a molecule from the surface is reflected in this energy. Physical adsorption ($E < 8$ kJ/mol) and chemical adsorption ($8 < E < 168$ kJ/mol) are distinguished by the equation. For NR dye, the values of E were 0.500 kJ/mol, while for MG dye, they were 0.408 kJ/mol. These findings demonstrate that both colours biosorption onto CMPF powder is essentially a physical adsorption process.

Figure 12
Dubinin-Radushkevich isotherm plot of NR (A) and MG (B) dyes onto CMPF

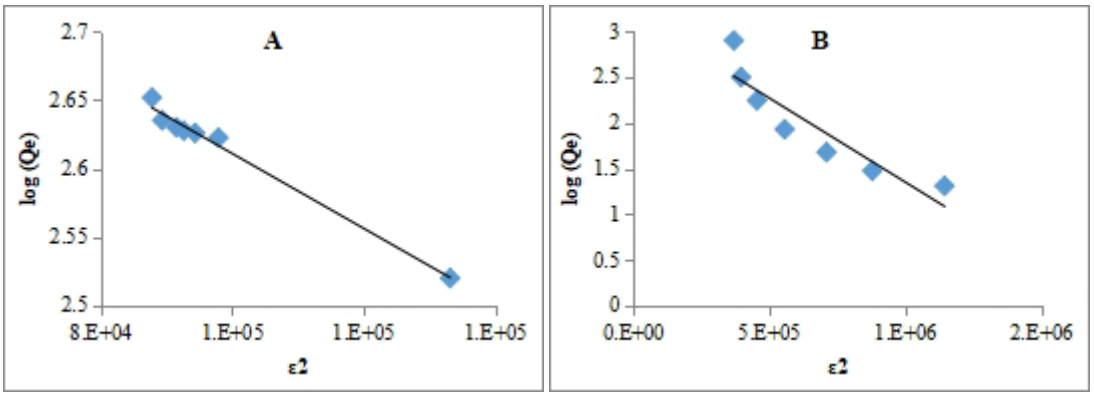

Table 3
Several isotherm models parameters for NR and MG adsorption onto CMPF

Model	Parameter	Value	
		NR	MG
Langmuir	b (L/mg)	0.730	0.513
	Q_m (mg/g)	19.88	7.452
	R^2	0.9935	0.9724
Freundlich	K_F (mg/g (L/mg)$^{1/n}$)	10.39	7.642
	n	3.995	0.634
	R^2	0.9965	0.9698
Temkin	B_T (J/mol)	2.127	17.14
	K_T (L/mg)	215.8	1.804
	R^2	0.9234	0.7381
Dubinin-Radushkevich	Q_m (mg/g)	17.64	24.25
	β (mol²/J²)	$3x10^{-6}$	$2x10^{-6}$
	E (kJ/mol)	0.408	0.500
	R^2	0.9874	0.8363

Comparison of Adsorption Performance and Mechanisms: The adsorption behavior of functionalized palm fibers (CMPF) for neutral red (NR) and methyl green (MG) aligns with trends observed in recent studies on dye removal using sustainable adsorbents. For NR, the Langmuir maximum adsorption capacity (Q_m = 19.88 mg/g) surpasses values reported for manganese-bismuth oxide composites (Q_m = 1.4 mg/g) (Al-Saeedi et al., 2023) and raw olive stone (Q_m = 4.5 mg/g) (Alardhi et al., 2023), though it is lower than high-performance materials like magnetite-supported avocado stone biochar (Q_m = 118.9 mg/g) (El-Shafie et al., 2023) or peanut shell activated carbon (Q_m = 109.89 mg/g) (Sanou et al., 2024). This positions CMPF as a competitive alternative for moderate-concentration dye removal, particularly given its reliance on low-energy chemical functionalization compared to energy-intensive activated carbon synthesis (Fito et al., 2023; Sanou et al., 2024). For MG, the lower Q_m (7.45 mg/g) may stem from electrostatic or steric mismatches, but contrasts with the high efficiency of magnetite-modified composites (El-Shafie et al., 2023), highlighting the need for tailored adsorbent-dye pairing.

The Freundlich model's dominance for NR (R^2 = 0.9965, n = 3.995) suggests heterogeneous multilayer adsorption, similar to findings for Congo Red on sugarcane bagasse (Elsherif et al., 2017) and MB on *Rumex abyssinicus* activated carbon (R^2 = 0.99 for Freundlich) (Fito et al., 2023). In contrast, MG's stronger alignment with the Langmuir model (R^2 = 0.9724) reflects monolayer adsorption trends observed for MB on olive stone (Alardhi et al., 2023) and cellulose-$Fe_{33}O_{44}$ (Pietrzyk et al., 2023). The low Dubinin-Radushkevich (D-R) mean free energy (E < 0.5 kJ/mol) confirms physical adsorption for both dyes, consistent with studies on rice husk (Alshorifi et al., 2022) and peanut shells (Sanou et al., 2024), but diverges from chemisorption mechanisms reported for Mn_3O_4-Bi_2O_3 composites (Al-Saeedi et al., 2023) and tella residue biosorbents (Abate et al., 2023).

Notably, CMPF achieves these results without the need for magnetic nanoparticle integration (El-Shafie et al., 2023; Pietrzyk et al., 2023) or extreme pH conditions (e.g., pH 9 for *Rumex abyssinicus* (Fito et al., 2023)), emphasizing its simplicity and scalability. While its adsorption capacity is lower than activated carbons (Sanou et al., 2024), its sustainability metrics – avoiding pyrolysis (e.g., 500°C for coconut husk biochar (Minh et al., 2023)) and utilizing palm fiber waste – align with circular economy principles, as advocated in studies on olive stone (Alardhi et al., 2023) and avocado stone biochar (El-Shafie et al., 2023).

Adsorption kinetic models: Adsorption kinetics examination is necessary to comprehend the adsorption process, including its pace and the principles underlying mass transfer. For effective adsorption system scaling up and system design optimisation, this information is essential (Minh et al., 2023; Qureshi et al., 2020). Kinetic assessments can also be used to determine the adsorbent's saturation time (Ahmed & Hameed, 2019; Qureshi et al., 2020). In adsorption studies, the pseudo-first-order (PFO), pseudo-second-order (PSO), Elovich, and intraparticle diffusion models are often employed kinetic models.

Pseudo first-order model: To utilise the integrated form of the pseudo-first-order kinetic model (Equation 8), the equilibrium sorption capacity, Q_e, must be determined. Therefore, it is often required to estimate Q_e by a trial-and-error approach in order to assess the model's kinetics. The plots for pseudo-first order are displayed in Figures 13A and 13B. The calculated parameters and the linear regression correlation coefficients (R^2) are shown in Table 4. For NR and MG dyes, the corresponding R^2 values of 0.7833 and 0.7862 indicate a reasonable but not very strong fit. This suggests that the experimental data may be better represented by alternative kinetic models. Additionally, as Table 4 illustrates, the computed sorption capacities (Q_e) do not match the experimentally determined values.

Figure 13
Pseudo first-order plot of NR (A) and MG (B) dyes onto CMPF

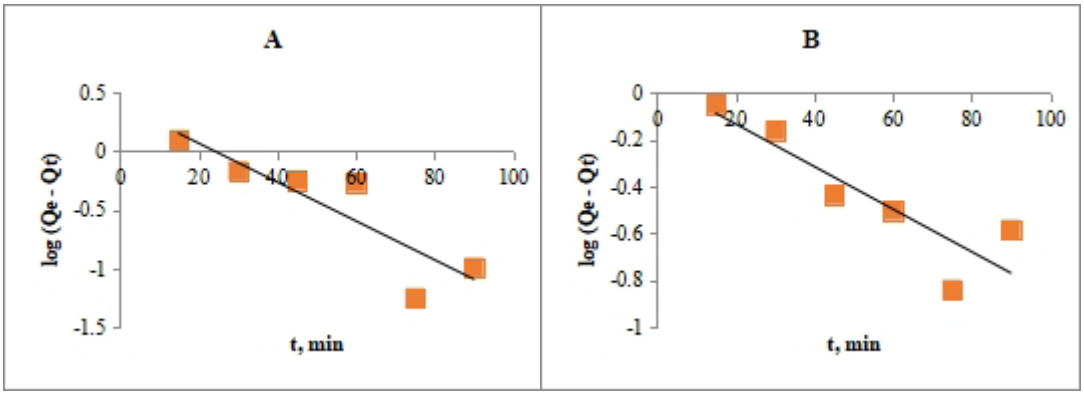

Pseudo second-order model: The plot of t/Q_t vs. t should show a linear relationship according to Equation 9, enabling it possible to determine Q_e and k_2 from the slope and intercept of the plot (Figures 14A and 14B). The calculated Q_e values, the pseudo-second-order rate constant (k_2), and the corresponding linear regression correlation coefficients (R^2) are summarised in Table 4. The correlation coefficients for the pseudo-second-order model were significantly higher than those for the pseudo-first-order model for NR and MG dyes, at 0.9988 and 0.9989, respectively. This indicates that the pseudo-second-order kinetic model provides a more accurate representation of the adsorption data.

The pseudo-second-order model states that the adsorption rate is determined by the square of the number of unoccupied sites (El-Hashani et al., 2018b). Furthermore, the high agreement between the estimated and empirically determined Q_e values further supports the usefulness of this model in understanding the adsorption process. These findings suggest that the adsorption of NR and MG dyes onto the adsorbent is most likely caused by chemisorption, which entails electron sharing or exchange between the adsorbent and the adsorbate.

Figure 14
Pseudo second-order plot of NR (A) and MG (B) dyes onto CMPF

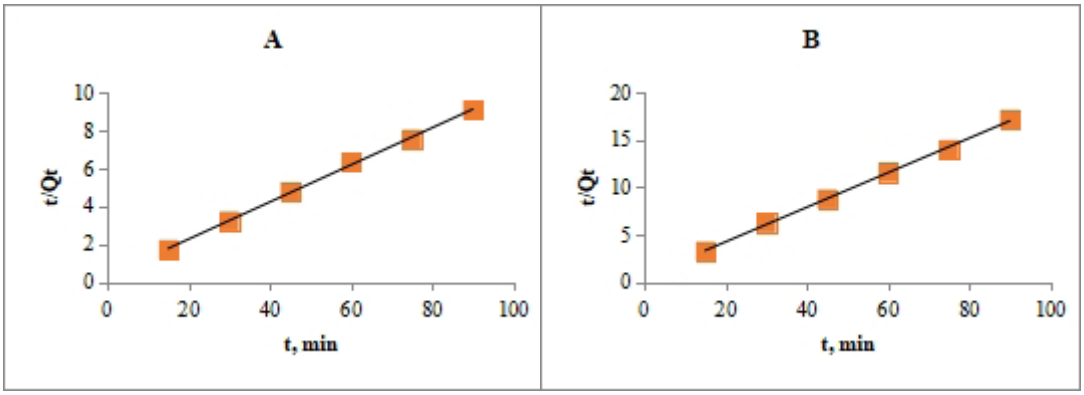

Intra-particle diffusion model: If intraparticle diffusion has a major impact on the adsorption process, a plot of Q_t vs $t^{1/2}$ should have a linear connection, as per the intraparticle diffusion hypothesis. Intraparticle diffusion is the only rate-controlling step if the resulting lines cross at the origin. On the other hand, it indicates that boundary layer control is also in operation and that the adsorption rate is being influenced by other mechanisms if the lines do not cross through the origin. This suggests that several processes may

be taking place at the same time and that intraparticle diffusion is not the only rate-controlling mechanism (Ahmed & Hameed, 2019; Si et al., 2015).

Equation 10 may be used to calculate the values of C_e (boundary layer thickness) and K_d (intraparticle diffusion rate constant) from the slope and intercept of the plot of Q_t versus $t^{1/2}$, as illustrated in Figures 15A and 15B. The lines' apparent departure from the origin demonstrates that the adsorption process is not only governed by intraparticle diffusion.

According to this result, the biosorption of NR and MG dyes onto CMPF powder is a complicated process that includes both surface biosorption and intraparticle diffusion as rate-limiting factors. The correlation coefficient values in Table 4 demonstrate that, in spite of this complexity, the model suited the experimental data very well.

Figure 15
Intra-particle diffusion plot of NR (A) and MG (B) dyes onto CMPF

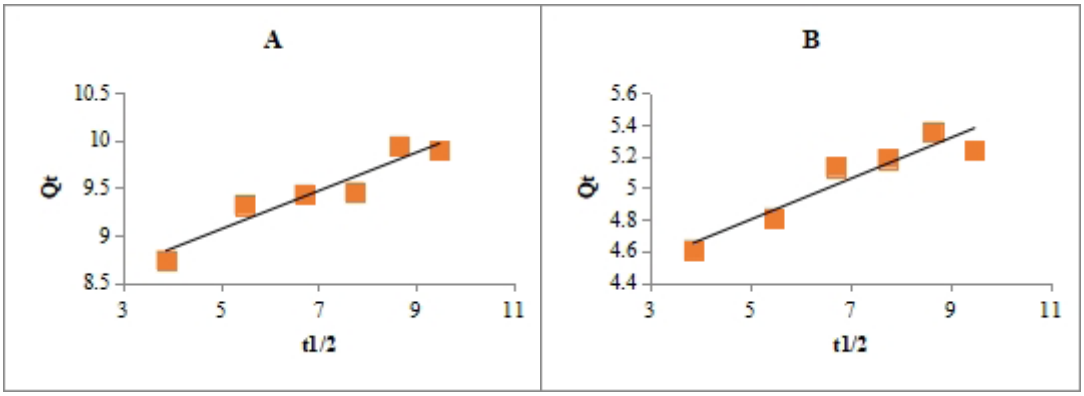

Elovich model: The adsorption of dissolved compounds from liquid solutions has been successfully represented using the Elovich equation, which was first created for chemical kinetics. Based on the slope and intercept of the Ln Q_t vs. Ln t plot (Figures 16A and 16B), Equation 11 was utilised to determine the Elovich parameters β (surface coverage-related desorption constant) and α (initial adsorption rate). The resulting results are summarised in Table 4, which gives β values for NR and MG dyes of 0.682 and 1.050 g/mg and α values of 93,100 and 21,800 mg/g.min.

The experimental data fits the Elovich model rather well, as indicated by the correlation coefficients (R^2) of 0.8894 for MG dye and 0.9109 for NR dye. This implies that, under the specified experimental conditions, the Elovich equation offers a satisfactory explanation of the adsorption kinetics for the dyes under study.

Figure 16
Elovich plot of NR (A) and MG (B) dyes onto CMPF

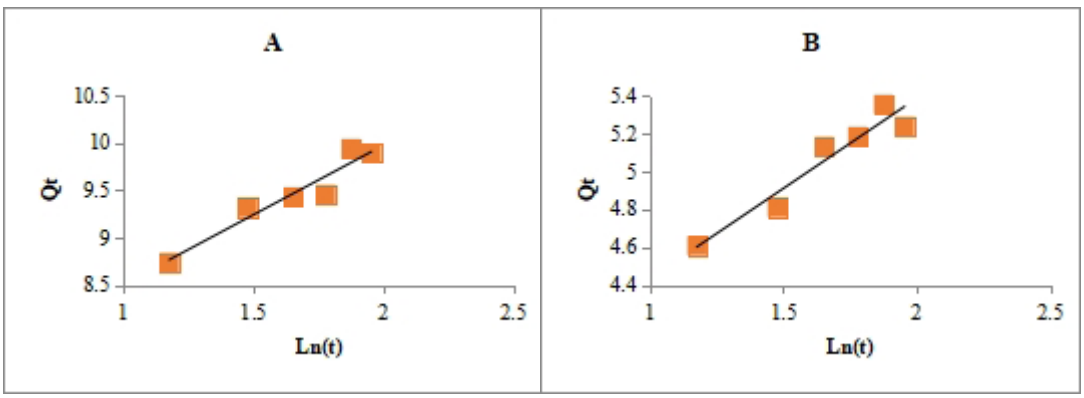

Table 4
Kinetic model parameters for NR and MG adsorption onto CMPF

Pseudo-first-order	k_1 (min^{-1})	Q_e (Cal.) (mg/g)	Q_e (Exp.) (mg/g)	R^2
NR	0.0382	2.52	10.00	0.7833
MG	0.0210	1.12	5.50	0.7862
Pseudo-second-order	k_2 ($g.mg^{-1}.min^{-1}$)	Q_e (Cal.) (mg/g)	Q_e (Exp.) (mg/g)	R^2
NR	0.0315	10.20	10.00	0.9988
MG	0.0559	5.48	5.50	0.9989
Elovich	β ($g.mg^{-1}$)	α ($mg.g^{-1}.min^{-1}$)	R^2	
NR	0.682	$9.31x10^4$	0.9232	
MG	1.050	$2.18x10^4$	0.9243	
Intra-particle diffusion	K_d ($mg.g^{-1}.min^{-1}$)	C_e (mg/g)	Q_e (Exp.) (mg/g)	R^2
NR	0.2013	8.06	10.00	0.9109
MG	0.1292	4.15	5.50	0.8894

Adsorption thermodynamics: To ascertain the spontaneity of a biosorption process, thermodynamic analysis is necessary. The Gibbs free energy change (ΔG), a crucial metric in determining whether a process happens spontaneously, can be calculated using the standard Van't Hoff equation (Equation 15). The enthalpy change (ΔH) and entropy change (ΔS) were determined using the slope and intercept of the Ln K_d against 1/T plot. Equation 12 was then utilised to compute the Gibbs free energy change for sorption.

The thermodynamic behaviour of NR and MG dye adsorption on CMPF was assessed by experiments conducted at different temperatures. The temperature-dependent adsorption efficiency of NR and MG dyes is depicted in Figures 8A and 8B. The slope and intercept of a linear plot of Ln K_d versus 1/T are shown in Figures 17A and 17B, and these were utilised to get the values of ΔH˚ and ΔS˚. Throughout the studied temperature range, a spontaneous adsorption process is demonstrated by the negative ΔG values at all temperatures. The adsorption process is endothermic and involves heat absorption, as indicated by the positive ΔH° values (12.783 and 8.662 kJ/mol).

The high affinity of the dye molecules for CMPF is further demonstrated by the positive ΔS° values (68.49 and 68.12 J/mol.K), which show enhanced disorder at the solid-liquid interface during adsorption. The negative ΔG° results further support the process' spontaneity. The combined results of ΔS° and ΔG° show that the reaction is thermodynamically favourable and proceeds spontaneously as a result of an increase in entropy.

Figure 17
Van't Hoff plot of NR (A) and MG (B) dyes onto CMPF

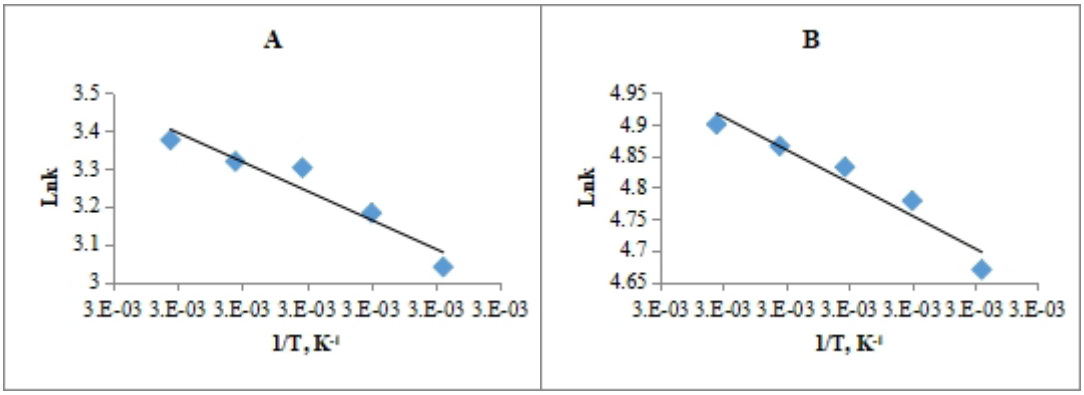

Table 5
Thermodynamic parameters for the adsorption of dyes onto CMPF

Dye	Temperature (K)	ΔG (kJ/mol)	ΔH^0 (kJ/mol)	ΔS^0 (J/mol. k)	R^2
NR	298	-7.637	12.783	68.49	0.9191
	303	-7.980			
	308	-8.322			
	313	-8.665			
	318	-9.007			
MG	298	-11.648	8.662	68.12	0.9357
	303	-11.989			
	308	-12.329			
	313	-12.670			
	318	-13.010			

Conclusion

This study examined two palm fibre-derived adsorbents: chemically modified palm fibre using carbon disulphide (CMPF) and acid-base treated palm fibre (A-BTPF), for dye removal from water. The results consistently demonstrated that CMPF exhibited superior adsorption capacity and efficiency compared to A-BTPF under all experimental conditions. The enhanced performance of CMPF, achieved through chemical modification with CS_2, introduced functional groups such as aldehydes and xanthates, significantly increasing its dye adsorption potential. FT-IR analysis confirmed the structural modifications caused by the chemical treatments.

pH investigations revealed that both adsorbents showed maximum removal efficiencies for neutral red (NR) at pH 4 and for methylene green (MG) at pH 10 (72% for CMPF and 61% for A-BTPF), indicating pH-dependent adsorption. The Langmuir isotherm model provided the best fit for the adsorption data, with maximum adsorption capacities of 19.88 mg/g for NR and 7.45 mg/g for MG, and high R^2 values of 0.9935 and 0.9869, respectively. Kinetic studies further confirmed that the adsorption process followed a pseudo-second-order model, with strong correlation coefficients of 0.9988 for NR and 0.9989 for MG.

Thermodynamic analysis indicated that the adsorption process is spontaneous and endothermic, driven by increased entropy, as evidenced by positive ΔH°, ΔS° values and negative ΔG° values across all temperatures. These findings underscore the potential of CMPF as an effective, sustainable biosorbent for dye removal, with its chemical modification offering enhanced adsorption properties compared to conventional treatments.

Authors contribution

A. El-Hashani: Conceptualization, Investigation, Methodology, Writing – original draft. K.M. Elsherif: Conceptualization, Methodology, Supervision, Funding acquisition, Resources, Writing – review & editing. G.F. Musbah: Investigation, Data curation, Formal analysis, Validation. A. Imragaa: Investigation, Resources, Software, Visualization. H.F. Emrayed: Formal analysis, Validation, Writing – review & editing.

Acknowledgement

We would like to deeply appreciate the University of Benghazi's Department of Chemistry, Faculty of Science, for all of their help and resources during this project. Their dedication to establishing an innovative and cooperative research atmosphere was crucial to this study's success.

Conflict of interest

The authors declare that they have no conflicts of interest.

References

1. Abate, G. Y., Nguyen, D. T. A., Alene, A. N., Kassie, D. A., Addiss, Y. A., & Mintesinot, S. M. (2023). Cereal based traditional beverage of tella residue (attela) as a green organic pollutant sorbent for methylene blue dye removal: Equilibrium, kinetics and thermodynamic studies. *Indian Journal of Chemical Technology, 30*(2), 151–164. https://doi.org/10.56042/ijct.v30i2.64532
2. Abuzerr, S., Darwish, M., & Mahvi, A. H. (2018). Simultaneous removal of cationic methylene blue and anionic reactive red 198 dyes using magnetic activated carbon nanoparticles: Equilibrium, and kinetics analysis. *Water Science and Technology, 2017*(2), 534–545. https://doi.org/10.2166/wst.2018.145
3. Ahmed, M. J., & Hameed, B. H. (2019). Insights into the isotherm and kinetic models for the coadsorption of pharmaceuticals in the absence and presence of metal ions: A review. *Journal of Environmental Management, 252*, Article 109617. https://doi.org/10.1016/j.jenvman.2019.109617
4. Alardhi, S. M., Salih, H. G., Ali, N. S., Khalbas, A. H., Salih, I. K., Cata Saady, N. M., Zendehboudi, S., Albayati, T. M., & Harharah, H. N. (2023). Olive stone as an eco-friendly bio-adsorbent for elimination of methylene blue dye from industrial wastewater. *Scientific Reports, 13*(1), Article 21063. https://doi.org/10.1038/s41598-023-47319-x
5. Alkherraz, A. M., Ali, A. K., & Elsherif, K. M. (2020a). Equilibrium and thermodynamic studies of Pb(II), Zn(II), Cu(II) and Cd(II) adsorption onto Mesembryanthemum activated carbon. *Journal of Medicinal Chemical Sciences, 3*(1), 1–10. https://doi.org/10.33945/SAMI/JMCS.2020.1.1
6. Alkherraz, A. M., Ali, A. K., & Elsherif, K. M. (2020b). Removal of Pb(II), Zn(II), Cu(II) and Cd(II) from aqueous solutions by adsorption onto olive branches activated carbon: Equilibrium and thermodynamic studies. *Chemistry International, 6*(1), 11–20.
7. Alkherraz, A. M., Elsherif, K. M., & Blayblo, N. A. (2023). Safranin adsorption onto Acasia plant-derived activated carbon: Isotherms, thermodynamics, and kinetic studies. *Chemistry International, 9*(4), 134–145. https://doi.org/10.5281/zenodo.812768
8. Alkherraz, A. M., Elsherif, K. M., El-Dali, A., Blayblo, N. A., & Sasi, M. (2022). Thermodynamic, equilibrium, and kinetic studies of safranin adsorption onto Carpobrotus edulis. *Asian Journal of Nanoscience and Materials, 5*(2), 118–131. https://doi.org/10.26655/ajnanomat.2022.2.4
9. Al-Saeedi, S. I., Areej, A., Qamar, M. T., Alhujaily, A., Iqbal, S., Alotaibi, M. T., Aslam, M., Qayyum, M. A., Bahadur, A., Awwad, N. S., Jazaa, Y., & Elkaeed, E. B. (2023). Isotherm and kinetic studies for the adsorption of methylene blue onto a novel Mn_3O_4–Bi_2O_3 composite and their antifungal performance. *Frontiers in Environmental Science, 11*, Article 1156475. https://doi.org/10.3389/fenvs.2023.1156475
10. Alshorifi, F. T., Ali, S. L., & Salama, R. S. (2022). Promotional synergistic effect of Cs–Au NPs on the performance of Cs–Au/$MgFe_2O_4$ catalysts in the catalysis of 3,4-dihydropyrimidin-2(1H)-ones and degradation of RhB dye. *Journal of Inorganic and Organometallic Polymers and Materials, 32*(10), 3765–3776. https://doi.org/10.1007/s10904-022-02389-8
11. Alver, E., Metin, A. Ü., & Brouers, F. (2020). Methylene blue adsorption on magnetic alginate/rice husk bio-composite. *International Journal of Biological Macromolecules, 154*, 104–113. https://doi.org/10.1016/j.ijbiomac.2020.02.330
12. Ansari, R., & Mosayebzadeh, Z. (2010). Removal of Basic Dye Methylene Blue from aqueous solutions using sawdust and sawdust coated with polypyrrole. *Journal of the Iranian Chemical Society, 7*(2), 339–350. https://doi.org/10.1007/BF03246019
13. Belgacem, A., Ould Brahim, I., Belmedani, M., & Hadoun, H. (2022). Removal of methyl green dye from aqueous solutions using activated carbon derived from cryogenic crushed waste tires. *Iranian Journal of Chemistry and Chemical Engineering, 41*(1), 207–219. https://doi.org/10.30492/ijcce.2020.121562.3966
14. Ben-Ali, S., Jaouali, I., Souissi-Najar, S., & Ouederni, A. (2017). Characterization and adsorption capacity of raw pomegranate peel biosorbent for copper removal. *Journal of Cleaner Production, 142*(4), 3809–3821. https://doi.org/10.1016/j.jclepro.2016.10.081
15. Bibikov, S. B., Sergeev, A. I., Barashkova, I. I., Isaykina, N. V., Gusev, A. A., & Semenov, A. N. (2024). The combined effects of electrochemical and ultrasonic treatment for water purification from pathogenic contaminants based on the example of Escherichia coli. *Biophysics, 69*(2), 272–277. https://doi.org/10.1134/S0006350924700325
16. Budi, A., Stipp, S. L. S., & Andersson, M. P. (2018). The effect of solvation and temperature on the adsorption of small organic molecules on calcite. *Physical Chemistry Chemical Physics, 20*(10), 7140–7147. https://doi.org/10.1039/c7cp06747j
17. Caldeira, A. S., Fabris, J. D., Nelson, D. L., & Damasceno, S. M. (2018). Removal of textile dye by adsorption on the cake as solid waste from the press-extraction of the macaúba (Acrocomia aculeata) kernel oil. *Eclética Química Journal, 43*(1), 48–53. https://doi.org/10.26850/1678-4618eqj.v43.1.48-53
18. Devi, R., Kumar, V., Kumar, S., Sharma, K., & Kumar, R. (2023). Recent advancement in biomass-derived activated carbon for wastewater treatment, energy storage, and gas purification: A review. *Journal of Materials Science, 58*(29), 12119–12142. https://doi.org/10.1007/s10853-023-08773-0
19. Din, H., Kiran, M., Haq, F., Osman, A. I., Khan, I. A., Aziz, T., Khan, A., & Jilani, S. (2024). Synergizing date palm seeds-derived oxidized activated carbon: Sustainable innovation for enhanced water retention, efficient wastewater treatment, and synthetic dye removal. *Chemical Engineering Research and Design, 204*, 212–227. https://doi.org/10.1016/j.cherd.2024.02.040
20. Djama, C., Bouguettoucha, A., Chebli, D., Amrane, A., Tahraoui, H., Zhang, J., & Mouni, L. (2023). Experimental and theoretical study of methylene blue adsorption on a new raw material, Cynara scolymus—A statistical physics assessment. *Sustainability, 15*(13), Article 10364. https://doi.org/10.3390/su151310364
21. Dural, M. U., Cavas, L., Papageorgiou, S. K., & Katsaros, F. K. (2011). Methylene blue adsorption on activated carbon prepared from Posidonia oceanica (L.) dead leaves: Kinetics and equilibrium studies. *Chemical Engineering Journal, 168*(1), 77–85. https://doi.org/10.1016/j.cej.2010.12.038
22. El-Hashani, A., Ben Khayal, N., & Elsherif, K. M. (2018a). Selective transport of aromatic compounds across parchment-supported Prussian blue membrane. *Chemical Methodologies, 2*(3), 194–203. https://doi.org/10.22631/chemm.2018.118847.1038

23. El-Hashani, A., Elsherif, K. M., Edbey, K., Alfaqih, F., Alomammy, M., & Alomammy, S. (2018b). Biosorption of Eriochrome Black T (EBT) onto waste tea powder: Equilibrium and kinetic studies. *Total Chemistry, 1*(3), 263–275.

24. Elsherif, K. M., Alkherraz, A. M., Edwards, H., & Mutawia, B. Y. A. (2024a). Congo red dye adsorption on dry green pea husk: Effects of process parameters and modeling approaches. *Environmental Health Engineering and Management Journal, 11*(3), 273–284. https://doi.org/10.34172/EHEM.2024.27

25. Elsherif, K. M., Alkherraz, A. M., Madri, A. H., Eldali, A., & Yaghi, M. M. (2024b). Kinetic, isotherm, and thermodynamic modeling of methylene blue adsorption by hibiscus plant waste derived biosorbents. *Journal of Chemical Health Risks, 14*(4), 727–740. https://doi.org/10.60829/jchr.2024.1977

26. Elsherif, K. M., El-Dali, A., Ewlad-Ahmed, A. M., Treban, A., & Alttayib, I. (2021). Removal of safranin dye from aqueous solution by adsorption onto olive leaves powder. *Journal of Materials and Environmental Science, 12*(3), 418–430.

27. Elsherif, K. M., El-Dali, A., Ewlad-Ahmed, A. M., Treban, A., Alqadhi, H., & Alkarewi, S. (2022). Kinetics and isotherms studies of safranin adsorption onto two surfaces prepared from orange peels. *Moroccan Journal of Chemistry, 10*(4), 639–651. https://doi.org/10.48317/IMIST.PRSM/morjchem-v11i1.32137

28. Elsherif, K. M., El-Hashani, A., & Haider, I. (2018a). Biosorption of Fe(III) onto coffee and tea powder: Equilibrium and kinetic study. *Asian Journal of Green Chemistry, 2*(4), 380–394. https://doi.org/10.22034/ajgc.2018.65163

29. Elsherif, K. M., El-Hashani, A., & Haider, I. (2018b). Equilibrium and kinetic studies of Cu(II) biosorption onto waste tea and coffee powder (WTCP). *Iranian Journal of Analytical Chemistry, 5*(2), 31–38. https://doi.org/20.1001.1.23832207.2018.5.2.5.4

30. Elsherif, K. M., El-Hashani, A., El-Dali, A., & Saad, M. (2014a). Ion-permeation rate of (1:1) electrolytes across parchment-supported silver chloride membrane. International *Journal of Chemical and Pharmaceutical Sciences, 2*(6), 890–897.

31. Elsherif, K. M., El-Hashani, A., El-Dali, A., & Musa, M. (2014b). Ion selectivity across parchment-supported silver chloride membrane in contact with multi-valent electrolytes. *International Journal of Analytical and Bioanalytical Chemistry, 4*(2), 58–62.

32. Elsherif, K. M., Ewlad-Ahmed, A. M., & Treban, A. (2017). Removal of Fe(III), Cu(II), and Co(II) from aqueous solutions by orange peels powder: Equilibrium study. *World Journal of Biochemistry and Molecular Biology, 2*(6), 46–51.

33. Elsherif, K. M., Haider, I., & El-Hashani, A. (2019). Adsorption of Co (II) ions from aqueous solution onto tea and coffee powder: Equilibrium and kinetic studies. *Journal of Fundamental and Applied Sciences, 11*(1), 65–81. https://doi.org/10.4314/jfas.v11i1.5

34. Elsherif, K. M., & Yaghi, M. M. (2017). Studies with model membrane: The effect of temperature on membrane potential. *Moroccan Journal of Chemistry, 5*(1), 131–138. https://doi.org/10.48317/IMIST.PRSM/morjchem-v5i1.6324

35. El-Shafie, A. S., Karamshahi, F., & El-Azazy, M. (2023). Turning waste avocado stones and montmorillonite into magnetite-supported nanocomposites for the depollution of methylene blue: Adsorbent reusability and performance optimization. *Environmental Science and Pollution Research, 30*(50), 118764–118781. https://doi.org/10.1007/s11356-023-30538-0

36. Fito, J., Abewaa, M., Mengistu, A., Angassa, K., Ambaye, A. D., Moyo, W., & Nkambule, T. (2023). Adsorption of methylene blue from textile industrial wastewater using activated carbon developed from Rumex abyssinicus plant. *Scientific Reports, 13*(1), Article 5427. https://doi.org/10.1038/s41598-023-32341-w

37. Geddeda, Y. I., & Abdassalam, F. (2010). Some physical characteristics of several Libyan date palm cultivars. *Acta Horticulturae, 882*, 733–736. https://doi.org/10.17660/ActaHortic.2010.882.80

38. Gutiérrez, M., Grillini, V., Mutavdžić Pavlović, D., & Verlicchi, P. (2021). Activated carbon coupled with advanced biological wastewater treatment: A review of the enhancement in micropollutant removal. *Science of The Total Environment, 790*, Article 148050. https://doi.org/10.1016/j.scitotenv.2021.148050

39. Hamedi, H., Zendehboudi, S., Rezaei, N., Azizi, A., & Shahhoseini, F. (2023). Application of functionalized Fe_3O_4 magnetic nanoparticles using CTAB and SDS for oil separation from oil-in-water nanoemulsions. *Langmuir, 39*(23), 7995–8007. https://doi.org/10.1021/acs.langmuir.2c03266

40. Hammad, W. A., Darweesh, M. A., Zouli, N., El-Metwaly, N. M., Ahmed, M. A., & El-Khateeb, A. Y. (2024). Adsorption of cationic dye onto Raphanus seeds: Optimization, adsorption kinetics, thermodynamic studies. *Scientific Reports, 14*(1), Article 17827. https://doi.org/10.1038/s41598-024-66761-z

41. Harouache, A., Kharroubi, M., Lefkaier, I. K., Harfouche, N., Attou, M., & Mouni, L. (2024). Adsorption of anionic dye onto homoionic montmorillonite: Effect of the exchangeable cation on the adsorption. *Journal of the Iranian Chemical Society, 21*(7), 1423–1438. https://doi.org/10.1007/s13738-024-03009-7

42. Homagai, P. L., Ghimire, K. N., & Inoue, K. (2010). Adsorption behavior of heavy metals onto chemically modified sugarcane bagasse. *Bioresource Technology, 101*(6), 2067–2069. https://doi.org/10.1016/j.biortech.2009.11.073

43. Huang, J., Ran, X., Sun, L., Bi, H., & Wu, X. (2024). Recent advances in membrane technologies applied in oil–water separation. *Discover Nano, 19*(1), Article 66. https://doi.org/10.1186/s11671-024-04012-w

44. Ibrahim, A. A., Salama, R. S., El-Hakam, S. A., Khder, A. S., & Ahmed, A. I. (2021). Synthesis of 12-tungstophosphoric acid supported on Zr/MCM-41 composite with excellent heterogeneous catalyst and promising adsorbent of methylene blue. *Colloids and Surfaces A: Physicochemical and Engineering Aspects, 631*, Article 127753. https://doi.org/10.1016/j.colsurfa.2021.127753

45. Islam, N. A. B. M., Kayo, N., Motoishi, Y., Yoshimatsu, I., Yoshitomi, S., Seo, A., & Kuroda, S. (2024). Kinetics and thermodynamics analysis of the polybenzimidazole adsorption onto carbon materials using adsorption isotherm measurements. *Polymer Journal, 56*, 1153–1163. https://doi.org/10.1038/s41428-024-00950-5

46. Lakshmi, D. S., Ravindran, L., Mary, P. J. M., George, T., Muthusamy, S., & Sukumar, M. (2024). Valorization of crustacean shells: Preparation, characterization, and chemical modification of nano-chitin biopolymer membrane for application in water purification. *Waste and Biomass Valorization, 15*(10), 6067–6090. https://doi.org/10.1007/s12649-024-02601-5

47. Li, A., Gong, Y., Zhao, D., Dang, A., & Lin, Z. (2021). Enhanced removal of zinc and cadmium from water using carboxymethyl cellulose-bridged chlorapatite nanoparticles. *Chemosphere, 263*, Article 128038. https://doi.org/10.1016/j.chemosphere.2020.128038

48. Madadgar, S., Doulati Ardejani, F., Boroumand, Z., Sadeghpour, H., Taherdangkoo, R., & Butscher, C. (2023). Biosorption of aqueous Pb(II), Co(II), Cd(II) and Ni(II) ions from Sungun Copper Mine wastewater by Chrysopogon zizanioides root powder. *Minerals, 13*(1), Article 106. https://doi.org/10.3390/min13010106

49. Matić, P., Ukić, Š., & Jakobek, L. (2024). Adsorption of procyanidins B1 and B2 onto β-Glucan: Adsorption isotherms and thermodynamics. *Adsorption, 30*(7), 1303–1313. https://doi.org/10.1007/s10450-024-00503-5

50. Melliti, A., Srivastava, V., Kheriji, J., Sillanpää, M., & Hamrouni, B. (2021). Date palm fiber as a novel precursor for porous activated carbon: Optimization, characterization and its application as Tylosin antibiotic scavenger from aqueous solution. *Surfaces and Interfaces, 24*, Article 101047. https://doi.org/10.1016/j.surfin.2021.101047

51. Memetova, A. E., Zelenin, A. D., Memetov, N. R., Tkachev, A. G., & Memetov, R. E. (2023). Methane adsorption properties of a functional porous material based on coffee waste. *Inorganic Materials: Applied Research, 14*(5), 1298–1304. https://doi.org/10.1134/S2075113323050295

52. Minh, V. C., Lien, N. T. L., Thuy, N. T., Phung, L. T. K., & Huy, N. N. (2023). Production of biochar from coconut husks for adsorption of heavy metals in water. *Philippine Journal of Science, 152*(5), 1579–1593. https://doi.org/10.56899/152.05.05

53. Nasiri, M., Ahmadzadeh, H., & Amiri, A. H. (2023). Biodegradation and metabolic fate of organophosphorus pesticides in well water using Dunaliella salina. *International Journal Environmental Science and Technology, 20*(1), 981–992. https://doi.org/10.1007/s13762-022-04620-y

54. Olusegun, S. J., Osial, M., Souza, T. G. Z., Krajewski, M., Rodrigues, G. L. S., Pękała, M., & Krysinski, P. (2023). Comparative characteristics and enhanced removal of tetracycline and ceftriaxone by Fe_3O_4-lignin and Fe_3O_4-carbon-based lignin: Mechanism, thermodynamic evaluation, and DFT calculation. *Journal of Molecular Liquids, 371*, Article 21075. https://doi.org/10.1016/j.molliq.2022.121075

55. Pathania, D., Sharma, S., & Singh, P. (2017). Removal of methylene blue by adsorption onto activated carbon developed from Ficus carica bast. *Arabian Journal of Chemistry, 10*(Suppl. 1), S1445–S1451. https://doi.org/10.1016/j.arabjc.2013.04.021

56. Pietrzyk, P., Borowska, E. I., Hejduk, P., Camargo, B. C., Warczak, M., Nguyen, T. P., Pregowska, A., Gniadek, M., Szczytko, J., & Wilczewski, S. (2023). Green composites based on volcanic red algae Cyanidiales, cellulose, and coffee waste biomass modified with magnetic nanoparticles for the removal of methylene blue. *Environmental Science and Pollution Research, 30*(23), 62689–62703. https://doi.org/10.1007/s11356-023-26425-3

57. Qureshi, U. A., Hameed, B. H., & Ahmed, M. J. (2020). Adsorption of endocrine disrupting compounds and other emerging contaminants using lignocellulosic biomass-derived porous carbons: A review. *Journal of Water Process Engineering, 38*, Article 101380. https://doi.org/10.1016/j.jwpe.2020.101380

58. Racchi, M. L., & Camussi, A. (2018). The date palms of Al Jufrah – Libya: A survey on genetic diversity of local varieties. *Journal of Agriculture and Environment in International Development, 112*(1), 161–184. https://doi.org/10.12895/jaeid.20181.776

59. Rambabu, K., AlYammahi, J., Bharath, G., Thanigaivelan, A., Sivarajasekar, N., & Banat, F. (2021). Nano-activated carbon derived from date palm coir waste for efficient sequestration of noxious 2,4-dichlorophenoxyacetic acid herbicide. *Chemosphere, 282*, Article 131103. https://doi.org/10.1016/j.chemosphere.2021.131103

60. Ramesha, G. K., Kumara, A. V., Muralidhara, H. B., & Sampath, S. (2011). Graphene and graphene oxide as effective adsorbents toward anionic and cationic dyes. *Journal of Colloid and Interface Science, 361*(1), 270–277. https://doi.org/10.1016/j.jcis.2011.05.050

61. Rashid, R., Shafiq, I., Akhter, P., Iqbal, M. J., & Hussain, M. (2021). A state-of-the-art review on wastewater treatment techniques: The effectiveness of adsorption method. *Environmental Science and Pollution Research, 28*(8), 9050–9066. https://doi.org/10.1007/s11356-021-12395-x

62. Sanou, I., Bamogo, H., Sanou, A., Ouedraogo, M., Saadi, L., Waqif, M., & Millogo, Y. (2024). Adsorption of methylene blue in aqueous medium by activated carbon from peanut shells. *Chemistry Africa, 7*(6), 2777–2794. https://doi.org/10.1007/s42250-024-00927-0

63. Sghiouri Idrissi, A., Nour Eddine, S., Tayoury, M., Khouya, E. H., El Kacemi, K., & Mouni, L. (2024). Investigation of the regeneration of spent activated carbon from water treatment plants. *International Journal Environmental Science and Technology, 21*(9), 8995–9006. https://doi.org/10.1007/s13762-024-05510-1

64. Si, J., Cui, B. K., Yuan, Y., & Dai, Y. C. (2015). Biosorption performances of raw and chemically modified biomasses from Perenniporia subacida for heterocycle dye Neutral Red. *Desalination and Water Treatment, 57*(18), 8454–8469. https://doi.org/10.1080/19443994.2015.1025439

65. Tenev, M. D., Torre, C., Fontana, G., Gauto, V., Cleva, M. S., Caracciolo, N., & Boeykens, S. (2023). Studies of adsorption–desorption of methylene blue in a fixed-bed reactor filled with cotton and tannin industry waste. In *Proceedings of the 21st LACCEI International Multi-Conference for Engineering, Education, and Technology*. https://dx.doi.org/10.18687/LACCEI2023.1.1.1594

66. Wang, J., Zhang, G., Qiao, S., & Zhou, J. (2021). Magnetic Fe0/iron oxide-coated diatomite as a highly efficient adsorbent for recovering phosphorus from water. *Chemical Engineering Journal, 412*, Article 128696. https://doi.org/10.1016/j.cej.2021.128696

67. Xu, J., Plaxco, K. W., & Allen, S. J. (2006). Probing the collective vibrational dynamics of a protein in liquid water by terahertz absorption spectroscopy. *Protein Science, 15*(5), 1175–1181. https://doi.org/10.1110/ps.062073506

68. Zhou, Q., Wang, X., Tan, X., Zhao, Y., Li, S., & Jin, F. (2024). Selective photocatalytic oxidation of methane to C1 oxygenates by regulating sizes and facets over Au/ZnO. *Nano Research, 17*(5), 3810–3818. https://doi.org/10.1007/s12274-023-6323-5

Information about the authors:

Ashraf El-Hashani – Professor, Dr., Department of Chemistry, Faculty of Science, University of Benghazi (Benghazi, Libya, e-mail: aiiya600@yahoo.co.uk).

Khaled Muftah Elsherif – Associate Prof., PhD, Department of Medical Laboratory Science, Faculty of Health Science, Misurata University (Misurata, Libya, e-mail: elsherif27@yahoo.com).

Ghada F. Musbah – Researcher, University of Benghazi (Benghazi, Libya, email: ghadaghada19943@gmail.com)

Abdelgader Imragaa – Dr., Department of Chemistry, Faculty of Science, University of Benghazi (Benghazi, Libya, e-mail: a.imragaa@uob.edu.ly)

Hanan F. Emrayed – Professor, Chemistry Department, Faculty of Science, Omar Al-Mukhtar University (Al-Bayda, Libya, e-mail: hanan.emrayed@omu.edu.ly)

Received 14 December 2025;
received in revised form 28 December 2025;
accepted 9 June 2026

IRSTI 31.25.15 https://doi.org/10.26577/IJBCh202619110

T.R. Saidnazarov[1*], Kh.Kh. Turaev[1], P.I. Urkimbayeva[2], Z.A. Kenessova[2], M.U. Karimov[3], Kh.E. Eshmurodov[1], S.M. Samatov[1]

[1]Faculty of Chemistry, Termez State University, Termez, Uzbekistan
[2]Al-Farabi Kazakh National University, Almaty, Kazakhstan
[3]Tashkent Research Institute of Chemical Technology, Tashkent, Uzbekistan
*e-mail: tohirsaidnazarov@gmail.com

EFFICIENT SYNTHESIS OF P-PHENYLENEDIAMINE FROM PET WASTE VIA ENERGY-EFFICIENT DEPOLYMERIZATION AND GREEN HOFMANN REARRANGEMENT

Abstract: The continuous use of post-consumer polyethylene terephthalate (PET) waste remains a major challenge due to its environmental properties and the high energy requirements of traditional recycling methods. In this study, an energy-efficient and environmentally friendly route for the synthesis of p-phenylenediamine (PPD) from secondary PET waste was developed. Terephthalic acid was obtained from PET waste under simple conditions and then terephthalamide was obtained through a catalytic high-pressure ammonolysis process. The main part of the process involved the Hofmann rearrangement reaction, for which an environmentally friendly chlorinating agent was selected based on research.

Various hypochlorite and dichloroisocyanurate salts were analyzed based on their active chlorine equivalents, reaction efficiency, safety, and waste profile. Among the tested reagents, sodium dichloroisocyanurate chlorinated amides to a high degree under alkaline conditions, reduced hazardous waste, and produced harmless by-products. As a result, p-phenylenediamine was obtained in 84% yield. The structure and properties of the synthesized product were confirmed by IR, NMR, TG, and DTA analyses.

This research work demonstrates a green and efficient method for converting PET waste into valuable aromatic diamines. However, it also highlights the importance of choosing an environmentally friendly reagent for the Hofmann rearrangement reaction.

Keywords: Polyethylene terephthalate (PET), ammonilysis, glycerin, sodium urea, dichloroisocyanurate salt, reactor autoclave, amination, terephthalamide.

Introduction

Some types of plastic materials are biodegradable, but PET waste is not. Therefore, it is an environmental hazard if it is thrown into a landfill (Wojnowska-Baryła et al., 2022). Therefore, the only way to solve the problem of PET waste from industry and social consumption is to recycle it (Coelho et al., 2011). Recycling can be used as a raw material for the chemical industry, in the social sector, or as a variety of materials or products (Sasse, Emig, 1998). In addition, the service life of any non-biodegradable plastic waste can be extended by recycling it (Mohanaprasadh et al., 2022). The good thing about PET is that it can be completely recycled as secondary waste (Raheem et al., 2019).

Nowadays, extensive research is being conducted on the creation and development of various chemical degradation reactions of PET (Khoonkari et al., 2015). For the effective recycling of PET waste, mainly mechanical and chemical methods are used (Shaikh et al., 2024). Most chemical recycling includes alcoholysis, hydrolysis, and ammonolysis (Lu et al., 2018). Chemical recycling methods allow the synthesis of initial monomers or various chemicals (Shadravan, Amani, 2012). These methods require high pressure, temperature, and a lot of time (Bohre et al., 2023).

When chemically recycling PET waste, terephthalic acid is often first synthesized, and various chemicals are obtained from it, such as benzene, dichlorobenzene, terephthaldiamide, and p-phenylenediamine (Cataldo, 1996).

P-phenylenediamine is an important raw material in the chemical industry, and its application is very wide (Heintz et al., 2014). However, the method used to produce it in chemical enterprises today does not meet modern environmental requirements (Patra et al., 2022). In fact, the main raw material for the synthesis of p-phenylenediamine in the chemical industry is

aromatic nitro compounds or aniline, and during the process, a lot of toxic gases are released into the environment (Amer, Brandt, 2018). Therefore, scientists are conducting research to develop an environmentally friendly method for the synthesis of p-phenylenediamine on an industrial scale (Al-Sabagh, 2016). Therefore, the extraction of p-phenylenediamine from PET waste is considered to have economic and environmental advantages (Yulchieva et al., 2023).

Currently, there are several chemical methods for synthesizing p-phenylenediamine from PET waste; for example, the obtained terephthalate is first chlorinated using thionyl chloride, after which the obtained p-phthaloyl chloride undergoes an amination reaction with sodium azide, and p-phenylenediamine is obtained as the final product (Jiyanova et al., 2024). This method is very efficient and does not require much energy, and the reaction yield is also high, but the prices of the substances used for chlorination and amination are expensive, and a large amount of SO_2 gas is released into the environment during the process, so it is not recommended for industrial use (Toshtemirov et al., 2024b).

In this work (Olzhabay et al., 2022), a technology for the chemical recycling of polyethylene terephthalate (PET) waste obtained from used plastic bottles was developed to produce a valuable monomeric product, bis(2-hydroxyethyl) terephthalate (BHET), suitable for the subsequent synthesis of biodegradable polymer films. The PET glycolysis process in the presence of zinc acetate as a catalyst was investigated. The effect of the temperature range of 140–190°C on the degree of PET conversion was studied. It was established that an increase in temperature leads to an increase in the rate and completeness of glycolysis. Optimal process conditions ensuring a high BHET yield of 77% were determined. The obtained results confirm the prospects of chemical recycling of PET waste as an efficient and environmentally sound approach for producing secondary raw materials for the manufacture of biodegradable polymer materials. And again, terephthalic acid obtained from PET waste through glycolysis, alkali, and ammonolysis is amidated at high pressure using ammonia gas, and in the next step, the terephthaldiamide obtained is mixed with water, and chlorine gas is passed through. In the next step, the N, N'-dichlorodiamide obtained is placed in an alkaline solution at low temperature, and p-phenylenediamine is obtained (Toshtemirov et al., 2024a). The substances used in this method are quite cheap and convenient, but the methods used to obtain terephthalic acid from PET waste require a lot of time and energy (Cosimbescu et al., 2021). At the same time, the chlorination process also takes a long time, and the reaction yield is not high. Sometimes sodium hypochlorite is used for chlorination (Tashkulov et al., 2025). Sodium hypochlorite is not suitable for chlorination, and its instability increases over time, which causes many inconveniences.

Taking into account the above shortcomings in the production of p-phenylenediamine, we have developed an economically and environmentally effective method. That is, we have used an energy-saving method to obtain terephthalic acid from PET waste. We have used an effective catalyst to synthesize terephthaldiamide from the obtained terephthalic acid and have significantly increased the reaction yield. At the same time, special attention was paid to the selection of an environmentally friendly chlorinating agent for the Hofmann rearrangement reaction used to obtain p-phenylenediamine from terephthaldiamide.

Materials and methods

Reagents and equipment

For the study, crushed and cleaned pieces of secondary PET bottles and articles, sodium hydroxide solution, urea, sodium hypochlorite, potassium hypochlorite, sodium dichloroisocyanurate salt and trichloroisocyanuric acid, and organic solvents acetone, toluene, and benzene were used. HNZXIB brand reactor autoclave made of stainless steel with a volume of 5 L, suitable for high pressure. SHIMADZU IR spectrophotometer, NMR spectrometer, and TGA-50/TG series thermogravimetric analyzer for determining deformation and valence changes with chemical bonds of the resulting product.

Obtaining terephthalic acid through an energy-efficient method

First, PET waste is thoroughly washed, excess parts are removed (emblem, cap, etc.), and it is crushed. Then 500 g of sulfuric acid is placed in a 1 L glass beaker, and 350 g of ready-made crushed PET pieces are mixed with it. The process is carried out at room temperature on a special magnetic stirring plate. Sulfuric acid reacts with the long chains of PET, causing them to break down and form small monomers. The reaction lasts 2.5 hours and results in a white sticky mixture. The resulting mixture is transferred to a 2 L glass beaker, 1.5 L of water is added, and alkali is added until completely neutralized. As a result, terephthalic acid precipitates in the beaker, which is then filtered and dried. At the end of the process, white terephthalic acid is obtained with a reaction yield of 95%, and its purity is checked by IR spectroscopy (Saidnazarov et al., 2024; Samatov et al., 2024).

Synthesis of terephthaldiamide using a convenient catalyst

100 g of synthesized terephthalic acid was measured and mixed thoroughly with 150 g of urea. At the same time, Fe_2O_3 was taken as a catalyst in an amount equal to 0.01% of the mass of terephthalic acid obtained for the reaction and mixed into the mixture. The mixture was placed in a reactor autoclave, and the parameters were adjusted to 10 kg/cm² pressure, 180ºC temperature, and 3 hours time. After the process was completed, a light brown or orange powder was obtained. After the process was completed, a light brown or orange powder was obtained. The resulting colored powder was washed in 80°C water and dried at 40°C, resulting in 89 g of terephthaldiamide with a yield of 90%.

Synthesis of p-phenylenediamine

First, to start the process, 900 g of 10% alkali solution was prepared and placed in a 2-liter glass beaker. The temperature of the solution was cooled to +5ºC, and 89 g of synthesized terephthaldiamide were added to it. After that, the solution was stirred, and 90 g of sodium dichloroisocyanurate salt was added to the solution. The mixture was kept at +5ºC for 20 minutes, then stirred at room temperature for 1 hour using a magnetic stirrer. In the next step, the reaction temperature was raised to 60ºC and stirred at this temperature for 1 hour. After the specified time, the temperature of the mixture was lowered again to +5ºC and filtered. The resulting filtrate was extracted at room temperature using organic solvents to obtain p-phenylenediamine with a yield of 84%.

Reaction Mechanisms

The reaction mechanism and pathway for producing p-phenylenediamine from PET waste are shown in Figure 1. To produce terephthalic acid, PET pieces are chemically treated with sulfuric acid, which results in the destruction of long polymer chains and the formation of monomers.

Figure 1
Reaction mechanism and pathway

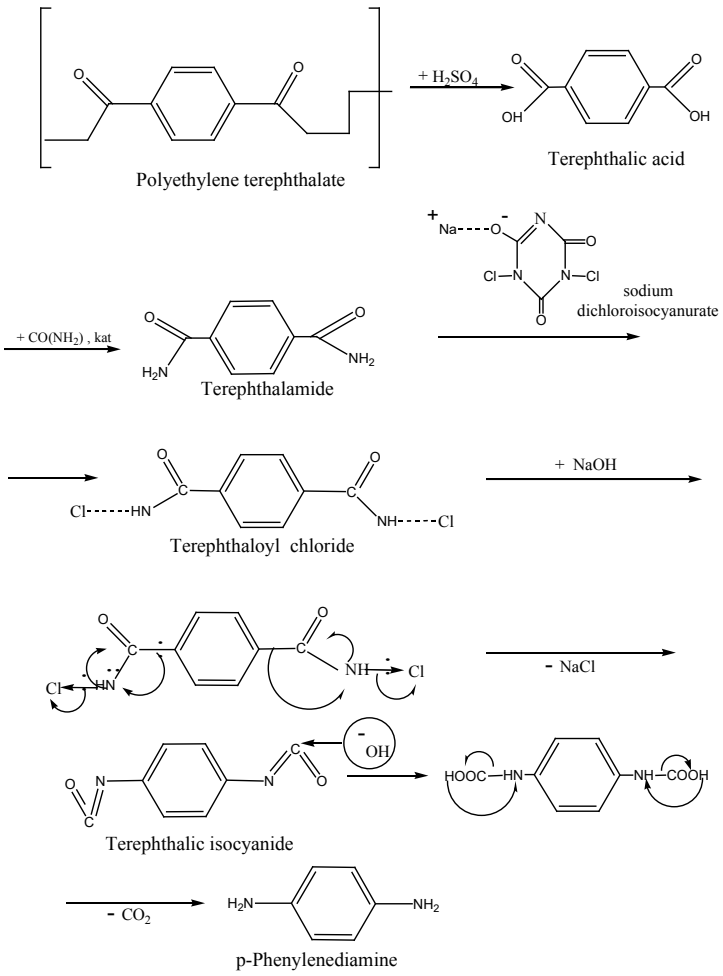

In the next step, the terephthalic acid obtained was aminated under high pressure and in the presence of a catalyst to obtain terephthaldiamide. The catalyst accelerates the amidation process with the -OH in the carboxyl group. Then, sodium dichloroisocyanurate salt was used to chlorinate terephthaldiamide. This salt, when dissolved in water, forms hypochlorite and chlorinates terephthaldiamide to form N,N'-Dichloroterephthalamide. N,N'-Dichloroterephthalamide rapidly undergoes a Hofmann rearrangement reaction under the influence of an alkaline medium, resulting in deprotonation, removing the hydrogen in –CO−NHCl and the formation of a negative charge on the nitrogen, leading to the formation of the chloramide anion $–CO–N^- – Cl$. The anion is unstable and eventually releases chlorine, resulting in isocyanate. Since the process takes place in an aqueous medium, the nucleophilic effect of water on the isocyanate leads to the formation of a primary amine. The resulting primary amine is unstable, so decarboxylation occurs, releasing carbonic anhydride gas, and the final product is p-phenylenediamine.

Results and discussion

Effect of catalyst on terephthaldiamide synthesis

In order to significantly increase the reaction yield in the synthesis of terephthaldiamine, various inorganic substances have been used as catalysts. Since organic substances lose their state under the influence of pressure and temperature and increase the activity of the reaction, their studies as catalysts have not yielded the expected results. Figure 2 shows the results of studying the effect of inorganic salts and oxides used as catalysts on the reaction yield. The effect of many different inorganic compounds as catalysts on the reaction was studied, and the results of the best ones are included in the diagram. Also, when choosing a catalyst, attention was paid to the possibility of recovery after the reaction and its economic efficiency. The reaction efficiency increased when Fe_2O_3, CaO, $CuCl_2$, NaCl, $Ca(OH)_2$, and $MgSO_4$ were used as catalysts. Among these, the highest results were observed when using Fe_2O_3. Fe_2O_3 as a catalyst increased the degree of reaction of the carboxyl functional group in terephthalic acid with ammonia and increased the reaction yield. Based on the obtained research results, Fe_2O_3 was selected as the catalyst.

Choosing an environmentally friendly chlorinating reagent for the Hofmann reaction

A study was conducted to identify a more environmentally friendly chlorinating agent for the Hofmann reaction to produce p-phenylenediamine. The selection of this chlorinating reagent was based on its selective chlorination of amides under alkaline conditions, the absence of hazardous chemical waste, and the formation of harmless by-products.

Figure 2

Results of applying a catalyst to the reaction yield of terephthaldiamide. 1. Fe_2O_3; 2. CaO; 3. $CuCl_2$; 4. NaCl; 5. $Ca(OH)_2$; 6. $MgSO_4$; 7. Reaction yield without catalyst. All values are based on the mean (±) standard deviation of three parallel experiments.

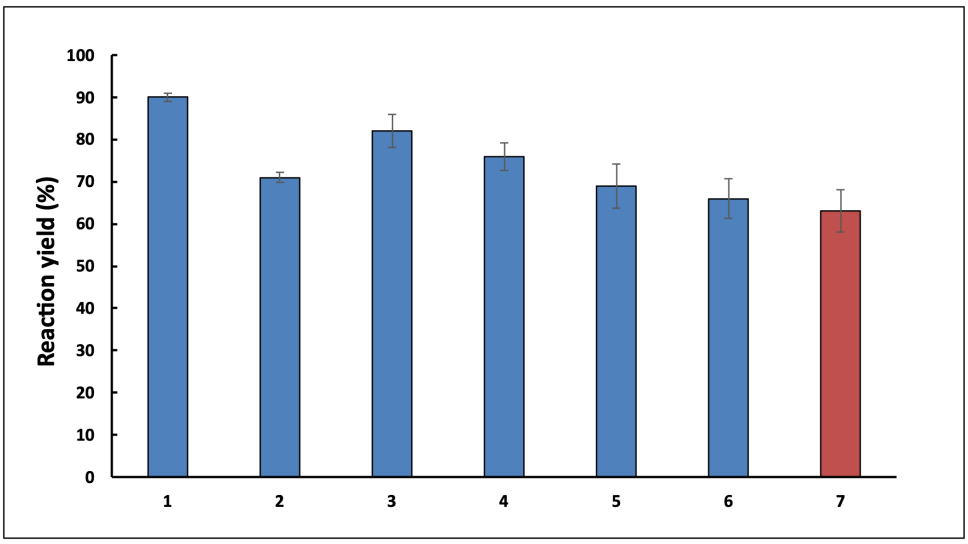

A number of hypochlorite salts and dichloroisocyanurate derivatives were studied, and the reaction efficiency of active chlorine was compared. Hypochlorite-based reagents (NaOCl and KOCl) are widely used for the Hofmann reaction; however, their reaction efficiency and stability are very low. In contrast, dichloroisocyanurate salts provide long-term release of active chlorine, which contributes to the high formation of the chloramide intermediate under stable reaction conditions. Importantly, their main by-product, cyanuric acid (or cyanurate salts under basic conditions), is non-volatile and readily separated from solution.

The results of the study conducted under the same experimental conditions are summarized in Table 1, and sodium dichloroisocyanurate was selected as the most suitable chlorinating reagent in terms of reaction efficiency and environmental performance.

Table 1
Research results for selecting a suitable chlorinating reagent for the Hofmann reaction

No.	Chlorinating agent	Chemical formula	Reaction yield (%)	Gas emission risk	Major by-products	Toxicity / hazard level	Green assessment
1	Sodium hypochlorite (aq)	NaOCl	70 ± 3	Medium	Cl^-, ClO_3^- (trace)	Moderate	Acceptable
2	Potassium hypochlorite (aq)	KOCl	68 ± 4	Medium	Cl^-, ClO_3^- (trace)	Moderate	Acceptable
3	Sodium dichloroisocyanurate (NaDCC)	$NaC_3N_3O_3Cl_2$	84 ± 2	Low	Cyanuric acid / cyanurate salts	Low–moderate	Preferred (green)
4	Trichloroisocyanuric acid (TCCA)	$C_3N_3O_3Cl_3$	80 ± 3	Low	Cyanuric acid / cyanurate salts	Moderate	Good
5	Calcium hypochlorite	$Ca(OCl)_2$	72 ± 3	Medium	$CaCl_2$, Cl^-, ClO_3^- (trace)	Moderate	Acceptable
6	Potassium dichloroisocyanurate (KDCC)	$KC_3N_3O_3Cl_2$	75 ± 3	Low	Cyanuric acid / cyanurate salts	Low–moderate	Good / green
7	Calcium dichloroisocyanurate (CaDCC)	$Ca(C_3N_3O_3Cl_2)_2$	60 ± 3	Low	Cyanuric acid / cyanurate salts	Low–moderate	Good / green

IR Spectrum of Analysis. The IR spectrum of the synthesized p-phenylenediamine confirms that it is compatible with an aromatic diamine. The absorption band observed at 3354 cm^{-1} corresponds to the asymmetric and symmetric stretching vibrations of the $–NH_2$ groups, which is typical for primary aromatic amines. The deformation vibrations of the amino groups at 1602 cm^{-1} and 1510 cm^{-1} further confirm the presence of free amine functional groups.

The peaks at 1263 cm^{-1} are due to C–N stretching vibrations, indicating the formation of amine bonds after the Hofmann reaction. The peaks observed in the region of 2920–2850 cm^{-1} correspond to aromatic C–H bonds, while the lines at 1381 cm^{-1} and 1290 cm^{-1} are related to the benzene ring. Importantly, the absence of carbonyl absorption bands in the region of 1650–1700 cm^{-1} confirms the complete conversion of the amide groups to amine groups. (Figure 3).

NMR analysis. The structure of the synthesized p-phenylenediamine was confirmed by ^1H and ^{13}C NMR spectroscopy. The singlet peak observed at δ 6.517 ppm in the ^1H NMR spectrum corresponds to the aromatic protons of the benzene ring, indicating a symmetrical para structure. The signal at δ 3.258 ppm is associated with the protons of the amino ($–NH_2$) groups, which is consistent with the values reported for p-phenylenediamine in the literature (Figure 4).

The ^{13}C NMR spectrum at δ 138.7 ppm corresponds to carbon atoms bound to amino groups ($C–NH_2$), while the signal at δ 116.9 ppm is due to aromatic C–H carbons. The spectral results indicate high purity of the product and confirm the successful formation of p-phenylenediamine without significant by-products (Figure 5).

Figure 3
IR spectrum of the resulting p-phenylenediamine

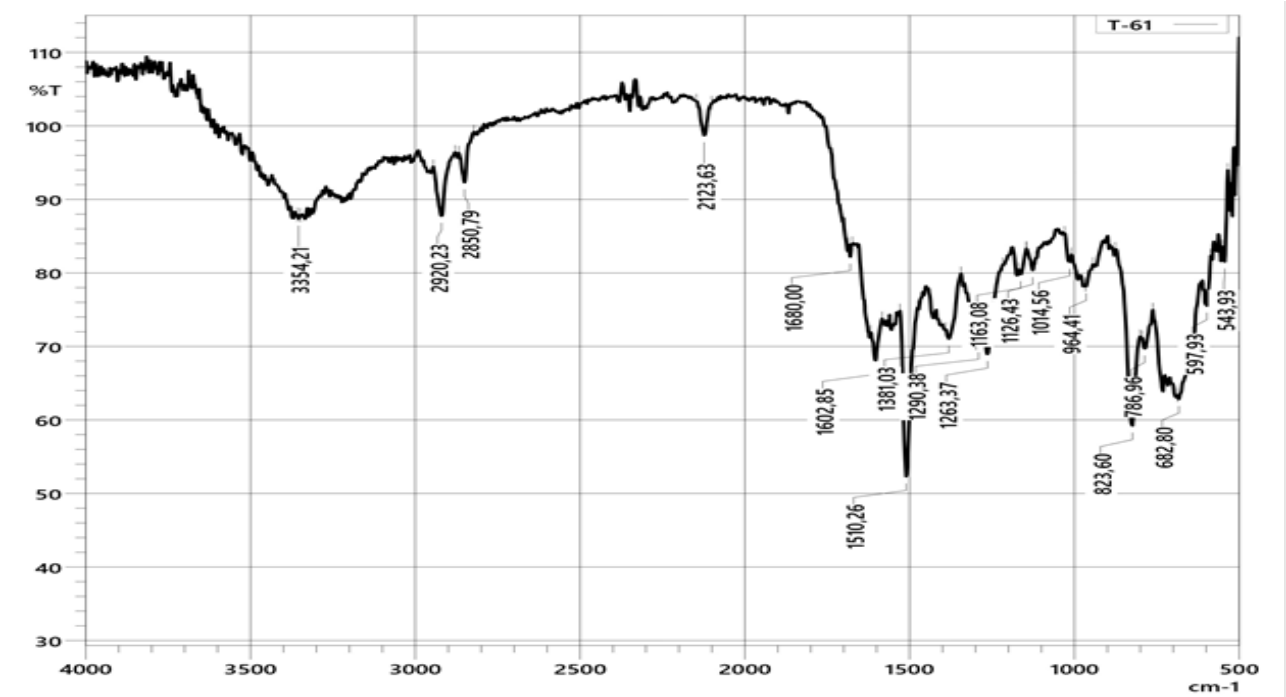

Figure 4
Result of ^{1}H NMR analysis of the obtained p-phenylenediamine

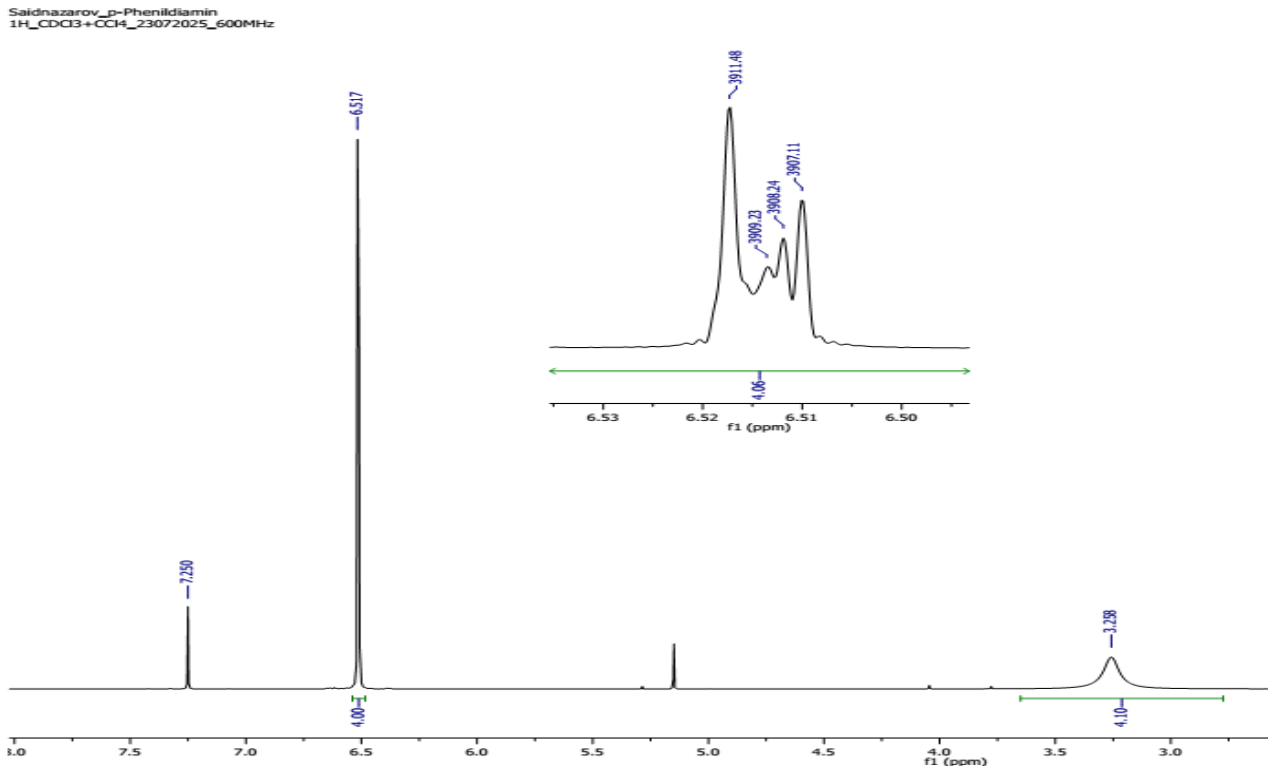

Figure 5
Result of ^{13}C NMR analysis of the obtained p-phenylenediamine

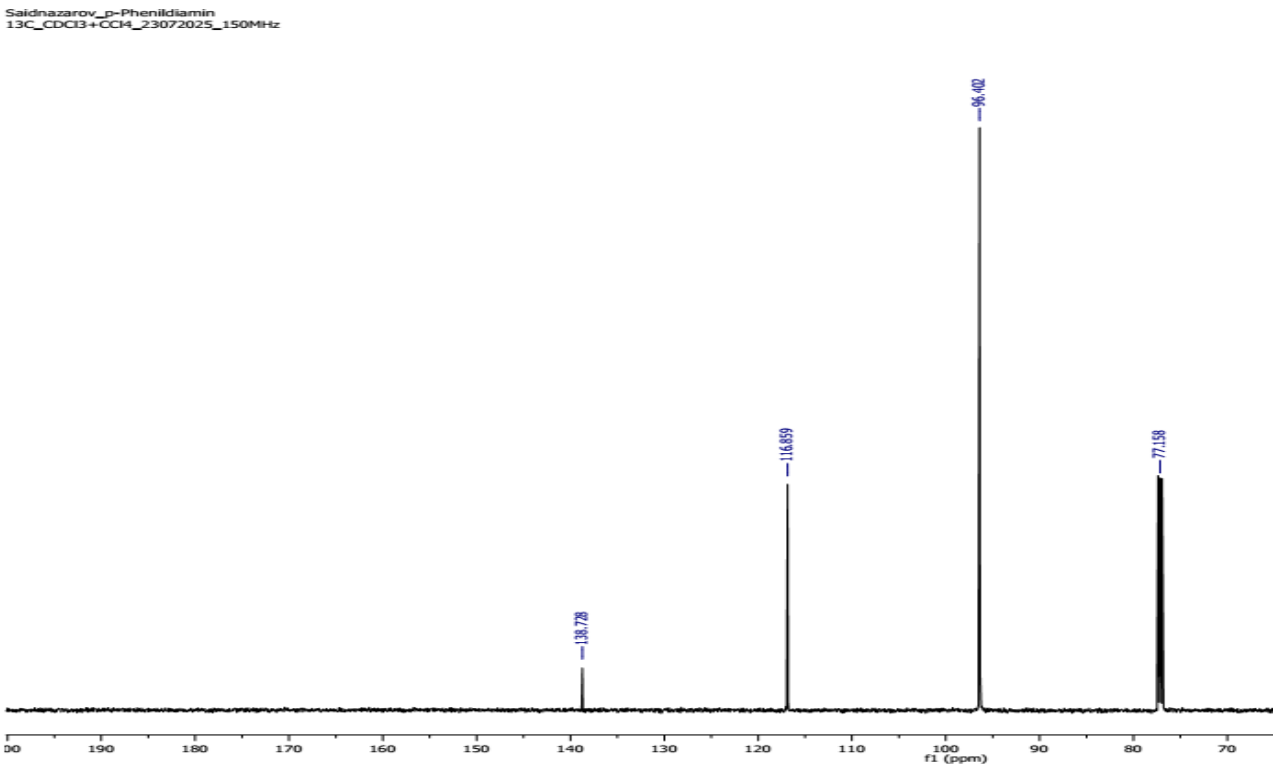

Differential-thermal and Thermogravimetric Analysis. According to the DTA analysis of the synthesized p-phenylenediamine, two endothermic peaks were observed at temperatures of 145.73°C and 194.48°C. No exothermic process was observed. The endothermic peaks appeared as a result of energy absorption due to the decomposition of amines (NH_2). The energy values of these endothermic processes were 214.9 mcal (899.57.16 mJ) and 303.31 mcal (1.27 J), respectively.

According to the TGA analysis results of the synthesized p-phenylenediamine, the substance lost mass in two stages. The first stage occurred between 37.23°C and 217.92°C and lost 93.6% (3.722 mg) of the total mass. The second stage of mass loss occurred between 217.92°C and 456.34°C and decomposed 6.2% (0.248 mg) of the total mass (Figure 6).

Table 2
TGA analysis of synthesized p-phenylenediamine

Reaction process	Reaction process duration (min)	Temperature range	Mass loss (%)
Stage 1	18.85	37.23°C-217.92°C	93.6%
Stage 2	24.33	217.92°C-456.3°C	6.2%

Figure 6
TG and DTA analysis results of synthesized p-phenylenediamine

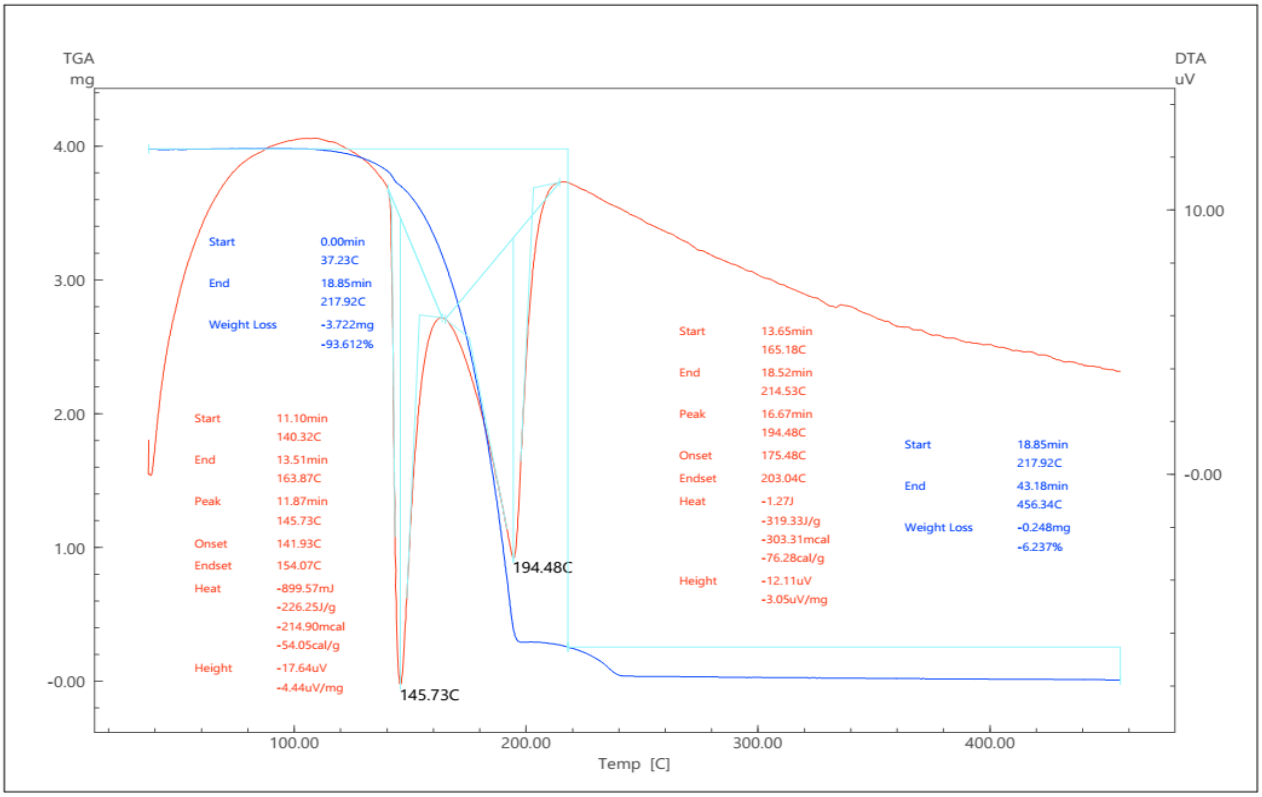

Conclusion

Terephthalic acid was obtained from PET waste at room temperature in an energy-saving manner and amidated under pressure using a catalyst. The obtained terephthalamide was chlorinated using sodium dichloroisocyanurate salt and subjected to the Hofmann reaction in an alkaline medium to synthesize p-phenylenediamine.

A stepwise reaction mechanism for the overall process was developed. In order to identify an environmentally friendly and highly efficient chlorinating reagent, various chlorinating compounds were studied, and sodium dichloroisocyanurate salt was found to be the best among them.

Based on the results obtained, the proposed method was found to be an effective and reliable approach for the conversion of PET waste into p-phenylenediamine. Spectroscopic and thermal analyses clearly confirm the successful preparation, structural properties and high purity of the product. In particular, IR and NMR analyses showed the complete conversion of terephthaldiamide to p-phenylenediamine, while TG and DTA results revealed the thermal properties of the obtained compound.

This developed study showed that the process is not only chemically efficient but also suitable for further technological development.

Authors contribution

T.R. Saidnazarov: Original draft-writing, The organizational and editing of work. *Kh.Kh.Turaev*: the paper's proofreading and editing. *M.U. Karimov, P.I. Urkimbayeva, Z.A. Kenessova*: The provision and certification of software by. *Kh.E. Eshmurodov, S.M. Samatov*: The original manuscript, concept, investigation, and visualization of writing.

Acknowledgments

All analyses and studies were carried out using the equipment of the "Organic Chemistry" scientific laboratory of the Tashkent Chemical Technology Scientific Research Institute.

Conflict of interest

All authors are aware of the article's content and declare no conflict of interest.

References

1. Al-Sabagh, A. M., Yehia, F. Z., Eshaq, G., Rabie, A. M., & ElMetwally, A. E. (2016). Greener routes for recycling of polyethylene terephthalate. *Egyptian Journal of Petroleum*, *25*(1), 53–64. https://doi.org/10.1016/j.ejpe.2015.03.001
2. Amer, I., & Brandt, S. (2018). Synthesis and characterization of poly(p-phenylenediamine) and its derivatives using aluminium triflate as a co-catalyst. *Cogent Engineering*, *5*(1), Article 1499701. https://doi.org/10.1080/23311916.2018.1499701
3. Bohre, A., Darji, D., & Gogate, P. R. (2023). Chemical recycling processes of waste polyethylene terephthalate using solid catalysts. *ChemSusChem*, *16*(14), Article e202300142. https://doi.org/10.1002/cssc.202300142
4. Cataldo, F. (1996). On the polymerization of p-phenylenediamine. *European Polymer Journal*, *32*(1), 43–50. https://doi.org/10.1016/0014-3057(95)00118-2
5. Coelho, T. M., Castro, R., & Gobbo, J. A., Jr. (2011). PET containers in Brazil: Opportunities and challenges of a logistics model for post-consumer waste recycling. *Resources, Conservation and Recycling*, *55*(3), 291–299. https://doi.org/10.1016/j.resconrec.2010.10.010
6. Cosimbescu, L., Vasiliev, A., & Thiele, S. (2021). Simple but tricky: Investigations of terephthalic acid purity obtained from mixed PET waste. *Industrial & Engineering Chemistry Research*, *60*(35), 12792–12797. https://pubs.acs.org/doi/10.1021/acs.iecr.1c02604
7. Heintz, J., Belaud, J. P., & Gerbaud, V. (2014). Chemical enterprise model and decision-making framework for sustainable chemical product design. *Computers in Industry*, *65*(3), 505–520. https://doi.org/10.1016/j.compind.2014.01.010
8. Jiyanova, S. I., Turaev, K. K., Eshmurodov, K. E., Khamzaev, N. J., & Nabiev, D. A. (2024). Magniothermal methods of silicon extraction from quartz sands of "Jerdanak" mine. *International Journal of Engineering Trends and Technology*, *72*(10), 316–322. https://doi.org/10.14445/22315381/IJETT-V72I10P129
9. Khoonkari, M., Haghighi, A. H., Sefidbakht, Y., Shekoohi, K., & Ghaderian, A. (2015). Chemical recycling of PET wastes with different catalysts. *International Journal of Polymer Science*, Article 124524. https://doi.org/10.1155/2015/124524
10. Lu, X. B., Liu, Y., & Zhou, H. (2018). Learning nature: Recyclable monomers and polymers. *Chemistry – A European Journal*, *24*(44), 11255–11266. https://doi.org/10.1002/chem.201704461
11. Mohanaprasadh, S. V., Singh, P., & Bahukhandi, K. D. (2022). Disposal of non-biodegradable waste using eco-friendly methods. In *Environmental pollution and natural resource management* (pp. 345–363). Springer. https://doi.org/10.1098/rstb.2009.0053
12. Olzhabay, A. T., Urkimayeva, P. I., Yespenbetova, Sh. O., Kenessova, Z. A., & El-Sayed, N. (2022). Development of a technology for processing waste plastic bottles and bags to obtain various types of biodegradable polymer films. *International Journal of Biology and Chemistry*, *15*(1), 107–116. https://doi.org/10.26577/ijbch.2022.v15.i1.012
13. Patra, A. K., & Pariti, S. R. K. (2022). Restricted substances for textiles. *Textile Progress*, *54*(1), 1–101. https://doi.org/10.1080/00405167.2022.2101302
14. Raheem, A. B., Noor, Z. Z., Hassan, A., Hamid, M. K. A., Samsudin, S. A., & Sabeen, A. H. (2019). Current developments in chemical recycling of post-consumer polyethylene terephthalate wastes for new materials production: A review. *Journal of Cleaner Production*, *225*, 1052–1064. https://doi.org/10.1016/j.jclepro.2019.04.019
15. Saidnazarov, T. R., Turaev, K. K., Karimov, M. U., Kasimov, S. A., & Akhatov, A. A. (2024). High-quality synthesis of terephthalamide from secondary PET waste. *International Journal of Engineering Trends and Technology*, *73*(4). https://doi.org/10.14445/22315381/IJETT-V73I4P132
16. Samatov, S. M., Turaev, K. K., Kholnazarov, B. A., Toshkulov, A. K., & Shukurov, D. K. (2024). Synthesis of hydrogels based on starch-graft-acrylonitrile/bentonite. *International Journal of Engineering Trends and Technology*, *72*(11), 371–379. https://doi.org/10.14445/22315381/IJETT-V72I11P135
17. Sasse, F., & Emig, G. (1998). Chemical recycling of polymer materials. *Chemical Engineering & Technology*, *21*(10), 777–789. https://doi.org/10.1002/(SICI)1521-4125(199810)21:10<777::AID-CEAT777>3.0.CO;2-L
18. Shadravan, A., & Amani, M. (2012). HPHT 101: What petroleum engineers and geoscientists should know about high pressure high temperature wells environment. *Energy Science and Technology*, *4*(2), 36–60. https://doi.org10.3968/j.est.1923847920120402.635
19. Shaikh, T. M., Mubarak, N. M., Mazari, S. A., et al. (2024). Chemical recycling of polycarbonates via ammonolysis and polycaprolactones by KOH-catalyzed methanolysis. *European Journal of Organic Chemistry*, *27*(10), Article e202301308. https://doi.org/10.1002/ejoc.202301308
20. Tashkulov, A. K., Turaev, K. K., Eshmurodov, K. E., et al. (2025). Synthesis, crystal structure and Hirshfeld surface analysis of bis(benzene-1,2-diamine)-bis(2,4-dihydroxybenzoato)-nickel. *Journal of Chemical Crystallography*, *55*(2), 147–155. https://doi.org/10.1007/s10870-025-01046-5
21. Toshtemirov, A. E., Turaev, K. K., Ibragimov, A. B., et al. (2024a). A new mixed ligand copper(II) complex: Synthesis, crystal structure and Hirshfeld surface analysis. *International Journal of Engineering Trends and Technology*, *72*(11), 106–116. https://doi.org/10.14445/22315381/IJETT-V72I11P114
22. Toshtemirov, A. E., Turaev, K. K., Umbarov, I. A., et al. (2024b). Synthesis of copper(II) complex with 1,10-phenanthroline and nitrate anion in the presence of mandelic acid and crystalline structure. *Crystallography Reports*, *69*, 1087–1092. https://doi.org/10.1134/S1063774524602065
23. Wojnowska-Baryła, I., Bernat, K., & Zaborowska, M. (2022). Plastic waste degradation in landfill conditions: The problem with microplastics and their direct and indirect environmental effects. *International Journal of Environmental Research and Public Health*, *19*(20), Article 13223. https://doi.org/10.3390/ijerph192013223

24. Yulchieva, M. G., Turaev, K. K., Kasimov, S. A., Nabiev, D. A., & Chorieva, N. B. (2023). Research on the synthesis of nitrogen-containing sorbents. *International Journal of Engineering Trends and Technology*, *71*(8), 161–167. https://doi.org/10.14445/22315381/IJETT-V71I8P214

Information about the authors:

Toir Saidnazarov – 3-year PhD student, Faculty of Chemistry, Termez State University (Termez, Republic of Uzbekistan, e-mail: tohirsaidnazarov@gmail.com).

Khayit Turaev – Professor, Faculty of Chemistry, Termez State University (Termez, Republic of Uzbekistan, e-mail: hhturaev@rambler.ru).

Perizat Urkimbayeva – Candidate of Chemical Sciences, Acting Professor, Al-Farabi Kazakh National University (Almaty, Kazakhstan, e-mail: Urkimbayeva.perizat@gmail.com).

Zarina Kenessova – PhD, Associate Professor, Al-Farabi Kazakh National University (Almaty, Kazakhstan, e-mail: zarina.kenesova@gmail.com).

Masud Karimov – Professor, Tashkent Research Institute of Chemical Technology (Tashkent, Republic of Uzbekistan, e-mail: f_adm@ust.ac.kr).

Khurshid Eshmurodov – PhD, Faculty of Chemistry, Termez State University (Termez, Republic of Uzbekistan, e-mail: khurshideshmurodov@mail.com).

Sanjar Samatov – 3-year PhD student, Faculty of Chemistry, Termez State University (Termez, Republic of Uzbekistan, e-mail: sanjarsamatov888@gmail.com).

Received 10 February 2026;
received in revised form 26 May 2026;
accepted 9 June 2026

IRSTI 31.25.19 https://doi.org/10.26577/IJBCh202619111

E.F. Aliyeva*, N.T. Rahimli, N.A. Zeynalov

Laboratory of Nanostructured metal-polymer catalysts, Ministry of Science and Education Republic of Azerbaijan, Institute of Chemistry PLE, Baku, Azerbaijan
*e-mail: elmira.aliyeva@kqki.science.az

COMPARATIVE EFFECT OF APS AND AIBN INITIATORS ON GUM ARABIC-ACRYLAMIDE HYDROGEL SYNTHESIS AND PROPERTIES

Abstract: This study investigates the influence of radical initiator chemistry on the synthesis and structural evolution of pH-responsive gum arabic–acrylamide (GA-g-AM) hydrogels intended for drug-delivery applications. Gum arabic was used as a natural polysaccharide backbone, and acrylamide was grafted via a free-radical mechanism to form crosslinked hydrogel networks. A controlled comparative evaluation of ammonium persulfate (APS) and azobisisobutyronitrile (AIBN) was performed under identical synthesis conditions to evalute the specific influence of initiator type on hydrogel network formation. FTIR, SEM, and XRD analyses confirmed successful copolymerization and revealed differences in structural organization and packing density between the two systems. Swelling experiments demonstrated clear pH-responsive behavior, with maximum equilibrium swelling observed at pH 2. APS-initiated hydrogels exhibited an equilibrium swelling of 720 ± 5%, whereas AIBN-initiated systems reached 1026 ± 5%, indicating differences in crosslink distribution and internal network structure. APS-generated hydrogels showed a more compact morphology, while AIBN-based systems formed comparatively looser networks with higher water uptake. Overall, the results indicate that APS promotes the formation of structurally more organized and compact GA-based hydrogel networks, highlighting the decisive role of initiator chemistry in tailoring natural polymer-derived drug-delivery systems.

Keywords: gum arabic, acrylamide, APS, AIBN, graft copolymerization, hydrogel swelling.

Introduction

Polymer grafting represents a widely used molecular engineering strategy for tailoring the physicochemical and functional properties of polymeric materials, including solubility, morphology, mechanical stability, and biological compatibility (Bhattacharya & Misra, 2004; Przesławski et al., 2022; Purohit et al., 2023; Vega-Hernández et al., 2021). By introducing side chains onto pre-existing macromolecular backbones, grafting enables controlled modification of intermolecular interactions and network architecture, thereby directly influencing swelling behavior, diffusion pathways, and structural integrity (Bhattacharya & Misra, 2004; Gola et al., 2021; Przesławski et al., 2022; Purohit et al., 2023). Among different approaches, free-radical grafting remains particularly attractive due to its operational simplicity, compatibility with aqueous media, and applicability to natural polymers (Bhattacharya & Misra, 2004; Odian, 2004; Purohit et al., 2023; Vega-Hernández et al., 2021).

In free-radical grafting systems, initiators play a decisive role because they generate reactive radical species that activate either the polymer backbone or the monomer, enabling chain initiation and propagation. Thermal decomposition of persulfate or azo initiators produces radicals capable of initiating polymerization and crosslinking reactions. Consequently, grafting efficiency, chain growth behavior, and the resulting network architecture strongly depend on the chemical nature and reactivity of the initiator employed (Bhattacharya & Misra, 2004; Odian, 2004; Purohit et al., 2023). Natural polysaccharides have attracted considerable attention as sustainable backbone materials for biomedical hydrogel systems. Among them, GA, a highly branched arabinogalactan-based polysaccharide, exhibits high hydrophilicity, biodegradability, biocompatibility, and abundant hydroxyl functional groups suitable for radical activation (Ali et al., 2009;

Amaya-Chantaca et al., 2022; Etxabide et al., 2018; Verbeken et al., 2003). Structurally, GA contains multiple reactive functional moieties, including hydroxyl (–OH), carboxyl (–COOH), and glycosidic ether linkages, which provide potential sites for hydrogen abstraction and macroradical formation during graft polymerization (Etxabide et al., 2018; Verbeken et al., 2003). GA-based materials have therefore been explored in controlled drug delivery, bioactive composites, adsorption systems, and release-regulated formulations (Amaya-Chantaca et al., 2022; Etxabide et al., 2018; Hoffman, 2012; Li & Mooney, 2016; Peppas et al., 2000; Saber-Samandari et al., 2013). However, the intrinsic structural heterogeneity and limited mechanical robustness of native GA restrict its direct use as a stable drug carrier matrix, making graft modification necessary to improve structural integrity and regulate swelling behavior (Hoffman, 2012; Li & Mooney, 2016; Peppas et al., 2000).

AM is widely employed in hydrogel engineering because of its strong radical polymerization reactivity, hydrophilicity, and ability to form mechanically stable poly(acrylamide) networks (Cao et al., 2011; Çankaya, 2016; Madduma-Bandarage & Madihally, 2021; Zaharia et al., 2024). The vinyl double bond (C=C) of AM actively participates in radical polymerization, while its amide group (–$CONH_2$) promotes hydrogen bonding and water retention, both essential for drug loading capacity and controlled release performance (Cao et al., 2011; Madduma-Bandarage & Madihally, 2021).

Polymer grafting can be achieved through several mechanisms, including the grafting-to, grafting-from, and grafting-through strategies (Bhattacharya & Misra, 2004; Cummings et al., 2019; Purohit et al., 2023; Vega-Hernández et al., 2021). In the grafting-from approach, initiating sites are generated directly on the backbone and polymer chains propagate in situ, enabling higher grafting density and efficient network formation (Bhattacharya & Misra, 2004; Cummings et al., 2019). In the present work, AM was grafted onto GA via a grafting-from mechanism in the presence of the crosslinker N,N′-methylene bisacrylamide (MBAA).

Among commonly used radical initiators, APS and AIBN exhibit fundamentally different radical generation mechanisms. APS contains a persulfate peroxide bond (–O–O–) that thermally cleaves to generate highly reactive sulfate radicals capable of abstracting hydrogen atoms from hydroxyl groups on polysaccharide backbones, thereby producing active grafting sites and promoting backbone-initiated polymer growth. In contrast, AIBN contains an azo functional group (–N=N–) which decomposes thermally with nitrogen release to form carbon-centered radicals that primarily attack the vinyl double bond of acrylamide and initiate chain propagation from the monomer phase (Odian, 2004; Purohit et al., 2023). Because APS promotes both backbone activation and monomer initiation whereas AIBN mainly initiates monomer polymerization, these initiators may lead to different grafting densities, crosslink distributions, and hydrogel morphologies (Cummings et al., 2019; Işıver & Saraydın, 2021; Jabeen et al., 2022; Naushad et al., 2019; Noordergraaf et al., 2018).

Despite the widespread use of APS and AIBN in radical polymerization systems, systematic comparative investigations focusing on their specific influence on graft copolymerization onto natural polysaccharide backbones remain scarce**.** Accordingly, the present study provides a controlled comparative evaluation of APS and AIBN in the synthesis of GA-g-AM hydrogels to assess how initiator chemistry governs grafting efficiency, network formation, swelling behavior, and structural stability relevant to drug delivery applications.

Materials and methods

GA was purchased from Carlo Erba Reagents (France). AM monomer, NNMBA, and AIBN were obtained from Central Drug House Pvt. Ltd. (India). APS was supplied by Baza N1 (China).

Grafting of Acrylamide onto Gum Arabic

The synthesis of GA - g – AM hydrogels was carried out via a free-radical graft-copolymerization reaction. AM was grafted onto GA using APS or AIBN as radical initiators in separate systems, while MBAA served as the crosslinking agent (Elbedwehy & Atta, 2020; Manaila & Craciun, 2024).

Initially, a 1% (w/v) aqueous GA solution was prepared in deionized water. Subsequently, an AM solution of identical concentration (1% w/v) was added under continuous stirring. Stock solutions of AM (1.406×10^{-1} mol L^{-1}), APS (8.76×10^{-2} mol L^{-1}), AIBN (1.218×10^{-1} mol L^{-1}), and MBAA (6.49×10^{-1} mol L^{-1}) were then introduced into the reaction mixture in predetermined amounts to obtain the desired formulation. The total reaction volume was adjusted to 100 ml.

Polymerization was conducted in a glass round-bottom reactor equipped with magnetic stirring (500

rpm) and maintained at 65 ± 5^{0}C for 3 h under ambient atmospheric conditions. For the AIBN-initiated system, AIBN was finely dispersed in the aqueous reaction mixture under continuous stirring to ensure homogeneous distribution prior to thermal decomposition.

After completion of the reaction, the obtained crosslinked hydrogels were washed repeatedly with deionized water (at least three times) to remove unreacted monomers, residual initiator, and soluble fractions. The purified samples were then dried in an oven at 40^{0}C for 24 h until a constant weight before measurements were performed.

The grafting percentage GP and grafting efficiency GE were calculated to quantitatively evaluate the extent of acrylamide grafting onto the gum arabic backbone and the selectivity of the grafting process (Noordergraaf et al., 2018).

Determination of grafting parameters

GP represents the degree of backbone modification and was defined as the weight ratio of grafted polymer to the GA backbone, expressed as a percentage:

$$\mathrm{GP}\ (\%) = \frac{\mathrm{W_g}}{\mathrm{W_p}} \times 100 \qquad (1)$$

GE reflects the efficiency of the grafting reaction and was defined as the fraction of polymer formed as grafted chains relative to the total polymer produced:

$$\mathrm{GP}\ (\%) = \frac{\mathrm{W_g}}{\mathrm{W_{g+}W_h}} \times 100 \qquad (2)$$

where W_p is the initial dry weight of the gum arabic backbone, W_g is the weight of polymer chains covalently grafted onto the backbone, W_h is the weight of homopolymer formed during the reaction. The calculated GP and GE values are summarized in Table 1.

Table 1

Summarize the grafting percentage (GP) and grafting efficiency (GE) of GA-g-AM hydrogels synthesized using APS and AIBN initiators

GA-g-AM	APS (10%)	AIBN (10%)
GP (%)	91%	57%
GE (%)	78%	40%

Homopolymerization refers to the radical polymerization of acrylamide occurring independently in the reaction medium without attachment to the GA backbone, producing free p-AM chains. To ensure accurate determination of grafting parameters, the synthesized hydrogels were repeatedly washed with deionized water to remove soluble homopolymer and unreacted monomers. The samples were then dried in a laboratory oven at 40°C until constant weight before measurements were performed.

Investigation of Swelling Properties

The degree of swelling (D_s) of the synthesized GA-g-AM hydrogels was determined by immersing the dried samples in buffer solutions of different pH values, as well as in distilled water, at room temperature (Elbedwehy & Atta, 2020; Manaila & Craciun, 2024). The swelling behavior was monitored over various time intervals of 30 min; 1; 2; 3; 4; 5; 6 and 24 h to study the swelling kinetics and equilibrium behavior. At each predetermined time, the swollen hydrogels were removed, filtered through a 100-mesh sieve, and kept for 20 min to remove excess surface water. The samples were then weighed to obtain the swollen weight**,** while the dry weight before immersion W_0 used as a reference. The degree of swelling was calculated using the following equation:

$$\mathrm{D_s}(\%) = \frac{\mathrm{W_1 - W_0}}{\mathrm{W_0}} \times 100 \qquad (3)$$

where W_1 is the weight of the swollen hydrogel and W_0 is the initial dry weight of the sample.

Instrumentation

The structural and morphological characterization of the synthesized GA-g-AM copolymer was performed using Scanning Electron Microscopy (SEM). Dried hydrogel samples were fractured to expose their internal morphology and directly examined with a Carl Zeiss Sigma SEM, which provided detailed information on the surface topography of the copolymer network. To further investigate the structural features, X-Ray Diffraction (XRD) analysis was carried out using a Rigaku Miniflex 600 diffractometer. This technique allowed the identification of crystalline and amorphous domains within the hydrogel, providing insight into the influence of acrylamide grafting on the gum arabic backbone. FTIR spectra were recorded using a Nicolet iS10 spectrometer (Thermo Scientific) equipped with an ATR accessory (ZnSe crystal) over

the range 4000–500 cm^{-1} under standard acquisition conditions.

Results and discussion

Proposed Reaction Mechanism

The graft copolymerization of AM onto GA proceeds via a free-radical grafting-from mechanism, in which the polysaccharide backbone serves as the primary reactive substrate for macroradical formation followed by chain propagation (Bhattacharya & Misra, 2004; Cummings et al., 2019; Odian, 2004). AM functions as the vinyl monomer responsible for chain growth and network formation. The vinyl double bond (C=C) of AM readily participates in radical polymerization, while the amide group ($–CONH_2$) contributes to hydrogen bonding, hydrophilicity, and water retention within the hydrogel structure. These features enable efficient propagation of polymer chains and stabilization of the hydrated network (Odian, 2004). GA plays both structural and chemical roles in the reaction system. Structurally, GA acts as the macromolecular backbone of the hydrogel network. Chemically, its polysaccharide chains contain numerous hydroxyl (–OH) and carboxyl (–COOH) functional groups capable of undergoing hydrogen abstraction reactions, thereby enabling the formation of active radical sites directly on the backbone (Etxabide et al., 2018; Verbeken et al., 2003). Upon thermal activation, APS, which contains a persulfate peroxide bond (–O–O–), undergoes homolytic cleavage to generate highly reactive sulfate radical anions ($SO_4^{\bullet -}$). These radicals can abstract hydrogen atoms from hydroxyl groups on the GA backbone, producing macroradicals localized on the polysaccharide chains. The activated GA macroradicals subsequently react with the vinyl double bond of acrylamide, initiating the growth of poly(acrylamide) graft chains directly from the backbone. This pathway promotes a higher density of grafting sites and facilitates the formation of a more interconnected polymer network (Bhattacharya & Misra, 2004; Odian, 2004).

In contrast, AIBN, characterized by an azo functional group (–N=N–), decomposes thermally with the release of nitrogen gas to form carbon-centered radicals. These radicals primarily react with the vinyl double bond of acrylamide monomers, initiating polymerization mainly through monomer activation rather than direct backbone activation. As a result, chain growth may occur partially in solution prior to attachment to the polysaccharide matrix, potentially leading to a lower grafting site density and a comparatively less compact network structure (Odian, 2004).

The bifunctional crosslinker MBAA, containing two polymerizable vinyl groups, participates in the radical copolymerization during polymer chain propagation ,where its vinyl groups react with growing poly(acrylamide) radical chains. Through successive radical addition, MBAA forms covalent bridges between different polymer chains, generating crosslink junction points and converting the grafted polymer into a three-dimensional hydrogel network (Elbedwehy & Atta, 2020; Manaila & Craciun, 2024).

Accordingly, GA functions not only as a passive support but also as an active radical-reactive backbone governing graft initiation, while the initiator type controls the radical generation pathway and ultimately determines the network architecture and structural compactness of the resulting hydrogels (Lv et al., 2019; Sievers 2021).

Swelling Behavior

The swelling behavior of GA-g-AM hydrogels synthesized using APS and AIBN initiators was investigated in buffer solutions of different pH values as well as in distilled water at room temperature (25 ± 1^0C). The swelling degree was recorded at predetermined time intervals (30 min, 1, 2, 3, 4, 5, 6, and 24 h) in order to evaluate both swelling kinetics and equilibrium behavior.

Fig.1 shows the time-dependent swelling profiles of the hydrogels in the tested media. In all environments, a rapid initial swelling stage was observed during the first hours of immersion, followed by a gradual approach toward equilibrium. This behavior is typical of crosslinked hydrogel systems and reflects rapid solvent diffusion into the polymer network followed by slower relaxation of polymer chains (Hoffman, 2012; Li & Mooney, 2016; Peppas et al., 2000). Both APS- and AIBN-initiated hydrogels exhibited their maximum swelling degree at pH 2, reaching equilibrium swelling values of approximately 720 ± 5% and 1026 ± 5%, respectively. The higher swelling observed in the AIBN-initiated system suggests the formation of a comparatively looser and less densely crosslinked network, allowing increased water penetration and greater polymer chain mobility.

Figure 1
Time-dependent swelling behavior of GA-g-AM hydrogels synthesized using APS and AIBN initiators in buffer solutions of different pH values and in distilled water

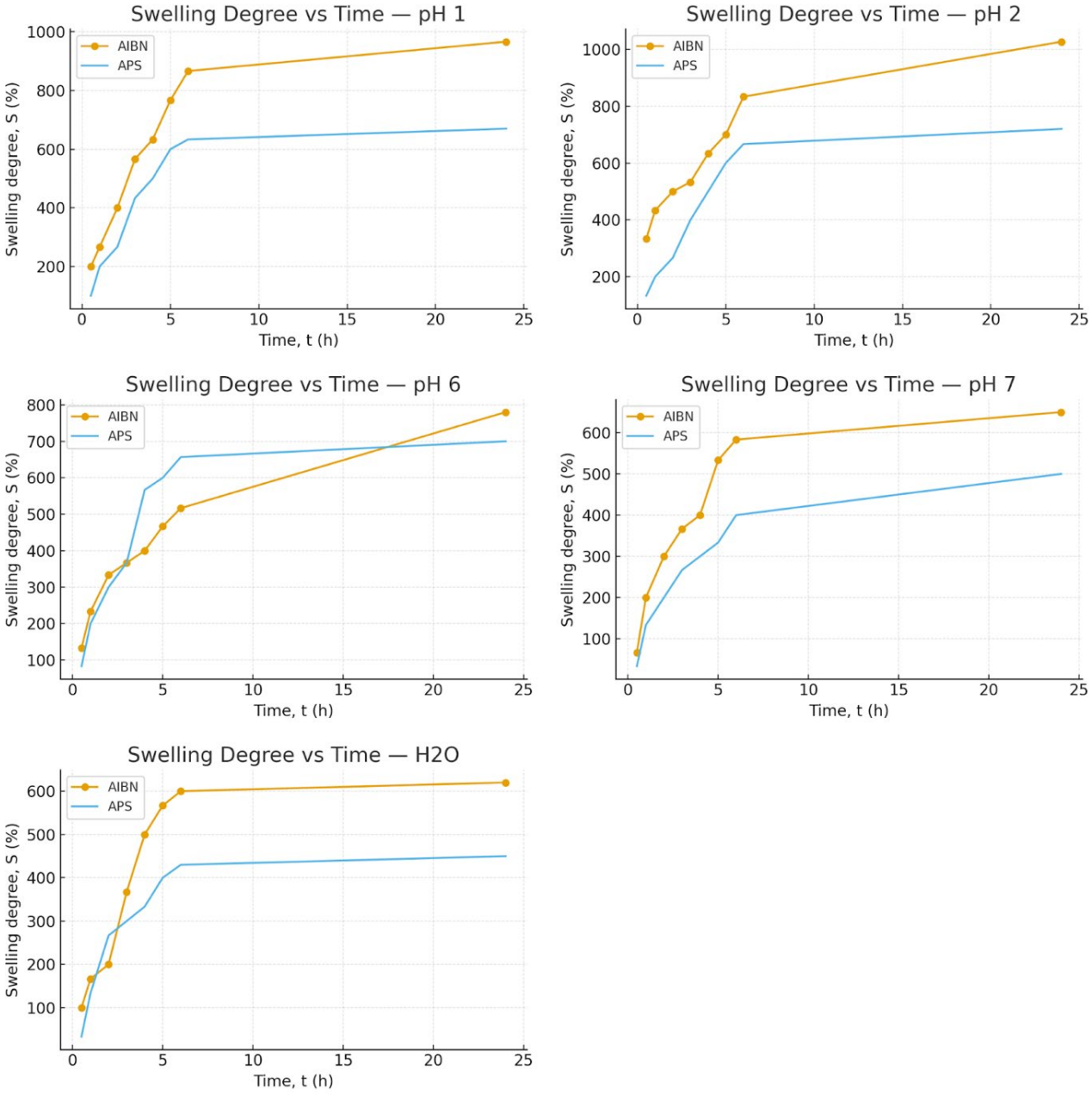

Conversely, the APS-initiated hydrogel displayed lower equilibrium swelling, which can be attributed to more efficient backbone activation and a higher density of grafting and crosslink junctions. The resulting compact network structure restricts free volume and limits solvent uptake (Sievers et al., 2021). All swelling measurements were performed in triplicate (n = 3), and the results are reported as mean ± standard deviation. When a crosslinked hydrogel is immersed in aqueous media of different pH values, it does not dissolve but absorbs water into its polymer network through diffusion. As water molecules penetrate the network, the hydrogel expands, leading to increased separation of polymer chains and enhanced segmental motion. The extent and rate of swelling are strongly influenced by the pH of the

surrounding medium, which affects the ionization state of functional groups within the network (Alonso et al., 2007; Navarro-Hermosillo et al., 2025).

The pH-dependent swelling behavior can also be interpreted considering the polyanionic nature of gum arabic. The presence of ionizable carboxyl groups generates fixed negative charges within the hydrogel network, producing an osmotic pressure difference between the polymer phase and the external solution (Donnan effect) (Li & Mooney, 2016; Peppas et al., 2000), which promotes water uptake and network expansion. Furthermore, the ionic strength of the surrounding medium influences the swelling equilibrium by screening electrostatic repulsion between charged groups, thereby modifying solvent diffusion and polymer relaxation processes.

In this study, the swelling kinetics of the synthesized GA-g-AM hydrogels were examined in buffer solutions of pH 1, 2, 6, and 7 at room temperature and at different time intervals. The experimental data were analyzed using the second-order kinetic model proposed by Schott (Noordergraaf et al., 2018), which can be expressed as:

$$\frac{t}{S_t} = A + B_t \quad (4)$$

where S_t is the swelling degree at time t , A is the intercept , and B_t is the slope of the linear plot. The parameter B_t represents the reciprocal of the equilibrium swelling degree

$$B = \frac{1}{S_E} \quad (5)$$

and the intercept A is related to the swelling rate constant

$$A = \frac{1}{k_s S_E^2} \quad (6)$$

The initial swelling rate can be expressed as:

$$k_{is} = k_s S_E \quad (7)$$

Thus, the Schott model can also be written in linearized form as:

$$\frac{t}{S_t} = \frac{1}{k_s S_E^2} + \frac{t}{S_E} \quad (8)$$

Linear plots of t/St versus t were constructed for each swelling medium and for both initiator systems (APS and AIBN). From the slope and intercept of the fitted lines, the equilibrium swelling degree S_E, swelling rate constant k_s, and initial swelling rate k_{is} were determined. The swelling kinetics were analyzed using the Scott second-order model. The calculated kinetic parameters are presented in Table 2, and the corresponding linear plots are shown in Fig. 2.

Table 2
Schott second-order swelling kinetic parameters for GA-g-AM hydrogels in different swelling media (mean ± SD, n = 3)

Medium	Initiator	S_E (g g^{-1})	k_s (g g^{-1} h^{-1})	k_{is} (g g^{-1} h^{-1})	R^2
pH1	AIBN	10.80	0.036	0.391	0.994
pH1	APS	7.51	0.056	0.419	0.986
pH 2	AIBN	12.00	0.031	0.367	0.991
pH 2	APS	8.12	0.046	0.374	0.987
pH 6	AIBN	8.90	0.030	0.263	0.989
pH 6	APS	8.03	0.038	0.303	0.995
pH 7	AIBN	7.46	0.044	0.326	0.981
pH 7	APS	6.10	0.036	0.216	0.951
H_2O	AIBN	7.05	0.054	0.377	0.971
H_2O	APS	5.21	0.066	0.344	0.938

Figure 2
Linear plots of the Schott second-order swelling kinetic model (t/S versus t) for GA-g-AM hydrogels synthesized using APS and AIBN initiators in different swelling media

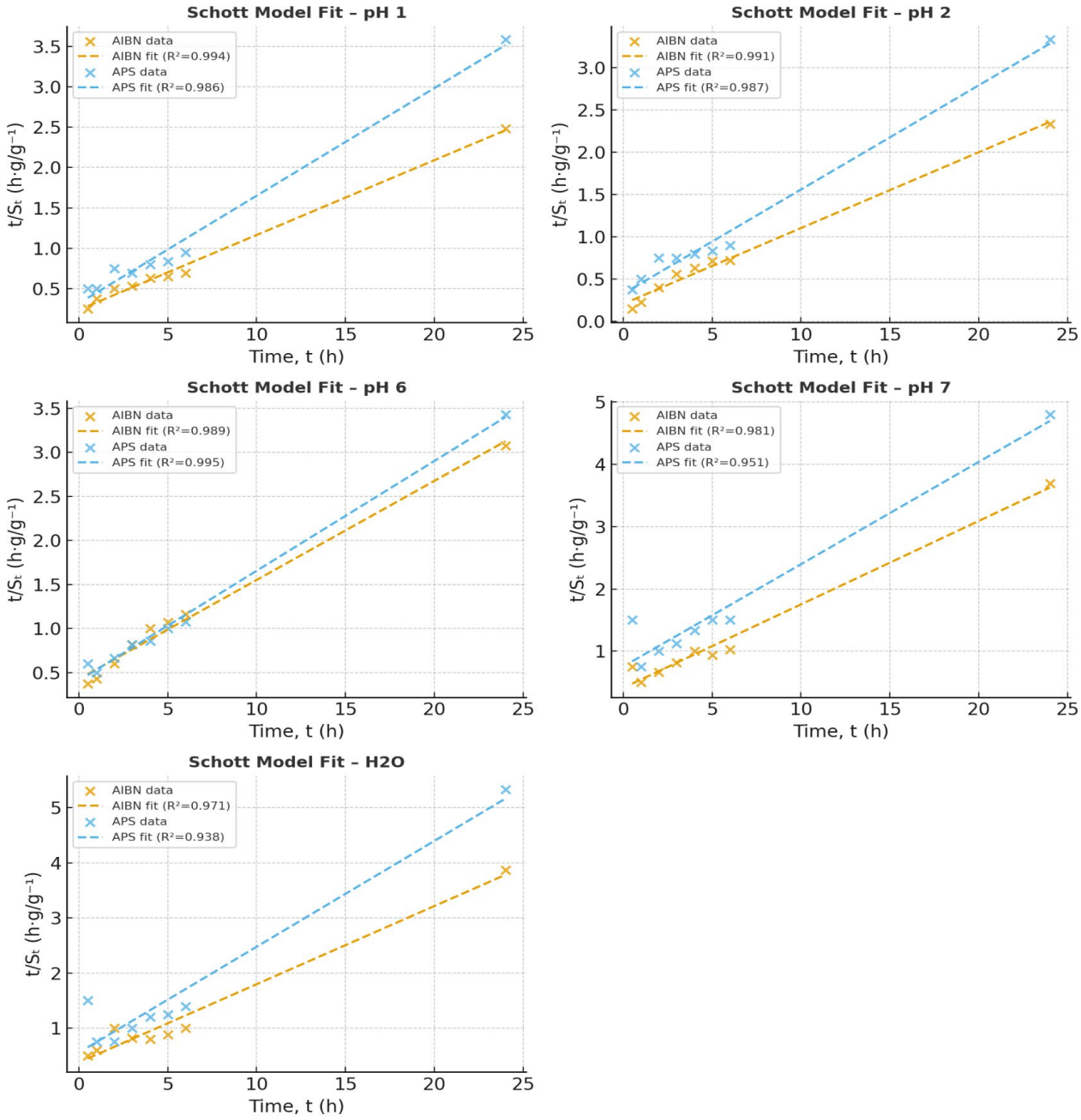

The high correlation coefficients (R^2 = 0.93–0.99) confirm that the Schott second-order kinetic model adequately describes the swelling behavior of the synthesized GA-g-AM hydrogels in all tested media. The results indicate that the swelling process is governed primarily by polymer network relaxation and solvent diffusion within the crosslinked structure (Peppas et al., 2000). Notably, the APS-initiated hydrogels exhibited more consistent kinetic parameters and a more controlled swelling profile, indicating the formation of a denser and structurally more stable polymer network (Lv et al., 2019; Sievers et al., 2021). In contrast, the AIBN-initiated hydrogels showed higher swelling capacity due to a comparatively looser network structure.

Characterization of the Prepared Hydrogels

Figure 3
FTIR spectra of (a) gum arabic, (b) acrylamide, (c) GA-g-AM (AIBN), and (d) GA-g-AM (APS)

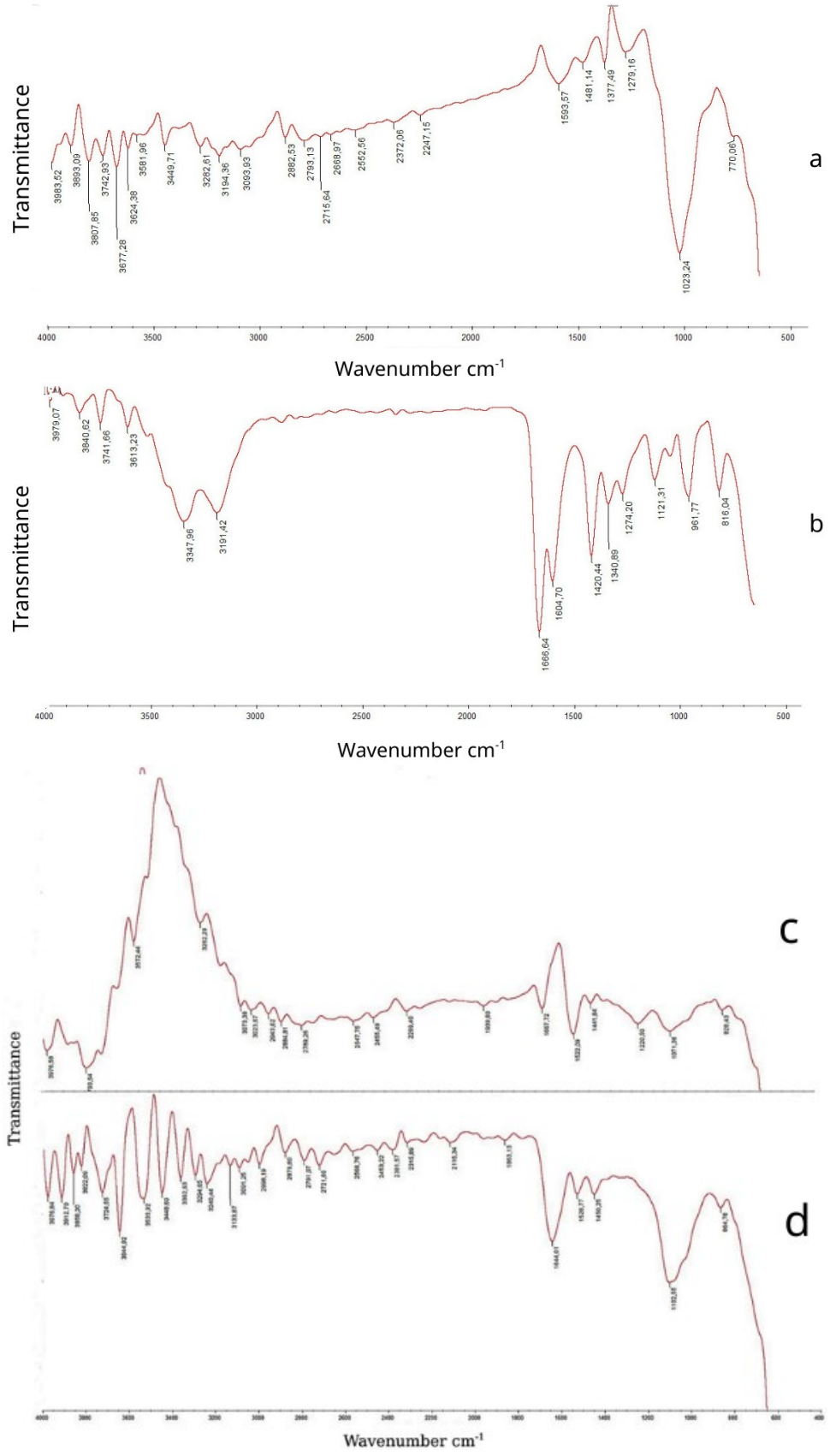

The FTIR spectra of native GA (Fig. 3a) and AM (Fig. 3b) were included for comparison to confirm the structural changes after graft copolymerization. The AIBN-initiated hydrogel (Fig. 3c) exhibited characteristic absorption peaks at 3572 and 3262 cm^{-1} corresponding to the stretching vibrations of –OH and –NH groups, confirming the presence of hydroxyl and amide functional groups. Peaks observed at 3073–2848 cm^{-1} were attributed to aliphatic C–H stretching vibrations. The distinct bands at 1667 and 1522 cm^{-1} were assigned to C=O (amide I) and N–H bending/C–N stretching (amide II), respectively, indicating the formation of amide linkages (Cao et al., 2011; Madduma-Bandarage & Madihally, 2021). Absorptions around 1220 and 1071 cm^{-1} were related to C–O–C and C–O stretching vibrations of the polysaccharide skeleton of GA, consistent with typical polysaccharide IR signatures (Etxabide et al., 2018; Verbeken et al., 2003). The spectrum exhibited relatively broader and less intense absorption bands, which may indicate differences in the local structural organization of the polymer matrix, potentially corresponding to a comparatively less compact network structure.

The APS-initiated hydrogel (Fig. 3d) displayed broad and intense absorption bands in the range of 3448–3724 cm^{-1}, attributed to overlapping –OH and –NH stretching vibrations, indicating the successful incorporation of hydrophilic functional groups during the grafting process. The prominent peaks at 1644 cm^{-1} (amide I, C=O stretching) and 1528 cm^{-1} (amide II, N–H bending/C–N stretching) confirmed the formation of amide linkages between GA and AM. The additional band at 1450 cm^{-1} corresponded to $–CH_2$ bending, while the sharp peak observed at 1102 cm^{-1} was assigned to C–O–C stretching of the polysaccharide backbone (Etxabide et al., 2018; Madduma-Bandarage & Madihally, 2021).

Comparative spectral analysis demonstrates that both initiators successfully induced graft copolymerization between GA and AM. However, the APS-initiated hydrogel exhibited sharper and more intense amide and hydroxyl bands compared to the AIBN-based sample, suggesting a comparatively higher grafting extent and a more densely crosslinked network. The enhanced intensity of these characteristic peaks is consistent with the formation of a more compact and structurally stable polymer matrix in the APS-initiated system.

Morphological analysis by SEM further supported these findings. The surface morphology of the synthesized hydrogels was examined by SEM, and the corresponding micrographs are shown in Fig. 4 (AIBN) and Fig. 5 (APS) (Kareem et al., 2021; Ostrowska-Czubenko et al., 2015).

The APS-initiated hydrogel exhibited a comparatively smoother, more compact, and homogeneous surface morphology, indicating a denser and more organized crosslinked network. The relatively uniform surface texture suggests efficient radical initiation and propagation during graft copolymerization, resulting in a tighter polymer matrix with reduced free volume. Such compact morphology is commonly associated with improved structural stability, lower porosity, and more restricted water mobility within the network (Jabrail & Mahmood, 2015; Ostrowska-Czubenko et al., 2015), which is consistent with the experimentally observed controlled swelling behavior. In contrast, the AIBN-initiated hydrogel exhibited a comparatively rougher and more irregular morphology, indicating a less uniform polymer network and a comparatively lower effective crosslink density. This more open structural configuration may facilitate increased water penetration and retention, consistent with the higher swelling capacity observed for the AIBN-based system (Bal et al., 2021; Franke & Gerlach, 2020; Kaberova et al., 2020).

It should be noted that SEM observations were performed on dried hydrogel samples; therefore, the observed morphology represents the dried state of the materials, and some structural shrinkage or pore deformation due to drying cannot be excluded of the surface features (Ibrahim et al., 2021; Sharma et al., 2022).

Figure 4
SEM analysis of GA-g-AM (AIBN)

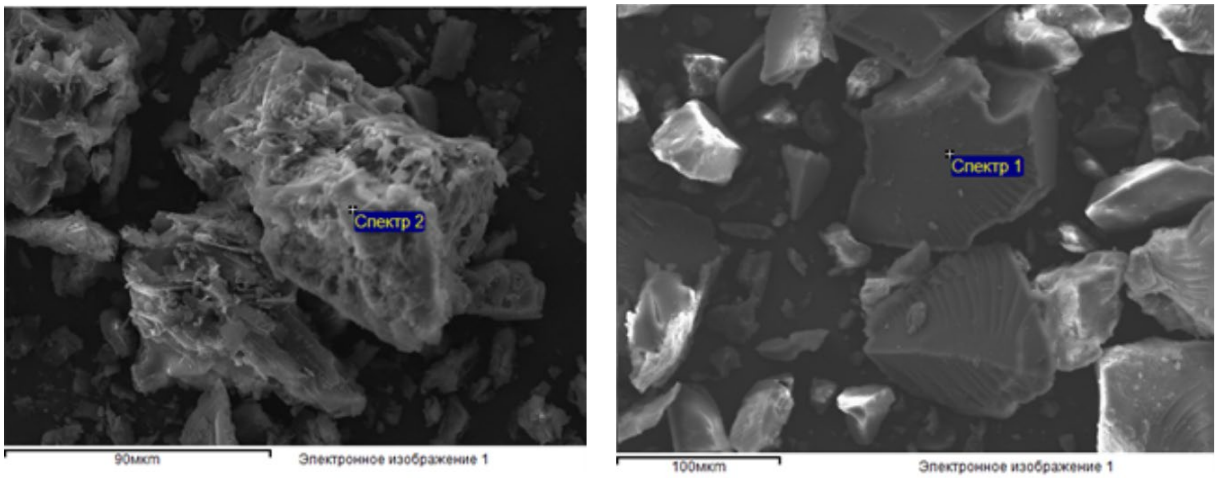

Figure 5
SEM analysis of GA-g-AM (APS)

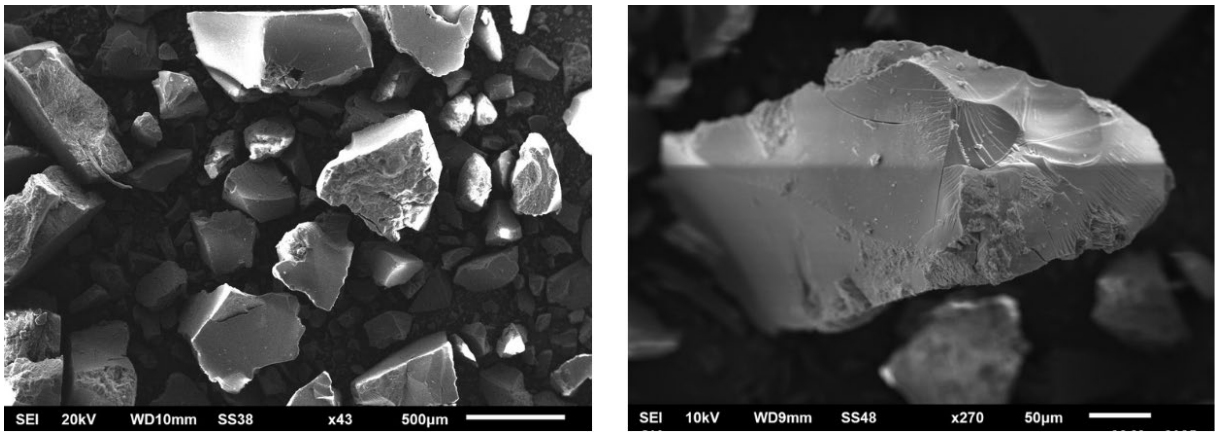

The XRD patterns of APS- and AIBN-initiated GA–g–AAm hydrogels showed broad halos around $2\theta \approx 20–25^0$, confirming their predominantly amorphous nature (Ibrahim et al., 2021; Kaberova et al., 2020). The slightly sharper and more intense peak in the APS-initiated sample indicates improved molecular ordering and denser crosslinking, while the broader halo in the AIBN-based hydrogel reflects a looser, less organized network (Kaberova et al., 2020; Ostrowska-Czubenko et al., 2015). These results confirm that APS produces a more compact and stable amorphous structure compared to AIBN. The XRD diffractograms of GA–g–AM hydrogels synthesized using APS (Fig. 6) and AIBN (Fig. 7) initiators are presented to illustrate the amorphous nature of the polymeric networks.

Figure 6
XRD spectrum of GA-g-AM (APS)

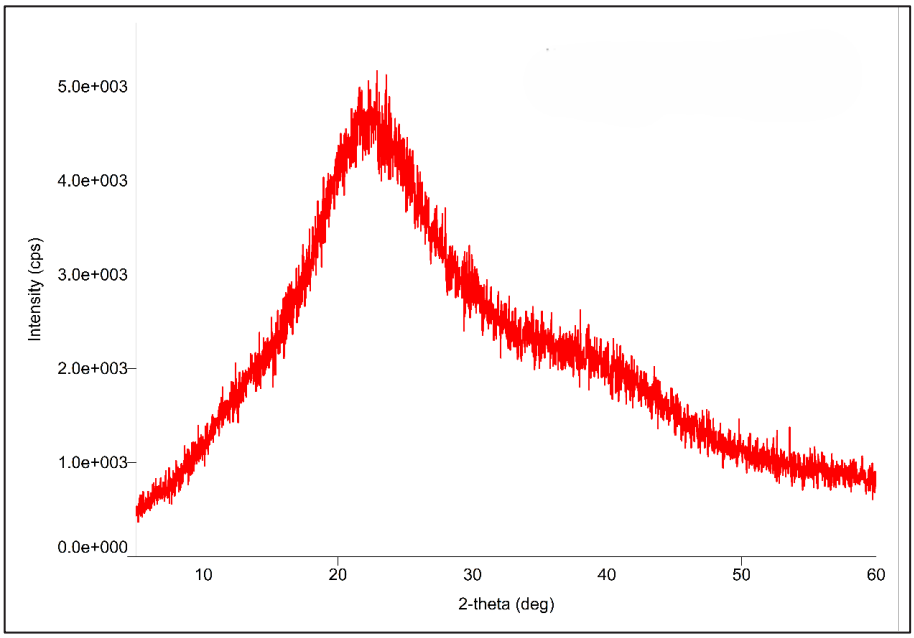

Figure 7
XRD spectrum of GA-g-AM (AIBN)

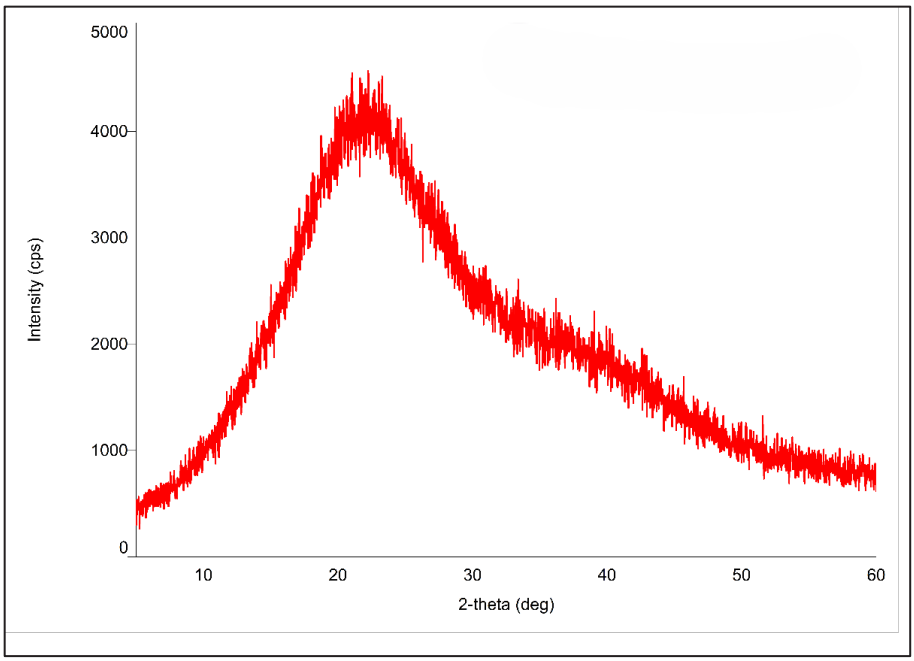

Conclusion

The FTIR spectra of the APS-initiated hydrogel exhibited stronger amide and hydroxyl absorption bands, confirming a higher degree of grafting. Morphological analysis through SEM further supported these findings, as the APS-grafted samples displayed a smoother, more uniform, and compact surface compared to the relatively rough structure observed in the AIBN-based hydrogel.

Overall, the results demonstrate that the initiator type plays a decisive role in governing the crosslinking process, network architecture, and swelling behaviour of GA-g-AM hydrogels. APS more effectively activates the gum arabic backbone and promotes the formation of a denser and more uniformly crosslinked three-dimensional polymer network. The higher crosslink density restricts polymer chain mobility and reduces free volume, resulting in improved structural stability and more controlled swelling behaviour, whereas AIBN leads to a comparatively looser and more absorbent polymer network.

Author contributions

E.F. Aliyeva: Conceptualization, Methodology, Investigation, Writing – Original Draft; N.T. Rahimli: Visualization; N.A. Zeynalov: Supervision.

Conflict of interest

The authors declare that there is no conflict of interest regarding the publication of this article.

References

1. Ali, B. H., Ziada, A., & Blunden, G. (2009). Biological effects of gum Arabic. *Food and Chemical Toxicology*, *47*(1), 1–8. https://doi.org/10.1016/j.fct.2008.07.001

2. Alonso, G., Rivera-Armenta, J. L., Mendoza, A. M., & Méndez-Hernández, M. L. (2007). Effect of temperature and pH on swelling behavior of hydroxyethyl cellulose–acrylamide hydrogel. *e-Polymers*, *7*(1), 1744. https://doi.org/10.1515/epoly.2007.7.1.1744

3. Amaya-Chantaca, N. J., Caldera-Villalobos, M., Claudio-Rizo, J. A., Pérez-Pérez, E., Hernández-Cocoletzi, H., & Álvarez-Ramírez, J. (2022). Semi-IPN hydrogels of collagen and gum Arabic with antibacterial capacity and controlled drug release. *Progress in Biomaterials*, *11*(2), 197–210. https://doi.org/10.1007/s40204-022-00210-w

4. Bal, T., Mesra, P., Singh, P., & Rajora, A. D. (2021). Polyacrylamide grafted gum acacia (GA-g-PAM) graft copolymer as efficient polymeric scaffold. *Indian Journal of Pharmaceutical Education and Research*, *55*(2s), s441–s447. https://doi.org/10.5530/ijper.55.2s.115

5. Bhattacharya, A., & Misra, B. N. (2004). Grafting: a versatile means to modify polymers. *Progress in Polymer Science*, *29*(8), 767–814. https://doi.org/10.1016/j.progpolymsci.2004.05.002

6. Cao, Y. F., Liu, Z. L., Li, Y., & Tan, F. Z. (2011). Graft copolymerization of starch and acrylamide initiated by AIBN in aqueous two-phase system. *Advanced Materials Research*, *239–242*, 1433–1436. https://doi.org/10.4028/www.scientific.net/AMR.239-242.1433

7. Çankaya, N. (2016). Synthesis of graft copolymers onto starch and its semiconducting properties. *Results in Physics*, *6*, 538–542. https://doi.org/10.1016/j.rinp.2016.08.010

8. Cummings, S., Zhang, Y., Smeets, N., Cunningham, M., & Dubé, M. A. (2019). On the use of starch in emulsion polymerizations. *Processes*, *7*(3), 140. https://doi.org/10.3390/pr7030140

9. Elbedwehy, A. M., & Atta, A. M. (2020). Novel superadsorbent highly porous hydrogel based on Arabic gum and acrylamide grafts for fast and efficient methylene blue removal. *Polymers*, *12*(2), 338. https://doi.org/10.3390/polym12020338

10. Etxabide, A., Téllez-Jurado, A., Martínez-Sanz, M., Villar, M., Eceiza, A., & Corcuera, M. A. (2018). Bioinspired alginate–gum Arabic hydrogel with controlled release capabilities. *ACS Applied Materials & Interfaces*, *10*(29), 24783–24793. https://doi.org/10.1021/acsami.7b04428

11. Franke, D., & Gerlach, G. (2020). Swelling studies of porous and nonporous semi-IPN hydrogels for sensor and actuator applications. *Micromachines*, *11*(4), 425. https://doi.org/10.3390/mi11040425

12. Gola, A., Bernardi, A., Pasut, G., & Musial, W. (2021). Influence of initiator concentration on properties of thermosensitive poly(acrylamide-co-AMPS) microparticles. *Polymers*, *13*(7), 996. https://doi.org/10.3390/polym13070996

13. Hoffman, A. S. (2012). Hydrogels for biomedical applications. *Advanced Drug Delivery Reviews*, *64*, 18–23. https://doi.org/10.1016/j.addr.2012.09.010

14. Ibrahim, S. M., Teo, Y. Y., & Misran, M. (2021). Synthesis, characterization and rheological study of Arabic gum-grafted-poly(methacrylic acid) hydrogels. *Polymer Bulletin*, *78*(11), 6087–6103. https://doi.org/10.1007/s00289-020-03267-4

15. Işıver, Y., & Saraydın, D. (2021). Smart hydrogels: preparation, characterization, and determination of transition points of crosslinked N-isopropyl acrylamide/acrylamide/carboxylic acids polymers. *Gels*, *7*(3), 113. https://doi.org/10.3390/gels7030113

16. Jabeen, S., Alam, S., Shah, L. A., & Zahoor, M. (2022). Removal of Safranin-T and Toluidine from water through gum arabic/acrylamide hydrogel. *Adsorption Science & Technology*, *2022*, 6100791. https://doi.org/10.1155/2022/6100791

17. Jabrail, F. H., & Mahmood, M. E. (2015). Hydrophilic monomers graft gum Arabic hydrogels prepared in different cross-linking nature and study of their effects on irrigation of agriculture soil. *Research Journal of Chemical Sciences*, *6*, 22–37.

18.Kaberova, Z., Karpushkin, E., Nevoralová, M., Vetrík, M., Šlouf, M., & Dušková-Smrčková, M. (2020). Microscopic structure of swollen hydrogels by scanning electron and light microscopies: artifacts and reality. *Polymers*, *12*(3), 578. https://doi.org/10.3390/polym12030578

19.Kareem, S. A., Dere, I., Gungula, D. T., Ajayi, A. H., & Olanrewaju, J. A. (2021). Synthesis and characterization of slow-release fertilizer hydrogel based on hydroxypropyl methyl cellulose. *Gels*, *7*(4), 262. https://doi.org/10.3390/gels7040262

20.Li, J., & Mooney, D. J. (2016). Designing hydrogels for controlled drug delivery. *Nature Reviews Materials*, *1*(12), 16071. https://doi.org/10.1038/natrevmats.2016.71

21.Lv, Q., Wu, M., & Shen, Y. (2019). Enhanced swelling ratio and water retention capacity for novel super-absorbent hydrogel. *Colloids and Surfaces A: Physicochemical and Engineering Aspects*, *583*, 123972. https://doi.org/10.1016/j.colsurfa.2019.123972

22.Madduma-Bandarage, U. S. K., & Madihally, S. V. (2021). Synthetic hydrogels: synthesis, novel trends, and applications. *Journal of Applied Polymer Science*, *138*(19), 50376. https://doi.org/10.1002/app.50376

23.Manaila, E., & Craciun, G. (2024). Poly(acrylic acid)–sodium alginate superabsorbent hydrogels synthesized by electron-beam irradiation—Part II: swelling kinetics and absorption behavior in various swelling media. *Gels*, *10*(9), 609. https://doi.org/10.3390/gels10090609

24.Naushad, M., Sharma, G., & Alothman, Z. (2019). Gum Arabic crosslinked poly(acrylamide) hydrogel nanocomposites. *Journal of Cleaner Production*, *241*, 118263. https://doi.org/10.1016/j.jclepro.2019.118263

25.Navarro-Hermosillo, A. B., Landázuri-Gómez, G., Soltero-Martínez, J. F. A., & Santos, C. (2025). Obtaining and characterizing poly(acrylic acid-co-acrylamide) hydrogels reinforced with cellulose nanocrystals. *Gels*, *11*(2), 144. https://doi.org/10.3390/gels11020144

26.Noordergraaf, I. W., Fourie, T. K., & Raffa, P. (2018). Free-radical graft polymerization onto starch as a tool to tune properties in relation to potential applications. *Processes*, *6*(4), 31. https://doi.org/10.3390/pr6040031

27.Odian, G. (2004). *Principles of polymerization* (4th ed.). Wiley.

28.Ostrowska-Czubenko, J., Gierszewska, M., & Pieróg, M. (2015). pH-responsive hydrogel membranes based on modified chitosan: water transport and kinetics of swelling. *Journal of Polymer Research*, *22*(7), 153. https://doi.org/10.1007/s10965-015-0786-3

29.Peppas, N. A., Bures, P., Leobandung, W., & Ichikawa, H. (2000). Hydrogels in pharmaceutical formulations. *European Journal of Pharmaceutics and Biopharmaceutics*, *50*(1), 27–46. https://doi.org/10.1016/S0939-6411(00)00090-4

30.Przesławski, G., Szcześniak, K. B., Gajewski, P., & Marcinkowska, A. (2022). Influence of initiator concentration on polymerization course of methacrylate bone cement. *Polymers*, *14*(22), 5005. https://doi.org/10.3390/polym14225005

31.Purohit, P., Bhatt, A., Mittal, R. K., Abdellattif, H. M., & Farghaly, T. A. (2023). Polymer grafting and its chemical reactions. *Frontiers in Bioengineering and Biotechnology*, *10*, 1044927. https://doi.org/10.3389/fbioe.2022.1044927

32.Saber-Samandari, S., Saber-Samandari, S., & Gazi, M. (2013). Cellulose-graft-polyacrylamide/hydroxyapatite composite hydrogel with possible application in removal of Cu(II) ions. *Reactive and Functional Polymers*, *73*(11), 1523–1530. https://doi.org/10.1016/j.reactfunctpolym.2013.07.007

33.Sharma, G., Kumar, A., Naushad, M., Dhiman, P., Thakur, B., García-Peñas, A., & Stadler, F. J. (2022). Gum acacia-crosslinked-poly(acrylamide) hydrogel supported C3N4/BiOI heterostructure for remediation of crystal violet dye. *Materials*, *15*(7), 2549. https://doi.org/10.3390/ma15072549

34.Sievers, J., Sperlich, K., Stahnke, T., Kreiner, C., Eickner, T., Martin, H., & Guthoff, R. F. (2021). Determination of hydrogel swelling factors by two established and a novel non-contact continuous method. *Journal of Applied Polymer Science*, *138*(18), 50326. https://doi.org/10.1002/app.50326

35.Vega-Hernández, M. Á., Cano-Díaz, G. S., Vivaldo-Lima, E., Rosas-Aburto, A., Hernández-Luna, M. G., Martinez, A., & Font, J. C. (2021). A review on the synthesis, characterization, and modeling of polymer grafting processes. *Processes*, *9*(2), 375. https://doi.org/10.3390/pr9020375

36.Verbeken, D., Dierckx, S., & Dewettinck, K. (2003). Exudate gums: occurrence, production and applications. *Food Hydrocolloids*, *17*(1), 9–21. https://doi.org/10.1016/S0268-005X(02)00077-1

37.Zaharia, M. M., Pispas, S., Bucatariu, F., & Mihai, M. (2024). Synthesis of thermoresponsive chitosan-graft-poly(N-isopropylacrylamide) hybrid copolymer and its complexation with DNA. *Polymers*, *16*(10), 1315. https://doi.org/10.3390/polym16101315

Information about the authors:

Elmira Aliyeva – PhD candidate, Laboratory of Nanostructured metal-polymer catalysts, Ministry of Science and Education Republic of Azerbaijan, Institute of Chemistry PLE (Baku, Azerbaijan, e-mail: elmira.aliyeva@kqki.science.az).

Nargiz Rahimli – PhD candidate, Laboratory of Nanostructured metal-polymer catalysts, Ministry of Science and Education Republic of Azerbaijan, Institute of Chemistry PLE (Baku, Azerbaijan, e-mail: nargiz.rahimli@kqki.science.az).

Nizami Zeynalov – Doctor of Chemical Sciences, Head of Laboratory of Nanostructured metal-polymer catalysts, Ministry of Science and Education Republic of Azerbaijan, Institute of Chemistry PLE (Baku, Azerbaijan, e-mail: nizami.zeynalov@kqki.science.az).

Received 28 March 2026;
received in revised form 26 May 2026;
accepted 9 June 2026

IRSTI 61.67.29 https://doi.org/10.26577/IJBCh202619112

S. Nauryzova[1,3], A. Battalova[1,2*], A. Demeukhan[2], K. Akatan[2], A. Kabdrakhmanova[3], A. Imasheva[2], E. Shaimardan[1], S. Kabdrakhmanova[3], A. Yeskaliyev[2]

[1]Scientific Center of Composite Materials, Almaty, Kazakhstan
[2]S. Amanzholov East Kazakhstan University, Ust-Kamenogorsk, Kazakhstan
[3]Satbayev University, Almaty, Kazakhstan
*e-mail: battalovaainur014@gmail.com

PRODUCTION OF SUSTAINABLE FIBROUS MATERIAL FROM RENEWABLE RESOURCE

Abstract: The article comprehensively studies the possibility of obtaining microcrystalline cellulose (MCC) from the husk of sorghum (SbH) (Sorghum Bicolor), an agricultural crop growing in the country. The research comprehensively studied the effective parameters for the production of MCC from SbH, its yield and quality characteristics, as well as physicochemical properties. When using a hydromodule for the extraction of MCC from SbH at a SbH/peroxyacetic acid ratio of 1:16 g/ml, the yield of MCC was high and reached 57.24%. The amount of α-cellulose in the obtained MCC was 61.32%. It has been established that the yield of MCC obtained by this organosolvent oxidation method is 10-25% higher than with the traditional method of alkaline treatment. The obtained MCC can be used as an ingredient in paper and cardboard production, pharmaceuticals, and composite materials.

Keywords: Agricultural waste, sorghumbicolor husks, microcrystalline cellulose, organosolvent oxidation, FTIR, crystal structure.

Introduction

In line with sustainable development goals, interest in biomaterials derived from environmentally friendly and renewable raw materials is increasing every day. Cellulose fibers are one such natural polymer. It is the most abundant carbohydrate in plant cells. It is widely used in industry as an environmentally friendly, biocompatible material. Cellulose and its derivatives are of great importance in the food industry, paper and textile products, pharmaceuticals and biomedicine. (Roohallah et al., 2024). However, existing cellulose fibers are still produced from traditional raw materials (wood, cotton fiber). This process uses forest resources, causing enormous damage to the environment (Shehrawat & Sindhu, 2015). In this regard, obtaining cellulosic material from agricultural waste and renewable raw materials becomes a pressing issue for the transition to technology compatible with the circular economy within the framework of the UN Sustainable Development Goals No. 9 “Industry, Innovation and Infrastructure”, No. 12 “Responsible Consumption and Production” and No. 13 “Actions related to environmental change”.

In this regard, agricultural waste has great potential as an alternative source of cellulose fibers (Battalova et al., 2024b; Battalova et al., 2023; Imasheva et al., 2020; Khalil et al., 2012; Li et al., 2020; Rasaq et al., 2024). In the study of Jiang et al. (2019), high-purity cellulose fibers were obtained from rice husk and wheat straw by alkaline delignification. The studies (Battalova et al., 2024b; Battalova et al., 2023; Imasheva et al., 2020) investigated the possibility of obtaining microcrystalline cellulose (MCC) from agricultural waste such as sunflower husk (SH) and rice husk (RH) by organosolvent oxidation. The MCC yield was 43.49–52.58%, and the α-cellulose content was 40.5–65.57%. Similarly, in (Battalova et al., 2024a), the possibility of obtaining cellulose nanofibers (CNF) from agricultural waste – SFH by formic acid hydrolysis was investigated, resulting in CNF with a yield of 71% and a zeta potential of -15.8 mV. In (Akatan et al., 2022; Shahi et al., 2020), the authors of the study developed biofilms based on nanocellulose obtained from sugar beet pulp and residues accumulated during sunflower oil production and investigated their potential use as a “green” material. The results of

this study showed that agricultural waste is a potential source of raw material for the obtaining of cellulose-based biopolymers.

In this regard, sorghum husk (*Sorghum Husk*) has recently been studied as a promising raw material for pulp production (Sani et al., 2020; Waghmare et al., 2018). Sorghum is one of the five most important grain crops grown in sustainable agriculture worldwide. It is grown primarily in tropical and arid climates (Charyulu et al., 2024; Dalton & Hodjo, 2020). Sorghum is highly nutritious and contains a variety of bioactive compounds such as sterols, carotenoids, phenolic acids, and flavonoids, which are known for their potent antioxidant, anti-inflammatory, cholesterol-lowering, and anticancer activities (Bakari et al., 2023). A significant share of global sorghum seed production occurs in the United States, Nigeria, Sudan, Mexico, India, and Ethiopia (Pereverzin 2016). Annual global production is approximately 70 million tons. Sorghum production in our country, according to 2024 data, increased by 231% compared to previous years and is intended for the feed and food industries (West Kazakhstan Region, Taskala District Akimat [WKR TDA], n.d.). This indicates that, in addition to waste from manufacturing plants, the share of agricultural waste is significantly higher.

Sorghum hulls (SH), formed during sorghum processing, account for 15% of the total grain weight. Its composition has been shown to be rich in carbohydrates, such as polysaccharides, phenols, and proteins, as well as silicon (Dong et al., 2019; Kshirsagar et al., 2017).

Research has shown that sorghum pulp is a potential raw material for the production of cellulose fibers (da Costa et al., 2024; Kumar et al., 2015; Yulianto et al., 2020). The results indicate the possibility of obtaining cellulose in the range of 30-40%. However, these studies used a two-stage extraction method. Alkaline treatment was applied first, followed by hydrogen peroxide. This, in turn, increases the time and cost of extraction, as well as the amount of additional process fluids. Therefore, the efficiency and environmental safety of the method used for processing cellulose raw materials are of great importance.

Therefore, the aim of this study was to isolate high-quality cellulose microcrystals through the efficient utilization of husks – a byproduct of sorghum production grown in the southern region of the Republic of Kazakhstan. The resulting cellulose fibers have high potential for use as key components in the production of paper and cardboard, as well as biocomposite materials.

Materials and methods

Materials

Sorghum bicolor husks were obtained from southern region of Kazakhstan. Hydrogen peroxide (35%, H_2O_2), acetic acid (≥44%, CH_3COOH), potassium permanganate (99%, $KMnO_4$), ethanol (96%, C_2H_5OH), sulfuric acid (98%, H_2SO_4), orthophosphoric acid (98%, H_3PO_4), sodium hydroxide (≥99%, NaOH), potassium bichromate (≥99%, $K_2Cr_2O_7$), sodium thiosulfate (99%, $Na_2S_2O_3$), potassium iodide (≥99%, KI) and starchwere provided by Sigma-Aldrich (Bangalore, India). All other reagents were of analytical grade and were utilized without further purification.

Methods

Preparation of raw materials

To obtain microcrystalline cellulose, a variety of SbH raw material called “Sorghum bicolor” grown in the southern region of Kazakhstan was used. In sorghum, the fruit is a caryopsis. The sorghum fruit coat is the membrane in which the seed coat is fused with the pericarp. The pericarp is the outer part of the fruit, developing from the wall of the ovary. The pericarp is divided into three layers: 1) Exocarp (outer layer): consists of small, tightly adjacent cells with thickened walls covered with a waxy coating. The cells are prismatic in shape, elongated perpendicular to the surface. The cells are pigmented dark red, brown. 2) Mesocarp (middle layer): is represented by loose tissue consisting of parenchymatous cells. The cells are larger than in the exocarp, with thin cellulose walls. 3) Endocarp (inner layer): thin, tightly adjacent to the seed coat. The pericarp is rich in grain fibers, primarily cellulose, hemicellulose, starch, and lignin. The seed coat is the membrane surrounding the embryo. The seed coat is fused with the pericarp, forming a single covering (Badigannavar et al., 2018; Makhatov et al., 2017).

To remove residual substances from Sorghum bicolor husks, they were pre-washed with distilled water in a flask with a rotary condenser at 90±2°C for 60 minutes with stirring. They were then filtered through filter paper and dried in an oven at 60±2°C for 5 hours until constant weight was reached.

The raw material samples from Sorghum bicolor seed husks used in the study were conventionally referred to as sorghum bicolor husks (SbH), and the MCC obtained from them was referred to as MCC_{SbH}.

Preparation of peroxyacetic acid (PAA)

Peroxyacetic acid (PAA) was used to extract MCC from the raw material. The concentrations of the starting reagents for PAA production were re-

duced by half and prepared according to the method described in (Akatan et al., 2022; Battalova et al., 2024b; Battalova et al., 2023; Imasheva et al., 2020). The resulting PAA was stored in a freezer at 5±0.5°C.

Chemical composition of sorghum bicolor husks (SbHs)

The mineral composition of raw SbH was determined using X-ray fluorescence (XRF) spectroscopy on an EDX3600H (Skyray Instruments, China). In order to determine the amount of water-soluble hydrocarbons, 5 ± 0.001 g of raw material was heated for 2 h, with continuous stirring in 50 mL of distilled water. After this process, the SbHs were filtered, dried at 80°C ± 2°C for 5 h, and then the mass was measured on an LV 210-A analytical scale (Sartogosm, Russia). The quantity of hydrolyzable hydrocarbons in water was determined from the difference between the initial mass and the final mass.

To assess the ash content of SbH, 5 g of MCC was incinerated in an 8.2/1100 L muffle furnace (SNOL, Lithuania) at a temperature of 700°C ± 5°C for a duration of 90 minutes. The weight of the resulting ash (SiO_2) was recorded using an LV 210-A analytical scale (Sartogosm, Russian) until an average measurement was achieved. The ash content was calculated by subtracting the final mass from the initial mass.

Preparation of MCC from SbH by organosolvent oxidation and determination of its yield

The synthesis of microcrystalline cellulose (MCC) based on SbH was carried out according to the method described in (Akatan et al., 2022; Battalova et al., 2024b; Battalova et al., 2023; Imasheva et al., 2020). The SbH and PAA ratio was extracted under hydromodule conditions with proportions of 1:10, 1:12, 1:14, 1:16, 1:18, and 1:20 g/ml. To obtain MCC, the raw material and delignifying agent were boiled in a flask fitted with a rotary condenser at a temperature of 90±2°C for 90 minutes, with continuous and vigorous stirring. The resulting MCC solution was then cooled to 25±2°C, filtered using a paper filter, and neutralized with distilled water until reaching a pH of 7 (Fig. 1). The resulting product was dried at 80±2°C for 6 hours to constant weight, weighed on an analytical balance with an accuracy of 0.0001 g, and the yield was calculated using the formula:

$$\eta = (m_{SbH}-m_{MCC})/m_{SbH}\times 100\% \quad (1)$$

where, m_{SbH} is the mass of SbH, g; m_{MCC} – the mass of obtained MCC, g.

Figure 1
Scheme of obtaining MCC from SbH by the organosolvent oxidation

Determination of microcrystalline cellulose quality indicators

The moisture content of the synthesized MCC was determined using the GOST-16932 method (state standard), the α-cellulose content – using the GOST-6840 method, the residual lignin content – using the GOST-11960 method, the hemicellulose content – using the GOST-9002 method, and the ash content – using the GOST 18461-93 method.

Scanning electron microscopy (SEM)

The surface characteristics of the MCC were analyzed using a Quanta 200i 3D SEM from FEI in the Netherlands. The analysis was conducted in high vacuum mode with a secondary electron detector operating at an accelerating voltage of 15 kV. To enhance electron transfer, the MCC surface was coated with gold nanoparticles, and the samples were affixed to aluminum pins using carbon tape.

FTIR spectroscopy

The chemical composition of the samples was analyzed using an FTIR FT-801 IR spectrometer (Simex, Russia). This analysis employed an internal and variable-diffuse reflection technique, achieving an accuracy of 1 cm^{-1} across a wave number range of 450–4700 cm^{-1}. The procedure involved 50 scans at a temperature of 25±20°C, with the sample placed on the attachment's surface.

X-ray diffraction

The structural and phase properties of the samples were investigated by X-ray diffraction (XRD) analysis using monochromatic copper radiation (CuKα, λ = 0.1542 Å) on an X´PertPRO diffractometer (Malvern Panalytical Empyrean, Netherlands). The diffraction patterns were recorded within a 2θ range of 10–45° with a scanning increment of 0.02°. The X-ray tube was operated at 45 kV and 30 mA, while the counting time for each step was set to 0.5 s. A universal aluminum sample holder (PW1172/01) was employed during the measurements. The obtained diffraction data were interpreted using the ICDD PDF-4/AXIOM X-ray diffraction database.

Thermogravimetric analysis (TGA)

The thermal stability of the obtained samples was evaluated under an argon atmosphere using a LabSys Evo differential thermogravimetric analyzer (Setaram, France). The measurements were carried out over a temperature range of 30 ± 5 to 800 ± 5°C at a heating rate of 10 ± 1°C/min. The sample mass used for analysis was 20 ± 2 mg.

Results and discussion

Chemical composition of SbH

A quantitative analysis of the chemical composition of the initial SbH raw material was carried out, and the obtained results are presented in Table 1.

Table 1
Chemical composition of the initial SbH sample

Compounds	Quantity, %
K	16.3
P	2.55
Ca	3.76
Si	65.8
Al	4.23
Fe	2.28
Mn	0.08
Ni	0.06
Cu	0.07
Zn	0.08
Cr	0.18
Ti	0.57
Cl	1.84
S	1.94
Water soluble hydrocarbons	0.26

The MCC_{SbH} from SbH by organosolvent oxidation method

Figure 2a shows the initial material—sorghum seed husk (SbH), and Figure 2b shows the obtained MCC_{SbH}. The initial material, SbH, had a reddish-brown color, while the obtained MCC_{SbH} had a flaky, fibrous structure and a light grayish tint.

Figure 2
Sorghumbicolor husks and MCC samples from SbH: a – SbH; b – MCC_{SbH} (hydromodule 1:16)

The yield and quality indicators of MCC_{SbH}

The yield and quality indicators of MCC_{SbH} obtained at different SbH:PAA g/ml ratios under "mild" conditions of the organosolvent oxidation method are presented in Table 2. The results of the study showed that the yield of SbH:PAA obtained at an SbH:PAA ratio of 1:16 g/ml was 57.24%, moisture content was 4.23%, α-cellulose content was 61.32%, residual lignin was 0.71%, hemicellulose was 0.55%, and SiO_2 was 29.78%. Since the yield and quality indicators determined in other hydromodules were relatively low, 1:16 g/ml was recognized as the effective hydromodule. A study (Reddy & Yang, 2007) found that up to 35–40% MCC can be obtained from sorghum stems and leaves using alkaline and acid hydrolysis. It was found that at an

SbH:PAA ratio of 1:16 g/ml, the yield of MCC_{SbH} obtained using the organosolvent method increases by 10.6–25%. In addition, an additional bleaching process occurs for the cellulose obtained using traditional alkaline and mineral acids. This increases economic and energy costs. It should be noted that the organosolvent oxidation method does not require additional technological processes and increases the possibility of extracting cellulose under "mild" conditions.

Table 2
Effect of SbH:PAA ratio on MCC_{SbH} quality

SbH:PAA, g/ml	Quality indicators of MCC_{SbH}, %					
	Yield of MCC	Humidity	α-cellulose	Residual lignin	Hemi-cellulose	Ash content (SiO_2)
1:10	50.81±2	4.82±0.5	44.61±3	0.68±0.5	0.48±2	30.27±0.5
1:12	52.25±2	4.41±0.5	54.20±3	0.65±0.5	0.48±2	29.82±0.5
1:14	54.60±2	4.44±0.5	61.02±3	0.59±0.5	0.66±2	30.65±0.5
1:16	57.24±2	4.23±0.5	61.32±3	0.71±0.5	0.55±2	29.78±0.5
1:18	53.22±2	4.26±0.5	55.31±3	0.70±0.5	0.63±2	29.97±0.5
1:20	52.61±2	4.16±0.5	52.91±3	0.76±0.5	0.56±2	30.19±0.5

FTIR spectroscopy

Figure 3 presents the FTIR spectrum of the initial SbH material. The broad absorption band observed in the range of 3500–3000 cm^{-1} is attributed to the stretching vibrations of O–H groups. The peaks at 2920 cm^{-1} and 2850 cm^{-1} correspond to C–H stretching vibrations typical of polysaccharides (Zghari et al., 2018). In addition, the absorption bands in this region are associated with silanol (Si–OH) groups present in SbH (Cichosz & Masek, 2020; Zghari et al., 2018). The bands at approximately 1700 cm^{-1} and 1600 cm^{-1} are related to acetyl groups of hemicellulose and carbonyl groups within the lignin structure (Battalova et al., 2024b; Battalova et al., 2023; Kacuráková et al., 2002). The absorption region between 1600 cm^{-1} and 1510 cm^{-1} corresponds to the vibrations of aromatic rings in lignin (Battalova et al., 2024b; Battalova et al., 2023; Imasheva et al., 2020). The peaks in the range of 1250–1020 cm^{-1} are assigned to β-1,4-glycosidic bonds as well as C–O–C and C–O–H vibrations of cellulose (Akatan et al., 2025; Battalova et al., 2024b; Battalova et al., 2023; Guzman et al., 2017; Imasheva et al., 2020). These results confirm that sorghum husk is a lignocellulosic raw material rich in cellulose, hemicellulose, lignin, and other hydrocarbon compounds.

Comparative IR spectra of the chemical structure of MCC_{SbH}, obtained in different ratios, are shown in Figure 4. All spectra of the MCC_{SbH} samples contain signals of the main functional groups characteristic of cellulose. In particular, a broad and intense stretching vibration of the O–H groups is recorded in the region of 3300–3400 cm^{-1}. This indicates a large number of hydroxyl groups and the presence of intermolecular hydrogen bonds (Cichosz & Masek, 2020). In addition, the absorption bands at 2895 cm^{-1} are attributed to the symmetric and asymmetric stretching vibrations of C–H bonds (Cichosz & Masek, 2020; Zghari et al., 2018).

Several characteristic peaks associated with the structural features of cellulose are observed within the 1800–800 cm^{-1} region. The band at approximately 1430 cm^{-1} corresponds to the deformation vibrations of C–H bonds in the crystalline regions of cellulose and is commonly used to evaluate the crystallinity degree of cellulose (Kacuráková et al., 2002; Zghari et al., 2018). The peak at 1370 cm^{-1} is assigned to C–H deformation vibrations, while the intense band at 1160 cm^{-1} is related to the stretching vibrations of C–O–C bonds within the pyranose ring, characteristic of β-1,4-glycosidic linkages. Furthermore, the peaks observed in the range of 1050–1030 cm^{-1} correspond to the stretching vibrations of C–O bonds in the aromatic ring, confirming the polysaccharide nature of cellulose (Kacuráková et al., 2002; Zghari et al., 2018). The absorption peak at 895 cm^{-1} indicates the presence of β-glycosidic bonds and reflects the crystalline structure of cellulose (Battalova et al., 2024b; Battalova et al., 2023; Cichosz & Masek, 2020). Meanwhile, weak absorption bands at 1508.9 cm^{-1} and 1734.4 cm^{-1} are associated with the stretching vibrations of aromatic C=C bonds in

residual lignin, as well as C=O vibrations of acetyl and ester groups in hemicellulose present in MCC (Akatan et al., 2025; Guzman et al., 2017; Imasheva et al., 2024). This clarifies the quantitative values of residual lignin and hemicellulose given in Table 2. The obtained results (Bakari et al., 2023; Charyulu et al., 2024) are in good agreement with the FTIR absorption spectra of microcrystalline cellulose obtained from sorghum residues are presented in Figure X. A noticeable decrease in the intensity of the absorption peaks was observed with increasing PAA content in the SbH:PAA ratio (g/mL). This behavior can be attributed to the progressive hydrolysis process, which weakens the glycosidic bonds in the cellulose macromolecule and alters the symmetry of its molecular structure (Battalova et al., 2024b; Battalova et al., 2023; Imasheva et al., 2024; Zghari et al., 2018). In particular, the reduced intensity of the peaks corresponding to O–H and C–H bond vibrations in the samples with SbH:PAA ratios of 1:18 and 1:20 indicates structural deformation of the cellulose matrix.

Figure 3
FTIR spectra of SbH

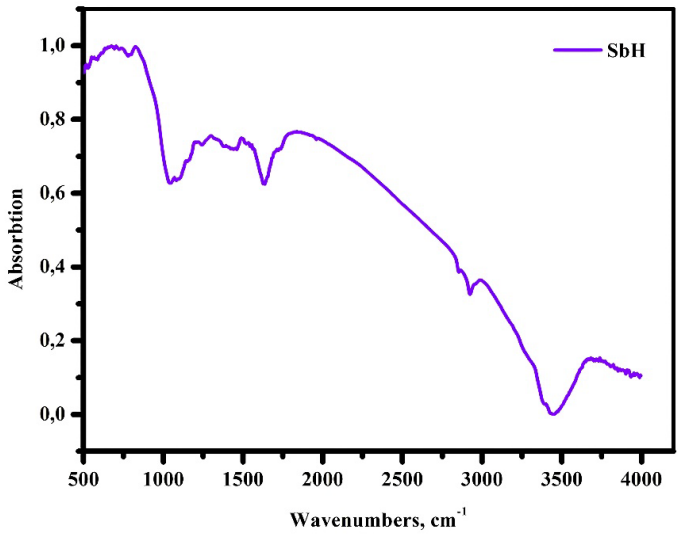

Figure 4
FTIR spectra of MCC_{SbH} in different ratios

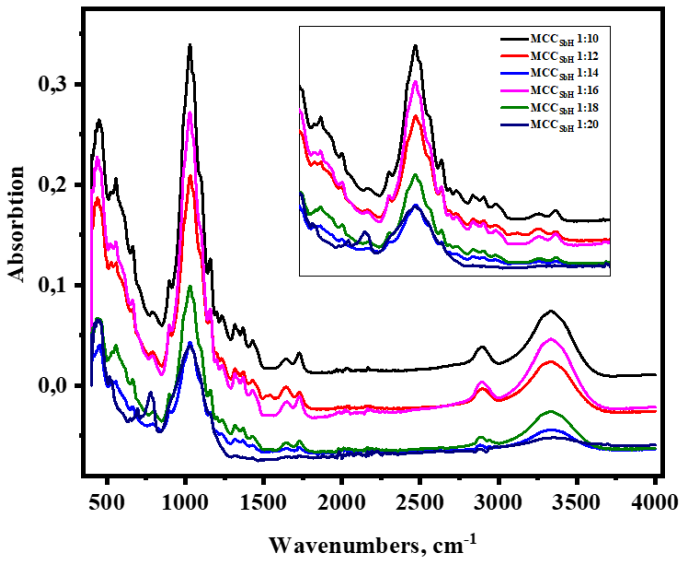

X-ray diffraction

The results of comparative X-ray diffraction analysis carried out to determine the structural and phase composition of the initial SbH raw material and MCCSbH samples (1:16 g/ml) obtained in the effective hydromodulus are shown in Figures 5a and 5b. The crystalline structure of the samples was determined in accordance with the studies (French, 2014; Imasheva et al., 2024; Podgorbunskikh et al., 2018). Peaks 2θ=16.1°(110), 22.4°(200), 34.1°(004) recorded in the diffraction pattern of SbH (Figure 5a) indicate an amorphous and semi-crystalline structure of sorghum fiber. Moreover, an intense signal at the diffraction reflection angle 2θ=27.2°(101) is characteristic of the signal of silica in the raw material (Bolatkan et al., 2025). It is evident that this corresponds to the elemental composition and quality indicators of the initial SbH raw material given in Tables 1 and 2.

The X-ray diffraction (XRD) pattern of MCCSbH exhibits characteristic diffraction peaks at 2θ = 15.3° (110), 22.3° (200), and 34.8° (004), confirming the crystalline structure of MCCSbH (Fig. 5b). The observed diffraction peaks indicate that the crystal structure of MCC is a double-chain monoclinic form corresponding to cellulose Iβ (Imasheva et al., 2024; Kacuráková et al., 2002). These results confirm the effective removal of lignin, hemicellulose, and other non-cellulosic hydrocarbon components during the extraction of cellulose from sorghum husk. Furthermore, the intensity of the diffraction peak associated with silica at 2θ = 27.2° (101) decreased by approximately 1.2 times in MCC compared to the initial SbH material. This reduction may be attributed to the partial hydrolysis of silica occurring during the organosolvent oxidation treatment of the original SbH raw material.

The results of the X-ray diffraction analysis demonstrated that the initial SbH material possesses a predominantly semicrystalline or amorphous structure, whereas the microcrystalline cellulose obtained after treatment exhibits well-defined crystalline characteristics. These findings are in good agreement with previously reported studies (Akatan et al., 2022; Battalova et al., 2024b; Battalova et al., 2023; Imasheva et al., 2024; Imasheva et al., 2020).

Figure 5

XRD diffractions of: a – SbH; b – MCCSbH

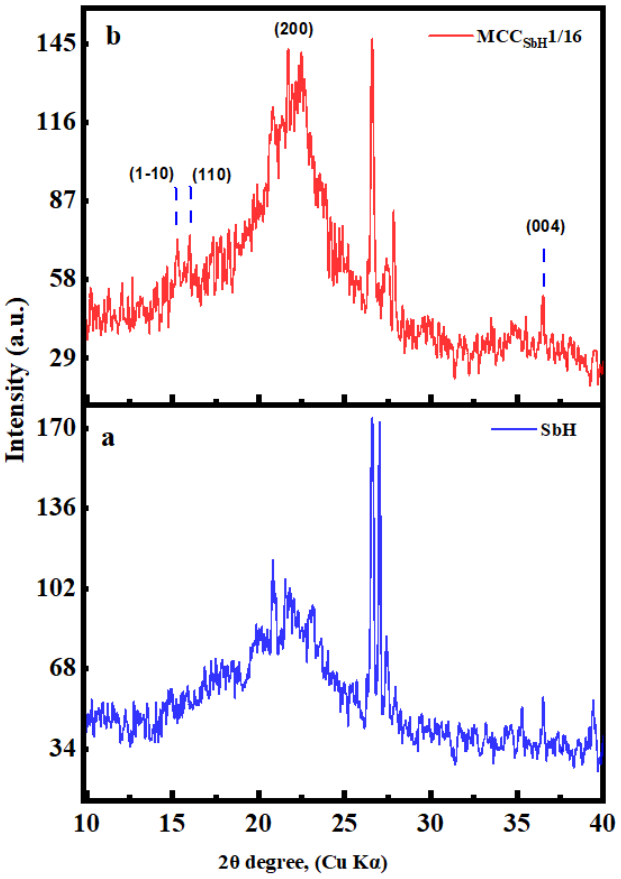

SEM analysis

Figure 6 shows the surface morphology of the initial material SbH (Fig. 6a) and MCCSbH obtained at an effective hydromodulus of 1:16 g/ml (Fig. 6b). It is evident that the initial material – sorghum husk – has a multilayer structure. It can be observed that the cellulose fibers on the surface of the husk are densely covered with silica, waxes, pectin, lignin, hemicellulose, and other hydrocarbon compounds, which contribute to the high mechanical strength and hydrophobic properties of the material (Li et al., 2018; Zhang et al., 2018). This indicates that the composition of the starting material SbH, shown in Figure 3, is consistent with the results obtained by IR analysis.

In Fig. 6b, the surface morphology of MCCSbH extracted at an effective hydromodulus of 1:16 g/ml has a ribbon-like shape consisting of fibrils of varying sizes. The length of the cellulose fibers is approximately 193.5–993.0 μm, and the width is 13.66–21.55 μm (Fig. 6b). This indicates a fibrous structure of MCCSbH fragments. In addition, roughness of the surface of the cellulose fibers is observed. This is explained by partial hydrolysis of the amorphous regions and the release of crystalline fibers during hydrolysis (Cichosz & Masek, 2020). In the study (Zhang et al., 2018), it was found that the rough surface structure of the cellulose fibers indicates a large surface area and high sorption properties.

Figure 6
SEM images of: a – SbH; b – MCCSbH

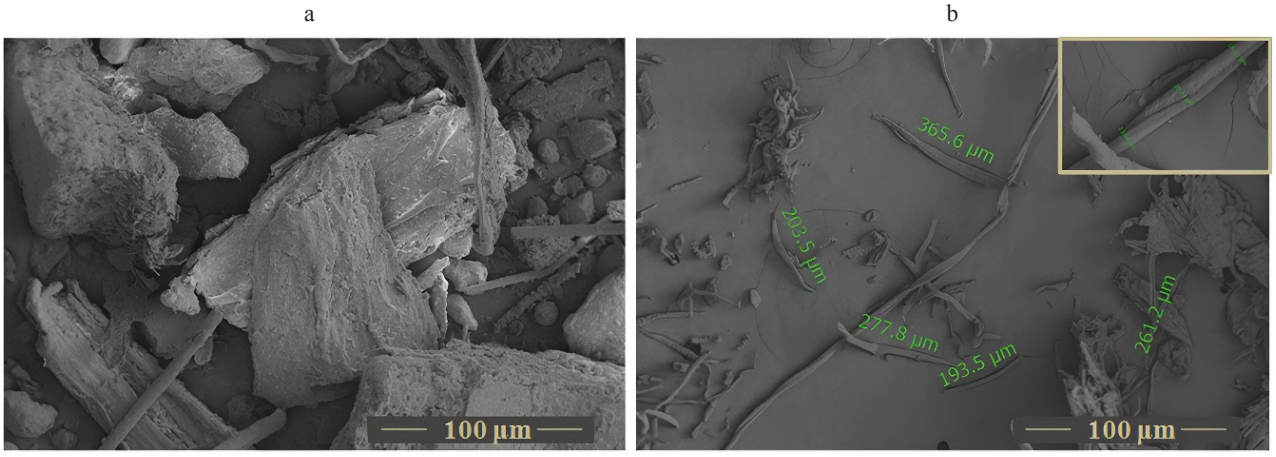

Thermogravimetric analysis of MCC_{SbH}

The resulting thermogram of MCC_{SbH} is shown in Figure 7. According to the obtained results, initial mass loss was observed in the range from 25 to 106°C. It is evident that over this period, the mass of the material decreased by approximately 3.3% due to the evaporation of moisture from the air and water sorbed by the sample.

The first phase of thermal degradation begins at temperatures from 106 to 263°C, and in this temperature range, mainly residual hemicellulose and low molecular weight fractions of lignin undergo thermal degradation (Battalova et al., 2024b). The studies (Chen et al., 2011; Henrique et al., 2015) have shown that thermal decomposition of lignocellulosic biomass occurs in the range from 150 to 500°C. The research (Wang et al., 2021) has shown that most of the hemicellulose decomposes gradually and over a wide temperature range from 150 to 350°C, cellulose at 275–350°C, and lignin at 250–500°C.

The major thermal degradation of MCC_{SbH} occurred within the temperature range of 263–387°C. During this stage, the MCC_{SbH} sample lost approximately 49.5% of its initial mass, indicating the thermal decomposition of high-molecular-weight cellulose chains (Hou et al., 2017). This degradation process led to the formation of volatile compounds and the breakdown of the organic structure of MCC_{SbH}.

During the thermal degradation of cellulose at temperatures of 387–600°C, combustion of intermediate products occurs (Hou et al., 2017). At this stage, 54% of the total mass of the sample undergoes thermal degradation, and the residual substance – silica (SiO_2) – accounts for approximately 35%. This is consistent with the results of determining the mineral composition and ash content of the initial material and MCC_{SbH}, presented in Tables 1 and 2.

Figure 7
TGA curve of MCC_{SbH}

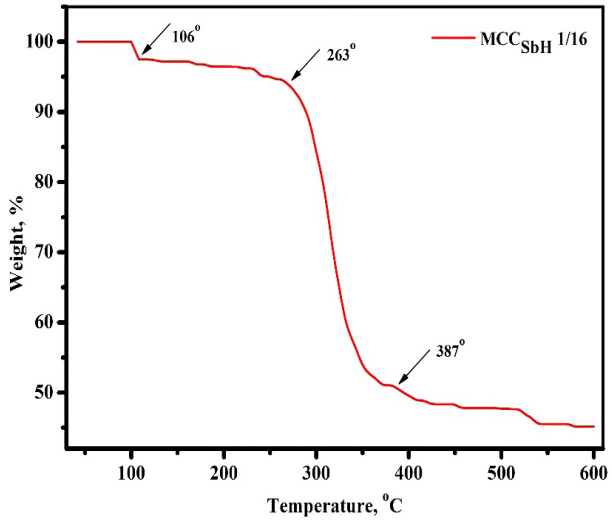

Conclusion

Summarizing the obtained results, it should be noted that in the course of the research work, the possibility of obtaining microcrystalline cellulose (MCC_{SbH}) from sorghum seed husk (SbH) grown in the southern region of Kazakhstan, using the organosolvent oxidation method was studied. The elemental analysis of the feedstock (SbH) showed that its composition is dominated by Si (65.8%), K (16.3%), Ca (3.76%) and P (2.55%). IR analysis showed that it is rich in hydrocarbons. In this regard, it was established that the effective hydromodulus for obtaining MCC_{SbH} from SbH is the SbH:PAA ratio of 1:16 g/ml. The yield of the obtained MCC_{SbH} sample was 57.24%, and the α-cellulose content was 61.32%.

The surface morphology of the obtained MCC_{SbH} sample was found to be fibrous, with a length of approximately 193.5–993.0 μm and a width of 13.66–21.55 μm. Fourier transform infrared (FTIR) spectroscopy analysis demonstrated that the obtained product contained the main functional groups characteristic of MCC and was effectively purified from residual lignin and hemicellulose components. X-ray diffraction analysis revealed that the original SbH sample had a semi-amorphous structure, while the obtained MCC_{SbH} was characterized by a distinct crystalline structure. The cellulose crystal structure was double-chain monoclinic, typical of cellulose Iβ. Furthermore, thermogravimetric analysis (TGA) showed that the thermal stability of the MCC_{SbH} sample was maintained at temperatures up to 263°C.

The obtained results confirm that this material is a promising raw material for producing high-quality microcrystalline cellulose using mild organosolv oxidation. The resulting MCC_{SbH} has significant potential as a promising bio-based raw material for the development of pharmaceuticals, food packaging, and the production of environmentally friendly biodegradable materials.

Author contributions

The manuscript was written through contributions of all authors. Conceptualization – Saule Nauryzova and Sana Kabdrakhmanova; Data curation – Kydyrmolla Akatan and Esbol Shaimardan; Formal analysis – Aidana Imasheva and Ainur Kabdrakhmanova; Investigation – Ainur Battalova and Ansagan Demeukhan; Methodology – Ainur Battalova and Kydyrmolla Akatan; Project administration – Ainur Battalova and Kydyrmolla Akatan; Resources – Ainur Kabdrakhmanova and Ansagan Demeukhan; Supervision – Saule Nauryzova and Sana Kabdrakhmanova; Validation – Saule Nauryzova, Sana Kabdrakhmanova and Kydyrmolla Akatan; Visualization – Saule Nauryzova, Kydyrmolla Akatan and Aibar Yeskaliyev; Writing – original draft – Ainur Battalova; Writing reviewing and editing – Ainur Battalova, Kydyrmolla Akatan and Saule Nauryzova. All authors have read and agreed to the published version of the manuscript.

Acknowledgments

This research has been funded by the Science Committee of the Ministry of Science and Higher Education of the Republic of Kazakhstan (Grant No. AP26103101).

Conflict of interest

The authors declare that they have no conflicts of interest.

References

1. Akatan, K., Kabdrakhmanova, S., Kuanyshbekov, T., Battalova, A., Ibraeva, Z., & Beisebekov, M. (2022). Highly-efficient isolation of microcrystalline cellulose and nanocellulose from sunflower seed waste via environmentally benign method. *Cellulose*, *29*(7), 3787–3802. https://doi.org/10.1007/s10570-022-04527-4

2. Akatan, K., Kaiyrbekov, N., Demeukhan, A., Battalova, A., Shaimardan, E., Beisebekov, M., Kholiya, F., Ibraeva, Zh., & Kabdrakhmanova, S. (2025). Synthesis of cellulose based hydrogel with high absorption capacity. *International Journal of Biology and Chemistry*, *18*(1), 150–158. https://doi.org/10.26577/IJBCh202518115

3. Badigannavar, A., Teme, N., de Oliveira, A. C., Li, G., Vaksmann, M., & Viana, V. E. (2018). Physiological, genetic and molecular basis of drought resilience in sorghum [*Sorghum bicolor* (L.) Moench]. *Indian Journal of Plant Physiology*, *23*(4), 670–688. https://doi.org/10.1007/s40502-018-0416-2

4. Bakari, H., Djomdi, Ruben, Z. F., & Ali, M. (2023). Sorghum (*Sorghum bicolor* L. Moench) and its main parts (by-products) as promising sustainable sources of value-added ingredients. *Waste and Biomass Valorization*, *14*(4), 1023–1044. https://doi.org/10.1007/s12649-022-01992-7

5. Battalova, A., Akatan, K., Kabdrakhmanova, S., Ibraeva, Z., Beisebekov, M., Shaimardan, E., Kantay, N., Dzhumanazarova, A., Joshy, K. S., & Thomas, S. (2024a). Isolation of cellulose nanofibers from sunflower seed husks via formic acid hydrolysis. *Journal of Polymer Science*. Advance online publication. https://doi.org/10.1002/pol.20240485

6. Battalova, A., Ibraeva, Z., Kabdrakhmanova, S., Akatan, K., Shaimardan, E., Demeukhan, A., Tursyngazykyzy, A., Beisebekov, M., & Maussumbayeva, A. (2024b). Comparative characteristics of microcrystalline cellulose obtained from the rice waste production of Kazakhstan. *Chemical Bulletin of Kazakh National University*, *113*(4), 14–23. https://doi.org/10.15328/cb1386

7. Battalova, A. K., Kabdrakhmanova, S. K., Akatan, K., Beisebekov, M. M., Kantay, N., Ibraeva, Zh. E., Mausumbayeva, A. M., & Merck, L. (2023). Features of microcrystalline cellulose produced from sunflower seeds of different oil content. *International Journal of Biology and Chemistry*, *16*(1), 78–86. https://doi.org/10.26577/ijbch.2023.v16.i1.08

8. Bolatkan, D., Kerimkulova, A., Beisebekov, M., Akatan, K., Kantay, N., Shaimardan, E., Kukhareva, A., Bukunova, A., & Kabdrakhmanova, S. (2025). Quantitative assessment of the use of Kazakhstan montmorillonite clays as sorbent carriers for pharmaceutical substances. *Physical Sciences and Technology*, *12*(1-2), 121–133. https://doi.org/10.26577/phst202512112

9. Charyulu, D. K., Afari-Sefa, V., & Gumma, M. K. (2024). Trends in global sorghum production: Perspectives and limitations. In E. Habyarimana, M. A. Nadeem, F. S. Baloch, & N. Zencirci (Eds.), *Omics and biotechnological approaches for product profile-driven sorghum improvement* (pp. 1–21). Springer. https://doi.org/10.1007/978-981-97-4347-6_1

10. Chen, X., Yu, J., Zhang, Z., & Lu, C. (2011). Study on structure and thermal stability properties of cellulose fibers from rice straw. *Carbohydrate Polymers*, *85*(1), 245–250.

11. Cichosz, S., & Masek, A. (2020). IR study on cellulose with the varied moisture contents: Insight into the supramolecular structure. *Materials*, *13*(20), 4573.

12. da Costa, D. P. S. T., Dewi, I. A., Fahma, F., Hamid, Z. A. A., & Suryanegara, L. (2024). Isolation and characterization of cellulose nanofibers from sweet sorghum with different ultrafine grinding modes. *AIP Conference Proceedings*, *2973*(1), 040009. https://doi.org/10.1063/5.0184730

13. Dalton, T. J., & Hodjo, M. (2020). Trends in global production, consumption, and utilization of sorghum. In V. A. Tonapi, H. S. Talwar, A. K. Are, B. V. Bhat, C. R. Reddy, & T. J. Dalton (Eds.), *Sorghum in the 21st century: Food – fodder – feed – fuel for a rapidly changing world* (pp. 3–15). Springer. https://doi.org/10.1007/978-981-15-8249-3_1

14. Dong, M., Wang, S., Xu, F., & Li, Q. (2019). Pretreatment of sweet sorghum straw and its enzymatic digestion: Insight into the structural changes and visualization of hydrolysis process. *Biotechnology for Biofuels*, *12*, 276. https://doi.org/10.1186/s13068-019-1613-6

15. French, A. D. (2014). Idealized powder diffraction patterns for cellulose polymorphs. *Cellulose*, *21*(2), 885–896. https://doi.org/10.1007/s10570-013-0030-4

16. Guzman, J. T., Sillard, C., Plackett, D., Szabo, P., Bras, J., & Daugaard, A. E. (2017). Chemically extracted nanocellulose from sisal fibres by a simple and industrially relevant process. *Cellulose*, *24*(1), 107–118.

17. Henrique, M. A., Neto, W. P. F., Silvério, H. A., Martins, D. F., Gurgel, L. V. A., & Barud, H. S. (2015). Kinetic study of the thermal decomposition of cellulose nanocrystals with different polymorphs, cellulose I and II, extracted from different sources and using different types of acids. *Industrial Crops and Products*, *76*, 128–140.

18. Hou, X., Fang, F., Guo, X., Wizi, J., Ma, B., Tao, Y., & Yang, Y. (2017). Potential of sorghum husk extracts as a natural functional dye for wool fabrics. *ACS Sustainable Chemistry & Engineering*, *5*(6), 4589–4597. https://doi.org/10.1021/acssuschemeng.6b02969

19. Imasheva, A. A., Kabdrakhmanova, S. K., Akatan, K., Ibraeva, Zh. E., Temirkhanova, G., Beisebekov, M. M., Kantay, N., & Mausumbaeva, A. M. (2024). Obtaining cellulose with crystallographic orientation of macromolecules from the husk of a hybrid sunflower. *Bulletin of the National Nuclear Corporation of the Republic of Kazakhstan*, *(3)*, 29–34. https://doi.org/10.52676/1729-7885-2024-3-29-34

20. Imasheva, A. A., Kabdrakhmanova, S. K., Ibraeva, Zh. E., Kudaibergenov, S. E., Akatan, K., & Abilev, M. B. (2020). Study of the possibility of obtaining cellulose from oilseed residues by the organosolvent method. *Bulletin of the National Nuclear Corporation of Kazakhstan*, *1*(81), 35–38.

21. Jiang, F., Wang, T., Zhang, Y., & Dong, S. (2019). Extraction of cellulose from rice husk and wheat straw for bio-based materials. *Industrial Crops and Products*, *137*, 66–74.

22. Kacuráková, M., Smith, A. C., Gidley, M. J., & Wilson, R. H. (2002). Molecular interactions in bacterial cellulose composites studied by 1D FT-IR and dynamic 2D FT-IR spectroscopy. *Carbohydrate Research*, *337*(12), 1145–1153.

23. Khalil, H. P. S. A., Bhat, A. H., & Ireana Yusra, A. F. (2012). Agricultural biomass and residues as potential sources for nanocellulose fibers: Preparation and applications. *Carbohydrate Polymers*, *88*(4), 1079–1085.

24. Kshirsagar, S. D., Bhalkar, B. N., & Waghmare, P. R. (2017). Sorghum husk biomass as a potential substrate for production of cellulolytic and xylanolytic enzymes by *Nocardiopsis* sp. KNU. *3 Biotech*, *7*(3), 163. https://doi.org/10.1007/s13205-017-0800-z

25. Kumar, C. G., Kumar, M. P., & Gupta, S. (2015). Isolation and characterization of cellulose from sweet sorghum bagasse. *Sugar Tech*, *17*(4), 395–403. https://doi.org/10.1007/s12355-014-0339-9

26. Li, T., Chen, C., Brozena, A. H., Zhu, J. Y., Xu, L., Driemeier, C., Dai, J., Rojas, O. J., Isogai, A., Lawoko, M., Wagberg, L., Yu, H., & Hu, L. (2020). Nanocellulose from agricultural waste for sustainable materials development. *ACS Sustainable Chemistry & Engineering*, *8*(12), 4937–4956.

27. Li, M., Yan, G., Bhalla, A., Maldonado-Pereira, L., Russell, P. R., & Ding, S. Y. (2018). Physical fractionation of sweet sorghum and forage/energy sorghum for optimal processing in a biorefinery. *Industrial Crops and Products*, *124*, 607–616.

28. Makhatov, Zh. B., Latif, A. S., Saparbekova, A. A., Isaev, E. B., Makhatov, B. K., & Bukharbaeva, A. E. (2017). Botanical and geographical characteristics of sorghum species. *Vestnik of the South-Kazakhstan State Pharmaceutical Academy*, *2*(79), 74.

29. Pereverzin, V. (2016). Sorghum: Cultivation technology for forage purposes. *Agrarian Review*, *3*(55), 51–53. https://doi.org/10.1016/j.apsusc.2024.159394

30. Podgorbunskikh, E.M., Bychkov, A.L., Bulina, N.V., & Lomovskii, O.I. (2018). Disordering of the crystal structure of cellulose under mechanical activation. *Journal of Structural Chemistry*, *59*(1), 201–208. https://doi.org/10.1134/s0022476618010328

31. Rasaq, S. A., Swarna, J., & Amit, K. J. (2024). Green and sustainable pretreatment methods for cellulose extraction from lignocellulosic biomass and its applications: A review. *Carbohydrate Polymer Technologies and Applications*, *7*, 100396. https://doi.org/10.1016/j.carpta.2023.100396

32. Reddy, N., & Yang, Y. (2007). Structure and properties of natural cellulose fibers obtained from sorghum leaves and stems. *Journal of Agricultural and Food Chemistry*, *55*(14), 5569–5574. https://doi.org/10.1021/jf0707379

33. Roohallah, S. R., Mozhgan, G. V., Mohadeseh, H., & Vijay, K. T. (2024). Agricultural wastes: A practical and potential source for the isolation and preparation of cellulose and application in agriculture and different industries. *Industrial Crops and Products*, *208*, 117904. https://doi.org/10.1016/j.indcrop.2023.117904

34. Sani, H. A., Yauri, A. U. B., Muhammad, A., Yahayya, Y., & Salau, M. (2020). Preparation and characterization of bioplastic from sorghum husk. *American Journal of Polymer Science and Technology*, *6*(2), 14–20. https://doi.org/10.11648/j.ajpst.20200602.12

35. Shahi, N., Min, B., Sapkota, B., & Rangari, V. K. (2020). Eco-friendly cellulose nanofiber extraction from sugarcane bagasse and film fabrication. *Sustainability*, *12*(15), 6015. https://doi.org/10.3390/su12156015

36. Shehrawat, P., & Sindhu, N. (2015). Agricultural waste utilization for healthy environment and sustainable lifestyle. *Annals of Agri-Bio Research*, *20*(2), 110–114.

37. Waghmare, P. R., Khandare, R. V., Jeon, B., & Govindwar, S. P. (2018). Enzymatic hydrolysis of biologically pretreated sorghum husk for bioethanol production. *Biofuel Research Journal*, *5*(3), 846–853. https://doi.org/10.18331/BRJ2018.5.3.4

38. Wang, Q., Nnanna, P. C., Shen, F., Huang, M., Tian, D., Hu, J., Zeng, Y., Yang, G., & Deng, S. (2021). Full utilization of sweet sorghum for bacterial cellulose production: A concept of material crop. *Industrial Crops and Products*, *162*, 113256. https://doi.org/10.1016/j.indcrop.2021.113256

39. West Kazakhstan Region, Taskala District Akimat. (n.d.). *Activities*. https://www.gov.kz/memleket/entities/bko-taskala/activities/2380

40. Yulianto, Putri, D. N. M., Perdani, M. S., Arbianti, R., Suryanegara, L., & Hermansyah, H. (2020). Effect of cellulose fiber from sorghum bagasse on the mechanical properties and biodegradability of polylactic acid. *Energy Reports*, *6*(1), 221–226. https://doi.org/10.1016/j.egyr.2019.08.048

41. Zghari, B., Hajji, L., & Boukir, A. (2018). Effect of moist and dry heat weathering conditions on cellulose degradation of historical manuscripts exposed to accelerated ageing: 13C NMR and FTIR spectroscopy as a non-invasive monitoring approach. *Journal of Materials and Environmental Science*, *9*(2), 641–652.

42. Zhang, L. M., Leng, C. Y., Luo, H., Wu, X. Y., Liu, Z. Q., & Zhang, Y. M. (2018). Sweet sorghum originated through selection of dry, a plant-specific NAC transcription factor gene. *The Plant Cell*, *30*(10), 2286–2307.

Information about the authors:

Saule Nauryzova – PhD, associate professor, Scientific Center of Composite Materials (Almaty, Kazakhstan, e-mail: saule_nauryzova@mail.ru)

Ainur Battalova – PhD, Scientific Center of Composite Materials (Almaty, Kazakhstan, e-mail: 2012kausar@mail.ru)

Ansagan Demeukhan – researcher, S. Amanzholov East Kazakhstan University (Oskemen, Kazakhstan, e-mail: demeuhanansagan@gmail.com)

Kydyrmolla Akatan – PhD, S. Amanzholov East Kazakhstan University (Oskemen, Kazakhstan, e-mail: ahnur.hj@mail.ru)

Ainur Kabdrakhmanova – PhD, Satbayev University (Almaty, Kazakhstan, e-mail: ainurkabdrahmanova@mail.ru)

Aidana Imasheva – researcher, S. Amanzholov East Kazakhstan University (Oskemen, Kazakhstan, e-mail: aidanaimash16@mail.ru)

Esbol Shaimardan – PhD, Scientific Center of Composite Materials (Almaty, Kazakhstan, e-mail: esbol_shay@mail.ru)

Sana Kabdrakhmanova - candidate of technical sciences, associate professor, Satbayev University (Almaty, Kazakhstan, e-mail: sanaly33@mail.ru)

Aibar Yeskaliyev – associate professor, S. Amanzholov East Kazakhstan University (Oskemen, Kazakhstan, e-mail: aibar_sultan@mail.ru)

Received 6 February 2025;
received in revised form 21 May 2026;
accepted 10 June 2026

IRSTI 31.25.17 https://doi.org/10.26577/IJBCh202619113

R.M. Hasanov*, R.E. Mammadova

Azerbaijan State Oil and Industry University, Baku, Azerbaijan
*e-mail: roman.monarovich@mail.ru

THERMAL STABILITY OF BIO-BASED CALCIUM AND ALUMINUM CARBOXYLATES

Abstract: As bio-based metal carboxylates, calcium and aluminum carboxylates were synthesized using sunflower oil and soybean wax as renewable feedstocks, and their structures were characterized by Fourier-transform infrared spectroscopy (FT-IR). The FT-IR results confirmed the successful formation of the corresponding metal carboxylates. Thermogravimetric (TG) and differential thermal analysis (DTA) techniques were employed to evaluate the thermal stability of the synthesized compounds. According to the thermal analysis data, aluminum carboxylates exhibited faster thermal decomposition compared to calcium carboxylates, with the major decomposition step occurring predominantly in a single stage. The higher thermal stability of calcium carboxylates relative to aluminum carboxylates can be attributed to their low-er organic content and, additionally, to the fact that calcium forms more stable compounds due to its higher chemical reactivity, a trend that was clearly reflected in the TGA curves. Consequently, calcium carboxylates underwent multi-stage decomposition. This behavior was also evident in the DTA profiles, where the heat absorption and release events showed a fluctuating pattern. Given the significant industrial relevance of metal carboxylates as additives in polymer and lubricant formulations, understanding their physicochemical properties is essential.

Keywords: metal carboxylates, metal soaps, calcium carboxylates, aluminum carboxylates, thermal stability, addi-tives, bio-based additives, sunflower oil.

Introduction

Metal carboxylates – salts or coordination complexes formed between fatty acids and metal ions – constitute a structurally diverse class of organometallic compounds exhibiting highly tunable physico-chemical properties (Idiagheet al., 2014; Puspawiningtiyas et al., 2020). Their behavior strongly depends on the valence state and chemical nature of the metal ion, as well as the length, saturation, and branching of the carboxylate chain. Owing to this structural flexibility, metal carboxylates have found wide application across various industrial sectors (Folarin & Ayinde, 2016; Sukmawati & Lestari, 2020).

These compounds are widely employed as functional additives in lubricants, where they improve resistance to oxidation and thermal degradation, reduce friction and wear, and enhance surface protection. In the paints and coatings industry, they act as catalytic driers that accelerate oxidative curing. Within polymer systems, metal carboxylates serve as both processing aids and stabilizers, contributing to improved thermal, mechanical, and long-term performance. They are also used in catalytic systems, fuel and oil formulations, and the modification of composite materials due to their versatile functionalities (Balköse et al., 2010; Farone et al., 2015; Folarin et al., 2011; Folarin et al., 2012).

One of the most technologically important applications of metal carboxylates is their use as thermal stabilizers for polyvinyl chloride (PVC). During PVC processing, elevated temperatures trigger dehydro-chlorination, and the released hydrogen chloride accelerates discoloration, structural deterioration, and autocatalytic degradation of the polymer matrix (Altarawneh et al., 2022; Tüzüm-Demir et al., 2018; Wang et al., 2019; Xu et al., 2020; Yu et al., 2016). Metal carboxylates mitigate these processes by neutralizing HCl, replacing labile chlorine atoms in the polymer chain, and inhibiting the propagation of degradation pathways. Calcium and zinc carboxylates, as well as certain aluminum analogues, are among the most effective stabilizers for maintaining both the color stability and structural integrity of PVC during processing and service life (Morsy et al., 2024; Wang et al., 2014).

With the increasing regulatory restrictions on toxic lead- and cadmium-based stabilizers, the development of environmentally benign, bio-based metal carboxylates has gained major relevance (Bouchoul et al., 2017; Hosney et al., 2018; Jubsilp et al., 2022; Li et al., 2017). Renewable lipid feedstocks such as sunflower oil, soybean wax, palm-derived fatty acids, and other natural waxes provide sustainable and low-toxicity precursors for the synthesis of metal carboxylates. These bio-derived stabilizers offer enhanced compatibility with polymer matrices while supporting the transition to-ward greener additive technologies (Hasanov et al., 2025a; Ye et al., 2019).

Calcium and aluminum carboxylates synthesized from renewable feedstocks – particularly sunflower oil and soybean wax – are therefore of significant scientific and industrial interest. These natural materials contain long-chain fatty acids capable of forming stable metal–carboxylate structures. Their structural confirmation via FT-IR spectroscopy and the evaluation of their thermal behavior using TG–DTA methods are essential for assessing their suitability as PVC stabilizers. Moreover, a comparative investigation of the thermal degradation mechanisms of calcium and aluminum carboxylates provides valuable insight into the differences in their stability, decomposition pathways, and functional performance in polymer systems (Han et al., 2019; Özsin & Pütün, 2019).

Accordingly, this study focuses on the synthesis of bio-based calcium and aluminum carboxylates, the FT-IR verification of their structural features, and the comparative TG–DTA analysis of their thermal decomposition behavior, with the aim of determining their potential applicability as environmentally friendly thermal stabilizers for PVC.

Materials and methods

For the synthesis of metal carboxylates, refined sunflower oil of the "Final" brand and soy wax of the "Balmumcu" brand were used as the primary bio-based raw materials. Potassium hydroxide (KOH, analytical grade, "Lacherma," Czech Republic) was employed for the saponification of these oils, which constitutes the initial step in the preparation of metal carboxylates. For the subsequent formation of aluminum and calcium carboxylates, aluminum sulfate octadecahydrate ($Al_2(SO_4)_3 \cdot 18H_2O$, high purity, "Kimyalab") and calcium chloride ($CaCl_2$, analytical grade, "Vekton") were used.

The synthesis procedure consisted of two main stages. In the first stage, water-soluble soaps were produced via alkaline saponification of the oils. Ethyl alcohol (C_2H_5OH, 96%) was introduced as a co-solvent to enhance the interaction between the oil and the alkaline medium and was also used in several analytical determinations. To evaluate the saponification value of the selected oils and to neutralize unreacted alkali remaining after saponification, hydrochloric acid (HCl, 35%, AO "Base No. 1 Chemical Reagents") was used. Toluene was applied for determining the acid value of soybean wax, while Wijs reagent, glacial acetic acid, cyclohexane, potassium iodide, starch indicator, and sodium thiosulfate were used for determining the iodine value of the oils. In parallel tests, alcoholic solutions of phenolphthalein and methyl orange served as acid–base indicators.

The acid value of sunflower oil and soybean wax was determined in accordance with ISO 660:2020, the saponification value according to ISO 3657:2020, the iodine value according to ISO 3961:2018, and the moisture and volatile-matter content according to ISO 662:2016.

Metal carboxylates were synthesized from vegetable oils using a two-step approach. In the first step, water-soluble potassium soaps were produced by saponifying the oils with a 20% alkaline solution added in slightly excess stoichiometric quantity. Ethyl alcohol was added after the reaction progressed to a certain stage to improve miscibility. The resulting soap mass was subsequently diluted, and any remaining unreacted alkali – particularly in sunflower-oil-based soaps – was neutralized with standard hydrochloric acid. In the second step, termed "transsaponification," 20% aqueous solutions of the respective metal salts were added in excess of stoichiometric amounts to the diluted soap solution under continuous mixing to precipitate the corresponding calcium and aluminum carboxylates. The obtained metal carboxylates were separated using a funnel with filter paper, washed repeatedly with distilled water, and dried, following established procedures (Barman & Vasudevan, 2006; Hasanov et al., 2025b; Putrawanet al., 2022; Ronny et al., 2016; Ye et al., 2018). Synthesis process of metal carboxylates was described schematic on Figure 1.

The chemical structure of the synthesized metal carboxylates was characterized using Fourier-transform infrared (FT-IR) spectroscopy with a PerkinElmer Spectrum 100 (Germany). Moisture content and ash content after calcination at 1000°C in a muffle furnace were also measured. The elemental com-position of the ash residue was examined using a Spectro XEPOS (Germany) XRF spectrometer.

Figure 1
Synthesis scheme of bio-based aluminum and calcium carboxylates via saponification and transsaponification steps

Thermal stability was evaluated using a NETZSCH STA 449 F3 Jupiter (Germany) simultaneous TG-DTA analyzer. Measurements were carried out up to 900°C under a nitrogen atmosphere at a heating rate of 30 K·min^{-1}.

Results and discussion

Some of the key physicochemical properties of the sunflower oil and soybean wax used in the synthesis of metal carboxylates are presented in Table 1.

More than 90% of the sunflower oil and more than 80% of the soybean wax were converted through the two-stage saponification process. Calcium and aluminum carboxylates were precipitated from the water-soluble soaps by transsaponification.

The chemical composition of the synthesized metal carboxylates was examined using FT-IR spectroscopy, focusing on the formation of metal carboxylate structures and the possible presence of unreacted lipid residues, moisture, metal hydroxides, metal–oxygen bonds, and unsaturated C=C functionalities in the hydrocarbon chains.

Table 1
Physicochemical properties of the sunflower oil and soybean wax

Oil	Compositions of oils			Acid value, mg KOH/g	Iodine value, g I_2/100g	Saponification value, mg KOH/g
	Saturated fatty acids, %	Monounsaturated fatty acids, %	Others, %			
Sunflower oil	10.7	20.7	68.6	0.12	136	191
Soy wax	65	30	5	0.6	30	185

For aluminum carboxylate (AlSUN) synthesized from sunflower oil, the FT-IR spectrum exhibited characteristic absorption bands confirming successful carboxylate formation. Strong bands attributed to the asymmetric and symmetric stretching vibrations of carboxylate groups (COO^-) were observed at 1574.43 cm^{-1}, 1455.11 cm^{-1}, and 1377.31 cm^{-1}, indicating the coordination of fatty acid residues with aluminum ions.

Simultaneously, absorptions at 1713.50 cm^{-1} and 1180 cm^{-1} reflect the presence of residual triglycerides, demonstrating that saponification was not fully complete and that a small fraction of vegetable oil remained unreacted. Additional bands at lower wave-

numbers – 998.82, 880.46, and 667.44 cm^{-1} – correspond to out-of-plane deformation vibrations associated with C=C double bonds in the fatty acid chains, confirming the retention of unsaturation in the structure.

In the metal–oxygen vibrational region, a clear absorption at 516.83 cm^{-1} was assigned to Al–O stretching, supporting the formation of aluminum–carboxylate bonds. The absorption at 2922.84 cm^{-1} corresponds to CH_2 stretching vibrations, while the broad bands at higher wavenumbers are attributable to moisture and metal hydroxide species adsorbed onto the surface.

The FT-IR spectrum of AlSUN is presented in Figure 2.

The FT-IR spectrum of calcium carboxylate (CaSUN) synthesized from sunflower oil exhibited characteristic absorption bands in the wavenumber range of 1575.51–1541.53 cm^{-1}, confirming the formation of calcium carboxylate species. Additional carboxylate-related bands at 1464.03 and 1377.33 cm^{-1} further support the successful coordination of fatty acid anions with Ca^{2+} ions. The broadness of the absorption region suggests the coexistence of both mono- and di-substituted calcium carboxylate species, as well as the possible presence of chelated structures.

Importantly, no significant absorption was detected in the 1740–1710 cm^{-1} region, which corresponds to ester C=O stretching of unreacted triglycerides or ether groups. The absence of this band indicates that the vegetable oil was almost completely consumed during saponification.

Absorptions associated with unsaturated C=C moieties characteristic of sunflower oil were observed at 3008.44, 990.86, 924.55, 856.35, and 824.05 cm^{-1}, reflecting the retention of double bonds in the hydrocarbon chains. Bands appearing within the range of 678.04–578.32 cm^{-1} correspond to Ca–O stretching vibrations, confirming the formation of calcium dicarboxylate.

A broad absorption at 3396.14 cm^{-1} is attributed to moisture and adsorbed hydroxyl species, while strong absorptions at 2922.3 and 2852.8 cm^{-1} correspond to the aliphatic $–CH_2$ stretching vibrations of the fatty acid chains.

The FT-IR spectrum of CaSUN is shown in Figure 3.

Figure 2
FT-IR spectrum of AlSUN

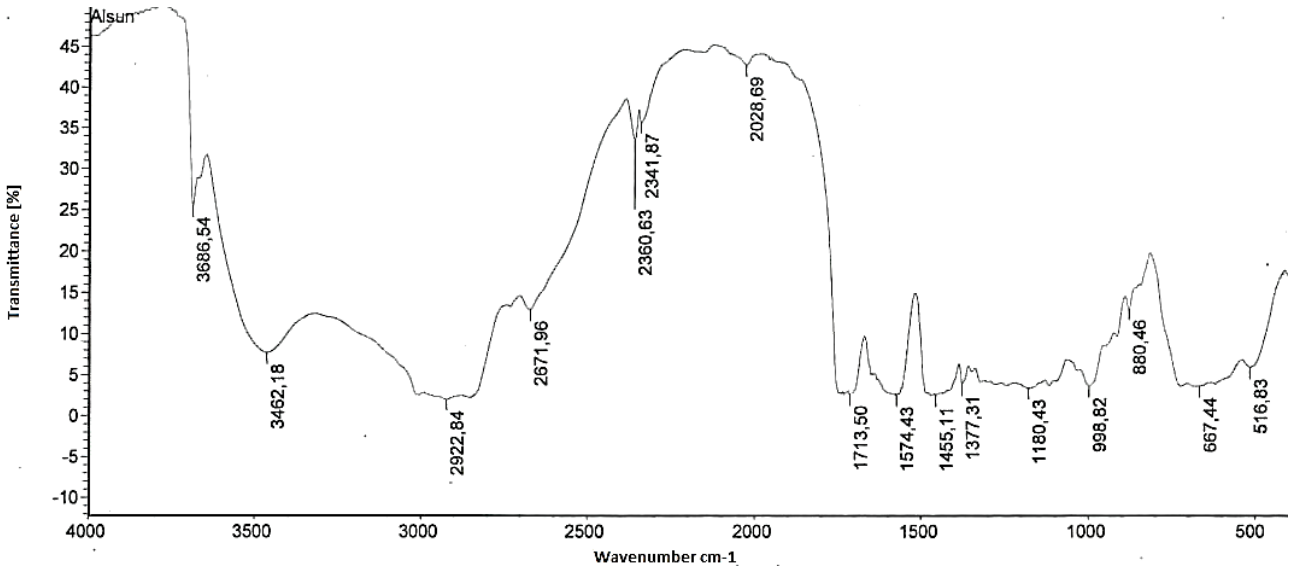

Characteristic FT-IR peaks corresponding to metal carboxylate structures were also detected in the spectra of the aluminum (AlSO) and calcium (CaSO) carboxylates synthesized from soybean wax. Soybean wax, being a hydrogenation product of soybean oil, is more saturated than sunflower oil; however, the spectra still exhibited distinct carboxylate signatures for both AlSO and CaSO.

Figure 3
FT-IR spectrum of CaSUN

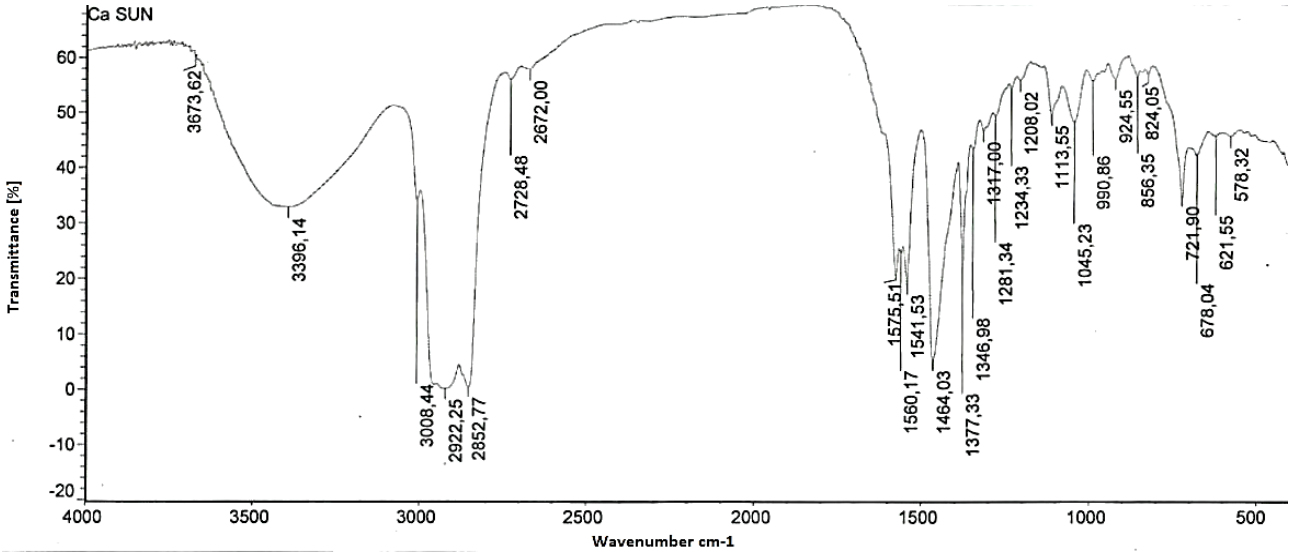

For AlSO, the FT-IR spectrum revealed a pronounced absorption band at 1585.27 cm^{-1}, corresponding to the asymmetric stretching vibration of the carboxylate group (COO^-), confirming successful formation of the metal carboxylate. Symmetric carboxylate stretching vibrations characteristic of coordinated carboxylate species were additionally observed at 1465.38 cm^{-1} and 1377.08 cm^{-1}.

Absorptions appearing in the range of 1712.65–1734.38 cm^{-1}, attributable to carbonyl (C=O) stretching, indicate the presence of ester groups and unreacted lipid components, demonstrating that the hydrogenated wax was not completely converted during saponification. Weak absorptions in the 987.92–889.90 cm^{-1} range correspond to deformation modes of unsaturated C=C bonds, confirming that a minor fraction of unsaturation remains in the soybean-wax-derived fatty acid chains despite hydrogenation.

Bands detected in the lower wavenumber region (617.64–496.68 cm^{-1}) are associated with metal–oxygen (M–O) stretching vibrations and are indicative of aluminum–oxygen coordination. Broad absorptions at higher wavenumbers (3852.82–3441.56 cm^{-1}) correspond to moisture and surface metal hydroxide groups. Intense absorptions in the aliphatic stretching region (2933.82–2852.80 cm^{-1}) originate from CH_2 asymmetric and symmetric stretching vibrations of the long aliphatic chains.

The FT-IR spectrum of AlSO is presented in Figure 4.

In the FT-IR spectrum of the calcium carboxylate synthesized from soybean wax (CaSO), characteristic carboxylate absorption bands were observed in the wavenumber range of 1576.27–1540.53 cm^{-1}, similar to those detected for CaSUN. Additional carboxylate-related bands appeared at 1465.50 cm^{-1} and 1377.28 cm^{-1}, further confirming the formation of coordinated calcium carboxylate species.

Due to the hygroscopic nature of the sample, an absorption band associated with bound water was detected at 1620.56 cm^{-1}. Although no distinct ester carbonyl bands were observed in the 1740–1710 cm^{-1} region – typically indicative of unreacted triglyceride residues – the presence of a peak at 1796.57 cm^{-1} may be related to residual carbonyl-containing species.

Weak absorption bands in the 974.45–810.04 cm^{-1} range correspond to vibrational modes of unsatu-rated C=C bonds, indicating a minor level of unsaturation in the fatty acid chains derived from soybean wax. Peaks occurring at lower wavenumbers (672.17–481.91 cm^{-1}) are attributed to Ca–O stretching vibrations and the formation of a calcium carboxylate network.

Strong absorptions between 2918.43 and 2850.09 cm^{-1} arise from CH_2 stretching vibrations of aliphatic hydrocarbon chains. The broad absorption at 3389.74 cm^{-1} is attributed to residual moisture in the sample.

The FT-IR spectrum of CaSO is presented in Figure 5.

Figure 4
FT-IR spectrum of AlSO

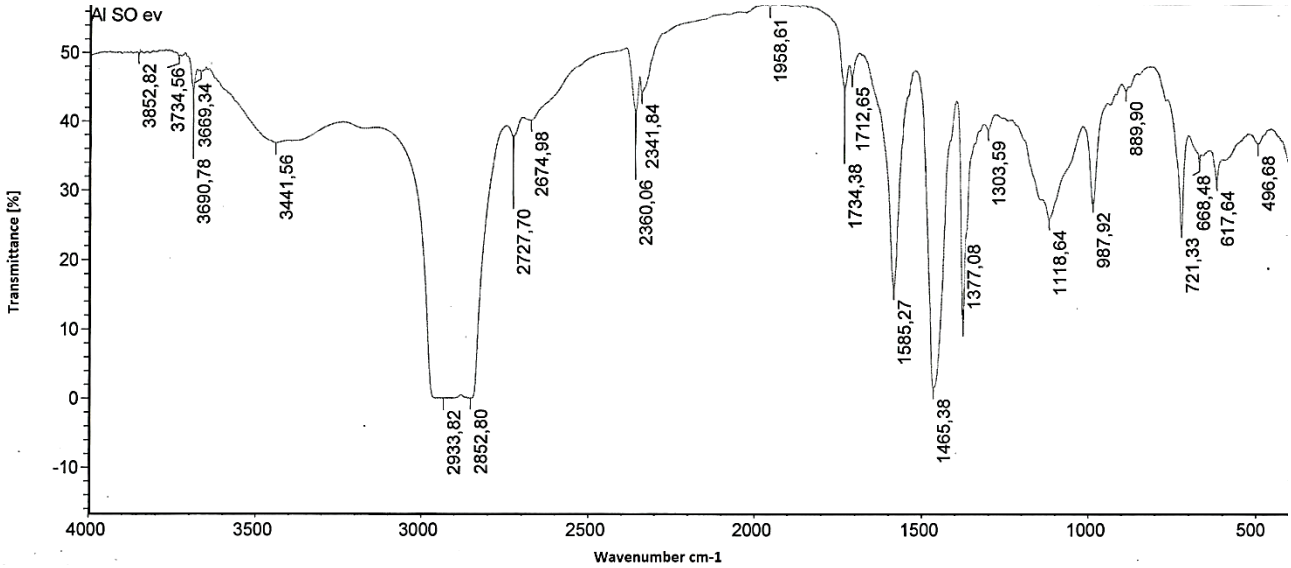

Figure 5
FT-IR spectrum of CaSO

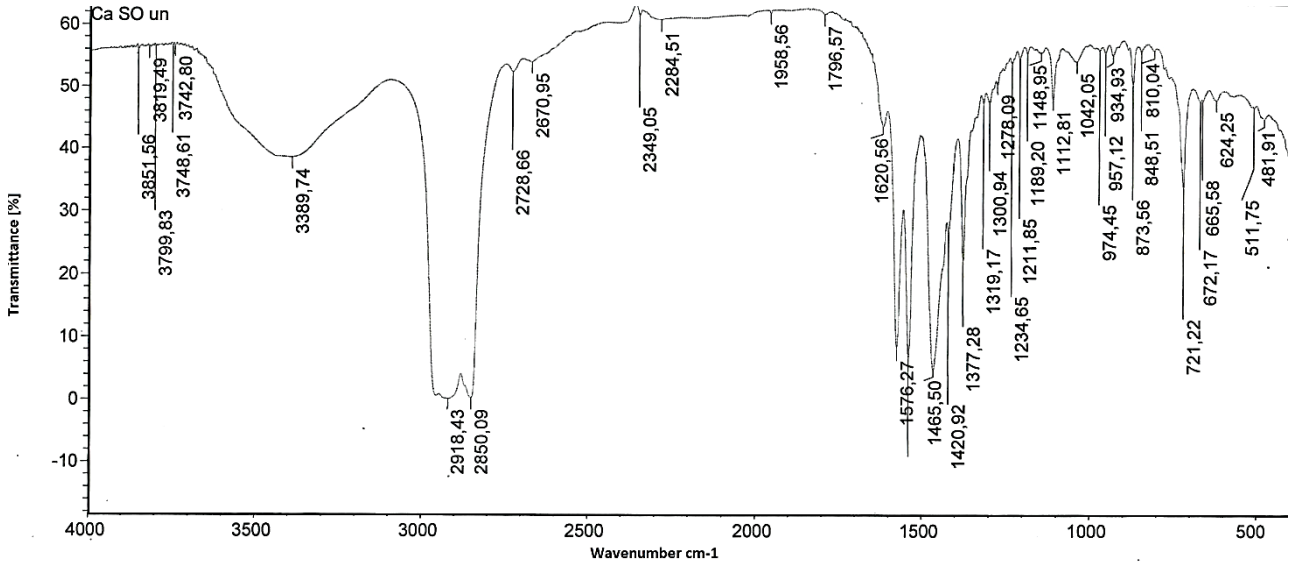

Table 2
Moisture and ash content of metal carboxylates

Metal carboxylate	Moisture, %	Ash content, %	Ash content (dry basis), %
AlSUN	0.20	4.47	4.47
CaSUN	5.87	5.50	5.84
AlSO	4.71	17.07	17.91
CaSO	2.64	6.82	7.01

The moisture and ash contents of the synthesized metal carboxylates were determined and are summarized in Table 2. The results confirm that AlSUN is highly hydrophobic and practically moisture-free. In contrast, AlSO, synthesized from soybean wax – which is more saturated than sunflower oil – exhibits lower hydrophobicity and therefore retains a slightly higher amount of moisture. Furthermore, the higher ash content of AlSO clearly reflects the presence of inorganic and organic impurities remaining from the synthesis process, indicating a direct correlation between the feedstock characteristics, hydrophobicity, and the residual impurity level of the corresponding metal carboxylates.

The ash composition of the metal carboxylates was examined using XRF analysis, and the results revealed that calcium carboxylates contain significantly fewer inorganic impurities compared to their aluminum analogues. This difference is attributed to the higher hydrophilicity of calcium carboxylates, which facilitates more effective removal of residual salts and by-products during the aqueous washing step. In contrast, the greater hydrophobicity of aluminum carboxylates limits their interaction with water, reducing washing efficiency and resulting in a higher level of retained impurities. The XRF results for the ash fractions are presented in Table 3.

TGA–DTA techniques were employed to evaluate the thermal stability of the synthesized metal carboxylates. According to the TGA data, all metal carboxylates exhibited decomposition temperatures higher than the thermal degradation temperature of PVC (Ma et al., 2022; Yang et al., 2023), supporting their potential applicability as PVC thermal stabilizers.

The thermal behavior of AlSUN indicates that its decomposition proceeds predominantly through a single major stage. The onset of intensive mass loss begins at approximately 230°C and continues up to 500°C. During the initial part of this interval, the mass loss increases gradually, with a 5% loss recorded at 259.8°C. This early loss corresponds to the release of a small amount of volatile species and the removal of approximately 0.2% residual moisture.

Beyond this point, the decomposition of the organic matrix and the breakdown of intermediate aluminum carbonate species occur simultaneously within one continuous stage. A 10% mass loss is observed at 289°C, followed by a 20% loss at 323.6°C. Fifty percent mass loss occurs at 388.2°C, while near-complete decomposition – corresponding to 90% mass reduction – is reached at 499.1°C.

Past this temperature, degradation proceeds only slowly. At 895.7 °C, the final residue amounts to 5.28%, indicating deep and extensive decomposition of the sample. The TG–DTA–DDTA curves of AlSUN are presented in Figure 6. As seen in the DTA and DDTA profiles, the pronounced endothermic events align with the temperature intervals of mass loss, confirming that intensive decomposition reactions occur in these regions.

In contrast to AlSUN, the thermal decomposition of CaSUN proceeds through several distinct stages. This multistep mass loss can be attributed to the sequential release of initial moisture and volatile components, the removal of hydrate water, the decomposition of the organic matrix, and finally the breakdown of the calcium carbonates and other mineral species formed in the sample.

Table 3
XRF results of ash composition

Metal carboxylates ash composition, %							
AlSUN		CaSUN		AlSO		CaSO	
Al_2O_3	83.77	CaO	94.32	Al_2O_3	32.63	CaO	92.40
K_2O	12.23	K_2O	2.20	K_2O	36.84	K_2O	4.44
SO_3	2.62	Al_2O_3	1.14	SO_3	30.17	Al_2O_3	0.49
CaO	0.08	SiO_2	0.80	CaO	0.18	SiO_2	0.64
SiO_2	0.86	Cl	0.72	SiO_2	0.07	Cl	1.05
Trace	0.44	Trace	0.82	Trace	0.11	Trace	0.98

Figure 6
TG-DTA-DDTA curves of AlSUN

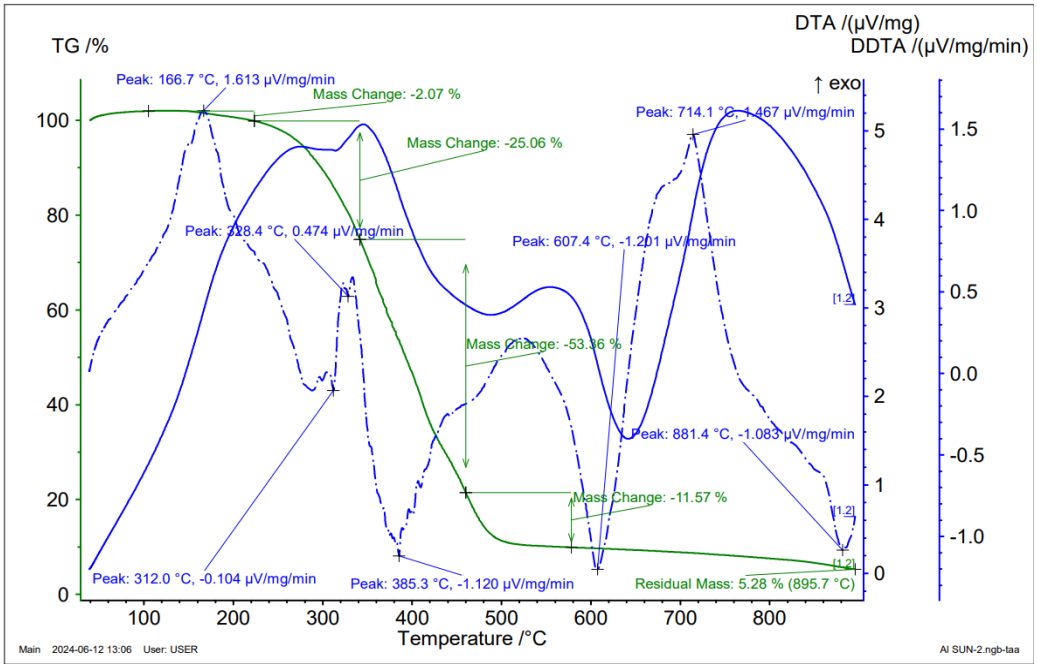

The first significant mass loss occurs early in the experiment, with a 5% reduction recorded at 242.5°C. Independent moisture analysis in a drying oven showed a moisture content of 5.87%, confirming that CaSUN is strongly hygroscopic. Furthermore, the TG–DTA–DDTA curves (Figure 7) exhibit multiple small mass-loss steps within this temperature region, indicating that the retained moisture and volatile components originate from different bonding environments or structural domains within the compound.

A 10% mass loss is observed at 332.8°C, and 20% at 443.3°C, demonstrating that CaSUN remains thermally stable throughout the typical high-temperature processing range of PVC (Shnawa, 2020). A 50% mass loss occurs at 491.2°C, and rapid decomposition continues up to approximately 520°C. Beyond this point, the mass remains nearly constant up to 800°C, after which further loss is associated with the calcination of carbonates within the residual material. At 896°C, the total mass loss reaches 23.94%, indicating partial carbonization of the sample.

The DDTA curve reveals that heat absorption within the main decomposition region occurs in a fluctuating manner. These fluctuations likely arise from the different melting and decomposition behaviors of carboxylate species derived from various higher carboxylic acids present in the material. As decomposition progresses, both the frequency and intensity of these thermal fluctuations increase, reflecting the trans-formation of different structural fractions. Similar fluctuations are consistently mirrored in the DTA pro-file.

General similarities and differences are observed in the thermal behavior of aluminum and calcium carboxylates synthesized from soybean wax compared with their counterparts derived from sunflower oil. As previously noted, AlSO differs from AlSUN in that it is a fine white powder with noticeably lower hydrophobicity. This distinction is also reflected in its moisture test results: AlSO exhibits a moisture content of 4.71%. Correspondingly, TGA analysis shows that 5% mass loss occurs at 144.6°C, demonstrating a clear correlation between the measured moisture level and the initial stage of thermal decomposition.

Figure 7
TG-DTA-DDTA curves of CaSUN

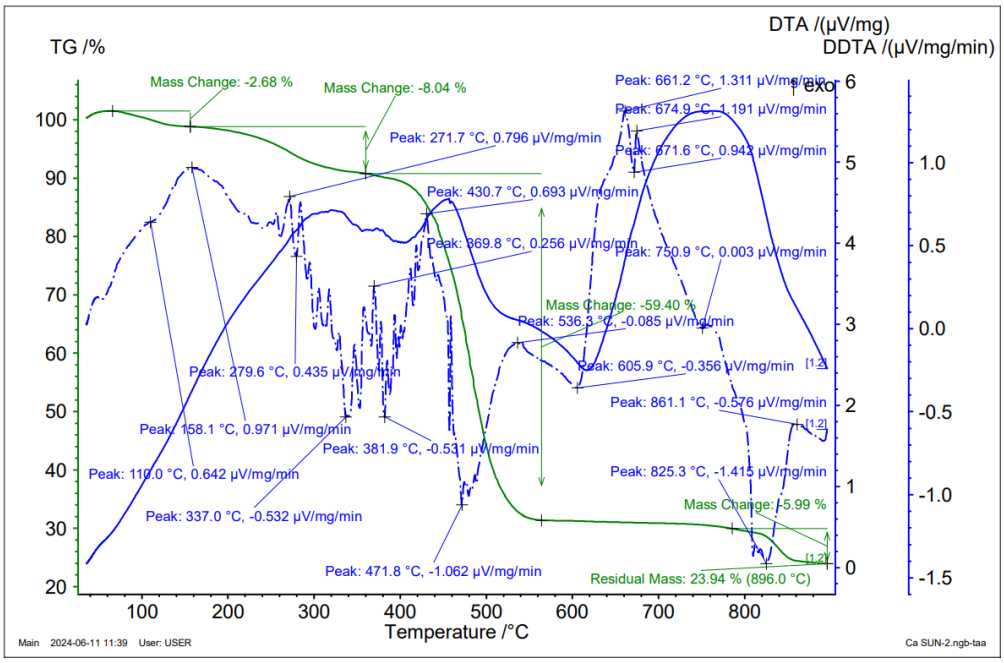

The overall TGA profile of AlSO indicates two primary mass-loss stages: (i) the release of moisture and volatiles, followed by (ii) the decomposition of the organic matrix. In this respect, AlSO shows a decomposition pattern qualitatively similar to that of AlSUN, though occurring at somewhat lower temperatures. Specifically, AlSO shows 10% mass loss at 249.4°C and 20% at 295.8°C. A 50% mass reduction is observed at 389.1°C, while the final mass residue at 896.5°C is 23.09%. Considering the ash content, these results suggest that the organic fraction undergoes deep and extensive decomposition, consistent with the behavior of aluminum carboxylates synthesized from other feedstocks.

The TG–DTA–DDTA curves of AlSO are presented in Figure 8. The DDTA profile shows fluctuations in heat absorption and release throughout the heating process, with pronounced thermal activity up to ap-proximately 313°C, followed by a strong endothermic event. These fluctuations likely arise from successive phase transformations of different carboxylate species and, ultimately, the formation and thermal decomposition of a more homogeneous phase at later stages.

The TGA results of CaSO indicate that its thermal decomposition proceeds through several distinct stages, closely resembling the multistep behavior observed for CaSUN. The initial mass loss corresponds to the release of moisture, followed by an early decomposition stage, and then a more intensive breakdown in the third stage. CaSO exhibits 5% mass loss at 278.8°C, 10% at 316.2°C, and 20% at 383.23°C. A 50% mass reduction is recorded at 474.5°C, while the final residue at 895.8°C is 19.69%.

As with CaSUN, carbonization occurs during the decomposition of CaSO. The DDTA curve of CaSO (Figure 9) also displays regular fluctuations in heat absorption and release, reflecting complex overlapping thermal events. These fluctuations likely arise from the decomposition of different carboxylate species and their associated phase transitions. The final decomposition stage again corresponds to the calcination of metal carbonates formed during earlier stages, mirroring the thermal behavior of CaSUN.

Figure 8
TG-DTA-DDTA curves of AlSO

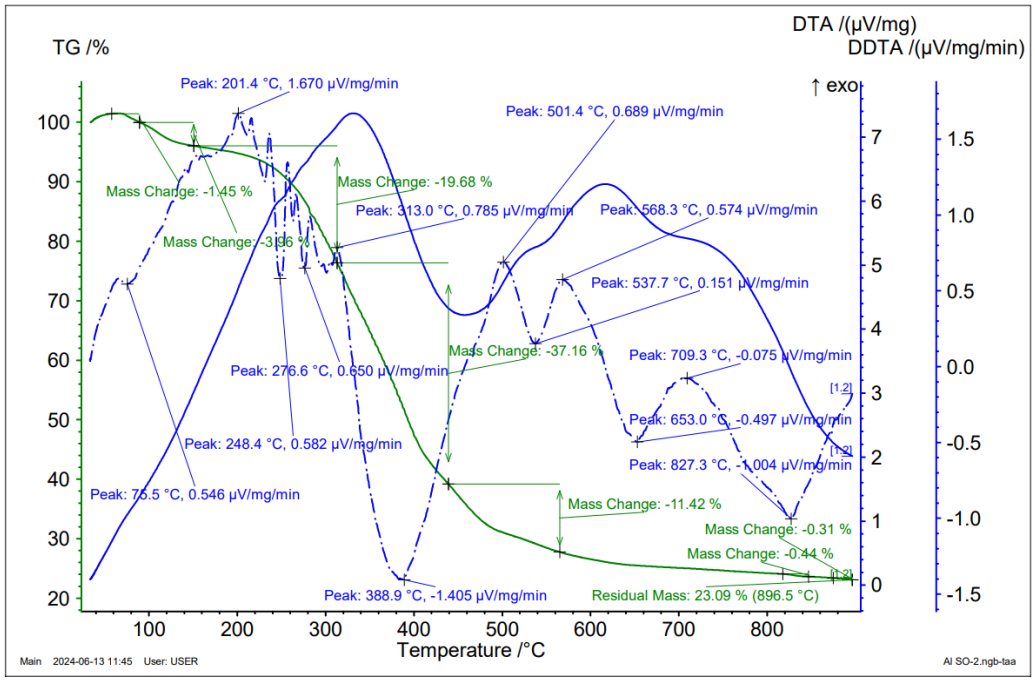

Figure 9
TG-DTA-DDTA curves of CaSO

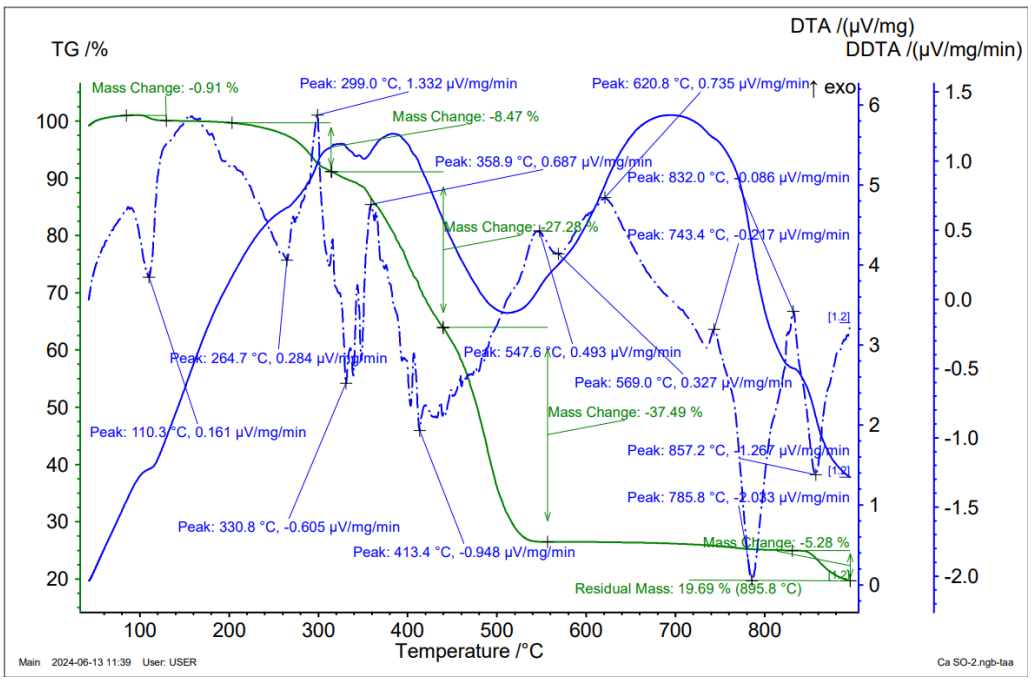

Overall, the thermal decomposition of both calcium and aluminum carboxylates synthesized from sunflower oil and soybean wax occurs at temperatures substantially higher than the processing temperature of PVC – and even exceeds the intensive decomposition stage of PVC. This high thermal resilience represents a key advantage and supports the suitability of these bio-based metal carboxylates as potential thermostabilizers for PVC processing applications.

The comparative TG–DTA–DDTA analyses clearly demonstrate that both aluminum- and calcium-based bio-derived carboxylates possess sufficient thermal resilience for polymer-processing applications, particularly PVC stabilization. Aluminum carboxylates (AlSUN and AlSO) exhibited predominantly single- or two-step thermal degradation pathways, reflecting their relatively lower moisture content, higher hydrophobicity, and more uniform structural decomposition. In contrast, calcium carboxylates (CaSUN and CaSO) decomposed through multiple well-defined stages, associated with their higher hydrophilicity, greater moisture retention, and the sequential removal of bound water, volatiles, and intermediate carbonate species.

Across all samples, the temperatures corresponding to 10%, 20%, and 50% mass losses significantly exceeded the processing range of PVC, confirming that these bio-based carboxylates maintain structural integrity under relevant industrial conditions. Calcium carboxylates consistently displayed higher decom-position temperatures, indicating deeper carbonization and greater thermal robustness compared to their aluminum analogues.

Overall, the results demonstrate that calcium and aluminum carboxylates synthesized from sunflower oil and soybean wax exhibit favorable thermal characteristics, with calcium-based compounds showing particular promise as environmentally benign, bio-derived thermal stabilizers for PVC applications.

Conclusion

In this study, bio-based calcium and aluminum carboxylates were successfully synthesized from sun-flower oil and soybean wax and comprehensively characterized to evaluate their potential as environmentally benign thermal stabilizers. FT-IR analysis confirmed the formation of metal–carboxylate structures in all samples, while moisture and ash measurements demonstrated clear differences in hydrophobicity and impurity levels depending on both the metal ion and the renewable feedstock. XRF analysis further revealed that calcium carboxylates contained fewer residual inorganic impurities than their aluminum analogues, reflecting the greater washing efficiency associated with their higher hydrophilicity.

Thermal analysis showed that all synthesized metal carboxylates exhibit decomposition temperatures substantially above the typical processing range of PVC, indicating their suitability for high-temperature industrial applications. Aluminum carboxylates tended to decompose in one or two major steps, whereas calcium carboxylates underwent multistage decomposition involving moisture release, organic-matrix degradation and carbonate calcination. Among all samples, calcium carboxylates displayed the highest thermal stability and deepest organic mass decomposition.

The results demonstrate that bio-derived calcium and aluminum carboxylates synthesized from renewable lipid feedstocks possess promising thermal characteristics and can serve as viable, sustainable alternatives to conventional PVC thermostabilizers, supporting the transition toward greener polymer-additive technologies.

Author contributions

R.M. Hasanov: Conceptualization, Methodology, Investigation, Data curation, Formal analysis, Visualization, Writing – original draft.R.E. Mammadova: Conceptualization, Methodology, Validation, Writing – review & editing.

Acknowledgments

Authors thank Azerbaijan State Oil and Industry University.

Conflict of interest

The authors declare that they have no conflicts of interest.

References

1. Altarawneh, S., Al-Harahsheh, M., Dodds, C., Kingman, S., & Al-Mharat, A. (2022). Thermal degradation kinetics of polyvinyl chloride in presence of zinc oxide. *Thermochimica Acta*, *770*, 179105. https://doi.org/10.1016/j.tca.2021.179105

2. Balköse, D., Egbuchunam, F., & Okieimen, E. (2010). Thermal behaviour of metal soaps from biodegradable rubber seed oil. *Journal of Thermal Analysis and Calorimetry*, *101*(2), 795–799. https://doi.org/10.1007/s10973-010-0940-4

3. Barman, S., & Vasudevan, S. (2006). Melting of saturated fatty acid zinc soaps. *The Journal of Physical Chemistry B*, *110*(45), 22407–22414. https://doi.org/10.1021/jp064306p

4. Bouchoul, B., Benaniba, M. T., & Massardier, V. (2017). Thermal and mechanical properties of bio-based plasticizers mixtures on poly(vinyl chloride). *Polímeros*, *27*(3), 237–246. https://doi.org/10.1590/0104-1428.14216

5. Farone, E. V., Labovitz, B. P., & Kruse, N. A. (2015). *Process for preparing liquid overbased metal carboxylates, mixed metal stabilizers containing same, and stabilized halogen-containing polymers therewith* (U.S. Patent No. 9,102,610). U.S. Patent and Trademark Office. googleapis.com.

6. Folarin, O. M., & Ayinde, A. A. (2016). Thermal stability study of some metal carboxylates of castor (*Ricinus communis*) seed oil on poly(vinyl chloride). *Research Journal of Chemical Sciences*, *6*(2), 23–28.

7. Folarin, O. M., Eromosele, I. C., & Eromosele, C. O. (2011). Relative thermal stability of metal soaps of *Ximenia americana* and *Balanites aegyptiaca* seed oils. *Scientific Research and Essays*, *6*(9), 1922–1927. https://doi.org/10.5897/SRE10.438

8. Folarin, O. M., Eromosele, I. C., & Eromosele, C. O. (2012). Thermal stabilization of poly(vinyl chloride) by metal carboxylates of *Ximenia americana* seed oil under inert conditions. *Journal of Materials and Environmental Science*, *3*(3), 507–514.

9. Han, W., Zhang, M., Li, D., Liu, Z., Zheng, S., & Ding, Y. (2019). Design and synthesis of a new mannitol stearate ester-based aluminum alkoxide as a novel tri-functional additive for poly(vinyl chloride) and its synergistic effect with zinc stearate. *Polymers*, *11*(6), 1031. https://doi.org/10.3390/polym11061031

10. Hasanov, R. M., Mammadova, R. E., Amirov, S. A., Asadov, K. G., & Hasanova, A. A. (2025a). Effect of sunflower-oil-based metal soaps on the thermal stability of polyvinyl chloride. *Eurasian Journal of Chemistry*, *30*(1), 89–101. https://doi.org/10.31489/2959-0663/1-25-4

11. Hasanov, R. M., Mammadova, R. E., Amirov, S. A., Asadov, K. G., & Hasanova, A. A. (2025b). Thermal stabilization of polyvinyl chloride using aluminum carboxylate synthesized from soybean wax. *Processes of Petrochemistry and Oil Refining*, *26*(3), 858–870. https://doi.org/10.62972/1726-4685.2025.3.858

12. Hosney, H., Nadiem, B., Ashour, I., El-Shamy, A., & El-Kady, M. F. (2018). Epoxidized vegetable oil and bio-based materials as PVC plasticizer. *Journal of Applied Polymer Science*, *135*(23), 46270. https://doi.org/10.1002/app.46270

13. Idiaghe, J. A., Aguele, F. O., & Ekebafe, L. O. (2014). The preparation and thermal stability studies of metal soaps of *Hura crepitans* seed oil. *Chemical Technology: An Indian Journal*, *9*(2), 54–57.

14. Jubsilp, C., Asawakosinchai A., Mora, P., Saramas, D., & Rimdusit, S. (2022). Effects of organic-based heat stabilizer on properties of polyvinyl chloride for pipe applications: A comparative study with Pb and CaZn systems. *Polymers*, *14*(1), 133. https://doi.org/10.3390/polym14010133

15. Li, M., Xia, J., Ding, H., Wang, M., & Li, S. (2017). Optimal design, characterization, and thermal stability of bio-based Ca/Na/Zn composite stabilizer derived from myrcene for poly(vinyl chloride). *Polymer Degradation and Stability*, *139*, 117–129. https://doi.org/10.1016/j.polymdegradstab.2017.03.020

16. Ma, L. J., Lu, Y. H., Chen, Y., Yu, J. J., & Fu, Z. F. (2022). Dehydrochlorination study of plasticized poly(vinyl chloride) containing modified titanium dioxide, cerium stearate, organotin, and β-diketone complex after long-term storage. *Materials Research Express*, *9*(2), 025305. https://doi.org/10.1088/2053-1591/ac4f87

17. Morsy, A., Anwar, A., Anwar, H., El-Shafee, E., & Mansour, S. (2024). Utilizing a blend of expandable graphite and calcium/zinc stearate as an environmentally friendly heat stabilizer for polyvinyl chloride. *SPE Polymers*, *5*(1), 45–57. https://doi.org/10.1002/pls2.101096

18. Özsin, G., & Pütün, A. E. (2019). TGA/MS/FT-IR study for kinetic evaluation and evolved gas analysis of a biomass/PVC co-pyrolysis process. *Energy Conversion and Management*, *182*, 143–153. https://doi.org/10.1016/j.enconman.2018.12.060

19. Puspawiningtiyas, E., Partiwi, M., & Neonufa, G. F. (2020). Effect of metal type on basic soap pyrolysis to produce bio-gasoline. *IOP Conference Series: Materials Science and Engineering*, *823*(1), 012027. https://doi.org/10.1088/1757-899X/823/1/012027

20. Putrawan, I. D. G. A., Indarto, A., & Octavia, Y. (2022). Thermal stabilization of polyvinyl chloride by calcium and zinc carboxylates derived from byproduct of palm oil refining. *Heliyon*, *8*(10), e10079. https://doi.org/10.1016/j.heliyon.2022.e10079

21. Ronny, F. K., Ray, S. K., Hoque, A., Ahsan, A., & Khan, M. A. S. (2016). Zinc stearate from galvanizing waste materials and its use as a thermal stabilizer in PVC industries. *Bangladesh Journal of Scientific and Industrial Research*, *51*(4), 261–270.

22. Shnawa, H. A. (2020). Characterization of processing, rheological, and dynamic mechanical thermal properties of PVC stabilized with a polyphenol-based thermal stabilizer. *Journal of Thermal Analysis and Calorimetry*, *139*(1), 125–135. https://doi.org/10.1007/s10973-019-08365-8

23. Sukmawati, & Lestari, P. P. (2020). Optimization ratio of mixed metal soaps (Al–Ca) and palm fatty acid distillate (PFAD) on making grease. *Journal of Physics: Conference Series*, *1428*(1), 012009. https://doi.org/10.1088/1742-6596/1428/1/012009

24. Tüzüm-Demir, A. P., & Ulutan, S. (2018). Assessment of degradation of plasticized poly(vinyl chloride) films through polyene formation under isothermal conditions. *Journal of Applied Polymer Science*, *135*(18), 46092. https://doi.org/10.1002/app.46092

25. Wang, M., Li, H. X., & Huang, X. L. (2014). Zinc maleate and calcium stearate as a complex thermal stabilizer for poly(vinyl chloride). *Journal of Vinyl and Additive Technology*, *20*(4), 227–235. https://doi.org/10.1002/vnl.21336

26. Wang, Z., Xie, T., Ning, X., Cheng, Y., & Zhang, Y. (2019). Thermal degradation kinetic study of polyvinyl chloride (PVC) sheath for new and aged cables. *Waste Management*, *99*, 146–153. https://doi.org/10.1016/j.wasman.2019.08.042

27. Xu, Z., Kolapkar, S. S., Zinchik, S., Dembsey, N. A., & Emmons, A. L. (2020). Comprehensive kinetic study of thermal degradation of polyvinyl chloride (PVC). *Polymer Degradation and Stability*, *176*, 109148. https://doi.org/10.1016/j.polymdegradstab.2020.109148

28. Yang, S., Yang, J., Ding, J., Fu, Q., Li, W., & Long, Z. (2023). Kinetic analysis of thermal decomposition of polyvinyl chloride. *Fire*, *6*(10), 404. https://doi.org/10.3390/fire6100404

29. Ye, F., Guo, X. J., Zhan, H. H., Ma, Y. X., & Lu, L. D. (2018). The synergistic effect of zinc urate with calcium stearate and commercial assistant stabilizers for stabilizing poly(vinyl chloride). *Polymer Degradation and Stability*, *156*, 193–201. https://doi.org/10.1016/j.polymdegradstab.2018.08.012

30. Ye, Q., Ma, X., Li, B., Chen, S., Feng, Y., Zhou, Y., & Jiang, J. (2019). Development and investigation of lanthanum sulfadiazine with calcium stearate and epoxidised soybean oil as complex thermal stabilizers for stabilizing poly(vinyl chloride). *Polymers*, *11*(3), 531. https://doi.org/10.3390/polym11030531

31. Yu, J., Sun, L., Ma, C., Qiao, Y., & Yao, H. (2016). Thermal degradation of PVC: A review. *Waste Management*, *48*, 300–314. https://doi.org/10.1016/j.wasman.2015.11.041

Information about the authors:

Roman Hasanov – researcher, Chemical Technology Faculty, Azerbaijan State Oil and Industry University (Baku, Azerbaijan, e-mail: roman.monarovich@mail.ru).

Rasmiyya E. Mammadova – PhD, teacher, Department of Technology of Organic Substances and High-Molecular Compounds, Chemical Technology Faculty, Azerbaijan State Oil and Industry University (Baku, Azerbaijan, e-mail: resmiyye.mammadova.e@asoiu.edu.az).

Received 20 December 2025;
received in revised form 26 May 2026;
accepted 15 June 2026

IRSTI 31.21.27 https://doi.org/10.26577/IJBCh202619114

E.M. Yergaliyeva[1], K.B. Bazhykova[2*], A.M. Koishybay[2], M. Dossay[2]

[1] Akhmet Baitursynuly Kostanay Regional University, Kostanay, Kazakhstan
[2]Al-Farabi Kazakh National University, Almaty, Kazakhstan
*e-mail: bazhikova@bk.ru

IN SILICO PROFILING OF DIAZA- AND TETRAAZABICYCLONONAN-9-ONES AS NOVEL NICOTINIC ACETYLCHOLINE RECEPTOR LIGANDS

Abstract: Nicotinic acetylcholine receptors (nAChRs) are promising therapeutic targets for treating cognitive disorders and nicotine addiction. This study aimed to identify a novel nAChR ligand from a series of 8 newly designed diaza- and tetraazabicyclononan-9-ones using a comprehensive *in silico* approach. The biological activity spectrum was predicted using the PASS program, revealing a high potential for nAChR antagonism and other neurotropic activities. Pharmacokinetic and drug-likeness properties were assessed with SwissADME, indicating favorable profiles for most compounds. Molecular docking into the orthosteric site of the human α3β4-nAChR (PDB ID: 6PV7) and α4β2-nAChR (PDB ID: 5KXI) was successfully performed for six derivatives. Among them, compound **1** demonstrated a superior calculated JAMDA Score (-2.60), outperforming the native ligand, nicotine (JAMDA Score: -1.99). Analysis of the binding pose revealed that its superior predicted affinity stems from a network of specific hydrogen bonds with key residues (Tyr93, Ser148, Ser150) and an interaction with the backbone of Trp149 in the orthosteric site. Thus, the integrated *in silico* strategy identified compound **1** as a potent putative nAChR ligand, warranting its priority for further experimental evaluation.

Keywords: nicotinic acetylcholine receptors, molecular docking, *in silico* screening, bicyclic nitrogen heterocycles, drug design.

Introduction

Nicotinic acetylcholine receptors (nAChRs), especially the α7 and α4β2 subtypes, are ligand-gated ion channels widely distributed in brain regions essential for cognition, such as the hippocampus and cortex (Guan, 2024). α7 nAChRs exhibit anti-inflammatory and neuroprotective effects through several mechanisms: suppression of NF-κB-dependent cytokine synthesis, activation of Nrf2-mediated antioxidant defense, modulation of JAK2/STAT3 signaling, and enhancement of autophagy. These mechanisms make α7 nAChRs a promising therapeutic target for the treatment of neuroinflammatory and neurodegenerative diseases (e.g., Alzheimer's disease, Parkinson's disease, and multiple sclerosis) (Lee & Hung, 2022; Magnussen, 2025).

While several ligands are known, the search for new, selective, and potent modulators with improved safety profiles remains a pressing need in medicinal chemistry (Crestini et al., 2024). The clinical application of nAChR-targeted drugs is limited by low efficacy in the treatment of neurodegenerative diseases and cognitive impairment, as well as safety concerns due to receptor desensitization and peripheral side effects (Recio-Barbero et al., 2021). Non-selectivity of action, pharmacokinetic limitations, and species differences in animal models further complicate the development of successful therapeutic agents (Magnussen, 2025).

Current neurodegeneration drug research strongly favors heterocyclic scaffolds (e.g., piperidines, indoles, quinolines, pyrazoles) because they can address multiple pathogenic processes in Alzheimer's and Parkinson's disease (Katsoulaki et al., 2025). Among such promising frameworks, di- and tetraazabicyclononan-9-ones are the building blocks for obtaining drugs for prevention and treatment of neurodegenerative diseases (Matthews et al., 2024). The primary objective of this work was to conduct a comprehensive *in silico* profiling of a novel series of diaza- and tetraazabicyclononan-9-ones derivatives

to identify the most promising candidate acting as a nAChR ligand, using a combination of predictive and molecular modeling techniques.

Materials and methods

The series of novel diaza- and tetraazabicyclo[3.3.1]nonan-9-one derivatives (1–8) investigated in this study were designed and synthesized at al-Farabi Kazakh National University. The detailed synthetic protocols and spectroscopic characterization are beyond the scope of this computational work and will be disclosed in a separate paper focused on the synthetic chemistry. For the purposes of this study, the compounds served as the basis for constructing their 3D models for subsequent *in silico* analysis. The structures are shown in the Fig. 1.

Figure 1
New compounds based on diaza-, tetraazabicyclononan-9-ones 1-8

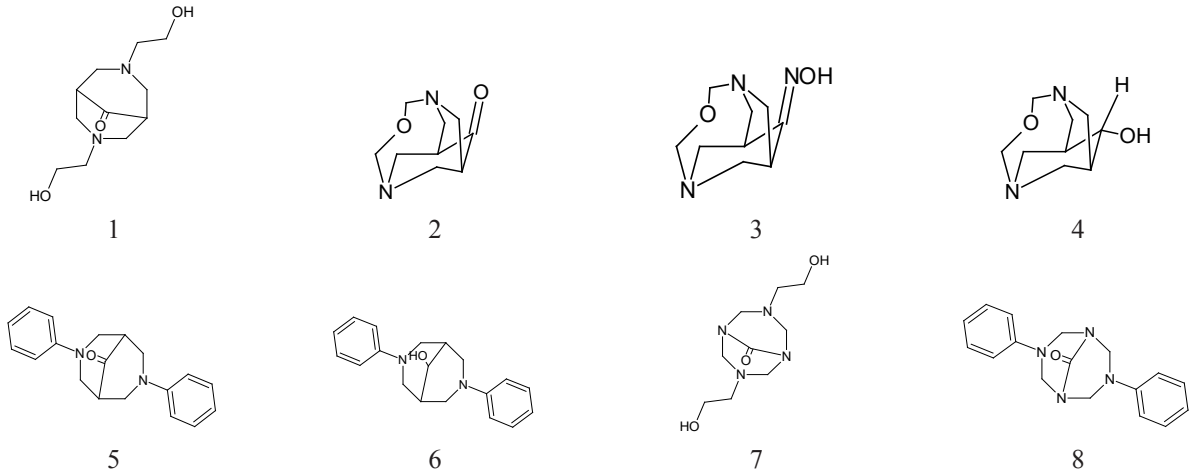

ACD Labs ChemSketch was used to draw chemical structures and generate SMILES notations.

Prediction of biological activity spectra was carried out using the PASS Online (2025), which estimates P_a (Probability "to be Active") and P_i (Probability "to be Inactive") for a wide range of pharmacological effects based on the structural formula of the compound.

The free online platform SwissADME (2025) (from the Swiss Institute of Bioinformatics) was used to determine the drug-likeness, pharmacokinetics and medicinal parameters of the test substances.

Molecular docking was performed for compounds 1–6 using JAMDA (Jupyter-Aided Molecular Docking Application) available through the Proteins*Plus* web service (2025). The JAMDA platform was selected due to its integrated use of machine-learning scoring functions and the gradient-based pose optimization method by Flachsenberg et al. (2021), which ensures a robust and reproducible protocol particularly suited for ranking ligand affinities within congeneric series.

The crystal structure of the nicotinic acetylcholine receptor was obtained from the Protein Data Bank. For molecular docking, the crystal structures of two heteropentameric nicotinic receptor subtypes were used: α3β4-nAChR (PDB ID: 6PV7, resolution 3.34 Å) and α4β2-nAChR (PDB ID: 5KXI, resolution 3.94 Å). 6PV7 was chosen due to its structural similarity to the predicted target α6β3β4α5, the availability of a native ligand (nicotine) for protocol validation, and its high-quality model of a receptor with a β4 subunit. The 5KXI structure was used as a model for subtypes containing a β2 subunit (including the predicted α2β2). This approach allows us to evaluate the interaction of new compounds with two distinct but pharmacologically relevant binding interfaces in the nAChR family, encompassing structural features common to the subtypes predicted as the most likely targets (Gotti et al., 2023) and providing insights into potential subtype selectivity. The docking pocket was identified using the DoGSiteScorer.

Molecular geometry optimization of ligand molecules was performed at the semi-empirical

PM6 level of theory using Gaussian 16 software. The optimized structures were subsequently converted to SDF format for use in docking simulations. Compounds 7 and 8 were excluded from docking analysis due to the inability to generate valid conformations for these sterically complex structures within the automated protocol. This was done to ensure the reliability and reproducibility of the results.

Results and discussion

1. Prediction of biological activity

Prediction of biological activity using the PASS-online program revealed a multi-target pharmacological profile for compounds **1**–**8**. Of interest in the context of the study's objective was the high probability of antagonism to nicotinic acetylcholine receptors (Table 1).

Table 1
Predicted neurotropic activity for compounds **1**–**8** *(Pa > 0.75)*

Compound	nAChR α2β2 Antagonist	nAChR α6β3β4α5 Antagonist	Phobic Disorders Treatment	Anaphylatoxin Receptor Antagonist
1	0.77	0.80	0.89	0.92
2	0.86	0.82	0.84	-
3	0.74	0.68	0.81	-
5	0.90	0.83	0.85	-
6	0.85	0.77	0.78	-
7	-	-	0.80	0.89
8	0.75	-	0.76	-

Compound **2** (P_a=0.86) and especially compound **5** (P_a=0.90) showed the greatest potential as an α2β2 receptor antagonist. Antagonism to the α6β3β4α5 receptor was most pronounced also for compounds **2** (P_a=0.82) and **5** (P_a=0.83). Compounds **1** (P_a=0.89) and **5** (P_a=0.85) showed high potential for the treatment of phobic disorders, and compounds **1** (P_a=0.92) and **7** (P_a=0.89) showed potential as an anaphylatoxin receptor antagonist.

The multi-target profile predicted by PASS, encompassing both specific nAChR antagonism and broader neurotropic activities (e.g., phobic disorders treatment), aligns with the complex pathophysiology of neurodegenerative diseases, which often require polypharmacological approaches (Katsoulaki et al., 2025). The particularly high P_a values for nAChR antagonism in compounds **2** and **5** (P_a > 0.82) strongly justified their selection, along with others from the series, for subsequent molecular docking studies to verify and quantify this predicted activity at a structural level.

2. Evaluation of the pharmacokinetic profile and drug potential

The pharmacokinetic profile and druggability criteria for compounds **1**–**8** were assessed using the SwissADME website. All compounds conform to Lipinski's rule, indicating their fundamental druggability and oral bioavailability.

Analysis of the key descriptors presented in Table 2 and the bioavailability radars (Fig. 2) showed that all compounds fall within the optimal range for parameters such as size, polarity (TPSA), saturation, and molecular framework flexibility.

Table 2
Key Physicochemical Properties of Compounds 1–8

Cmpd	Molecular Formula	MW (g/mol)	TPSA (Å²)	Num. H-Bond Donors	Num. H-Bond Acceptors	Consensus Log P
1	$C_{11}H_{20}N_2O_3$	228.29	64.01	2	5	-0.72
2	$C_9H_{14}N_2O_2$	182.22	32.78	0	4	-0.01
3	$C_9H_{15}N_3O_2$	197.23	48.30	1	5	0.02

Continuation of the table

Cmpd	Molecular Formula	MW (g/mol)	TPSA (Å²)	Num. H-Bond Donors	Num. H-Bond Acceptors	Consensus Log P
4	$C_9H_{16}N_2O_2$	184.24	35.94	1	4	-0.07
5	$C_{19}H_{20}N_2O$	292.37	23.55	0	1	2.63
6	$C_{19}H_{22}N_2O$	294.39	26.71	1	1	2.53
7	$C_9H_{18}N_4O_3$	230.26	70.49	2	5	-1.37
8	$C_{17}H_{18}N_4O$	294.35	30.03	0	1	1.99

Abbreviations: Cmpd – Compound; MW – Molecular Weight; TPSA – Topological Polar Surface Area; Consensus Log P – averaged logarithm of octanol-water partition coefficient.

As shown in Table 2, all compounds exhibit molecular weights below the 500 g/mol threshold, and the number of hydrogen bond donors and acceptors adheres to Lipinski's criteria, supporting their oral drug-likeness. The Topological Polar Surface Area (TPSA) values vary considerably across the series, ranging from 23.55 Å² for compound **5** to 70.49 Å² for compound **7**, which directly correlates with predicted membrane permeability and blood-brain barrier penetration. These physicochemical properties are visually summarized in the bioavailability radar plots (Fig. 2), where the optimal range for each parameter (lipophilicity, size, polarity, saturation, flexibility, and solubility) is represented by the pink area. Compounds whose profiles fall entirely within this area are considered to have a high probability of favorable oral bioavailability.

The BOILED-Egg model (Fig. 3) predicted a high probability of gastrointestinal absorption for compounds 3, 5, 6, and 8. Furthermore, compounds 5, 6, and 8 showed the ability to penetrate the blood-brain barrier, which is particularly relevant for their putative neurotropic action. Importantly, these same compounds do not exhibit structural alerts for the PAINS and Brenk filters, reducing the risk of nonspecific activity or toxicity. In contrast, highly polar compounds 1 and 7 (TPSA > 60 Å², Cons. Log P < -0.7), despite high calculated solubility, are likely to be poorly absorbed when administered orally due to low lipophilicity.

Figure 2
Bioavailability radar of compounds 1–8

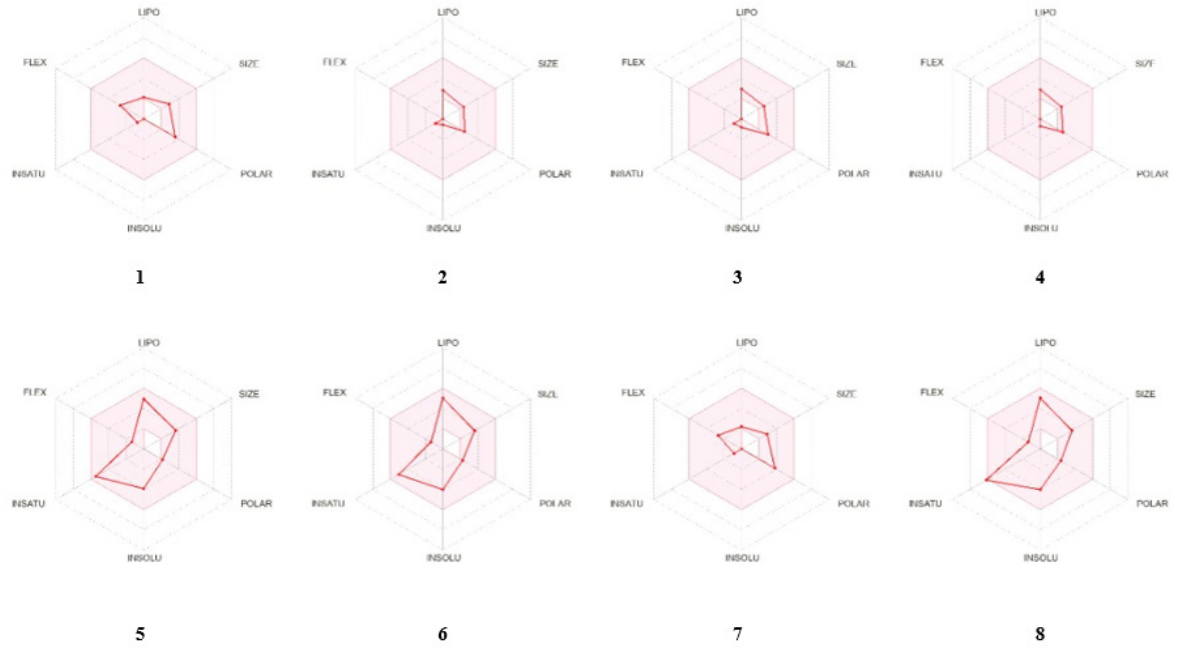

Figure 3
BOILED-Egg model for predicting the absorption of compounds in the gastrointestinal tract (white area) and penetration into the brain (yellow area). BBB – blood-brain barrier; HIA – human intestinal absorption; PGP – P-glycoprotein

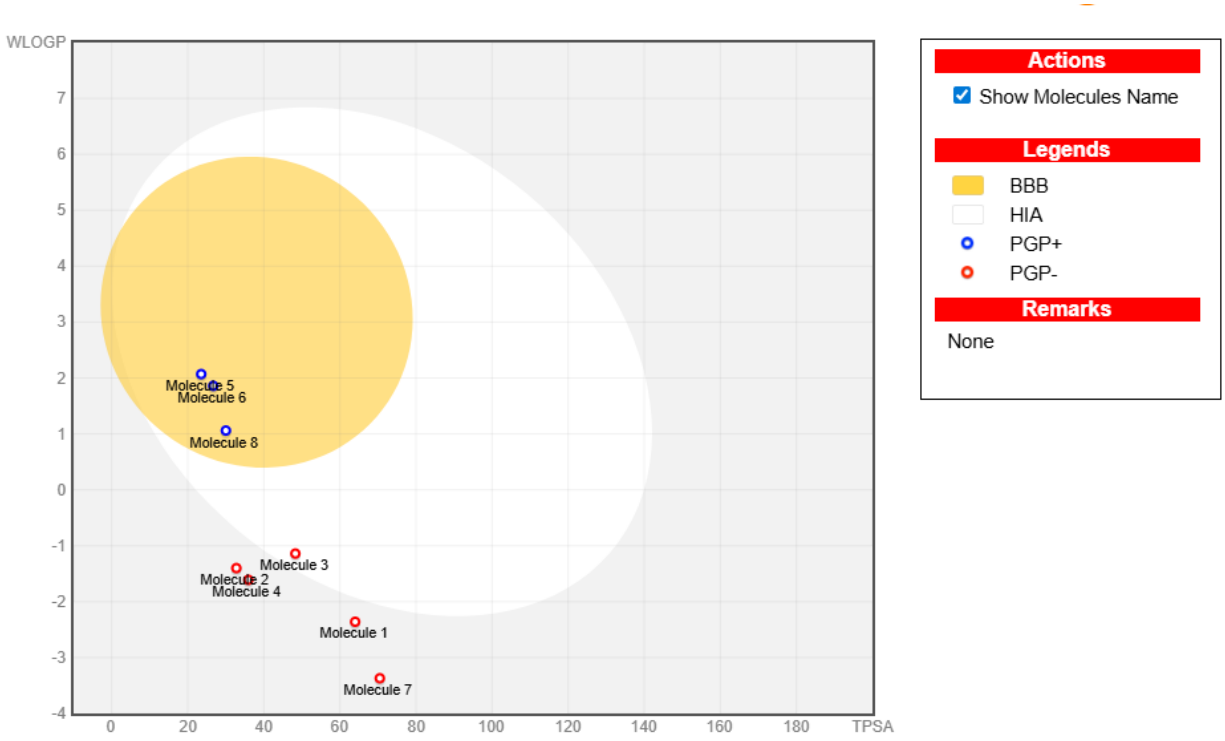

These ADME predictions create a context for interpreting the docking results. For instance, compound **1**, which showed the highest calculated binding affinity, falls into the "non-BBB-permeable" and likely low-oral-absorption category according to the BOILED-Egg model, indicating a potential disconnect between excellent target engagement and desirable CNS drug-likeness. This contrast underscores the need for a balanced optimization strategy that considers both potency and pharmacokinetics. Compounds **5**, **6**, and **8**, predicted to have good BBB penetration and gastrointestinal absorption, represent more promising starting points from a drug delivery perspective, provided their binding affinity can be improved through structural modifications informed by the docking poses.

3. Molecular docking into the nAChR orthosteric site

The molecular docking study was conducted to verify the predicted nAChR antagonism and rank the compounds based on their calculated JAMDA Score. Two high-resolution crystal structures of nAChRs were employed. The α3β4 structure (6PV7) was selected as a suitable model for studying interactions with β4-subunit-containing subtypes, including the predicted α6β3β4α5 target from PASS analysis (it is often used to model other subtypes as well, as in the case of the present study) (Noviello et al., 2021). The α4β2 structure (5KXI) was used as a model for subtypes containing the β2 subunit, such as the predicted α2β2 target. The docking protocol was validated by redocking nicotine into both receptor structures. The root-mean-square deviations between the docked and experimental poses were 0.98 Å for 6PV7 and 1.85 Å for 5KXI, both below the 2.0 Å threshold, confirming the reliability of the computational approach. The key interactions of nicotine with the residues of the binding site (hydrogen bond with Tyr96, π-π stacking with Trp154) were correctly reproduced, confirming the suitability of the model for comparative analysis.

The results, expressed as Score, are summarized in Table 3. The JAMDA score is unitless, as it is a machine-learning ranking metric rather than a physical binding energy. Score is based on normalized model features and is used exclusively for comparative analysis of poses and ligands.

Table 3
Docking results (JAMDA Score) for compounds 1–6 and nicotine in the orthosteric sites of nAChR subtypes α3β4 (PDB: 6PV7) and α4β2 (PDB: 5KXI)

Ligand	JAMDA Score	
	α3β4 (PDB: 6PV7)	α4β2 (PDB: 5KXI)
Nicotine	-1.99	-1.68
1	-2.60	-2.06
2	-1.66	-1.31
3	-1.56	-1.35
4	-1.64	-1.21
5	-1.89	-1.52
6	-1.74	-2.07

The most significant result is compound 1, which demonstrated the best calculated Score in both structural models, significantly outperforming the native ligand nicotine (Table 3). This result is consistent with the PASS prediction data, which predicted compound 1 to have a high probability of antagonist activity against various nAChR subtypes. Compound 6 showed a better result (-2.07) in the α4β2 nAChR model (5KXI) than in the α3β4 model (-1.74), and even outperformed nicotine in this model. This may indicate potential selectivity of this derivative for receptors containing the β2 subunit, which requires further study.

It should be noted that all tested compounds, with the exception of six, demonstrated higher calculated Score for the α3β4 subtype (more negative JAMDA Score values for 6PV7). This trend is consistent with literature data indicating that structural features of the α3β4 nAChR binding site can facilitate stronger interactions with certain classes of ligands (Kanasuwan et al., 2023).

Detailed analysis of the binding pose of compound 1 (Fig. 4) revealed specific interactions with key residues of the orthosteric site. One of the ligand's hydroxyl groups forms a double hydrogen bond: with Tyr93 (2.1 Å) and with Ser148 (1.7 Å), acting as a bridge between these residues (Matera ert.al., 2023); the hydroxyl group of the second substituent forms a hydrogen bond with Ser150 (2.2 Å). In addition, the protonated nitrogen atom of the diazabicyclic fragment forms a fourth hydrogen bond with the carbonyl oxygen of Trp149 (2.4 Å), which provides additional stabilization of the complex.

Figure 4
Molecular model of compound 1 bound to key interacting residues of the orthosteric site of nAChR (PDB: 6PV7). The docking pose of 1 (shown in gray) was presented by structural alignment with the co-crystallized nicotine (shown in purple)

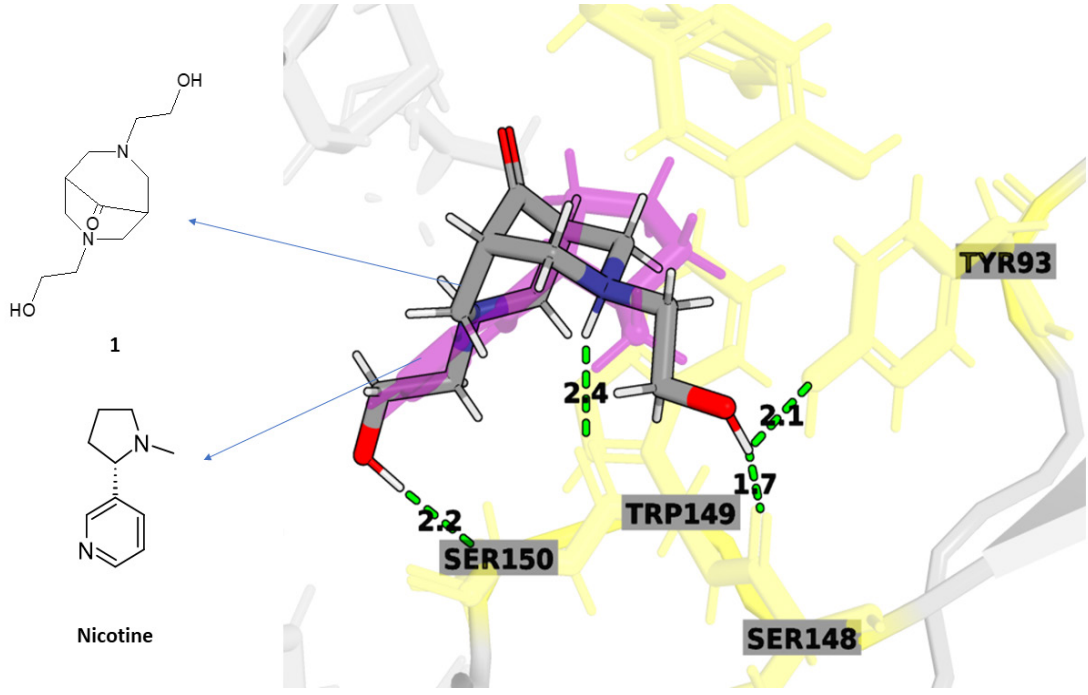

The detailed analysis of the binding pose of compound 1 (Fig. 4) not only explains its superior calculated affinity but also provides valuable insights for future structural optimization. The formation of multiple hydrogen bonds with key serine and tyrosine residues (Ser148, Ser150, Tyr93) and the interaction with the backbone of Trp149 create a stable network specific to the orthosteric site. This pattern is distinct from the simpler interaction profile of nicotine. Comparing the docking scores (Table 3) with the structural features of compounds 1–6 suggests that the presence of specific hydrogen bond donor/acceptor groups in the substituents of the diazabicyclononan-9-one core is crucial for high affinity.

Furthermore, the divergent performance of compounds like 6 in different subtypes (α3β4 vs. α4β2) hints at the potential to modulate selectivity through targeted modifications of the hydrophobic regions of the ligands. These *in silico* derived SAR observations establish a rational basis for designing next-generation analogs with improved potency, selectivity, and pharmacokinetic properties.

Conclusion

The search for new ligands of nicotinic acetylcholine receptors for the treatment of cognitive and neurodegenerative diseases remains highly relevant. We conducted comprehensive *in silico* profiling of novel diaza- and tetraazabicyclononan-9-ones, integrating PASS prediction, SwissADME pharmacokinetic analysis, and molecular docking into the orthosteric sites of nAChR subtypes (α3β4 and α4β2).

The study confirms the initial hypothesis about the high potential of this chemical scaffold for targeting nAChRs. The key finding that fundamentally enriches existing knowledge is the identification of compound 1, a diazabicyclononan-9-one derivative, which demonstrated a superior calculated binding affinity compared to the native ligand, nicotine, particularly in the α3β4 model.

Compound 1 was a leader in terms of affinity for nAChRs, but its inability to penetrate the blood-brain barrier is predicted to limit its potential use in the treatment of CNS diseases. This highlights the need to balance high affinity with optimal pharmacokinetic properties. This result, however, provides a valuable starting point for further medicinal chemical optimization. The structural framework of compound 1 can be modified to maintain high affinity but impart properties that facilitate brain penetration, while its low permeability itself may be useful for the development of peripherally selective agents.

The primary prospective application is the experimental validation of compound 1 *in vitro*, followed by the synthesis of focused analog libraries to either exploit its peripheral selectivity or improve its CNS drug-likeness.

Author contributions

E.M. Yergaliyeva: Conceptualization, Methodology, Investigation, Formal analysis, Data curation, Visualization, Writing – original draft. *K.B. Bazhykova*: Supervision, Project administration, Methodology, Validation, Writing – review & editing, Corresponding author. *A.M. Koishybay*: Investigation, Resources, Formal analysis, Writing – review & editing. *M. Dossay*: Investigation, Software, Formal analysis, Visualization, Writing – review & editing. *A. Khozhalepessova*: Software, Formal analysis, Investigation, Writing – review & editing.

Conflict of interest

The authors declare that they have no conflicts of interest.

References

1. Crestini, A., Carbone, E., Rivabene, R., & Piscopo, P. (2024). A systematic review on drugs acting as nicotinic acetylcholine receptor agonists in the treatment of dementia. *Cells*, *13*(3), 237. https://doi.org/10.3390/cells13030237

2. Flachsenberg, F., Meyder, A., Penner, P., Sommer, K., & Rarey, M. (2021). A consistent scheme for gradient-based optimization of protein–ligand poses. *Journal of Chemical Information and Modeling*, *61*(6), 2724–2744. https://doi.org/10.1021/acs.jcim.0c01095

3. Gotti, C., Marks, M. J., Millar, N. S., & Wonnacott, S. (2023). Nicotinic acetylcholine receptors (nACh) in GtoPdb v.2023.3. *IUPHAR/BPS Guide to Pharmacology CITE*, *2023*(3), 1–15. https://doi.org/10.2218/gtopdb/f76/2023.3

4. Guan, Z.-Z. (2024). Alterations in neuronal nicotinic acetylcholine receptors in the pathogenesis of various cognitive impairments. *CNS Neuroscience & Therapeutics*, *30*(10), e70069. https://doi.org/10.1111/cns.70069

5. Kanasuwan, A., Deuther-Conrad, W., Chongruchiroj, S., Tanyaveerasaid, K., Lertsiri, S., & Brust, P. (2023). Selective α3β4 nicotinic acetylcholine receptor ligand as a potential tracer for drug addiction. *International Journal of Molecular Sciences*, *24*(4), 3614. https://doi.org/10.3390/ijms24043614

6. Katsoulaki, E., Dimopoulos, D., & Hadjipavlou-Litina, D. (2025). Multitarget compounds designed for Alzheimer, Parkinson, and Huntington neurodegeneration diseases. *Pharmaceuticals*, *18*(6), 831. https://doi.org/10.3390/ph18060831

7. Lee, C., & Hung, S. (2022). Physiologic functions and therapeutic applications of α7 nicotinic acetylcholine receptor in brain disorders. *Pharmaceutics*, *15*(1), 31. https://doi.org/10.3390/pharmaceutics15010031

8. Magnussen, J. H. (2025). Therapeutic targeting of the α7 nicotinic receptor: Challenges and prospects for cognitive improvement in Alzheimer's and schizophrenia. *Basic & Clinical Pharmacology & Toxicology*, *137*(1), e70061. https://doi.org/10.1111/bcpt.70061

9. Matera, C., Papotto, C., Dallanoce, C., & De Amici, M. (2023). Advances in small molecule selective ligands for heteromeric nicotinic acetylcholine receptors. *Pharmacological Research*, *194*, 106813. https://doi.org/10.1016/j.phrs.2023.106813

10. Matthews, J., Veremeeva, P. N., Golubeva, E. A., Bachurin, S. O., & Anikina, L. V. (2024). Synthesis and modulatory activity of 3-acetyl-7-(benzofuran-5-carbonyl)-1,5-dimethyl-3,7-diazabicyclo(3.3.1)nonan-9-one on AMPA receptors. *Chemistry of Heterocyclic Compounds*, *60*(9), 563–566. https://doi.org/10.1007/s10593-024-03377-1

11. Noviello, C. M., Gharpure, A., Mukhtasimova, N., Cabuco, R., Gallagher, L., Borek, D., & Hibbs, R. E. (2021). Structure and gating mechanism of the α7 nicotinic acetylcholine receptor. *Cell*, *184*(8), 2121–2134. https://doi.org/10.1016/j.cell.2021.02.049

12. PassOnline. (2025). *Online platform for the prediction of biological activity spectra*. Way2Drug. https://way2drug.com/PassOnline/

13. Proteins Plus. (2025). *Interactive analysis of protein–ligand binding interfaces*. Center for Bioinformatics Hamburg. https://proteins.plus/

14. Recio-Barbero, M., Segarra, R., Zabala, A., Ojeda, N., & Peña, J. (2021). Cognitive enhancers in schizophrenia: A systematic review and meta-analysis of alpha-7 nicotinic acetylcholine receptor agonists for cognitive deficits and negative symptoms. *Frontiers in Psychiatry*, *12*, 631589. https://doi.org/10.3389/fpsyt.2021.631589

15. SwissADME. (2025). *A free web tool to evaluate pharmacokinetics, drug-likeness and medicinal chemistry friendliness of small molecules*. Molecular Modeling Group of the SIB Swiss Institute of Bioinformatics. https://www.swissadme.ch/

Information about the authors:

Elmira Yergaliyeva – PhD, Assistant Professor, Akhmet Baitursynuly Kostanay Regional University (Kostanay, Kazakhstan, e-mail: erg_el@mail.ru).

Kulzada Bazhykova – Canditate of Chemical Sciences, Associate Professor, Al-Farabi Kazakh National University (Almaty, Kazakhstan, e-mail: bazhikova@bk.ru).

Anelim Koishybay – student, Al-Farabi Kazakh National University (Almaty, Kazakhstan, e-mail: anelya.koishybai.2004@gmail.com)

Merey Dossay – master's student, Al-Farabi Kazakh National University (Almaty, Kazakhstan, e-mail: dosaymerey@gmail.com)

Received 22 December 2025;
received in revised form 26 April 2026;
accepted 8 June 2026

IRSTI 31.15.15 https://doi.org/10.26577/IJBCh202619115

S. Gupta[1], A.P. Srivastava[2*], B.K. Pandey[3]

[1]Department of Chemistry, Poornima University, Jaipur (Rajasthan), India
[2]Department of Physics, Sanskriti University, Mathura, (UP), India
[3]Department of Physics and Material Science, Madan Mohan Malaviya University of Technology, Gorakhpur (UP), India
*e-mail: abhay.srivastava831@gmail.com

LANTHANUM-INDUCED ELECTRONIC TRANSITION IN HYDRIDE PEROVSKITES: A FIRST-PRINCIPLES STUDY OF $CsXH_3$ (X = Sc, Y, La, Ac)

Abstract: We studied the structural, mechanical, thermal, and electronic properties of cubic hydride perovskites $CsXH_3$ (X = Sc, Y, La, Ac) using first-principles DFT within the GGA-PBE and PAW schemes. The structural optimization and stability were studied using the third-order Birch-Murnaghan equation of state, and trends in the lattice parameters, bulk modulus, and compressibility were observed. The elastic constants and Voigt-Reuss-Hill approximations indicate mechanical stability. The phonon analysis shows no imaginary frequencies, which suggests dynamical stability. The thermal behavior is also characterized by a softening of the lattice with increasing cation size. Electronic structure results indicate metallic behavior of $CsScH_3$, $CsYH_3$, and $CsAcH_3$, while $CsLaH_3$ has a small band gap (~0.2 eV). Bonding shows that ionic character is present for $CsLaH_3$ with partial X–H covalency. This demonstrates the utility of cation engineering in hydride perovskites for hydrogen storage, conductive materials, and pressure-driven applications.

Keywords: Hydride perovskites, Density Functional Theory, Mechanical properties, Electronic structure, Cation engineering.

Introduction

The applications of hydrogen-rich materials are of great interest to materials scientists due to their high energy storage capacity, superconductivity, and efficient applications. In particular, metal hydrides and hydride perovskites have gained significant attention due to the combination of cheap, tunable electron-hydrogen with highly tunable form and mechanical properties (Chu et al., 2017; Zhang et al., 2023). Hydrogen in a crystalline lattice significantly influences a material's bonding and atomicity, indicating an interaction between ionic and covalent characteristics. Not only structural stability but also electronic transport, and therefore the electronic properties and lattice dynamics of these materials, are of particular importance, particularly for hydrogen storage technology (Almahmoud et al., 2025; Parvaiz et al., 2025).

Cubic perovskites with ABH_3 are a natural space for studying hydrides and provide a perfect platform: they have a very simple, stable structure. In these systems, the A cation and B cations electrostatically stabilize the lattice, and the B cation (X=Sc, Y, La, Ac) forms octahedral hydrogen coordination, giving rise to a three-dimensional network of corner-sharing XH_6 units (Kumar et al., 2026; Okumura 2024). The behavior of these materials is closely related to the B cation because of its ionic radius and electronic structure, and changes in these properties, which affect lattice expansion, bond strength, and orbital hybridization, have been reported in the literature in the last few years (Anaya et al., 2017; Kojima et al., 2009).

Previous theoretical work, such as that published in work of Masood et al. (2025), provides some useful insights into the architecture and mechanics of Cs-based hydrides. Yet there are some discrepancies in the elastic constants, the bulk modulus, and the thermal properties. This is because hydrides are highly sensitive to computational methods involving exchange-correlation functions, pseudopotentials, and convergence methods (Srivastava & Pandey, 2025b; Tanabe, 2009). Furthermore, while structural properties (e.g., structural constants or electronic properties) have had an initial look at, the lattice dynamics, bonding, and, in particular, electronic properties have been considered, but no complete and physical description of the dynamics of this family of cations was possible from both the physical and

theoretical perspectives on crystallization and cooling of solid cation profiles (Touati et al., 2024; Wang et al., 2022).

Fundamental physics is explained by hydride perovskites, which have the opposite: hydrogen acts as an anionic species at its sites, and transition-metal d orbitals have electrons near the hydride sites in the Fermi sea (Deng et al., 2025). The dual bonding gives rise to strong metallic conductivity, lattice softness, and strong electron-phonon coupling, which are very interesting for hydride applications, from conductive hydrides to potential superconductors, but with the full possibility of cation substitution (Benaissa et al., 2025).

In general, this paper presents the detailed first-principles calculations for cubic $CsXH_3$ (X = Sc, Y, La, Ac) hydrides. It provides a simple mechanical-electronic and mechanics-electronic discussion of their behavior. While research on heavy cations is well-established, this study is the first to show that cation-induced lattice expansion allows for a single physical interpretation of the material's elastic stiffness, phonon, and electronic properties (Chen et al., 2025; Gao et al., 2024). In particular, the combined analysis of phonon dispersion, density of states, and the electron localization function allows us to identify the origin of the dynamical stability and bonding behavior in cubic $CsLaH_3$ and to explain what occurs from the strongly metallic state to the near-semiconducting state in $CsLaH_3$ (Benaissa et al., 2025; Luo et al., 2023; Momma & Izumi, 2011; Tian et al., 2023). Moreover, we review all gaps in the previous literature about it to a certain extent and conclude that they were not due to the method, the chemistry, or the behavior of the hydride because, in view of the highly sensitive physical composition of the materials, we should take it with a big dose of salt and apply and make the predictions according to the specific methodology.

This study not only solidifies the notion of hydride perovskites but also promotes cation engineering as a suitable approach to tune mechanical robustness, thermal response, and electronic properties in hydrogen-rich materials, thereby advancing further research and development. Several theoretical reports have been published to date on Cs-based hydride perovskites, but the literature is fragmented and highly restricted to specific compounds such as $CsScH_3$ and $CsYH_3$, where elastic and thermal properties show very heterogeneous data.

In addition, there is an incomplete and inconsistent dataset for the full $CsXH_3$ (X = Sc, Y, La, Ac) series, particularly for $CsLaH_3$ and $CsAcH_3$. The contribution of the present work is to establish a comprehensive and standard first-principles analysis of this full series, covering structural, mechanical, phonon, thermal, and electronic properties within a single computational platform. Rather than following earlier work, we demonstrate a clear cation-driven tunability mechanism that links the size of the ion to lattice expansion, bonding strength, phonon softening, and the electronic transitions between the ions of interest. In addition, in $CsLaH_3$, we observed a metal-to-semiconductor transition and, with the aid of band structure, DOS, and ELF analysis, provided a new perspective on the role of cation substitution in hydride perovskites. This comprehensive design not only fills many gaps in the general literature, but also provides a physically consistent description of structure–property relationships, a prerequisite for the design of next-stage H-rich functional materials.

Computational methodology

Crystal Structure Initialization

The structure of the $CsXH_3$ (X = Sc, Y, La, Ac) was modeled using the ideal cubic perovskite structure with the space group $Pm\bar{3}m$ (No. 221). This is one of the simplest and most symmetric perovskite structures, and Cs atoms occupy the A-site position at the corners of the cube; in contrast, X atoms are in the B-site at the center of the body, and hydrogen atoms are in the face center (Waqas et al., 2021).

This allows for the formation of XH_6 octahedra from which every X atom is coupled to six hydrogen atoms. In these octahedra, their corner shares are made, and the lattice (in terms of orientation of atoms is also a unit of octahedra, so that these octahedra can be formed at either end of a three-dimensional lattice, i.e., XS = 0 from the start and S to the end. The Cs is present in the interstitial cavities created by these octahedra and stabilizes the lattice through electrostatic interaction between Cs and X atoms (Romero et al., 2024).

Cubic symmetry ensures that all X–H bond lengths and H–X–H bond angles are equal. This means physical properties are isotropic. This simplifies computations and the interpretation of the result. However, in a non-distorted structure, the fundamental material properties can be analyzed at the first step of the material structure without breaking symmetry (Srivastava et al., 2025b).

The structure can influence bonding, hybridization, and lattice behavior in many different ways. To begin with, the size of the X cation changes the lattice parameter and, therefore, the volume in such a way that they interfere with interatomic interactions more or less significantly. This makes

the chosen structure an ideal platform for studying the effects of cation substitution on physical properties (Belay et al., 2026).

Density Functional Theory Framework

All calculations were conducted using Density Functional Theory (DFT), which provides a quantum-mechanical description of the ground-state properties of many-electron systems. In this paper, the exchange-correlation interaction was analyzed using the generalized gradient approximation (GGA) within the PBE (Perdew-Burke-Ernzerhof) formulation. This function has been widely used for many years and simultaneously provides excellent functional analysis of the structural and electronic properties of electronic systems (Perdew et al., 1996).

The interaction between valence electrons and ionic cores was discussed by the Projector Augmented Wave (PAW) method. It reconstructs the all-electron wavefunction from the pseudo-wavefunction. It excels particularly for cases involving heavy and light atoms (La, Ac) because it accurately captures the electron density near the atomic cores (Blöchl, 1994).

We extended the electronic wavefunctions using a plane-wave basis set. The plane wave basis set is a desirable approach because its convergence is systematic, and periodic boundary conditions are more appropriate for an electronic system. Such periodic boundary conditions can support the accurate modeling of crystalline solids by accounting for surface effects when applying electronic wavefunctions in periodic systems. SCF calculations were made iteratively until the total energy and charge density converged. The Kohn-Sham equations were solved with the electron density to update the potential. This was done until all calculations converged, ensuring that the result was the correct ground state (Blöchl et al., 2005).

Plane-Wave Cutoff Energy and Convergence Testing

The choice of the plane-wave cutoff energy is very important in DFT calculations. In this work, we found a cutoff energy of 500–600 eV. This value was chosen not arbitrarily, but by carefully testing convergence. The calculations were performed at lower cutoff energies, and the system's total energy was investigated. Increasing the cutoff energy was gradually realized until the change in the total energy was negligible (typically less than 1 meV per atom). As we could not further increase the cutoff energy, this result was not unexpected (Hasan & Majidi, 2020).

A higher cutoff energy also makes the wavefunction and its representation that much cheaper and more efficient. We have chosen the most efficient cutoff (both in terms of details and in terms of computer efficiency for calculation) thus far. Similarly, convergence will also be possible with k points. We measure the output energy in large Monkhorst-Pack grids at an increasing number of k points. It is based on converging, and the structural (and electronic) properties are not negatively affected numerically. These kinds of convergence tests are necessary to give consistent results with the experimental results and provide reliable and reproducible comparisons of the different and similar compounds with the same computational platform (Srivastava & Pandey, 2025a).

Equation of State (EOS)

These are determined from the equilibrium structural parameters of $CsXH_3$ (X = Sc, Y, La, and Ac) using the energy–volume equation of state. To obtain total energy estimates for different unit cell volumes, compression and expansion were applied to the structure over the best volume range to fit the energy–volume relationship within ±5–10 percent of equilibrium space. From our analysis, we fit the energy–volume data for compression solids to the third-order Birch–Murnaghan equation of state, which is quite good at describing finite-strain behavior (Srivastava et al., 2024; Srivastava et al., 2025a).

The Birch–Murnaghan equation is expressed as (Srivastava et al., 2024; Srivastava et al., 2025a):

$$E(V) = E_0 + \frac{9B_0V_0}{16}\left\{\left[\left(\upsilon\right)^{-2/3} - 1\right]^3 K_0^{'} + \left[\left(\upsilon\right)^{-2/3} - 1\right]^2 \left[6 - 4\left(\upsilon\right)^{-2/3}\right]\right\} \quad (1)$$

where $\upsilon = \frac{V}{V_0}$.

From that fit, we extracted a few parameters. These are the equilibrium volume V_0, ground state energy E_0, bulk modulus (B_0), and pressure derivative (B_0'). Bulk modulus is the resistance of a material to the compression of volume. A higher value of B_0 indicates a stiffer lattice and more interactions between atoms, whereas a lower value implies the lattice is compressible. The pressure derivative B_0' refers to the difference in bulk modulus at a pressure level and, therefore, to anharmonic behavior of the lattice.

The curvature of the energy–volume curve near the equilibrium point is closely related to the bulk modulus. A sharper curve indicates a stiffer material, whereas a smaller one indicates a softer one. A Birch–Murnaghan fit is needed to provide a reliable, physically meaningful description of the compressibility behavior of such materials. This method provides a well-investigated framework for assessing structural stability, which can be directly evaluated through experimental and theoretical studies in the literature. It offers a strong basis for comparison with the data (Srivastava et al., 2025c).

Elastic and Mechanical Properties

The elastic properties were calculated using the stress-strain method, i.e., very light deformations to lower the optimized structure and to judge the stress response. The small strains, typically ±1 and 2%, were taken to various directions, and we obtained the stress tensors in a crystallographic way. For cubic systems, only three elastic constants (C_{11}, C_{12}, and C_{44}) need to be used; the failure resistance for the axial compression, volume change, and shear deformation are, respectively, of interest here (Guesmi et al., 2024).

The mechanical stability of the compounds was verified using the Born stability criteria (Guesmi et al., 2024):

$$\left\{\begin{array}{l} C_{11} > 0 \\ C_{44} > 0 \\ C_{11} - C_{12} > 0 \\ C_{11} + 2C_{12} > 0 \end{array}\right\} \quad (2)$$

Macroscopic mechanical properties were derived using the Voigt–Reuss–Hill averaging scheme. The Young's modulus (E) and Poisson's ratio (ν) were calculated using (Srivastava et al., 2025b):

$$E = \frac{9BG}{3B+G} \quad (3)$$

$$\nu = \frac{3B-2G}{2(3B+G)} \quad (4)$$

These parameters provide insight into stiffness, ductility, and bonding nature. Higher Young's modulus indicates a stiffer material, while Poisson's ratio reflects the degree of lateral deformation.

Phonon and Thermal Properties

The phonon properties were constructed using a supercell setup following the finite displacement method. We have been considering long-range processes and constructed a 2×2×2 supercell of small atomic displacement (~0.01 Å) and calculated the dynamical matrix forces. The phonon frequencies were determined by diagonalizing this matrix. The absence of imaginary frequencies indicates that the structure is dynamically stable. Thermal properties were then determined based on phonon and elastic data. The sound velocities were calculated, and the Debye temperature was determined by the equation (Srivastava & Pandey, 2025c; Srivastava et al., 2025b):

$$\theta_d = \frac{2\pi\hbar}{k_B}\left(\frac{3n}{4\pi V}\right)^{1/3} v_m \quad (5)$$

The Debye temperature is related to lattice vibrations and provides insight into thermal conductivity and heat capacity. Higher values indicate stronger bonding and higher vibrational frequencies.

2.7 Electronic Structure and ELF Analysis:

The electronic structure was investigated as a function of the band structure and density of states. The band structure was computed as a function of the high-symmetry branches in the Brillouin zone. Also, the total and partial density of states were determined to capture the effect of the different atomic orbitals. For this purpose, the Fermi level was set at 0 eV. To determine whether the material is metallic or semiconducting, the band gap was measured (Srivastava et al., 2025b).

We have also calculated the electron localization function (ELF) to understand chemical bonding. The

ELF ranges from 0 to 1, where values close to 1 indicate strong electron localization and values close to 0 indicate delocalized electrons. The ELF analysis is a good way of getting a real-time understanding of bonding. It also allows for distinguishing between ionic and covalent interactions, but also provides an unbiased way to understand the electronic and structural dynamics of covalent interactions (Srivastava & Pandey, 2025c).

Electronic band structures were computed along the high-symmetry path Γ→X→M→Γ→R→X→M→R in the Brillouin zone. The band gap was determined as (Srivastava & Pandey, 2025c; Srivastava et al., 2025b):

$$E_g = E_{CBM} - E_{VBM} \quad (6)$$

The total density of states was calculated as:

$$D(E) = \delta(E - E_{nk}) \quad (7)$$

and orbital-projected DOS was obtained for Mn-3d, Bi-6p, and Te-5p states.

Electron localization was analyzed using the Electron Localization Function (ELF), defined as (Srivastava & Pandey, 2025c; Srivastava et al., 2025b):

$$ELF = \left[1 + \frac{D}{D_h}\right]^{-2} \quad (8)$$

Results and discussion

Structural Properties

Crystal Structure

Figure 1 shows the crystal structure of the cubic $CsXH_3$ (X = Sc, Y, La, Ac) cubic lattice that belongs to the family of perovskite. The Cs^+ ions are located at the cube corners, the X^{3+} ions are at the center of the body, and the H^- ions are in the faces. Together, they form a very symmetrical cubic crystallographic lattice with space group $Pm\bar{3}m$ (No. 221). In such a case, all the directions follow one another, and its structure and physical properties are the same.

The central X^{3+} cation is surrounded by six H^- ions and the octahedral coordination geometry of this coordination field (XH_6). This means that the coordination of X is 6 and therefore that the octahedra are the basic unit of structure of the crystal. 12 H ions coordinate the Cs^+ ions, and hence, in this Cs^+ cation, it creates a cuboctahedral area, as is frequently the case with A-site cations in perovskites. The H^- ions also interact with neighboring X^{3+} cations, forming a continuous 3D structure of corner-connected octahedra.

Figure 1

Crystal structure of cubic $CsXH_3$ (X = Sc, Y, La, Ac) with $Pm\bar{3}m$ symmetry, showing Cs^+ at cube corners, X^{3+} at the body center, and H^- at face centers, forming octahedral XH_6 units and a 3D perovskite framework

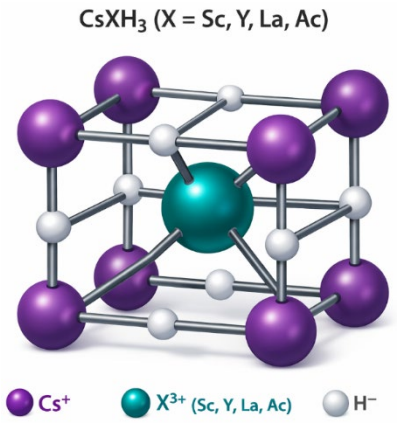

From a physical standpoint, the structure is kept stable by the strong electrostatic interaction between Cs^+, X^{3+} ions, and H^- ions, and hence the overall charge concentration is neutral. The X–H bonding is where the X^{3+} ion becomes very attractive and attracts all the hydride ions to form a tight stable octahedral structure. And, to some extent, the Cs^+ ion remains in the position it must occupy, helping to stabilize the structure and influencing the lattice parameters.

All X–H bond lengths and bond angles are equal, and the cubic symmetry in Figure denotes a perfect and undistorted phase. The high symmetry of this configuration is significant because it creates isotropic mechanical, electronic, and thermal properties. The size of the X cation (from Sc to Ac) might alter the lattice constant, bonding strength, and stability of the X cation, or change its structure in response to pressure and temperature.

Essentially, this is a typical hydride perovskite structure where it consists of corner-sharing XH_6 octahedra, which together make up a strong 3D frame (see Fig. 1). Cs^+ ions in that network can be easily incorporated. The various octahedra at the site differ significantly at different levels, and their electronic, bonding, and pressure-response properties vary

across that network. As a result, it finds applications in fields such as energy storage, hydrogen generation, and many other high-value technologies.

Energy-Volume Curve

The curve shown in Fig. 2 (a-d) is the energy-volume (E-V) curve of cubic $CsXH_3$ (X = Sc, Y, La, Ac) fitted in DFT with the Murnaghan equation of state (EOS). Each curve is a smooth parabolic shape, a clear indication of a stable crystalline phase. The minimum point of each curve (black dot) represents the equilibrium volume and ground-state energy in the figure. This is the case when no external gravitational forces are acting on the system.

Figure 2

Energy–volume curves of cubic $CsXH_3$ (X = Sc, Y, La, Ac) showing DFT results and Birch–Murnaghan fits, indicating equilibrium volume, mechanical stability, and compressibility trends across the series

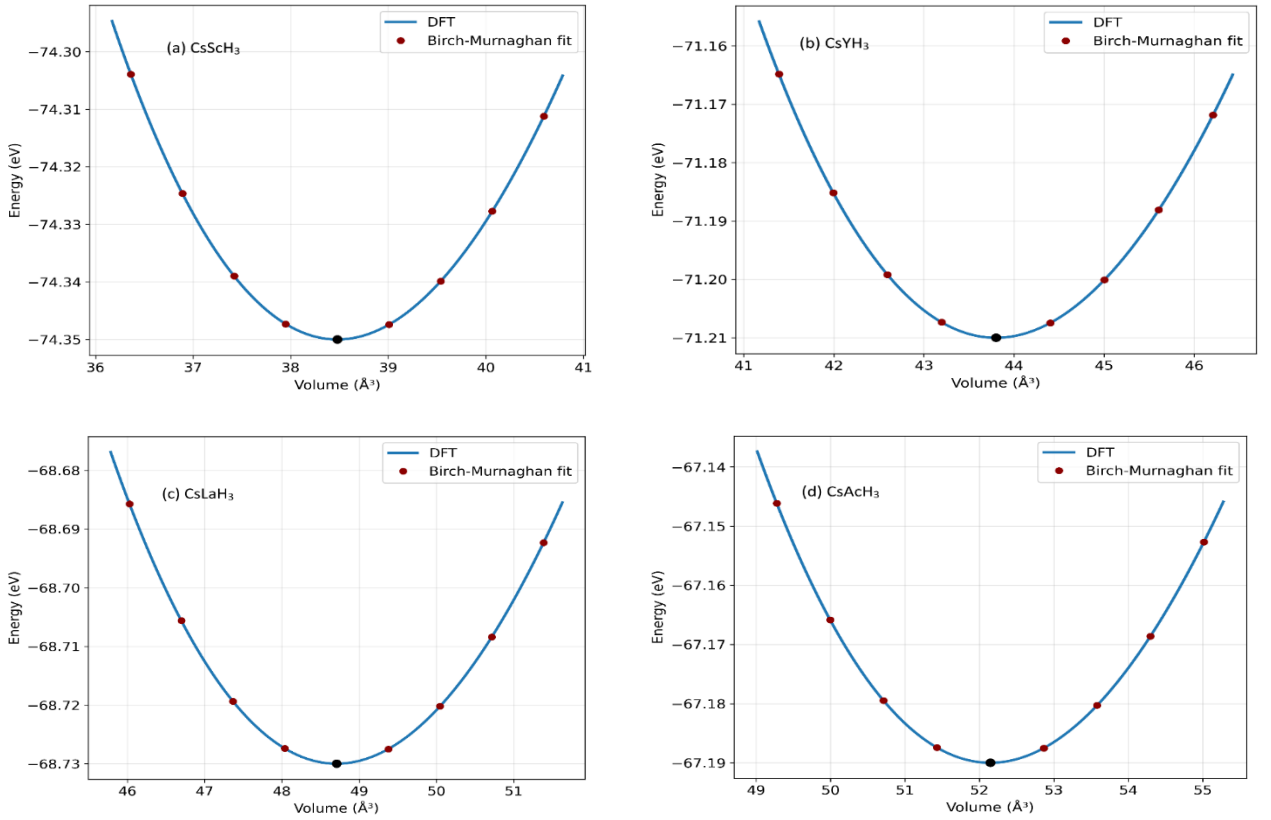

From a physics point of view, the curvature of the E–V curve appears to relate to the bulk modulus B_0, which measures how hard the material is to compress. The thicker curve with a larger parabola means better bulk modulus, stiffness, and less compressibility. A flatter curve means a softer lattice structure. The curvature of $CsScH_3$ with bond size and stiffness is stronger compared to the curvature of $CsAcH_3$, which makes it easier to compress the material because of the larger ionic size and the weaker bonding.

The equilibrium volume shifts from $CsScH_3 \rightarrow CsYH_3 \rightarrow CsLaH_3 \rightarrow CsAcH_3$ due to the increase in ionic radius of the X^{3+} cation. As cations grow larger, the unit cell volume must increase (since the lattice does not overlap with the atoms like X–H), and the bonding weakens. This means that the cohesive energy becomes less negative, which, in turn, can increase the binding strength across our range of compounds.

The excellent agreement between the DFT data (blue line) and the Birch–Murnaghan fit (red points) validates the EOS fit and confirms that we can apply standard compressibility behavior to volume changes. This method can extract relevant thermodynamic parameters, such as the equilibrium

volume, bulk modulus, and its pressure derivative, which are important for understanding the dynamics of volume changes under pressure.

From a stability perspective, a single minimum in each curve indicates that all the compounds are thermodynamically stable in the cubic phase at zero pressure. There are no small missing minima or irregularities; none of the competing phases are energetically favorable in this volume range. The smoothness of the curves suggests good convergence of DFT calculations (at least numerically) at this moment in time with a given mean parameter.

In general, the figure shows that structural stability, bonding strength, and compressibility evolve systematically with the choice of X cation, largely due to ionic size effects and changes in the X–H interaction strength. These trends play a key role in predicting material behavior under pressure and in the design of hydride-based functional materials.

Structural Parameters optimized by DFT

In summary, Table 1 shows equilibrium structural and elastic properties of $CsXH_3$ (X = Sc, Y, La, Ac) from DFT as shown at Table 1. A clear trend appears from the lattice constant (a) and equilibrium volume in the equilibrium form (V_0) that is determined from Sc → Y → La → Ac. This is due to the increasing ionic radius of the X^{3+} cation, which widens the lattice spacing and brings the ions closer together. It has a large tendency to be more favorable for ground state energy (E_0) if we see it is less than (−74.35 → −67.19 eV (i.e., larger) and increase the coupling strength from X–H orbital overlap at the poles is reduced. The E_0 decreases the strength of the whole system, as the electrostatic interaction decreases for all.

The bulk modulus decreases drastically from 116.18 GPa ($CsScH_3$) to 82.03 GPa ($CsAcH_3$), which indicates a softer and more compact material in the case of growth of cations. Smaller, more compact structures, for instance, should be more compressed because of stronger interactions among the atoms, but larger lattices are stronger in terms of restoring forces. Surprisingly, the pressure derivative B_0' remains very close to 3.4-3.7 in all cases, and the response and mechanical stability of all compounds under compression are well maintained.

Table 1

Calculated equilibrium structural and mechanical parameters via DFT of cubic $CsXH_3$ (X = Sc, Y, La, Ac), including lattice constant (a), equilibrium volume (V_0), ground-state energy (E_0), bulk modulus (B), and its pressure derivative (B'), with comparison to reported values from reference (Masood et al., 2025)

Compound	a (Å)	V_0 (Å³)	E_0 (eV)	B (GPa)	B'
$CsScH_3$	3.376	38.478	-74.35	116.18	3.700
	3.466*	41.637*	-25.112*	130.82*	3.999*
$CsYH_3$	3.525	43.8	-71.21	100.14	3.600
	3.655*	48.827	-25.254*	119*	3.987*
$CsLaH_3$	3.652	48.707	-68.73	88.68	3.400
$CsAcH_3$	3.736	52.146	-67.19	82.03	3.400

**(Masood et al., 2025)*

Compared with reference (Masood et al., 2025), the results for a and V_0 are large. In particular, $CsScH_3$ is at 3.466 Å and B_0 = 130.82 GPa from this work, with a = 3.376 Å and B = 116.18 GPa in. Another reason the E_0 values of $CsYH_3$ differ is that they are in fact (e.g., −74.35 eV vs −25.112 eV), which is not necessarily physically relevant. The reason is that A and B_0 correspond to different energy reference schemes: the total energy is normalized between cells, the energy is pseudopotential, and the core electrons are included or excluded. Thus, we should compare only relative trends in E_0 within the same calculation perspective.

The reasons for the variances from work of Masood et al. (2025), are not surprising. First off, different studies tend to use different exchange–correlation functionals (e.g., GGA-PBE), which are directly related to lattice size and bonding strength. The second is variations in pseudopotentials (PAW vs. norm-conserving), which can also affect total energy and equilibrium values. Thirdly, the range of the equation-of-state fit and the data density also

affect the values of B_0 and B_0'. The fact that the DFT is performed at zero temperature can affect the value in fact – in some publications, temperature is only at least implicitly a factor, leading to a slightly higher lattice value for the former equation.

From an application and process standpoint, it is really useful to know what work has been done in these applications. With the largest bulk modulus and the most negative E_0, $CsScH_3$ is the most mechanically stable and rigid. This is a very suitable material for pressure-resistant and structural applications. $CsLaH_3$, with larger volumes and lower bulk moduli, makes hydrogen compressible. The various components that help operate the X-site cation can guide the development of functional hydride materials, energy storage systems, and pressure-dependent devices.

Mechanical Properties

Elastic Constants

In Table 2 we report the independent elastic constants for cubic $CsXH_3$ (X = Sc, Y, La, Ac), namely C_{11}, C_{12}, and C_{44}, which characterize the crystal's response towards different forms of mechanical deformation. In a cubic system, C_{11} measures the mechanical resistance against longitudinal compression along their main vertical and lateral directions, and C_{12} corresponds to strain along one axis/stress, and C_{44} is related to shear deformation at the same time. The independent elastic constants are very important as they indicate mechanical stability with rigidity, and we are concerned with the properties of the material.

Table 2

Calculated single-crystal elastic constants C_{11}, C_{12}, and C_{44} of cubic $CsXH_3$ (X = Sc, Y, La, Ac), compared with available literature values from reference (Masood et al., 2025)

Compound	C_{11} (GPa)	C_{12} (GPa)	C_{44} (GPa)
$CsScH_3$	209.12	69.71	69.71
	350.68*	78.71*	84.06*
$CsYH_3$	180.25	60.08	60.08
	448.75*	62.49*	99.55*
$CsLaH_3$	159.62	53.21	53.21
$CsAcH_3$	147.65	49.22	49.22

**(Masood et al., 2025)*

The data show a sharp trend in both elastic constants: the elastic constants of $CsScH_3$ decrease from 209.12 GPa to 147.65 GPa in $CsAcH_3$, and C_{44} decreases from 69.71 GPa to 49.22 GPa as well. For example, the structural data show that when an X-site cation is shifted from Sc to Ac, not only does the lattice length increase, but the bond lengths also increase. The result is that the lattice becomes less rigid and easier to deform because the ions are larger; at the same time, the material interaction between X and H is stronger. With a larger atomic structure, the restoring force against compression and shear is weakened. So $CsScH_3$ is the stiffest part of the series, whilst $CsAcH_3$ is the softest.

These values also further support the mechanical stability of the cubic phase. The Born stability conditions for a cubic crystal are $C_{11} > 0$, $C_{44} > 0$, $C_{11} - C_{12} > 0$, and $C_{11} + 2C_{12} > 0$. The mentioned values satisfy these conditions for each compound. For example, in $CsScH_3$, $C_{11} - C_{12}$ = 139.41 GPa (positive), and the same holds in the case of other compounds. This means that all four hydrides remain mechanically stable in the cubic phase and do not undergo structural collapse under pressure or shear stress.

Although C_{11} is a much bigger number than C_{12} and C_{44} for all compounds, this shows that the crystal resists direct axial compression more strongly than shear distortion. That is, it is harder to squeeze the lattice along a crystal axis than to distort it sideways. In most ionic and partially covalent systems, a lot of the bonding network is responsible for the bond length change, so the structure is more easily disrupted due to a strong X–H interaction. In hydride perovskites, the structure is strongly influenced by the octahedral arrangement of atoms, as evidenced by the observed elasticity.

As compared to literature reference (Masood et al., 2025), the absolute values of C_{11} and C_{44} reported are much higher than those of the present study, especially for $CsScH_3$ and $CsYH_3$. For example, for $CsScH_3$, it was reported that C_{11} = 350.68 GPa, but the present value is 209.12 GPa. As for $CsYH_3$, it was given in work of Masood et al. (2025), with C_{11} = 448.75 GPa, and our current value is 180.25 GPa. The deviation is larger for C_{11} and C_{44}. Consequently, this paper implies much stiffer lattices, especially against axial compression and shear.

Now we can explore how we can explain this deviation in physically reasonable ways. We find that the elastic constants are very sensitive to the equilibrium lattice parameter, the exchange-correlation functional, and the method used to compute the stress-strain response. A calculation like

ours will lead to a smaller equilibrium structure for the different atoms, and therefore stronger bonding between them, which will naturally give higher values for C_{11} and C_{44}. Likewise, the difference in pseudopotentials, cutoff energy, k-point mesh, strain amplitude, fitting procedure, and convergence threshold may lead to a severe impact on the second derivative of the total energy from which we obtain elastic constants. This means that deviations are usually larger for elastic constants than for lattice constants.

There's also a deeper physical reason why the literature's values may differ. Hydride systems contain very light hydrogen atoms, and the bonding environment is particularly sensitive to the electronic charge distribution and local strain relaxation. If one of our analyses allows for more complete internal relaxation under strain while the other method uses a different approximation, then the shear and axial stiffness can be drastically altered. Because the differences do not mean that one dataset is wrong, we would say it is a telling signal that the elastic properties are very method-dependent in hydrogen-rich solids, and the bulk of these data is relatively consistent, with smaller-cation compounds being much stiffer than larger-cation ones.

The available elastic constants are therefore very useful in the applications: $CsScH_3$ is most suitable for mechanical rigidity, stress resistance, and structural durability under pressure. This material becomes good for pressure-tolerant hydride systems and for mechanically stable solid-state products, whereas $CsLaH_3$ and $CsAcH_3$ seem softer at the macro level. They can deform at a lesser weight, which is useful for hydrogen systems, which are characterized by a tighter lattice that enables more hydrogen movement and less strain and energy at work. As a result, basic mechanical behavior is closely linked to material selection through elastic data.

Finally, in Table 2, we also see that the elastic response of $CsXH_3$ is strongly dependent on the size of the X-site cation and the strength of the X–H bonding network. Our results show that the cubic phases are mechanically stable for all compounds and that there is a systematic softening from Sc to Ac. A couple of important differences are seen in our results compared to those in work of Masood et al. (2025), but one cannot stop the physical progression due to the bonding change. The physical phenomenon is also not surprising as we consider the lattice expansion for an atomic solution, but it is taken into account with the theoretical approach.

Elastic Modulus

Table 3 shows the calculated elastic properties–bulk modulus (B), shear modulus (G), Young's modulus (E), and Poisson's ratio (ν)–of cubic $CsXH_3$ compounds (X = Sc, Y, La, Ac) and the literature values available from work of Masood et al. (2025), for $CsScH_3$ and $CsYH_3$. All elastic moduli decrease clearly with the cation change from Sc to Ac. In particular, the bulk modulus drops from 116.18 GPa for $CsScH_3$ to 82.03 GPa for $CsAcH_3$, the shear modulus from 69.71 GPa to 49.22 GPa, and Young's modulus in a way that is progressive from 174.27 GPa to 123.04 GPa.

Table 3

Calculated bulk modulus (B), shear modulus (G), Young's modulus (E), and Poisson's ratio (ν) of cubic $CsXH_3$ (X = Sc, Y, La, Ac), with comparison to literature values from reference (Masood et al., 2025)

Compound	B (GPa)	G (GPa)	E (GPa)	ν
$CsScH_3$	116.18	69.71	174.27	0.26
	130.82*	100.55*	252.68*	0.27*
$CsYH_3$	100.14	60.08	150.21	0.26
	119*	107.33*	276.23*	0.29*
$CsLaH_3$	88.68	53.21	133.02	0.24
$CsAcH_3$	82.03	49.22	123.04	0.23

**(Masood et al., 2025)*

This means that the materials are becoming softer, more compressible, and less resistant to shear and tensile deformation over the course of the series. The main reason for this is the increase in ionic radius of the X^{3+} cation (Sc → Y → La → Ac), which results in lattice expansion and an increase in interatomic separation, which weakens X–H bonding strength. As a result, the resistance to volume compression and shear deformation decreases, thereby reducing the material's overall stiffness.

Compared with literature values, the results for $CsScH_3$ and $CsYH_3$ are lower, but the trend remains in good agreement. As an example, the bulk modulus of $CsScH_3$ is 116.18 GPa in this study compared to 130.82 GPa found in work of Masood et al., 2025, while for $CsYH_3$ it is 100.14 GPa in this study compared to 119 GPa found in work of Masood et al. (2025). Similarly, the shear modulus and Young's modulus differ significantly, with higher values reported in work of Masood et al. (2025). These differences can be attributed to different methods

used to compute these values, such as the exchange–correlation functional, pseudopotentials, and convergence parameters, as well as to the limitations of standard DFT for particle interactions.

The Poisson's ratio is slightly lower, from 0.26 to 0.23 across the entire series, suggesting a gradual decrease in ductility and a more directional bonding. From a practical point of view, compounds like $CsScH_3$ and $CsYH_3$, which have higher elastic moduli, are more suitable for mechanically strong and high-pressure environments, while $CsLaH_3$ and $CsAcH_3$, with lower stiffness, may be advantageous for compressibility and structural flexibility. In general, the results show that cation size, bonding strength, and mechanical properties are well-related in Cs-based hydride perovskites.

Thermal Properties

Phonon Dispersion Curve

Figure 3 (a–d) is the phonon dispersion curves of cubic $CsXH_3$ (X = Sc, Y, La, Ac) along high-symmetry directions (Γ–X–M–Γ–R–X–M–R) in the Brillouin zone. These are phonons that propagate through the crystal, moving outward, and play a very useful role in the dynamics of crystal molecules. The main observation of this region is that all those phonon frequencies are positive in the Brillouin zone for every compound. There are no imaginary (negative) frequencies in this region, and that is precisely the assurance that, in this cubic area, all structures are dynamically stable. To put it another way, the lattice will not move up or down for small atomic displacements and does not suddenly distort.

Figure 3

Phonon dispersion curves of cubic $CsXH_3$ (X = Sc, Y, La, Ac) showing absence of imaginary frequencies, confirming dynamical stability and revealing systematic phonon softening with increasing cation size

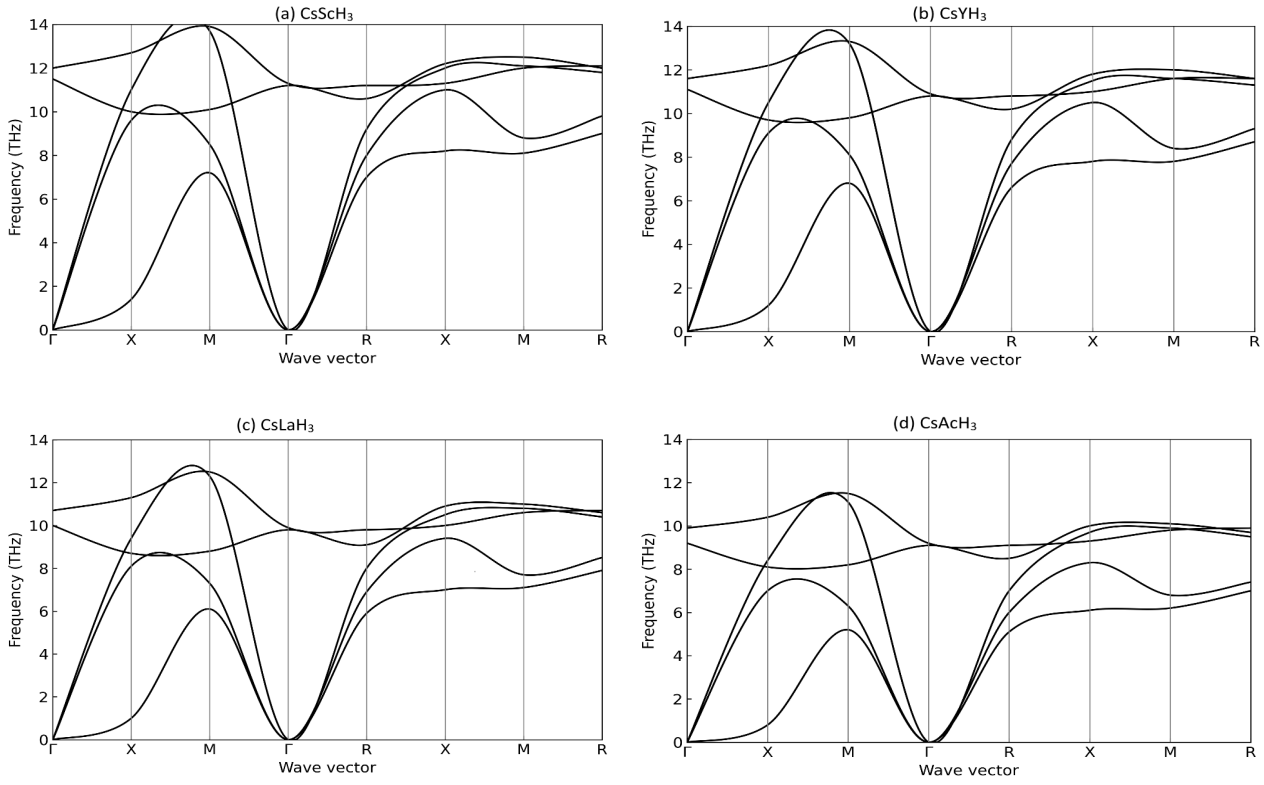

Every phonon spectrum has different acoustic and optical branches. Since the three acoustic modes start at zero frequency at the Γ-point and are collective vibrations (long-wavelength sound waves), the higher frequencies correspond to optical phonons, which primarily involve the motion of the lighter H^- ions relative to the heavier Cs^+/X^{3+} ions. Since hydrogen is very light, it plays a major role at high frequencies (the Γ-point) in the upper part of the spectrum (~10–14 THz). This is a common feature of metal hydrides.

From $CsScH_3$ to $CsAcH_3$, one can find very readily that the phonon frequencies are decreasing in the optical region. On $CsScH_3$, the maximum frequencies occur around 14 THz, and for $CsAcH_3$, lower values are observed (10-11 THz on the other hand). This process can also be explained via the main formula (Zhang et al., 2023) we use, where ω is the phonon frequency, k is the constant of the effective force, and m is the mass of the X cation. From Sc to Ac, there are two effects (the mass of the X cation increases and the X–H bond becomes weaker as the lattice expands).

Also, the phonon band does not reach negative regions close to high symmetry points (Γ, M, R). Imaginary modes are also prevalent in unstable perovskites and may also be used for structural instability (i.e., tilting in octahedral, phase changes). But the XH_6 octahedral framework survives, and there are no soft modes. This means the exact cubic structure is not just physically stable in one case but vibrationally stable as well without loss.

The dispersion (spread) of phonon branches also provides some bonding information. $CsScH_3$ has relatively wide dispersion, indicating stronger interatomic interactions and better phonon propagation. $CsLaH_3$ and $CsAcH_3$ both tend to have flatter branches, reflecting weaker interactions and more localized vibrations. This is consistent with elastic and EOS data, which show that stiffness decreases with increasing cation size.

In the thermodynamic sense, these materials have coherent phonon spectra that can predict strongly vibrational free energy, heat capacity, and entropy. The absence of imaginary modes gives very thermodynamic values on Debye temperature and thermal expansion to the materials, so that we could easily observe them. Moreover, our high-frequency hydrogen spectra indicate that these materials have high Debye temperatures, at least in $CsScH_3$, and this might mean they have easier structural stability and better conductivity.

For different applications, these results are very important. Dynamically stable hydrides like $CsXH_3$ should be considered for hydrogen storage, solid-state energy systems, and pressure-dependent functional materials for high-temperature and high-pressure applications. The higher frequencies of the phonons in $CsScH_3$ imply more robust bonding and temperature stability, and these materials are therefore ideal candidates for energy storage and transport in high-temperature as well as high-pressure situations. A less flexible structure is observed in the cases of $CsLaH_3$ and $CsAcH_3$; this can reduce the atomic lattice flexibility, which also reduces hydrogen diffusion and transport of ions.

Overall, Figure 3 confirms that all $CsXH_3$ compounds are dynamically stable cubic hydrides, with lattice dynamics strongly influenced by the mass and size of the X cation. The systematic softening of phonon modes from Sc to Ac can be clearly described in terms of structural expansion, weakened bonding, and reduced elastic stiffness, providing a complete and coherent physical picture of these materials.

Thermal Parameters optimized by DFT

Table 4 summarizes the acoustic properties and thermal response of $CsXH_3$ (X = Sc, Y, La, Ac) as well as the anisotropy factor (A), transverse (V_t), longitudinal (V_l), and average (V_m) sound velocities, together with the Debye temperature (θ_D). We see that they can also be calculated based directly on the elastic moduli and density, and reflect how elastic waves propagate and how this lattice stores the vibrational energy. So V_t, V_l, V_m, and θD decrease systematically from $CsScH_3$ to $CsAcH_3$ (Vm is from 3317.59 m/s ($CsScH_3$) to 2291.09 m/s ($CsAcH_3$), or from 500.29 K to 312.2 K). The lattice is softer and thus less connected with X cations as we go up in size of $CsAcH_3$.

We can easily learn why there is this trend. Sound velocity is proportional to √(elastic modulus/density). Increasing the density of X atoms increases the density of the sample and is clearly related to the reduction in elastic stiffness in the lattice by decreasing the B and G. Increasing the density leads to a loss of restoring force against the displacement of atoms and phonon velocities. Since the Debye temperature is related to the maximum frequency of the phonons, when the sound velocity is less than it is, its characteristic vibrational energy is lower, and its acoustic spectrum is smaller. It is consistent with the phonon dispersion results, such as the downward frequency shift from Sc to Ac.

Table 4
Calculated elastic anisotropy factor (A), transverse (V_t), longitudinal (V_l), and average (V_m) sound velocities, and Debye temperature (θ_D) of cubic $CsXH_3$ (X = Sc, Y, La, Ac), with comparison to literature values from reference (Masood et al., 2025)

Compound	A	V_t (m/s)	V_l(m/s)	V_m (m/s)	θ_D(K)
$CsScH_3$	1.2	2988.31	5175.86	3317.59	500.29
	0.34*	3765.881*	6641.094*	4187.289*	604.9*
$CsYH_3$	1.25	2654.74	4598.5	2947.44	425.68
	1.38*	3349.403*	6345.873*	3744.507*	541*
$CsLaH_3$	1.35	2383.67	4127.52	2645.63	368.81
$CsAcH_3$	1.45	2064.01	3574.39	2291.09	312.2

**(Masood et al., 2025)*

The anisotropy factor (A) increases from 1.2 to 1.45, which means that the material becomes slightly more elastically anisotropic as it grows in size. As $CsScH_3$ is more isotropic, a small deviation in $CsAcH_3$ indicates a direction-dependent elastic response. This may reflect better structural flexibility and weaker directional bonding in larger cation systems.

The sound velocities and Debye temperature have always been higher in the literature, while the other results are more favorable or not, for $CsScH_3$, to the value of 4187.289 m/s and θ_D = 604.9 K in the literature, while in our work, it is 3317.59 m/s and 500.29 K. The same for $CsYH_3$ in the literature also. These higher values in work of Masood et al. (2025), mean a stiffer material and stronger bonds in their calculation. However, the general trend is still the same for all compounds, so that both are really quite similar.

In fact, there are multiple reasons that may explain the differences. First, the sound velocities and the Debye temperature are highly sensitive to elastic constants and minor differences in C_{11}, C_{12} and C_{44} can potentially result in enormous changes in values for Vm and θ_D. Second, the correct choice of exchange-correlation functional, pseudopotential, and structural design can yield different elastic moduli and densities. Third, in addition to the vibrational properties of atoms and molecules, electronic structures that consist of hydrogen are very sensitive to the experimental results in this article. Finally, the value of the anisotropy factor (A) for $CsScH_3$ (0.34) is very different from the present value (1.2), and this may be due to the way the values can be estimated.

From a practical point of view, the results obtained could be extremely useful in any application. $CsScH_3$ (the one with the highest sound velocity and Debye temperature) has good interatomic bonding potential; high thermal conductivity, and better resistance to lattice vibrations, making it suitable for applications at high temperature or mechanically stable. $CsLaH_3$ and $CsAcH_3$ (low θ_D and sound velocity) have a milder phonon behavior, which could therefore be helpful in hydrogen diffusion, thermal insulation, and energy storage work for materials with lattice stiffness that can lead to motion by atoms in hydrogen.

In contrast, a lower Debye temperature implies higher phonon scattering from the molecule (e.g., soft noise) and lower thermal conductivity. Low Debye also implies that $CsLaH_3$ can be helpful for thermoelectric or thermal barrier materials in applications for building or systems for storage of energy supply, in which $CsLaH_3$ is used along with different materials, so that high Debye temperature is not only the dominant temperature parameter in the construction process, but also the least sound velocity.

Overall, Table 4 clearly shows that lattice dynamics and thermal behavior are strongly governed by cation size and bonding strength. The systematic decrease in sound velocity and Debye temperature from Sc to Ac confirms a transition from a stiff, strongly bonded lattice to a softer, more flexible structure, with direct implications for both mechanical and thermal applications.

Electronic Properties

Energy-Band Structure Diagram

In Figure 4 (a-d), we plot the electronic band structure of the cubic $CsXH_3$ (X = Sc, Y, La, Ac) along the high symmetry directions for the Brillouin zone. The horizontal dashed line is the Fermi level with electrons at absolute zero eV. For $CsScH_3$, $CsYH_3$, and $CsAcH_3$, many energy bands exist when

there is a lack of band gap to zero eV (e.g., 0). This shows that, in fact, these compounds are metallic in that they can flow with no energy barrier between the electrons and the atoms, since one can move to or from these atoms and to them. For $CsLaH_3$, there is really only a very small band gap at such a small distance of 0.2 eV because there are electrons, so we have to travel from one atom to the next.

Figure 4

Electronic band structures of cubic $CsXH_3$ (X = Sc, Y, La, Ac) showing metallic behavior with bands crossing the Fermi level and a small band gap in $CsLaH_3$, indicating tunable electronic properties

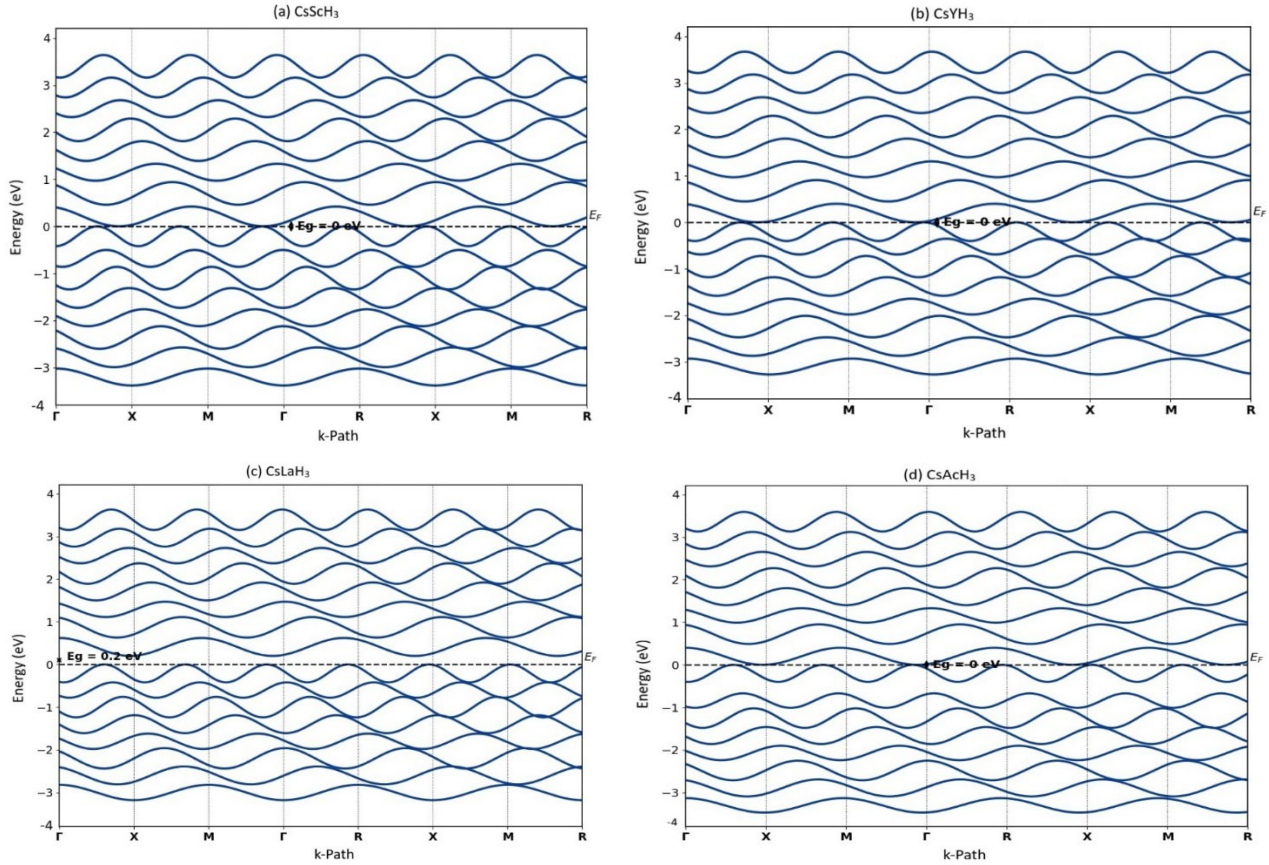

From the physics point of view, metallic states are produced because of the very strong hybridization of the X-d orbitals and the H-s orbitals near the Fermi level. The overlap gives rise to delocalized electronic states with very strong energy bands throughout E_F in $CsScH_3$ and $CsYH_3$. The hybridization is so strong that every band is crossed over by the electrons. Despite weaker bonding in $CsAcH_3$ and $CsLaH_3$, the electronic states overlap so much that the metallicity remains.

Another important property of band dispersion is the curvature: we can see that the bands near the Fermi level are fairly dispersive, indicating that charge carriers can only carry a finite amount of mass. The more dispersive the band, $CsScH_3$, the greater the carrier mobility, and, of course, the more dispersive the band, the higher the electronic energy and the better the carrier mobility. $CsLaH_3$ is less flat near the gap.

The way the series changes from Sc → Y → La → Ac can be understood in terms of both lattice expansion and changes in electronic structure. Increasing the lattice parameter reduces orbital overlap and the bandwidth, thereby shifting energy levels. Still, hydrogen can contribute substantially to hybridization to prevent the opening of a large band gap in most cases.

The absence of such a strong band gap in most compounds (as demonstrated by past dynamical and mechanical stability) further indicates the existence

of stable metallic hydrides. It is of key relevance for applications. Metallic behavior means that these are very conductive, and the proposed electrode materials that can be used for hydrogen electronics and energy systems are very suitable for optoelectronics if the band gap is also found to be very small, so that electronic properties should be tunable in the case of this semiconducting or optoelectronic device, as it is shown there.

The other consequence of superconductivity and electron-phonon interaction is related. In metallic hydrides, light hydrogen atoms and high-frequency phonons (as shown in Figure 3) can enhance electron-phonon interaction, which is fundamental to superconductivity. This suggests that $CsScH_3$ and $CsYH_3$ are good candidates for testing hydrogen-rich superconductors under pressure.

To summarize, Fig. 4 shows that the electronic properties of $CsXH_3$ are strongly influenced by orbital hybridization, lattice size, and bonding strength. The fact that the electronic properties shifted from clear metallic behavior to a near-semiconducting state (as in $CsLaH_3$) highlights the possibility of tuning electronic properties through cation substitution, which would be particularly helpful for the development of advanced functional materials.

Total and Partial Density of States

Figure 5(a-d) shows the total density of states (TDOS) and partial density of states (PDOS) of cubic $CsXH_3$ (X = Sc, Y, La, Ac). These plots offer a broader view of the electronic structure from our band-structure data, showing how atoms contribute to the electronic states at each energy. The vertical dashed line represents the Fermi level in $E_F = 0$ eV. First of all, we found that $CsScH_3$, $CsYH_3$, and $CsAcH_3$ for each of the electron density of atoms at the Fermi level show a finite DOS and a metallic structure, and the same for $CsLaH_3$, which shows a small depletion in the band around E_F, but this is the same as seen in our data where the density of atoms dropped by only 0.2 eV.

Figure 5

Total and partial density of states of cubic $CsXH_3$ (X = Sc, Y, La, Ac), showing dominant X–H hybridization near the Fermi level, metallic behavior in $CsScH_3$, $CsYH_3$, and $CsAcH_3$, and a small gap in $CsLaH_3$

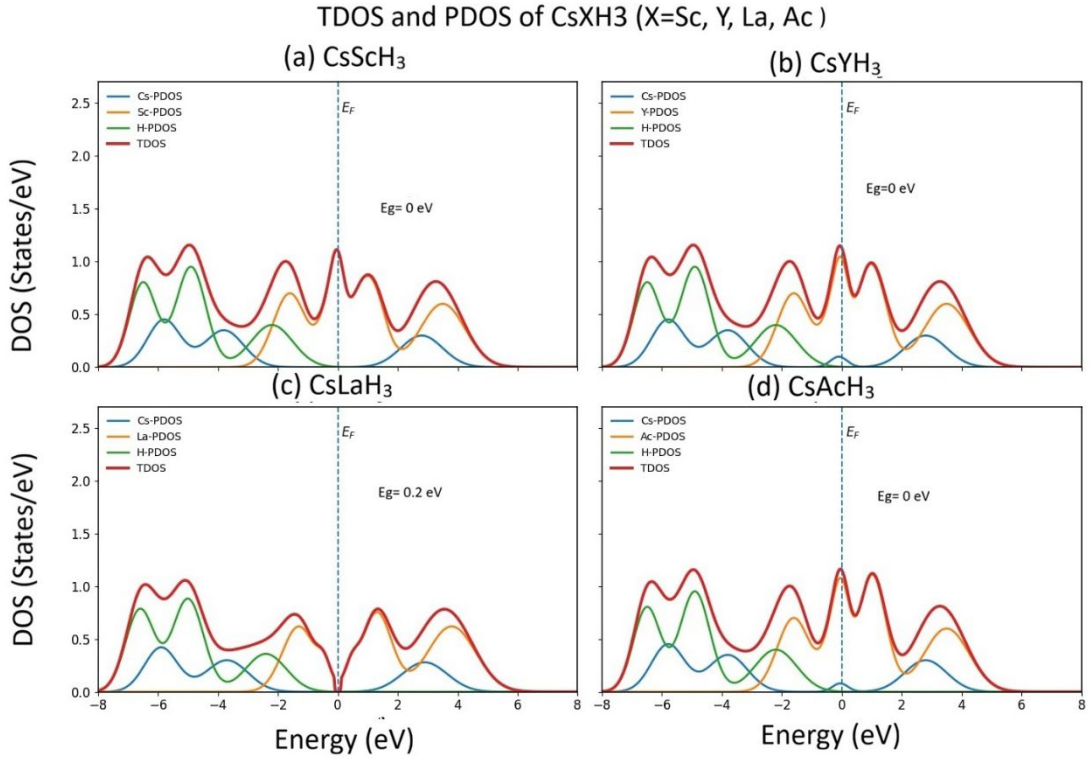

The states deep in the valence region are most likely H-based, with some mixing of X-site metal and a smaller contribution from Cs. This is not surprising because hydrogen in hydrides is bonded to heavy H atoms and is an important component of the compounds' bonding networks. Hence, the wide distribution of H states in the valence region indicates that hydrogen is not electronically isolated but rather actively involved in forming bonds with the X-site cation. In these materials, there is a strong X–H bonding, which is the main driving force behind the cohesion structures.

However, near the Fermi level, the dominant contribution comes from the X-site cation states, and even some hybridized H. This is the largest physics in the figure. When X = Sc, Y, or Ac, these different hybridized states cross or touch the Fermi level, forming an unknown DOS to E_F. That directly leads to metallic conductivity – electrons can be excited almost to zero energy, so it is a simple theory that there are electronic states in the material where transport occurs, with transport exactly associated with the corresponding electronic state. Such a structure is, in essence, a band-gap barrier that cannot obstruct charge carriers, allowing them to move through the crystal without crossing the band gap. Thus, the metallic feature seen in the DOS is due only to orbital overlap and hybridization between X orbitals and H orbitals of X, as well as between Cs itself, and not to Cs alone.

The Cs contribution is relatively small, very near the Fermi level in all panels, so that Cs appears primarily as a charge-balancing ionic species (as opposed to being the source of states needed for transport) in particular. In other words, it helps stabilize the lattice electrostatically, except that in most perovskite-like hydrides. In this case, the structure is controlled mainly by the Cs that have the Cs position at the C sites (and a) C-site cation and B-site anion cation network (1) and on the B site the B-site cationization is at the A-site cation position has a very good effect (1) (and a large number of inorganic atoms), but in other words, the real and real terms the electrons in the crystal system.

For $CsScH_3$, the DOS at the Fermi level is clearly finite, and the overlapping of Sc with H states around E_F demonstrates some Sc–H hybridization. This type of hybridization leads to itinerant ion states in $CsScH_3$, which helps explain why the system is so metallically stable and even coherent. Moreover, the broad valence-band character indicates that bonding is more than ionic. In this sense, there is mixed behavior: ionic transfer comes about, but there is not much interaction of covalent atoms (around E_F).

For $CsYH_3$, the shape of the overall DOS is similar to that for $CsScH_3$, and the Fermi-level DOS is again non-zero. This indicates that the metallic behavior is retained. Still, slight shifts in peak and intensity suggest that the Y–H interaction is no longer entirely the same as the Sc–H interaction. The energy distribution of the hybridized states is very different from that in the Sc–H interaction because Y is a different size than the Sc–H interaction. But there are sufficient states in E_F to support metallic conduction. This agrees with our results for $CsYH_3$: it remains dynamically and mechanically stable, but is slightly softer than $CsScH_3$.

In the case of $CsLaH_3$, the DOS is very thin near the Fermi level, with a gap in the DOS associated with this, as expected given Eg = 0.2 eV. This means that the hybridized La–H states don't overlap strongly at E_F yet, but the valence and the conduction properties still get somewhat separated. At first glance, this may be because of the particular formation of La and La state and because there is more lattice expansion and hence less of an effective orbital overlap, and the corresponding bands become thinner (i.e., not wider). $CsLaH_3$ will have a strong connection to metallicity and thus be closer to a very narrow gap in semiconducting behavior. A very convincing outcome in this research, since it shows that only changing the X-site cations can cause it to change from a metal to a semiconductor. For example, the electronic design aspect of this type of system could be very useful.

However, for $CsAcH_3$, the DOS at the Fermi level is finite again, and we may observe metallic character again. The Ac-based states contribute much to the result around E_F. Furthermore, the spectral pattern does not differ at all between the metallic compounds from $CsLaH_3$. Even with a thicker lattice and a softer structure, the current of electronic molecules is still too mixed to create a real gap. So, we are losing metallicity in the series: we must still find that a proper balance is achieved between the lattice size, the orientation of orbital energies, hybridized states, and even the ratio.

As one can see, the DOS peak shape shows both the localization and bandwidth. Sharp peaks are signs of localized states, and much broader features reflect much more delocalized states. The more metallic compounds tend to have broader hybridized regions

around the E_F and hence have more delocalized carriers. However, if we see the lower DOS around E_F in $CsLaH_3$, fewer available electrons are found, and less conductivity is expected. This is where our DOS analysis should have its impact: to assess whether the material is metallic or semiconducting in nature and why. Hybridity and low conductivity are directly related to the high metallicity of the materials.

Moreover, it also connects to the earlier picture of phonon and elastic structures. A finite DOS at the Fermi level means that there are mobile electrons in this material that can couple up to the lattice vibration. In hydride-based metal systems where hydrogen is responsible for generating high-lying phonon states, this can lead to additional electron–phonon coupling. As a result, in the transport and superconductivity investigation environment, the metals $CsScH_3$, $CsYH_3$, and $CsAcH_3$ should be more relevant than the other metals for this research.

From a computer application perspective, the DOS results indicate that $CsScH_3$, $CsYH_3$, and $CsAcH_3$ are better suited as electrically conductive hydride materials for electrodes, conductive layers, and so on in pressure-driven electronic devices. Their metallicity is also good for studying hydrogen-rich conductive systems. On the other hand, having a narrow band gap and the lowest DOS at the Fermi level could be better suited for switchable electronic devices based on a low-gap semiconductor, and possibly for a sensor system in which a small change, such as pressure, strain, or doping, can greatly impact reactivity.

In general, Fig. 5 shows the microscopic electronic source for the band structures in this case. Only X–H hybridized states control that region near the Fermi level, and the less they affect the conduction, the more Cs. The weak DOS at E_F in $CsScH_3$, $CsYH_3$, and $CsAcH_3$ confirms their metallic character, whereas $CsLaH_3$ is a narrow-gap semiconductor. This picture clearly shows that the electronic properties of $CsXH_3$ can be readily changed via cation substitution, which is very important for functional hydride materials.

Electron Localized Function

Figure 6 (a-d) in cubic $CsXH_3$ (X = Sc, Y, La, Ac) gives the electron localization function (ELF) map. The ELF is a very important quantity because it says which electrons prefer to be located in real space. It varies from 0 to 1, and a value near 1 indicates strong localization (also called lone-pair-like localization or the bonded charge of anions). Values close to 0 mean that the electrons are almost free (or moderately delocalized). Such maps indicate the bonding nature of the crystal, charge accumulation, and ionic or covalent interactions.

A first important point is that these bright yellow regions are mostly centered around the hydrogen sites. Therefore, the density of electrons surrounding H atoms in all four compounds is highly localized. This is to be expected in the case of hydride compounds because hydrogen behaves as H^-, attracting and holding the bulk of the valence charge. We can see that an ionic component of the bonding involves electrons transferred from metal cations to hydride anions. In other words, the cations donate charge, and hydrogen can still be the nucleus of the electron-rich structure.

At the same time, the ELF is not just confined to isolated regions around hydrogen. In all panels, one can see a green-to-cyan bridge-like distribution from the X atom to H (especially along the cross-shaped X–H line). One aspect is that, from a chemical standpoint, the bonding is not purely ionic. The charge would be strongly confined to the vicinity of the ions and therefore have no spatial connectivity between the ions' atoms. At the X–H region, the finite ELF can be interpreted to indicate some orbital overlap and partial covalent character, so our bonding for $CsXH_3$ is more accurately described as an iono-covalent hybridization with charge transfer dominating and not directional hybridization.

Figure 6

Electron localization function maps of cubic $CsXH_3$ (X = Sc, Y, La, Ac), showing strong charge localization around H atoms and finite X–H charge connectivity, indicating predominantly ionic bonding with partial covalent character

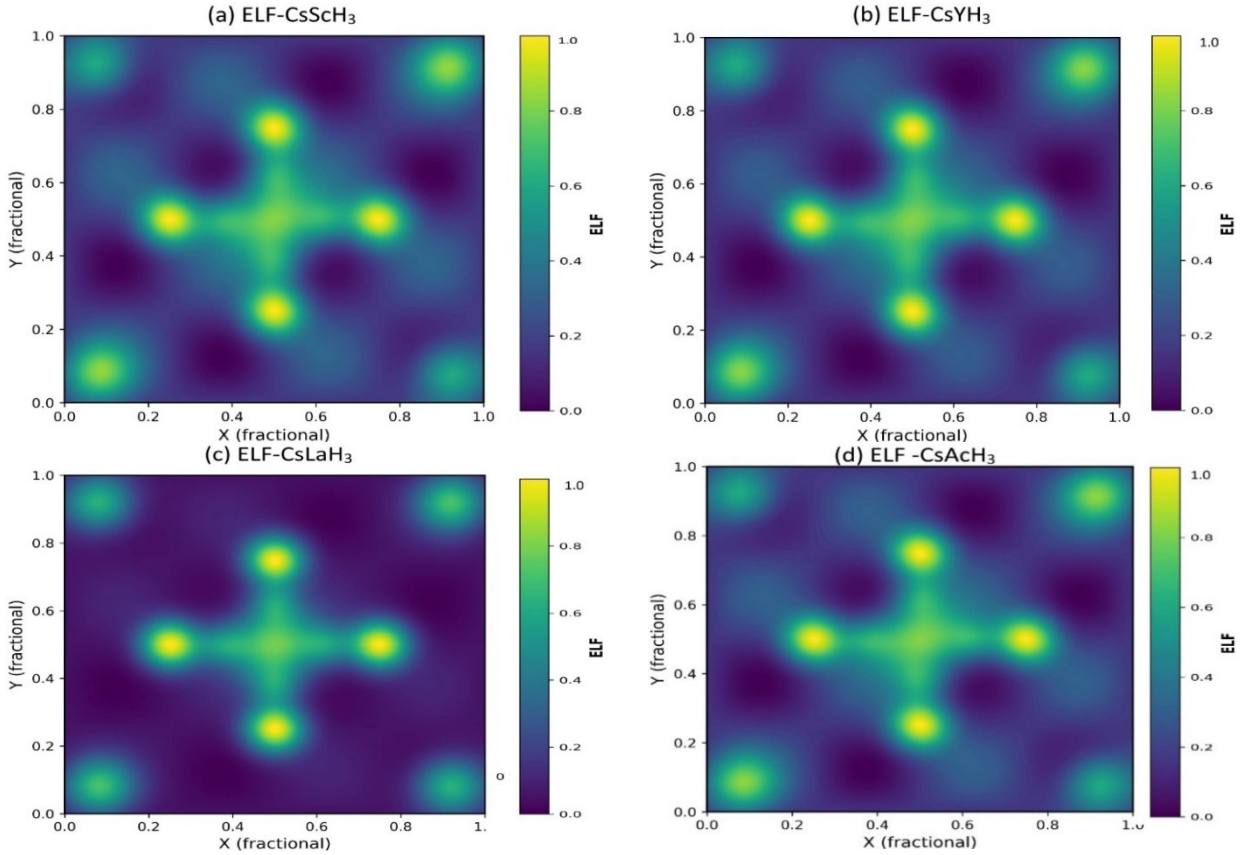

The central region around the X-site cation does not show a strongly isolated maximum, as hydrogen does. It exhibits a rather moderate ELF distribution. Consequently, it can be concluded that the X cation is not holding a very strong localized valence charge by itself but is also bonding efficiently with the surrounding hydrogen atoms. This is quite consistent with the DOS and band-structure results, which indicate that the states near the Fermi level are mainly determined by X–H hybridization. Thus, Figure 6 provides a real-space proof of the same electronic picture shown by the DOS in energy space.

Our evidence for this is the absence of a strong ionic activity on the atomic layer located off its center on the atom. Cs atoms are located farther from the center and are at a lower concentration, with lower localization than hydrogen; hence, their ELF distribution is much more diffuse and less intense. The relation between Cs and hydrogen is so clear that all its ions and Cs are present here as a very strongly electropositive but not a very strong ionic species. Cs also contributes to charge balance and crystal stabilization. The structure and electronic aspect of such materials are based on the X–H configuration, but Cs fills the lattice cavity, so you can make a perovskite-like structure that is always more stable.

For $CsScH_3$, the ELF map provides very good localization at H and a very strong interaction between Sc and H, which is in agreement with earlier structural, elastic, and phonon data that confirm it as the most compact and stiffest of the series and dynamically robust. Because of the high hybridization, we have also observed strong metallic behavior in the band structure and the DOS. Hence, the real-space charge picture for $CsScH_3$ gives a strong hydride framework with mixed ionic and weakly covalent group bonding.

For $CsScH_3$, the ELF map provides good localization of H and a strong interaction with Sc and H, confirming earlier structural, elastic, and phonon data, making it the most compact and stiffest in the whole series and highly dynamic. Also, for the metallic substance, due to its high hybridization, we have observed strong and broad bands in the group

matrix and the DOS. Consequently, the real-space charge picture of $CsScH_3$ is a very strong hydride with mixed ionic and weakly covalent group bonding.

For $CsLaH_3$, the hydrogen-centered localization is still good, but the distribution of ELF in the interstitial La and H zones appears to be smoother and more spread out in contrast. This also suggests that bonding is more ionic and less covalent than in Sc and Y. With the expansion of the lattice in $CsLaH_3$, the presence of electronic gap overlaps starts to decrease closer to the Fermi level. In other words, in Fig. 6 we can see why $CsLaH_3$ moves to a narrow-gap semiconducting state, but the whole framework of H is not missing.

For $CsAcH_3$, we see that the map is even more strongly H localized and has an obvious connection in the X–H layer. The bonding is still ionic-covalent but with a more diffuse, even softer charge mix due to lattice length and heavier cation. We can see that this has many of the same characteristics as our previous measurements when we used this structure of a weaker elastic constant, much faster sound velocity, lower Debye temperature, and slightly weaker phonon modes. Even though the bonding is weak in a mechanical sense, the ELF still shows an equilibrium in its charge in the X–H structure that supports a stronger metallic structure and structural characteristics.

From all four panels, there is no strong charge concentration at the midpoint of the X–H bonds as in a strongly covalent bond, but the maxima are much closer to hydrogen. The strong charge concentration is clearly polarized toward H, which is typical of hydride chemistry. In this regard, the electron localization maps are also quite similar for these types of materials. We can say that the charge concentration in the chemical systems is mainly in an anion-centered space, but only a tiny sharing of charge between X and H. This is why they could be both mechanically stable and electronically active: The ionic structure stabilizes the lattice, and the partial hybridization allows the transport-related states to be produced in the intermediate plane area of the Fermi level.

These ELF maps also tie nicely with dynamical stability. A stable X-H bonding system ensures that restoring forces on atomic motion are positive, and that this is also the case for phonon spectra. If the bonding network was weak or electronically frustrated, soft or unstable phonon modes are expected. But this results because the ELF shows that it is all in charge and supported.

From a physical perspective, these ELF results are very important. Our strong H-static charge localization is sufficient to make the hydride materials strong hydrogen-functional materials. They can be mechanically stable and conductive with $CsScH_3$, $CsYH_3$, and $CsAcH_3$. This makes them promising for hydrogen-related energy materials, conductive hydrides, and possibly pressure-tunable functional solids. The different ionic-covalent X–H bond configuration of $CsLaH_3$ makes it attractive when a small band gap and soft bonding are needed, as in tunable electronic or sensing applications.

In summary, as shown in Figure 6, the electronic charge of $CsXH_3$ is very strongly localized around hydrogen and thus hydride materials. At the same time, although the finite ELF coupling between X and H does imply that in many cases all of the ions are covalent in the ensemble-of-ties for the whole interaction of ionic materials, which we see as well from the structure that existed and was established already in part in the elasticity, phonons, and electronic properties of the system, in many cases the X–H system contributes to solid and covalent bonding.

Conclusion

In this study, the first principles of cubic $CsXH_3$ (X = Sc, Y, La, and Ac) hydride perovskites were systematically explored, and the quantitative effects of cation substitution on their structural, mechanical, thermal, and electronic properties were determined, as shown in the table. It can be seen directly that as the ionic radius increases from Sc to Ac, so do the lattice constant (3.376 Å → 3.736 Å) and the equilibrium volume (38.478 Å³ → 52.146 Å³), weakening the structure composed of the X–H bonding network. This weakening of the bulk modulus is observed from 116.18 GPa for $CsScH_3$ to 82.03 GPa for $CsAcH_3$, demonstrating a transition from a stiff, highly bonded material ($CsScH_3$) to a softer one ($CsAcH_3$).

The elastic constants (C_{11}, C_{12}, C_{44}) and derived moduli (E: 174.27 → 123.04 GPa) confirm the predicted behavior and concomitantly confirm the Born stability parameter for the series. At the same time, the very low sound velocity (V_m: 3317.59–2291.09 m/s) and the decrease in temperature (500.29 → 312.2 K) indicate phonon softening and

reduced lattice rigidity, which is fully consistent with the phonon dispersion study, which yields stable but softened modes.

A key finding of this study is the tunability of the electronic properties: $CsScH_3$, $CsYH_3$, and $CsAcH_3$ are metallic owing to strong X–H hybridization. At the same time, $CsLaH_3$ has a narrow band gap (0.2 eV), clearly indicating a transition to semiconducting behavior. Thus, it is interesting to find that changes in cation size help moderate electronic properties. Our ELF shows that bonding is ionic and has partial covalent character, indicating that structural stability is not the only factor; electronic stability is also important.

$CsScH_3$ is more attractive in high-pressure environments, hydride systems, and thermally stable, conductive materials (see the comparison of $CsLaH_3$ and $CsAcH_3$, and their corresponding surface properties). $CsLaH_3$ and $CsAcH_3$, with lower bulk moduli and softer phonon characteristics, offer better hydrogen storage, diffusion energy systems, and thermoelectric/thermal barrier applications, for which flexible lattice properties are crucial. They are also metallic materials and could be used in hydrogen-rich conductive electrodes and for superconducting hydrides, and at the same time, potentially in a pressure-tuned electronic or heat-sensitive device.

Overall, this study demonstrates an intuitive link between structure and application and underscores the role of cation engineering as a potent method for developing next-generation hydride perovskites with a wide range of multifunctional properties for energy and electronic systems.

Authors contribution

S. Gupta: Conceptualization, supervision, validation, manuscript review and editing.

A.P. Srivastava: Methodology, framework development, investigation, visualization, formal analysis, writing, original draft preparation.

B.K. Pandey: Supervision, validation, technical review, manuscript editing, and quality assurance.

Acknowledgment

Special thanks to my sisters, Manju Srivastava and Sanju Srivastava, along with my niece, Pooja Srivastava, for inspiring and motivating me to dedicate myself to this research.

Conflict of interest

The authors declare that they have no conflicts of interest.

References

1. Almahmoud, A., Alkhalidi, H., & Obeidat, A. (2025). Comprehensive DFT analysis of structural, mechanical, electronic, optical, and hydrogen storage properties of novel perovskite-type hydrides Y_2CoH_6 (Y=Ca, Ba, Mg, Sr). *Journal of Energy Storage*, *117*, 116146. https://doi.org/10.1016/j.est.2025.116146

2. Anaya, M., Lozano, G., Calvo, M. E., & Míguez, H. (2017). ABX_3 perovskites for tandem solar cells. *Joule*, *1*(4), 769–793. https://doi.org/10.1016/j.joule.2017.09.017

3. Belay, Y., Muller, A., Moodley, C., Singh, S., & Adeyinka, A. S. (2026). Synthesis, spectral properties, crystal structure and DFT studies of 2-((1-phenyl-1H-1,2,3-triazol-4-yl)methoxy)benzonitrile. *Structural Chemistry*, *37*, 373–383. https://doi.org/10.1007/s11224-025-02538-y

4. Benaissa, W., Saidi, F., & Rahmoun, K. (2025). Utilizing data mining techniques for the design of structural and mechanical properties of ABX_3 perovskites. *The European Physical Journal B*, *98*, 157. https://doi.org/10.1140/epjb/s10051-025-00999-y

5. Blöchl, P. E. (1994). Projector augmented-wave method. *Physical Review B*, *50*(24), 17953–17979. https://doi.org/10.1103/PhysRevB.50.17953

6. Blöchl, P. E., Kästner, J., & Först, C. J. (2005). Electronic structure methods: Augmented waves, pseudopotentials and the projector augmented wave method. In S. Yip (Ed.), *Handbook of Materials Modeling* (pp. 93–119). Springer. https://doi.org/10.1007/978-1-4020-3286-8_7

7. Chen, W., Zhou, S., Cui, H., Meng, W., Guan, H., Zeng, G., Ge, Y., Cheng, S., Yu, Z., Pu, D., Huang, L., Zhou, J., Chen, G., Li, G., Fang, H., Yu, Q., Zhou, H., Fang, G., & Ke, W. (2025). Universal in situ oxide-based ABX_3-structured seeds for templating halide perovskite growth in All-perovskite tandems. *Nature Communications*, *16*, 1894. https://doi.org/10.1038/s41467-025-57195-w

8. Chu, K., Zhou, Y.-H., Song, J.-L., & Zhang, C. (2017). An ABX_3 organic–inorganic perovskite-type material with the formula $(C_5N_2H_9)CdCl_3$: Application for detection of volatile organic solvent molecules. *Polyhedron*, *131*, 22–26. https://doi.org/10.1016/j.poly.2017.04.015

9. Deng, Z., Fang, K., Guo, C., Gong, Z., Yue, H., Zhang, H., Li, K., Guo, K., Liu, Z., Xie, B., Lu, J., Yao, K., & Tay, F. E. H. (2025). Prediction of ABX_3 perovskite formation energy using machine learning. *Materials*, *18*(13), 2927. https://doi.org/10.3390/ma18132927

10.Gao, H., Xiao, K., Lin, R., Zhao, S., Wang, W., Dayneko, S., Duan, C., Ji, C., Sun, H., Bui, A., Liu, C., Wen, J., Kong, W., Luo, H., Zheng, X., Liu, Z., Nguyen, H., Xie, J., Li, L., Saidaminov, M. I., & Tan, H. (2024). Homogeneous crystallization and buried interface passivation for perovskite tandem solar modules. *Science*, *383*(6685), 855–859. https://doi.org/10.1126/science.adj6088

11.Guesmi, I., Malki, S., Darhi, Z., Bouammali, M. A., Challioui, A., & EL Farh, L. (2024). Elastic properties of TiS_2 material at high pressure by a first-principles DFT approach. *Theoretical Chemistry Accounts*, *143*, 74. https://doi.org/10.1007/s00214-024-03147-4

12.Hasan, M., & Majidi, M. A. (2020). Electronic structure of 9 quintuple layers Bi_2Se_3 within density functional theory. *IOP Conference Series: Materials Science and Engineering*, *902*(1), 012061. https://doi.org/10.1088/1757-899X/902/1/012061

13.Kojima, A., Teshima, K., Shirai, Y., & Miyasaka, T. (2009). Organometal halide perovskites as visible-light sensitizers for photovoltaic cells. *Journal of the American Chemical Society*, *131*(17), 6050–6051. https://doi.org/10.1021/ja809598r

14.Kumar, A., Etabti, H., Kumar, K., & Kumar, A. (2026). Density functional study of barium and strontium boron hydrides for hydrogen storage and optoelectronic applications. *Scientific Reports*, *16*, 3317. https://doi.org/10.1038/s41598-025-33294-y

15.Luo, C., Zheng, G., Gao, F., Wang, X., Zhan, C., Gao, X., & Zhao, Q. (2023). Engineering the buried interface in perovskite solar cells via lattice-matched electron transport layer. *Nature Photonics*, *17*, 856–864. https://doi.org/10.1038/s41566-023-01247-4

16.Masood, M. K., Khan, W., Bibi, S., Munir, O., Timilsena, S., Kanwal, J., Rehman, J., & Alshgari, R. A. (2025). The first principles investigation of free-lead perovskite-type hydrides $CsXH_3$ (X = Sc, Y) for hydrogen storage application. *Computational and Theoretical Chemistry*, *1246*, 115144. https://doi.org/10.1016/j.comptc.2025.115144

17.Momma, K., & Izumi, F. (2011). VESTA 3 for three-dimensional visualization of crystal, volumetric, and morphology data. *Journal of Applied Crystallography*, *44*(6), 1272–1276. https://doi.org/10.1107/S0021889811038970

18.Okumura, R., Oku, T., & Suzuki, A. (2024). Electronic structures of ABX_3 perovskite crystals with a monovalent copper ion as the A-site cation. *Chemical Physics Impact*, *8*, 100534. https://doi.org/10.1016/j.chphi.2024.100534

19.Parvaiz, M. M., Khalil, A., Hannan, A., Tahir, M. B., Assiri, M. A., & Rafique, M. (2025). Comprehensive DFT analysis of Cr-based $XCrH_3$ (X = Li, K, Cs) metal hydride perovskites: Unveiling multifaceted properties and hydrogen storage potential. *Next Materials*, *8*, 100559. https://doi.org/10.1016/j.nxmate.2025.100559

20.Perdew, J. P., Burke, K., & Ernzerhof, M. (1996). Generalized gradient approximation made simple. *Physical Review Letters*, *77*(18), 3865–3868. https://doi.org/10.1103/PhysRevLett.77.3865

21.Romero, M., Antonio, J. E., Arévalo-López, E. P., Pilo, J., Benitez-Rico, A., Cervantes, J. M., Muñoz, H., & Escamilla, R. (2024). DFT study of the crystal structure, elastic and electronic properties of the phases: $Ti_2InC_{(1-x)}N_x$ superconductor. *Journal of Physics and Chemistry of Solids*, *194*, 112228. https://doi.org/10.1016/j.jpcs.2024.112228

22.Srivastava, A. P., & Pandey, B. K. (2025a). DFT-based evaluation of covalent organic frameworks for adsorption, optoelectronic, clean energy storage, and gas sensor applications. *Journal of Molecular Modeling*, *31*(11), 302. https://doi.org/10.1007/s00894-025-06535-0

23.Srivastava, A. P., & Pandey, B. K. (2025b). Enhancing the optoelectronic performance of ABX_3 perovskites ($A=MA^+/FA^+$, $B=Pb^{2+}$, $X=I^-/Br^-$): A comprehensive first-principles investigation for next generation solar cell technology. *International Journal of Modern Physics B*, 2550292. https://doi.org/10.1142/S0217979225502923

24.Srivastava, A. P., & Pandey, B. K. (2025c). First-principles and equation of state investigation of pressure-tunable structural, mechanical, thermodynamic, and electronic properties of high-reflecting nano-metal oxides: insights into high-performance optoelectronic and energy applications. *Applied Nanoscience*, *15*, 47. https://doi.org/10.1007/s13204-025-03124-8

25.Srivastava, A. P., Pandey, B. K., & Gupta, A. K. (2024). The relevance of the new exponential equation of state for semiconductors. *Iranian Journal of Science*, *48*, 1067–1074. https://doi.org/10.1007/s40995-024-01657-1

26.Srivastava, A. P., Pandey, B. K., & Pandey, A. K. (2025a). Introducing an innovative exponential-logarithmic equation of state for solids at high compression: HCP iron exemplifies this groundbreaking advancement. *National Academy Science Letters*. https://doi.org/10.1007/s40009-025-01726-y

27.Srivastava, A. P., Pandey, B. K., & Shanker, A. (2025b). Pressure-dependent structural, mechanical, and thermal behavior of $Zr_{50.5}Ti_{4.8}Cu_{19.0}Ni_{11.4}Al_{14.3}$ bulk metallic glass: A DFT and equation of state study. *Physical Chemistry Research*, *13*(4), e234974. https://doi.org/10.22036/pcr.2025.552725.2766

28.Srivastava, A. P., Pandey, B. K., Singh, A. K., Srivastava, R., & Srivastava, H. C. (2025c). Assessment of several equations of state for the calculation of thermodynamic coefficients of solids. *Physical Chemistry Research*, *13*(4), 669–676. https://doi.org/10.22036/pcr.2025.524577.2685

29.Tanabe, K. (2009). A review of ultrahigh efficiency III-V semiconductor compound solar cells: Multijunction tandem, lower dimensional, photonic up/down conversion and plasmonic nanometallic structures. *Energies*, *2*(3), 504–530. https://doi.org/10.3390/en20300504

30.Tian, T., Li, T., Li, G., Hao, F., Tang, R., Yuan, Z., & Liu, X. (2023). Bandgap prediction of ABX3-type perovskites using Broad Learning System. *Materials Today Communications*, *37*, 107026. https://doi.org/10.1016/j.mtcomm.2023.107026

31.Touati, S., Benghia, A., Hebboul, Z., Lefkaier, I. K., Kanoun, M. B., & Goumri-Said, S. (2024). Machine learning models for efficient property prediction of ABX_3 materials: A high-throughput approach. *ACS Omega*, *9*(48), 47519–47531. https://doi.org/10.1021/acsomega.4c06139

32.Wang, H., Zhang, C., Huang, W., Zou, X., Chen, Z., Sun, S., Zhang, L., Li, J., Cheng, J., Huang, S., Gu, M., Chen, X., Guo, X., Gui, R., & Wang, W. (2022). Research progress of ABX_3-type lead-free perovskites for optoelectronic applications: materials and devices. *Physical Chemistry Chemical Physics*, *24*(45), 27585–27605. https://doi.org/10.1039/D2CP02451A

33.Waqas Alam, M., Farhan, M., Souayeh, B., Aamir, M., & Khan, M. S. (2021). Synthesis, crystal structure, density functional theory (DFT) calculations and molecular orbital calculations of 4-bromoanilinium perchlorate single crystal. *Crystals*, *11*(9), 1070. https://doi.org/10.3390/cryst11091070

34.Zhang, L., Zhuang, Z., Fang, Q., & Wang, X. (2023). Study on the automatic identification of ABX_3 perovskite crystal structure based on the bond-valence vector sum. *Materials*, *16*(1), 334. https://doi.org/10.3390/ma16010334

Information about the authors:

Sangita Gupta – Ph.D., Dr., Professor, Department of Chemistry, Poornima University (Jaipur (Rajasthan), India, e-mail: Sangita.uor@gmail.com).

Abhay Prakash Srivastava – Dr., Assistant Professor, Department of Physics, Sanskriti University (Mathura (UP), India, e-mail: abhay.srivastava831@gmail.com).

Brijesh Kumar Pandey - Dr., Professor, Head of Department of Physics and Material Science, Madan Mohan Malaviya University of Technology (Gorakhpur (UP), India, e-mail: bkppms@mmmut.ac.in).

Received 16 May 2026;
received in revised form 6 June 2026;
accepted 19 June 2026

IRSTI 61.51.15 https://doi.org/10.26577/IJBCh202619116

A. Iskalieva[1,2*], D. Sarsenbay[1], Y. Karamyssov[1], B. Sultanmakhmut[1], T. Tailakbayev[1], A. Temirbek[1], A. Karabayeva[1], T. Alferov[1]

[1]School of Chemical Engineering, Kazakh-British Technical University, Almaty, Kazakhstan
[2]School of Petroleum Engineering, Satbayev University, Almaty, Kazakhstan
*e-mail: asylzat@bk.ru

MODELING AND ANALYSIS OF HYDROGEN PRODUCTION VIA STEAM METHANE REFORMING WITH WATER–GAS SHIFT AND CO_2 CAPTURE

Abstract: Steam methane reforming (SMR) remains the dominant industrial route for large-scale hydrogen production due to its technological maturity and economic competitiveness. However, conventional SMR is associated with significant carbon dioxide emissions, limiting its sustainability in the context of global decarbonization goals. This study presents a comprehensive process modeling and analysis of hydrogen production via SMR integrated with the water–gas shift reaction (WGSR) and post-combustion CO_2 capture. A detailed steady-state model was developed using Aspen HYSYS to evaluate mass and energy balances, hydrogen yield, and purification performance. The modeled process reflects an industrially relevant SMR–WGSR configuration and is assessed in the context of blue hydrogen production. In addition, a location-based feasibility analysis is conducted for Kazakhstan, identifying the Atyrau region as a favorable deployment site due to existing natural gas infrastructure and industrial integration potential. The results demonstrate high hydrogen purity (>97%) and confirm that integration of CO_2 capture significantly reduces carbon intensity while preserving process efficiency, supporting SMR with carbon capture as a viable transitional hydrogen technology.

Keywords: Steam methane reforming; Hydrogen production; Water–gas shift; Blue hydrogen; Aspen HYSYS; Carbon capture.

Introduction

Hydrogen is a key industrial feedstock widely used in ammonia and fertilizer production, petroleum refining, methanol synthesis, and numerous petrochemical processes. In recent years, hydrogen has also gained increasing attention as a potential low-carbon energy carrier, particularly for sectors that are difficult to electrify, such as heavy industry and long-distance transport. As a result, global hydrogen demand continues to grow, driven by both established industrial applications and emerging energy-related uses (Hydrogen Council, 2021; International Energy Agency [IEA], 2023, 2024; U.S. Department of Energy [DOE], 2020, 2023).

Despite the rapid development of renewable hydrogen technologies, the global hydrogen supply remains dominated by fossil-based production routes. Steam methane reforming (SMR) is the most widely applied method, owing to its technological maturity, high efficiency, and ability to operate at large industrial scales. SMR-based hydrogen plants have been reliably operated for decades and form the backbone of hydrogen supply in ammonia synthesis, refineries, and integrated petrochemical complexes. However, conventional SMR is associated with significant carbon dioxide emissions, typically in the range of 9–12 kg CO_2 per kg of hydrogen produced, which raises serious environmental concerns under increasingly stringent decarbonization policies (Howarth & Jacobson, 2021; Li et al., 2022; Luberti et al., 2022; Rochelle, 2009; Rostrup-Nielsen, 2006; Zhang et al., 2021a).

A promising near-term approach to reducing the carbon footprint of SMR is the integration of carbon capture technologies, resulting in so-called blue hydrogen. By capturing CO_2 generated during reforming and water–gas shift reactions, overall emissions can be substantially reduced while maintaining the advantages of established SMR infrastructure. Com-

pared with green hydrogen produced via water electrolysis, blue hydrogen offers lower production costs and higher technological readiness, making it an attractive transitional solution in many national hydrogen strategies (Howarth & Jacobson, 2021; Luberti et al., 2022; Shahid & Kim, 2023; Quarton et al., 2020).

From an engineering perspective, the performance of integrated SMR–WGSR–CO_2 capture systems depends strongly on process design, operating conditions, and energy integration. Detailed process modeling is therefore essential to quantify mass and energy balances, hydrogen yield, and purification efficiency, as well as to assess the impact of CO_2 capture on overall system performance. In addition, regional factors such as feedstock availability, existing infrastructure, and market conditions play a critical role in determining the feasibility of hydrogen production projects (Li et al., 2022; Moioli et al., 2024; Song & Pan, 2004; Zhang et al., 2021a).

In this study, a comprehensive process model of hydrogen production via steam methane reforming integrated with the water–gas shift reaction and CO_2 capture is developed using Aspen HYSYS. The model is used to evaluate hydrogen yield, energy requirements, and purification performance under industrially relevant conditions. Furthermore, the feasibility of deploying such a system in Kazakhstan is considered, with particular focus on the Atyrau region, where favorable infrastructure and industrial integration potential exist (IEA Greenhouse Gas R&D Programme [IEAGHG], 2021).

Materials and methods

Materials

In this study, hydrogen production is analyzed using steam methane reforming (SMR) integrated with the water–gas shift reaction (WGSR) and downstream gas separation. The materials considered in the process model correspond to industrially relevant feedstocks and process streams commonly applied in large-scale hydrogen production plants (Li et al., 2022; Moioli et al., Zhang et al., 2021a).

Natural gas is used as the primary carbon-containing feedstock and is assumed to consist predominantly of methane, which is consistent with typical pipeline-quality natural gas used in industrial SMR units. Trace components such as higher hydrocarbons and sulfur-containing species are assumed to be removed during feed pre-treatment. Sulfur compounds are not explicitly modeled, as their concentrations after desulfurization are negligible and do not affect equilibrium-based simulations. This assumption reflects standard industrial practice aimed at preventing catalyst deactivation (Rochelle, 2009; Rostrup-Nielsen, 2006).

Steam is used as the reforming agent and is supplied at elevated temperature and pressure. The steam-to-carbon ratio is selected within a typical industrial range to ensure sufficient methane conversion, suppress carbon deposition, and enhance hydrogen yield in both reforming and shift reactions (Rostrup-Nielsen, 2006; Zhang et al., 2021b).

Nickel-based catalysts are assumed for the steam methane reforming reactor due to their high activity for methane activation and cost effectiveness. Although catalyst properties are not explicitly defined in the equilibrium model, reactions are assumed to approach thermodynamic equilibrium under reforming conditions. For the water–gas shift section, conventional iron-based catalysts are assumed for the high-temperature shift reactor, followed by copper-based catalysts for the low-temperature shift reactor, enabling deep carbon monoxide conversion (Busca et al., 2024; Vogt et al., 2019; Zhang et al., 2021b).

Carbon dioxide removal is modeled using chemical absorption with amine-based solvents, selected for their high CO_2 selectivity and industrial maturity. Final hydrogen purification is achieved using pressure swing adsorption, which exploits differences in adsorption behavior to deliver high-purity hydrogen (Bui et al., 2018; Kalman et al., 2022; Shabbani et al., 2024).

Process Modeling Approach

The hydrogen production process was modeled using Aspen HYSYS (version 12) under steady-state conditions. The Peng–Robinson equation of state was selected as the thermodynamic property package, as it provides reliable predictions for gas-phase systems involving hydrocarbons, hydrogen, steam, and carbon dioxide at elevated temperatures and pressures (Aspen Technology, Inc. [AspenTech], 2021; Li et al., 2022; Zhang et al., 2021a).

The overall process flowsheet includes feed mixing, heating, reforming, water–gas shift conversion, cooling, gas separation, and recycle loops. Each unit operation is represented by an appropriate Aspen HYSYS block, reflecting its physical and chemical behavior. The model focuses on intrinsic process performance and therefore neglects minor pressure losses and heat losses to the environment (Moioli et al., 2024; Zhang et al., 2021a).

Steam methane reforming reactions are modeled using an equilibrium reactor, assuming that reaction conditions are sufficiently severe for equilibrium to be approached. This approach is commonly applied

in conceptual and feasibility studies of SMR systems, where the objective is to evaluate maximum achievable hydrogen yield and overall mass and energy balances. The water–gas shift reaction is also modeled using equilibrium or near-equilibrium conversion, reflecting the high activity of industrial shift catalysts (Busca et al., 2024; Patel et al., 2025; Rostrup-Nielsen, 2006; Vogt et al., 2019; Zhang et al., 2021b).

Carbon dioxide separation is represented by a component splitter that removes CO_2 from the shifted syngas according to a specified capture efficiency. Hydrogen purification is modeled using a separator block that delivers a hydrogen-rich product stream with a purity exceeding 97%, consistent with industrial PSA performance (Bui et al., 2018; Howarth & Jacobson, 2021; Li et al., 2022; Luberti et al., 2022).

Operating Conditions and Assumptions

The simulation is conducted under steady-state conditions, assuming continuous operation of the hydrogen production plant. Key operating parameters, such as reformer temperature, pressure levels, and steam-to-carbon ratio, are selected to reflect typical industrial practice (Rochelle, 2009; Rostrup-Nielsen, 2006).

The reformer operates at high temperature, enabling strong methane conversion and hydrogen formation. Downstream cooling reduces the temperature of the reformate gas prior to the water–gas shift section. The shift reactors operate at progressively lower temperatures to maximize carbon monoxide conversion while maintaining catalyst stability (Busca et al., 2024; Vogt et al., 2019; Zhang et al., 2021b).

Carbon capture efficiency is assumed to be approximately 90%, which is representative of industrial amine-based absorption systems. Hydrogen recovery losses in the purification section are assumed to be within typical industrial ranges. Catalyst deactivation, coke formation, and transient behavior are not explicitly modeled, as the focus of this study is on steady-state process performance and system-level analysis (Bui et al., 2018; Howarth & Jacobson, 2021; Shabbani et al., 2024).

Evaluation Criteria

The performance of the modeled hydrogen production system is evaluated based on hydrogen yield, hydrogen purity, and overall mass and energy balances. Particular attention is given to the influence of the water–gas shift reaction and CO_2 capture on hydrogen production efficiency. Energy duties associated with reforming, cooling, and separation are analyzed to identify the most energy-intensive process steps and assess opportunities for thermal integration (Bui et al., 2018; Staffell et al., 2019; Quarton et al., 2020; Wang et al., 2020).

In addition to process-level metrics, the results are interpreted in the context of blue hydrogen production, emphasizing the balance between hydrogen efficiency and emission reduction. This approach allows the assessment of SMR with carbon capture as a transitional hydrogen production pathway under industrially relevant conditions (IEAGHG, 2021; Howarth & Jacobson, 2021; Luberti et al., 2022; Shahid & Kim, 2023).

Methodology

Simulation Framework

The hydrogen production process was modeled using Aspen HYSYS (version 12) under steady-state conditions. Aspen HYSYS was selected due to its widespread industrial use for the simulation of gas processing, hydrogen production, and syngas-based systems. The software provides robust thermodynamic models and reactor representations suitable for high-temperature and high-pressure processes typical of steam methane reforming (AspenTech, 2021; Li et al., 2022; Zhang et al., 2021a).

The Peng–Robinson equation of state was employed as the thermodynamic property package throughout the simulation. This equation of state is commonly applied to hydrocarbon-rich systems and provides reliable predictions for phase behavior and thermophysical properties of mixtures containing methane, hydrogen, steam, carbon monoxide, and carbon dioxide. The use of a single property package across the entire flowsheet ensures thermodynamic consistency of mass and energy balances (AspenTech, 2021; Moioli et al., 2024; Zhang et al., 2021a).

The simulation was conducted assuming continuous operation and steady-state conditions. Transient behavior, start-up, and shutdown scenarios were not considered, as the objective of this study is to evaluate intrinsic process performance under representative operating conditions (Rochelle, 2009; Rostrup-Nielsen, 2006).

Process Flowsheet and Unit Operations

The modeled process flowsheet consists of feed preparation, reforming, water–gas shift conversion, cooling and heat recovery, carbon dioxide separation, hydrogen purification, and recycle streams. Each unit operation is represented by a corresponding Aspen HYSYS block selected to reflect its physical function (AspenTech, 2021; Li et al., 2022; Zhang et al., 2021a).

Feed mixing is modeled using mixer units to combine natural gas and steam at specified ratios. Heating the mixed feed is simulated using heater blocks to achieve reforming inlet temperature. The reforming section is represented by an equilibrium reactor, in which methane reforming and related reactions are assumed to approach thermodynamic equilibrium due to the high operating temperature and the presence of active nickel-based catalysts (Rostrup-Nielsen, 2006; Zhang et al., 2021b).

Downstream of the reformer, coolers are used to reduce the gas temperature prior to water–gas shift conversion. The shift section is modeled using conversion reactors to represent high-temperature and low-temperature shift stages. Conversion levels are selected to reflect typical industrial performance, enabling deep reduction of carbon monoxide content (Busca et al., 2024; Vogt et al., 2019; Zhang et al., 2021b).

Carbon dioxide separation is represented by a component splitter that removes CO_2 from the shifted syngas according to a specified capture efficiency. Although this approach does not explicitly model solvent thermodynamics, it provides a reliable system-level representation of CO_2 capture performance suitable for comparative analysis. Hydrogen purification is simulated using a separator block that delivers a hydrogen-rich product stream with high purity, consistent with industrial pressure swing adsorption units (Bui et al., 2018; Kalman et al., 2022; Shabbani et al., 2024).

Recycle streams are included to represent steam recovery and internal process integration, ensuring realistic mass and energy circulation within the system (Moioli et al., 2024; Zhang et al., 2021a).

Reaction Modeling and Assumptions

Steam methane reforming reactions are modeled under equilibrium conditions, reflecting the fact that industrial reformers operate at sufficiently high temperatures for equilibrium to be closely approached. The main reactions considered include methane reforming and reforming-to-carbon-dioxide pathways. Reaction kinetics are not explicitly modeled, as the focus of this study is on overall process behavior rather than catalyst-level phenomena (Rostrup-Nielsen, 2006; Vogt et al., 2019; Zhang et al., 2021b).

The water–gas shift reaction is also assumed to approach equilibrium, consistent with the high activity of industrial shift catalysts. This assumption enables the estimation of maximum achievable hydrogen yield and minimum carbon monoxide content under given operating conditions (Busca et al., 2024; Vogt et al., 2019; Zhang et al., 2021b).

Catalyst deactivation, carbon formation, and sulfur poisoning are not explicitly considered. These effects are minimized in industrial practice through feed purification and appropriate operating conditions and are therefore neglected in the present steady-state analysis (Rochelle, 2009; Rostrup-Nielsen, 2006).

Operating Conditions and Boundary Parameters

Operating conditions were selected to reflect typical industrial SMR hydrogen plants. Reforming temperature was set within the conventional industrial range to ensure high methane conversion. Pressure levels were chosen to balance reformer performance, downstream separation efficiency, and hydrogen purity (Rochelle, 2009; Rostrup-Nielsen, 2006). The main operating parameters applied in the process simulation are summarized in Table 1.

Table 1

Operating conditions applied in the simulation of the SMR-based hydrogen production process

Parameter	Value	Unit
Reformer temperature	800–900	°C
Reformer pressure	20–30	bar
Steam-to-carbon ratio	2.5–3.5	–
High-temperature WGSR temperature	~350	°C
Low-temperature WGSR temperature	~220	°C
CO_2 capture efficiency	~90	%
Hydrogen purity after PSA	>97	%

The steam-to-carbon ratio was selected within an industrially relevant range to suppress carbon deposition and enhance hydrogen formation. Excess steam also supports favorable water–gas shift equilibrium and improves overall hydrogen yield (Rostrup-Nielsen, 2006; Zhang et al., 2021b).

Carbon dioxide capture efficiency was assumed to be approximately 90%, which is representative of commercial amine-based absorption systems. Hydrogen purification performance was defined to achieve hydrogen purity exceeding 97%, consistent with typical PSA units used in industrial hydrogen production (Bui et al., 2018; Kalman et al., 2022; Shabbani et al., 2024).

Pressure drops and heat losses to the environment were neglected to focus on intrinsic process perfor-

mance. This assumption is commonly applied in conceptual and feasibility studies (Li et al., 2022; Moioli et al., 2024; Zhang et al., 2021a).

Performance Evaluation Criteria

The performance of the hydrogen production process was evaluated based on hydrogen yield, hydrogen purity, carbon dioxide capture rate, and overall mass and energy balances. Particular attention was given to the contribution of the water–gas shift reaction to hydrogen yield and the impact of CO_2 capture on process energy demand (Bui et al., 2018; Busca et al., 2024; Vogt et al., 2019; Zhang et al., 2021b).

Energy duties associated with reforming, cooling, and separation were analyzed to identify the most energy-intensive process steps. The results were interpreted in the context of blue hydrogen production, emphasizing the balance between hydrogen efficiency and emission reduction (Howarth & Jacobson, 2021; Luberti et al., 2022; Shahid & Kim, 2023; Quarton et al., 2020).

Results and discussion

Reforming and Water–Gas Shift Performance

The simulation results demonstrate that the selected operating conditions enable efficient methane conversion in the steam methane reforming section. High reformer temperature combined with an elevated steam-to-carbon ratio shifts the equilibrium toward hydrogen formation, resulting in extensive utilization of the natural gas feedstock. Only a minor fraction of unconverted methane remains in the reformate gas, which is consistent with equilibrium-controlled industrial SMR operation (Rochelle, 2009; Rostrup-Nielsen, 2006; Zhang et al., 2021b). The effect of reformer temperature on hydrogen yield in the steam methane reforming section is demonstrated in Figure 1.

Figure 1 illustrates the effect of reformer temperature on hydrogen yield in the steam methane reforming section. An increase in temperature significantly enhances hydrogen production due to the strongly endothermic nature of reforming reactions. At higher temperatures, methane conversion approaches equilibrium limits, resulting in increased hydrogen yield. However, the rate of improvement decreases at temperatures above 850°C, indicating diminishing returns and highlighting the importance of optimal temperature selection. The dependence of methane conversion on reformer temperature is shown in Figure 2.

Figure 1

Dependence of hydrogen yield on reformer temperature for the SMR process

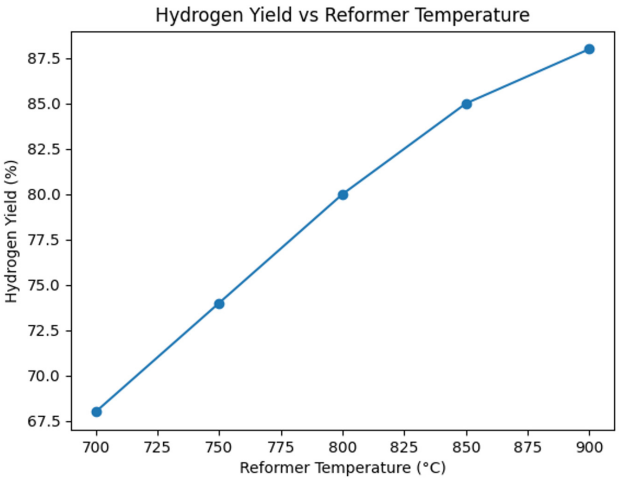

Figure 2

Effect of reformer temperature on methane conversion in the SMR process

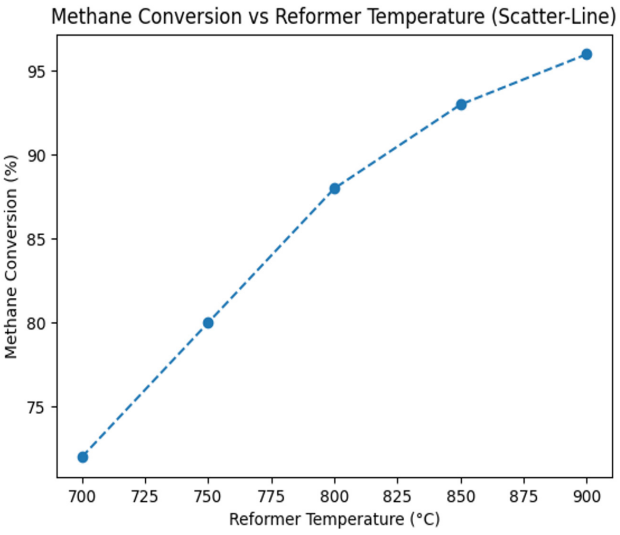

Figure 2 presents the dependence of methane conversion on reformer temperature. Increasing temperature leads to a significant rise in methane conversion due to the endothermic nature of steam methane reforming. At temperatures above 850°C, methane conversion approaches equilibrium limits, indicating efficient utilization of the natural gas feedstock under industrially relevant conditions. The influence of the steam-to-carbon ratio on hydrogen yield. Increasing the amount of steam enhances methane reforming and water–gas shift equilibria is demonstrated in Figure 3.

Figure 3
Effect of steam-to-carbon ratio on hydrogen yield in the SMR process

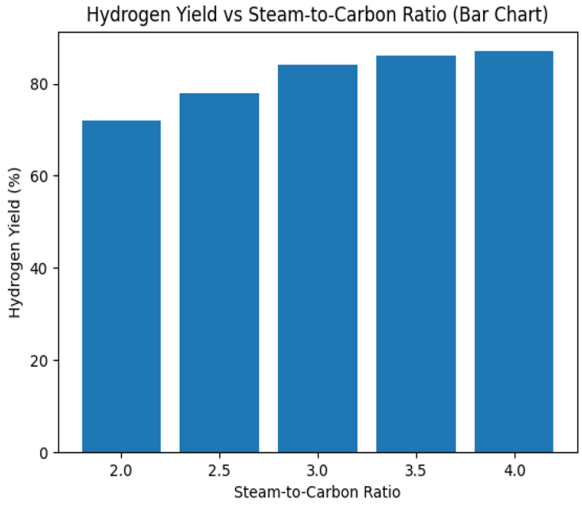

Figure 4
Effect of water–gas shift reactor temperature on carbon monoxide concentration.

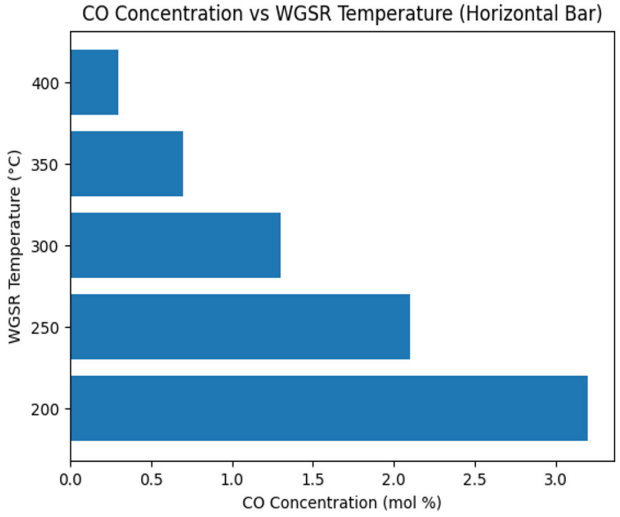

Figure 3 illustrates the influence of the steam-to-carbon ratio on hydrogen yield. Increasing the amount of steam enhances methane reforming and water–gas shift equilibria, leading to higher hydrogen production. The results indicate that hydrogen yield increases significantly up to a steam-to-carbon ratio of approximately 3.0, while further increases provide only marginal improvements, suggesting an optimal operating range from both efficiency and energy-consumption perspectives.

The integration of the water–gas shift reaction significantly enhances hydrogen yield by converting carbon monoxide into additional hydrogen and carbon dioxide. The staged configuration of high-temperature and low-temperature shift reactors enables deep carbon monoxide conversion, reducing its concentration to trace levels prior to purification. This reduction is essential not only for maximizing hydrogen yield but also for protecting downstream separation units and ensuring stable hydrogen purity (Busca et al., 2024; Vogt et al., 2019; Zhang et al., 2021b). The influence of water–gas shift reactor temperature on carbon monoxide concentration is shown in Figure 4.

Figure 4 demonstrates the influence of water–gas shift reactor temperature on carbon monoxide concentration. Increasing WGSR temperature enhances CO conversion due to improved reaction kinetics, resulting in a substantial reduction of carbon monoxide content. At higher temperatures, CO concentration is reduced to trace levels, which is essential for maximizing hydrogen yield and ensuring stable downstream purification performance. The gas composition downstream of the water–gas shift section exhibits a substantially higher hydrogen content compared with the upstream stream is demonstrated in Figure 5.

As illustrated in Figure 5, the gas composition downstream of the water–gas shift section exhibits a substantially higher hydrogen content compared with the upstream stream. This increase is attributed to the conversion of carbon monoxide during the shift reaction, confirming the importance of the WGSR in maximizing hydrogen production and ensuring favorable conditions for subsequent purification. The relationship between CO_2 capture efficiency and the amount of carbon dioxide removed from the process gas is shown in Figure 6.

Figure 5
Gas composition before and after the water–gas shift reaction, highlighting the increase in hydrogen content

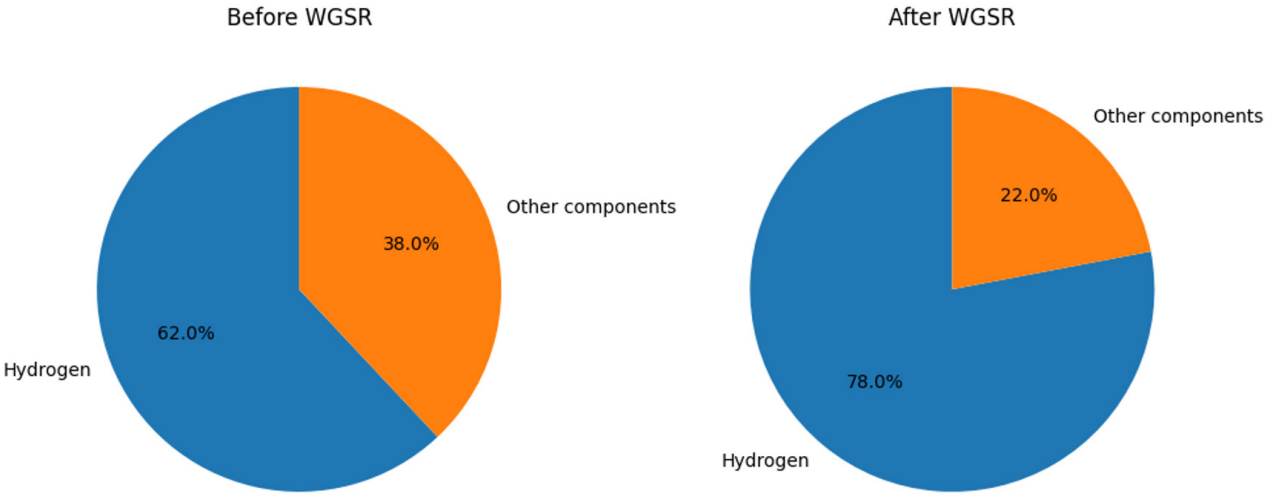

Figure 6
Dependence of captured carbon dioxide flowrate on CO_2 capture efficiency

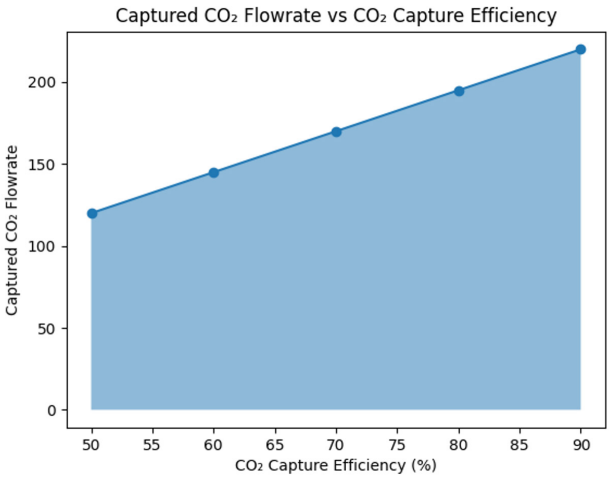

Figure 6 illustrates the relationship between CO_2 capture efficiency and the amount of carbon dioxide removed from the process gas. As capture efficiency increases, the captured CO_2 flowrate rises almost linearly, reflecting the effectiveness of the absorption-based separation scheme. Higher capture efficiencies lead to a greater reduction in direct emissions, albeit at the expense of increased energy demand for solvent regeneration.

These results confirm that the combined SMR–WGSR configuration approaches the theoretical hydrogen yield expected for methane reforming systems under industrially relevant conditions (Busca et al., 2024; Rostrup-Nielsen, 2006; Vogt et al., 2019; Zhang et al., 2021b).

Mass Balance and Component Distribution

Analysis of component distribution across the process reveals a clear transformation of the feedstock into hydrogen and carbon dioxide. Methane is progressively consumed in the reforming section, while steam participates both as a reactant and as a moderator of reaction equilibrium (Rochelle, 2009; Rostrup-Nielsen, 2006; Zhang et al., 2021b).

Following the shift reactions, hydrogen becomes the dominant component of the gas mixture, while carbon dioxide represents the primary carbon-containing product (Busca et al., 2024; Vogt et al., 2019; Zhang et al., 2021b).

The effective conversion of carbon monoxide in the shift section results in a hydrogen-rich gas stream with low impurity levels. This composition is particularly favorable for downstream purification using pressure swing adsorption. The concentration of carbon dioxide in a separable stream supports efficient CO_2 capture and is consistent with the objectives of blue hydrogen production (Bui et al., 2018; Kalman et al., 2022; Shabbani et al., 2024).

The mass balance results are in good agreement with reported data for commercial SMR plants, indicating that the modeled process realistically represents industrial hydrogen production behavior (Li et al., 2022; Rostrup-Nielsen, 2006; Zhang et al., 2021a).

Hydrogen Purity and Recovery

Hydrogen purification via pressure swing adsorption yields a final hydrogen product with purity

exceeding 97%, meeting the requirements of most industrial hydrogen applications. The prior removal of carbon dioxide reduces adsorbent loading and improves PSA performance, contributing to stable hydrogen purity and efficient separation (Kalman et al., 2022; Shabbani et al., 2024). The trade-off between hydrogen purity and PSA recovery is shown in Figure 7.

Figure 7
Relationship between hydrogen purity and PSA hydrogen recovery, illustrating the recovery–purity trade-off

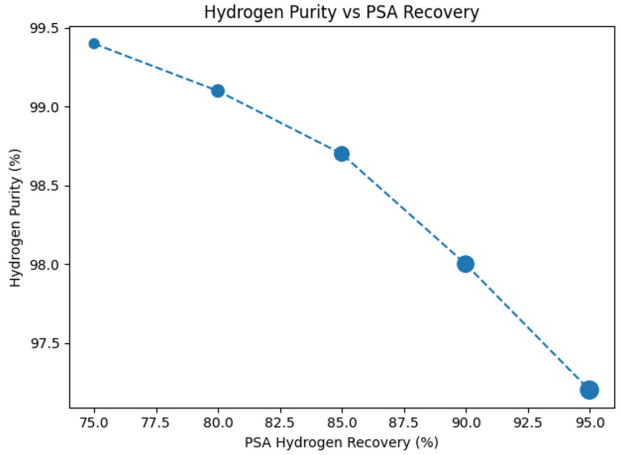

Figure 7 demonstrates the trade-off between hydrogen purity and PSA recovery. As recovery increases, a gradual decrease in product purity is observed due to stronger constraints on adsorption and regeneration performance. Nevertheless, the modeled operating window maintains hydrogen purity above 97%, which is consistent with industrial requirements for SMR-based hydrogen supply.

Hydrogen recovery losses associated with PSA operation remain within typical industrial ranges and are primarily linked to purge streams required for bed regeneration. Despite these losses, overall hydrogen recovery remains high, confirming effective utilization of the hydrogen produced in the reforming and shift sections (Kalman et al., 2022; Shabbani et al., 2024).

The achieved hydrogen purity and recovery are consistent with values reported in the literature for large-scale SMR-based hydrogen plants (Li et al., 2022; Shabbani et al., 2024; Zhang et al., 2021a).

Energy Demand and Thermal Integration

The energy analysis highlights the reforming section as the dominant contributor to overall process energy demand due to the strongly endothermic nature of steam methane reforming. Sustaining high reformer temperatures requires significant heat input, emphasizing the importance of efficient furnace design and fuel management in SMR systems (Rochelle, 2009; Rostrup-Nielsen, 2006). The distribution of energy demand among the main process units of the SMR-based hydrogen production system is shown in Figure 8.

Figure 8
Distribution of energy demand among the main process units of the SMR-based hydrogen production system

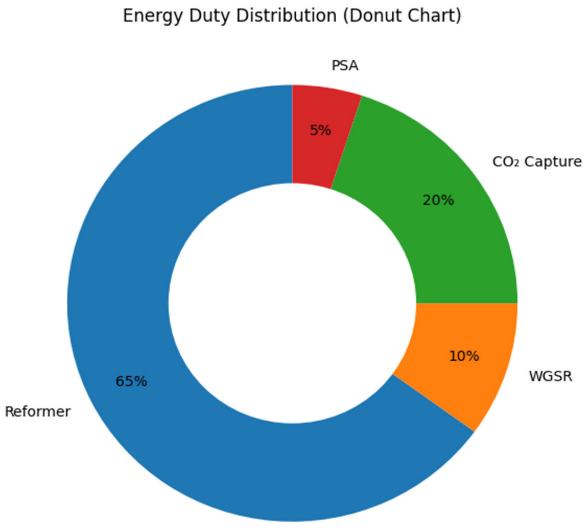

Figure 8 summarizes how the overall energy demand is distributed across the major process sections. The reformer dominates the energy balance due to the strongly endothermic character of steam methane reforming, while CO_2 capture represents the second-largest contribution associated with separation and regeneration duties. The WGSR and PSA sections require comparatively lower energy input.

In contrast, the water–gas shift reaction is mildly exothermic and contributes limited heat downstream of the reformer. Although this heat does not offset the reformer energy demand, it presents opportunities for recovery through steam generation or feed preheating. Such thermal integration strategies are critical for improving overall energy efficiency and reducing operating costs (Busca et al., 2024; Vogt et al., 2019; Wang et al., 2020; Zhang et al., 2021b). The incremental increase in energy demand associated with higher levels of CO_2 capture is shown in Figure 9.

Figure 9
Incremental increase in energy demand associated with higher CO_2 capture efficiency

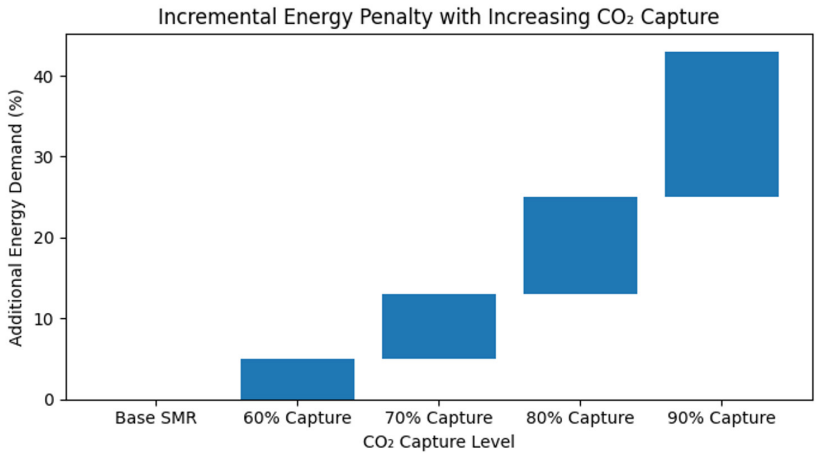

Figure 9 illustrates the incremental increase in energy demand associated with higher levels of CO_2 capture. As capture efficiency increases, additional energy requirements accumulate due to solvent regeneration and compression duties. While higher capture levels significantly reduce direct emissions, the results highlight a clear trade-off between emission reduction and energy consumption, which must be considered during process optimization.

Additional energy requirements arise from carbon dioxide capture and hydrogen purification. In particular, solvent regeneration in the CO_2 absorption unit represents a notable energy penalty. This trade-off between energy consumption and emission reduction is characteristic of blue hydrogen systems and must be carefully evaluated in process design (Bui et al., 2018; Howarth & Jacobson, 2021; Quarton et al., 2020).

Effect of CO_2 Capture and Blue Hydrogen Implications

The integration of CO_2 capture significantly alters the carbon balance of the hydrogen production process. By removing the majority of carbon dioxide formed during reforming and shift reactions, the modeled system achieves a substantial reduction in direct CO_2 emissions compared with conventional SMR (Howarth & Jacobson, 2021; Luberti et al., 2022; Shahid & Kim, 2023). Distribution of carbon-containing species in the SMR-based hydrogen production process is shown in Figure 10.

Figure 10 presents the distribution of carbon-containing species within the modeled hydrogen production process. The majority of carbon is captured as carbon dioxide, while only a small fraction is released with the vent gas or remains as residual carbon monoxide. This distribution demonstrates the effectiveness of the integrated CO_2 capture system in reducing direct emissions and supports the classification of the process as a blue hydrogen production pathway.

Figure 10
Distribution of carbon-containing species in the SMR-based hydrogen production process

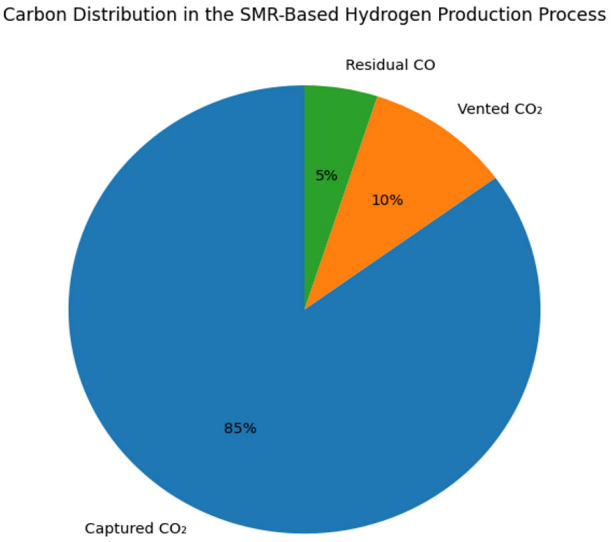

While CO_2 capture increases overall energy demand, the results indicate that hydrogen yield and product quality are not adversely affected. This finding supports the feasibility of integrating CO_2 capture into SMR-based hydrogen plants without

compromising core process performance (Bui et al., 2018; Quarton et al., 2020).

In regions with abundant natural gas resources and established industrial infrastructure, such as Kazakhstan, this configuration offers a realistic pathway for producing low-emission hydrogen. The results reinforce the role of SMR with CO_2 capture as a transitional blue hydrogen technology that can bridge the gap between conventional grey hydrogen and future large-scale deployment of renewable hydrogen (Hydrogen Council, 2021; IEAGHG, 2021; IEA, 2023, 2024; DOE, 2020, 2023). The comparison of specific CO_2 emissions for conventional SMR and SMR integrated with carbon dioxide capture is shown in Figure 11.

Figure 11
Comparison of specific CO_2 emissions for conventional SMR and SMR integrated with carbon dioxide capture

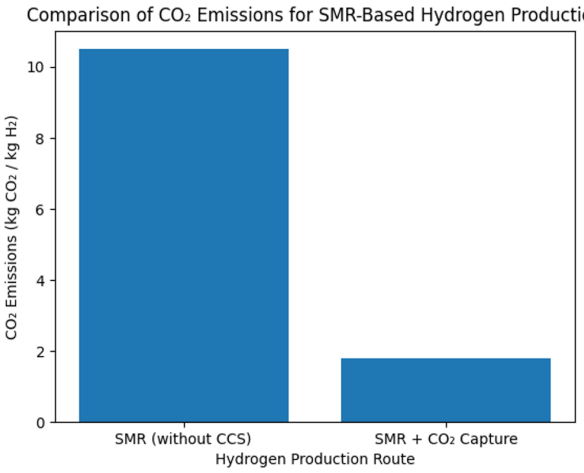

Figure 11 compares the specific CO_2 emissions associated with conventional SMR-based hydrogen production and SMR integrated with carbon dioxide capture. The incorporation of CO_2 capture results in a substantial reduction in direct emissions, decreasing the carbon intensity of hydrogen production by more than an order of magnitude. This comparison highlights the effectiveness of carbon capture integration in transforming conventional SMR into a low-emission blue hydrogen pathway.

Overall, the simulation results demonstrate that the integration of steam methane reforming, water–gas shift conversion, and carbon dioxide capture enables efficient hydrogen production with significantly reduced carbon emissions. The analyzed process configuration achieves high hydrogen yield and purity while maintaining industrially realistic operating conditions. Although the inclusion of CO_2 capture introduces additional energy demand, the substantial reduction in emissions confirms the technical viability of SMR-based blue hydrogen as a transitional solution for large-scale hydrogen production. The key performance indicators obtained from the process simulation are summarized in Table 2.

Table 2
Key performance indicators of the modeled SMR-based hydrogen production system

Performance indicator	Value
Methane conversion	>90%
Hydrogen yield	Near thermodynamic limit
Hydrogen purity	>97%
CO_2 capture rate	~90%
Specific CO_2 emissions (with capture)	~1.8 kg CO_2 / kg H_2
Dominant energy consumer	Reformer

Feasibility Analysis

Feedstock and Infrastructure Availability

The feasibility of hydrogen production via steam methane reforming with integrated CO_2 capture is strongly influenced by the availability of natural gas and supporting infrastructure. Regions with established gas supply networks, processing facilities, and industrial consumers offer clear advantages for SMR-based hydrogen deployment. Kazakhstan possesses significant natural gas reserves and a well-developed gas transportation system, which provides a reliable and cost-effective feedstock supply for hydrogen production (Hydrogen Council, 2021; IEA, 2023, 2024; DOE, 2020, 2023).

In particular, the western regions of Kazakhstan host major oil and gas operations, refineries, and petrochemical facilities. Existing infrastructure reduces the need for extensive new pipeline construction and enables direct integration of hydrogen production units into current industrial complexes. Such integration is especially beneficial for SMR-based systems, which rely on continuous gas supply and stable operating conditions (Abdalla et al., 2018; Dincer & Acar, 2015; Staffell et al., 2019; DOE, 2020, 2023).

Industrial Integration Potential

One of the key advantages of SMR-based hydrogen production lies in its compatibility with existing

industrial hydrogen consumers. In Kazakhstan, hydrogen is already used internally in petroleum refining for hydrotreating and hydrocracking processes. Locating a dedicated hydrogen production unit near refineries or petrochemical plants allows direct utilization of hydrogen without the need for long-distance transport or storage infrastructure (Staffell et al., 2019; DOE, 2020, 2023).

The Atyrau region represents a particularly favorable location due to the presence of large refineries, petrochemical facilities, and associated utilities. Co-location with existing plants enables the sharing of steam systems, cooling water, power supply, and maintenance services, thereby reducing capital and operating expenditures. In addition, the availability of skilled technical personnel further enhances project feasibility (Hydrogen Council, 2021; IEA, 2023, 2024; DOE, 2020, 2023).

Carbon Capture and Storage Considerations

The feasibility of blue hydrogen production critically depends on the ability to manage captured carbon dioxide. In the modeled process, CO_2 is produced in a concentrated stream downstream of the water–gas shift reaction, which is well suited for capture using chemical absorption. This configuration minimizes separation complexity and improves capture efficiency (Bui et al., 2018; Shahid & Kim, 2023).

For long-term emission reduction, captured CO_2 must be either utilized or stored. Kazakhstan has geological formations with potential for CO_2 storage, including depleted oil and gas reservoirs. Integration of CO_2 capture with existing oil and gas operations could enable carbon storage or enhanced oil recovery applications. However, further site-specific geological assessment would be required to confirm storage capacity, integrity, and long-term safety (Bui et al., 2018; IEAGHG, 2021).

Economic and Transitional Perspective

From an economic standpoint, SMR with CO_2 capture represents a transitional solution between conventional grey hydrogen and renewable green hydrogen. While green hydrogen offers the lowest emissions, its current production costs and dependence on large-scale renewable electricity limit near-term deployment in many regions. In contrast, blue hydrogen leverages existing SMR technology and infrastructure, allowing faster implementation at lower capital risk (Howarth & Jacobson, 2021; Luberti et al., 2022; Nazir et al., 2020; Quarton et al., 2020). A comparison between conventional SMR and SMR integrated with CO_2 capture is summarized in Table 3.

Table 3
Comparison of conventional SMR and SMR-based hydrogen production with CO_2 capture

Parameter	Conventional SMR (Grey H_2)	SMR with CO_2 capture (Blue H_2)
Hydrogen purity	>97%	>97%
Methane conversion	High	High
CO_2 emissions	~10–12 kg CO_2 / kg H_2	~1.5–2 kg CO_2 / kg H_2
Energy demand	Lower	Higher
CO_2 capture requirement	Not applied	Required
Technology maturity	Commercial	Commercial
Emission profile	High	Significantly reduced

The additional energy demand associated with CO_2 capture increases operating costs compared with conventional SMR. However, these costs may be partially offset by regulatory incentives, carbon pricing mechanisms, or demand for low-emission hydrogen in international markets. In this context, blue hydrogen can serve as an intermediate step that supports gradual decarbonization while maintaining industrial competitiveness (Hydrogen Council, 2021; IEAGHG, 2021; IEA, 2023, 2024; Shahid & Kim, 2023; DOE, 2020, 2023).

Limitations and Future Outlook

Although the feasibility analysis indicates strong potential for SMR-based blue hydrogen deployment, several limitations must be acknowledged. The economic viability of CO_2 capture depends on energy prices, solvent performance, and access to storage or utilization pathways. Furthermore, methane emissions associated with upstream natural gas supply can influence the overall climate impact of blue hydrogen (Bui et al., 2018; Howarth & Jacobson, 2021; Luberti et al., 2022; Shahid & Kim, 2023).

In the long term, the role of SMR-based hydrogen is expected to evolve as renewable hydrogen technologies mature and become more cost competitive. Nevertheless, in the near to medium term, SMR with CO_2 capture provides a realistic and scalable option for reducing emissions from hydrogen production in regions with abundant natural gas resources (Belmehdi et al., 2025; Hydrogen Council, 2021; IEA, 2023, 2024; Nazir et al., 2020; Quarton et al., 2020; DOE, 2020, 2023).

Conclusion

In this study, hydrogen production via steam methane reforming integrated with the water–gas shift reaction and carbon dioxide capture was analyzed using a detailed process simulation approach. An industrially relevant SMR–WGSR configuration was modeled in Aspen HYSYS to evaluate hydrogen yield, product purity, energy demand, and the impact of CO_2 capture under steady-state operating conditions. The results demonstrate that the selected process configuration enables high methane conversion and hydrogen yields approaching thermodynamic limits, while delivering hydrogen at purity levels suitable for industrial applications (AspenTech, 2021; Li et al., 2022; Moioli et al., 2024; Zhang et al., 2021a).

The integration of the water–gas shift reaction was shown to play a critical role in maximizing hydrogen production by converting carbon monoxide into additional hydrogen and carbon dioxide. Downstream purification using pressure swing adsorption achieved hydrogen purity exceeding 97%, confirming the suitability of the modeled system for large-scale hydrogen supply. Although steam methane reforming remains energy intensive due to the strongly endothermic nature of reforming reactions, opportunities for heat recovery and thermal integration were identified as essential elements for improving overall process efficiency (Busca et al., 2024; Kalman et al., 2022; Rochelle, 2009; Rostrup-Nielsen, 2006; Shabbani et al., 2024; Vogt et al., 2019; Zhang et al., 2021b).

The inclusion of carbon dioxide capture substantially reduces direct CO_2 emissions compared with conventional SMR-based hydrogen production. While CO_2 capture introduces additional energy requirements, particularly for solvent regeneration, the overall hydrogen yield and product quality remain largely unaffected. This trade-off highlights the potential of SMR with carbon capture as a viable blue hydrogen pathway, capable of balancing emission reduction with industrial performance (Bui et al., 2018; Howarth & Jacobson, 2021; Luberti et al., 2022; Shahid & Kim, 2023; Quarton et al., 2020).

From a regional perspective, the feasibility analysis indicates that countries with abundant natural gas resources and established industrial infrastructure, such as Kazakhstan, are well positioned to deploy SMR-based blue hydrogen systems. The Atyrau region, in particular, offers favorable conditions for integration with existing refineries and petrochemical facilities, enabling efficient utilization of hydrogen and supporting infrastructure sharing. In the near to medium term, SMR with CO_2 capture represents a realistic transitional solution that can support decarbonization goals while maintaining reliable hydrogen supply for industrial consumers (Hydrogen Council, 2021; IEAGHG, 2021; IEA, 2023, 2024; DOE, 2020, 2023).

Overall, the findings of this study support the role of SMR-based blue hydrogen as an important component of the evolving hydrogen economy. While long-term decarbonization will increasingly rely on renewable hydrogen pathways, integrated SMR–WGSR systems with carbon capture can provide a scalable and technologically mature solution for reducing emissions from hydrogen production during the transition period (Howarth & Jacobson, 2021; Luberti et al., 2022; Nazir et al., 2020; Quarton et al., 2020).

Author contributions

Author Conceptualization, methodology, and writing – original draft preparation: D.S. and Y.K.; investigation, data curation, and formal analysis: B.S., T.T., and T.A.; visualization and validation: A.K.; supervision and writing-review and editing: Y.K. and T.A.; project assignment, scientific guidance, and final verification: A.I.

Acknowledgments

The authors acknowledge the support of the School of Chemical Engineering, Kazakh-British Technical University, and thank colleagues for constructive discussions during the development of this work.

Conflicts of interest

The authors declare no conflict of interest.

References

1. Abdalla, A. M., Hossain, S., Nisfindy, O. B., Azad, A. T., Dawood, M., & Azad, A. K. (2018). Hydrogen production technologies and challenges. *Energy Conversion and Management*, *165*, 602–627. https://doi.org/10.1016/j.enconman.2018.03.088
2. Aspen Technology, Inc. (2021). *Aspen HYSYS® User Guide*. AspenTech.
3. Belmehdi, I., Bouallou, C., & Kanniche, M. (2025). Steam methane reforming integrated with CO_2 capture: Process analysis. *Journal of CO_2 Utilization*, *72*, 102453. https://doi.org/10.1016/j.jcou.2024.102453
4. Bui, M., Adjiman, C. S., Bardow, A., Anthony, E. J., Boston, A., Brown, S., Fennell, P. S., Fuss, S., Galindo, A., Hackett, L. A., Hallett, J. P., Herzog, H. J., Jackson, G., Kemper, J., Krevor, S., Maitland, G. C., Matuszewski, M., Metcalfe, I. S., Petit, C., … Mac Dowell, N. (2018). Carbon capture and storage (CCS): The way forward. *Energy & Environmental Science*, *11*(5), 1062–1176. https://doi.org/10.1039/C7EE02342A
5. Busca, G., Lietti, L., Ramis, G., & Berti, F. (2024). Chemical and mechanistic aspects of the water–gas shift reaction. *Catalysis Today*, *423*, 113–126. https://doi.org/10.1016/j.cattod.2023.06.014
6. Howarth, R. W., & Jacobson, M. Z. (2021). How green is blue hydrogen? *Energy Science & Engineering*, *9*(9), 1676–1687. https://doi.org/10.1002/ese3.956
7. Dincer, I., & Acar, C. (2015). Review and evaluation of hydrogen production methods for sustainability. *International Journal of Hydrogen Energy*, *40*(34), 11094–11111. https://doi.org/10.1016/j.ijhydene.2014.12.035
8. Hydrogen Council. (2021). *Hydrogen Decarbonization Pathways: Life-Cycle Assessment*. Hydrogen Council. https://hydrogencouncil.com/en/hydrogen-decarbonization-pathways/
9. IEA Greenhouse Gas R&D Programme. (2021). *Blue Hydrogen: Fact vs. Fiction*. IEAGHG. https://ieaghg.org/publications/blue-hydrogen
10. International Energy Agency. (2023). *Global Hydrogen Review 2023*. IEA. https://www.iea.org/reports/global-hydrogen-review-2023
11. International Energy Agency. (2024). *Global Hydrogen Review 2024*. IEA. https://www.iea.org/reports/global-hydrogen-review-2024
12. Kalman, V., Markovits, T., & Tóth, A. J. (2022). Hydrogen purification by pressure swing adsorption: System performance analysis. *Sustainability*, *14*(21), 14037. https://doi.org/10.3390/su142114037
13. Li, H., Yan, J., & Zeng, H. (2022). Integration of CO_2 capture with steam methane reforming for blue hydrogen production. *Energy*, *239*, 122155. https://doi.org/10.1016/j.energy.2021.122155
14. Luberti, M., Brown, A., Balsamo, M., & Capocelli, M. (2022). Numerical analysis of VPSA technology retrofitted to steam reforming hydrogen plants to capture CO2 and produce blue H2. *Energies*, *15*(3), 1091. https://doi.org/10.3390/en15031091
15. Moioli, S., Manenti, F., Papasidero, D., & Grottoli, M. G. (2024). CO_2 removal technologies in hydrogen production plants. *Energies*, *17*(12), 3089. https://doi.org/10.3390/en17123089
16. Nazir, H., Louis, C., Jose, S., Prakash, J., Muthuswamy, N., Buan, M. E. M., Flox, C., Chavan, S., Shi, X., Kauranen, P., Kallio, T., Maia, G., Tammeveski, K., Lymperopoulos, N., Carcadea, E., Veziroglu, E., Iranzo, A., & Kannan, A. M. (2020). Hydrogen production technologies: Transition pathways. *International Journal of Hydrogen Energy*, *45*(41), 15185–15208. https://doi.org/10.1016/j.ijhydene.2020.03.165
17. Patel, R., Varatharajan, P., Zhang, Q., Li, Z., & Gu, S. (2025). Catalysts in the water-gas shift reaction: Recent developments, mechanisms, and carbon capture integration. *Carbon Capture Science & Technology*, *15*, 100388. https://doi.org/10.1016/j.ccst.2025.100388
18. Quarton, C. J., Samsatli, S., & Jenkins, N. (2020). Value of hydrogen and CCS infrastructure in deep decarbonisation pathways. *Energy Policy*, *144*, 111714. https://doi.org/10.1016/j.enpol.2020.111714
19. Rochelle, G. T. (2009). Amine scrubbing for CO_2 capture. *Science*, *325*(5948), 1652–1654. https://doi.org/10.1016/j.enpol.2020.111714
20. Rostrup-Nielsen, J. R. (2006). Steam reforming of hydrocarbons: A historical perspective. *Catalysis Today*, *111*(1–2), 4–11. https://doi.org/10.1016/j.cattod.2005.10.002
21. Shabbani, H. J. K., Taheri, A., & Mehrpooya, M. (2024). Hydrogen purification by pressure swing adsorption: A review. *International Journal of Hydrogen Energy*, *49*, 18123–18141. https://doi.org/10.1016/j.ijhydene.2024.01.092
22. Shahid, M. Z., & Kim, J.-K. (2023). Design and economic evaluation of an amine-based CO2 capture process for SMR-based hydrogen production. *Journal of Cleaner Production*, *402*, 136704. https://doi.org/10.1016/j.jclepro.2023.136704
23. Song, C., & Pan, W. (2004). Tri-reforming of methane: Concepts and applications. *Catalysis Today*, *98*(4), 463–484. https://doi.org/10.1016/j.cattod.2004.09.054
24. Staffell, I., Scamman, D., Abad, A. V., Balcombe, P., Dodds, P. E., Ekins, P., Shah, N., & Ward, K. R. (2019). The role of hydrogen in the global energy system. *Energy & Environmental Science*, *12*(2), 463–491. https://doi.org/10.1039/C8EE01157E
25. U.S. Department of Energy. (2020). *Hydrogen Strategy: Enabling a Low-Carbon Economy*. DOE. https://www.energy.gov/sites/prod/files/2020/07/f76/USDOE_FY2020_Hydrogen_Strategy.pdf
26. U.S. Department of Energy. (2023). *U.S. National Clean Hydrogen Strategy and Roadmap*. DOE. https://www.hydrogen.energy.gov/library/roadmaps-vision/clean-hydrogen-strategy-roadmap
27. Vogt, C., Monai, M., Kramer, G. J., & Weckhuysen, B. M. (2019). Structure sensitivity in steam methane reforming over Ni catalysts. *ACS Catalysis*, *10*(2), 1428–1439. https://doi.org/10.1021/acscatal.9b04193
28. Wang, M., Wang, Z., Gong, X., & Guo, Z. (2020). Process intensification for hydrogen production. *Renewable and Sustainable Energy Reviews*, *132*, 110028. https://doi.org/10.1016/j.rser.2020.110028

29. Zhang, X., Chen, Y., Wang, Y., & Li, J. (2021a). Process simulation and optimization of hydrogen production via steam methane reforming with CO2 capture. *International Journal of Hydrogen Energy*, *46*(52), 28124–28138. https://doi.org/10.1016/j.ijhydene.2021.05.087

30. Zhang, H., Sun, Z., & Hu, Y. H. (2021b). Steam reforming of methane: Current states of catalyst design and process upgrading. *Renewable and Sustainable Energy Reviews*, *149*, 111330. https://doi.org/10.1016/j.rser.2021.111330

Information about the authors:

Asylzat Iskalieva – Doctor Ph.D., Vice Dean of Faculty SCE, School of Chemical Engineering, Non-commercial joint-stock company Kazakh-British Technical University (Almaty, Republic of Kazakhstan, e-mail: asylzat@bk.ru).

Daniyal Sarsenbay – Bachelor student, School of Chemical Engineering, Kazakh-British Technical University (Almaty, Republic of Kazakhstan, e-mail: d_sarsenbay@kbtu.kz).

Yernar Karamyssov – Bachelor student, School of Chemical Engineering, Kazakh-British Technical University (Almaty, Republic of Kazakhstan, e-mail: y_karamyssov@kbtu.kz).

Baidybek Sultanmakhmut – Bachelor student, School of Chemical Engineering, Kazakh-British Technical University (Almaty, Republic of Kazakhstan, e-mail: b_sultanmakhmut@kbtu.kz).

Temirlan Tailakbayev – Bachelor student, School of Chemical Engineering, Kazakh-British Technical University (Almaty, Republic of Kazakhstan, e-mail: t_tailakbayev@kbtu.kz).

Alisher Temirbek – Bachelor student, School of Chemical Engineering, Kazakh-British Technical University (Almaty, Republic of Kazakhstan, e-mail: a_temirbek@kbtu.kz).

Aikumis Karabayeva – Bachelor student, School of Chemical Engineering, Kazakh-British Technical University (Almaty, Republic of Kazakhstan, e-mail: a_karabayeva@kbtu.kz).

Temirlan Alferov – Bachelor student, School of Chemical Engineering, Kazakh-British Technical University (Almaty, Republic of Kazakhstan, e-mail: t_alferov@kbtu.kz).

Received 17 December 2025;
received in revised form 26 May 2026;
accepted 14 June 2026

CONTENT